Acoustic measurements of flowing and quasi-static particulate suspensions

Thesis

Acoustic measurements of flowing and quasi-static particulate suspensions

---

Thesis submitted by

Simon H.O. Moss BA (Hons)

for the degree of

Doctor of Philosophy

June 1997

Engineering Mechanics Discipline
The Open University
Milton Keynes
MK7 6AA
UK

ABSTRACT

Flowing suspensions of solid particles in gas can be found in various industrial applications, as a method for transporting powdered solids (known as "pneumatic conveying"). The problem of measuring the mass concentration of the solid fraction has not yet been satisfactorily resolved.

This thesis explores acoustic techniques to measure the particle concentration. Controlled suspensions — both flowing and quasi-static — were generated in cylindrical tubes, and their acoustic properties were measured over three frequency ranges, requiring a variety of different measuring techniques:

- Plane wave region (200 – 4 kHz): the attenuation of plane waves travelling along the flow tube was measured. A simple method of measuring the characteristic impedance of the suspension was also devised and preliminary measurements were made.
- Reverberant region (4 – 20 kHz). Three parameters were measured: the decay rate of the reverberant field in certain frequency bands; the level of actively-excited steady state sound; and the frequency of transverse resonant modes of the pipe.
- Ultrasonic region (40 – 75 kHz): the attenuation of ultrasound was measured across the pipe diameter.

The measurements were compared with theoretical predictions. They showed the predicted linearity of acoustic attenuation with concentration, although the frequency dependence was less well predicted. In general, the larger particle sizes produced the greatest discrepancy; an explanation is proposed. Ultrasonic measurements showed significant differences from the predicted frequency dependence.

A method of isolating acoustic transducers from the flow with a column of clean air is described. However, measurements may be complicated by interactions at the orifice into the flow pipe. Further work is needed in this area.

It is concluded that acoustic methods could be used to measure particle concentration. However, to remain insensitive to changes in the properties of the particles — size in particular — measurements must be made at more than one frequency.

BL form

MOSS,

EX12

RESEARCH DEGREES CENTRE

LIBRARY AUTHORISATION FORM

Please return this form to the The Research Degrees Centre with the two bound copies of your thesis to be deposited with the University Library.
All students should complete Part 1. Part 2 only applics to PhD students.

Student: Simon H.O. Moss PI: P0091057

Degree: PhD

Thesis title: Acoustic Measurements on flowing and quasi static particulate suspensions

Part 1 Open University Library Authorisation [to be completed by all students]

I confirm that I am willing for my thesis to be made available to readers by the Open University Library, and that it may be photocopied, subject to the discretion of the Librarian.

Signed: [signature] Date: 8-11-97

Part 2 British Library Authorisation [to be completed by PhD students only]

If you want a copy of your PhD thesis to be available on loan to the British Library Thesis Service as and when it is requested, you must sign a British Library Doctoral Thesis Agreement Form. Please return it to the Research Degrees Centre with this form. The British Library will publicise the details of your thesis and may request a copy on loan from the University Library. Information on the presentation of the thesis is given in the Agreement Form.

The University has agreed that your participation in the British Library Thesis Service should be voluntary. Please tick either (a) or (b) to indicate your intentions.

✓ [a] ➳ I am willing for the Open University to loan the British Library a copy of my thesis. A signed Agreement Form is attached.

[b] ➳ I do not wish the Open University to loan the British Library a copy of my thesis.

Signed: [signature] Date: 8-11-97

ACKNOWLEDGEMENTS

Firstly, I would like to thank my internal supervisor, Prof. Keith Attenborough. The speed with which he read and commented on my work was outstanding; his encouragement and faith in me made my years at the Open University very enjoyable.

I am very grateful to my external supervisor, Dr Stephen Woodhead, for all of his friendly advice and practical assistance. Furthermore, he made available the flow rig, for which I would like to thank him and the Wolfson Centre for Bulk Solids Handling Technology, at the University of Greenwich.

Thanks also to the examiners, Dr Alan Cummings and Prof Clive Greated, whose useful comments have improved this work.

I am extremely indebted to Peter Seabrook: he really deserves to be a joint author. Peter executed all of the mechanical construction in the project, was instrumental in several of the nifty designs (including the dust "blow gun", the magnetic weighing end, and the sliding coupling of the twin tubes), and many of his creations would not look out of place in a nuclear submarine. Furthermore, his interest, encouragement and friendship was vital for me to maintain my momentum at times.

Everyone in the Acoustics group at the Open University contributed to this work in some way. In particular, Dr Jon Evans assisted in matters theoretical (chapters 2 and 7 especially), and my conversations with him helped to clarify my own murky thinking. He also provided me with very thorough and useful feedback on several chapters. Everyone else (Kris, Nick, Patrice, Qiang, Shahram & Tim) I would like to thank for their help and friendship. It is probably the most harmonious group of work colleagues I have ever experienced.

Dr Andrew Watson helped me greatly in my first year of this project (especially the work in Appendix E), and placed me on a firm footing. Much credit for the eventual unfoldment of the project goes to him.

My thanks, too, to Prof. V.E. Ostashev for some illuminating conversations about the mechanisms of turbulent loss .

And then there are all the friends outside of my subject area who provided encouragement and support. I will mention, in particular, my greatly-missed friends Dr Sarah Bush and Dr Teresa Valverde, as well as the umpteen members of my family who believed in me so much that my finishing the thesis was never even an issue.

Finally, my thanks to the SERC & EPSRC for funding this work. It is humbling to imagine how much this volume has cost the nation.

CONTENTS

FIGURES

TABLES

NOTATION

SYMBOLS

(#.#) refers to the equation number in which the symbol is first defined

a Particle radius

$\bar{a}, \bar{a}_{rr}, a_{32}$ Mean radius, fineness parameter (Rosin Rammler PSD), Sauter mean radius (Chapter 2)

A_0, A_1 Individual particle scattering coefficients (2.3, 2.4).

A Tube cross sectional area

B Filter bandwidth

c Sound velocity

C_p Specific heat capacity at constant pressure

C Reverberant decay curvature (3.8); electrical capacitance.

d Interparticle spacing (2.7); reverberant decay (3.7); hole diameter (chapter 5)

D Pipe diameter

E Reverberant sound energy (7.11)

$f, f_{m,n}$ Frequency; cut-on frequency of transverse mode (m,n) (3.14)

G (3.6); goodness of fit (7.18)

h Impulse response (3.3)

H (2.5); transfer function

i $\sqrt{-1}$

k Propagation constant; constants in (3.7)

K Oversampling ratio (G.10)

L Path length; time duration of reverberant record (3.7); electrical inductance.

M Mach number

n Noise signal (3.4); number of points

N Number of samples in a sequence (3.1); noise power per unit bandwidth (3.3).

p	Sound pressure
Pr	Prandtl number (2.22)
Q	Reverberant decay rate (7.2); quality factor of resonant system (C.1)
r	Characteristic flow resistance (4.3); correlation coefficient (7.14)
r_{det}, r_{ψ}	Correlation coefficients: (7.15), (7.17)
R	Pipe radius (3.12), electrical resistance.
Re	Reynolds number (2.25)
s	Reverberant decay curve (3.3)
T	Temperature (K)
T_{60}	Time for reverberant sound level to decay by 60 dB
v	Voltage
V	Volume of chamber (chapter 5)
w	(2.15)
x	Various distances in section 4.9.1
Y	(4.15)
z	(2.5)
Z	Impedance
α, α_{ss}	Plane wave attenuation coefficient; single scattering attenuation coefficient
β	Sound speed dispersion
δ_v, δ_t	Boundary layer thickness: viscous and thermal
δ, δ'	Unit impulse (4.5), periodic unit impulse (3.2)
ϕ_v, ϕ_m	Particle volume concentration, mass concentration
γ	Ratio of specific heats of gas C_p/C_v; extinction coefficient (3.20)
Λ	Source sound power (7.13)
Γ	Constant related to sound absorption (7.1)
κ	Thermal conductivity, or adiabatic compressibility (2.33 - 2.35)
λ	Sound wavelength
μ	Dynamic viscosity

Θ	Coefficient of thermal (volume) expansion; phase (chapter 4, Appendix F)
ρ	Density
σ	Logarithmic standard deviation
σ_{rr}	Fineness parameter in Rosin Ramler PSD (Chapter 2)
τ_t, τ_v	Relaxation times (thermal, viscous)
ω	Angular frequency
$\Phi(a)$	Volume fraction of particle size a
$\Phi_{cum}(a)$	Cumulative volume fraction of particle size a
ψ	Decay sensitivity (7.16)

Subscripts $_{f,s}$ refer to fluid and solid quantities, respectively.

ABBREVIATIONS

A/D, ADC	Analogue to Digital (Converter)
ANL	Argonne National Laboratory
ASTM	American Society for Testing Materials
BCURA	British Coal Utilisation Research Association
CSIRO	Commonwealth Scientific and Industrial Organisation
D/A, DAC	Digital to Analogue (Converter)
DC	Direct current
DFT	Discrete Fourier Transform
FFT	Fast Fourier Transform
F800, F1000...	Different size grades of alumina powder
IEC	International Electrotechnical Commission
IL	Insertion loss
IR	Impulse Response
ISO	International Organisation for Standardisation
LDV	Laser Doppler Velocimeter

LMS	Least Mean Squares
MLS	Maximum Length Sequence
MLSSA	Maximum Length Sequence System Analyser
PF	Pulverised Fuel
ppm	parts per million (in measurement of particle volume concentration)
PSD	Particle Size Distribution or Power Spectral Density (depending on context)
PZT	Lead Zirconate Titanate
rms	Root Mean Square
SAV	Superficial air velocity
SNR	Signal / Noise Ratio
SPL	Sound Pressure Level
VI	Virtual instrument (LABVIEW subroutine)

The small code letters adjacent to graphs refer to the name of the dataset from which each graph was generated – for the use of people with access to the datasets.

1

INTRODUCTION

This thesis presents an experimental investigation into the acoustic properties of aerosols. The emphasis is on developing equipment to test acoustic theories, with the intention that the resulting information will be useful in developing an acoustic device for measuring the solids mass flow-rate of pneumatically-conveyed powders.

1.1 AIMS

The aims of this work are to:

- Implement current and devise new experimental techniques to measure the acoustic effects of particulate suspensions;
- Measure the acoustic properties of reference particulates, over a range of frequencies and concentration densities;
- Compare the measured acoustic properties with theoretical predictions, and to assess the applicability of such predictions;
- Report on the most promising techniques to measure the mass flow rate of suspended, flowing particulates – pulverised fuel in particular.

1.2 STRUCTURE OF THESIS

This thesis is divided into two parts. The first half (Chapters 2 - 5) consists of literature reviews, equipment design and methods, while the second half (Chapters 6 - 8) presents the experimental results.

The literature review is split between two chapters. Chapter 2 reviews – somewhat briefly – the many different theoretical models that predict the acoustic effects of suspensions, and attempts to assess their applicability within the "parameter space".

Chapter 3 reviews experimental work conducted on aerosols: including acoustic and non-acoustic measurements, quasi-static laboratory experiments and measurements on large-scale flowing suspensions. The measurement techniques used in this thesis are placed in context, and some of the physical processes associated with flowing suspensions are reviewed, where these have a relevance to the experimental work that is presented.

The design of equipment is also split between two chapters. Chapter 4 describes the rig that was built for measurements on quasi-static suspensions, and describes the data analysis that extracted the

plane wave propagation constant. Chapter 5 describes the design of equipment for use with the (existing) flow rig that generated concentrated, flowing suspension.

Experimental results are presented in Chapters 6 to 8, covering plane wave measurements (6), reverberation measurements (7), ultrasonic measurements (8), while preliminary measurements of admission impedance are presented in Appendix A.

Chapter 9 presents some conclusions and suggestions for further work, and also summarises acoustic measurement techniques and the regimes in which they are useful.

This structure is not adhered to rigidly. Where the assimilation of information would be made unnecessarily difficult by splitting and separating it into logical subdivisions, then logical nicety may be sacrificed in favour of clarity.

1.3 TERMINOLOGY & CONVENTIONS

In the broadest sense, this work concerns the acoustics of two-phase media. The important application area of three-phase media is not mentioned beyond this chapter. Theoretical models treat a two-phase medium as a particulate phase distributed within a continuous phase. The term "suspension" refers to a solid particulate distributed in a fluid. Where the fluid is a liquid, the suspension can be called a slurry; in the case of a gaseous fluid, the medium is referred to as an aerosol. The work in this thesis focuses on aerosols in which the gas is air.

Where liquid particles are distributed within another (immiscible) liquid, the term emulsion will be used. Gaseous particles in liquid (e.g. bubbles) and solid particles in solid (e.g. alloys) will not be considered.

The main parameters of a suspension are its particle concentration, particle size, and the material constants of both phases. These are treated individually below.

1.3.1 Suspension concentration

The particle concentration, indicated by the symbol ϕ, may be quoted by volume or mass. The volume concentration, ϕ_v, is calculated as (volume of particles / volume of fluid) in a test volume; while it is dimensionless, units of m^3/m^3 may be quoted for clarity. This is the preferred measure in the acoustic literature. For measurements on quasi-static aerosols, the volume concentration is usually a small number, and so figures may be quoted in parts per million (p.p.m.); i.e. 10^{-6} m^3/m^3.

The mass concentration, ϕ_m, is similarly calculated as (mass of particles / mass of fluid) in a test volume, and will indicated by units of kg/kg. This is the preferred measure in industrial applications of pneumatic conveying, where very much higher concentrations are achieved than is possible in the laboratory. Mass concentration is evidently related to the volume concentration by a

factor of (particle density of solid / density of fluid). Note that for a powdered solid, the particle density is usually somewhat higher than its bulk density, due to airspaces in the bulk powder.

A further hybrid quantity is the (mass of particles / volume of fluid) in kg/m^3. This pragmatic measure reflects the fact that solids are usually measured by mass, and fluids by volume; it is used, for example, in quantifying particulate air-pollution. Where the fluid is air, this measure will differ from the mass concentration by a factor of approximately 20%.

1.3.2 Particle size and particle size distribution

References in the literature to "particle size" usually refer to particle diameter, although theoretical models usually employ the particle radius, a. There is an implicit assumptions that particles are modelled as spheres; this may be difficult to justify, except that any more realistic quantity is so hard to measure, and harder to model. Theories that attempt this are reviewed in Chapter 2 and the impact of non-sphericity on experimental measurements is discussed in Chapter 6. If a powder contains only particles of a single size, it is referred to as "monodispersed". Any practical powder will contain a range of particle sizes, and will be characterised by its particle size distribution (PSD). Chapter 2 will discuss ways of modelling the PSD, and the effect that this parameter has on acoustic predictions. Methods of inferring the PSD from acoustic measurements will also be covered in Chapters 2 and 9.

1.3.3 Material constants

Theoretical models require a knowledge of the material constants of both phases. Some of these parameters have a large effect on the predictions (e.g. density) while others have virtually no effect (e.g. sound speed in solid) in the regime of interest. A listing of the constants used is given in Appendix F.

1.4 APPLICATION AREAS

1.4.1 General survey

Understanding the acoustics of two-phase media is important in two main areas: I shall call them the "forward" and "inverse" problems. Forward problems require a prediction of acoustic effects from known physical parameters of the medium: for example, predicting the propagation of sound from fog-horns in fog (water particles in air) [37]; in oceanographic experiments, understanding underwater sound transmission, in which the sea can be modelled as a 3 phase medium of water, solid suspended particles and air bubbles [164].

The major application of the "inverse" problem is in the development of instrumentation, that enables deduction of the physical parameters of a medium from acoustic measurements. An inverse problem is involved since a theoretical or empirical model of sound transmission is used to deduce

the input (physical) parameters from the output (acoustic) measurements. The usual pitfalls of finding inverses will apply, such as non-uniqueness of solutions, and extreme sensitivity to measurement errors and certain parameters.

As a radiation source to probe a medium, sound complements electromagnetic radiation and radionucleotide sources, since it has a considerably different speed of propagation, and interacts with matter differently. It has the advantage of being non-ionising and non-hazardous, and associated devices are non-intrusive and non-destructive. In many applications involving optically-opaque, non-conducting media, there are few alternatives to acoustic interrogation. In common with other radiation types, information can be collected from an insonified medium by observing either the transmitted wave or the scattered (reflected) wave. In flowing media, the backscattered signal will be Doppler-shifted; this effect is used in Doppler flowmeters.

Sound is widely used in single-phase flow metering, and many areas of non-destructive testing [87]. Its use in two-phase systems is largely restricted to ultrasound, and consists either of parameter deduction (e.g. flow velocity) or imaging. In medical applications, backscattered ultrasound is used for imaging of hard and soft tissue; indeed, tissue itself can be modelled as an emulsion [70]. Blood flow-rate can be measured from the Doppler shift of signals scattered from blood cells [134].

Underwater back-scattered sound has been used to monitor suspended sediments [119], sea-bed sediments, and fish [137]. The time of flight of the backscattered signal identifies the volume of space from which it was scattered, and so, with the additional information provided by Doppler shift, a profile of flow speeds may be calculated. This led to the development of the Acoustic Doppler Current Profiler, which can monitor, for example, the movement of sediment plumes [118,104], pollution [157], and plankton [88].

Process industries have a large need for two-phase flow-meters to measure flow in pipes. The oil industry, in particular, frequently encounters emulsions of oil and water, and even three-phase flows with the inclusion of sand particles or gas bubbles. The flow regimes of two phase flows are complicated, and measurements of flow need to be insensitive to changes in regime: for example, from uniformly suspended particles, to roping flow (in which particle are concentrated in a small, meandering area of the tube cross-section [95]), to bed flow (in which particles are carried along on "dunes"), to plug flow (in which dense plugs of particles are separated by dilute cushions of air [10]).

One approach to identifying the flow regime, and compensating for it, is to form an image of the flow by ultrasonic tomographic methods [31, 61], in which the pipe-flow is interrogated by numerous beams of ultrasound.

Backscattering of acoustic energy is significant only when the particle size is comparable to or larger than the wavelength. Measurements of sound transmission, however, can yield information at lower frequencies or particle sizes. Measurements of ultrasonic transmission have been used to characterise food emulsions [94], drilling muds [58], coal slurries [116] and metallurgical slurries [18]; further

proposed uses are to monitor paint-making, chemical reactions involving precipitation, and homogenisation of emulsions.

In particular, measurements of ultrasonic attenuation over a wide bandwidth have been used to estimate the particle size distribution of emulsions [123], slurries [110, 120], and aerosols [17].

This project started life as an attempt to measure levels of particulate emissions from power station chimneys, by using measurements of audio frequency transmission. In agreement with another study [59], it was concluded that the acoustic effects of typical emissions would be too small to measure accurately at low frequencies, and masked by air absorption and non-classical effects at higher frequencies. An alternative application was found, in which the concentration of particulate would be considerably higher (typically a factor of 10^4, from 100 mg/m^3 to 1 kg/m^3): the application is pneumatic conveying, in which powdered and granulated solids are transported by suspension in a moving air-stream. Pneumatic conveying is widespread in process industries as a transport device, and there is currently no satisfactory in-line method of monitoring the mass flow rate of the solid. An acoustically-based flow-meter would therefore have a generic demand.

There is, however, a special case of pneumatic conveying, which is used in many coal-burning applications; most notably coal-fired power stations, cement kilns and steel mills. Here, coal is pulverised, suspended in air and conveyed into a combustion chamber. In this case, the air also acts as the oxidising agent, and obtaining the correct ratio of coal to air is critical for efficient combustion. This particular application area is discussed in the following section.

1.4.2 Application to pulverised fuel (PF) flow

In a coal-fired power station, the coal is pulverised in a small number of mills and conveyed pneumatically through successive bifurcations to the combustor, which is fed by numerous burner pipes (over 60 per unit at Drax power station). The result of so many bifurcations is that the pulverised fuel (PF) flow to each burner will inevitably become unbalanced, leading to sub-optimal combustion in some burners. The British Coal Utilisation Research Association (BCURA) measured the flow imbalance after a pipeline trifurcation to be approximately ± 18% [86]. Although flow between burners can be crudely balanced – for example, using orifice plates [149] – such methods cannot account for changes in load conditions. Excess oxygen in the waste gas is the parameter typically measured to control combustion, but this cannot address imbalance in individual burners [51]. An in-line flow monitor would allow frequent rebalancing of burners. More importantly, in the long term, if coupled with techniques to control flow-splitting at bifurcations, the combination creates the opportunity for dynamic control of PF flow [128].

The efficiency of coal-fired stations would be improved if the coal dust/air stream at the burners could be monitored and controlled more accurately [128]. BCURA has estimated that a maximum of 3% of coal remains unburnt due to inefficient combustion, and that optimal control could reduce losses by more than 10%. This wastage results in greater coal consumption than necessary,

and hence excess emissions of gaseous and particulate pollutants. The unburnt carbon is problematic in three ways: it results in greater particulate emissions, since electrostatic precipitators perform poorly on carbon [90]; it makes the application of low NO_x technologies more difficult [51]; and it contaminates the ash which can be sold to the cement industry only if it has a low carbon content, but must otherwise be disposed of as waste [90]. In addition, future clean coal technology, being investigated by National Power, would benefit greatly from PF flow measurement since there will be no excess oxygen to be detected – the usual parameter for combustion control.

Currently, the only commercial way to measure the flow rate of PF is using multipoint isokinetic sampling; this is labour-intensive and unsuitable for real-time monitoring. The lack of a suitable measurement technique impedes the application of control strategies that would increase combustion efficiency and reduce gaseous and particulate waste [159].

In financial terms, if a suitable PF measuring systems were to become available, the savings to a single U.K. power company (National Power) have been estimated at £15 million annually [91]. While the market for clean coal-combustion is small in the U.K., it is growing strongly in the Pacific rim countries, Eastern Europe and North America. Clearly there is a great need for a suitable PF flow meter, for both financial and environmental reasons.

An ultrasonic mass-flow meter has been tested on a PF feed-pipe of a power station [1], and was found to perform satisfactorily. There are, however, complicating factors which were not addressed. The major problem is that the PSD of the pulverised coal can be expected to vary with time, both randomly, and systematically increasing as the pulverising mills wear [136]. This is predicted to have a large effect on acoustic propagation, and will be discussed in Chapter 2. Other factors that will not be addressed include changes in the moisture content of the coal, and in the coal composition. Moisture in the coal is expected to produce an additional acoustic loss through the mechanism of mass transfer (evaporation and condensation synchronously with acoustic pressure variations); variations in coal composition could affect material properties, of which particle density and heat capacity are the most important.

Measurable acoustic parameters are few, while the physical variables are many. Hence, it is not expected that acoustic measurements will, on their own, be able to resolve unambiguously all the physical variables. One possibility is to restrict the scope to relative measurements, hence to identify relative imbalance between different PF pipes – assuming a common coal source.

However, it will be argued that absolute flow-rate measurements should be possible, provided that acoustic measurements are made over a range of carefully-chosen frequencies. The spectral information may not only be analysed to provide a measure of flow-rate, but may also indicate shifts in PSD, which is potentially useful data itself.

1.5 SUMMARY OF NOVEL WORK

Acoustical measurement of slurries and emulsions is an area of active interest, and much experimental work has been published — Evans [43] gives a good review of the work. Less work has been directed to aerosols — this will be reviewed in Chapter 3.

In general, it may be said that previous measurements on aerosols consist either of laboratory-based experiments with sound theoretical grounding, but which avoid the more rigorous conditions imposed by a concentrated, flowing suspension; or else there are studies of flowing suspensions, with results that are presented empirically, and avoid theoretical analysis of the results. This current work presents measurements on moderately concentrated, flowing suspensions, typical of those encountered in pneumatic conveying applications, and also attempts to make theoretical comparisons with a variety of theories.

Chapter 6 presents measurements of plane wave parameters in both quasi-static and flowing suspensions. The novelty of audio frequency measurements in quasi-static suspensions lies simply in the range of sizes of particulates tested, enabling some general conclusions to be drawn about the validity of theoretical models.

A recent paper by Tallon & Davies [140] describes the first published measurements at audio frequencies in large-scale flowing suspensions; continuous sine waves were transmitted along the axis of flow of coarse sand. The work reported in this thesis attempts more rigorous measurements across a wide audio range. Impulse measurements have allowed the removal of the effect of internal reflections, and variations in orifice impedance have been investigated. A variety of materials were tested, including fine powders that were predicted to have a significant effect on audio-frequency propagation (unlike coarse sand).

Chapter 7 consists of predominantly original material, including a method of correlating particle concentration with the rate of reverberant decay in a tube. Experimental evidence is gathered to test theoretically predicted by Vetter & Culick [151]. There are also some preliminary attempts to correlate the steady state amplitude of modal frequencies (under continuous excitation) with the particle concentration.

Chapter 8 describes measurements made at several frequencies at the low end of the ultrasonic range (40 - 75 kHz). Previous work [55, 136, 2] on flowing aerosols measured at a single, higher, frequency — a decision that was possibly based on the misconception that appreciable effects will only be observed where the wavelength is comparable to the particle size [108, 55]. The advantage of lower frequency measurements is that they are less complicated by effects due to turbulence and beam drift.

Appendix A describes a preliminary attempt to detect changes in the characteristic impedance of the aerosol. A very simple apparatus was devised to measure the acoustic load on a loudspeaker that radiated into the suspension; this load is affected by the characteristic impedance of the

environment into which it radiates. To my knowledge, the application of such a technique to suspensions is novel.

Finally, some of the equipment that has been built to make these measurements may be considered to contain novel elements; in particular, the acoustic design of the transducer probes (Chapter 5), and the dynamic weighing apparatus (Appendix C).

2

LITERATURE REVIEW: MODELS & PREDICTIONS

This chapter concentrates on theoretical aspects of sound propagation in suspensions.

Section 2.1 introduces the physical mechanisms that are involved in sound transmission through suspensions, and section 2.2 defines the notation that will be used to describe the problem.

Section 2.3 presents an overview of two classes of theory that predict the acoustic effects of suspensions: scattering and coupled-phase theories. For a more thorough review and development, the reader is referred to Evans [43].

Section 2.4 discusses the predicted acoustic effects across a wide range of input variables. It indicates a variety of regimes in which scaling laws are different, and different theories are more or less valid.

Section 2.5 describes ways to model the particle size distribution (PSD) in a suspension. The predicted acoustic effect of changing PSD will be examined, and the discussion in Section 2.4 is applied to understand how the PSD may be deduced from acoustic measurements — in particular, from changes in the scaling regimes. Attempts to deduce PSD from acoustic measurements are reviewed.

Section 2.6 presents a model to predict the characteristic acoustic impedance of a suspension.

2.1 PHYSICAL MECHANISMS

Suspended particles in a continuous medium represent inhomogeneities to an incident sound wave. The degree of inhomogeneity will govern the magnitude of the acoustic effect, and can be in any of several physical parameters: including density ρ, specific heat capacity C_p, sound speed c, and hence characteristic impedance ρc. If a particle has a higher density than the fluid, then its oscillatory motion due to a passing compressional wave will lag that of the fluid (this is known as acoustophoresis). In the case of a viscid fluid, the relative motion between particle and fluid will lead to viscous losses.

A difference in heat capacity will cause a temperature difference between the particle and the oscillating temperature of the fluid (which is induced by acoustic compression and rarefaction). This will lead to irreversible heat flow between particles and fluid, again leading to losses.

A discontinuity in characteristic impedance will cause partial reflection of an incident compressional wave. The remaining energy will propagate into the particle and may be re-radiated.

Although not a lossy mechanism, it causes energy to be removed from the direction of propagation and to be radiated incoherently in other directions.

For the case of liquid particles in a gas, then an oscillating mass transfer occurs between the phases, as liquid evaporates and condenses in the oscillating acoustic pressure. This leads to a further loss mechanism.

Provided that the contribution from the scattered compressional wave is small, the coherent portion of the propagating plane wave is dominant, and the effect of the particles can be represented by an attenuation and modified sound speed. These are found by solving for the complex wavenumber, k. Essentially, the two-phase medium can then be represented by a continuum with this wavenumber.

There are two main classes of theory that attempt to model these mechanisms: scattering theory and coupled-phase theory. These will be summarised in the Section 2.3. Evans [43] has shown that a further type of theory – porous media theory, in which the continuous phase is a solid – can be applied to suspensions, and he has demonstrated its equivalence to coupled-phase theory in this particular case.

2.2 NOTATION

The suspension will be represented by spheres of radius a distributed in the fluid, at a concentration of ϕ. The sound has frequency f, angular frequency ω. Subscripts $_f$ and $_s$ will denote the continuous phase (fluid) and particulate phase (usually solid). Where no subscript is given, the variable refers to the bulk suspension.

The three most important variables are three characteristic lengths: the inter-particle spacing, governed by ϕ_v, the particle radius, a, and the sound wavelength, λ. Together, these form a three-dimensional "parameter space", in which the assumptions of some theories are more valid than others, and in which the acoustic effects pass through several scaling regimes. These will be addressed in Section 2.4.

A significant controlling parameter is $k_f a$, where $k_f = \omega/c_f$ is the wavenumber in the fluid. Where $k_f a \ll 1$, the acoustic wavelength is much larger than the scatterer size; this is called the "long wavelength" regime, and some important simplifications can be made.

The desired quantity from each theory is the wavenumber,

$$k = \frac{\omega}{c} + i\alpha \tag{2.1}$$

where α is the plane wave attenuation coefficient in Np/m. The acoustic parameters of speed and attenuation are related to the real and imaginary parts, respectively by:

$$c = \frac{\omega}{\mathrm{Re}(k)} \quad \text{and} \quad \alpha = \mathrm{Im}(k) \tag{2.2}$$

In the following discussion, the attenuation of the continuous phase will be ignored, and therefore the acoustic effects are "excess" quantities, in addition to those of the continuous phase.

2.3 MODELS FOR SOUND PROPAGATION IN SUSPENSIONS

2.3.1 Scattering theory

Scattering theory treats the suspension as an array of randomly-distributed scatterers. An incident plane wave is represented by a compressional wave. If viscous and thermal effects are included, the interaction with a single scatterer creates three new scattered waves in the fluid, although the scattered viscous and thermal waves are attenuated rapidly with distance, and are considered to be confined to a boundary layer. Three waves are also created within the scatterer: compressional, thermal, and shear or viscous, depending on whether the scatterer is solid or liquid, respectively. The boundary layers of individual scatterers are assumed not to overlap; hence, in evaluating the interaction at each scatterer, the latter can be assumed to be surrounded by an infinite volume of the continuous phase — the "isolated particle" assumption.

The waves scattered by a single particle are expressed as infinite sums of weighted spherical harmonics; the magnitude of successive terms decreases with increasing frequency, and can be truncated according to the uppermost value of $k_f a$. The problem consists of solving for the 6 unknown waves by reference to the boundary conditions at the scatterer. In the long wavelength regime, $k_f a \ll 1$, the series representation of the waves can be approximated by the first two terms, A_0 and A_1, defined below.

To find the effect of many scatterers, the simplest technique is to sum the effect due to each individual one, assuming no interaction between scatterers and an equal field at each scatterer. Hence, the resultant expression for α is linear in ϕ. This is known as the single scattering, or Born, approximation. A further development, multiple scattering, takes account of re-scattering of scattered waves, and introduces higher powers of ϕ into the expression.

Some of the earliest theoretical formulations attempted to model fogs. Sewell [129] treated water droplets as rigid, stationary spheres in a viscous medium, and neglected effects of heat and mass transfer. Epstein & Carhart [40] removed the constraint of particles to be stationary, and modelled them as a visco-elastic fluid. The effect of heat transfer was included, and they showed that the viscous and thermal losses were additive in the long wavelength regime.

Allegra and Hawley [6] extended the work from fluid/fluid to solid/fluid suspensions. They allowed for (isothermal) deformations of the solid, and included the effect of compressional wave scattering.

By making the long wavelength approximation, they derived explicit expressions for the first two scattering coefficients of a single sphere, A_0 and A_1 :

$$A_0 = \frac{i(k_f a)^3}{3}\left(\frac{\rho_f {c_f}^2}{\rho_s {c_s}^2} - 1\right) - {k_f}^2 a c_f T_f \rho_f \kappa_f H\left(\frac{\Theta_f}{\rho_f C_{pf}} - \frac{\Theta_s}{\rho_s C_{ps}}\right)^2 \tag{2.3}$$

$$A_1 = \frac{-i(k_f a)^3}{3}\left\{\frac{3\rho_f}{(\rho_s - \rho_f)} + 2\left[1 + 3(1+i)\frac{\delta_v}{2a} + 3i\frac{{\delta_v}^2}{2a^2}\right]^{-1}\right\}^{-1} \tag{2.4}$$

$$\text{where} \quad H = \left\{\frac{1}{(1 - iz_f)} - \frac{\kappa_f}{\kappa_s}\frac{\tan(z_s)}{\tan(z_s) - z_s}\right\}^{-1}, \quad z = (1+i)a/\delta_t \tag{2.5}$$

$$\delta_t = \sqrt{\frac{2\kappa}{\omega\rho C_p}}, \text{ and } \quad \delta_v = \sqrt{\frac{2\mu_f}{\omega\rho_f}} \tag{2.6}$$

Here, T is the absolute temperature, μ is the shear viscosity of the fluid, C_p is the specific heat capacity (at constant pressure), Θ is the coefficient of thermal volume expansion, and κ is the thermal conductivity. δ_t and δ_v are the thermal and viscous boundary layer thicknesses (respectively), and represent the distance for the scattered wave amplitude to decay by $1/e$.

The isolated particle assumption requires that the boundary layer thicknesses are smaller than half the inter-particle spacing, d. The average spacing can only be estimated: Evans [43] justified the use of Zuber's expression [167] :

$$d = 2a\left(\phi_v^{-\frac{1}{3}} - 1\right) \tag{2.7}$$

This gives the following expressions for the maximum volume fraction:

$$\phi_v < \left(\frac{\delta_v}{a} + 1\right)^{-3} \text{ and } \phi_v < \left(\frac{\delta_t}{a} + 1\right)^{-3} \tag{2.8}$$

where the limitation is caused by overlapping viscous and thermal boundary layers, respectively. These conditions are illustrated (for the case of air) in Figure 2-1.

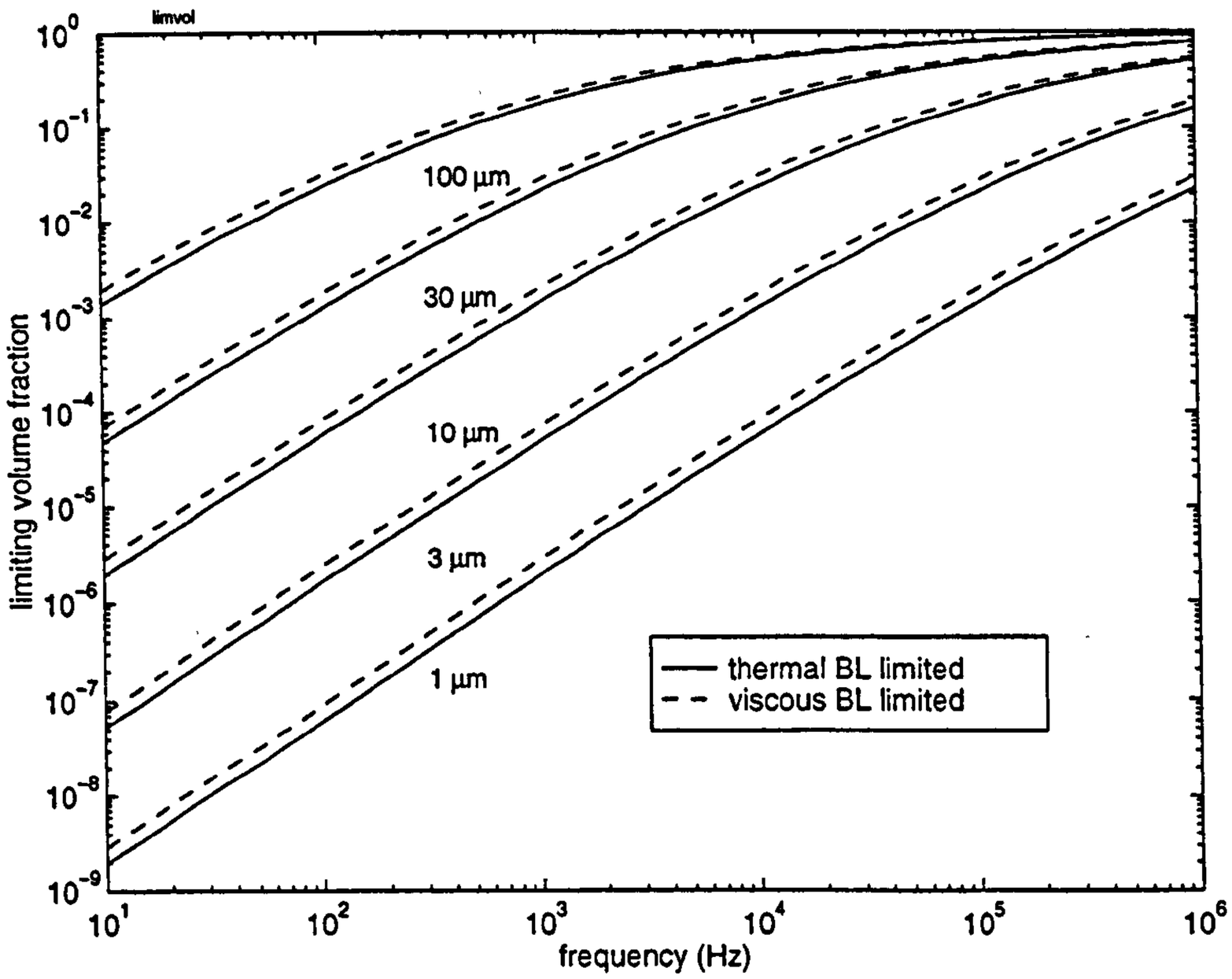

Figure 2-1 *The limiting values of volume fraction at which thermal (solid line) and viscous (dashed line) boundary layers begin to overlap in air, for varying particle radii . The area below the curves signifies the region in which there is no overlap.*

For air, δ_t is always provides the limiting case. The smaller particle sizes result in surprisingly low limiting volume fractions: less than 1 ppm at low frequencies. However, McClements & Povey [92] found that measurements still agreed with theory somewhat beyond this limitation.

Single scattering theory assumes that the wave incident on each scatterer is equal, which requires that the total signal attenuation in the scattering volume is small. This condition is expressed as [43]:

$$\alpha_{ss} L \ll 1 \tag{2.9}$$

where α_{ss} is the attenuation coefficient calculated according to single scattering, and L is the path length. If 0.1 Np is chosen as a limiting value, then this implies a maximum of 10% signal loss $[1-\exp(0.1)]$ across the test volume. If this loss is exceeded, then a multiple scattering theory should be used.

Allegra and Hawley developed a single scattering theory. However, their expressions for the coefficients A_0 and A_1 are still used in contemporary multiple-scattering formulations.

A commonly encountered multiple scattering theory is that due to Waterman and Truell [154]. Lloyd and Berry [85], and Ma *et al* [89] both suggested improvements by adding some higher order statistics in the multiple scattering analysis. Twersky [147] and Tsang *et al* [146] arrived at the same long wavelength approximation as Ma *et al*.

McClements [93] compares the predictions of these theories with experimental measurements on a concentrated emulsion. He also introduced a method of accounting for a polydispersed suspension, which involves summing the A_n coefficients for each particle size.

$$A_0' = -3i\sum_j \left[\Phi_j \cdot A_{0j} / (ka_j)^3\right] \tag{2.10}$$

$$A_1' = 3i\sum_j \left[\Phi_j \cdot A_{1j} / (ka_j)^3\right] \tag{2.11}$$

where Φ_j is the volume fraction of particles (relative to the total volume of particles) with radius r_j and A_{0j} and A_{1j} are the single particle scattering coefficients for radius a_j. These modified coefficients are then substituted into one of the multiple scattering equations below.

According to Waterman and Truell [154]:

$$k^2 = k_f^2\left(1+\phi_v A_0'\right)\left(1-3\phi_v A_1'\right) \tag{2.12}$$

Lloyd and Berry [85] extended the expression thus:

$$k^2 = k_f^2\left(1+\phi_v A_0'\right)\left(1-3\phi_v A_1'\right) + 6\phi_v^2 A_1' \tag{2.13}$$

Ma *et al* [89] derived an expression that included still higher order statistics, and predicts the transition into the region where compressional wave scattering is significant:

$$k^2 = k_f^2 \frac{\left(1+\phi_v A_0'\right)\left(1-\phi_v A_1'\right)}{\left(1+2\phi_v A_1'\right)}\left\{1+\frac{i\left(k_f a\right)^3 \phi_v w}{6}\left[\frac{A_0'^2}{\left(1+\phi_v A_0'\right)}+\frac{3A_1'^2}{\left(1+2\phi_v A_1'\right)\left(1-\phi_v A_1'\right)}\right]\right\}^2 \tag{2.14}$$

$$\text{where } w = \frac{\left(1-\phi_v\right)^4}{\left(1+2\phi_v\right)^2} \tag{2.15}$$

Ma *et al* use A coefficients for lossless scatterers: this is justified for $k_f a \geq 0.1\pi$, where compressional wave scattering starts to overshadow viscous and thermal losses; however, McClements [93] suggests that the expression may be valid also in the long wavelength regime if one uses the coefficients for a lossy scatterer. The validity of this assumption is not clear.

By comparing their predictions to optical measurements made of latex spheres in water, Ma *et al* showed that, at high concentration ($\phi_v > 0.1$) their expression was a considerable improvement over that of Waterman & Truell [154].

2.3.2 Coupled phase theory

Coupled phase theories treat the medium as a continuum, with a single plane wave propagating through it. The conservation equations and equations of state of both phases are coupled by terms

that describe momentum and heat transfer between phases. All the variables are volume-averaged to account for the presence of two phases in the control volume, and are allowed time and space dependency. This set of equations can be written as the matrix equation:

$$\mathbf{A}\mathbf{y} = 0 \tag{2.16}$$

where $\mathbf{y}$ is the vector of unknown amplitudes of field variable fluctuations, $\mathbf{A}$ is a vector containing known physical parameters, and coupling terms between the variables as a function of the unknown k. Non-trivial solutions require:

$$\det \mathbf{A} = 0 \tag{2.17}$$

which yields an equation that can be solved for k.

This approach ignores compressional wave scattering, and so is only valid in the long wavelength regime ($k_f a \ll 1$) where this mechanism is negligible. Like the scattering approach, it is only valid where the coherent wave is dominant. The field is assumed to be uniform throughout the volume, and so the limitation of the Born approximation in equation (2.9) applies.

In order for the volume-averaging approach to be valid, the suspension must appear as a continuum to the sound wave and therefore the inter-particle spacing should be much less than a wavelength. This is the limitation quoted by Gumerov *et al* [54]:

$$\phi \gg (2a\lambda)^3 \tag{2.18}$$

Crowe [35] applied the condition that there should be a statistically-large number of particles in a control volume with sides λ: he suggested 10^4 particles by analogy with the statistical mechanics of molecules in a gas. This gives the following criterion:

$$\phi > \tfrac{4}{3}\pi \times 10^4 (a\lambda)^3 \tag{2.19}$$

While these inequalities set the lower limits on the volume fraction, the upper limits restricting overlap of boundary layers still apply, since the isolated particle assumption is made. Therefore equation (2.8) applies also to coupled-phase theories (except where a correction for hydrodynamic interaction is made, as described later).

Temkin & Dobbins [141] presented an early – and still popular – coupled phase theory. It assumed a low volume concentration and that the drag force on particles could be represented by Stokes' law only. This restricted its use to suspensions with a high density contrast between phases, and to comparatively low frequencies. The heat transfer was modelled by Newton's law of cooling. Particles were treated as incompressible, and mass transfer was ignored.

The beauty of their theory is in the simplicity of its presentation, which shows the acoustic effects to be due to the sum of thermal and viscous relaxation mechanisms (at low values of ϕ_m). Each mechanism shows a peak in the specific attenuation (attenuation per wavelength, $\alpha\lambda$) – and a

corresponding maximum rate-of-change of sound speed — as a function of frequency. This is given by its relaxation time, and is easily calculated explicitly:

$$\tau_v = \frac{2a^2\rho_s}{9\mu} \tag{2.20}$$

$$\tau_t = \frac{\mathrm{Pr}\ C_{ps}\, a^2\rho_s}{3\mu C_{pf}} \tag{2.21}$$

Here τ_v and τ_t are the viscous and thermal relaxation times, respectively, and Pr is the Prandtl number:

$$\mathrm{Pr} = \mu C_{pf}/\kappa_f \tag{2.22}$$

Their predictions are expressed in terms of specific attenuation, and dispersion, both normalised with respect to mass fraction:

$$\overline{\alpha} = \frac{\alpha c_f}{\omega\phi_m} = \frac{\omega\tau_v}{1+(\omega\tau_v)^2} + (\gamma-1)\frac{C_{ps}}{C_{pf}}\frac{\omega\tau_t}{1+(\omega\tau_t)^2} \tag{2.23}$$

$$\overline{\beta} = \frac{1}{\phi_m}\left[\left(\frac{c_f}{c}\right)^2 - 1\right] = \frac{1}{1+(\omega\tau_v)^2} + (\gamma-1)\frac{C_{ps}}{C_{pf}}\frac{1}{1+(\omega\tau_t)^2} \tag{2.24}$$

Mednikov [97] extended this theory to account for sound pressures of finite amplitude.

Mecredy and Hamilton [96] considered gas/liquid and liquid/gas media, similarly with an incompressible liquid phase. They extended the work of Temkin and Dobbins in many areas. To the Stokes law drag, they added the effect of the "induced mass" force, and the extended representation of heat transfer. They also modelled the effect of mass transfer. Evans [43] showed that by removing the terms describing mass transfer, an analytical solution for k could be found.

Gumerov *et al* [54] arrived at a similar treatment, with the addition of unsteady components of the viscous force (Bassett history term) and heat transfer, and included the effects of mass transfer.

A parallel treatment was used by Harker & Temple [56], who neglected heat transfer but included the effects of particle compressibility. Evans [43] extended their work by introducing terms for heat transfer, thus formulating a theory that includes the effects both of heat transfer and particle compressibility. This makes it the only coupled phase theory that is suitable for use with emulsions, where both mechanisms are important. However, the method results in an 8×8 A matrix, the solution of which must be found partly numerically (except at the limiting frequencies of $f = 0$ and $f = \infty$). Evans also gives an explicit expression for k that includes heat transfer, but not viscous momentum transfer, and is a useful approximation.

Ahuja [4] made the first attempt to model the effect of non-spherical particles. He derived the drag force (modified Stokes' drag, Bassett history and induced mass) for spheroids (3D ellipses), and included it within a coupled-phase theory. Using these expressions, Evans [43] showed that the effect of changing the particles' shape while keeping volume constant, or changing their orientation relative to the sound field, could be modelled by a sphere of a given effective radius (in fact two radii: one giving an equal drag, one giving an equal heat transfer as the spheroid). It is expected that surface roughness of a particle is not significant if the particle size is much smaller than the viscous boundary layer; ie. the roughnesses are invisible on the scale of the viscous wave [162].

Strout [139] modelled the effect on the momentum transfer term of hydrodynamic interactions between particles, which happen when their viscous boundary layers overlap. He introduced a correction term into Harker & Temple's theory, although no account was taken of the similar effects due to overlap of thermal boundary layers. Hence this theory should be more accurate at very concentrated suspensions, relaxing the restriction of equation (2.8). An attempt to introduce a similar correction term into a multiple scattering theory was less successful.

2.3.3 Comparison and the "preferred" model

In general, coupled-phase theories are more valid than scattering theories at high volume concentrations, and therefore tend to be more useful for emulsions and slurries, where ϕ_v can exceed 0.5. A further advantage of coupled-phase theories is their apparent extensibility, for example, to include non-spherical particles and interactions between particles. Their fundamental limitation is the neglect of compressional wave scattering, and hence they cannot be used at frequencies above the long wavelength limit.

By contrast, multiple scattering theories can be extended, numerically if not symbolically, to an arbitrarily high frequency, by including higher terms in the expansion of the single-particle scattering coefficients. Their validity at high concentrations is, however, inferior to coupled-phase theories. In almost all cases, scattering theories are not "self-consistent": as ϕ_v approaches 1, the predicted bulk acoustic parameters do not converge to those of the particulate phase. In particular, single scattering theory predicts an attenuation that increases linearly as ϕ_v approaches 1, instead of decreasing back to zero.

The current work is concerned with aerosols, where the upper limit of ϕ_v is far below that of emulsions and slurries: in "dilute phase" pneumatic conveying (where each particle is surrounded by gas) the highest achievable value of ϕ_v is approximately 0.01. However, there is the prospect that ultrasonic measurements on large particles could approach the long wavelength limit. Therefore, unless otherwise stated, predictions in this thesis will use the multiple-scattering theory of Lloyd & Berry [85]. The relevant equations are (2.3) to (2.6) in the previous section. Occasionally, where

predictions at high $k_f a$ are required, the theory of Ma *et al* [89] will be used (using scattering coefficients for lossy scatters) . It should be noted that the validity of this method is uncertain.

Evans [43] has shown that for dilute aerosols there is negligible difference between predictions using Lloyd & Berry's multiple-scattering theory and the coupled-phase theory of Mecredy & Hamilton.

2.4 REGIMES IN PARAMETER SPACE

It has been stated that the variables $a, f,$ and ϕ together form a three dimensional parameter space within which the acoustic effects pass through several regimes. These regimes will be discussed successively in terms of frequency, particle size, and concentration.

Below the long wavelength limit, the "vocabulary" will be that of coupled-phase theory. The loss mechanisms mentioned will be the momentum transfer terms: exactly analogous losses also occur with the equivalent thermal mechanism. The significant controlling variable is the Reynolds number, Re, which measures the ratio between the inertial forces, represented by the particle size, and the viscous forces, represented by the viscous boundary layer thickness:

$$\mathrm{Re} = \frac{a}{\delta_v} = a\sqrt{\rho_f \omega / 2\mu} \qquad (2.25)$$

Above the long wavelength limit, the dimensionless wavenumber, ka, is more useful, and the "vocabulary" will be that of scattering theory.

For the case of hard particles suspended in gas, there are four main acoustic regimes: viscous, inertial, Rayleigh scattering and resonant scattering.

2.4.1 Attenuation as a function of frequency

Long wavelength

At low frequencies where $\mathrm{Re} \ll 1$, the boundary layer thickness is much larger than the particle size. Stokes law drag dominates the momentum transfer expression, and the relaxation times (given in equations (2.20) and (2.21)) are shorter than the sound period. Strictly, this is the region in which the theory of Temkin & Dobbins [141] applies, although it appears useful up to a frequency decade higher. The attenuation scales as $\frac{a^2}{\mu}\omega^2$ and sound speed is independent of frequency. This is known as the viscous regime.

As $\mathrm{Re} \geq 1$, the Basset history force becomes significant.

In the inertial regime, $Re >> 1$, the viscous boundary layer becomes very thin, and the bulk of the fluid is dominated by inviscid inertial effects (the induced mass force). This is, however, a lossless mechanism, and so loss occurs through the in-phase component of the Basset history force.

Kytömaa [80] states the attenuation scaling to be $\frac{\sqrt{\mu}}{a}\sqrt{\omega}$.

The viscous and inertial regimes, and the transition between them, are well-characterised by the coupled-phase formulations of Mecredy & Hamilton and the long-wavelength approximation of Lloyd & Berry's approach. This region is illustrated Figure 2-2, where Lloyd & Berry's predictions of attenuation coefficient and sound speed are plotted for a wide range of frequency (extending above the long wavelength limit, and so beyond the region of validity).

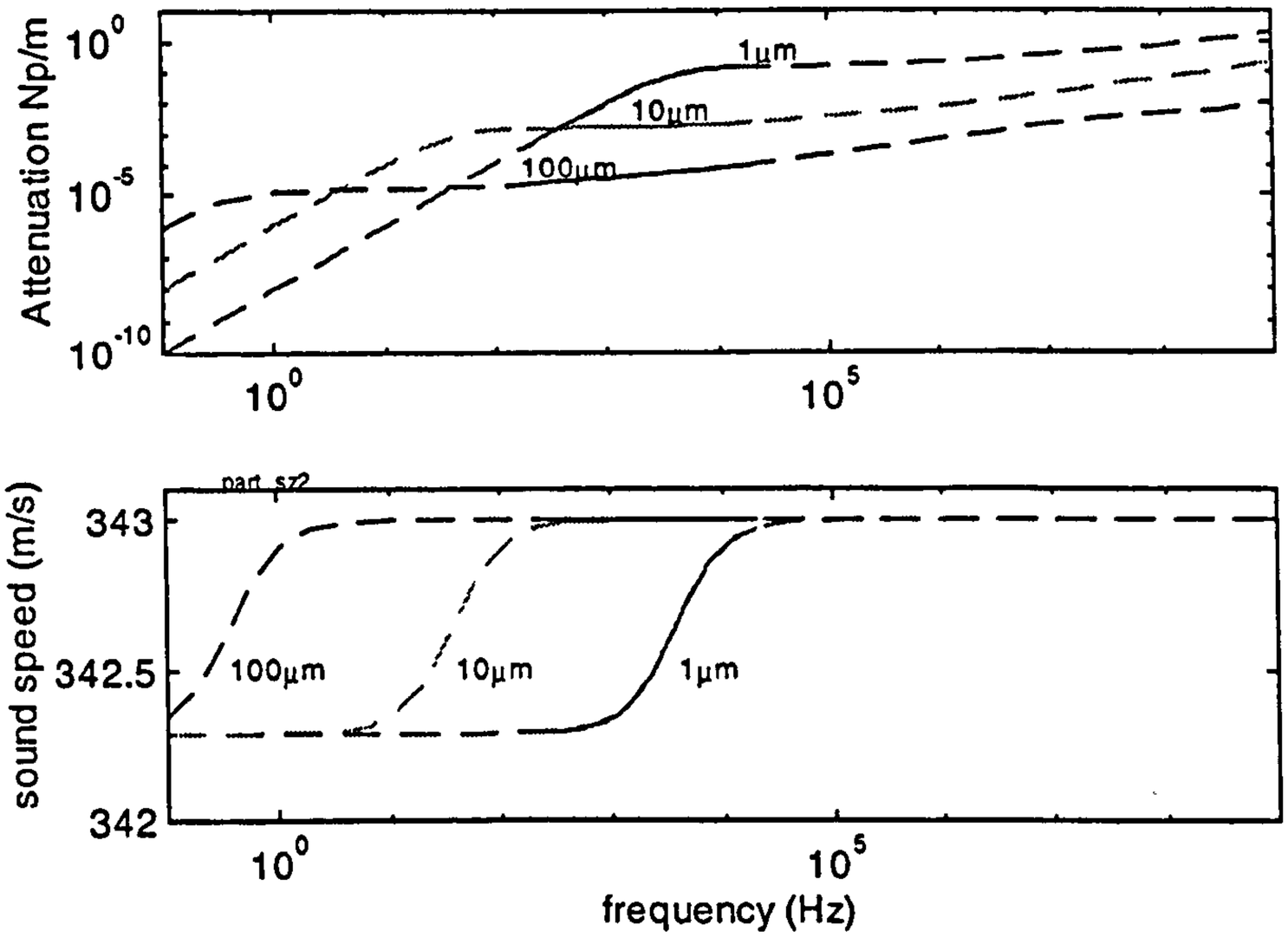

Figure 2-2 Theoretical attenuation (top) and sound speed (bottom) for 3 particle radii of monodispersed spheres of alumina in air. The solid lines span the frequency range 200Hz - 20kHz. Particle concentration $\phi_v = 10^{-6}$.

Solid lines are drawn to indicate the audio bandwidth, and to show how the particle size influences the shape of the attenuation-frequency curve. The transition from ω^2 to $\omega^{0.5}$ scaling clearly occurs at lower frequencies, as the particle size is increased. The sound speed has two asymptotes. At low frequency (viscous regime) the value is easily found from Temkin & Dobbins, equation (2.24):

$$c_{(f\to 0)} = c_f\left[\phi_m(\gamma-1)\frac{C_{ps}}{C_{pf}}+1\right]^{-\frac{1}{2}} \qquad (2.26)$$

In the inertial regime, the sound speed converges to that of the fluid:

$$c_{(f\to\infty)} = c_f \qquad (2.27)$$

The transition from one asymptote to the other marks the start of the transition from viscous to inertial regimes.

Temkin and Dobbins make the transition region more explicit through their formulation in terms of relaxation frequency, given in equation (2.20). Figure 2-3 shows the same predictions as Figure 2-2 (ie. using Lloyd & Berry's theory), but the abscissa is normalized frequency, $\omega\tau_v$. It is now clear that

the transition starts around $\omega\tau_v = 1$ and is complete by approximately $\omega\tau_v = 10^3$. In the transition, the attenuation curve is marked by a plateau area before the $\omega^{0.5}$ scaling begins.

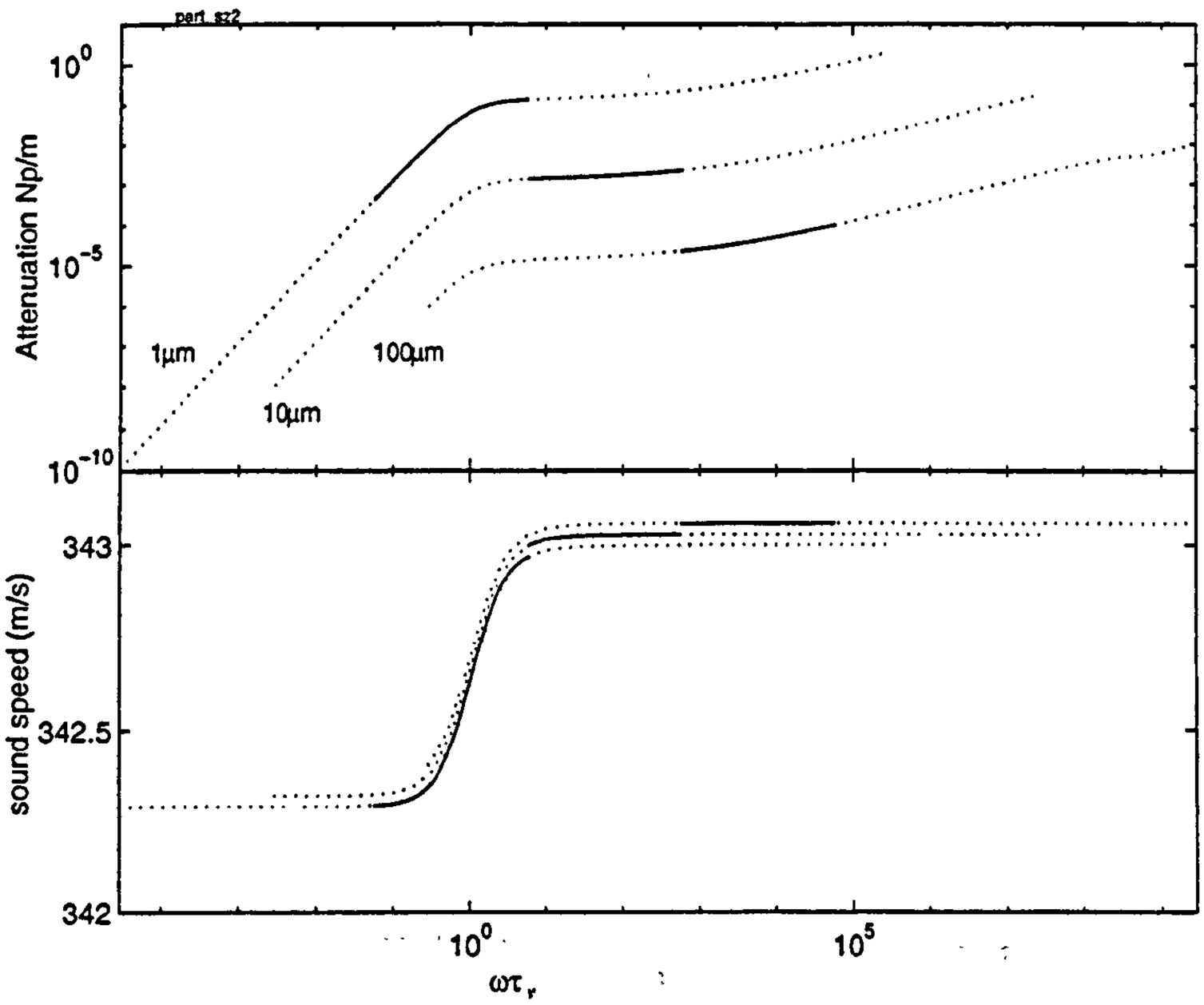

Figure 2-3 Theoretical attenuation (top) and sound speed (bottom) plotted against normalised frequency, for 3 particle radii of monodispersed spheres of alumina in air. The sound speed curves for sizes 10 and 100μm are offset for clarity: they actually overlie the 1μm curve. The solid lines span the frequency range 200Hz - 20kHz. Particle concentration $\phi_v = 10^{-6}$.

The sound speeds for different particle sizes have collapsed onto a single curve. Temkin and Dobbins' theory also demonstrates how to collapse the attenuation onto a single curve. The specific attenuation $\alpha\lambda$ (attenuation per wavelength) is plotted against normalised frequency, in Figure 2-4.

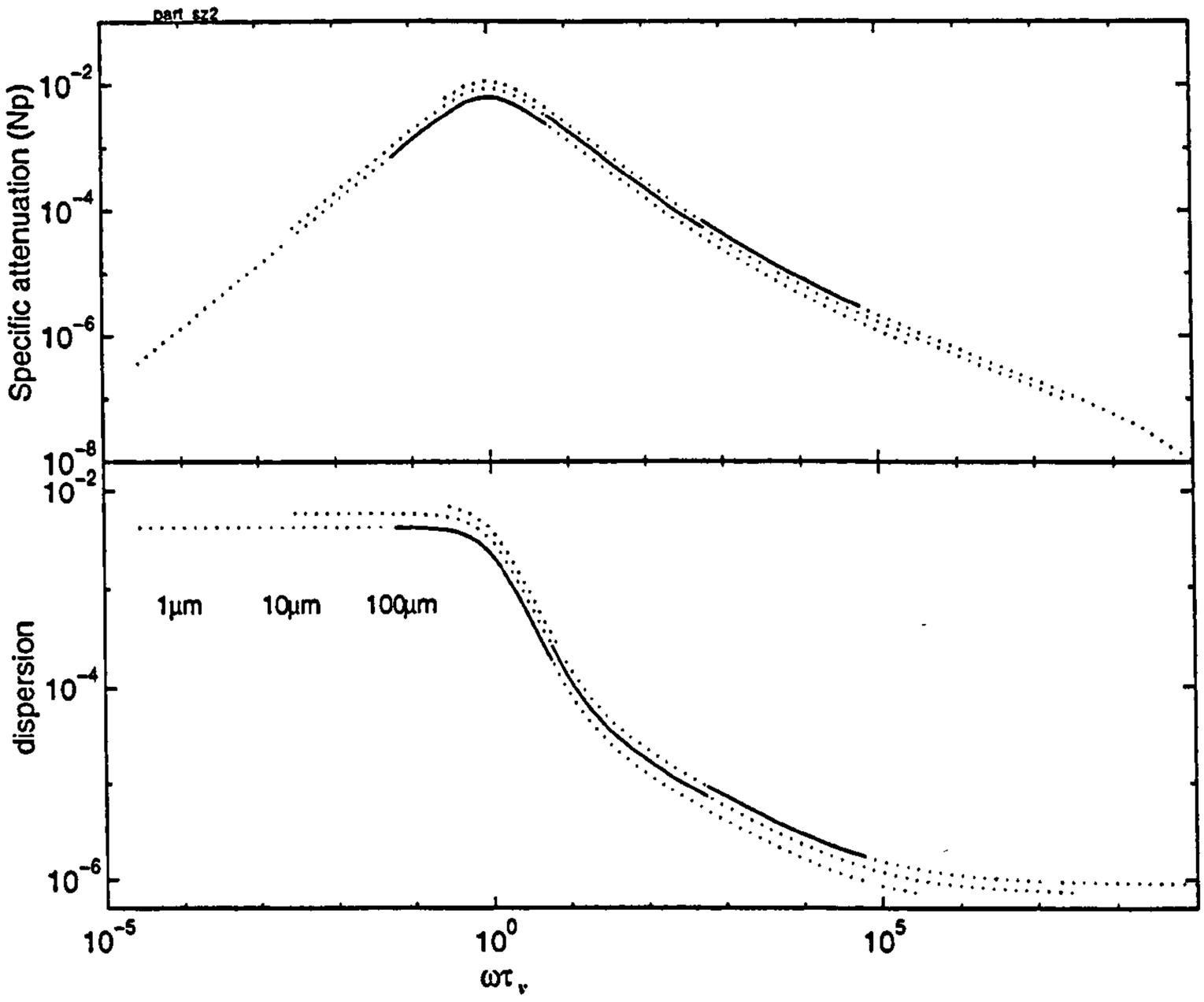

Figure 2-4 *Theoretical specific attenuation plotted (top), and sound speed dispersion (bottom) against normalised frequency, for 3 particle sizes in long wavelength limit (monodispersed spheres of alumina in air). The solid lines span the frequency range 200Hz - 20kHz. The 10 and 100µm curves are slightly offset for clarity: they actually the 1µm curve. Particle concentration $\phi_v = 10^{-6}$.*

The peak in specific attenuation occurs at $\omega\tau_v = 1$. The same effect occurs for polydispersed aerosols if the relaxation time is based on the Sauter mean radius of the distribution (see section 2.5): in this case, the peak in the attenuation curve broadens.

Further exploration of the complex structure of the long wavelength region may be found in the review by Kytömaa [80].

Scattering regime

In the entire long wavelength region, compressional wave scattering occurs and is known as Rayleigh scattering. However, its effect on attenuation scales as $(ka)^4$, and is negligible compared to viscothermal loss mechanisms. When $ka > 0.1$, the particle size becomes a significant proportion of the wavelength, and so the long wavelength approximation breaks down. Rayleigh scattering begins to dominate the viscothermal losses for $ka > 0.1\pi$. The regime in which Rayleigh scattering dominates is limited to the decade $0.1\pi \leq ka \leq \pi$, in which attenuation scales as $(ka)^4$. This region is predicted by the theory of Ma *et al* [89] – presented in equations (2.14) & (2.15) – despite making a long wavelength approximation. Figure 2-5 shows the attenuation as a function of *ka*, and demonstrates the transition to Rayleigh scattering at approximately 0.1π. The predictions of the long-wavelength formulation of Lloyd & Berry [85] are shown for comparison.

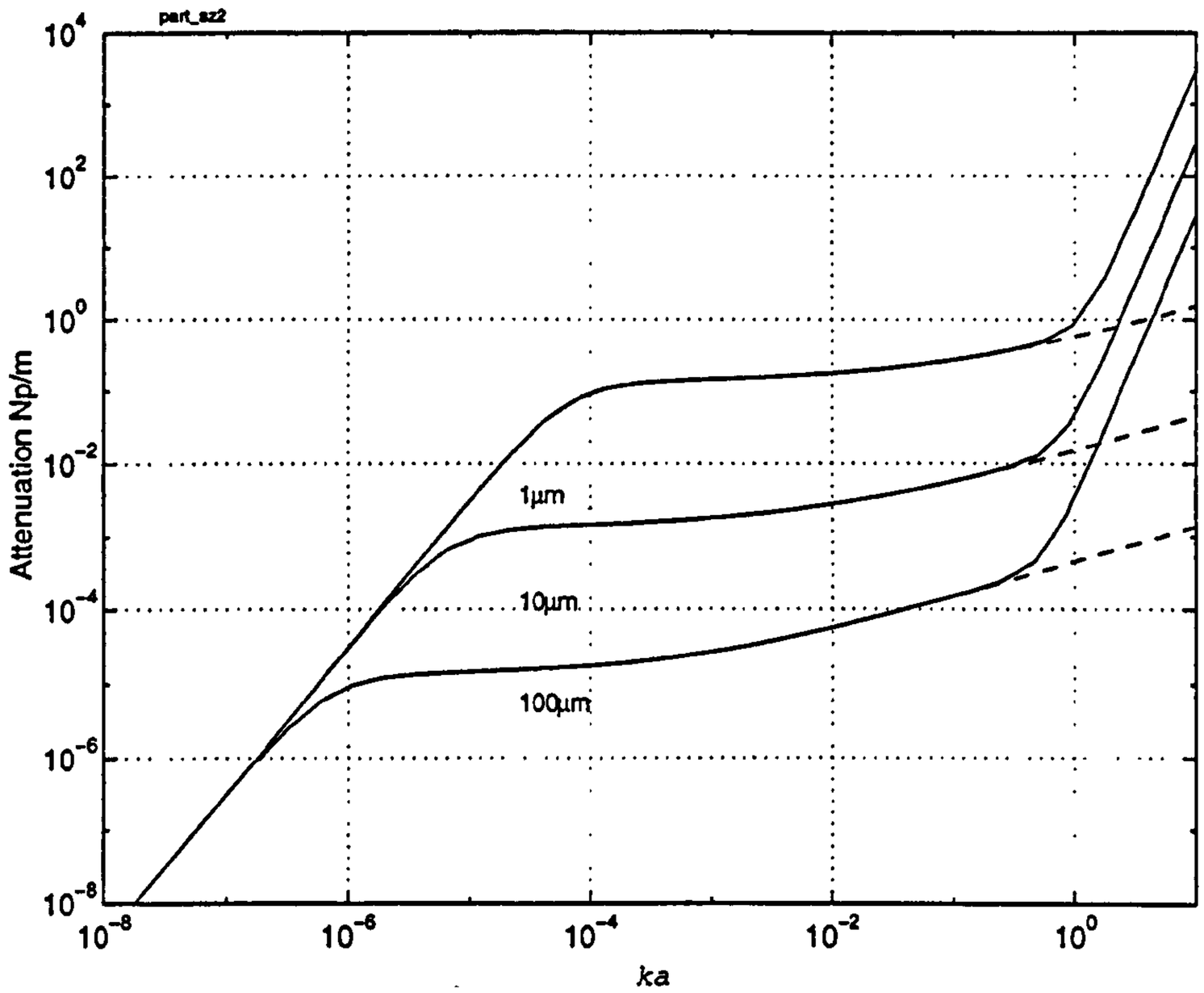

Figure 2-5 Theoretical attenuation plotted against dimensionless wavenumber, for 3 particle radii of monodispersed spheres of alumina in air. The solid line is calculated from Ma et al *[89], the dashed line from Lloyd & Berry [85]. Particle concentration* $\phi_v = 10^{-6}$.

The graph also shows how, in the viscous regime, the attenuation is a function of *ka* only.

When $ka > \pi$, the particle is large enough to support internal structural resonances, which lead to re-radiation. The resulting sound field is complex in its variation in both polar direction and frequency. This "resonant scattering" regime displays an attenuation that reaches a plateau (not shown) that is dominated by resonant phenomena. To predict attenuation in this regime requires a lengthy numerical expansion of the scattering coefficients. For airborne particulates of practical size, this regime is not encountered because of the very high frequencies that would be required.

2.4.2 Attenuation as a function of particle size

The same information is presented in Figure 2-6 as a function of particle size instead of frequency.

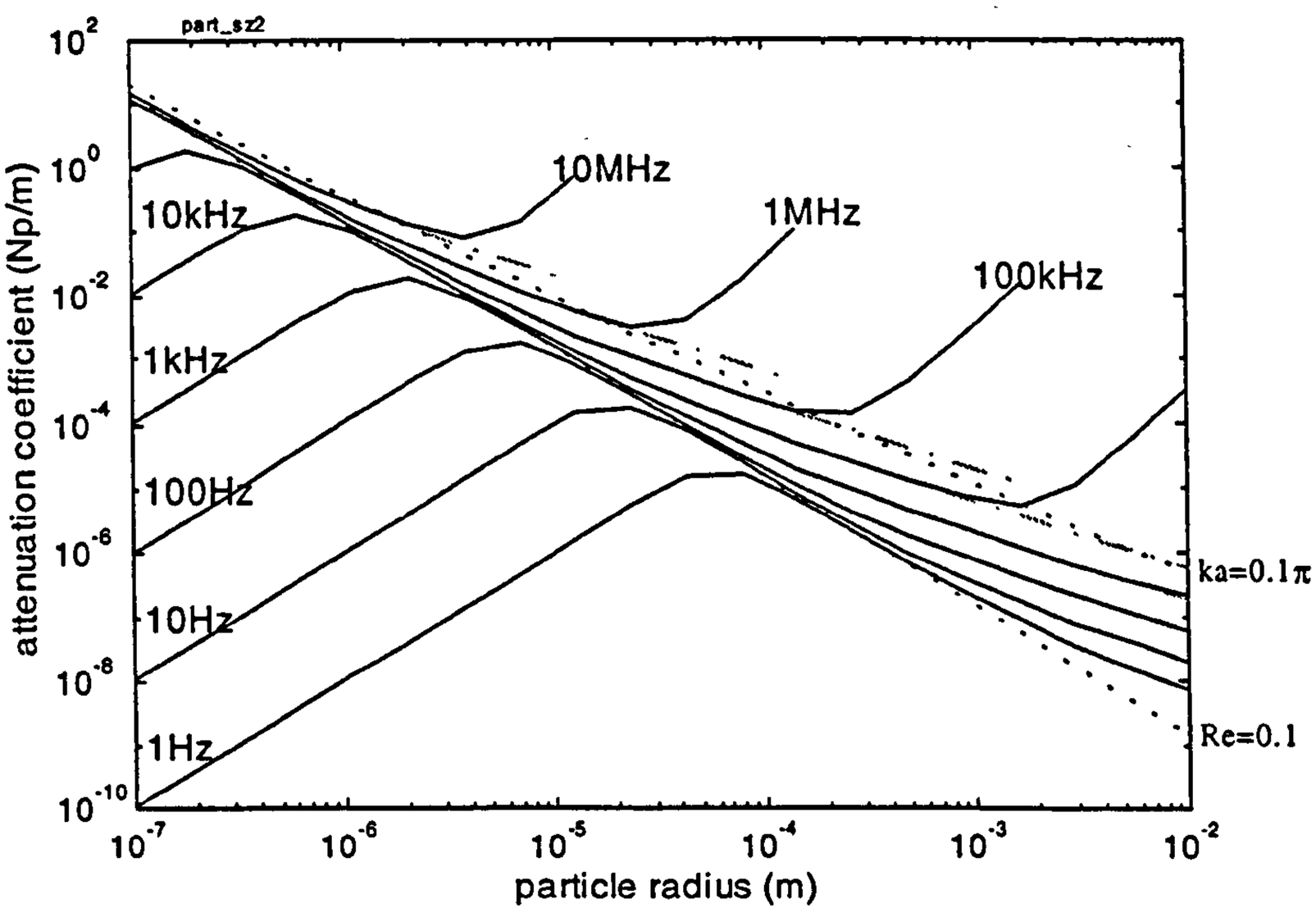

Figure 2-6 Theoretical attenuation coefficient for alumina spheres as a function of radius (and frequency). Solid lines are predicted with the theory of Ma et al, *dot-dash lines using Lloyd & Berry. The area to the left of the* Re = 0.1 *line marks the viscous regime; that to the right of the* $ka = 0.1\pi$ *line marks the Rayleigh scattering-dominated regime, and the area in between is the inertial regime. Lines cease at* $ka = \pi$, *marking the transition to the resonant scattering regime. Particle concentration* $\phi_v = 10^{-6}$.

Several points are noteworthy:

- In the viscous regime, $Re < 0.1$, the a^2 scaling is clear, although the transition to a^{-1} scaling in the inertial regime is slow, and the transition to Rayleigh scattering appears to happen before the a^{-1} scaling is fully established. Kytömaa [80] points out that for very small particles, the viscous regime can pass directly into the Rayleigh-scattering regime.
- Each frequency shows an attenuation maximum at the viscous-to-inertial transition, and a minimum at the inertial-to-Rayleigh scattering transition. For audio frequency measurements, the particles of size such that $Re \approx 0.1$ will therefore have the greatest effect on attenuation. However, since measurements usually take place above this value, the smallest particles will have the greatest effect, unless the largest particles are such that $ka > 0.1\pi$.
- The clustering of curves around the $Re = 0.1$ line shows that there is little frequency dependence of attenuation coefficient in the inertial regime. The theory of Temkin & Dobbins [141], which does not include higher order terms for momentum and thermal transfer, predicts that all curves would converge onto this line.

2.4.3 Attenuation as a function of volume concentration

In the case of aerosols, there is less structure to predicted attenuation as a function of volume fraction. Figure 2-7 shows that the multiple scattering extension has little effect, and so attenuation is closely linear over the range of interest (up to $\phi_v \approx 10^{-3}$).

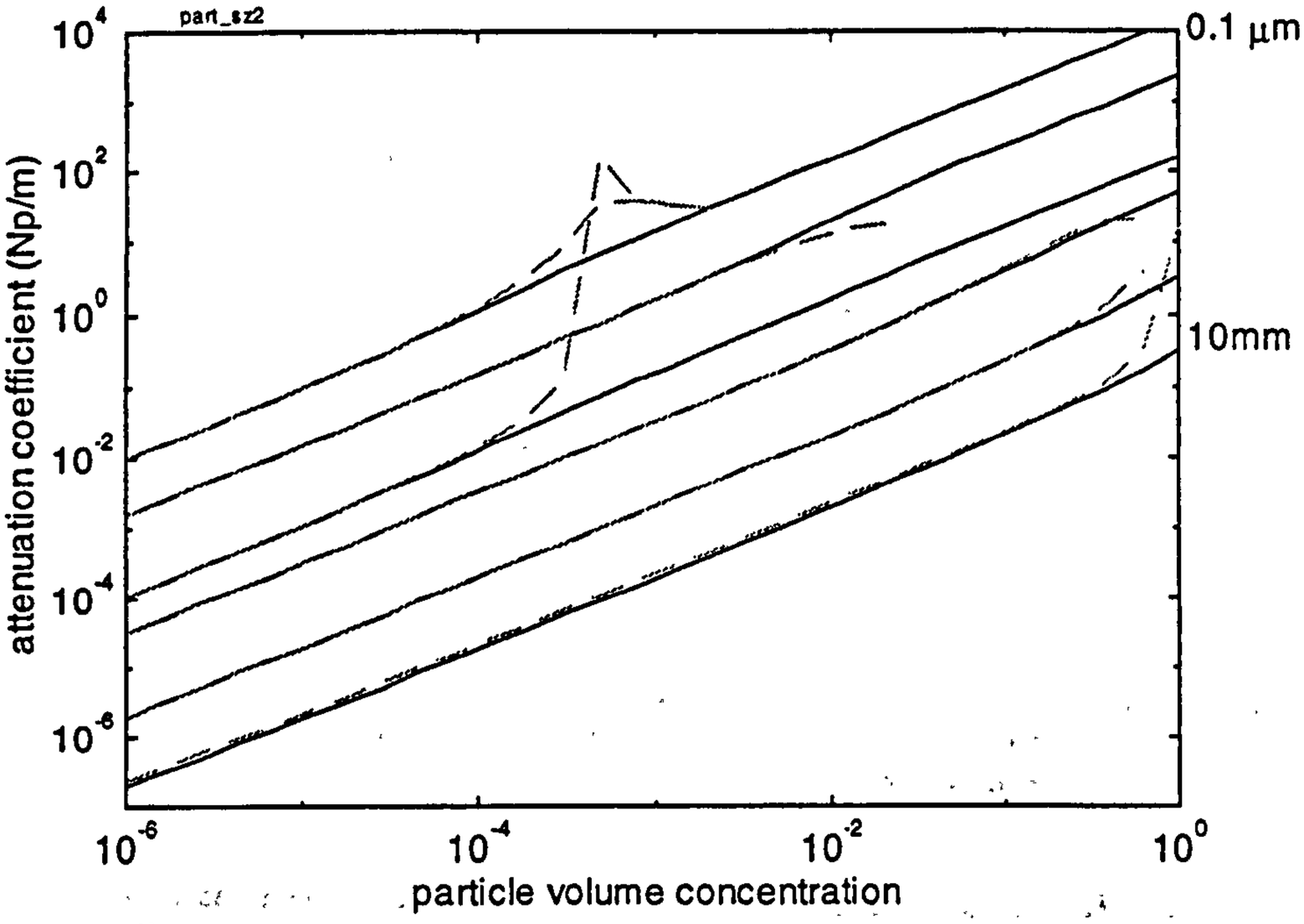

Figure 2-7 Theoretical attenuation coefficient for alumina spheres as a function of volume concentration (and radius). Solid lines are predicted with the theory of Lloyd & Berry, dashed lines using Ma et al. *Frequency = 1000 Hz. Parallel lines correspond to particle radii 0.1μm, 1μm, 10μm, 100μm, 1mm, 10mm (bottom to top).*

The theory of Lloyd & Berry predicts near-linear dependence on concentration (gradient of 1 in the log-log plot). However, the Ma *et al* theory diverges occasionally in a complex way; this appears to be due to numerical instability at low frequencies and high concentrations.

Neither theory can be expected to produce useful results above $\phi_v \approx 10^{-2}$, where coupled phase theories would be chosen. Linear dependence of attenuation on concentration will be assumed in this work.

2.4.4 Implications for particle sizing

It can be seen from Figure 2-7 that a given measurement of attenuation could be produced by an infinite number of pairs of a and ϕ_v. Therefore a measurement of attenuation at a single-frequency can not provide values for a and ϕ_v separately.

On the other hand, a broadband (spectroscopic) measurement may be used to infer both the particle size and concentration, but only under certain conditions. Figure 2-2, for example, shows that the attenuation curves of alumina spheres of 1, 10 and 100μm exhibit almost identical scaling in the inertial regime above 100kHz. Therefore, once again, a broadband signal above 100kHz (but under

$ka = 0.1\pi$) will not be able to discriminate between the particle sizes if their concentration is unknown.

The key to deducing PSD lies in the structure of attenuation-frequency curves that is provided by transitions between regimes. In the previous discussion, three such transitions have been identified: from viscous to inertial (ω^2 to $\omega^{0.5}$), from inertial to Rayleigh scattering ($\omega^{0.5}$ to ω^4), and from Rayleigh scattering to resonant scattering[1]. If the frequency band incorporates one of these transitions for each particle size of interest, then, theoretically, the PSD can be deduced without knowledge of the concentration.

In the following section, three experimental techniques are reviewed, which use different transitions to attempt particle sizing. Kytömaa [80] points out that the particle sizing process would more robust if measurements encompassed more than one transition, but there are great practical problems in making a measurement of such a high bandwidth (>6 decades).

2.5 PARTICLE SIZE DISTRIBUTION: MODELS AND ACOUSTIC DEDUCTION

It will be demonstrated in section 2.5.2 that the particle size distribution (PSD) of the particulate phase has a large influence on the predicted acoustic effects. Theoretical formulations that model a PSD do so by weighting acoustic parameters according to the volume (or, equivalently, mass) fraction of the particles; see, for example, equations (2.10) and (2.11). The larger particle fractions will therefore have a strong influence on the predictions, due to the cubic power relation between their volume and size. Because of this sensitivity, a good knowledge of the PSD is necessary to make accurate acoustic predictions.

2.5.1 Models of PSD

The PSD can be displayed by either a frequency distribution or a cumulative frequency distribution. A frequency distribution is a bar-graph that plots the volume fraction of particles in a given size range ("bin") against the size. The cumulative frequency distribution is (potentially) a continuous curve that plots the percentage by volume of particles under a particular size. The forms are demonstrated in Figure 2-8 below for a hypothetical PSD.

[1] Kytömaa [80] treats the Rayleigh and resonant scattering regimes as a single one: geometrical scattering.

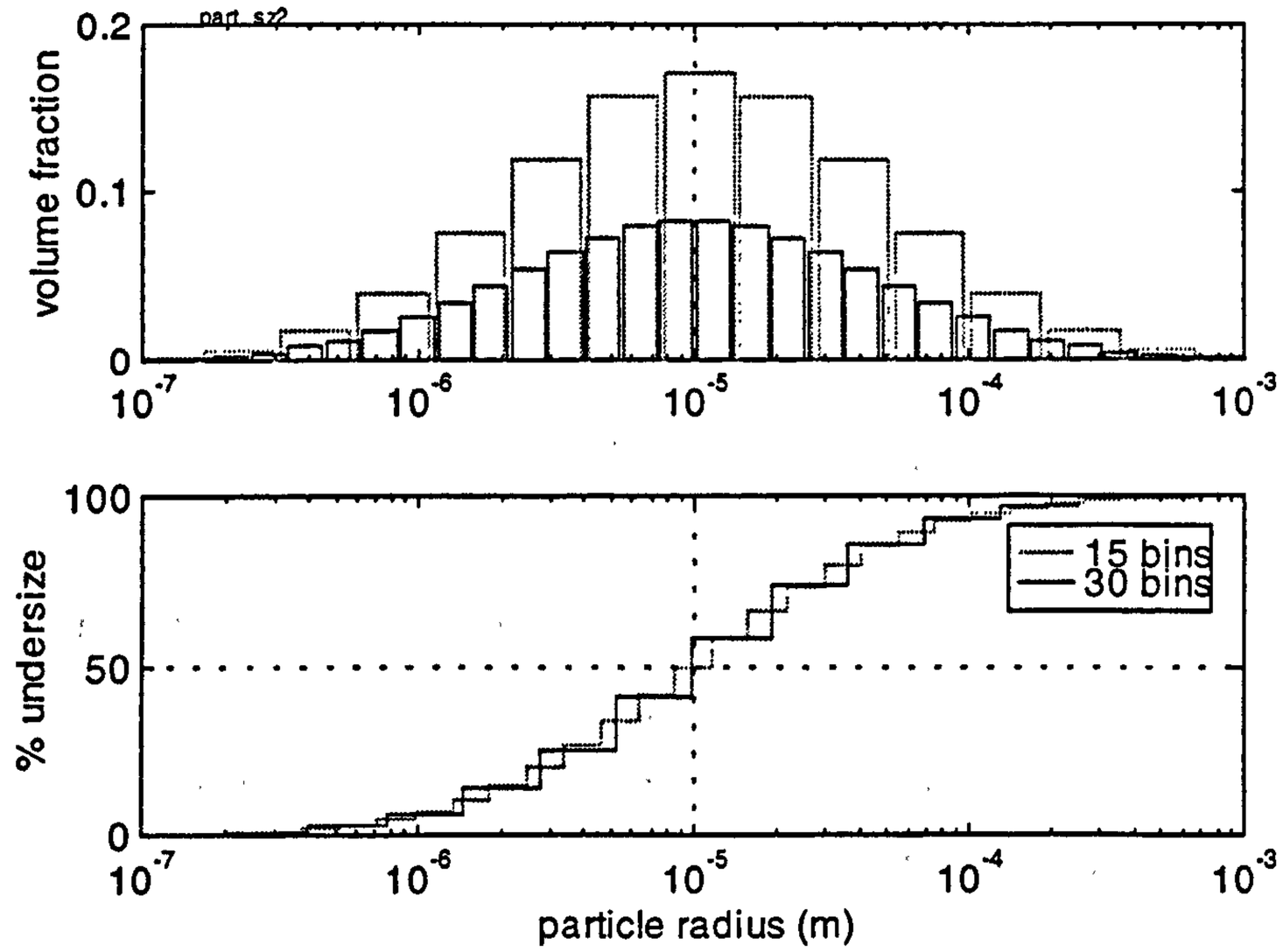

Figure 2-8 A hypothetical PSD evaluated with 15 and 30 size bins (log-normal, with mean 10μm and standard deviation 1.5). Top: the volume fraction scales according to the number of bins. Bottom: the cumulative frequency distribution converges to a single curve as the number of bins increase. Dotted lines demonstrate that the cumulative distribution curves passes through 50% at the mean particle size (10μm).

The volume fraction is used in the theoretical models, while the cumulative distribution is more useful for visual presentation, since the shape and scaling of the curve are insensitive to the number of size bins chosen, and to statistical fluctuations that can make volume fraction distributions appear rather "jagged". The mean size of a distribution may be read off a cumulative distribution curve, by noting the size for which the curve crosses 50%.

A further useful statistic is the Sauter mean radius, a_{32}, which is the ratio of volume to surface area, defined by [142]:

$$a_{32} = \frac{\sum_k n_k a_k^3}{\sum_k n_k a_k^2} \tag{2.28}$$

Where n_k is the **number** fraction (not volume fraction) of particles of size a_k. The Sauter mean radius is biased to higher particle sizes, and is the relevant characteristic size for acoustic predictions in the long wavelength region; i.e. it is a good predictor of the position the viscous-to-inertial transition (demonstrated in section 2.5.2.)

It is useful to have an analytical model of a typical PSD curve, in order to characterise a measured PSD in a few parameters, or else to produce predictions for a hypothetical PSD. Two such models are described below.

Log-normal

The log-normal curve models the volume fraction curve (upper graph in Figure 2-8). It is a normal (Gaussian) distribution when plotted with a logarithmic abscissa.

$$\Phi(a) = \frac{1}{\sigma\sqrt{2\pi}} \exp\left\{ -\frac{1}{2}\left[\frac{1}{\sigma} \log\left(\frac{a}{\overline{a}} \right) \right]^2 \right\} \tag{2.29}$$

where $\overline{a}$ is the mean particle radius, σ is the logarithmic standard deviation, and $\Phi(a)$ is the volume fraction of particles with radius a. This distribution was demonstrated in Figure 2-8.

Rosin Rammler

The Rosin Rammler distribution models the cumulative distribution curve. It was designed specifically to model the distribution that results from grinding a brittle, isotropic substance, [133] and has been found very useful in characterising pulverised fuel [151, 152].

$$\Phi_{cum}(a) = 100\left\{ 1 - \exp\left[-\left(\frac{a}{\overline{a}_{rr}} \right)^{\sigma_{rr}} \right] \right\} \tag{2.30}$$

Here, $\Phi_{cum}(a)$ is the cumulative volume distribution of size a (percentage undersize); $\overline{a}_{rr}$ is a measure of average particle size, known as the "fineness", such that $\Phi_{cum}(\overline{a}_{rr}) = 100[1 - \exp(-1)] = 63.1\%$; σ_{rr} is a measure of spread of the distribution, known as the "dispersion" – high values of σ_{rr} create a narrowly dispersed distribution.

To form a volume fraction curve from the cumulative distribution requires a numerical differentiation; similarly, to form the cumulative distribution from a log-normal volume fraction requires a numerical integration. Numerical scaling constants are required in both operations to account for the finite width of the radius "bins".

Figure 2-9 demonstrates the fit of both models to the measured PSD of alumina powder (tabulated in Appendix F).

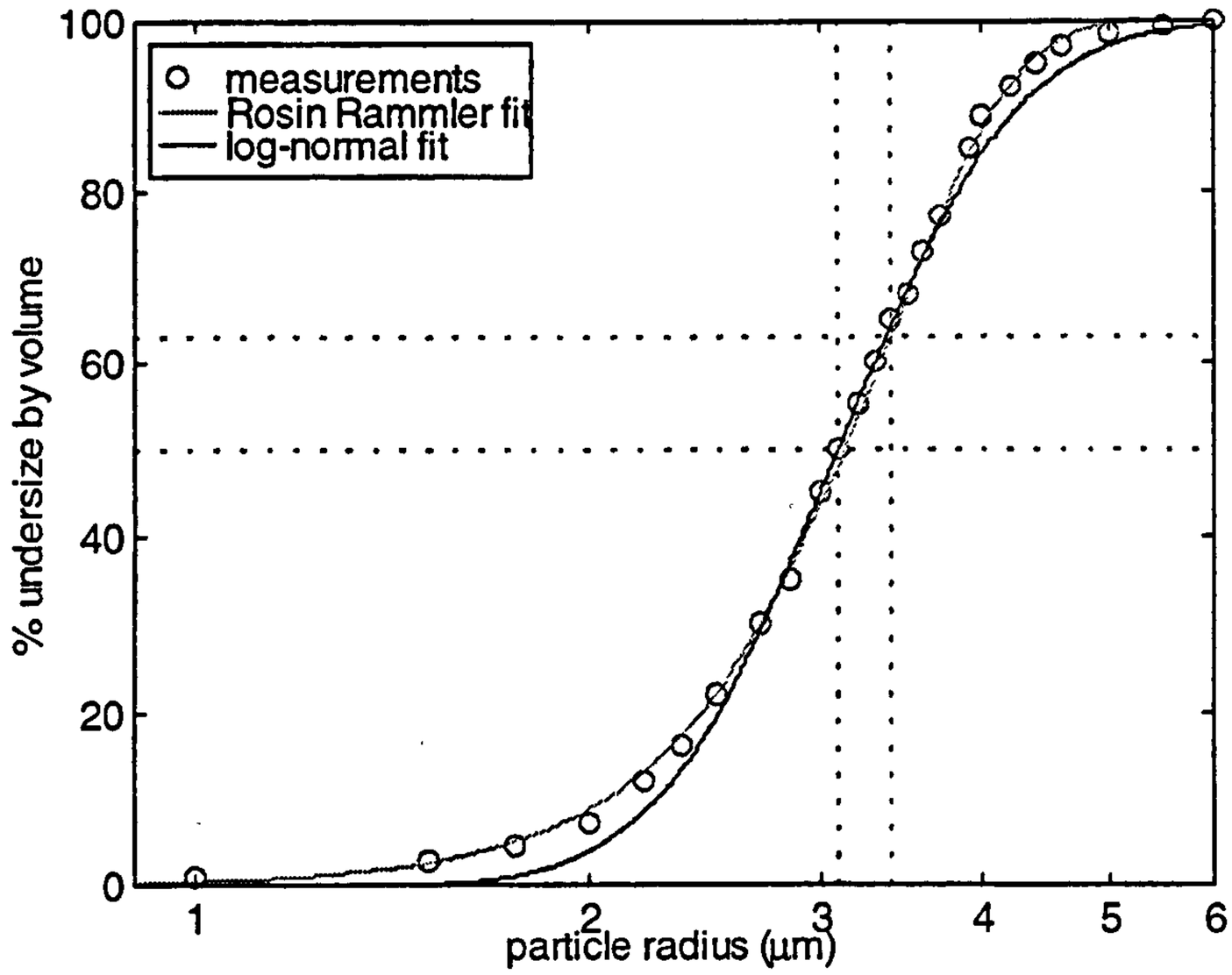

Figure 2-9 Rosin Rammler and log-normal curves, fitting a measured PSD (of grade F800 alumina). Dotted lines show the 63.1% & 50% values, indicating the fineness and mean radius of 3.4 and 3.1 μm respectively. $\sigma = 0.25$, $\sigma_{rr} = 4.5$

Clearly the Rosin Rammler distribution provides a much closer fit to the data than the log-normal curve. This is because real powdered solids tend to be skewed towards smaller particle sizes, especially if larger particles have been screened out by sieving. The Rosin Rammler curve reflects this skew, whereas the log-normal plot is symmetric about the mean size (on a logarithmic axis).

2.5.2 Acoustic effect of PSD variation

It has been stated that variations in the PSD of a suspension, even while maintaining the same mean, will have an acoustic effect. This is demonstrated in Figure 2-10, which shows predicted attenuation parameters for four different log-normal distributions with the same mean radius.

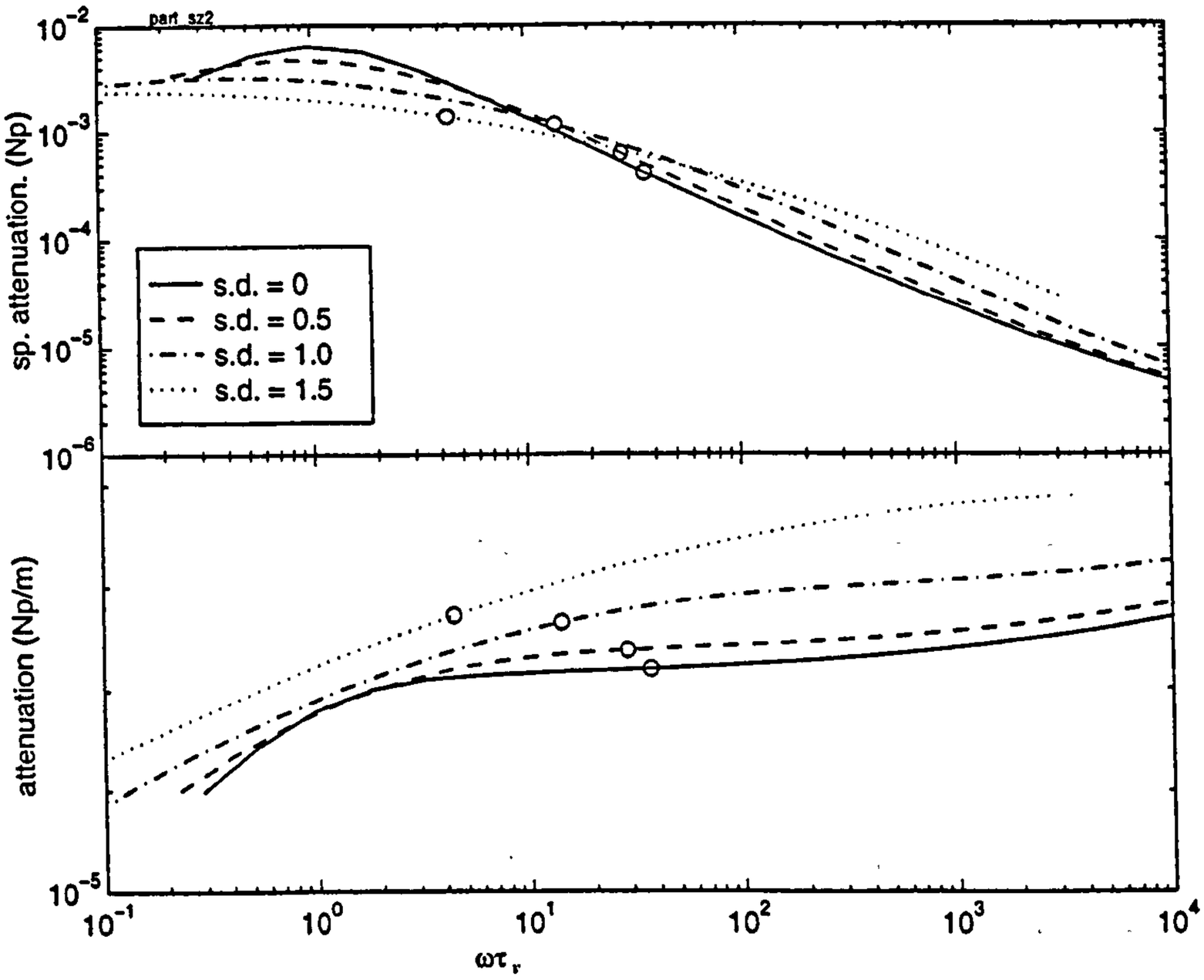

Figure 2-10 *Theoretical specific attenuation (top) and attenuation (bottom) for 4 suspensions with parametrically varied standard deviation σ, plotted against normalised frequency; predictions are for alumina spheres with log-normal distribution, mean radius $\overline{a}$ = 1μm. Circles show values at a single frequency of 1.3kHz. Viscous relaxation period, τ_v, is based on Sauter mean radius a_{32}.*

Increasing the standard deviation of the distribution has the effect of broadening the relaxation peak, and reducing the clarity of the frequency-dependent structure. The peak in the specific attenuation curve remains around $\omega\tau_v = 1$, when τ_v is calculated using the Sauter mean radius of the distribution (equation (2.28)); this justifies the assertion in section 2.5.1 that the Sauter mean radius is the characteristic particle size in the long wavelength regime.

Above the viscous regime, it can be seen that increasing the standard deviation increases the attenuation. This can be explained as follows: the additional smaller particles produce a larger attenuation increment than the decrement due to the additional larger particles (see Figure 2-6); since the log-normal distribution is symmetric about the size axis, the net effect is an increment in attenuation. This effect can be expected to be more pronounced if the model used a Rosin-Rammler distribution, since it is skewed to smaller sizes.

2.5.3 Acoustic determination of PSD

While several experimental studies have measured acoustic effects due to differing particle sizes, few have tried to infer the particle size distribution from acoustic measurements. Three are presented below.

They all rely on a theoretical model, and an iterative solution, using the general form:

$$\alpha(f) = \phi \int_{x_{min}}^{x_{max}} K(f,x) \cdot n(x)\, dx \qquad (2.31)$$

where $\alpha(f)$ is the measured attenuation at frequency f, ϕ is the overall particle concentration, $K(f,x)$ is a kernel function that is based on the theoretical attenuation at f due to a particle defined by its size (area or radius) x, and $n(x)$ is the particle distribution function to be found. The problem of deducing $n(x)$ from a known $\alpha(f)$ is known as a Fredholm integral problem of the first kind, and is well known in mathematics.

By characterising the particle distributions as a sum of monodispersed particles, equation (2.31) may be expressed:

$$\boldsymbol{m} = \phi \boldsymbol{K} \boldsymbol{n}$$

where $\boldsymbol{m}$ is the measurement vector, $\boldsymbol{K}$ is the kernel matrix, and $\boldsymbol{n}$ is the number distribution to be found. Hence, solving for $\boldsymbol{n}$ involves inverting the kernel matrix. This usually leads to numerical instabilities, and several approaches have been used, differing chiefly in the algorithmic solution and the way in which physical constraints (e.g. no negative values of n) are imposed on the solution.

While several different algorithms are used to solve for $n(x)$, the main difference in approach is in the theory used for the kernel function, due to the different acoustic regimes.

Riebel & Löffler

Riebel & Löffler [120] measured ultrasonic attenuation in a suspension of glass beads in water. The frequency range was 1.7 - 81 MHz, and the particle size was 20 - 1000 µm diameter. This corresponds to a *ka* range of:

	20 µm	1000µm
1.7 MHz	0.07	3.2
81 MHz	3.2	153

It appears that the frequency range is chosen such that, for the each particle size of interest, the frequency range encompasses the value $ka = \pi$. Hence the technique appears to be "latching onto" the transition from the ω^4 to the resonant scattering regime. The frequency bandwidth defines the range of particles that may be sized, and the number of frequency points equals the number of particle sizes that may be solved.

They do not try to measure the particle concentration; indeed, they say that the concentration may vary over one decade without seriously affecting the results.

The theoretical foundations are cast in the form of an optical analogy; the measurement is of "ultrasonic extinction", and the distribution is of particle area distribution (not radius); the kernel

function is the relative extinction coefficient, which is based on a theory due to Lamb [82]. An explicit formula is not given, and the assumptions are not clear. The concentration variable is the particle projection area per unit suspension volume. This has the advantage that differing particle shapes may be simply accommodated, by calculating their projection area/volume — a variable that is measurable through microscopic inspection, or theoretically if their shape is well-defined. The kernel function may still have to be measured experimentally to account for different shapes; the relative extinction coefficient is shown to differ by a factor of approx. 2 - 3 between glass beads and polyamide fibres.

Their limited results on near-monodispersed glass beads show that the PSD and concentration may be inferred (although it is not clear if both are calculated for the same dataset). The influence of systematic errors (such as an imperfect kernel function) seems reasonably low for the mean particle size, but higher for concentration & size distribution.

Beckord & Höfelmann

Beckord & Höfelmann [17] measured the attenuation of wideband sound (1kHz - 200kHz) in a monodisperse aerosol contained in a tube (they also measured dispersion, but concluded that the measurement was unreliable due to temperature drift). They describe an inversion technique that uses a kernel function based on Temkin & Dobbins [141]. The algorithm apparently assumes a knowledge of particle concentration, but it might be modified to deduce concentration also. The particle size which was fitted using the given bandwidth is 0.1µm to 10µm. The corresponding values of $\omega\tau_v$ and ka are shown below.

	0.1µm		10µm	
	$\omega\tau_v$	ka	$\omega\tau_v$	ka
1kHz	0.0015	9.2×10^{-7}	15	9.2×10^{-5}
200kHz	0.3	1.8×10^{-4}	3000	1.8×10^{-2}

Clearly the entire regime lies below the scattering region, since $ka << 1$.

The rationale for the choice of frequency or size range is unclear. For a given frequency, the size range spans the point $\omega\tau_d = 1$, hence ensuring that the transition point is included in the range. However, the smallest sizes are not probed by a frequency which reaches $\omega\tau_d = 1$ (remaining in the viscous regime) so it would appear that they could not be inferred correctly.

The algorithm is demonstrated to work for theoretical attenuation curves — i.e. an attenuation curve is generated using the theory for a selected PSD, and the algorithm works backward to solve for

PSD. Calculated PSDs are also shown for 3 measurements using sub-micron size monodispersed aerosols of an un-specified substance; the technique appears to work, but the results shown are limited.

Pendse & Sharma

Pendse & Sharma [110] describe an acoustic spectrometer for measuring attenuation over the frequency range 1 - 100 MHz. They report that the commercial instrument ("Acoustophor") can measure the particle size distribution of submicron slurries with a volume concentration of up to 50%. The kernel function that they used is based on a coupled-phase theory using the high concentration correction factor of Strout [139] – as such, it is limited to the long wavelength regime, and therefore very fine particles. They report promising results for a size range of 0.1 - 10 μm, which produce attenuation measurements of between 0.1 - 1500 dB/cm, thus placing a great demand on the dynamic range of the instrument.

2.6 CHARACTERISTIC IMPEDANCE

The focus so far has been on characterising a suspension by its acoustic propagation parameters; that is, the wavenumber k, which contains information on the attenuation coefficient and the phase velocity. However, a medium can also be characterised by its characteristic impedance. Therefore measurements of impedance might provide an alternative way of gaining information about the suspension.

The characteristic impedance of a medium measures the ratio of sound pressure to resultant particle motion, and is found by:

$$Z = \rho_0 c \tag{2.32}$$

where ρ_0 is the medium density, and c is the sound speed in the medium. For a multiphase system, such as a suspension or porous material, ρ_0 can be replaced by an effective density, ρ. The sound speed in the suspension can be found by:

$$c^2 = \frac{1}{\kappa\rho} \tag{2.33}$$

where κ is the effective adiabatic compressibility. Hence:

$$Z = \sqrt{\frac{\rho}{\kappa}} \tag{2.34}$$

Both scattering theory and coupled-phase theory can be used to calculate κ and ρ. Scattering theory is used here for consistency with other predictions. Modifying McClements' expressions [92] (valid in the long wavelength limit) to account for a particle size distribution gives:

$$\kappa = \kappa_f \mathrm{Re}\left(1 - 3i\phi_v \sum_j \frac{\Phi_j A_{0j}}{k_f^3 a_j^3}\right) \tag{2.35}$$

$$\rho = \rho_f \mathrm{Re}\left(1 - 9i\phi_v \sum_j \frac{\Phi_j A_{1j}}{k_f^3 a_j^3}\right) \tag{2.36}$$

By substituting Equations (2.35) & (2.36) into (2.34), we are now in a position to predict the characteristic impedance for a given suspension, as a function of frequency.

A measurement technique that relies on changes in characteristic impedance will be introduced in Appendix A.

2.7 EFFECTS OF FLOW

The theories presented in this chapter assume that there is no mean flow in the medium. In this work, however, the theories will be applied to flowing suspensions. The effect of the flow is assessed below.

To ensure validity of the theories, it is necessary to take the suspension as the stationary frame of reference, with a moving acoustic souce and receiver. Their relative motion creates a Doppler shift, dependent on the component of suspension velocity along the acoustic path.

Suppose the suspension velocity is v, and the sound path is axially downstream (the configuration used in Chapter 6). A transmitted frequency f_s then is reduced to f in the suspension, which is found [183] by assuming the source is receding at a velocity of $v_s = v$:

$$f = f_s\left(\frac{1}{1 + v_s/c}\right) \tag{2.37}$$

The received frequency is the same as that transmitted, since there is no relative motion between them: alternatively, the observer is approaching at $v_0 = v$ relative to the moving medium, and so the observed frequency f_0 is given by [183]:

$$f_o = f\left(1 + \frac{v_o}{c}\right) = f_s \tag{2.38}$$

Therefore, for the predictions to be strictly applicable on moving suspensions, the frequency axis should be corrected by the amount shown in (2.37). The predictions in this thesis are applied to suspensions flowing at 20 m/s. Where sound propagation is along the line of flow – giving the maximum Doppler shift – the reduction in frequency is 6%. For propagation perpendicular to the flow, no Doppler shift is predicted (although the turbulent motion of the flow could be expected to cause slight broadening of spectral lines).

This small effect of flow was ignored in all the predictions in this work.

2.8 CONCLUSIONS

A survey of scattering and coupled-phase theories has been presented. A multiple scattering theory (a long wavelength approximation of Lloyd & Berry [85, 93]) has been chosen for predictions in this work, due to its inclusion of both thermal and viscous effects, and extensibility to higher frequencies. No coupled phase theory is valid above the long wavelength limit. There is very little difference between predictions of coupled-phase theories (that include thermal losses), single scattering, and multiple scattering theories for the case of solid particles in air, in the long wavelength regime. The predictions diverge at high frequencies, high concentrations, and in some special cases depending on the material parameters of the two phases.

Acoustic effects pass through four different regimes in which different mechanisms dominate: viscous, inertial, Rayleigh scattering and resonant scattering. In the first two regimes, lossy visco-thermal mechanisms dominate; in the latter two regimes, geometrical scattering dominates, reducing the amplitude of the transmitted wave by scattering in all directions rather than by absorption. The regimes have their own characteristic scaling exponents, in terms of f or a (except for the resonant scattering regime, which has complex structure). In the frequency domain, the transitions between regimes provide structure to the curves. This structure may be used to deduce both the particle size distribution, and the concentration, given measurements across a frequency range that encompasses a transition between regimes. Measurements at a single frequency, or across a frequency range that lies within a single scaling regime, will not be able to resolve the ambiguity between a and ϕ.

3

LITERATURE REVIEW: EXPERIMENTAL WORK & METHODS

This chapter has four sections:

- Section 3.1 reviews past measurements of the acoustic properties of aerosols, covering the range from small-scale, quasi-static suspensions, to large-scale flowing suspensions.
- To set this work into the context of two-phase flow measurement techniques, in section 3.2 a variety of alternative in-line instruments are reviewed, predominantly non-acoustically based.
- Section 3.3 reviews the literature that is relevant to the experimental techniques that are used in this work.
- Since some experimental work is conducted on flowing suspensions, Section 3.4 reviews the reported physical and acoustic effects of ducted flow.

3.1 MEASUREMENTS OF THE ACOUSTIC PROPERTIES OF AEROSOLS

3.1.1 Laboratory scale, quasi-static suspensions

Acoustic studies of two-phase systems have concentrated on propagation of ultrasound through liquid/solid (slurries) and liquid/liquid media (emulsions). As the scatterers are usually quite large, and the ultrasonic wavelength is small, the size of the scatterers can be comparable to or larger than the acoustic wavelength, and so non-dissipative scattering is the dominant mode of loss.

There have been relatively few studies of the acoustic properties of gas/solid media (aerosols), possibly because it is more difficult to create a controlled and stable aerosol. This section will review the work that has been conducted on laboratory scale equipment, usually with quasi-static aerosols. The following section describes some relevant measurements of acoustic parameters in a non-intrusive way on large flow rigs.

Laidler & Richardson (1938)

Laidler & Richardson [81] measured ultrasonic attenuation in "smokes" of lycopodium and stearic acid at 42, 98 and 695 kHz. They used an ingenious device (a Pierce interferometer) that consisted of a quartz crystal radiating into a small box (70 × 70 × 120 mm) that was filled with recirculating aerosol. The pressure wave reflected off an opposite face, and impinged back on the crystal. The

reaction force of the reflected wave altered the supply current to the driving oscillator; by moving the reflector to create a series of reaction dips, the rate of change of dip amplitude with distance could be used to infer the attenuation coefficient of the transmission medium.

The measurements were compared with predictions calculated according to Sewell's theory, in which the particles are assumed stationary and thermal effects ignored [129]; although at these high frequencies such an approximation is more justified than at audio frequencies, the theory underestimated the frequency-dependence of the attenuation coefficient.

Knudsen *et al* (1948)

Knudsen *et al* [76] measured the sound decay rate in a reverberation chamber that was filled successively with water fog, oil fog and ammonium chloride smoke. They compared one set of results quantitatively with values predicted by a simple theoretical formulation and achieved remarkably good agreement (20 - 30 % error).

Zink and Delsasso (1958)

In a much cited paper (based on Zink's doctoral thesis [165]), Zink & Delsasso [166] measured attenuation and sound velocity change through alumina particles suspended in various gases. They were among the first to measure the sound velocity change (dispersion), and develop an expression to predict it. The expression included only the effects of increased heat capacity and density due to the particles. The attenuation was predicted by summing the expressions that Epstein and Carhart derived for viscous and thermal losses [40]. The apparatus consisted of a rotating horizontal tube (200mm diameter × 1.7m), in which alumina particles were suspended by virtue of the rotary motion of the tube. The ends of the tube were sealed with a mylar membrane, and a burst of sine waves was transmitted through the tube by externally mounted transducers. The received signal was displayed on an oscilloscope, from which the attenuation and time delay were measured. The particle concentration was measured by counting from a photomicrograph of settled particles, and the particle size distribution was modelled as the sum of four monodisperse distributions (5, 7.5, 10, 15μm diameters). Results are reported for four suspending gases: air, oxygen, argon and helium. Measurements were made at single frequencies over a range of 500 - 13600 Hz.

Uncertainty surrounds the acoustic arrangement, in which the plane wave parameters were deduced from signals radiating from an enclosure in which both longitudinal and transverse modes existed. The effect of transverse modes was "filtered out" by measuring the sound pressure at some distance from the end of the tube, with the reasoning that the pressure distribution across the vibrating membrane will sum to zero at a distance.

Despite the poorly-controlled acoustic environment, the measured results (Figure 3-1) agreed quite closely with the theory that was presented. In general, all measurements of attenuation were higher

than predicted, and dispersion was lower than predicted. The reported data have been used for comparison with several later theoretical predictions [141].

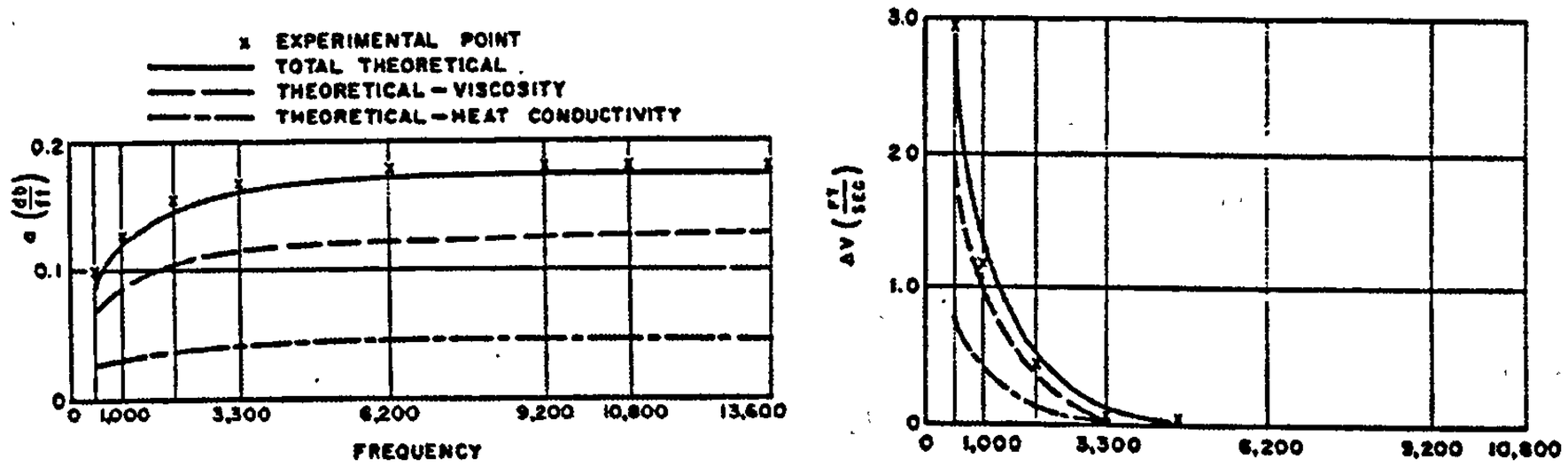

Figure 3-1 Attenuation (left) and change in sound velocity (right) of alumina particles in air. Reproduced from Zink [165]

Temkin & Dobbins (1966)

In a classic paper, Temkin & Dobbins [142] measured the attenuation and dispersion of an aerosol of oleic acid in nitrogen, using a modified standing wave apparatus. The aerosol was generated by condensing a hot vapour of oleic acid (which is liquid at room temperature) around solid nuclei; the phase of the particles is therefore a little uncertain, although they were treated as solid particles, and their material parameters were drawn from those of oleic acid. The particle size was controlled by varying the parameters of the aerosol generator (i.e. temperature and nuclei generation rate), and varied between mean diameters of 0.8 to 4.7 μm. The concentration was measured with an optical scattering photometer.

The suspension filled a standing-wave tube, in which pressure minima and maxima were ascertained using a travelling probe attached to a micrometer screw. Attenuation and sound speed were calculated at single frequencies using the standing wave ratio and spacing of the minima, in the usual way [8].

To cover the frequency range 1000 – 9450 Hz, two tubes were used: 44.5mm diameter × 1m for low frequencies, and 9.5mm × 400mm for the higher frequencies. The probe had a diameter of 3mm, therefore accounting for 10% of the cross-sectional area of the smaller tube; it should be noted that the A.S.T.M. [8] recommend that probes should account for less than 5% of the tube area, and so may cast doubt on the accuracy of measurements using the smaller tube.

Nonetheless, the measurements (Figure 3-2) were extremely consistent, and generally confirmed their relaxation theory. The dispersion, especially, matched theoretical predictions well, while the measured specific attenuation was lower than predicted (by about 10%) above the relaxation frequency. In particular, this was the first study to have clearly confirmed the predicted existence of a maximum in specific attenuation, at the relaxation frequency, and a low frequency maximum of dispersion. This was possible due to the low particle density (895 kg/m^3), and very small particle size that could be generated; most other studies have operated well above the relaxation frequency.

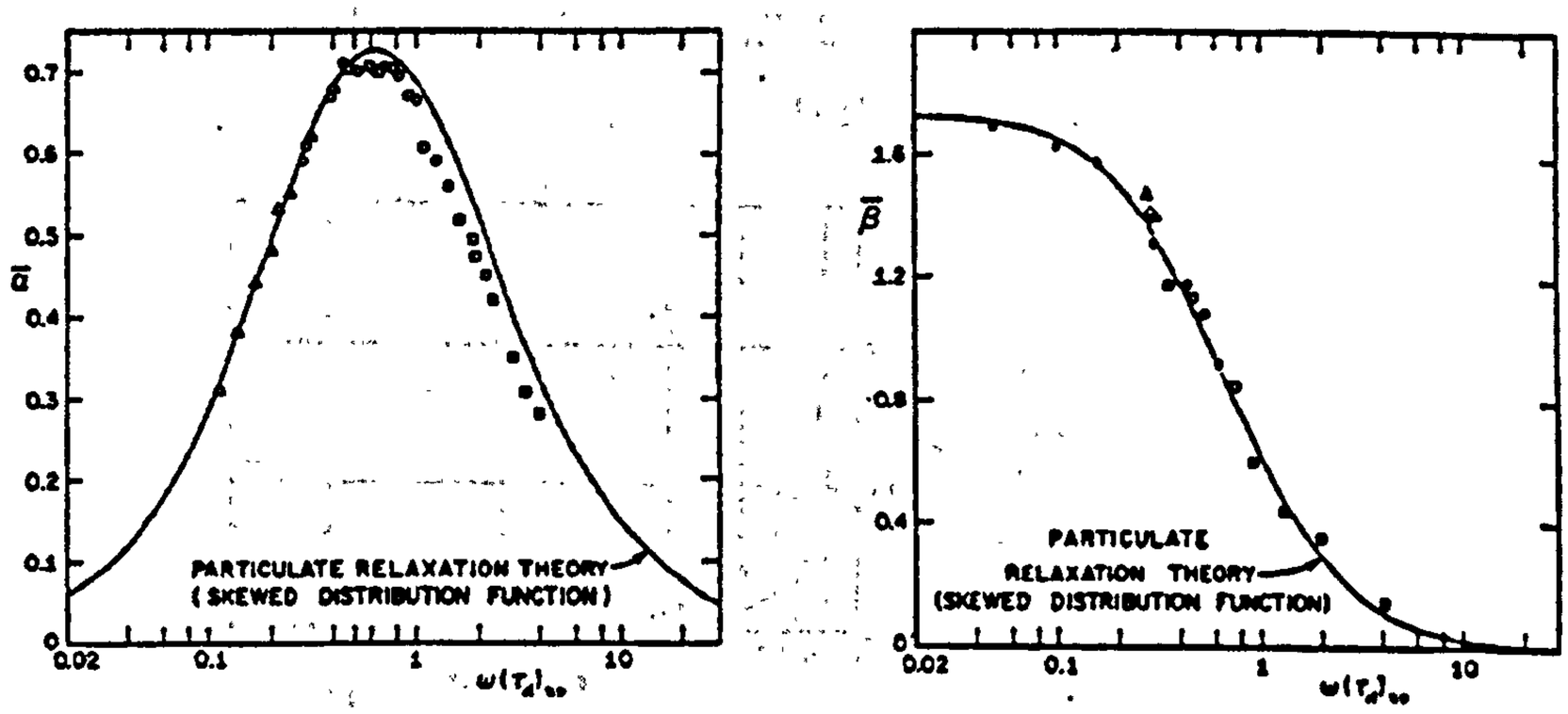

Figure 3-2 Specific attenuation (left) and dispersion (right) of oleic acid particles in nitrogen. Δ: 4900 Hz. O: 6400 Hz. □: 9450 Hz. Reproduced from Temkin & Dobbins [142].

Steen (1986)

Steen [138] built an "acoustical particle monitor" that, unusually, measured the sound speed dispersion of an aerosol to deduce its concentration. To remove errors due to the temperature dependance of sound speed, he transmitted tone bursts of two frequencies (5 and 40 kHz) and measured the relative phase difference between them. This pair of frequencies appears to be chosen to produce a maximum phase difference for a particle size of 2μm; dispersion is almost at its low frequency maximum at 5kHz , and almost zero at 40kHz. The method of measuring small phase differences was unstated, although it involved amplitude-limiting the sinusoids to produce square waves, thus enabling either a visual inspection or use of a phase comparator circuit. He calculated the concentration required to produce a given phase shift using the theory of Mednikov [97].

An aerosol of talc was injected into either a 0.4 m^3 box or a 1.5 m long tube. The particle size distribution was measured with an impactor, although the particles were only described as being under 7μm. Limited results were reported, although it was stated that the device produced linear phase shifts up to a concentration of several g/m^3, and had a sensitivity of about 10 mg/m^3.

Höfelmann & Beckord (1990)

Höfelmann & Beckord [60] measured the transmission loss of an unspecified aerosol in a narrow tube using a swept sine signal from 1kHz to 100kHz. The particles were generated by a monodisperse aerosol generator, and had a diameter of 2μm. The received signal was demodulated by multiplying it by an analytical (complex) version of the transmitted signal, and processed to yield the attenuation (the phase velocity was too temperature sensitive to be useful).

In a later paper [17], Beckord *et al* use an inversion technique to reconstruct the particle size distribution of the aerosol in the range 0.1 - 10 μm (as discussed in Chapter 2).

3.1.2 Large scale, flowing suspensions

Experimental measurements on dense pneumatic flows require large scale, specialised equipment, and so have been restricted to a few sites.

Hamade (1982)

For his doctorate, Hamade [55] built a large-scale test facility based on the experiences of BCURA and ANL (see the following section). This consisted of a recirculating loop, made of 300mm diameter pipe with a total length of 20.4 m. The test material was pulverised coal (with various distributions and compositions), suspended in nitrogen to reduce the chance of ignition. The suspension density was varied between 0 - 3 kg/kg, according to the weight of material that was added at the start of the experiment.

He measured ultrasonic attenuation of tone bursts at 459 kHz diametrically across the flow, using a pair of lead zirconate titanate (PZT) transducers. This frequency was chosen to give a wavelength of 10× the mean particle diameter (80% particles < 75μm), based on the incorrect assumption that significant attenuation would only occur when the wavenumber was comparable with the particle size.

The high frequency – and consequent narrow beam-width – gave problems with beam drift due to flow (the receiving transducer was moved according to flow speed), and losses due to gas turbulence, which were not easily predictable or understandable. The high frequency gave additional problems due to excessive attenuation at high particle loadings. Comparisons of these measurements with theory were made, but agreement was fairly poor. The results were further reported in reference [84].

The other major problem was the degradation of particles during an experiment, caused, presumably, by particle impact on the fan blades, as well as on each other and on the pipeline walls at bends. This led to time-varying acoustic measurements during the course of an experiment (see Figure 3-3)

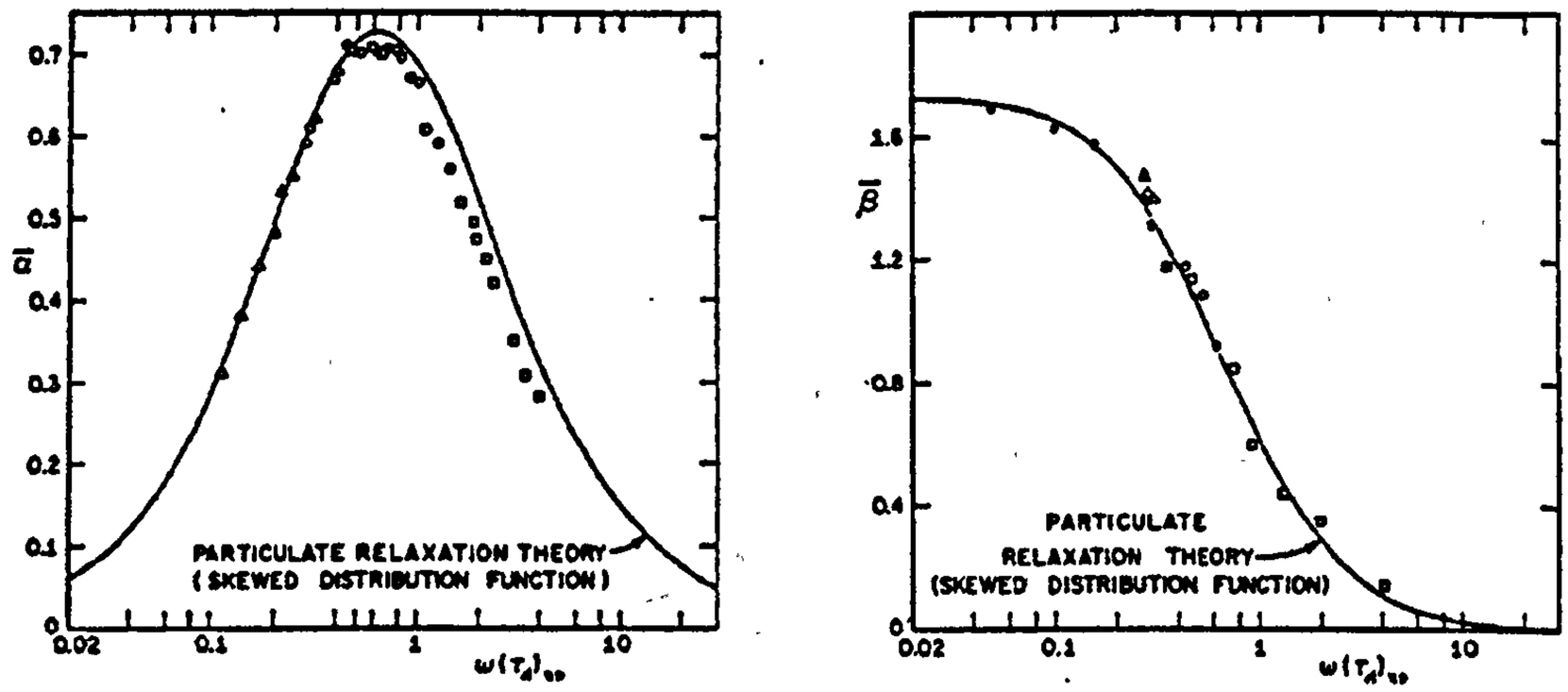

Figure 3-2 Specific attenuation (left) and dispersion (right) of oleic acid particles in nitrogen. Δ: 4900 Hz. O: 6400 Hz. □: 9450 Hz. Reproduced from Temkin & Dobbins [142].

Steen (1986)

Steen [138] built an "acoustical particle monitor" that, unusually, measured the sound speed dispersion of an aerosol to deduce its concentration. To remove errors due to the temperature dependance of sound speed, he transmitted tone bursts of two frequencies (5 and 40 kHz) and measured the relative phase difference between them. This pair of frequencies appears to be chosen to produce a maximum phase difference for a particle size of 2μm; dispersion is almost at its low frequency maximum at 5kHz , and almost zero at 40kHz. The method of measuring small phase differences was unstated, although it involved amplitude-limiting the sinusoids to produce square waves, thus enabling either a visual inspection or use of a phase comparator circuit. He calculated the concentration required to produce a given phase shift using the theory of Mednikov [97].

An aerosol of talc was injected into either a 0.4 m^3 box or a 1.5 m long tube. The particle size distribution was measured with an impactor, although the particles were only described as being under 7μm. Limited results were reported, although it was stated that the device produced linear phase shifts up to a concentration of several g/m^3, and had a sensitivity of about 10 mg/m^3.

Höfelmann & Beckord (1990)

Höfelmann & Beckord [60] measured the transmission loss of an unspecified aerosol in a narrow tube using a swept sine signal from 1kHz to 100kHz. The particles were generated by a monodisperse aerosol generator, and had a diameter of 2μm. The received signal was demodulated by multiplying it by an analytical (complex) version of the transmitted signal, and processed to yield the attenuation (the phase velocity was too temperature sensitive to be useful).

In a later paper [17], Beckord *et al* use an inversion technique to reconstruct the particle size distribution of the aerosol in the range 0.1 - 10 μm (as discussed in Chapter 2).

3.1.2 Large scale, flowing suspensions

Experimental measurements on dense pneumatic flows require large scale, specialised equipment, and so have been restricted to a few sites.

Hamade (1982)

For his doctorate, Hamade [55] built a large-scale test facility based on the experiences of BCURA and ANL (see the following section). This consisted of a recirculating loop, made of 300mm diameter pipe with a total length of 20.4 m. The test material was pulverised coal (with various distributions and compositions), suspended in nitrogen to reduce the chance of ignition. The suspension density was varied between 0 – 3 kg/kg, according to the weight of material that was added at the start of the experiment.

He measured ultrasonic attenuation of tone bursts at 459 kHz diametrically across the flow, using a pair of lead zirconate titanate (PZT) transducers. This frequency was chosen to give a wavelength of 10× the mean particle diameter (80% particles < 75μm), based on the incorrect assumption that significant attenuation would only occur when the wavenumber was comparable with the particle size.

The high frequency – and consequent narrow beam-width – gave problems with beam drift due to flow (the receiving transducer was moved according to flow speed), and losses due to gas turbulence, which were not easily predictable or understandable. The high frequency gave additional problems due to excessive attenuation at high particle loadings. Comparisons of these measurements with theory were made, but agreement was fairly poor. The results were further reported in reference [84].

The other major problem was the degradation of particles during an experiment, caused, presumably, by particle impact on the fan blades, as well as on each other and on the pipeline walls at bends. This led to time-varying acoustic measurements during the course of an experiment (see Figure 3-3)

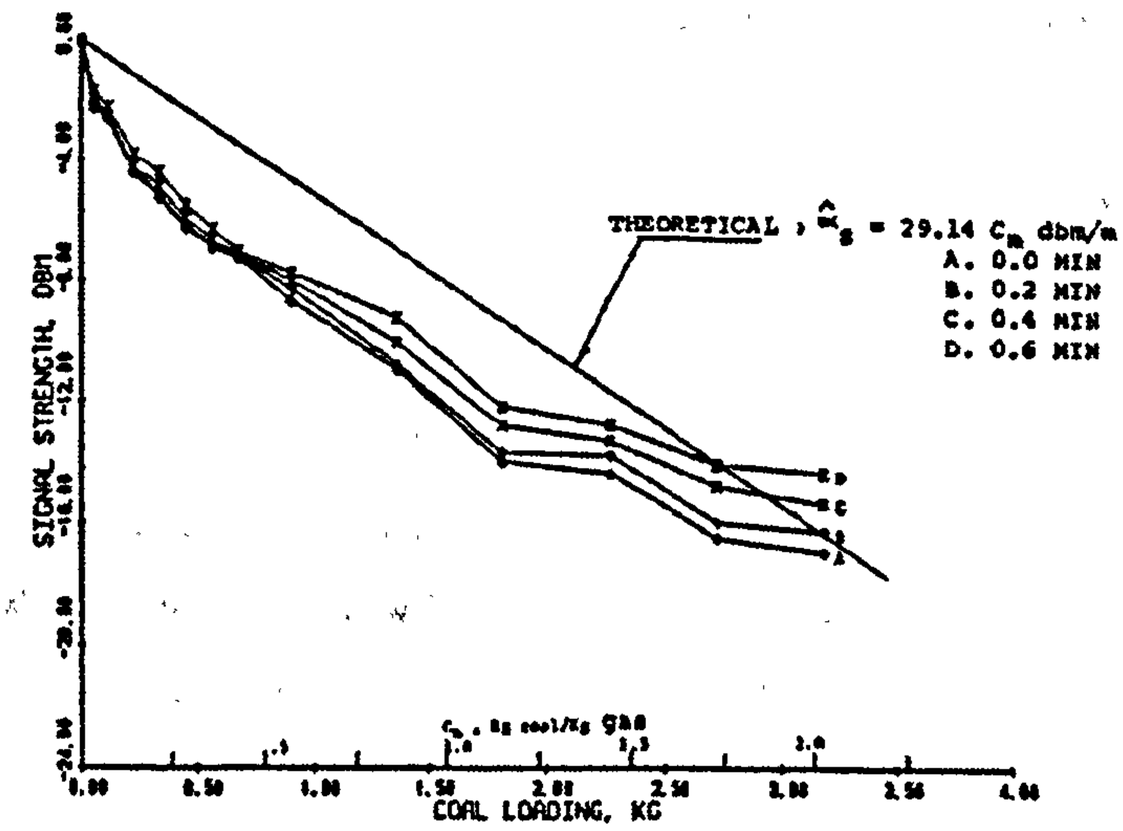

Figure 3-3 Received signal strength as a function of time and coal mass concentration, for an unspecified coal grade. Reproduced from Hamade [55].

Commonwealth Scientific and Industrial Research Organisation (CSIRO) (1991-6)

The recirculating loop at CSIRO is similar to that built by Hamade, consisting of 310mm diameter pipe with 20 m length.

Following some experience with nuclear and microwave techniques, Sowerby *et al* [136] tested an ultrasonic device similar to that of Hamade, but at the lower frequency of 215kHz. The reason for this choice of frequency is not clear: the reduced frequency apparently increases beam-width sufficiently to eliminate the need to move the receiver to account for beam-drift, but effects due to turbulence are still significant, and require correction. They used two pairs of PZT transducers: a directly opposed pair to measure attenuation, and a pair inclined at 45° to measure air velocity using the contrapropagating time-of-flight method [87]. The transducers were mounted flush with the inside of the tube, and protected by soft rubber faces.

In the first paper [136], measurements of ultrasonic attenuation were correlated with measurements of beta-particle absorption that were supplied by a reference device. Unspecified corrections were made to the acoustic measurements to account for turbulence and temperature. Glass beads (of unspecified size) were used as the test material, at a concentration of 0.1 - 1 kg/kg. At a constant air velocity of 22.5m/s, the mean relative error was 5%, rising to 8% when the velocity was allowed to vary between 22.5 - 32.5 m/s.

No comparison with theory was attempted and attenuation measurements were not reported: this is unfortunate, since it is the only such study of a substance as well-characterised as glass beads.

The second paper (Abernethy *et al* [2]) relates the trial of this equipment on the burner feed pipe (diameter 500mm) of a power station. The acoustic absorption data was again correlated against the beta absorption reference. The mean relative error was estimated at 4%, for concentrations between 0.25 - 0.75 kg/kg.

This study is important because it shows the feasibility of the acoustic technique. Its weakness is the lack of a theoretical basis; in particular, the possible effect due to changes in particle size distribution is not well addressed. Nevertheless, they predict a change of 7% in the indicated concentration due to a change in p.s.d. that is typical of that caused by mill wear (from 75% to 40% of particles < 75μm). The basis of this prediction is unstated; my own calculations[1] predict a change of 160%, which is clearly a significant shift that should be considered.

It is also unfortunate that the method of turbulence compensation is not described. It seems to be an empirical correlation that uses knowledge of the flow velocity to apply a correcting factor. Since the accuracy of the device deteriorates when the velocity is varied, it is possible that the turbulence compensation is not well-characterised over a range of flows.

Tallon & Davies (1996)

Tallon & Davies [140] made audio frequency measurements in an open-circuit flow rig (74mm diameter). They measured the variation of background noise and introduced continuous sine waves in sand flowing between 15 - 35 m/s. The sand had a mean diameter of 155μm, (log-normal standard deviation of approx. 0.19), and a mass concentration of up to 5 kg/kg. Measurements were made in both horizontal and vertical pipe sections. The received signal level was measured by digitally filtering the continuous signal into 3 frequency bands, between 200 - 1050 Hz; the narrow band signal level was then correlated with the solids concentration. This bandwidth lies below the cut-on frequency of the first transverse mode of the pipe, and therefore sound was assumed to propagate as plane waves.

The narrow-band level of background noise exhibited a reasonable negative correlation with volume concentration, presumably due to attenuation due to the sand. There was, however, much point scatter at zero loading which was attributed to "resonance" caused by reflections from the air blower; the effect of these reflections was attenuated when particles were present.

Measurements of attenuation coefficient were made by transmitting a continuous low-level signal into the pipe, and detecting the signal 3m further downstream. The data was rather less clear. Attenuation along the vertical pipe segment showed a roughly linearly-increasing trend with concentration. Attenuation over the horizontal section was negligible, which they explained by gravitational settling of the sand causing a concentration gradient, thus leaving a clean air path to "short-circuit" the attenuating path. Scatter at zero loading was again attributed to end reflections — the inherent problem of using continuous excitation.

No comparison with theory was made. Generally, the particle size was too large to produce significant attenuation. It is not clear why the measurements of background noise show up to 30 dB

[1] Assume a Rosin Rammler distribution with a typical dispersion parameter of 0.8 [152], and a fineness parameter increasing from 50 to 170μm (giving the required change in <75μm percentage). The long wavelength approximation of Lloyd & Berry [93] was used for the prediction.

attenuation (compared to clean air) when predictions according to Lloyd & Berry predict a maximum of 5dB over the 15m path length.

This paper represents the first published audio-frequency investigation of flowing particulates in a large scale facility.

3.2 OTHER IN-LINE MEASUREMENTS OF AEROSOL FLOWS

This section will briefly review the types of devices and techniques that can measure aerosol properties in-line and non-intrusively; that is, devices that measure parameters in the pipeline without intruding into the flow, or requiring severe alterations to the flow pipework, and that operate in real-time. Except for ultrasonic time-of-flight flowmeters, all such acoustic techniques have been reviewed in the previous section.

The three basic parameters of interest in metering aerosol flows are:

- solid mass concentration (kg/kg)
- solid mass flow rate (kg/s)
- flow velocity of solid or gas phase (m/s)

There is additional interest in measuring the particle size distribution and particle composition but these topics are not addressed here.

Some references are given to general review papers that survey the use of each particular device.

3.2.1 Mass concentration

The literature reports the following techniques (both experimental and industry-proven) for measuring mass concentration in aerosol flows:

Ionising-radiation attenuation

All these devices work by measuring the attenuation of a beam of radiation or energetic particles passing through the flowing medium. Methods that have been tried include: beta-particles, neutrons, gamma rays and X-rays. The absorption depends on the atomic weight of the particulate [107] and so measurements are sensitive to changes in particle composition and moisture – indeed, they have been used to detect such changes [74]. All these methods tend to be unpopular on safety grounds since they require a radioactive source. In addition, radionucleotide particles require a window at the entry and exit points of the beam, which must be thin to prevent excessive absorption by the window; this is susceptible to wear by the flow [136, 111, 63].

Such sensors, after calibration off-line, have been used as references for comparison with other devices [2, 136].

Non-ionising radiation

While working on the same principle as ionising radiation, other devices use a more benign form of radiation: principally microwaves [63, 109, 74] and light [109,74]. (Acoustic methods also fall into this category). The necessity for a transparent window renders optical methods impractical for all but research purposes. Microwave methods require a non-conducting window, or antennae mounted within the tube.

Capacitance transducers

The dielectric constant of the flow will vary according to the concentration of suspended solid, and the dielectric constant of the solid. Capacitative transducers work by creating a capacitor around the flow, and detecting the change in capacitance due to change in the dielectric constant [156, 158]. A portion of the pipeline is divided into annular segments, electrically insulated from each other, and therefore forming the plates of the capacitor, with the interior of the pipe acting as the dielectric. The capacitance of the sensor can then be correlated with the mass concentration of the flow. This technique works best at relatively high concentrations (> 2kg/kg [159]), above those normally encountered in P.F. feed systems.

Electrostatic (Triboelectic) transducers

Flowing particles tend to become electrostatically charged. This charge can be detected if the particle collides with, or passes nearby, an electrode, thereby inducing a current. This current is a function of the particle concentration and velocity, as well as of many particle parameters (size, density, conductivity, permittivity), gaseous humidity and the pipe dimensions. Nonetheless, the principle has been used successfully down to very low concentrations (2×10^{-9} kg/m^3) [158]. Physically, the sensor is often similar to a single "plate" of the capacitative transducer; that is, an annular insulated segment.

3.2.2 Flow velocity

Most measurements of mass flow rate rely on multiplying separate measurements of mass concentration and flow velocity. For this to be accurate, either the particle velocity must be measured, or the particle velocity deduced from the gas velocity by making assumptions about the relative slippage between the two phases. The following techniques have been identified:

Cross-correlation (particle velocity)

Two mass concentration transducers (of any high-bandwidth type) are placed in the flow pipe, axially separated by a known distance. The inherent fluctuations of mass concentration will modulate the steady-state output of both transducers, but there will be a time delay between the signals, as the time-of-flight of any fluctuation propagates from the upstream to the downstream sensor. The real-time cross-correlation of the two signals should therefore show a peak at a time

delay corresponding to the time-of-flight, from which the average particle velocity can be calculated. A high velocity resolution will require high bandwidth sensors.

This technique has been tested widely, and has the advantage that it requires little more hardware other than a duplication of the mass concentration sensor. Indeed, a concentration sensor is not required; any local signal that is modulated by the flow can be used [130].

Doppler measurements (particle velocity)

A beam of radiation is emitted into the flow tube, angled into the flow; a portion of the radiation will be back-scattered from the moving particles, and hence its frequency is Doppler shifted. This radiation is mixed with the original signal to produce a Doppler spectrum that contains information about the spectrum of particle velocities (in the direction of the beam). While this technique has been applied successfully in liquid/solid flows, its use in aerosol flows has been limited by practicalities. Laser Doppler Velocimeters (L.D.V.) have been used for experimental studies [158, 145, 77], but the requirement for an optically transparent window limits their use in practical flows. Preliminary trials with a microwave device have also been reported [63].

Ultrasonic time-of-flight (air velocity)

The propagation velocity of an acoustic signal in a flowing medium will be modified by the speed of the flow. If the speed of propagation is measured both up- and down-stream, then both the speed of flow, and the inherent sound speed in the (static) medium can be calculated. This is the basis of the well-known contrapropagating time-of-flight meter, in which two transducers transmit at an angle to the flow, acting alternately as transmitter and receiver. Ultrasonic signals are almost always used to provide high resolution (for a good review see Lynnworth [87]). The technique has been used widely in single phase flow, but is also becoming accepted in aerosol flow [107,136]

Particle / gas slip ratio

If the particle velocity is to be inferred by measuring the gas velocity, then some knowledge is required of the relative slip of the two phases. In general, for the particles to be conveyed in the air flow, their velocity will be lower than that of the air. However, for small particles, the velocity difference can be negligible. Some work on the percentage slip has been reported. Parkinson & Hiorns [108] stated that for particles under 50μm diameter, the velocity difference is under 1%; and for a typical P.F., the particle velocity can be assumed to be 98.5% of the gas velocity. Kolansky *et al* [77] used a L.D.V. and a hot-film anemometer to measure the particle and gas velocities respectively across a flow of glass beads (36μm diameter). They found negligible slip in the core of the flow, increasing to around 8% slip near the tube wall.

Woodhead *et al* [161] also used a L.D.V. to measure the velocity of particles (mean size 60 μm), and found the velocity difference to be less than 2% (indiscernible difference within the accuracy of the

instrument). Abernethy *et al* [1] compared velocity data from a cross-correlation measurement (based on beta-ray absorption) with an ultrasonic time-of-flight gauge, and concluded that the slip velocity was less than 2m/s between a flow speed of 23 to 32 m/s . Tsuji & Morikawa [145] used an L.D.V. to measure the particle and air velocity in a flow of large (>200μm) plastic pellets. The air velocity was measured by seeding the flow with a "smoke" of fine particles (0.5μm); they therefore assume that the slip velocity between the air and "smoke" particles is negligible.

3.2.3 Mass flow rate

Almost all measurements of mass flow rate are derived from knowledge of mass concentration and particle velocity. An exception is the coriolis flow meter, which works by inserting a U-shaped pipe segment into the pipework [74]. The Coriolis force causes a twisting moment in the pipe, which can be measured and related directly to the mass flow rate. However, the contorted flow path will induce additional pipe wear and pressure drop, and so the technique can be considered intrusive.

3.2.4 Mass concentration profile

So far, reference to mass concentration has been implicitly to a mean across the pipe diameter. As the solid phase is very much more dense than the conveying gas, gravitational force will exert an important influence on the behaviour of the suspension. Similarly the inertia of the particulate phase means that a change in direction of the pipe can lead to complex behaviour following the bend, such as "roping flow" — in which a thin, high density "rope" forms in the tube — and maybe even settling-out. Some work has investigated how the concentration varies across the pipe section, in dependence upon the orientation of the pipe and proximity to bends.

Soo *et al* [135] used a LDV and electrostatic probe to measure the velocity and concentration of 100μm glass beads in a 51mm pipe. In a vertical pipe, the particle density profile followed a similar curve to air velocity distribution; while a horizontal pipe produced an asymmetrical profile with much higher density towards the bottom of the pipe.

McCluskey *et al* [95] designed an optical apparatus to visualise the flow of particles, and calculate their velocity vectors through image processing. They induced a roping flow by subjecting the flow to a vertical → horizontal 90° bend. At the bend, as expected they found that the particles were concentrated towards the outside of the bend radius. Progressing horizontally downstream, the rope gradually descended towards the lower wall, until it formed a stable deposit approximately 10 pipe diameters after the bend.

Inhomogeneous density profiles such as this are important, since the accuracy of any concentration meter will depend upon being able to measure the mean concentration (and velocity) across the profile. Most devices rely on interrogating the tube volume with a narrow beam (such as ultrasonics or radionucleotide absorption), or are more sensitive to the peripheral flow (electrostatic or

ultrasonic cross-correlation), and so are prone to sampling error. Some investigators have tried to solve this problem using multiple interrogation paths [2, 87].

3.2.5 Experimental Teams

This section will review some teams that have made important experimental attempts to measure flow parameters.

British Coal Utilisation Research Association (BCURA)

Parkinson & Hiorns [108] built a mass flow-meter, based on a β-particle absorption device to measure particle concentration, and a continuous-wave ultrasonic device to measure the air velocity. The apparatus was found to measure mass flow to an accuracy of 10% [86].

During field trials, problems with the apparatus were encountered, especially due to the nylon windows for the β source, which suffered from erosion and particle build-up. The mass-flow meter was consequently not recommended for industrial use [111].

Howard [63] experimented later with a microwave device, in addition to re-evaluating the beta-particle absorption method. The microwave signal was transmitted along the tube axis. This arrangement necessitated offsetting a straight tube segment by two 90° bends, and transmitting the signal into and out of the bends (made of plastic). As such, the technique cannot be considered completely non-intrusive. Howard correlated the microwave attenuation signal with coal dust concentration successfully. In addition, the backscattered microwave signal was used to form a Doppler spectrum, and hence give information about particle velocity. However, the signal processing necessary to extract velocity was not attempted. Unfortunately, the microwave attenuation is very dependent also on coal composition and moisture content, and so the technique is useful only for relative measurements (e.g. comparing the flow rate to separate pipes). In evaluating the beta-particle technique, he suggested that careful installation and choice of window could extend its lifetime, but only to a few months at most.

Argonne National Laboratory (ANL)

A team from ANL has published widely on coal / air flowmeters, especially on experiments performed with their large test facility; this permits instrumented flows with concentrations above 10kg/kg in 75mm pipework [130]. They have attempted to measure mass flow rate with active and passive acoustic devices, and capacitative transducers, using cross-correlation to measure flow velocity.

Sheen & Raptis [130, 132] measured ultrasonic emissions caused by particle/wall collisions in a flow of 1mm limestone particles. The acoustic signal was found to depend on both flow velocity and mass concentration, but in a rather complex way. Although data was limited, a power law relationship to velocity was found, in which the power varies according to concentration [132]. The

noise level of a dilute flow was 20dB higher than airflow alone, although increasing the concentration led to lower emissions. A further paper reports that the emissions are correlated with mass concentration [131]. Other investigators have used acoustic emissions to characterise the particle size distribution [83, 42]. Such diverse correlations of acoustic emissions suggests that their interpretation is likely to be complicated.

Sheen & Raptis [130, 132] also report trials of an active ultrasonic instrument, in which two pairs of transducers (transmitting continuous waves) recorded the acoustic modulation due to particles and flow turbulence; the cross-correlation of the signals was used to measure the flow velocity. The device under-read by 30–50%, apparently because it measured flow velocity mainly in the low velocity region near the wall. No attempt was made to relate the received ultrasonic signal to the mass concentration, despite earlier such experience with coal/water slurries [116]. The high ultrasonic frequency (900kHz) and large particle size place the experiment well into the resonant scattering regime ($ka = 16$), and so significant absorption could be expected.

Bobis *et al* [21] describe a successful attempt to measure the mass flow rate of very dense flows (up to 22kg/kg) of 1mm glass beads. The device used several sets of capacitative transducers to measure the mass concentration, and derived the particle velocity by cross-correlation of the density signals.

Wolfson Centre for Bulk Solids Handling Technology

Woodhead [158] built a coal / air flow facility (described in Chapter 5) in which to test the performance of existing mass-flowmeters. The most relevant test [160] was on an electrostatic device (similar to that developed at ANL) which measured mass concentration, and particle velocity by cross-correlation. Below densities of 0.5kg/kg, the device performed reasonably: the velocity measurement under-read by 5%, again indicating sensitivity to slower particles travelling near the wall; the mass concentration measurements showed some scatter and dependence on velocity, but correlated reasonably well with reference measurements. Above 0.5kg/kg the velocity measurement degraded, and concentration measurement became useless.

3.3 ACOUSTIC MEASUREMENT TECHNIQUES

Either the attenuation coefficient or the velocity dispersion may be measured to determine the particle concentration acoustically; however, attenuation is more sensitive to medium characteristics and easier to measure. The attenuation coefficient in a medium may be deduced by: measurement of propagation constant over a fixed distance [55, 60, 99, 166]; measurement of decay rate inside an enclosure when excitation stops [76, 9]; interferometer techniques [9, 81] ; measurement of level, during steady state excitation of an enclosure by a source of known sound power [79].

The first two methods are employed in this work. Section 3.3.1 will review the technique used to measure the propagation characteristics of a suspension, while Section 3.3.2 reviews the background to the measurement of reverberant decay.

Velocity dispersion was measured only in the case of audio frequency measurements on quasi-static suspensions: above low audio frequencies, dispersion is negligible, while the presence of flow tends to smother the small phase difference that need to be measured. Two main methods of measuring dispersion have been reported in the literature:

- Measuring changes in the time of arrival of a single-frequency tone burst [166,138]. If a pulse is used instead of a tone burst, then the group velocity is measured.
- Measuring changes in the phase spectrum of the system transfer function, using wideband excitation: either using FFT analysis [eg. 30] or synchronous demodulation of a swept sine wave [60].

Appendix G justifies the use in this thesis of using the second, frequency domain technique.

3.3.1 System analysis using MLSSA

This section will describe the principle behind the apparatus (MLSSA) that was used for much of the data-collection.

Introduction to system analysis

System analysis refers to the process of deducing the relationship between the output and input of a linear system. In general, the system is excited by a test signal, the response signal is measured, and the system transfer function is calculated from the knowledge of the input and output signals.

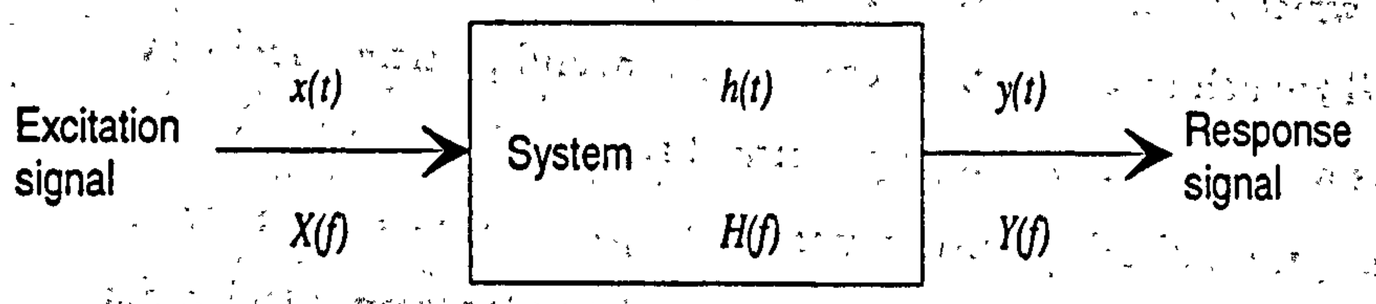

In the time domain: $y(t) = x(t) * h(t)$,

where *h(t)* is known as the impulse response of the system, * signifies a convolution, and lower case letters indicate a time domain description.

In the frequency domain: $Y(f) = X(f)\,H(f)$,

where *H(f)* is known as the transfer function of the system, and upper case letters indicate a frequency domain description.

Therefore, extracting the system description requires a division in the frequency domain, or a deconvolution in the time domain. The complexity of deconvolution is one reason why frequency domain analysis is the more popular. In practice, real systems will have some degree of non-linearity, and all measurements will contain noise. Therefore, the measurement of the transfer function is only an estimate.

The selection of the input signal is arbitrary, and depends on many factors. The main parameters are:

- *Bandwidth*: the range of frequencies in which sufficient energy is present.
- *Signal type:* continuous or transient. If continuous, periodic or random: periodic signals will repeat after a fixed duration, and therefore have a line spectrum; random signals are aperiodic and have a continuous spectrum.
- *Crest factor*: the ratio of the signal's peak amplitude to its RMS value. Since, to avoid overload, the power to a transducer is often limited by the peak amplitude, the mean output power of signals with high crest factors will be lower than low crest factor signals, and hence the resulting measurements will have a worse signal/noise ratio (S.N.R.)
- *Estimation accuracy*: some signals permit more robust estimation techniques than others.

The following table summarises the properties of some commonly-used excitation signals:

	Bandwidth	Signal Type	Crest Factor	Accuracy
Sine	single frequency ⇒ slow analysis	Continuous, periodic	3 dB	Good for non-linearity & noise.
Swept sine	arbitrarily wide & flat response	Continuous, aperiodic	3dB	Good for non-linearity & noise. Allows time-delay identification.
Random "noise"	arbitrarily wide & flat response	Continuous, aperiodic	11 dB	Good statistical characterisation, good estimates with non-linearities, poor SNR, slow due to need for averaging.
Impulse	wide, limited low frequencies	Transient. Can simulate impulse response	very high (low energy)	Poor: high CF gives low SNR and excites non-linearites. Repeatability suspect. Allows time-delay identification & editing
Pseudo-random	arbitrarily wide & flat, low frequencies limited by period	Continuous, periodic	arbitrary, depending on phase spectrum	Good for noise (synchronous averaging possible), poor for non-linearities, always excites them similarly.

Table 3-A Properties of commonly-used excitation signals

Pseudo-random signals attempt to appear locally random, but with a fixed pattern that repeats each time and after a fixed duration. This has three advantages:

- If the duration is synchronised with the data collection window, then the line spacing of the (periodic) signal is identical to that of sampled waveform, and therefore no windowing is required, and no frequency "leakage" occurs [115].
- Since the same signal repeats periodically, the measured data block can be averaged in the time domain, with the recording synchronised with the generated signal, to reduce the level of uncorrelated noise. This technique — called synchronous averaging — increases the SNR of the measurement, and can recover the signal even in the presence of considerable background noise.
- Unlike excitation by random "noise", spectral averaging is not necessary to remove the effect of random fluctuations.

While the amplitude spectrum of pseudo-random signals is flat in the frequency range of interest, the phase spectrum may be manipulated to achieve certain goals; for example, low crest factor, Gaussian amplitude distribution etc.

Maximum-length sequence (M.L.S., or "m-sequence")

The M.L.S. is a special type of pseudo-random signal, first proposed by Schroeder [126] for use in room acoustics. It is a binary sequence, taking the values +1 and -1 in equal number, and therefore having the lowest possible crest factor of 0dB. The sequence is conveniently generated by an *n*-stage shift register [33], yielding a sequence length of $N = 2^n - 1$. Since the spectrum is flat (in a given range), their circular autocorrelation function, *r(m)*, approximates to an impulse.

In fact,

$$r(m) = \frac{1}{N}\sum_{k=1}^{N} x(k)x(k+m) = 1 \qquad m \bmod N = 0$$
$$= \frac{-1}{N+1} \qquad \text{otherwise} \tag{3.1}$$

Since N is chosen to be high (typically 32767 for n = 15), the value of $r(m)$ for m mod N $\neq 0$ is small. Therefore this approximates a periodic unit pulse:

$$\delta'(m) = 1 \qquad m \bmod N = 0$$
$$= 0 \qquad \text{otherwise} \tag{3.2}$$

where the dash signifies a periodic quantity.

This leads to the property that the periodic impulse response of the system under test can be approximated by cross-correlating the sampled response signal with the original MLS sequence. Rife

& Vanderkooy [121] prove this rigorously, and describe many properties and limitations of analysis with MLS.

Testing with MLS became popular when an efficient method of performing the cross-correlation was found (using a fast Hadamard transform [34, 7])

The advantages of this technique are:

- The signal approximates to the same flat amplitude response as a delta pulse (-3 dB at ½ the pulse generation frequency, and hence at the Nyquist frequency of the sampled signal).
- The crest factor is very much lower than a pulse (due to the very erratic phase spectrum of the MLS). With a crest factor of 0 dB, the maximum possible power is delivered to the transmitter, given a limit to maximum amplitude. For an amplitude-limited system, the energy content of a MLS signal is a factor N higher than that of a single pulse. In consequence, the SNR is higher by $10\log_{10} N$; for example, the SNR of a $n = 15$ sequence is 45dB higher than a pulse of the same amplitude.
- This method can therefore be likened to testing with impulses, but with very much higher SNR and reduced risk of exciting non-linearites. In particular, reflecting paths in the system can be readily identified, and edited in the time-domain, if necessary.
- The impulse response is very long (up to N samples). Therefore, very reverberant environments may be measured, with remarkably little noise in the low-amplitude "tails" of the response, and long duration records may be collected at a high bandwidth. Furthermore, if a Fourier transform is applied to the long time sequence, a very high resolution frequency spectrum will be obtained without the necessity for zoom processing — the usual method with analysers that are typically limited to 2 - 8 ksample transforms.
- Cross-correlation makes the resulting impulse response quite immune to noise: for example, a single noise transient in the response signal will have its energy spread evenly throughout all N samples in the impulse response. And since each repetition of the MLS is identical, the signal may be synchronously-averaged to reduce uncorrelated noise, increasing the SNR by $10\log_{10}(\text{no. of averages})$ dB.
- Instead of driving a linear transducer, the digital output of the MLS can trigger, for example, spark gaps, or booms for use in oceanography [20]. The cross-correlation algorithm effectively acts as a matched inverse filter, to compress the energy spread out over the N pulses back into a single pulse.

The disadvantages of MLS testing are:

- It is not good at estimation in the presence of non-linearities, since they are always excited in the same way. However, their presence is easily detectable, since non-linearity shows up as "fixed pattern" noise in the time-of-flight gap, or after the I.R. should have decayed — that is, regions where the I.R. should be zero actually show a noise signal that is the same each time the measurement is taken.
- The signal contains no energy at D.C. (0 Hz). This is not usually a problem in acoustic testing.
- The technique applies only to time-invariant systems. The same is true of all other signals, but the long duration of the MLS signal means that the time-scale over which a system must be time-invariant is longer than, say, an impulse.
- The statistical estimation techniques are not as well developed as for Gaussian noise, so making error estimates of a resulting transfer function more difficult. Rife & Vanderkooy [121] have developed a limited method of deriving coherence from a MLS-derived impulse response.
- The duration of the sequence must be longer than the impulse response of the system, otherwise "time-aliasing" will result [121]. This is not usually a problem, due to the long durations possible (for example, a $n = 16$ sequence measuring at 20kHz bandwidth lasts over 1s).

Maximum-length sequence system analyser (M.L.S.S.A.)

MLSSA (usually pronounced "Melissa") is a proprietary P.C. card and software that performs as a single-channel system analyser. Most system analysers have two channels — for system input and output — but since the MLS signal output is "known", only a single input channel is provided. It incorporates an antialiasing filter with programmable corner frequency, shape and gain. The measurement bandwidth is variable from 1 - 40 kHz, with the sample clock, signal generation clock, and antialiasing filter automatically changing according to the bandwidth. The supplied software performs the cross-correlation, and further post-processing functions.

For all the reasons mentioned above, the device has become popular in acoustic testing [50,153].

3.3.2 Reverberant decay

Chapter 7 describes measurements of the decay of a reverberant field within an enclosed suspension (static and flowing), and attempts to find frequency bands in which near- exponential decay exists. A quantity named "decay rate" could thus be defined — related to the inverse of the more usual T_{60} — and measured to assess the change due to medium attenuation. As this work was particularly concerned with decay in non-diffuse fields, in which the decay is not necessarily exponential, a

literature survey was undertaken to discover a means of assessing the "goodness" of the exponential decay. Existing experimental techniques were also investigated.

Almost all of the experimental papers reviewed were directed at sound decay in the context of measurement in reverberation chambers or semi-reverberant rooms. Little was found about reverberant decay inside geometrical enclosures.

Experimental techniques

Several techniques for measuring decay curves can found in the literature:

Decay of Interrupted noise

The technique of measuring decay from interrupted noise is still the standard. A random noise source excites the enclosure to a stationary level, and is then interrupted. The sound pressure is measured, filtered, averaged, and recorded as a decaying level. Due to the variation between individual noise bursts, many measurements must be averaged in the time domain, a method known as "ensemble averaging".

Integrated impulse response

In an important paper, Schroeder [127] proved that the ensemble average decay can be derived from a single measurement of the impulse response of the enclosure:

$$\left\langle s^2(t)\right\rangle = N\int_t^\infty h^2(\tau)d\tau \tag{3.3}$$

where N is the sound power per unit bandwidth, $h(t)$ is the impulse response, and $s(t)$ is the sound pressure at the measurement point.

Initially, the method was limited by the experimental problem of measuring the impulse response, due to the low energy content of any pulse excitation and the consequently poor SNR. Furthermore, the reverse integration method is especially affected by noise, because the noise floor in the decay tail is integrated, so that it appears as a second decay slope. One effect of contaminating noise is that the resulting decay curve will be sensitive to the (necessarily finite) upper integration limit in equation (3.3), illustrated in Figure 3-4.

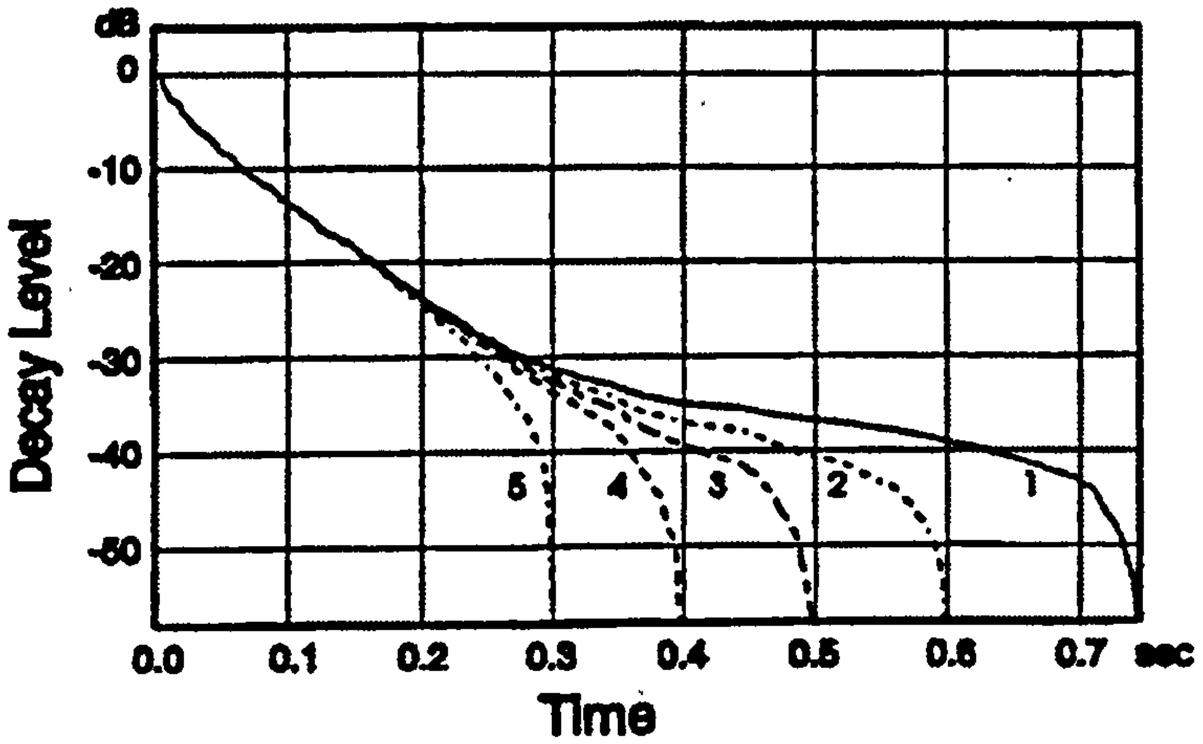

Figure 3-4 *Decay curves calculated using the integrated impulse response method, showing dependence on the upper integration limit. Curves 1 - 5 are evaluated from the same impulse response, using successively decreasing upper integration limits. Reproduced from Xiang [163].*

Chu [32] reduced this sensitivity by introducing a noise subtraction term into Schroeder's equation.

$$\left\langle s^2(t)\right\rangle = N\int_t^{(\infty)} h^2(\tau) - \overline{n}^2 \, d\tau \qquad (3.4)$$

where $\overline{n}^2$ is the mean square noise pressure, usually calculated from the time-of-flight gap. This is an approximate correction only, but Chu demonstrated that it worked effectively, and the resulting decay curves compared well with those obtained by the more usual technique of interrupted noise [32].

Schroeder [126] first proposed that pseudo-random noise could be used as the excitation signal and that the impulse response could be derived computationally by cross-correlating the noise response with the original signal. As explained above, this technique has the advantage of considerably increasing the SNR, and making the reverse-integrated impulse method more attractive. Schroeder [126] demonstrated this property by measuring the room response of a lecture theatre, using soft background excitation, and synchronously-averaging during the course of a lecture to improve the SNR.

Fourier-transformed impulse response

Aoshima [11] proposed an interesting alternative method for deriving the decay curve from the (measured or derived) impulse response. Instead of performing a reverse integration of the squared sound pressure values, he showed that an integration of the time-varying Fourier coefficients can also yield the decay curve.

$$\left\langle s^2(t)\right\rangle = \int_{-\infty}^{\infty} \left|G(f,t)\right|^2 \Phi(f) df \qquad (3.5)$$

where $\Phi(f)$ is the power spectrum of the excitation signal, and

$$G(f,t)=\int_{t}^{\infty}h(\tau)e^{-2\pi f\tau}d\tau \qquad (3.6)$$

The advantage of this technique is that the impulse response of any associated filter may be separated from the enclosure response. Furthermore, the method may be used to predict the response to any arbitrary excitation signal. Its greatest disadvantage is the large computational overhead of having to calculate $2N$ discrete Fourier transforms of size N, where N is usually >10k. Consequently the method has been largely ignored, although maybe contemporary PC's now have sufficient power and memory to make the method worth revisiting.

Measurement of decay rate

If a sound field decays exponentially, then a graph of the log sound pressure level against linear time will yield a straight line. The slope of this line can therefore be characterised by a decay rate in dB/s, or, more usually, a time to decay by a certain level; for example, the T_{60} time to decay by -60dB.

The measurement of this gradient is usually accomplished graphically or by linear regression from the decay record [22, 32]. Xiang [163] used a non-linear regression method, designed specifically for curves that had been calculated using Schroeder's reverse integration technique. He modelled the resulting curves as the sum of an exponential decay and a linearly decreasing noise curve, due to the integration of a constant noise level. He stated the general decay model in terms of 3 unknowns:

$$d(t)=k_1\exp(-k_2t)+k_3(L-t) \qquad 0\le t\le L \qquad (3.7)$$

where $k_1 = 1$ if the curve has been normalised, $k_2 = 13.8\,/T_{60}$, $k_3 = \dfrac{\overline{n^2}}{N}$, and L is the time duration of the record. The three unknowns are found using an iterative least-squares fit of this model on the measured decay curve. A further description of this technique is given in Appendix H, and an algorithm for its implementation is listed in Appendix B. The advantage of the method is that it is reasonably insensitive to the upper integration limit, and no estimate of the noise power is required (except as an initial value for iteration).

Measurement of decay curvature

A decay record is described as "curved" when it deviates from simple exponential decay; that is, when the (log) sound pressure level curve deviates from being linear. This can occur when, in the frequency range being analysed, there are multiple dominant modes with greatly different decay rates. For example, if two dominant modes are excited, the early part of the decay will be governed by the fastest decaying mode, and the later part by the slower decaying mode, leading to a dual slope decay curve.

The concept of curved decay enters into the literature in two guises:

1. To assess how "good" a reverberation chamber is, and how valid the resulting measurements are, by characterising the diffusivity of the sound field [155]. A fully diffuse sound field would display a linear decay curve, and hence zero curvature.

2. To characterise the acoustical behaviour of "real" rooms; these will be expected to display a non-diffuse sound field with non-exponential decay, and any resulting curvature can be used as a measure of the extent of this [16]. Familiar concepts are those of "early" and "late" decay.

Definitions of Curvature

While the term "curvature" is widely used, its definition varies between authors.

The ISO standard [66] defines curvature by using the ratio of the decay rates of two subsections of the curve, each covering a range of at least 10dB, with one extending to an SPL at least 10dB lower than the other. This is not a tight definition, and so alternatives have flourished, some within, others without this definition.

Some authors fit either several linear regression lines [16, 155], or a quadratic curve [39], and arrive at a variety of descriptors of curvature.

Bodlund [23] defined a measure of curvature as:

$$C = 1000(1 - |r|) \tag{3.8}$$

where r is the correlation coefficient of the decay curve. Hence C will vary between 0 for a perfectly linear decay, up to a theoretical value of 1000 for a completely uncorrelated time series of sound pressure levels. An advantage of this definition over regression techniques is that irregularities in the decay record other than monotonic curvature (eg. steps) are also flagged by a degradation in C.

Signal Processing Considerations

Jacobsen appears to be the first author to consider the effects of signal processing on the measured decay curve. In one note [67] he displays that a band-pass filter introduces a time lag into the decay, and produces distortion due to its own impulse response.

Through experimental work and visual inspection of the resulting curves, he states guidelines for the filter bandwidth. If the reverberation time of the enclosure is T_{60}, and the filter 3dB bandwidth is B, then

$$T_{60}\ B > 16 \tag{3.9}$$

is a suitable criterion to use, provided only the average decay time of the system is required.

Furthermore, the linear fit should ignore the early (distorted) part of the decay, delimited by

$$0 < t < 1/B \tag{3.10}$$

If the early decay rate is also needed, then a much more stringent requirement should be imposed: a factor of 64 is suggested instead of 16.

In a later note, Jacobsen [68] suggested reversing the time sequence of the reverberation data before it was filtered. In this way, the effect of the filter impulse response is reduced, due to its time asymmetry, and the bandwidth limitation becomes correspondingly less stringent. Jacobsen suggested:

$$T_{60}\ B > 4 \tag{3.11}$$

However, these figures must also be modified according to the roll-off behaviour of the filter: a steep roll-off tends to extend the impulse response of the filter, and hence lead to greater distortion and lag.

Time-reversed filtering was found necessary in this work to measure the decay rate in flowing suspensions (section 7.3).

3.4 THE EFFECT OF FLOW AND TURBULENCE IN DUCTS

Since the targeted application involves flow in a duct, the acoustic effect of this flow and the associated turbulence is reviewed in this section.

The study of turbulence occupies a massive field in the literature. The following section only attempts to summarise some areas that are important to the present work.

3.4.1 Flow velocity profile

There will always be a velocity profile across the pipe diameter due to shear stress at the wall.

Where the flow turbulence is fully developed, the profile is usually represented by a power law. In clean air flow, a 1/7 power is usually assumed (e.g. Pridmore-Brown [113]).

$$M(y) = M_0\left(\frac{y}{R}\right)^{\frac{1}{7}} \tag{3.12}$$

where $M(y)$ is the Mach number at radial distance y, $0 \le y \le R$, where R is the pipe radius. Kolansky *et al* [77] experimentally measured a 1/6.3 power law. This leads to a steep velocity gradient near the tube wall, indicating a region of high shear, and high turbulent intensity. The effects of this will be discussed in the following sections.

The presence of particles affects the flow profile. In the same study, Kolansky *et al* [77] found that, when glass beads were introduced into the flow, the profile flattened out in the core region, indicating increased levels of turbulence – since turbulence increases the momentum diffusion

across adjacent toroidal "layers". Maybe surprisingly, they found that smaller particles (22μm) caused greater flattening than larger (36μm) particles, indicating higher levels of turbulence.

They also measured the turbulent intensity directly, and found that the smaller particles did indeed increase the intensity more than larger particles, and that the intensity increased greatly at the tube walls.

Tsuji & Morikawa [145] found the opposite tendency, with much larger particles: 3.4 mm plastic pellets tended to increase the turbulent intensity, while 0.2mm pellets decreased the intensity. Increasing the mass loading caused increased intensity in both cases. It was suggested that the 3.4mm pellets were large enough to create their own wake, and hence increase turbulence, while the smaller particles had the effect of damping the turbulence. Interpretation of the data was complicated by the horizontal orientation of the flow pipe, leading to an axially-asymmetric profile, due to gravity.

Woodhead *et al* [160] also used a L.D.V. to measure the flow velocity profile of suspensions of pulverised fuel and flour (mean size of 60μm). They found that the power law of the profile model depended on the particle loading, albeit with significant point-scatter. The power varied from around 1/7.5 at low concentrations, up to 1/10 at 0.3 kg/m^3, yielding the same flattening of the profile as observed by Kolansky *et al*.

3.4.2 Variation of orifice impedance

In the experiments described later, acoustic energy is coupled into and out of the flow tube through an orifice in the tube wall. As the coupling ratio into the tube will depend on the impedance of the orifice, it is important to know how the impedance might vary with flow conditions. Little work has been conducted in this area, most of it in the field of duct-silencing using perforated liners.

Cummings [36] measured the impedance of various sized orifices in the wall of a square section duct. He expressed the impedance in terms of the (real) resistance, and the mass end correction (a measure of the imaginary part), and related them to the friction velocity. The friction velocity is related to the wall shear stress, which depends both on mean air velocity and the wall roughness; Cummings did not explain how he measured it.

By reducing the parameters to dimensionless numbers based on the dimensions of the orifice, he was able to find empirical relationships between them. Notably, the resistance θ_f increased linearly with friction velocity u_*, with a gradient that depended on the orifice dimensions, thickness t, diameter d:

$$\frac{\theta_f c_0}{fd} = \left[12.52\left(\frac{t}{d}\right)^{-0.32} - 2.44\right]\left(\frac{u_*}{fd}\right) - 3.2 \qquad (3.13)$$

while the mass end correction decreased in a non-linear fashion, and with much point scatter. He concluded that the increasing intensity of boundary layer turbulence causes these effects.

3.4.3 Acoustic effects of flow

Apart from any considerations of turbulence, the presence of mean flow in the pipe will affect the sound pressure distribution of an acoustic signal.

Up & Downstream propagation in mean flow

Ingard & Singhal (64), ignoring turbulence and velocity profile, measured the propagation of tone bursts (1000 Hz and 1477 Hz) in a flow of clean air. The sound pressures at equal distances up and downstream, p_+ and p_- respectively, were measured and expressed as a ratio $\left|\frac{p_+}{p_-}\right|$. This was found to be related to the Mach number, M, of the flow by a $\left(\frac{1+M}{1-M}\right)^2$ curve up to approximately $M < 0.1$, with a transition to a $\left(\frac{1+M}{1-M}\right)$ curve for $M > 0.2$. They explained the transition mathematically as a change in boundary conditions at the orifice of the acoustic source, due to a shift from streamlined to turbulent flow. Although it seems unlikely that the flow could be streamlined at $M=0.1$, the presence of particles could conceivably induce a similar change in boundary conditions. This is relevant for later experiments on plane wave propagation, since the sound pressure received at a point downstream from the transmitter will show variations due to the flow speed, and possibly, due to changes in the boundary conditions at the transmitting orifice which could depend on turbulent variations or the presence of particles.

Sound pressure re-distribution due to a velocity profile

A flow velocity profile has the additional effect of altering the transverse sound pressure distribution. Studies of this effect are, to my knowledge, limited to theoretical work.

Pridmore-Brown [113] calculated the sound pressure level of a plane wave propagating between two parallel plates, in the presence of mean flow; a velocity profile with a 1/7 power law was assumed (as well as a rather unrealistic linear profile). He predicts that the sound pressure becomes concentrated near to the wall, by an amount that increases with Mach number and frequency. For example, at M = 0.1 and a sound wavelength three times larger than the boundary layer, he predicts the SPL at the plate to be 35 dB higher than midway between the plates.

Mungur & Gladwell [102], investigating circular pipes, extended this work to include predictions of the first symmetric transverse mode; only the effect of a linear velocity profile was evaluated, but this is expected to give qualitatively similar results to the power law profile [113]. The effect of flow

is to change the modal shape quite significantly, turning the U-shaped pressure profile into a W-shape. Again, the effect becomes more pronounced as frequency and Mach number increase.

Nagel & Brand [103] modelled the flow profile in a circular duct by a combining a uniform velocity core and a boundary layer of variable thickness, in which velocity varies according to a 1/4 period sinusoid. They were able to model this as a duct with a (complex) admittance at the boundary layer that depended on boundary layer thickness, thus simplifying analysis. In particular, it becomes fairly easy to calculate the acoustic pressure distribution of plane waves and transverse modes by re-solving the wave equation with revised boundary conditions. The reactive part of the boundary layer admittance is the most affected by flow.

For plane waves, the effect of increasing the boundary layer thickness is to increase refraction towards the wall for propagation upstream, and refract away from the wall for propagation downstream. Transverse modes are affected in a more complex way, depending on their order. Most of the analysis considers the effect on the attenuation constant for a duct with finite wall admittance (due to an attenuating duct-liner). It is not clear if attenuation will still occur if the walls have zero admittance.

Change in modal frequencies

Fuller & Bies [49] analysed the effects of mean flow (without a velocity profile) in a rectangular section duct with rigid, zero-admittance walls. They predict that the modal cut-on frequencies will be reduced, according to the flow Mach number:

$$f_{m,n}' = f_{m,n}\left(1-M^2\right)^{1/2} \qquad (3.14)$$

where $f_{m,n}$ is the cut-on frequency of the (m,n) mode in the absence of flow, and the dashed quantity indicates the presence of flow. Clearly, the direction of the flow is irrelevant in this expression.

Their experimental measurements (of a reactive attenuator) did not have sufficiently high resolution to observe the expected 0.5% reduction in modal frequency (for $M = 0.08$). They made a further prediction: without flow, the wavenumber of a mode below cut-on is purely imaginary, leading to an evanescent, reactively-attenuated mode; whereas, in the presence of flow, the wavenumber becomes complex, and so the mode is convected as a "pseudo-wave" with a reduced rate of decay compared with the no flow case.

Erikson [41] applied equation (3.14), without justification, to modes in a circular duct.

Agarwal & Bull [3], also considering a circular duct, extended the work to cover the case of a flow velocity profile that closely mimics the case in turbulent pipe flow (although no account is taken of the acoustic effects of the turbulence). With their numerical method, each cut-on frequency must be calculated individually. Overall, they predicted that the presence of a turbulent velocity gradient

tends to reduce the cut-on frequency less than the case of a uniform flow. A simplified method is described which involves calculating an effective Mach number by integration across the velocity profile, and using equation (3.14).

3.4.4 Acoustic effects of turbulence

Scales of turbulence

Theoretical predictions of fields in inhomgeneous media make assumptions about the wavelength of radiation in comparison to the size scale of inhomogeneities. The scale of inhomogeneities l, is usually thought to be bounded by the outer scale, L_0, and the inner scale, l_0. In the case of optics (and most short-wave electromagnetic radiation), the regime is usually characterized by the inequality:

$$\lambda < l_0 < L_0 \tag{3.15}$$

that is, the wavelength λ is smaller than all scales of inhomogeneity. For the case of outdoor sound propagation, theoretical predictions are based on the following assumption:

$$l_0 < \lambda < L_0 \tag{3.16}$$

since the outer scale of atmospheric turbulence is usually very large compared with the acoustic wavelength.

In both the above cases, while $\lambda < L_0$, it can be assumed that the dominant effect is that of forward scattering.

For the case of plane wave propagation in pipes, where the turbulent medium flows axially, the outer scale is given approximately by the pipe diameter. Since the wavelength, for plane wave propagation, is larger than the diameter, we have the following inequality:

$$l_0 < L_0 < \lambda \tag{3.17}$$

Most of the theories developed for predicting outdoor sound attenuation in the presence of turbulence are not valid in this regime. However, Ostashev [105] does give an expression for the extinction coefficient, γ, of the mean coherent field in such a case, using a theory of multiple scattering. The mean coherent field $\overline{p}(t)$ is calculated by ensemble-averaging a set of realizations (blocks of time series data) of the sound pressure:

$$\overline{p}(t) = \left\langle a(t)\cos\left[\omega t + \phi(t)\right]\right\rangle \tag{3.18}$$

This leads to a time record, with the same length as the realization, whose mean amplitude and phase can be measured, and the spatial decay of amplitude with distance, x, will yield the extinction coefficient:

$$\overline{p}(t,x) = \overline{a}_{x=0} \exp(-\gamma x) \cdot \exp(i\omega t + \overline{\phi^2}) \tag{3.19}$$

In the absence of temperature and humidity fluctuations, Ostashev's prediction of γ (his eqn (87)) reduces to:

$$\gamma = 2\pi^2 k^2 \int_0^{2k} K\left(1 - \frac{K^2}{2k^2}\right)^2 \left(1 - \frac{K^2}{4k^2}\right) \frac{F(K)}{c_0^2} dK \tag{3.20}$$

where k is the acoustic wavenumber, K is the air velocity wavenumber, and $F(K)$ is the 3 dimensional spectral density of K.

The reduction of the mean coherent field is caused mainly by the shifting of the energy from the mean component to the fluctuating component due to the phase fluctuations; i.e. in the expression for the pressure field, p:

$p = \overline{p} + \tilde{p}$, representing the mean and fluctuating components respectively, turbulence causes the mean component, $\overline{p}$, to decrease, and the fluctuating component, $\tilde{p}$, to increase, without necessarily any change in the signal energy. This leads to a divergence between the the mean coherent amplitude, and the mean intensity, which remains high due to the high fluctuating component.

Experimental studies

While there is a large mass of literature on theoretical and experimental aspects of outdoor propagation in the presence of turbulence, there is far less concerning acoustic propagation in ducts with turbulent flow. There has, apparently, been no experimental verification of the insignificance of turbulence at long wavelengths. All the following studies investigate high frequency propagation where it can be be assumed that $\lambda < L_0$.

Müller & Matschat [101] modelled turbulence as a statistically-distributed ensemble of vortices. They predicted that the effects of scattering by the vortices will lead to an attenuation that increases according to a f^5 law at low frequencies, changing to a f^2 scaling at higher frequencies, with a transition between the regimes when the sound wavelength has the same order as the vortex radius.

To confirm the theory, Schmidt (in [101]) measured the change in level of ultrasonic tone bursts transmitted across a 300mm diameter duct. Turbulence was encouraged in the 25 m/s flow by placing a grid of rods upstream of the test section. The frequency was varied between 60 - 400 kHz. The scaling confirmed the existence of the two regimes.

Hamade measured the signal level of tone bursts at 459 kHz, transmitted across a duct carrying gas flow of varying speeds. The measurements of log signal level varied linearly with velocity. If the turbulent velocity field was homogeneous and isotropic (as assumed), then the turbulent energy spectrum, $E(k)$ could be expected to follow a $k^{-5/3}$ law, where k is the velocity wavenumber.

However, this leads to the prediction that the signal level should fall with a power law. In fact, the linear dependence was consistent with the turbulent spectrum following a $k^{-1/3}$ scaling.

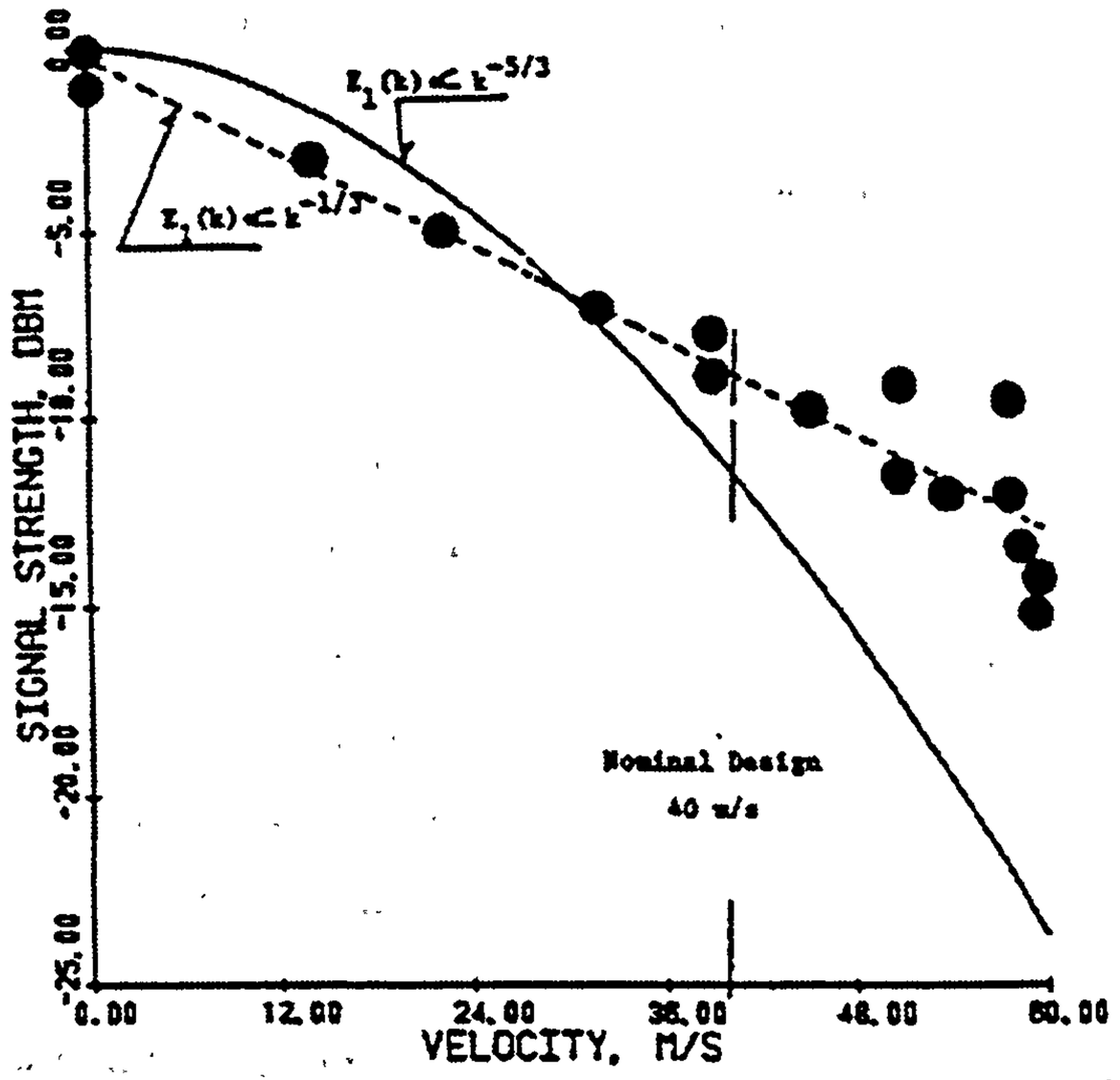

Figure 3-5 *Theoretical and measured (•) change in signal level of tone bursts, at 459 kHz transmitted across a duct carrying flowing clean air. Reproduced from Leffert* et al *[84].*

Baerg & Schwartz [15] measured the angular dependence of scattering intensity, for tone bursts between 25 – 65 kHz. Both velocity and temperature fields were tested, using a heated grid upstream of the measuring volume. The shape of the curves closely follows that predicted if the turbulent fluctuations are assumed to follow a Kolmogorov spectrum.

3.5 CONCLUSIONS

The acoustic propagation characteristics of an aerosol have been measured chiefly in laboratory apparatus. These few experiments have confirmed the validity of theoretical formulations in the long wavelength limit to a reasonable degree of certainty. Most work above the long wavelength limit was either performed on emulsions or slurries (not reviewed here), or at a single frequency on aerosols.

Ultrasonic measurements across flowing suspensions have confirmed that the particle concentration can be correlated with the attenuation at a single frequency. However, as explained in Chapter 2, a single frequency measurement will not be able to distinguish between changes in particle concentration and changes in particle size. Hence, for a measurement system to be immune to changes in p.s.d. (or maybe even be able to indicate such changes), multi-frequency measurements are necessary, in the absence of any *a priori* knowledge of p.s.d. Such measurements have so far only been conducted in the laboratory.

No work has adequately investigated the effects of varying the particle size, shape and composition. Any practical sensor will have to be relatively insensitive to such parameters.

Any measurement of mass flow rate will have to solve the problem of concentration and velocity inhomogeneity across the tube section. This could be by using multiple sensors to interrogate a number of paths, or by finding a technique that inherently averages within the tube volume: acoustic measurements at audio frequencies can be expected to display the latter quality, due to the long acoustic wavelength.

Measurements of particle velocity are relatively more developed than particle concentration. Both cross-correlation techniques and contrapropagating ultrasonic devices have been proven successful.

Most industrial applications of mass flowmeters will involve a small velocity range ("turndown ratio"), as low speeds cause particles to fall from suspension, and high speeds cause excessive wear. Therefore, for the relatively small particles in P.F., the particle velocity can be inferred from measurements of gas velocity; changes in slip velocity due to changes in p.s.d. or air velocity can be assumed negligible. Hence the measurement of particle velocity is comparatively easy for the applications of interest, and so this work will concentrate on the problem of measuring particle concentration.

No truly satisfactory method of measuring particle concentration has yet been reported for the application considered.

The measurement techniques used in this work have been reviewed. The operation of the MLSSA device was explained and justified as offering excellent SNR (important in the noisy environment of pneumatic conveying), and the ability to measure both propagation characteristics and reverberant decay. Its analysis in terms of impulse response is advantageous in allowing time domain editing, and derivation of the reverberant decay curve, respectively.

Reverberant decay does not appear to have been used to measure medium attenuation in a geometrical enclosure. A lack of diffusivity of the sound field has been found to lead to curvature of the decay records; ways of characterising this curvature have been reviewed.

The acoustic effects of flow in pipes have been reviewed. Many inter-dependant mechanisms were described. The sound field depends on the mean flow, the flow profile, and the turbulence parameters. These are themselves affected by the concentration and size of the particles. Figure 3-6 summarises the dependencies.

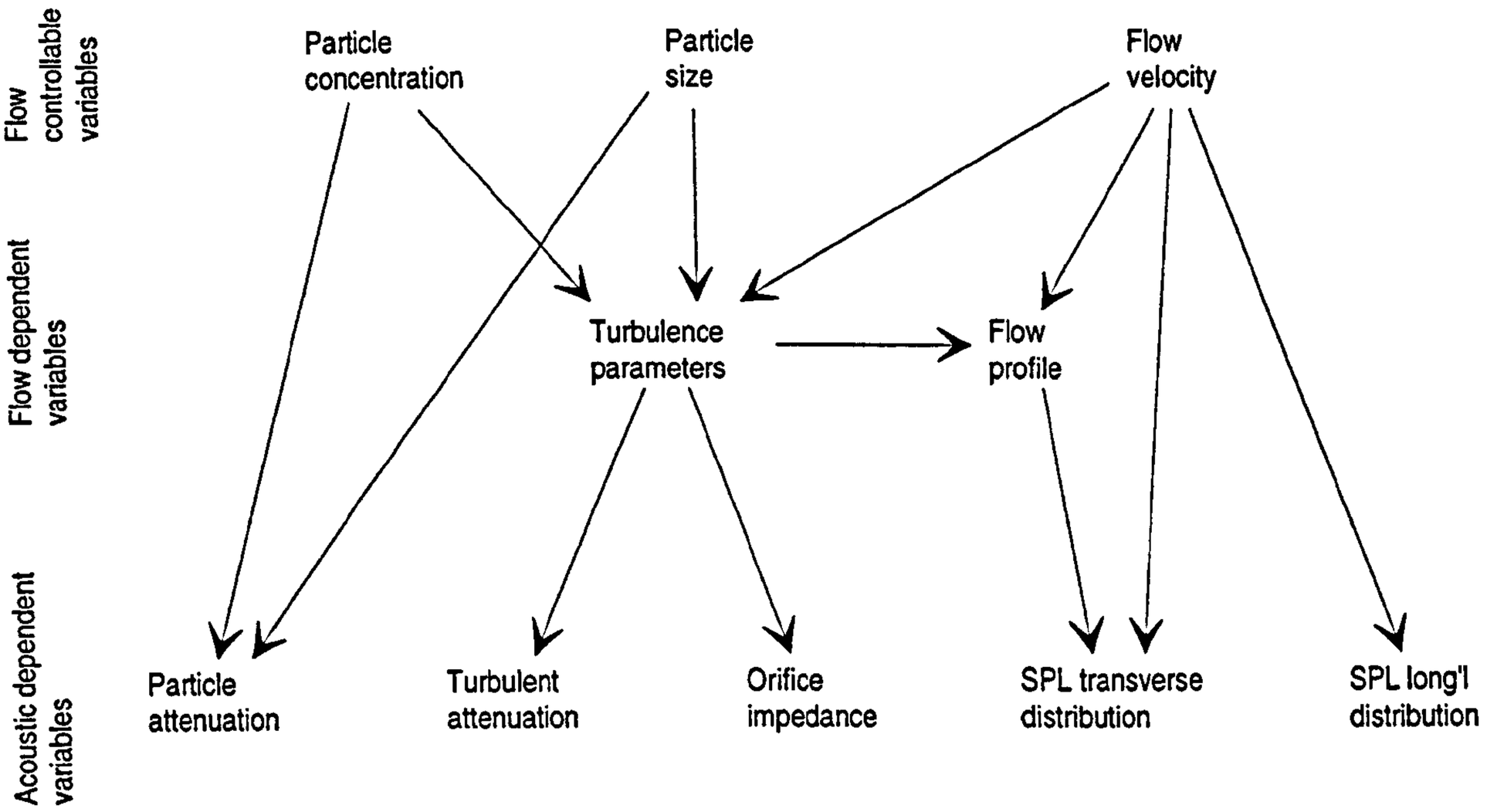

Figure 3-6 *Chart summarising the inter-dependencies of flow parameters, and acoustic effects.*

Therefore, in order to measure the attenuation due to particles alone, it is necessary to be able to separate or ignore all the other effects. It is partly this combination of complex interactions that makes measurements in flow more complicated than quasi-static suspensions.

4

DESIGN & USE OF EQUIPMENT: QUASI-STATIC APPARATUS

4.1 INTRODUCTION

This chapter describes the equipment that was designed and built to measure the acoustic properties of "static" suspensions. Of course, the suspension is only quasi-static, as the particles settle out under gravity[1], and the term is used to contrast with the moving suspensions generated in the flow rig. The static apparatus is intended to provide a well-controlled and benign environment in which to make acoustic measurements, in contrast to the more complex and aggressive environment of a high concentration, flowing suspension.

The lack of flow with which to keep the particles in suspension means that the apparatus is restricted to tests on small particles (approximately < 10μm), so that their settling rate is not excessively large. Less obviously, there is a difficulty in achieving a high suspension density: a volume concentration of 11 parts per million (ppm) was the maximum attained (mass concentration of 33 g/kg.)

The apparatus was designed primarily for plane wave measurements, and so this aspect will be discussed in the greatest detail. Modifications to the apparatus which were made, for example, to make measurements of reverberant decay will be described in the relevant chapters.

Many of the solutions presented in this chapter are refinements based on experience gained on a more crude apparatus, that nevertheless yielded publishable results [99] — the paper is reproduced in Appendix E.

While the experimental methods are outlined in this chapter, the details are found in Appendix D.

4.2 AIMS

The aims of this part of the project were to:

- Design apparatus to measure the acoustic properties of a stable aerosol in a control volume, with a means of measuring its suspension concentration and particle size independently.
- Devise an experimental and computational procedure to ensure maximum repeatability and accuracy of measurements.

[1] Temkin and Dobbins [142] have shown that the additional drag due to settling under gravity has no acoustic effect

4.3 OBJECTIVES

To fulfil these aims, it was necessary to be able to:

- Generate and disperse a stable, uniform suspension of a variety of powdered solids.
- Contain the suspension with an enclosure that would meet the acoustic constraints and permit acoustic access to the test volume via orifices.
- Measure the concentration of the suspension.
- Measure the stability of the suspension.
- Measure the particle size distribution of the suspension.
- Model the system under measurement, extract the desired quantities, and hence devise a suitable signal processing algorithm.
- Assess the repeatability and accuracy of the resulting measurements.

These individual project stages are addressed below.

4.4 GENERATION OF SUSPENSION

Finely divided powders tend to be cohesive, and so a high energy environment is required to separate the particles and suspend them individually. Compressed air was chosen as the medium to provide this environment.

An initial trial consisted in placing the powder in a concave bowl at the base of the tube, and directing a downwards-pointing air jet into the powder. It was intended that the air would divide and suspend the particles, and then be deflected by the concave end to travel upwards, so as to disperse the suspension throughout the height of the tube. However, trials of this technique showed that the suspension settled much faster than expected, and therefore that the dispersal mechanism was not being effective, either as a result of generating too large clumps of particles and/or not raising the suspension to a sufficient height within the tube.

Hence, a technique was adopted that used the "paint sprayer" approach. A fast moving stream of air was directed through a venturi, into which the dust was gravity fed through an orifice. The feed rate – and hence the concentration of the resulting suspension – could be varied by using orifices of different sizes, achieved with interchangeable nozzles. (See Figure 4-1). The suspension is directed into the enclosure and upwards by the tube arrangement. The length of this tube had to be minimised, as even a short additional length was found to create a backpressure that produced a positive pressure in the venturi, blowing dust out of the top of the hopper.

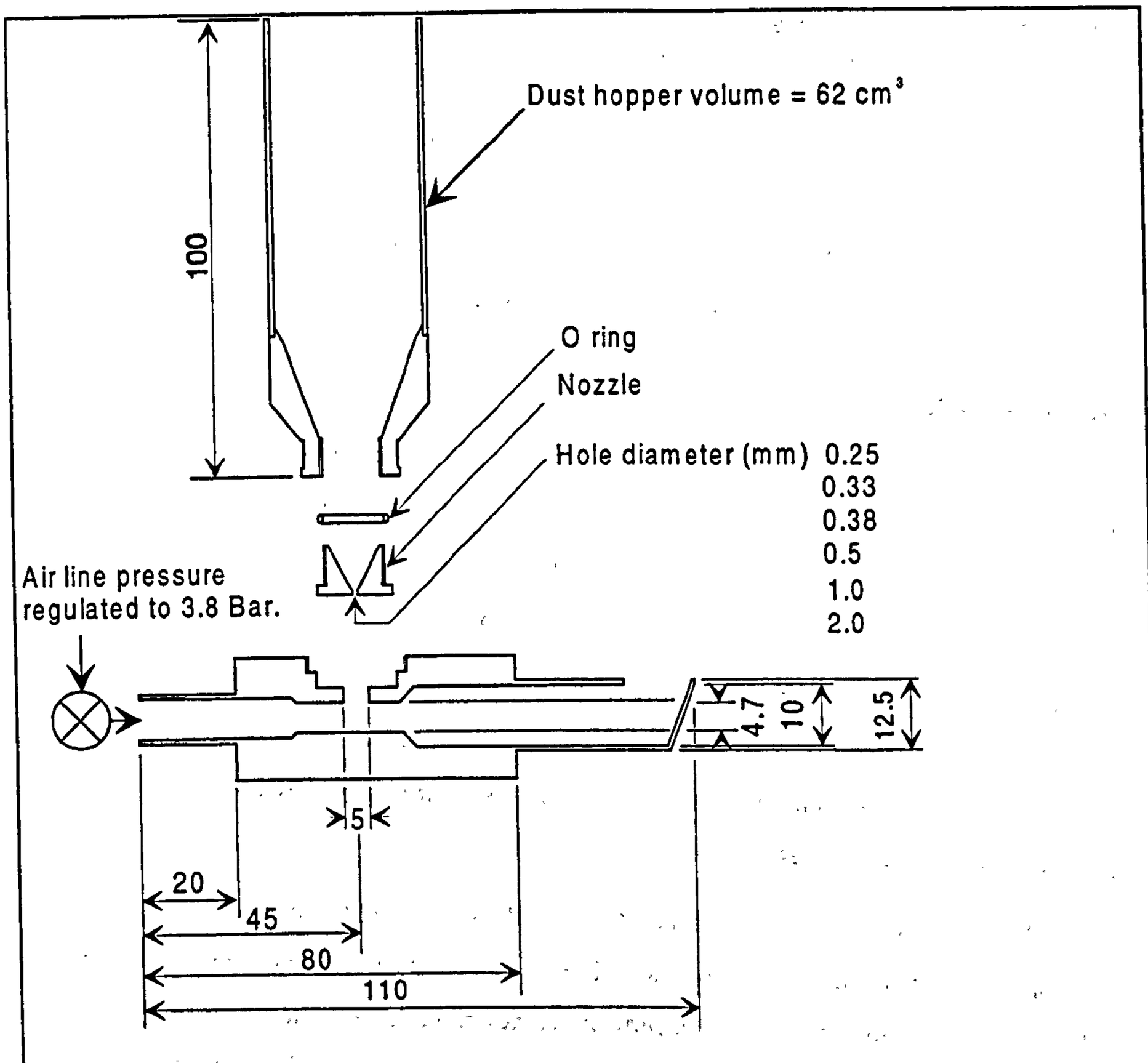

Figure 4-1 *Cross section of the dust "blow gun" drawn in elevation.*

An air pressure of 3.8 bar (50 p.s.i) was found to deliver the highest dust concentration (for a given nozzle), and was used in all following experiments. This pressure was chosen by varying the line pressure, and measuring the air and dust mass flow rate separately, to arrive at the dust concentration. This peak in concentration is presumably because reduced pressure created less suction in the venturi, and more pressure diluted the suspension by an increasing amount.

To deliver the suspension, the blower tube was placed into a filling boss towards the base of the enclosure, and a 5 second burst of compressed air was delivered to the "blow gun". This duration was chosen to be long enough – given the air flow rate of 4.6 l/s and tube volume of 15.7 litres – to change the air with a little excess, but also to make the filling event comparatively short.

The hopper was chosen to be taller than was necessary to contain the volume of particulate used. Earlier tests with a shorter hopper had shown a propensity for a "rat hole" to develop as material is drawn only from the centre of the hopper, and a clean air path can form in only a second or two. Hence a larger hopper was built, with a shallower convergence cone to improve material feed.

4.5 DESIGN OF ENCLOSURE

The acoustic requirement of the enclosure was to measure the plane wave characteristics of a suspension, in the audio frequency range, preferably down to the frequency of maximum specific attenuation that is predicted theoretically. While this could be achieved by measuring the free-field propagation constant, and correcting for spherical spreading, such an approach was impractical since the enclosure would have to be large or non-existent, thus creating dust-control problems.

4.5.1 Plane wave tube

The solution adopted was a modified standing-wave tube. Below a critical frequency, a cylindrical tube acts an acoustic waveguide; that is, only a single mode of propagation — plane wave propagation — is possible without rapid reactive attenuation. The critical frequency is that at which the first transverse mode is excited, and is equal [41] to 0.586c/D.

A 100mm diameter tube was chosen, giving a cut-off frequency for plane waves — and hence an upper working frequency — of 1992Hz. While a smaller diameter would be desirable for an extended frequency range, it was anticipated that the increased (wall area / enclosed volume) ratio would cause problems due to dust adhesion.

Two 2m lengths of tube were aligned with their axes vertical, thus allowing the dust to settle out onto the lower end, which was closed by a heavy cap. (The final weight of settled dust was used to measure the concentration of dust initially in suspension, as described later). The two tubes coupled together in the middle to form a 4m length. The upper end was closed by a mid-range loudspeaker. Towards the top of the lower tube, a microphone was mounted flush with the inside wall.

The walls of the lower tube were coated with a layer of bitumen panels to reduce structural vibration, hence reducing two mechanisms: the interchange of energy between acoustic and mechanical modes, and transmission via mechanical flanking paths. The panels also formed an insulation layer to reduce heat exchange with outside air, and the consequent variations in temperature during the course of an experiment; as the air inside the tube had been discharged from a compressed air line, a temperature difference could be expected.

4.5.2 Measurement technique

The impulse response between the loudspeaker and microphone was measured using the MLSSA system (described in Chapter 3). The resulting impulse response shows the downwards travelling downwards pulse, following by an upwards travelling pulse that had been reflected from the lower end, and traversed the lower tube twice. Further reflections from the loudspeaker cone and lower end followed.

The lower tube forms the measurement volume and was filled with suspension. The purpose of the upper tube was to increase the path length between the loudspeaker and microphone, and hence

increase the time gap between the first reflected pulse and the reflection from the loudspeaker cone. A typical impulse response is shown in Figure 4-2. Note that the pulses rise from and fall to approximately zero, and are clearly separated; the importance of this will be discussed below. Crudely speaking, the direct pulse acts as a reference, and the first reflection measures the acoustic effect of travelling twice through the suspension in the lower tube.

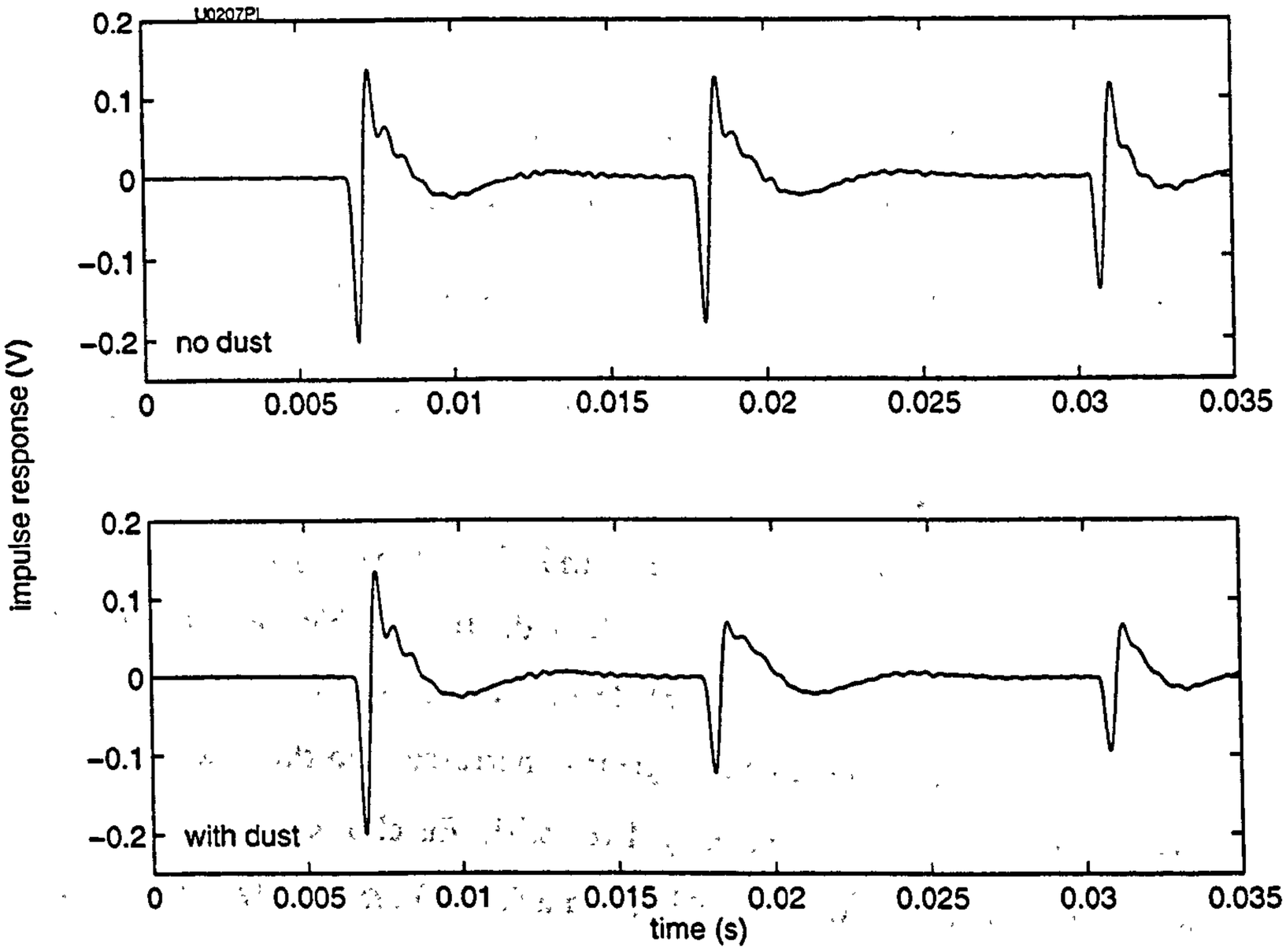

Figure 4-2 Examples of measured impulse response. Upper trace: measured with clean air in tube; lower trace: with 8.1 ppm of grade F1000 alumina in suspension. The first pulse is direct, before interaction with the suspension, and so remains unchanged by the presence of the suspension; the second pulse is the first reflection after two passes through suspension – it is clearly attenuated; the third pulse is the first reflection from the loudspeaker cone. For clarity, traces have been filtered digitally by a 2000Hz Butterworth low-pass filter (n=6) to remove reverberant high frequency ripple.

4.5.3 Filling the tube with suspension

It was necessary to ensure that all of the dust that had settled at the end of the experiment was in suspension during the measurement, and included in the acoustic path. If some dust was suspended *above* the microphone, it would have no acoustic effect, yet its mass would be measured, and hence the concentration would be estimated too high. To eliminate this error, the tube was divided into two equal lengths, with a sliding coupling in the middle.

Before the lower tube was filled, the upper tube was raised to provide access to the open top end of the lower tube. As suspension was blown into the lower end of the lower tube, displaced air and excess suspension was vented from the top end, into either a vacuum cleaner nozzle, or a large plastic bag. After the filling was completed, the nozzle or bag would be removed, and the upper tube replaced onto the lower. This method ensured that the upper tube was substantially free from suspended particles. The coupling provided a continuous, smooth inner wall to prevent stray reflections, and closely-toleranced surfaces to ensure an airtight fit whilst still sliding freely.

The suspension was blown into the tube through a filling boss near the lower end. The nozzle on the blow-gun deflected the suspension upwards, thus flushing out the clean air, and reducing the incidence of suspension directly onto the weighing apparatus. This mode of filling was found to produce the most uniform suspension compared to other methods tried (e.g. filling from the top). Visual inspection of the filling process showed a spiral filling pattern that distributed the suspension evenly across the tube section – confirmed by the even axial distribution of settled dust at the end of the experiment.

The filling boss was positioned 370 mm above the lower end in an attempt to produce a clean air buffer above the weighing shim, and hence reduce premature settling.

After filling, the blow-gun nozzle was withdrawn from the boss, and the orifice sealed with a bung whose end fitted flush with the inside of the tube wall.

4.5.4 Acoustic transducers

An unbaffled loudspeaker, mounted on a wooden surround, fitted coaxially onto the open top end of the upper tube. A mid-range driver was selected (Goodmans 4", 125W 8 ohm) despite the fairly low frequency range required (down to 200Hz). The reason is that, when coupled to a waveguide, the low-frequency radiation efficiency is greatly increased, and the spectrum of the resulting signal is weighted heavily to low frequency. Even with this choice of loudspeaker, a 16 μF series capacitor was used to attenuate low frequencies, and achieve a reasonably flat response in the frequency range of interest (see Figure 4-3).

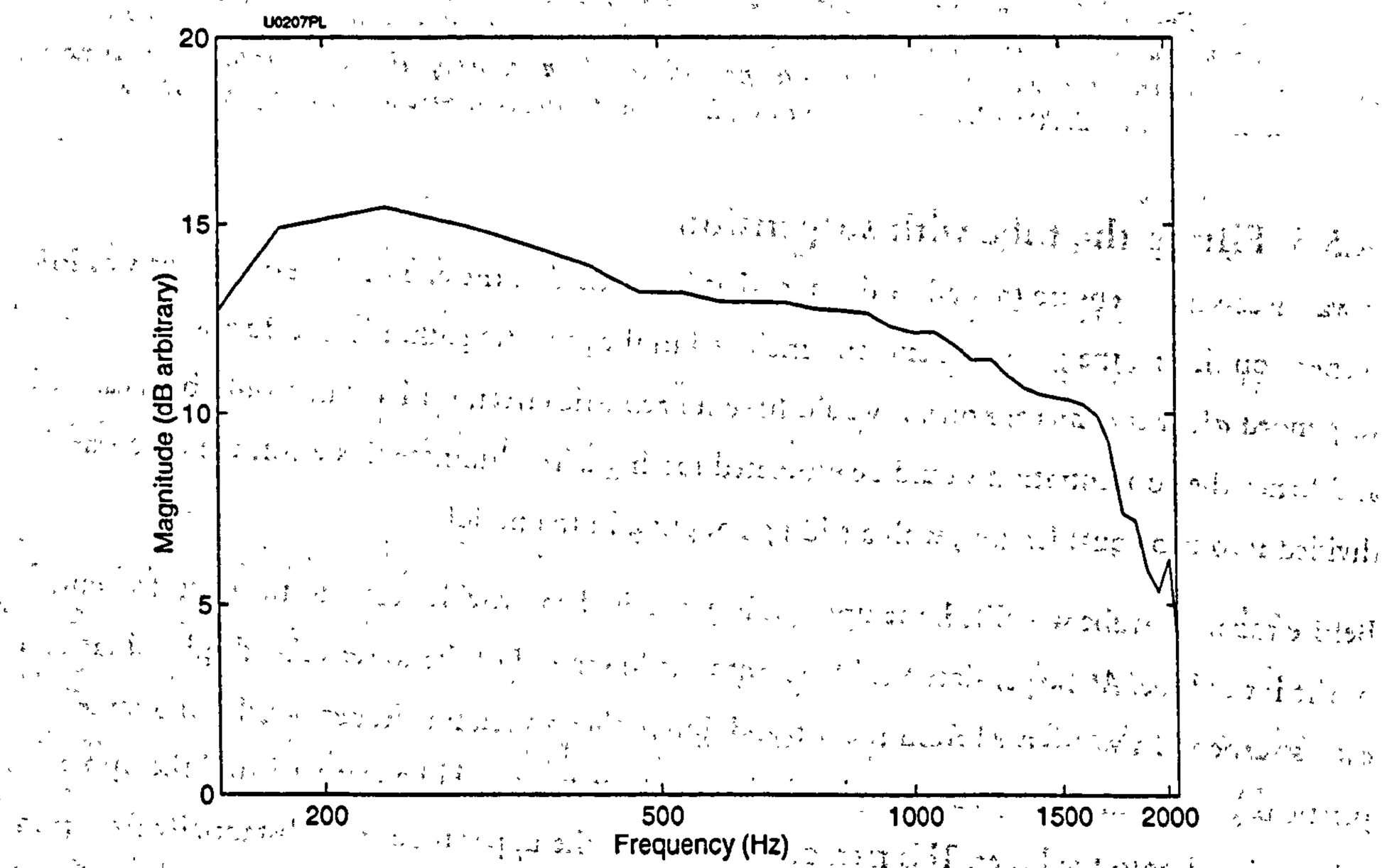

Figure 4-3 Spectrum of the direct pulse in Figure 4-2 (with no filtering). The cut-on of the first transverse mode (1,0) is visible at 2000Hz.

The microphone was a Brüel & Kjær 4133 1/2" capsule on a Type 2639 preamplifier. It was mounted with the grid flush with the inside wall, and protected with a thin layer of 50μm gauze. It is important that the capsule was "side-vented", meaning that the rear of the diaphragm was connected via a low frequency equalisation duct to the front of the diaphragm, rather than the rear of the preamp which is outside of the tube. As the tube assembly is substantially air-tight, the static pressure inside the tube can fluctuate sharply when, for example, the tubes are coupled and decoupled. If these fluctuations appeared across the diaphragm instead of on both sides of it, the microphone might be damaged.

The microphone was held in a boss by two O-rings that provided an air-tight seal and vibration isolation.

4.6 MEASUREMENT OF SUSPENSION CONCENTRATION

It was important to be able to make an independent measurement of the particle concentration within the tube by non-acoustic means. Optical densimeter techniques were considered, but these suffer from the disadvantage of sampling along a line (or cylinder) only. To account for the inevitable variations in concentration throughout the enclosure volume, a method of measuring mean concentration was required. A gravimetric method was chosen, in which the suspension was allowed to settle after a measurement, and the mass of settled particles was measured. Hence, knowing the volume of the tube, the concentration could be calculated.

The measurement of settled mass is complicated by the relatively small amounts of dust (10 - 400 mg), and the requirement for a heavy, acoustically reflective lower end. The solution adopted (see Figure 4-4) was to clamp magnetically a thin metal shim to the end cap , so that this could be removed and weighed on a sensitive balance. The shim is slightly undersized (85mm diameter) to avoid errors due to dust falling off the tube onto the shim, and the likelihood that particles falling near the wall could stick to the wall during settling.

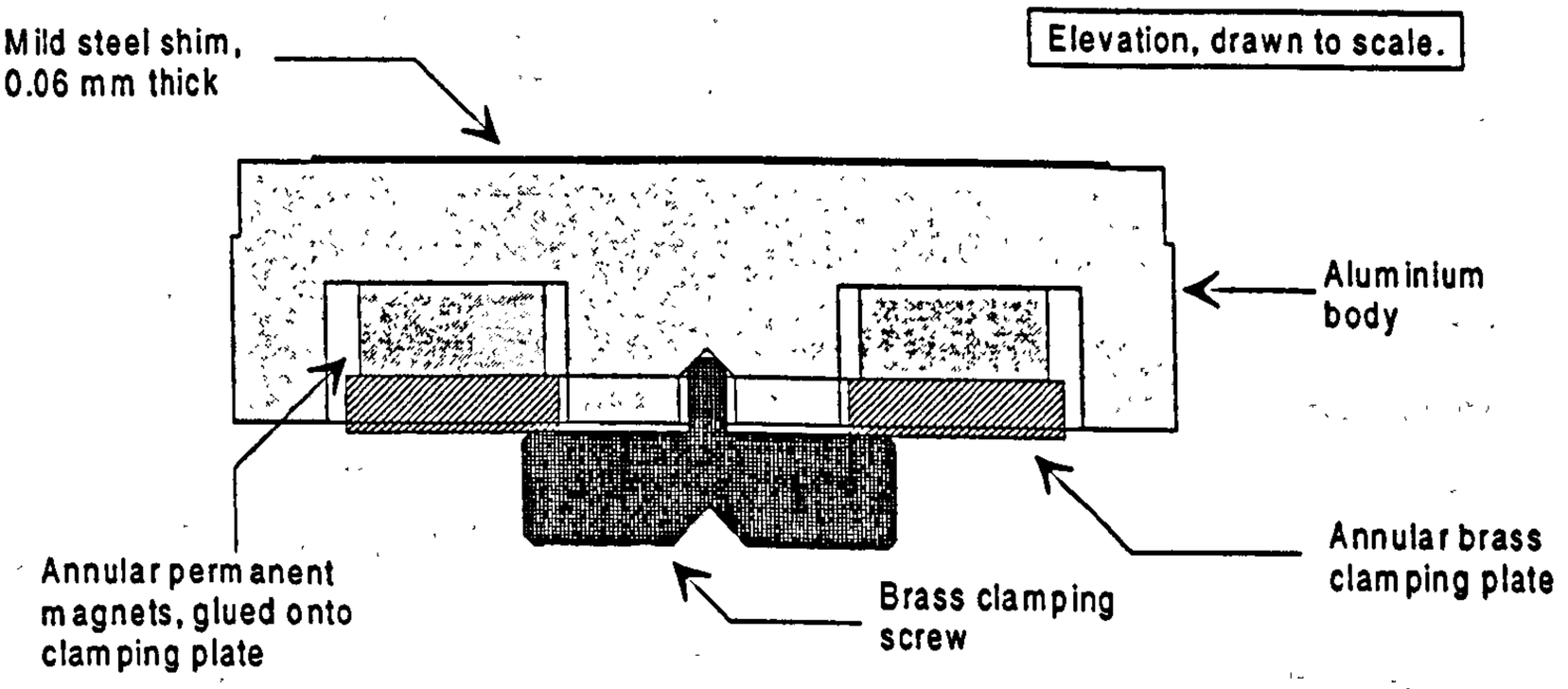

Figure 4-4 *Cross section of the lower end cap and shim clamping device. To weigh the shim, the clamping screw is removed, thus releasing the clamping plate and magnets, and the shim is thus freely removed. The whole assembly is clamped into the tube by a strap that hooks onto lugs brazed onto the tube, and a screw that locates in the recess in the brass clamping screw.*

4.7 MEASUREMENT OF SUSPENSION STABILITY

The volume concentration of dust in the static rig is measured by weighing the settled-out dust at the end of the experiment. For this to give a true representation of the actual volume fraction during the acoustic measurement, we need to be sure that the quantity of dust that settles before or during the acoustic measurement is negligible; any such premature settlement would tend to lead to an overestimation of the volume fraction.

Hence it was desirable to estimate the amount of dust settling prematurely, in order to give error margins to the concentration measurements. This required real time measurements of the settled mass, with a time resolution of < 1 second, and for this to be accomplished with as little modification to filling airflow as possible.

4.7.1 Dynamic weighing device

A device was designed which would measure dynamically the mass of dust as it settled onto the lower end-cap. The physical principle used was to measure the resonant response of a lightly damped mass-spring system, in which the resonant frequency is dependent on the value of the mass.

A special lower end-cap was devised, with a thin brass shim suspended above the surface of the cap. The shim was excited to vibrate at resonance by insonifying it from below, via a hole in the end cap which was coupled through a plastic tube to a low frequency compression driver (see Figure 4-5).

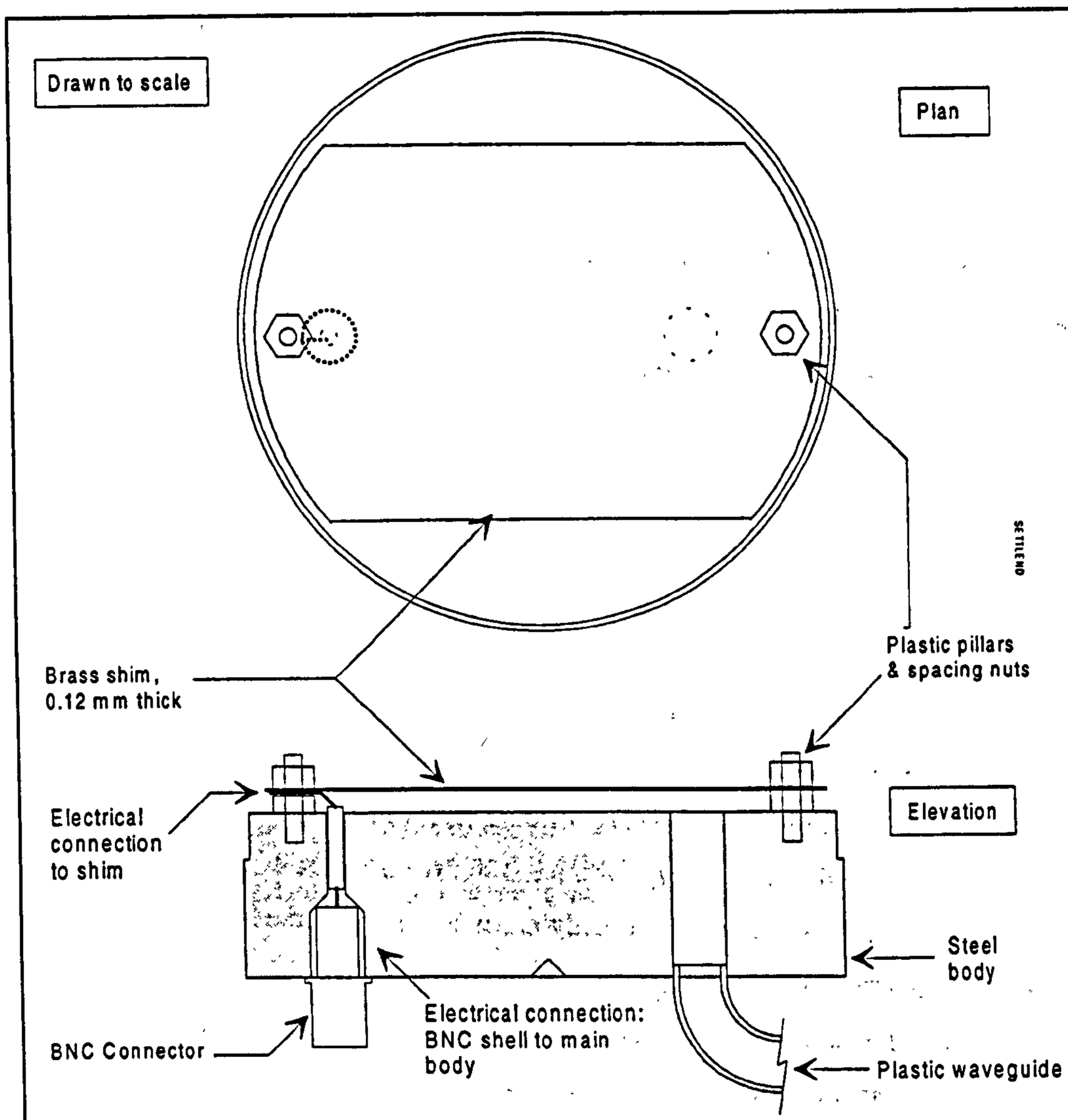

Figure 4-5 *Drawing of the dynamic settled-mass measurement device. The shim is held in slight tension by the spacing of the plastic (insulating) pillars.*

The displacement of the shim was measured by treating it as the diaphragm of an electrostatic microphone; insulating posts maintained an airgap between the shim and metal end cap, and hence oscillations of the shim resulted in a change of capacitance of the shim/cap system. This system was wired to a microphone preamplifier and measuring amplifier in the usual way, so that the shim was maintained with a polarisation voltage of 200V.

The shim has a complex set of resonances, some of which are extremely lightly damped ($Q > 100$). By exciting the shim to a low-order, lightly-damped resonance, and measuring its vibration amplitude as a function of time, very small quantities of dust settling on the shim may be detected. This is because the dust affects the resonant system in two ways:

- The resonant frequency is lowered, because the mass of the system is increased.
- The Q of the resonance is reduced.

These mechanisms both lead to a reduction in vibration amplitude, provided the same excitation frequency is maintained. The higher the Q, the more sensitive is the system to added weight.

Further detail on the theory and testing of this device is given in Appendix C.

4.7.2 Use of the dynamic weighing device

As the device presents a complex reflective surface, it cannot be used during acoustic measurements: so separate tests were made to ascertain the stability and settling rate of the different particulates used.

To make a measurement, the tube was filled with suspension in the normal way, but with the device in place of the usual lower end cap. The output of the device was recorded through the experiment (although for the period that the tubes are uncoupled, the output is invalid). The change in weight of the brass shim was measured after the dust had settled out, and so, after processing of the signal output, the dynamically-measured mass could be expressed as a percentage of the final settled mass. Assuming that similar settling conditions would prevail in an acoustic test, the device gave an indication of the mass percentage of dust that would have adhered to the weighing shim before the acoustic test started. A typical trace is shown in Figure 4-6. As the first acoustic measurement on a suspension-filled tube is usually taken 10s after the start of filling, it can be seen that approximately 6% of the final mass would have settled on the shim before the acoustic measurement. Repeated measurements on several different grades of material gave similar results, as so it was concluded that the process of filling tended to prematurely deposit this amount on the weighing shim, presumably due to recirculating flow below the filling boss as filling takes place. The implications on accuracy are discussed in section 4.10.1.

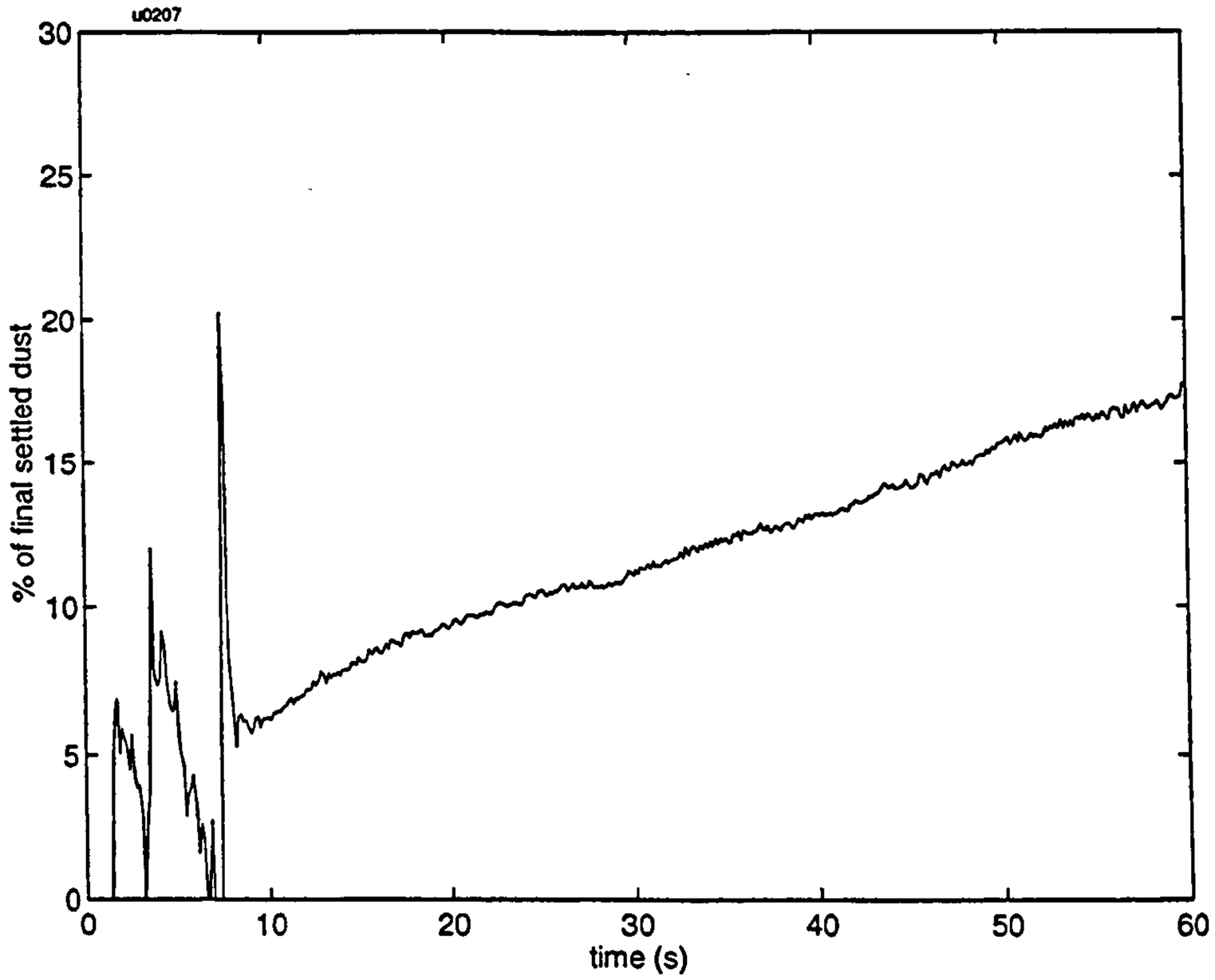

Figure 4-6 *Typical graph of particle settling, measured by the dynamic weighing device. The particulate is grade F1000 alumina, mean size 4μm. The trace before the spike at 9s is invalidated by the filling process: the spike indicates the re-coupling of the two tubes and start of validity of the trace.*

4.8 MEASUREMENT OF PARTICLE SIZE DISTRIBUTION

Most of the test powders were supplied with an indication of particle size distribution. This was generally measured by the photosedimentation technique, in which the distribution of settling rates in a liquid was measured, from which was calculated the distribution of the Stokes' diameter of the particles. However, since the introduction of dust into the tube involves some venting of excess suspension, there is the possibility that the resulting size distribution will be skewed; presumably a higher proportion of the finer particles will be vented, skewing the distribution to larger sizes. To account for this effect, the dust that settled onto the shim at the end of each experiment — after being weighed — was collected, and then its overall size distribution was measured with a photosedimentometer.

To illustrate the size of the shift, Figure 4-7 shows the distributions of the raw material and of the settled material, for one grade of alumina particles. An increase in mean radius from 3.1 to 3.25μm is discernible.

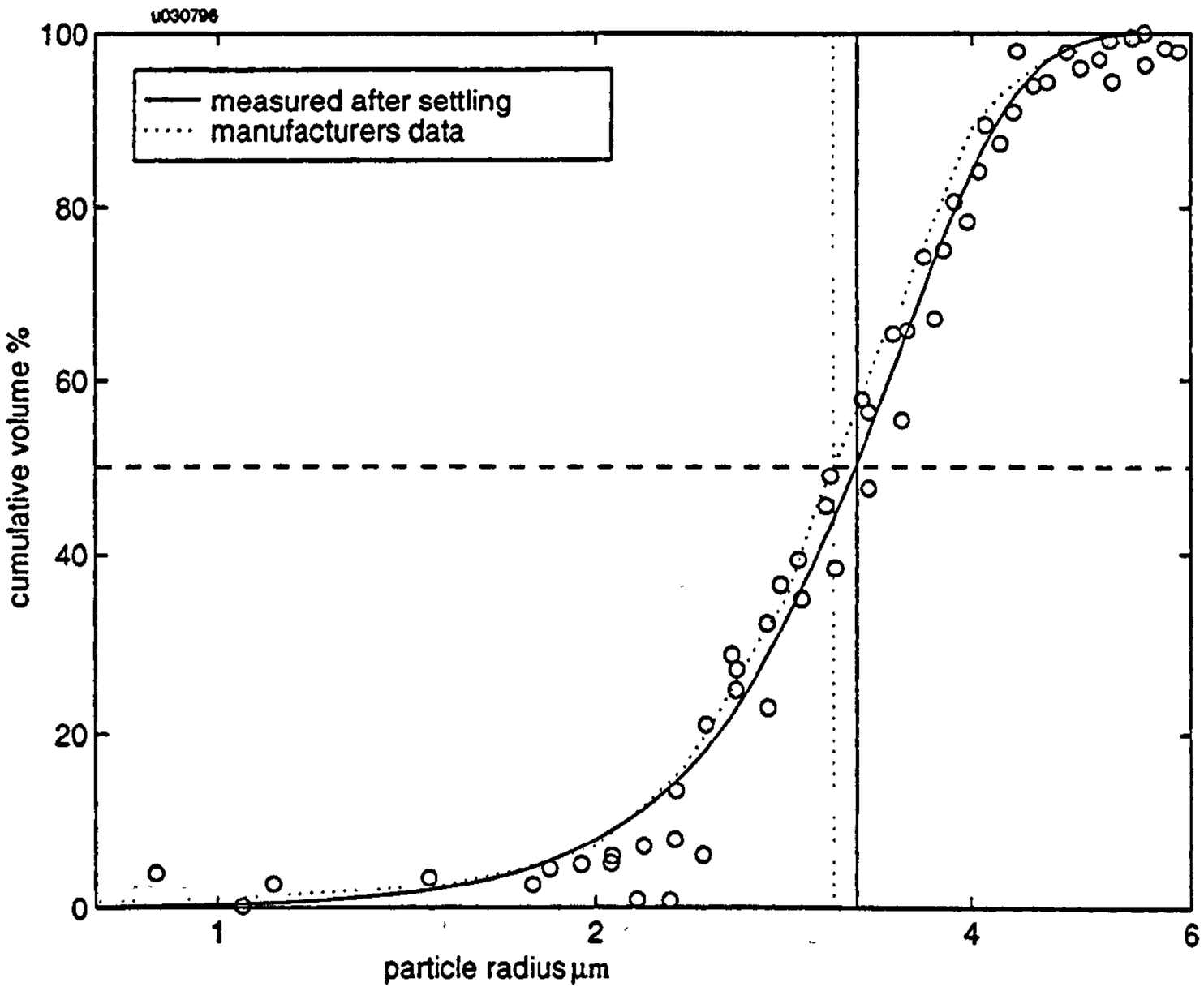

Figure 4-7 *The particle size distribution of grade F800 alumina. Dotted: supplied by manufacturer ; circles: measured points, three sets of data; solid: data points fitted by a Rosin-Rammler distribution [133] (3.4µm fineness, 4.5 dispersion). Vertical lines show the mean sizes of the two distributions (50% by volume)*

4.9 ANALYSIS OF DATA

This section will examine how the acoustic parameters of a suspension can be deduced from the impulse response measured in the equipment described above. Initially, the constant temperature case will be considered, before examining the effect of temperature drift on measurements of dispersion.

4.9.1 Constant temperature

Consider the measured impulse response (I.R.) between the output & input of the MLSSA system, $x(t)$. It will be composed of the direct pulse, and multiple delayed and modified versions of the pulse, and can be expressed in terms of the following individual I.R.s.

x_o : MLSSA stimulus output to a point in front of the loudspeaker.

x_m : the measurement chain from the microphone to the MLSSA card.

x_1 : passage of the upper tube, from in front of the loudspeaker to the microphone.

x_2 : two passages of the lower tube, including reflection from the lower end; from the microphone, back to the microphone.

x_s : additional effect above x_2 due to the presence of suspension.

x_L : reflection from the loudspeaker cone.

For the case where there is no dust in suspension, we can write:

$$x_a^T = x_m * (x_0 * x_1 + x_0 * x_1 * x_2 + x_0 * x_1 * x_2 * x_1 * x_L * x_1 + \ldots) \tag{4.1}$$

where x_a^T represents the total I.R. for an air-filled tube, and the symbol * represents a convolution in the time domain, so that, for example,

$$x_1(t) * x_2(t) = \int_{-\infty}^{\infty} x_1(\tau) \cdot x_2(t-\tau)\, d\tau \tag{4.2}$$

and τ is a dummy integration variable.

A similar expression can be written for the I.R., x_s^T, when the lower tube is filled with suspension:

$$x_s^T = x_m' * \left(x_0' * x_1 + x_0' * x_1 * x_2 * x_s + x_0' * x_1 * x_2 * x_s * x_1 * x_L * x_1 + \ldots\right) \tag{4.3}$$

Here, for the sake of generality, we allow the equipment IRs to drift to the dashed variables.

For the moment, we can approximate many of these IRs as weighted delta functions, to impose the necessary time delay (and so neglecting any frequency dependent terms):

$$x_1(t) \approx k_1 \delta\left(t - \frac{l_1}{c}\right) \tag{4.4}$$

$$x_2(t) \approx k_2 \delta\left(t - \frac{2l_2}{c}\right) \tag{4.5}$$

where $\delta(t-\tau) = 1 \quad t = \tau$ $\quad = 0 \quad t \neq \tau$ is the unit delta function, c is the velocity of sound in air at the prevailing temperature, and k_1 and k_2 are numerical constants to account for losses.

Therefore, if x_0 decays to a negligible quantity in a time less than $\left(\frac{2l_2}{c}\right)$, then the bracketed terms in (4.1) can be separated by editing in the time domain; we can see from Figure 4-2 that this is a reasonable assumption. The importance of this separability is explored below.

With the assumption that we can separate the individual terms, we define the following "sub-IRs", extracted using a rectangular window.

$$x_a^0 = x_m * x_0 * x_1 = \begin{cases} x_a(t) & \text{for } t_1 \le t \le t_2 \\ 0 & \text{otherwise} \end{cases} \tag{4.6}$$

$$x_a^1 = x_m * x_0 * x_1 * x_2 = \begin{cases} x_a(t) & \text{for } t_2 \le t \le t_3 \\ 0 & \text{otherwise} \end{cases} \tag{4.7}$$

Here, the superscript ^{0} refers to the direct pulse, and ^{1} refers to the first reflected pulse.

Similarly for the IRs measured with suspension.

$$x_s^0 = x_m{}' * x_0{}' * x_1, \quad x_s^1 = x_m{}' * x_0{}' * x_1 * x_2 * x_s \tag{4.8}$$

Now, making a transform into the frequency domain, we represent the transformed variables in upper case letters, and replace convolutions by multiplications [115].

$$X_a^0 = X_m X_0 X_1 \tag{4.9}$$

$$X_a^1 = X_m X_0 X_1 X_2 \tag{4.10}$$

$$X_s^0 = X_m{}' X_0{}' X_1 \tag{4.11}$$

$$X_s^1 = X_m{}' X_0{}' X_1 X_2 X_s \tag{4.12}$$

To arrive at an expression for the desired quantity X_S, without the other unknowns, we form the following transfer functions.

$$H_a = \frac{X_a^1}{X_a^0} = X_2 \tag{4.13}$$

$$H_s = \frac{X_s^1}{X_s^0} = X_2 X_s \tag{4.14}$$

$$Y = \frac{H_s}{H_a} = X_s \tag{4.15}$$

Hence we see that, by measuring two IRs – one with and one without suspension in the tube – and editing them appropriately, transforming the edited segments into the frequency domain and forming transfer functions, one can deduce the frequency domain effect of two passes through the suspension. The technique is robust, since it automatically rejects drift in the electronic components. The analysis above ignores variations in the temperature of the air/suspension column, although this case will be investigated later.

From (4.15) we can deduce the conventional acoustic parameters. The plane wave attenuation coefficient of the medium is given simply by:

$$\alpha = \frac{|Y|}{8.69 \times 2l_2} \quad \text{Np/m, if } |Y| \text{ is expressed in dB.} \tag{4.16}$$

This can be expressed in the dimensionless form used by Temkin & Dobbins [141], known as the specific attenuation, $\overline{\alpha}$, or attenuation per wavelength:

$$\overline{\alpha}(f) = \alpha(f)\frac{c}{f} \quad \text{Np} \tag{4.17}$$

Dispersion may also be defined in a dimensionless manner as:

$$\beta(f)=\left(\frac{c_0}{c_s(f)}\right)^2-1 \tag{4.18}$$

Here, c_0 and c_s refer to the phase velocities in clean air and suspension, respectively.

The advantage of this definition is that, as shown explicitly by Temkin and Dobbins [141], the dispersion is directly proportional to dust concentration (at low values of concentration), whereas the phase velocity of the suspension decreases in a non-linear way. Therefore sets of experimentally-measured dispersion curves may be collapsed onto a single curve by normalising with respect to their concentration. The same process can also be applied, more obviously, to either the attenuation or specific attenuation.

It will be shown in the next section that the dispersion can be computed from the argument of Y thus:

$$\beta=\left(1-\frac{c_a \arg(Y)}{4\pi f l_2}\right) \tag{4.19}$$

4.9.2 Dispersion measurement in the presence of temperature drift.

In a practical set of measurements, there will be a time lag between the measurement without, and that with suspension. In the previous section, we acknowledged this by allowing the IRs of the stimulus and measuring equipment to drift between the expressions for x_a and x_s — equations (4.1) and (4.3). However, the values of x_1 and x_2 were held constant, implicitly assuming that the propagation constants for the columns of air remained constant, and therefore that the temperature does not drift between the two measurements. To assess the error due to such a drift, consider the approximate expression for the velocity of sound in air:

$$c_a=C\sqrt{\frac{T}{T_0}} \tag{4.20}$$

Where C = 331 ms^{-1}, T is the temperature in °K, and T_0 = 273.1 °K. We allow the temperature to drift from T to $T+\Delta T$, and investigate the apparent dispersion[1], in the absence of any other changes. Substitute this expression into (4.18):

$$\beta_T=\left(\frac{C\sqrt{T/T_0}}{C\sqrt{T+\Delta T/T_0}}\right)^2-1=-\frac{\Delta T}{T+\Delta T} \tag{4.21}$$

For example, assume a drift of +0.2K from 293K. The apparent dispersion would then be -6.8×10^{-4}. Compare this with the dispersion of a suspension of 6μm alumina spheres, which formed the

[1] Temperature drift does not cause true dispersion, since the velocity change is constant with frequency. In a real measurement, the apparent dispersion due to temperature drift will therefore appear as an offset on top of a frequency dependent curve due to the suspension.

most used test material: at 2000Hz and a volume concentration of 1 ppm (towards the lower end of the experimental range) the predicted dispersion is 3.5×10^{-4}. So it is clear that, at low concentrations and higher frequencies (dispersion due to suspension falls with frequency), the actual dispersion due to the suspension could be swamped by quite small variations in temperature. This problem was encountered by Höfelmann and Beckord [60], who abandoned their attempt to measure phase velocity in suspensions.

Let us investigate whether the effect of temperature drift can be removed through signal processing, in the same way that equipment drift was nulled.

The dispersion can be computed from only the phase spectra of the transfer functions, and so, in the following, only the argument of the complex variables will be considered.

Consider two measurements: the first one, without suspension, with a uniform air temperature yielding a sound speed of c_0 ; the second one, with suspension, and a temperature drift such that the speed of sound in clean air (in the upper tube) is $c_0 + \Delta c_T$, and that in the lower tube is $c_0 + \Delta c_T + \Delta c_s$. Our aim is to measure the dispersion due to Δc_s while ignoring that due to Δc_T.

Referring to (4.9), define the "intrinsic phase" of the equipment:

$$\Theta_0 \equiv \arg(X_m X_0) \tag{4.22}$$

In this analysis, we remove the allowance of phase drift in the instruments, so that $\Theta_0' = \Theta_0$. This condition will be discussed later.

$\arg(X_1)$ is formed by a phase lag due to the time-of-flight over distance l_1, and the phase lead due to editing, since the transform is taken of a data segment between times t_1 and t_2. It is easy to show that:

$$\arg\left(X_a^0\right) = \Theta_0 - \frac{\omega l_1}{c_0} + \omega t_1 \tag{4.23}$$

Similarly, for (4.10):

$$\arg\left(X_a^1\right) = \Theta_0 - \frac{\omega(l_1 + 2l_2)}{c_0} + \omega t_2 + \Theta_2 \tag{4.24}$$

where Θ_2 is the phase change due to the reflection at the lower end. Similarly for (4.11) and (4.12):

$$\arg\left(X_s^0\right) = \Theta_0 - \frac{\omega l_1}{c_0 + \Delta c_T} + \omega t_1 \tag{4.25}$$

$$\arg\left(X_s^1\right) = \Theta_0 - \frac{\omega l_1}{c_0 + \Delta c_T} - \frac{2\omega l_2}{c_0 + \Delta c_T + \Delta c_s} + \omega t_2 + \Theta_2 \tag{4.26}$$

We can now express the phase spectra of the transfer functions in these terms. For convenience, we label the phase spectra as P, defined below. Substituting (4.23) and (4.24) into (4.13):

$$P_a \equiv \arg\left(\frac{X_a^1}{X_a^0}\right) = \omega\left[\frac{-2l_2}{c_o} + (t_2 - t_1)\right] + \Theta_2 \tag{4.27}$$

Substitute (4.25) and (4.26) into (4.14):

$$P_s \equiv \arg\left(\frac{X_s^1}{X_s^0}\right) = \omega\left[\frac{-2l_2}{c_o + \Delta c_s + \Delta c_T} + (t_2 - t_1)\right] + \Theta_2 \tag{4.28}$$

Substitute (4.27) and (4.28) into (4.15):

$$P_Y \equiv \arg(Y) = P_s - P_a = 2\omega l_2\left(\frac{1}{c_0} - \frac{1}{c_0 + \Delta c_s + \Delta c_T}\right) \tag{4.29}$$

Define a further transfer function and substitute (4.23) and (4.25) :

$$P^0 \equiv \arg\left(\frac{X_s^0}{X_a^0}\right) = \omega l_1\left(\frac{1}{c_0} - \frac{1}{c_0 + \Delta c_T}\right) \tag{4.30}$$

It can be seen from (4.30) that P^0 may be used to assess the value of Δc_T, since all other variables are known; essentially, it is the transfer function formed from the two direct (clean air) pulses.

While a further transfer function, $P^1 \equiv \arg\left(\frac{X_s^1}{X_a^1}\right)$, can be defined, it yields us no further information, since it can be shown that $P^1 = P_Y + P^0$.

For the moment, let us set $\Delta c_T = 0$ to check the validity of (4.19). Substitute (4.29) into (4.19):

$$\beta = \left(\frac{c_0}{c_0 + \Delta c_s}\right)^2 - 1 \tag{4.31}$$

which accords with the definition of dispersion in (4.18).

Now, to remove the effect of temperature drift, we make two further definitions:

$$Q^0 \equiv \left(1 - \frac{c_0 P^0}{\omega l_1}\right)^{-1} = \frac{c_0 + \Delta c_T}{c_0} \tag{4.32}$$

$$Q^Y \equiv \left(1 - \frac{c_0 P_Y}{2\omega l_2}\right)^{-1} = \frac{c_0 + \Delta c_s + \Delta c_T}{c_0} \tag{4.33}$$

$$\text{then } 1 + Q^Y - Q^0 = \left(\frac{c_0 + \Delta c_s}{c_0}\right) \tag{4.34}$$

And finally $\beta = \left(\frac{1}{1+Q^Y - Q^0} \right)^2 - 1$ (4.35)

Therefore, if there was a spatially-uniform temperature drift between the two measurements, then some simple signal processing can be used to extract the dispersion due to the suspension alone. It was necessary to assume zero equipment phase drift, since otherwise a term in $\Delta\Theta_0$ would remain in Q^0. The attenuation coefficient can still be calculated using the earlier expression, (4.16), in which amplitude drift is removed, while the dispersion can be calculated using either (4.35) or (4.19), depending on which is found to give the most stable measurements.

4.9.3 Signal processing

The calculations described above were performed using a program written in MATLAB [1]. The program accepts as input an array of impulse responses, one of which is taken as the clean air reference, and performs the following steps:

1. Calculates the sound velocity in clean air, using the time of flight between the direct pulse, and a subsequent high order reflection.
2. Displays the direct and reflected pulses and prompts the user to manually select the beginning and end of pulses. A high order reflection can be chosen for the reflected pulse, if required.
3. The IRs are filtered to reduce reverberant high frequency noise, divided into segments, and windowed with leading and trailing Hamming windows.
4. The required FFT transforms are taken, and transfer functions calculated.
5. The output variables are displayed and returned. They are: specific attenuation, uncorrected dispersion and temperature-corrected dispersion.

4.10 ASSESSMENT OF MEASUREMENT ERRORS

There are two areas in which the errors may fall: errors in creating and measuring the controlled suspension, and errors in measuring the acoustic effects of the suspension. The latter will mainly be discussed in Chapter 6, Discussion, although some measurements are given later in this chapter to assess the stability of the apparatus.

4.10.1 Errors in the controlled suspension

These errors relate to the accuracy of the independent variables, that are used as inputs to the acoustic model to compare with the measured acoustic (dependent) variables. The sources of error and the ways in which they were assessed and minimised are listed below:

[1] See listing of PLAN7MC.M in Appendix B

Volume concentration

The balance that was used to measure the dust-covered shim (Mettler H10W) had a resolution of 0.1mg, and a repeatability of approx. 0.2mg. Hence, allowing for a 5% weighing error, the minimum measurable concentration was 300mg/kg (4mg of settled dust, corresponding to a volume concentration of 0.1 parts per million of alumina). At a more typical concentration of 20g/kg, the error due to weighing resolution is negligible at 0.06%. While the linearity of the balance is not quoted, the maximum error above a concentration of 1ppm was assumed to be 0.5%.

The data gained from the dynamic weighing apparatus (Figure 4-6) indicated that approximately 6% of the dust at the end of an experiment will have been deposited during the course of filling, and therefore that the measured concentration will be 6% too high. Therefore, all concentration measurements are derated by 6%. The uncertainty in this value is approximately 3%, caused by the extreme sensitivity of the dynamic weighing device at low values of added mass.

A less quantifiable error may be caused by the assumption that all dust in suspension eventually settles on the end cap, without adhering to the tube walls. This was minimised by using an undersized weighing shim, so that errors due to dust adhesion are reduced.

Overall, it is estimated that the accuracy of the concentration measurement (after the 6% adjustment) was ±5%.

Vertical inhomogeneity

It would be surprising if the suspension inside the tube were distributed perfectly homogeneously, although this is the assumption made in the theoretical acoustic predictions. Intuitively, we can see that the inhomogeneity will have little effect for the following reason. At low concentrations, the acoustic effects are directly proportional to concentration; and as the final measured effects have been integrated over the path length by the travelling plane wave, the exact spatial distribution of dust should be irrelevant as long as the spatially averaged values can be measured. To check this assumption, a computer program simulated the effect of vertical inhomogeneity in two ways:

1. A linear concentration gradient was imposed, ranging from zero at the top of the tube, to double the average concentration at the bottom. The particle size distribution was maintained uniform. The acoustic predictions with and without the inhomogeneity were computed[1], and the error caused by disregarding the inhomogeneity is shown Figure 4-8.

[1] See listing of STRAT.M in Appendix B

2. Vertical stratification of particle size was simulated by dividing the air column into nine segments, with each segment containing only one particle size[1]. The concentration of each segment varied according to the abundance of that particle size. The percentage error was calculated as above, and shown in Figure 4-9.

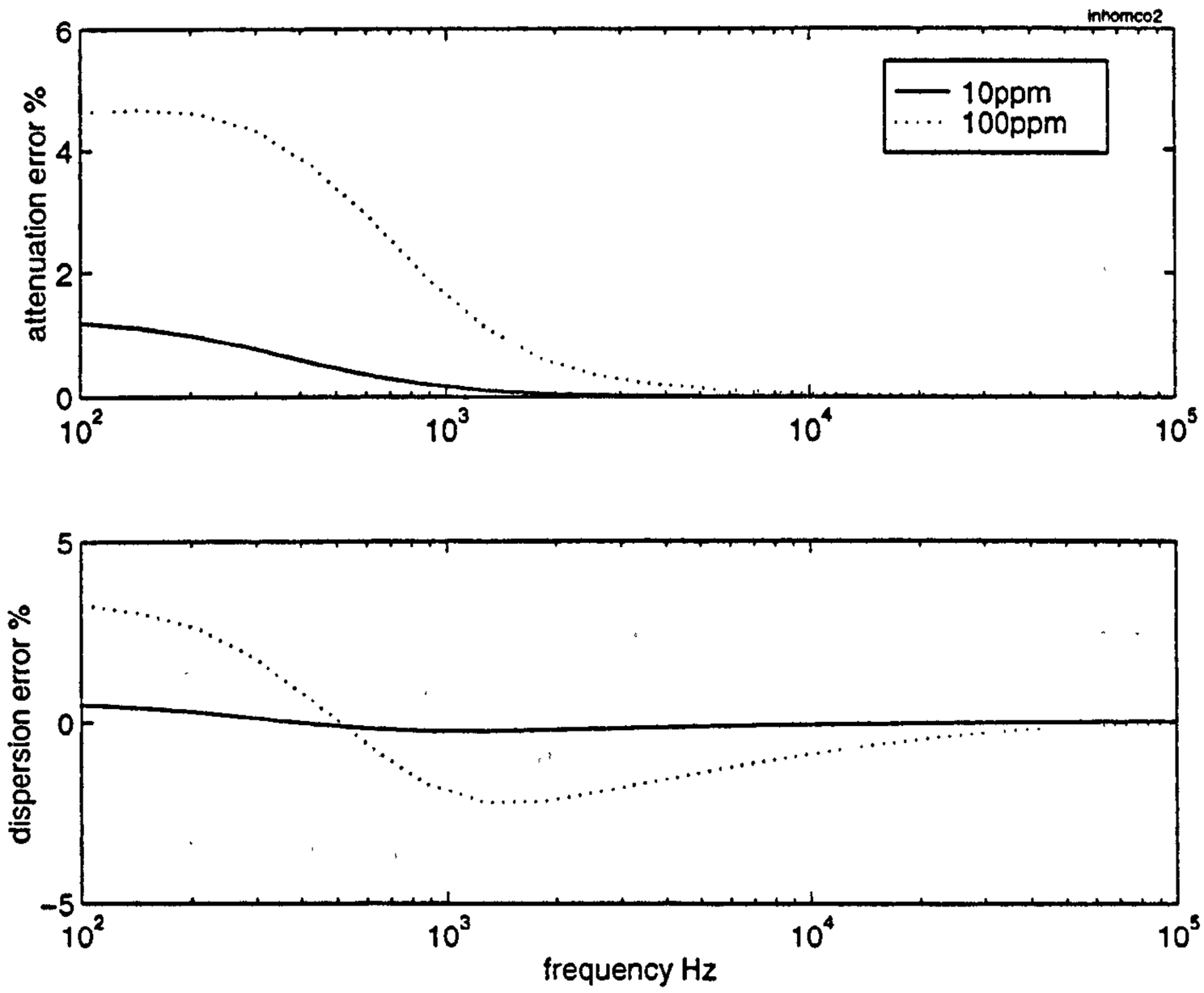

Figure 4-8 Theoretical percentage error caused by assuming homogeneity in the presence of a vertical linear concentration gradient, for two mean concentrations: 10ppm (the usual maximum), and 100ppm.

[1] See listing of VER_INH.M in Appendix B.

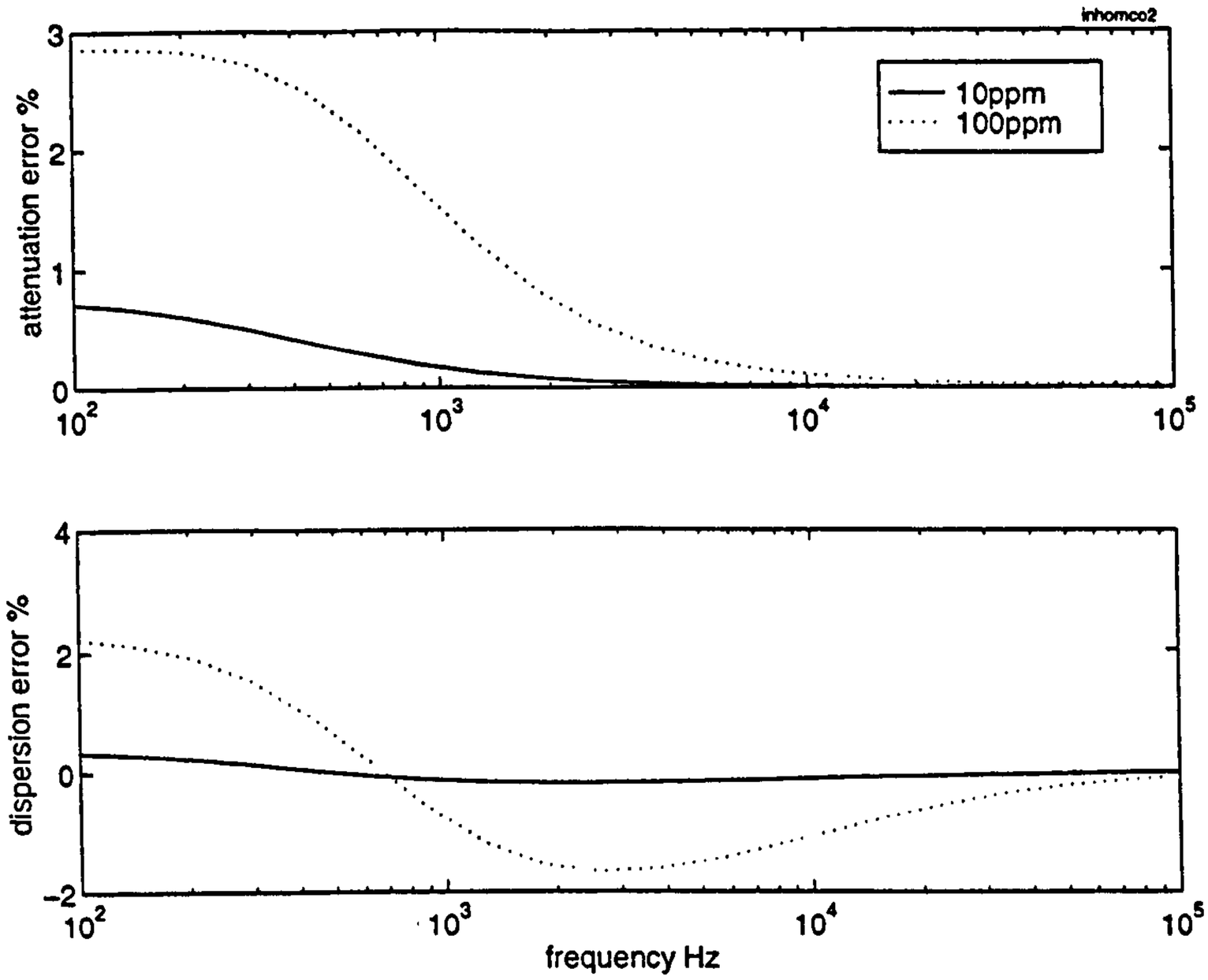

Figure 4-9 Theoretical percentage error caused by assuming homogeneity in the presence of vertical stratification of particle sizes, for two mean concentrations: 10ppm (the usual maximum), and 100ppm.

At the usual maximum volume concentration of 10ppm, both cases show a maximum error of <1% at 200Hz, decreasing with frequency. The error increases with concentration, as the non-linearity in the relationship becomes more marked.

Since the situations presented here are extreme in their level of inhomogeneity, it was felt justifiable to ignore such effects.

4.10.2 Errors in the measuring equipment

MLSSA Stability

Initially, the stability of the MLSSA system alone was tested. Its output was connected directly to the input, and measurements taken over the period of 50mins, having been left to warm up for 1 hour. These measurements were essentially the IR of the anti-aliasing filter.

While the amplitude was found to be constant to <0.05dB, the phase showed a steady drift. The phase spectrum as a function of frequency (referenced to the first measurement) was a reasonably straight line with a negative gradient, and so could be described by a time lag (since the phase spectrum due to a time lag Δt is $\Theta(\omega) = \omega \cdot \Delta t$). This lag showed a monotonic increase with time, as seen in Figure 4-10.

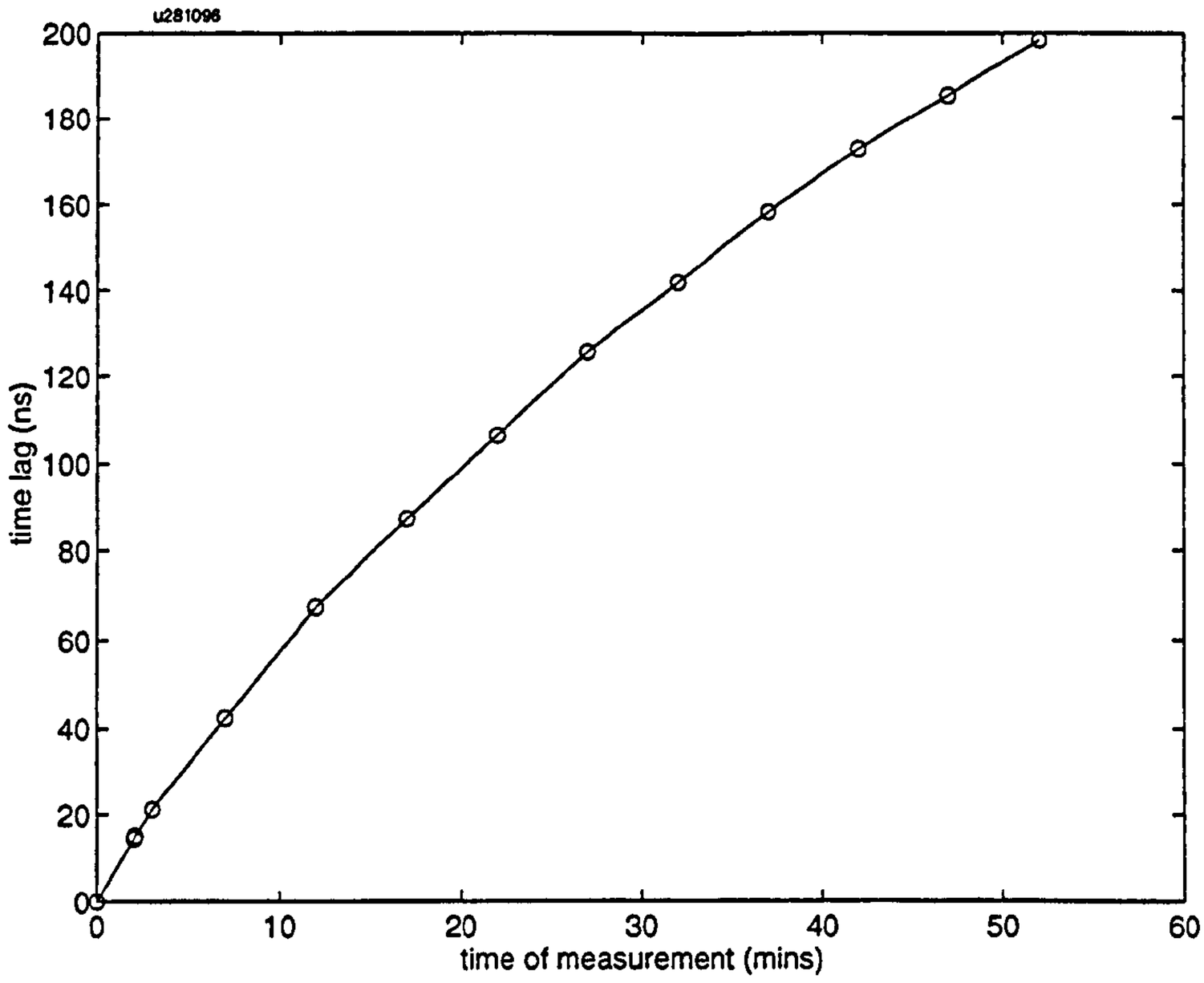

Figure 4-10 The drift in the phase spectrum of MLSSA's antialiasing filter can be described as an increasing time lag.

The impact of this drift on the apparent attenuation and dispersion was calculated by synthesising a double pulse IR – similar to the electro-acoustic IR – simply by concatenating two identical (single pulse) IRs. This was then processed as usual; the results are shown in Figure 4-11. It is clear that there is no drift in specific attenuation – just a small random error. The drift in temperature-corrected dispersion is clear, whereas the uncorrected dispersion almost perfectly rejects system phase drift, as predicted in the analysis above.

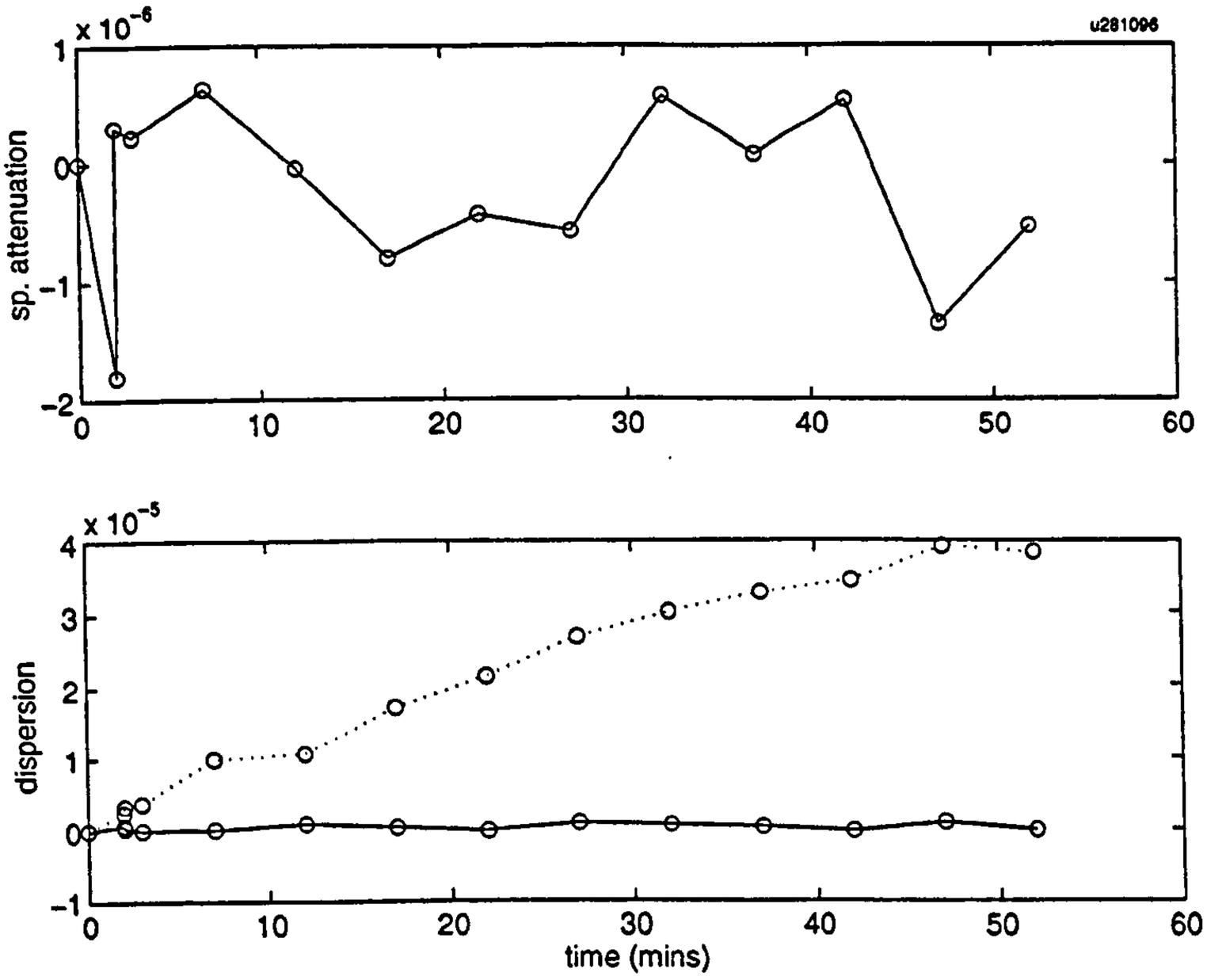

Figure 4-11 Upper: apparent specific attenuation at 2000Hz due to MLSSA's amplitude repeatability/stability. Lower: apparent dispersion at 2000Hz due to MLSSA's phase repeatability/ stability; dotted curve is with temperature compensation, solid line is without.

Acoustic stability

To assess the stability of the acoustic measurement, and the relative importance of various sources of error, control (no dust) measurements were made over a period of 30mins. These were initiated by a "mock" filling, that is, the suspension-generation procedure was followed, except that no dust was placed in the hopper, so that only the effects of drift and disturbance due to the filling would be measured. Three IRs were measured repeatedly: the overall electro-acoustic IR, the IR of the electronic components (by connecting the power amplifier output to the microphone amplifier input), and the IR of MLSSA (by connecting MLSSA output to its input). The IRs were processed as above to calculate the apparent values of specific attenuation and dispersion (using as references the IRs before filling). The equipment had been allowed to warm up for 3 hours.

The errors were greatest at the bottom and the top of the useful frequency range ; so the worst-case plots are shown, for 240Hz, and 1960Hz, in Figure 4-12 and Figure 4-13 respectively.

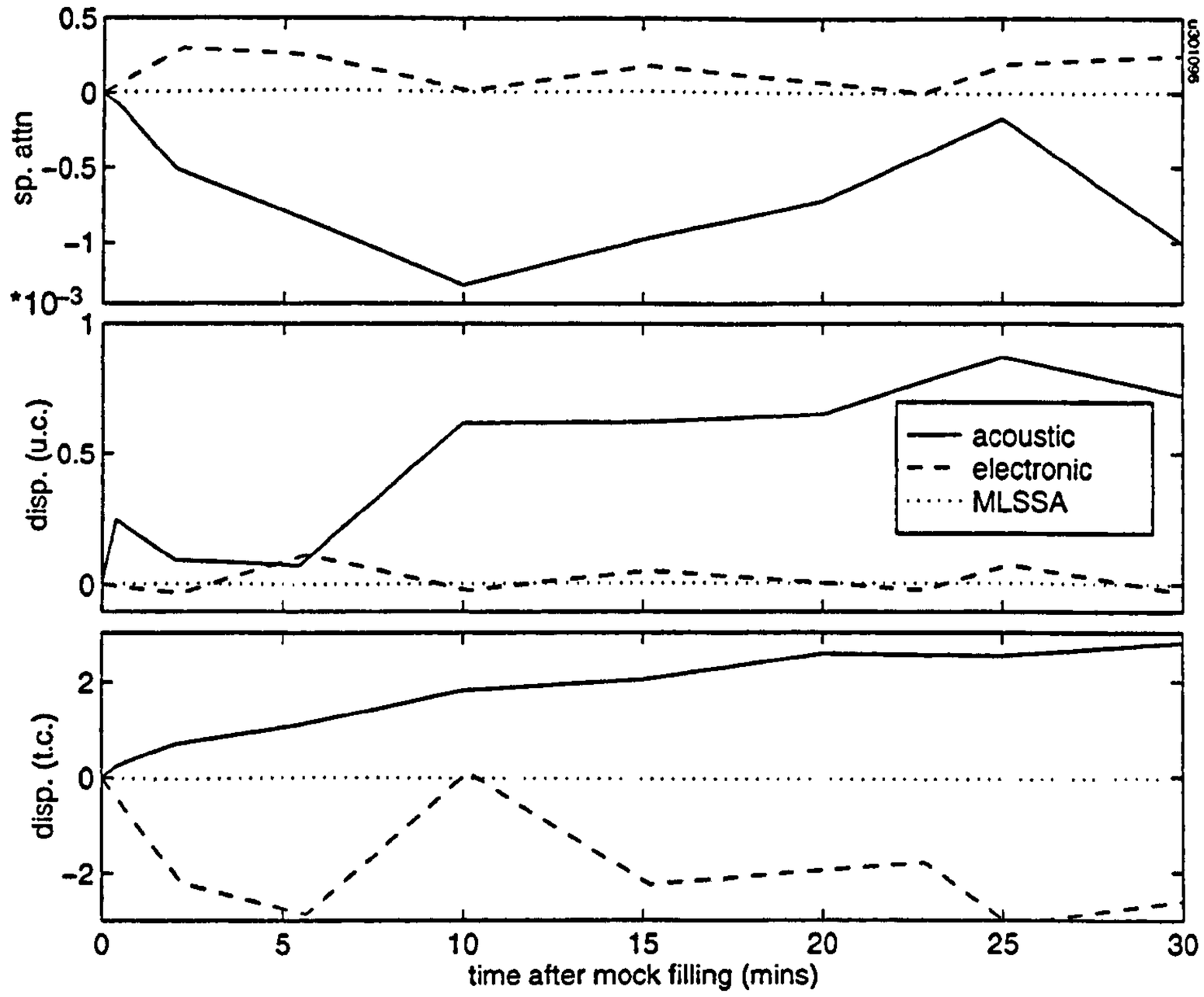

Figure 4-12 Drift in acoustic measurements at 240Hz, after "mock filling", referenced to value before filling (t=0). Upper: specific attenuation; Middle: uncorrected dispersion; Bottom: temperature-compensated dispersion. Solid line: calculated from overall electro-acoustic IR; Dashed line: contribution from electronic measuring equipment only; Dotted line: contribution from MLSSA system only.

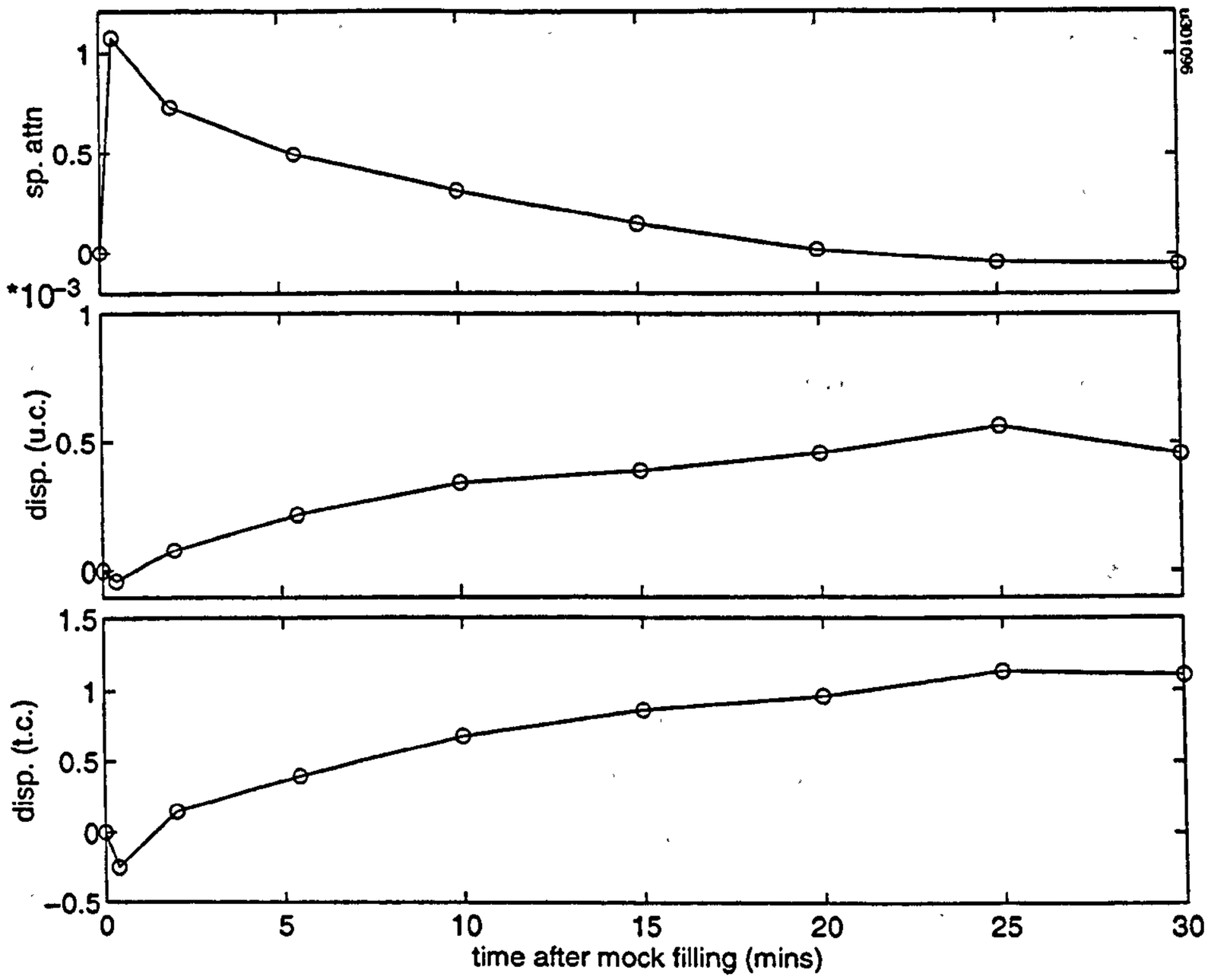

Figure 4-13 Drift in acoustic measurements at 1960Hz, after "mock filling", referenced to value before filling (t=0). Upper: specific attenuation; Middle: uncorrected dispersion; Bottom: temperature-compensated dispersion. Overall electro-acoustic value only is shown: contributions from electronic system and MLSSA are negligible.

Several points are of significance:

1. Above 500Hz, the contributions due to the measurement chain (electronic components and MLSSA) are negligible compared with the acoustic drift, and so are not shown in Figure 4-13.

2. At low frequencies, there is a small but finite contribution($<0.3\times10^{-3}$) towards specific attenuation drift from the measuring chain. This is thought to be due to the finite length (12.6ms) of the time window: although this should theoretically give a minimum useable frequency of around $\frac{1}{12.6\times10^{-3}} = 80Hz$, in practice the effect of the uncertainty is present but decreasing up to approximately 500Hz. The effect of the uncertainty is that the equal drift in both direct and reflected pulses is not completely cancelled, leading to the visible error.

3. Towards the cut-on frequency of the first transverse mode (1992Hz), spurious errors increase again, presumably due to an extreme sensitivity to conditions.

4. The "temperature compensated" dispersion shows uniformly more drift than the uncorrected dispersion, and does not appear to be related to electronic drift. This suggests that the drift is acoustic in nature, presumably due to fluctuations which are not removed by the algorithm; for example, differential temperature variations between

the upper and lower tubes. So, in later analyses, only the "uncorrected" dispersion will be displayed.

5. As the acoustic measurements on a suspension will be taken just before, and 12seconds after filling, we need only to consider the initial part of these curves to assess the magnitude of errors. From this, we are justified in assuming that the error for both specific attenuation and dispersion will be approximately $< 10^{-3}$, and reducing to $< 10^{-4}$ at mid frequencies.

4.11 SUMMARY

Equipment has been designed to measure the attenuation and dispersion of suspensions of small particles in air. The suspension was confined in a vertical tube, and the acoustic properties extracted by measuring a pulse before and after travelling through the suspension. These measurements are valid between approximately 200 and 2000Hz. The particle concentration was measured by weighing the particles that settled at the end of each experiment, and their particle size distribution was measured using a photosedimentometer. The accuracy of the apparatus was assessed as approximately ±5% error in the particle concentration, and between 10^{-4} and 10^{-3} absolute error in both specific attenuation and dispersion, being highest at either extreme of the quoted frequency range.

5

DESIGN & USE OF EQUIPMENT:

FLOW RIG

5.1 INTRODUCTION

This chapter describes the equipment that was built to measure the acoustic effect of moderately dense, flowing suspensions. In particular, it will describe the rigs that generated flow, the probes that formed the interface between the flow and the acoustic transducers, and some of the hardware that controlled the experiments. Furthermore, results will be presented to describe the acoustic characteristics of the environment, and the performance of the equipment.

Measurements on flowing suspensions were desirable for two reasons:

1. They would be more representative of the type of environment encountered in the target application — measuring the concentration of flowing particulates.

2. The flowing environment is necessary to suspend larger particles (> 10μm), and to achieve the high densities that would be encountered in the target application (0.1 - 10 kg/kg).

The aim of this part of the project was to build apparatus that would measure the acoustic properties of a suspension flowing through a pipeline, with an independent means of measuring its suspension concentration, flow rate and particle size.

5.2 OBJECTIVES

To fulfil this aim it was necessary to be able to:

- Generate a flowing suspension of a variety of powdered solids, with controllable concentration and flow rate, contained within a pipeline.
- Measure the concentration and particle size distribution of the suspension.
- Gain acoustic access to the pipeline via orifices suitably placed to permit a variety of experiments.
- Ensure that, where necessary, the acoustic transducers are isolated from the suspension by a structure that optimises their acoustic performance. In particular, the following transducers should be accommodated:
  - 1/4" microphone to act as receiver

- Low frequency driver, for plane wave measurements
- Mid/high frequency driver, for reverberation and modal excitation measurements.
- Ultrasonic transmitter.

- Assess the background noise of the environment, due to flow and the presence of particulates.

These individual project stages are addressed below.

5.3 FLOW TEST FACILITIES

Flowing suspensions of calibrated concentration can be created in two main ways:

- Closed loop: a known mass of particulate is inserted into a closed loop in which flow is maintained by an in-line fan. The concentration is found from the volume of air in the loop, and the mass of particulate (see, for example, Hamade [55], Sowerby [136])
- Open loop: clean air is accelerated to the required flow rate, particulate is fed into the flow at a steady rate, and then further downstream the particulate is separated and collected, while clean air is discharged. The concentration is found from the mass feed rate of particulate, and the mass flow rate of air (see, for example, Sheen & Raptis [132], Woodhead [158]).

The closed loop has the advantages that only small samples of particulate are required and the flow can be maintained continuously. However, to calculate the concentration it is necessary to assume that the entire mass of particulate is in uniform suspension, and, therefore, that there is no adhesion to walls, or "slugs" of deposited material. Furthermore, the conditions tend to be unsteady, either through heating up of the suspension, or degradation of the particulate (a problem encountered by Hamade [55]). The physical construction is complicated by the need to expose the fan to the suspension, with consequent problems of erosion and environmental sealing of bearings.

The open loop has the advantage of achieving steadier flow conditions and more accurate measurement of concentration. However, the particulate must be fed into the flow continuously, and usually cannot be recirculated, so that the flow can be maintained only for a period that is governed by the quantity of particulate: to achieve a reasonable duration of experiment at a high concentration, large samples are required.

The building of either of the above flow rigs represents a significant expenditure of time and money. Although plans for a small-scale open loop rig were drawn up, a kind offer for the use of an existing rig at the University of Greenwich was made and accepted.

5.3.1 Description of the flow test facility

The rig used for all measurements on flowing suspensions was built at the Wolfson Centre for Bulk Solids Handling Technology, University of Greenwich, by Woodhead as part of his doctoral work. A detailed description of the rig and its sub-systems is given in his thesis [158], and that of Bradley [24]. A brief overview will be presented here.

The facility is of the open loop type. Air from a laboratory supply at 4.0 bar is fed into two banks of valves. These valves can meter a known and controllable mass-flowrate of air into two separate lines: the supplementary air line, and the venturi air line. The latter feeds into a venturi (a narrowing of the pipe which creates a reduced air pressure), into which the particulate is gravity-fed from a feeder tank. The resulting suspension is mixed with the supplementary air. The diluted suspension passes through the working section of pipeline, before being introduced into a storage hopper that sits on top of the feeder tank. The sudden deceleration encourages the particulate to drop out of suspension, and the air is vented to atmosphere via large bag filters.

After all the contents of the feeder tank have been conveyed to the storage hopper, the air flow is turned off, and the particulate is allowed to fall under gravity from the storage hopper into the feeder tank by opening valves that connect the two. Particulate can be shaken out of the filters and off the walls of the hopper by actuators that impose vibratory motion. A simplified diagram of the facility is shown in Figure 5-1, and Figure 5-2 illustrates the facility with a photograph.

The feeder tank can hold approximately 0.4 m^3 of particulate, weighing over 100kg. While the air feed system could provide up to 0.15 m^3/s of free air, corresponding to a velocity of 76 m/s, the velocity was usually maintained at 20 m/s (nominally). To give an example of the available run time, at a concentration of 1 kg/kg and flow velocity of 20 m/s, 100kg of material would be exhausted in approximately 30 mins.

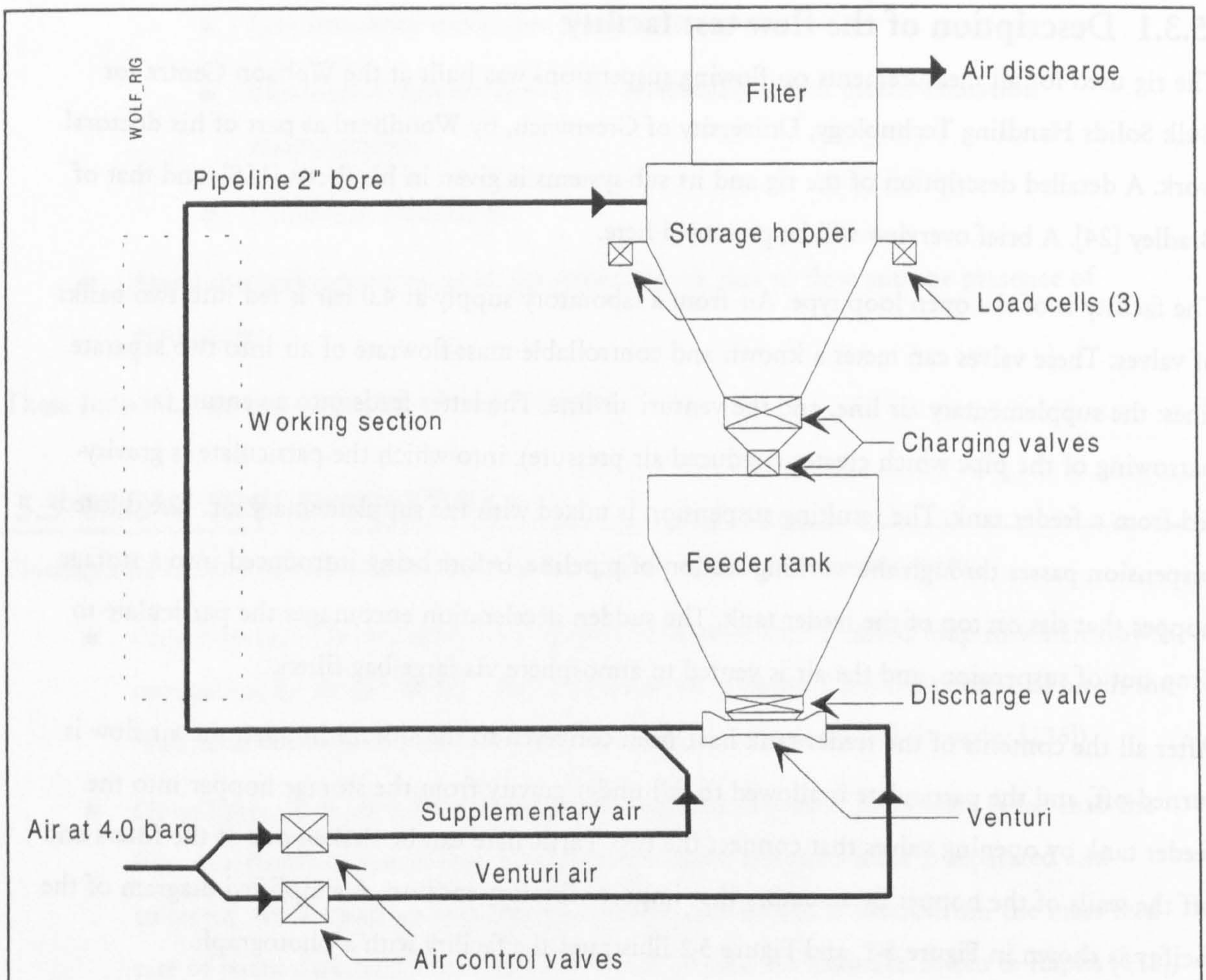

Figure 5-1 *The flow test facility at the Wolfson Centre (after Woodhead [158]).*

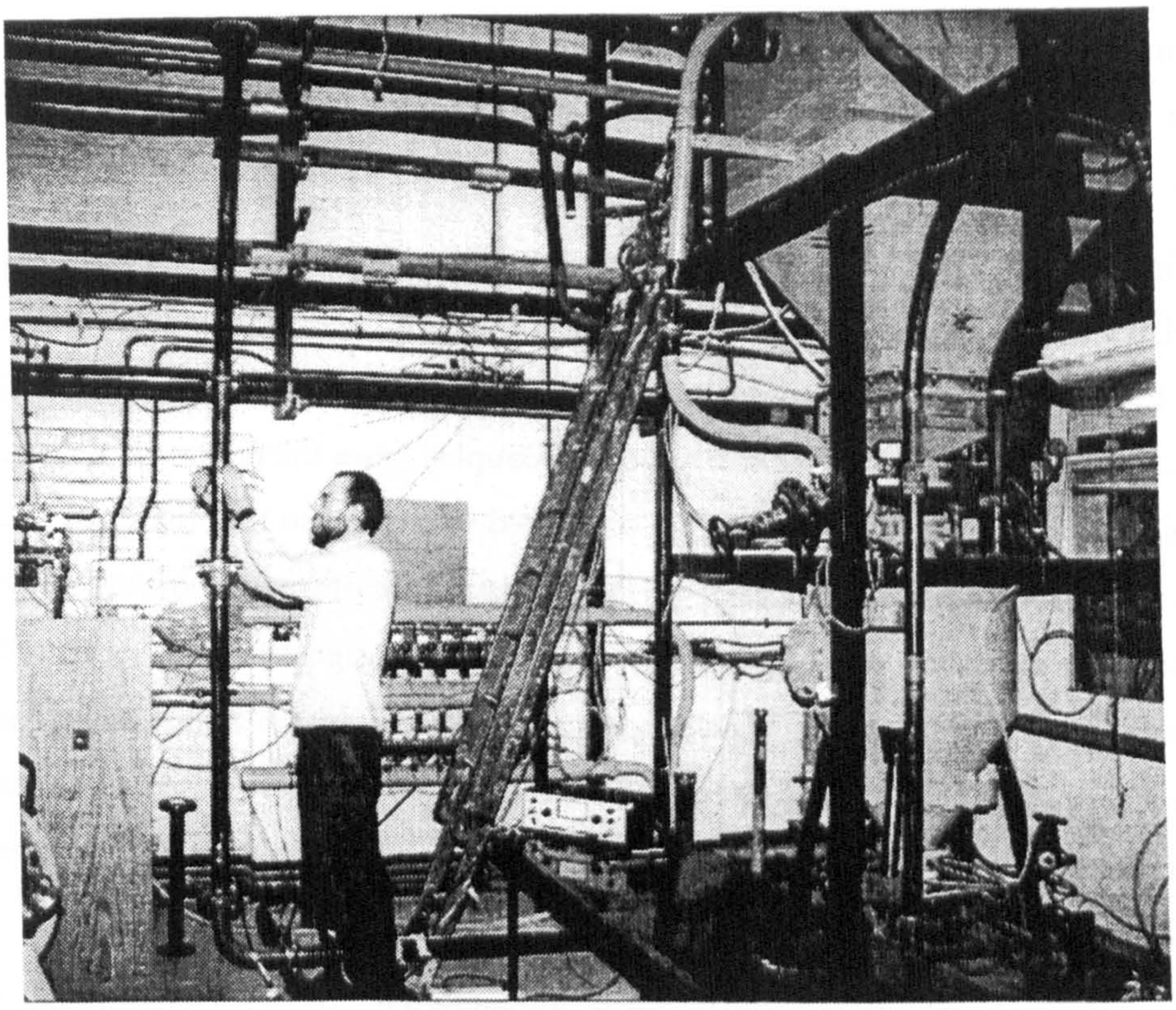

Figure 5-2 *Photograph of the ultrasonic transducers being installed on the working section of the flow test facility. The nozzle bank is visible on the rear wall; the feeder tank is visible to the right, with the lower portion of the storage hopper above it.*

5.3.2 Instrumentation of the flow test facility

Air flow control

Both banks of air control valves are composed of eight individual valves that each feeds a choke-flow nozzle. This type of nozzle has the characteristic that the mass flow rate of air through it is independent of the back-pressure across the nozzle, provided the back-pressure remains above approximately 1.5 barg [28, 26]. The flow rate is determined by the size of the nozzle orifice. The orifice sizes were chosen such that, for each bank, the mass flow rate of the nozzles formed a power-of-two sequence; the eight valves therefore gave a turn-down ratio (maximum/minimum flow rate) of 255. The valves were controlled electronically from a control room, from where the mass flow rate of air in each line could be controlled by activating the appropriate valves.

The purpose of having two banks of nozzles and two air lines is to give independent control over both air velocity and suspension concentration. For example, to generate a set of test points with constant air velocity but increasing suspension density, a collection of nozzle settings is chosen such that the sum of the venturi and supplementary flow rates remains constant, but the ratio of venturi/supplementary flow rates increases.

Measurement of suspension concentration

The mass flow rate transmitted by each nozzle had been calibrated when the facility was built. Therefore, for a given experiment, the air mass flow-rate is found by summing the flow rate of each activated nozzle.

The other variable that is needed to calculate the concentration is the mass flow rate of particulate. This is found by measuring the gain-in-weight of the storage hopper. The weight of the hopper (and filter) is distributed between 3 load cells, and is decoupled from the pipework and the feed tank by flexible couplings. The strain gauges are connected in parallel so that their total output voltage indicates the total weight of the hopper. Therefore the rate of increase of the hopper's weight is equal to the mass flow rate of particulate. The combined signal from the load cells is indicated (usually) on a chart recorder. The voltage sensitivity is calibrated by hanging a known mass onto the hopper and noting the deflection. The feed rate of the chart paper is known and selectable; therefore, the mass flow rate of the particulate is found by measuring the gradient of the trace on the chart recorder.

Further details on operating the facility are found in Appendix D.

5.3.3 Pipe test sections and air-only flow rig

The pipeline test sections were constructed from 2" bore welded steel pipe with standard end flanges, so that they would be accommodated into the working section of the Wolfson Centre facility. Two sections were made: a short (0.6 m long) section with two diametrically opposed ports, designed for measurements across the pipe section; and a longer section (1.4 m) with a single port, designed to accommodate a transmitter for measurement along the pipe to a receiver in the short section. By placing the port asymmetrically along the length, two different path lengths (0.7 and 1.3 m) could be obtained according to the configuration.

Two further sections were also fabricated, to allow arrangement into an open loop, airflow-only rig. This was built for convenience, so that measurements could be made at the Open University on the acoustic effect of airflow only. Therefore, the same working sections could be used either in the air-only rig, or the dust-flow rig.

The extra sections consisted of an entrance and exit section of 2m and 0.6m length respectively, to produce fully-developed flow conditions in the working sections. In total, four ports with threaded bosses permitted the introduction of probes nominally flush with the inside of the tube wall; these are labeled A – D in Figure 5-3. The air-flow was generated by a pneumatic amplifier ("Airmover") which uses small volumes of high pressure air to accelerate large volumes of ambient air. By adjusting the air supply pressure, velocities of between 5 to 50m/s could be achieved. The velocity was measured by positioning a hot-wire anemometer at the centreline of the tube at port C.

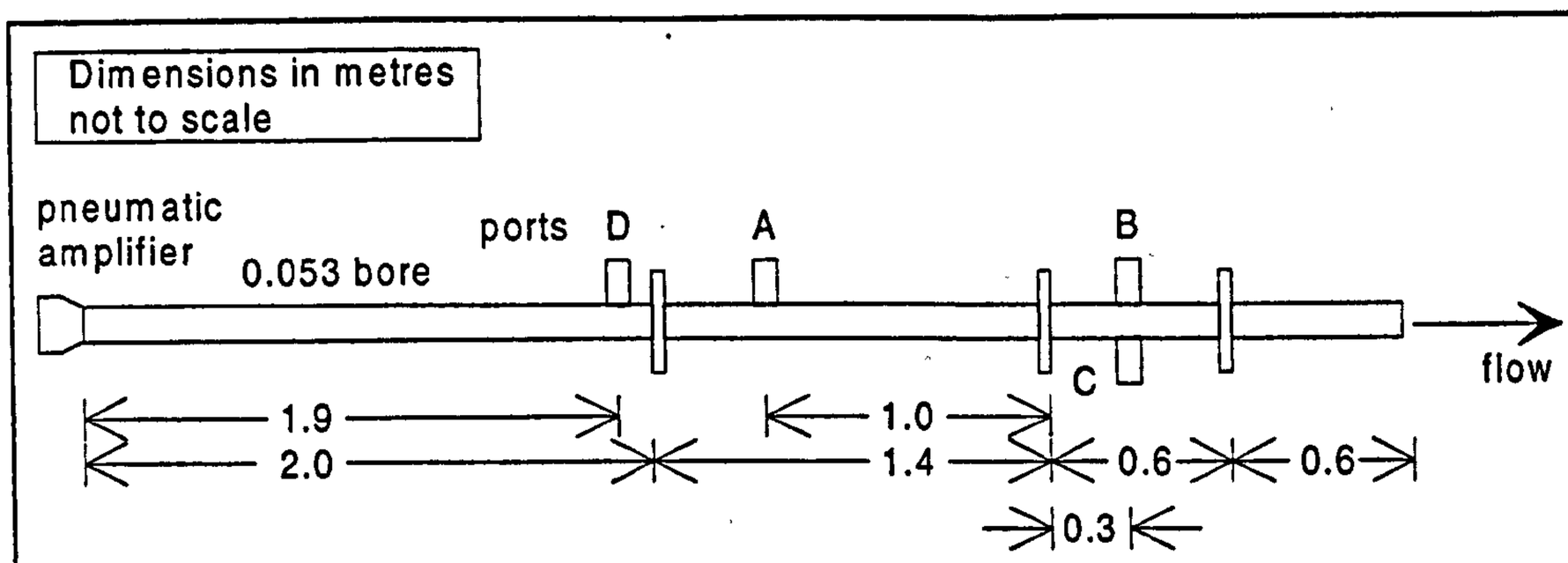

Figure 5-3 *Schematic diagram of air-only flow rig and test sections.*

5.4 TRANSDUCER PROBES – AUDIO TRANSDUCERS

5.4.1 Design Requirements

The probes are structures that protect the acoustic transducers, and couple acoustic energy between the transducer and the environment inside the pipeline through a port. The requirements are as follows:

a) the transducers must not come in contact with the dust flow, to prevent contamination, and explosion in the case of transducer failure.

b) the transfer of energy (from transmitters) should be as efficient as possible to maximise signal/noise ratio (SNR)

c) the magnitude of the coupler's transfer function should be as flat as possible within the desired range, to maximise SNR.

d) the duration of the probe's impulse response should be as short as possible (to allow time-domain editing of separate pulses).

5.4.2 Probe tube: flushing arrangement

The physical isolation of the transducers was achieved by coupling the transducer to the port by a tube. To prevent dust ingress into the probe tube, air was used to flush continuously in two ways;

- A high velocity, annular jet of air exiting circumferentially around the port.
- A low speed flow of air, flushing along the length of the probe tube, through the port.

Both of these techniques were incorporated into the microphone probe, and tested individually in flow. A portion of the probe is shown in Figure 5-4 to illustrate the flushing arrangements.

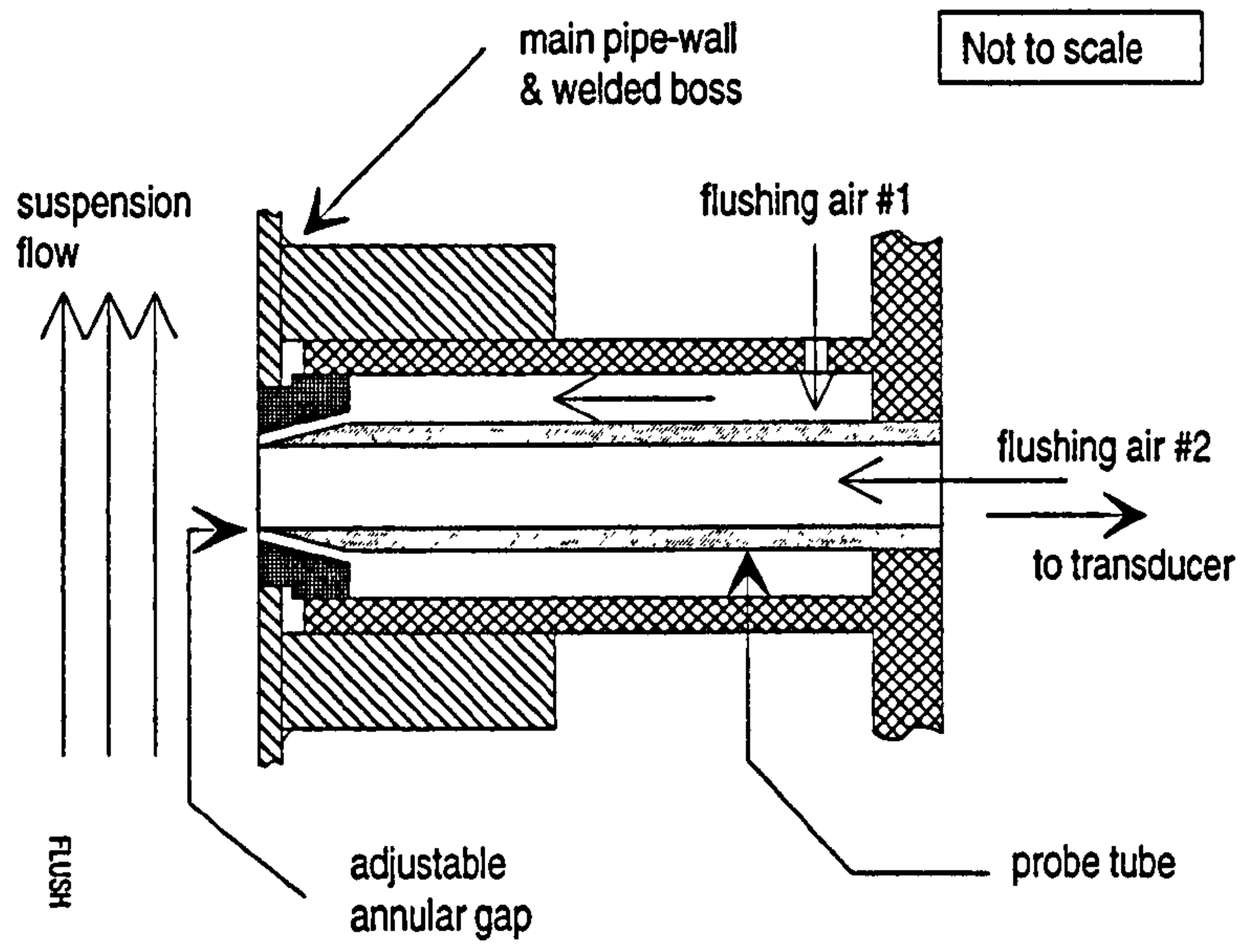

Figure 5-4 Schematic diagram of the two types of flushing arrangement attempted: a high velocity annular jet, and a low velocity flow along the probe tube.

The low speed, rear-flushing technique (shown as #2 in Figure 5-4) was found to be the most effective at maintaining cleanliness in the probe tube. For the microphone probe, with a probe tube diameter of 5mm, an air mass-flow rate measured at 3.3×10^{-4} kg/s (air velocity approx. 14 m/s) was found sufficiently high to exclude the largest particles tested (0.3mm). This flow was supplied by a choke-flow nozzle with an orifice of 0.64mm. The flushing air for the microphone probe corresponded to 0.06% of the main conveying airflow (0.053 kg/s at a nominal 20m/s) and so its dilution effect on the suspension was neglected.

The rear-flushing technique had the additional advantage that a long buffer of clean air was maintained between the suspension flow and the transducer, thereby reducing the risk of ignition in case of transducer failure.

The flushing airflow had the undesired effect of increasing the background noise level. It was found that the rear flushing arrangement produces over 10dB less noise than the annular jet. This is presumably because the flow is slower and more likely to be laminar, whereas the annular jet is an arrangement similar to an acoustic whistle, and likely to produce very turbulent and oscillatory flow.

Therefore the rear flushing arrangement was used in this and later designs.

5.4.3 Probe tube: acoustic design

The acoustic requirements of the probe tube were stated to be a flat transfer function and short impulse response. These are essentially the same constraint in the frequency and time domain respectively: they require the minimization of reflections that would lead to periodic impulses in the time domain, and a harmonic structure in the frequency domain. The reflections occur for the following reason. The essence of the probe arrangement is a tube terminated at one end by the

transducer, and the other end by an expansion into the larger conveying pipe (essentially free space). In acoustic terms, this represents a transmission line terminated by two mismatched impedances, and it is this mismatch that creates reflections at either end.

The periodic reflections cause the impulse response to lengthen, and the periodic time structure leads to a "peaky" frequency response with a harmonic structure.

Lumped-parameter modeling

To tackle the problem of internal reflections, the acoustical system was represented by a lumped-parameter model. This technique uses the analogy between electrical current and air particle flow to convert acoustical elements into equivalent electrical elements. The advantage is that, instead of having to solve an acoustic wave equation with complicated boundary conditions, one can use simple electrical circuit theory to solve for system variables. A requirement for the transformation to be valid, is that dimensions should be smaller than the wavelength, so that acoustic pressure can be considered constant within each volume. Where one dimension is larger than the wavelength — specifically, the length of the tube — then distributed-parameter modelling may be possible, so that the tube may be modelled as a waveguide with a certain impedance. All the theory in this section is based on reference [73], chapter 10.

Figure 5-5 shows the representation of a simple tube terminated by the two impedances, using both distributed and lumped parameter modelling.

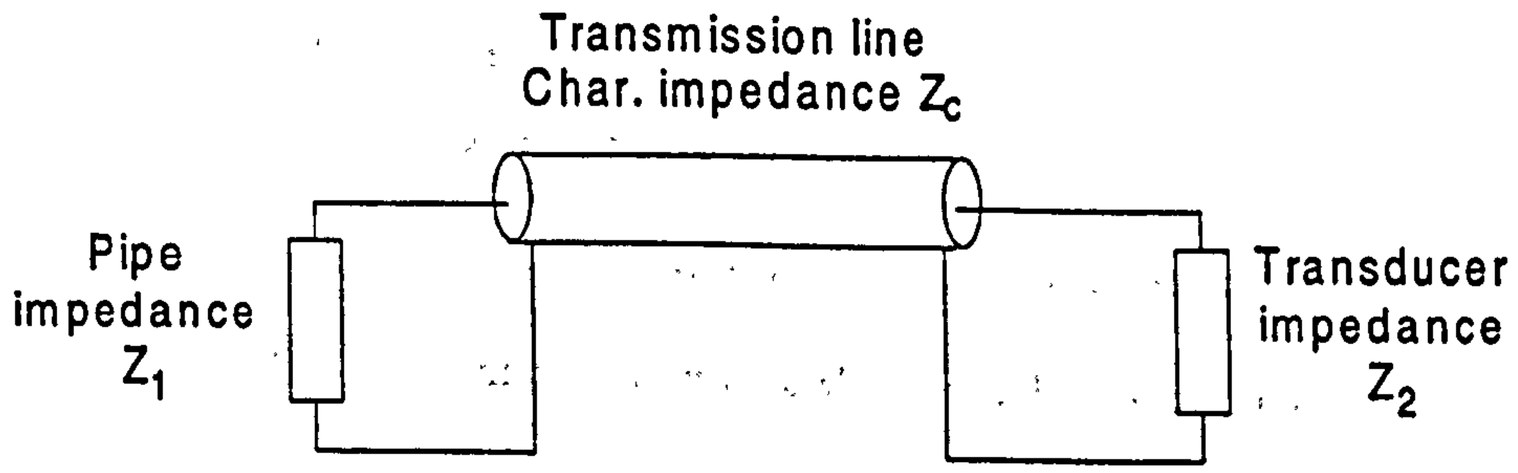

Figure 5-5 *Equivalent circuit of a waveguide terminated by two impedances*

The impedance of the waveguide is a function of the tube cross-sectional area, A:

$$Z_c = \rho c / A \tag{5.1}$$

where ρc is the characteristic impedance of free space. The impedance of the conveying pipe will typically be much lower than Z_c (having a large area), while the transducer impedance is much higher. Equation (5.1) shows that the only control over the impedance mismatch between the probe and pipe is the diameter of the probe tube, which is set by the size of the connecting hole.

Attention was directed to the mismatch at the transducer face. Being a high impedance termination, it should be possible to shunt it by a lower impedance to match that of the waveguide. This is the approach taken below.

Matching channel

The matching channel is an acoustic method of loading the waveguide with a matching impedance.

A resistive flow element was placed in the wall of the waveguide as close as possible to the transducer face. Its flow resistance was chosen to match the impedance of the waveguide.

The flow resistance of a resistive element is defined as:

$$R = \Delta p / Q \quad (\text{Pa.s.m}^{-3}) \tag{5.2}$$

where Δp (Pa) is the pressure drop across the element for a volume flow of Q (m^3/s) through the element.

The characteristic flow resistance of a given material is given by:

$$r = \Delta p / v \quad (\text{Pa.s.m}^{-1}) \tag{5.3}$$

where v is the particle velocity through any area of the material.

To select the resistance material, the criterion was chosen that a given area of material would have a flow resistance equal to the impedance of a waveguide of the same area. It then follows that the waveguide can be equalised by arranging holes in the wall of the tube with total area equal to the cross sectional area, and placing a patch of material over the holes.

So then: flow resistance · hole area = r Pa s m^{-1}

From (5.1): characteristic impedance · hole area = ρc Pa s m^{-1}

So ideally we chose, $r = \rho c \approx 412$ Pa s m^{-1}

That is, the characteristic resistance of the flow material should equal the characteristic impedance of free space.

The characteristic flow resistance of different woven materials were measured on a low-velocity air-flow rig. A finely-woven polyester fabric ("Microfine") was selected which had $r \approx 340$ Pa s m^{-1}.

Equalisation chamber

Ideally the element would vent to atmosphere, and hence provide a shunt to acoustic "ground". However, since the conveying pipe operates at an overpressure (maximum 1 bar), the probe assembly must be pressure-tight. Hence the resistive element is vented to a large, sealed chamber of volume V. Such a chamber acts as a compliance; its equivalent capacitance is

$$C = V/\rho c^2 \qquad (5.4)$$

By choosing its volume to be large enough, then its impedance, $1/j\omega C$ at the angular frequency of operation ω, can be made arbitrarily small.

The large volume of the chamber means that the condition of small dimensions relative to the wavelength is not necessarily satisfied. To damp the occurrence of standing waves within the volume, it was filled with wadding.

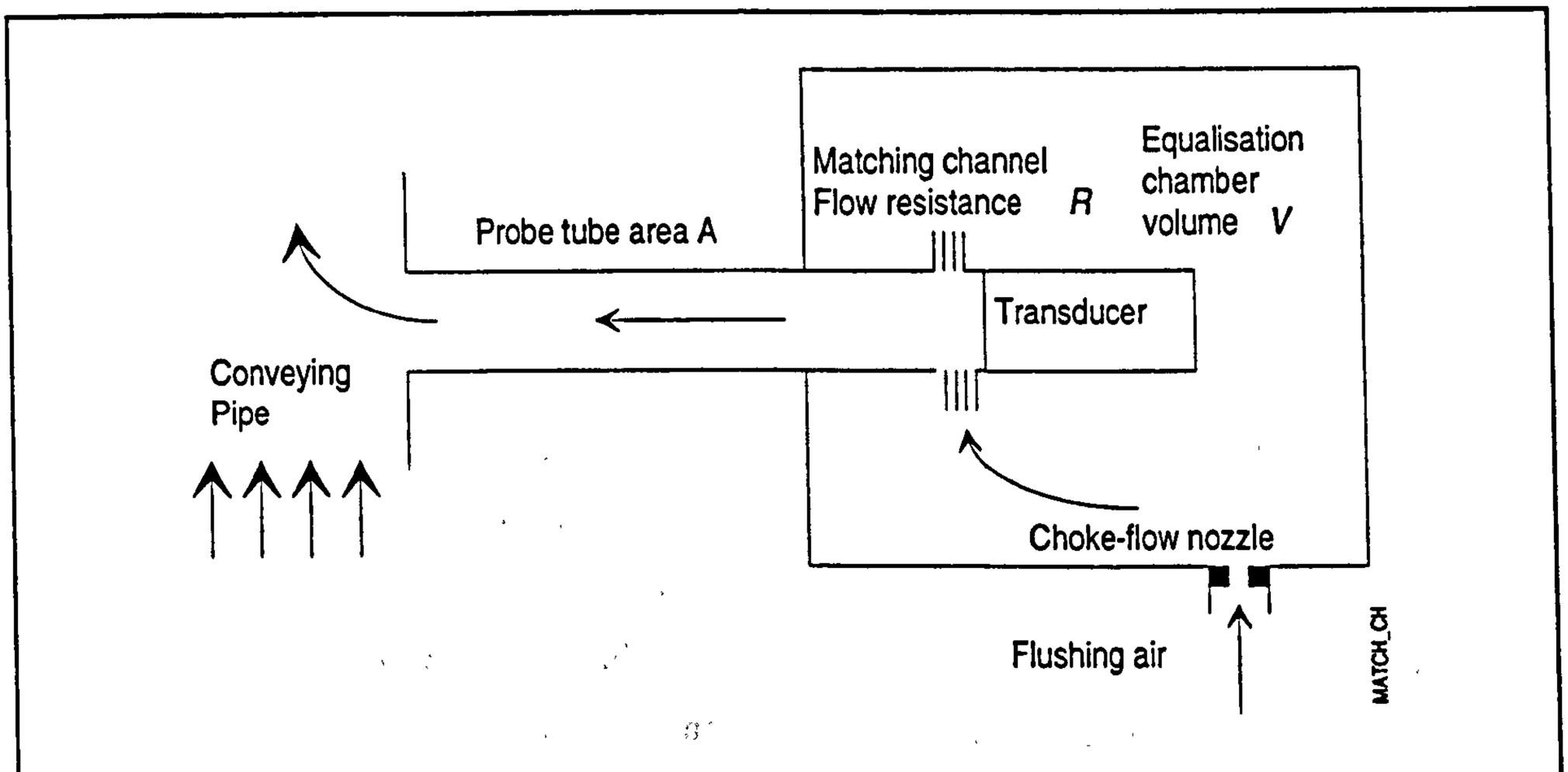

Figure 5-6 Schematic arrangement of matching channel and equalisation chamber to improve termination of the probe tube.

This physical arrangement also provided the mechanism for introducing flushing air into the probe. Air at 4.0 bar pressure discharged into the chamber through a choke flow nozzle. The nozzle ensured that the air-flow remained constant and known despite variations in the conveying line pressure. The flow passed through the resistive element, and along the probe tube. The scheme is outlined in Figure 5-6.

5.4.4 Final design

This ideal situation cannot be achieved in practice because of practical constraints of construction, so compromises had to be made. The detail of the design is described for the microphone and loudspeaker probes separately.

Microphone

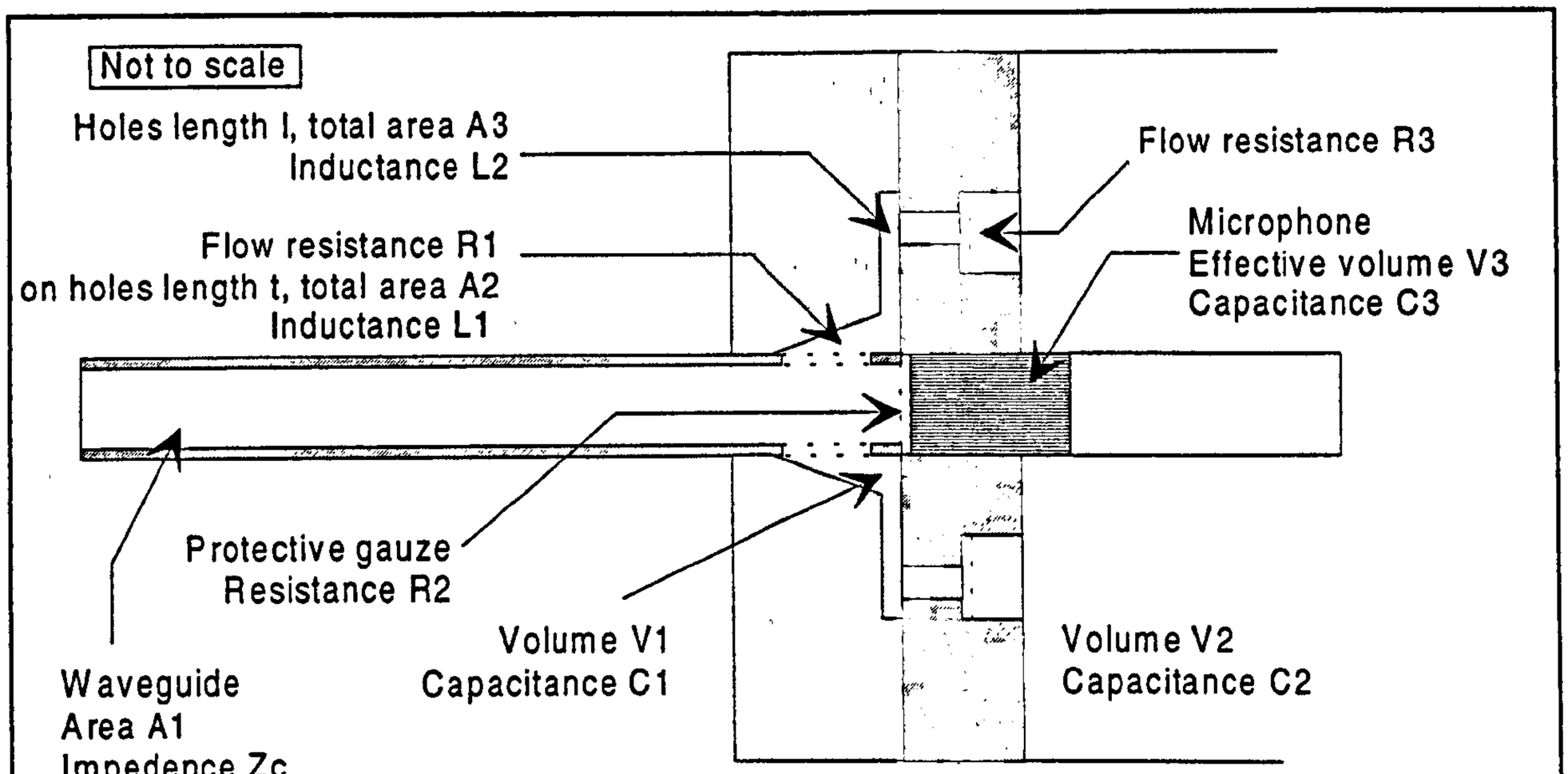

Figure 5-7 *Schematic diagram of the matching arrangements of the microphone probe*

The required bandwidth of the microphone probe was 200Hz — 20kHz. The wavelength at 20kHz is 1.7 cm, and this dimension places a constraint on the size of probe elements. Efficiency of coupling into the probe tube was not considered important, due to the high sound power level inside the pipe. A probe tube with internal diameter of 5mm was chosen. A sketch of the physical arrangement is shown in Figure 5-7.

A twin chamber design was chosen for practicality; the small equalisation chamber V_1 vents through a series of holes into the much larger, internally damped chamber V_2. Any interconnecting holes, length l, area A, contain plugs of air that act as inductors of equivalent inductance:

$$L = \rho l' / A \qquad (5.5)$$

where l' is the effective length = l + 1.7 d, and d is the hole diameter.

A protective gauze (50μm hole size) of very low flow resistance ($r \approx 26$ Pa s m^{-1}) was placed in front of the microphone, for protection in case of dust ingress. The microphone is modelled by a compliance with an effective volume given in its datasheet.

The acoustical system may be modelled by the equivalent electrical circuit shown in Figure 5-8. This schematic was entered into a linear circuit analyser. By imposing a signal V_{in} at the probe opening, it is possible to calculate the resulting signal V_{out} at the microphone face, and therefore estimate the signal response due to the lumped elements shown. This will not account for reflections due to impedance mismatch; for this purpose, the impedance "seen" by the end of the waveguide, Z_{in} was also calculated. The aim was to iterate on the physical dimensions to arrive at a

compromise between flat frequency (and smooth phase) response, and a value of Z_{in} that is close to Z_c . The parameters that were chosen finally are shown in Table 5-A.

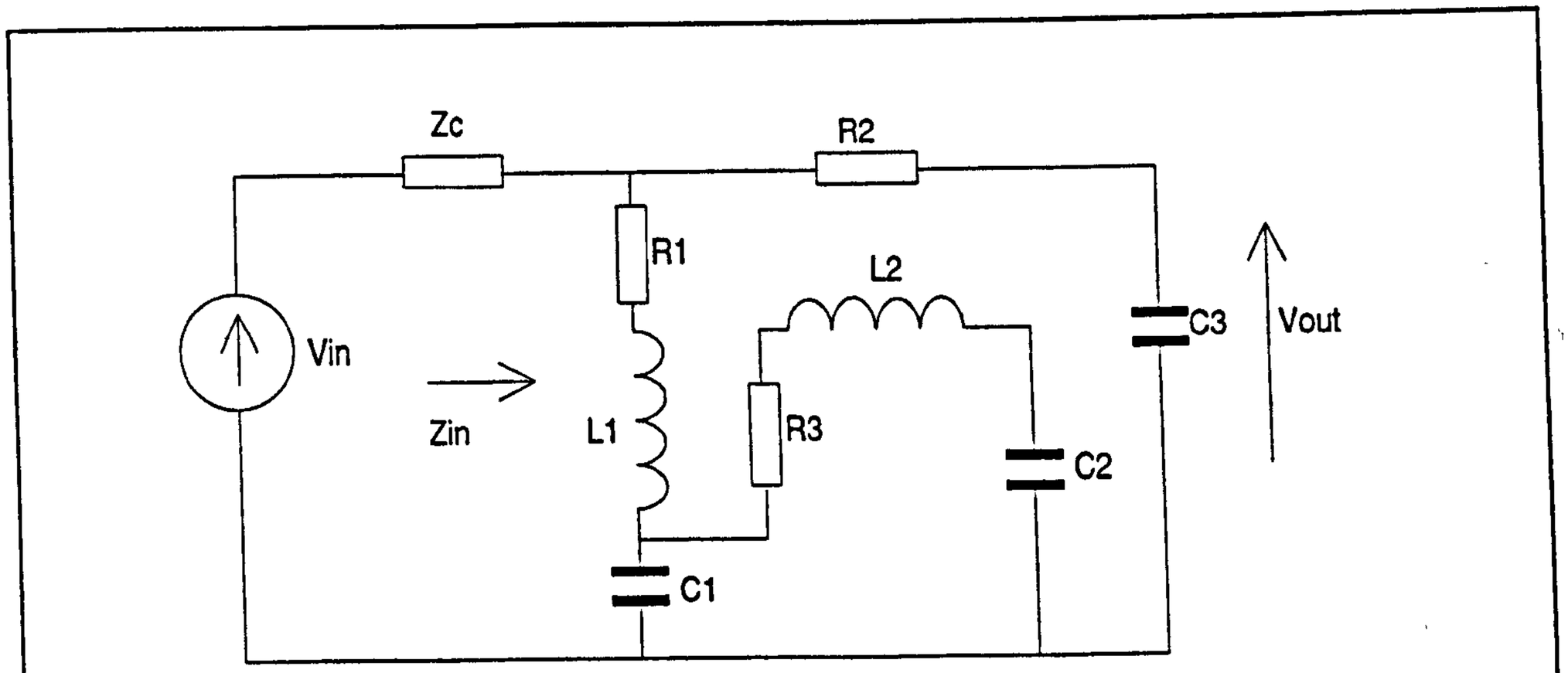

Figure 5-8 *Equivalent circuit of microphone probe using lumped parameters.*

Element	Physical Dimensions	Electrical equivalent
Waveguide	$A_1 = 19.6\ mm^2$	$Z_c = 21\ M\Omega$
Volume 1	$V_1 = 331\ mm^3$	$C_1 = 2.4\ pF$
Volume 2	$V_2 = 75\ 200\ mm^3$	$C_2 = 54\ nF$
Volume 3	$V_3 = 0.6\ mm^3$	$C_3 = 0.004\ pF$
Holes 1	$A_2 = 18.8\ mm^2$, $t = 1mm$, $d = 2mm \times 6$	$L_1 = 281\ H$
Holes 2	$A_3 = 15.7\ mm^2$, $l = 8\ mm$, $d = 2\ mm \times 5$	$L_2 = 871\ H$
Resistance 1		$R_1 = 18M\Omega$
Resistance 2		$R_2 = 1.3\ M\Omega$
Resistance 3		$R_3 = 22\ M\Omega$

Table 5-A Physical dimensions and electrical analogues of acoustic elements in the microphone probe.

Care was taken to isolate the microphone from the probe assembly, both electrically (to avoid earth loops) and physically (to reduce pick-up of structural vibration). The microphone was supported within two rubber O-rings that also provided the pressure seal. A side-venting microphone (Brüel & Kjær type 4165) was selected to ensure that the pressure equalisation port

vented to the front face of the microphone rather than the rear chamber that could be at a slight pressure differential. Figure 5-11 shows a photograph of the finished probe containing the microphone.

Loudspeaker

The analysis of the loudspeaker probes is slightly different, because the imposed signal in this case is at the other end of the waveguide. The first reflection from the interface between the waveguide and the conveying pipe is inevitable, so the matching technique works by reducing the second reflection from the loudspeaker face. A disadvantage is that the matching network shunts the output of the speaker, and therefore can be expected to reduce the radiated power (by 6dB, if the electrical power remains constant).

Notwithstanding the matching circuit, the loudspeaker is driving an impedance far higher than that of free space. For this reason, compression drivers where chosen; their main characteristic is a more massive magnet assembly, so that larger forces may be generated to drive high impedance loads.

It was desired to generate signals over a frequency range 400 - 20000 Hz. No single driver can achieve this efficiently, so two separate drivers were chosen:

Community M200, 0.4 - 3.5 kHz, 75 W, 2 inch throat;
Fane MD2151, 1.5 - 20 kHz, 50W, 1 inch throat.

The low frequency driver was used for plane wave measurements, and the high frequency driver for reverberation measurements; since no experiment required the full frequency range, the probe assembly only needed to accommodate one driver at a time.

To reduce non-linear effects in the waveguide due to high sound pressures, the largest practical diameter of 12mm was chosen. An approximate exponential horn was constructed in two sections to fit either driver; one reduced the diameter from 51mm to 25mm, and a second section from 25mm to 12mm. The exponential shape was approximated by straight line segments. The flare constant of the horn, m, was chosen for a lower cut-off frequency, f_c, of 350Hz, according to [73, chapter 14]:

$$f_c = \frac{mc}{4\pi} \tag{5.6}$$

The acoustical design of the probe is similar, with the addition of the exponential horn, which is modeled by an impedance converter (transformer). It was, however, decided not to provide impedance matching for the high frequency driver, because:

- It would only be used for reverberation measurements, where the signal/noise ratio is critical.

- The reflection coefficient at these higher frequencies is lower than for the low frequency driver
- The throat of the driver contained some acoustic foam, which, together with the additional wadding, was considered adequate to damp internal reflections.

The mechanical design is substantially different from the microphone probe, due to the larger dimensions, and lower frequencies that need to be considered.

It was necessary to consider the effect of an over-pressure on the loudspeaker cone. If a pressure differential existed across the cone, the sensitivity of the loudspeaker may be affected, or the cone could even be damaged. To reduce this problem, a static equalisation channel was introduced into each driver, to ensure that the rear of the cone had a low frequency equalisation path to the front of the cone. The drivers were also modified to ensure that the necessary surfaces were pressure-sealed.

The physical arrangements of the probes are shown in Figure 5-9 for the low frequency driver, and Figure 5-10 for the high frequency driver. It can be seen that some components are common to both assemblies. Figure 5-11 shows a photograph of low frequency driver and its probe.

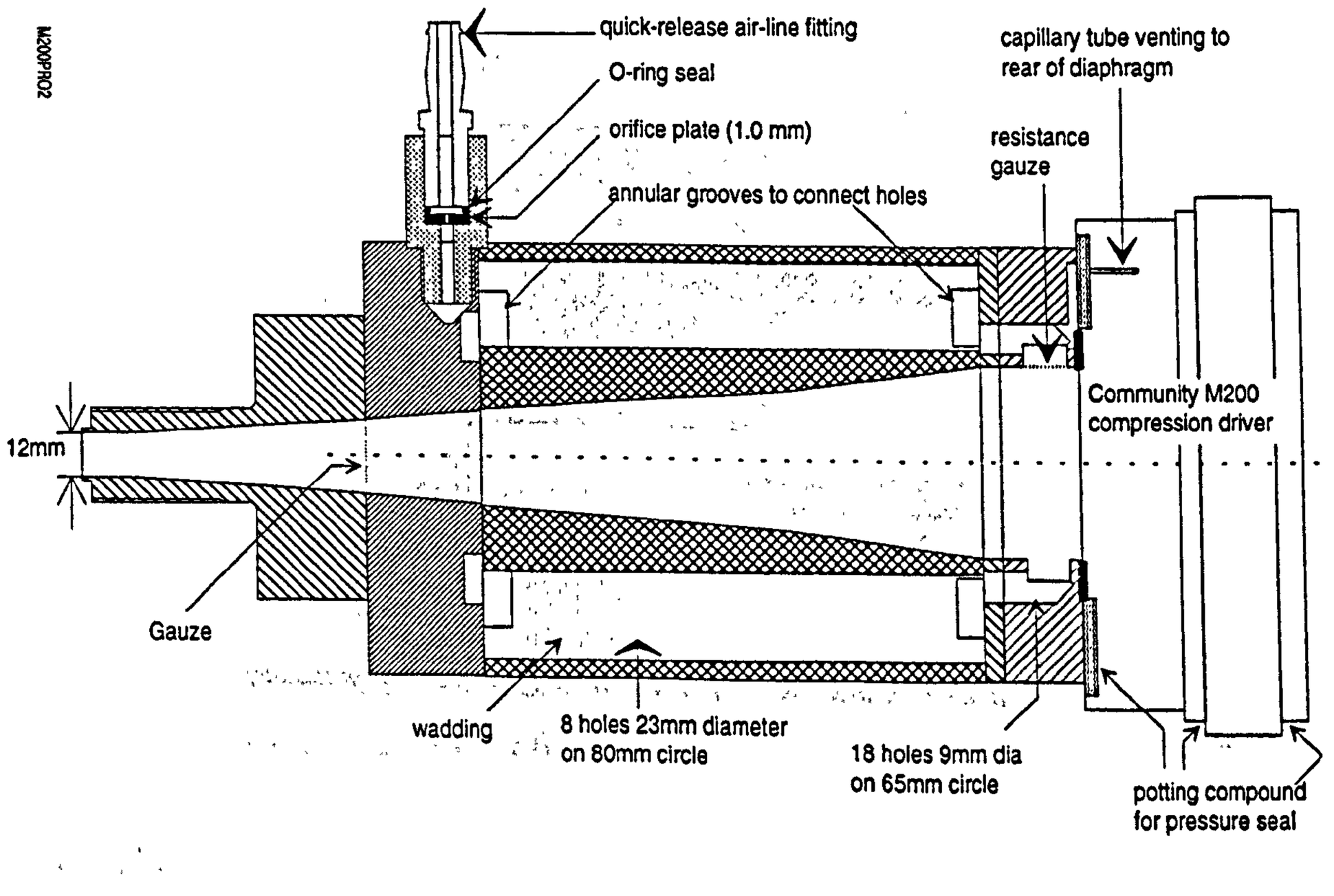

Figure 5-9 Cross section through the probe assembly for the low frequency driver (drawn to scale). For clarity, the fasteners are not shown.

The 1.0 mm orifice was found to provide sufficient flushing air. The flow was measured at 1.42×10^{-3} kg/s, corresponding to 2.7% of the main flow at 20 m/s. As the driver probe was always

arranged to be upstream of the receiver, this causes a slight dilution of the suspension, and so this effect was taken account in calculations of suspension concentration.

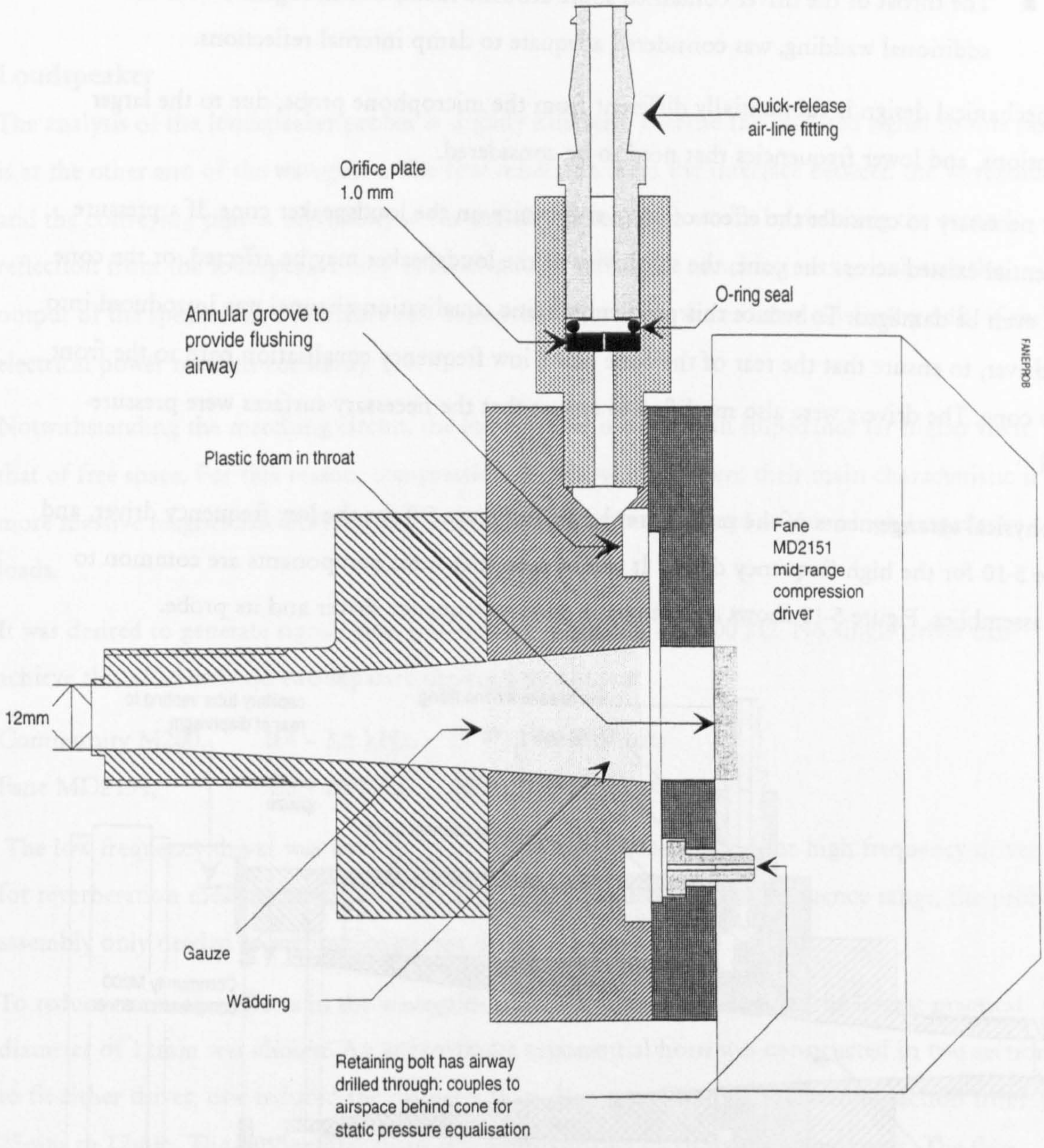

Figure 5-10 Cross section through the probe assembly for the mid-range driver (drawn to scale). For clarity, most fasteners are not shown.

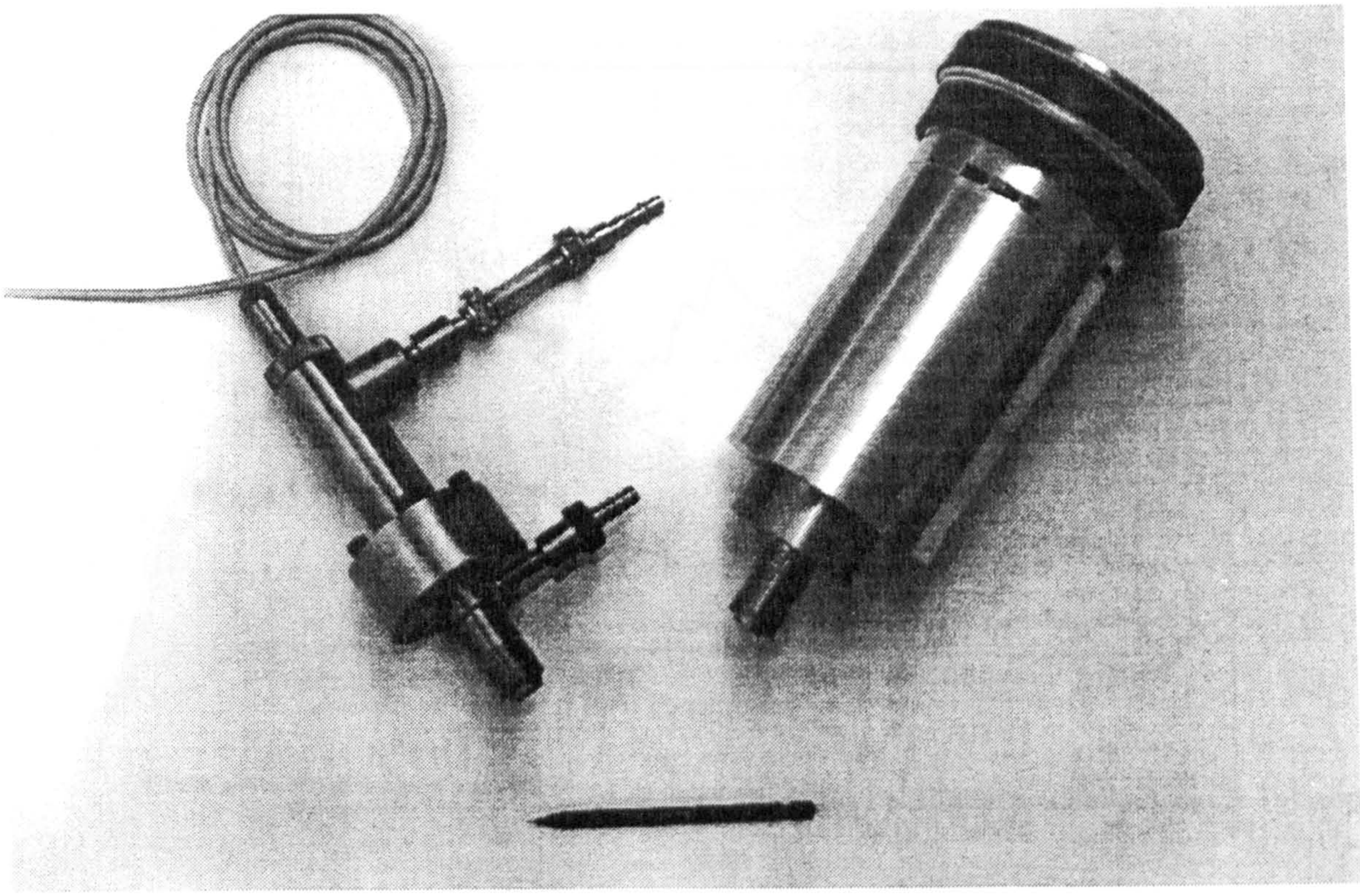

Figure 5-11 *Photograph of the microphone probe (left) and low frequency driver probe (right). The pencil is shown for scale.*

5.4.5 Acoustic measurements of probe performance

Although the probe assemblies were designed to be attached to the conveying pipe, for simplicity they were tested in a free field. This can be expected to modify their response somewhat: the characteristic impedance of free space is lower than that of the tube, affecting the reflection coefficient at the exit; and the microphone probe is designed for use as a pressure microphone (that is, a high impedance point replacing a solid wall), rather than a free field microphone, and so it will tend to distort the sound field.

Nonetheless, for the assessment purposes of this work, it was not considered worthwhile to overcome the practical problems in trying to assess response *in situ* and hence remove the acoustic effect of the conveying pipe.

The measurements were made with MLSSA, and used time domain editing to remove external reflections, and hence simulate a free field.

Microphone

The microphone response was compared to the response of a free field microphone placed at the same point in a sound field. The resulting spectrum is shown in Figure 5-12. It is fairly uneven, but the excursions are limited to ± 5dB over most of the frequency range. Since all measurements made with it are compared with a reference, a flat frequency response is required only to give a good SNR across the useful range, rather than for an absolute calibration.

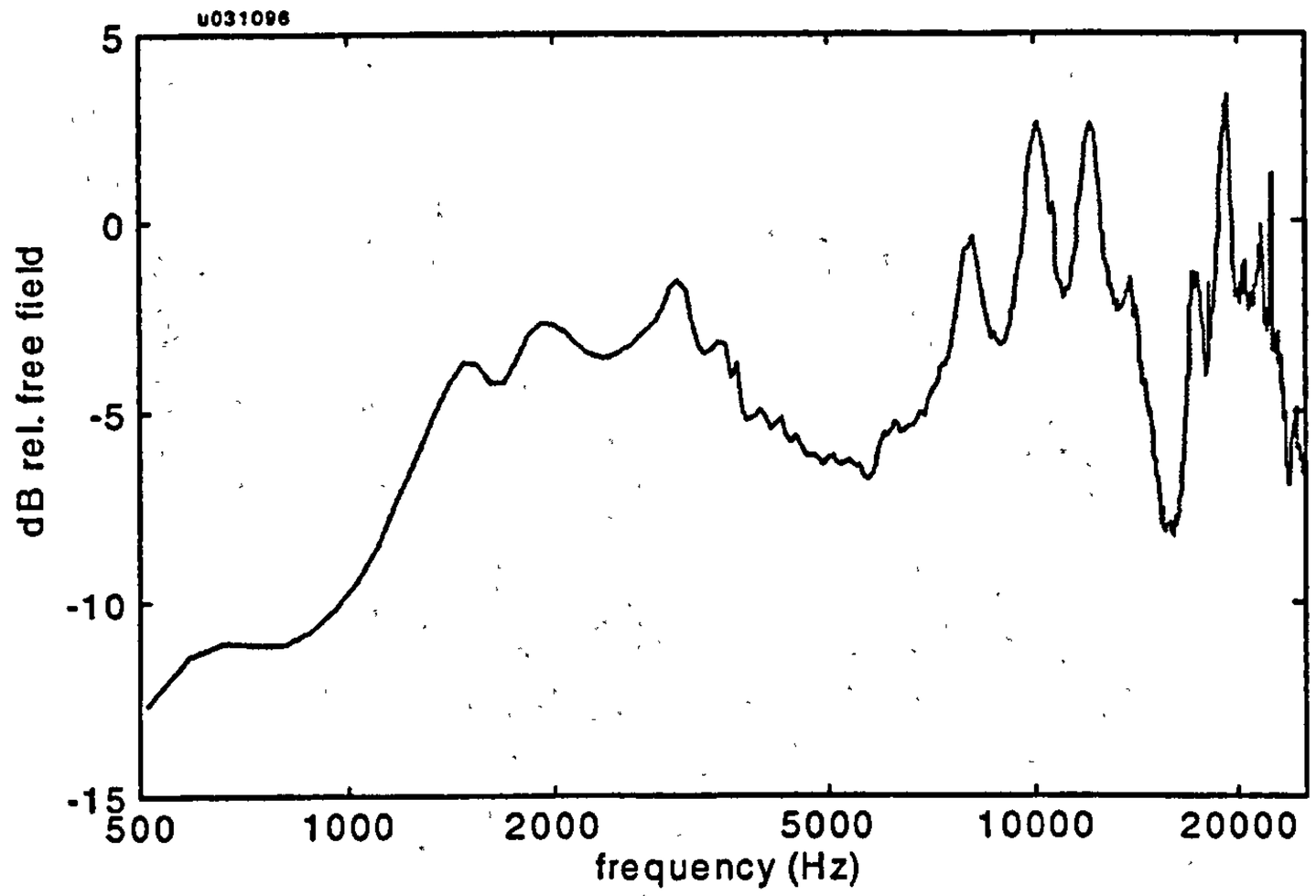

Figure 5-12 *Response of the microphone probe, relative to the free-field sound pressure at the probe mouth.*

Loudspeaker probe

Low frequency driver

The impulse response was measured for four stages of development of the probe:

1. Without the matching channel
2. With the matching channel, but with no resistance material
3. With the resistance material over the matching channel
4. With resistance material, and a plug of gauze of 25mm length inside the tube.

The Schroeder decay plot is shown below, to demonstrate the rate of decay of the impulse response.

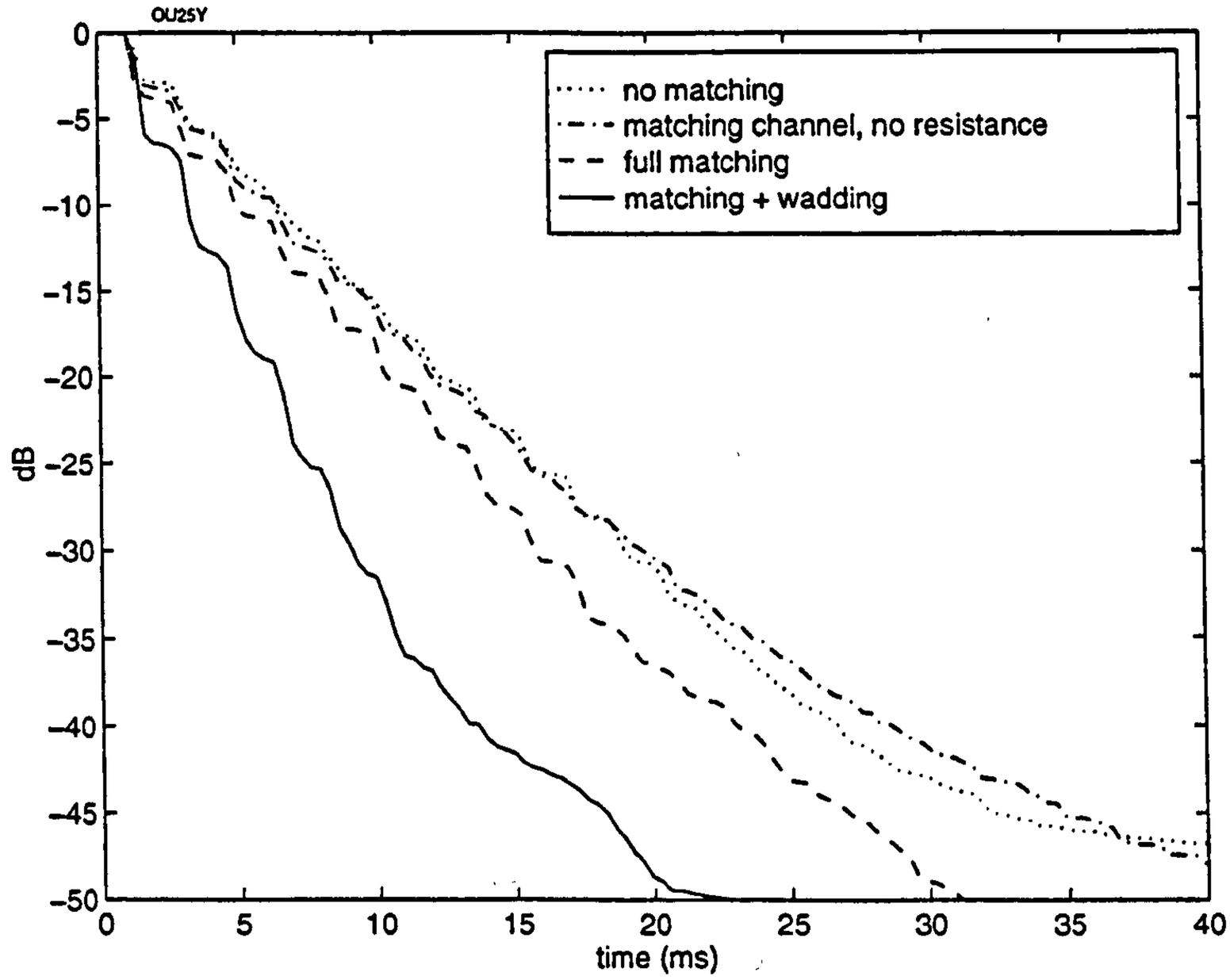

Figure 5-13 *Schroeder (energy) decay plot of low frequency driver in probe: different stages of build.*

It can be seen that addition of the flow resistance increases the decay rate by approximately 27%. The largest effect, as may be expected, is gained by the damping material that increases the decay rate by a further 79% to 3.4 dB/ms.

Therefore, the final design contained this plug of wadding, near to the opening of the probe (where the particle velocity is greatest, for the largest damping effect). It was held in place by a screen of fine gauze, which also protected the loudspeaker from dust contamination.

The anechoic spectrum of the final design is shown in Figure 5-14.

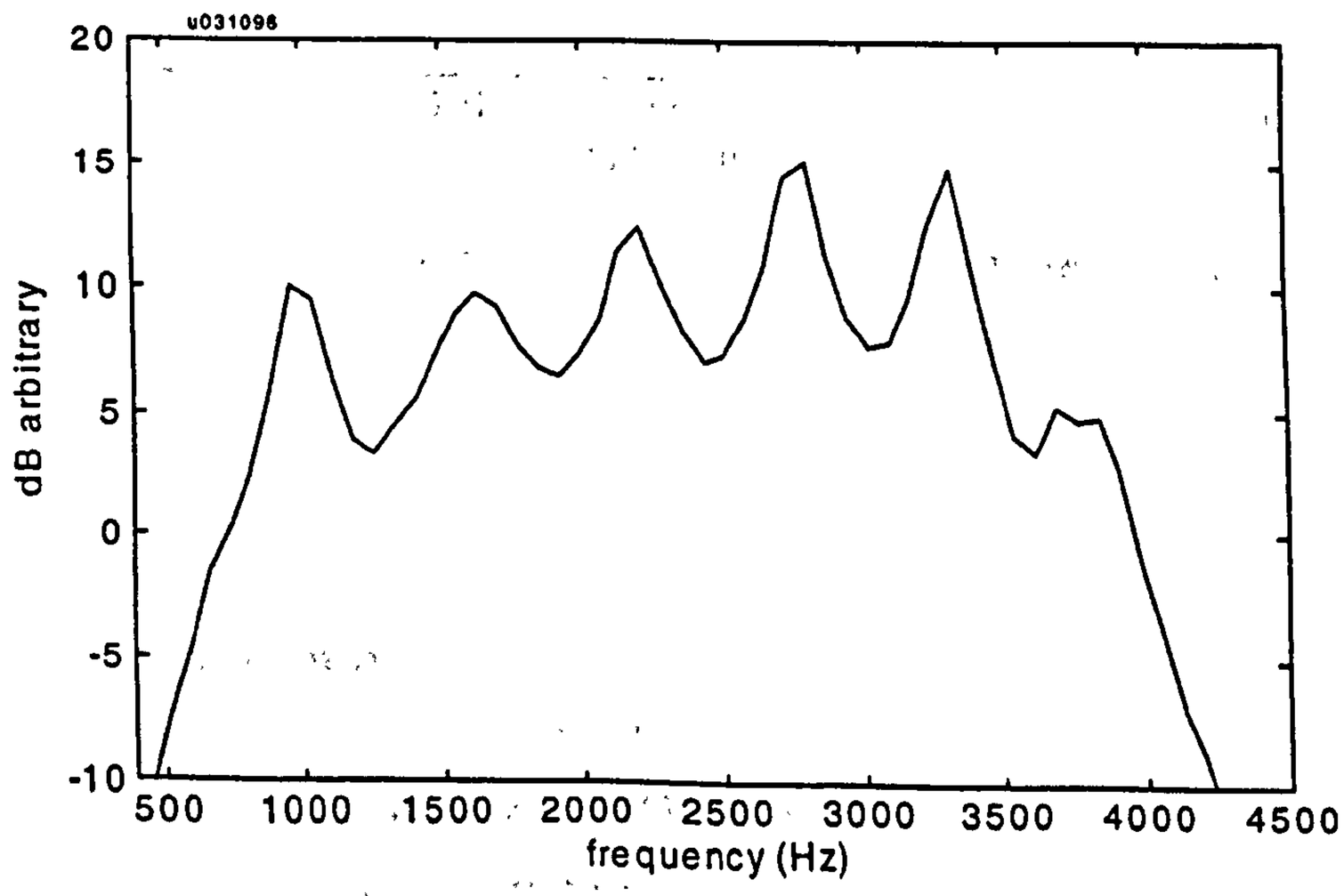

Figure 5-14 *Anechoic spectrum of low frequency driver mounted in probe*

The harmonic peaks are evidence of internal reflections in the tube; the second peak appears to be the most sensitive to internal damping. The difficulty of completely matching the impedance presented by the low frequency driver is probably due to the large internal cavity within the driver: this will tend to present a large compliance that is not easily compensated.

The low frequency performance is worse than predicted: a high-pass characteristic is visible below 600 Hz. This is thought to be due to the approximation of the exponential horn by a series of conical segments, causing the cut-off frequency to be higher than 400 Hz (the design value).

The high frequency roll-off is caused by a low-pass filter set to 3500 Hz – the nominal upper frequency of the driver. A high pass filter was similarly set to 400 Hz. Together, they protected the driver, and maximised its useful power output.

High frequency driver

The anechoic spectrum is shown in Figure 5-15. The lower frequency roll-off was due to a high-pass filter set to 1500 Hz. The decay rate of the impulse response is 10dB/ms.

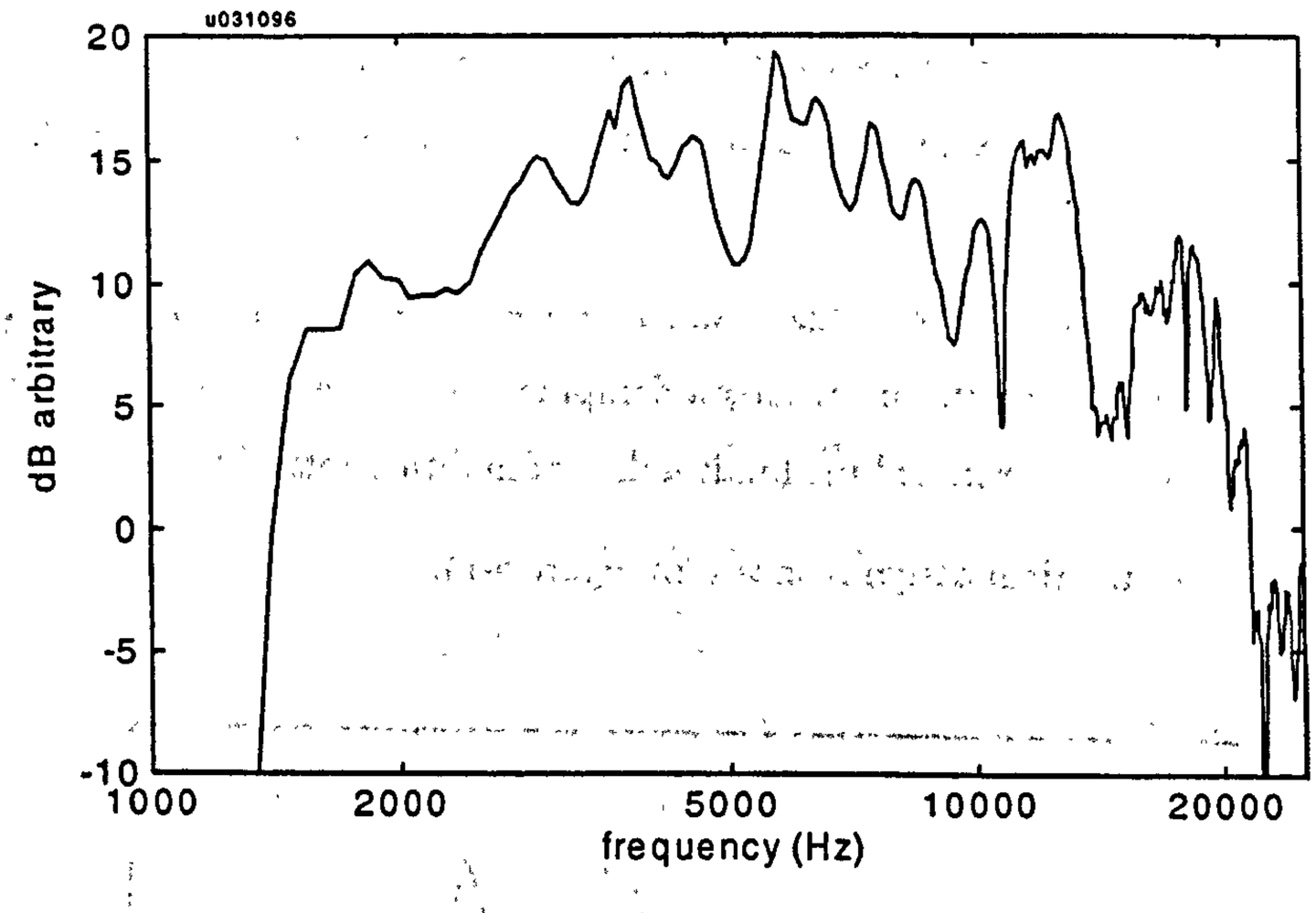

Figure 5-15 *Anechoic spectrum of high frequency driver mounted in probe.*

5.5 ULTRASONIC TRANSMITTING PROBE

The literature search identified a lack of measurements on suspensions made at the lower end of the ultrasonic frequency range. To make attenuation measurements in this frequency range, an appropriate transducer was selected. This selection, and the design of a suitable probe and driving hardware, is described in this section. The software to control and analyse the measurements is described in Chapter 8.

Transducer selection

There are two main types of transducer capable of coupling ultrasonic energy into air: electrostatic and piezoelectric. Their relative advantages and disadvantages are summarised in Table 5-B:

	Advantages	Disadvantages
Electrostatic 10 kHz - 500 kHz	Cheap Easy to self-build Relatively efficient coupling Relatively broadband	Fragile membrane (2 - 5 μm) Long-term instability Sensitive to static pressure variations
Piezoelectric 100 kHz - 5 MHz	Rugged Elements can be bought pre-tuned Long-term stability? Insensitive to static pressure	Narrow-band or very inefficient Inefficient coupling Expensive elements

Table 5-B *Advantages & disadvantages of ultrasonic transducer types for use in air*

An electrostatic transducer was selected due to its good coupling efficiency, and the reasonable performance at the low-ultrasonic frequency range of interest. The type was a Polaroid Environmental ultrasonic transducer, which is cheap, readily available, and has a wide transmitting bandwidth of 42 - 77 kHz approx. (the same transducer may be used as a receiver, but its bandwidth is narrower at 40 - 65 kHz approx.)

As a receiver, the existing 1/4" microphone and flushing probe were found to have a useful frequency range up to 80kHz.

Transducer driving circuitry

The Polaroid transducer requires a driving voltage of up to 400V for maximum output power. Conceivably, it may be driven from -400 - +400V; however, its transfer function becomes non-linear about 0V, thus introducing new frequency components and leaking energy away from the

frequency of interest. Hence, the drive signal was operated about a D.C. bias of 200V, with a 180V peak-peak swing.

In order to achieve this voltage from the amplifier available (Rotel RA-870BX), a step-up transformer was wound with a turns-ratio of 44. The input impedance at 50kHz was chosen to be 8Ω (nom.) to match the usual load of the amplifier. This gave an output impedance of 15kΩ which appeared low enough in order to drive the cable and transducer effectively with very little distortion. The diagram of the driving circuitry is shown in Figure 5-16

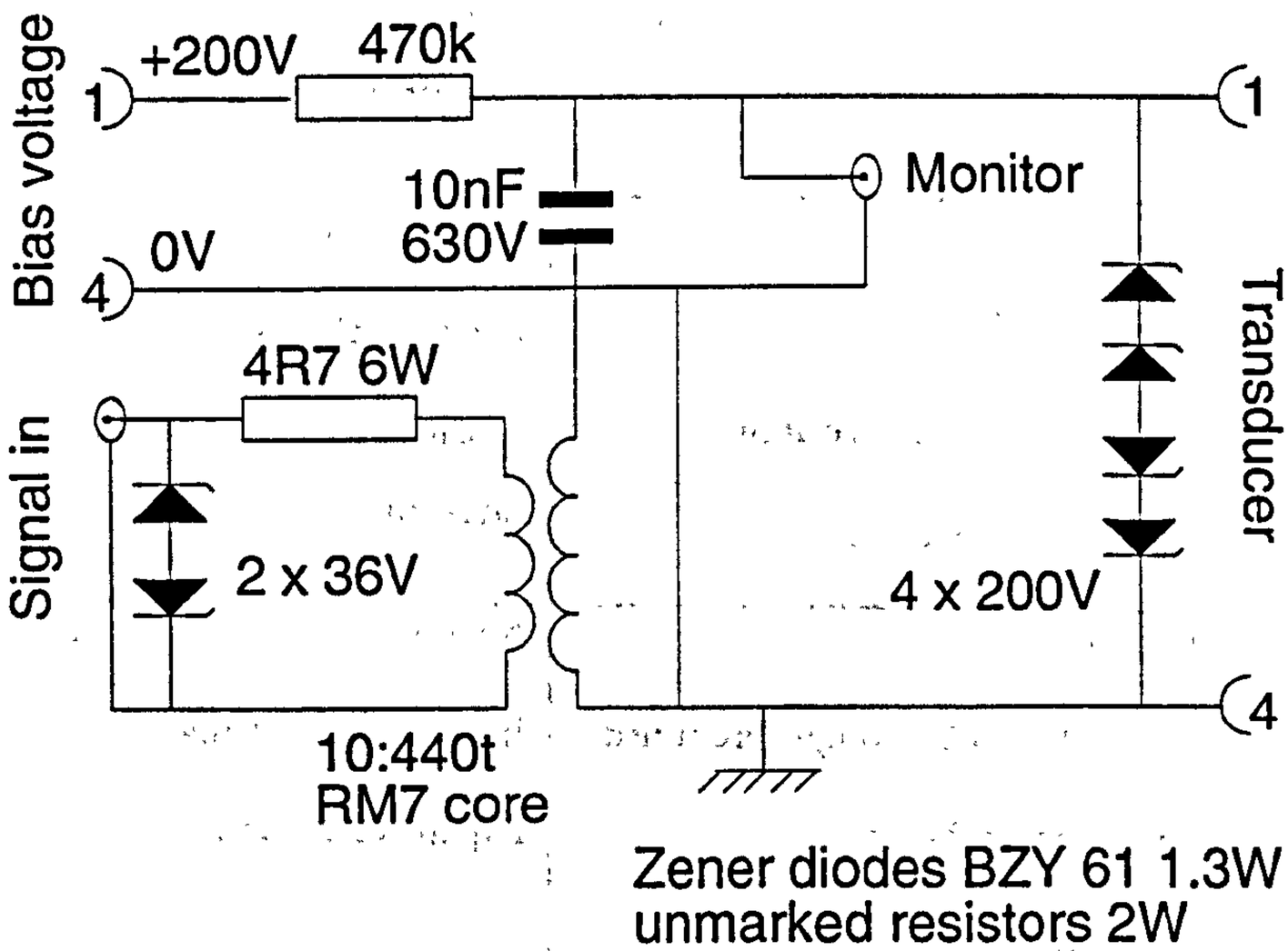

Figure 5-16 Circuit diagram of ultrasonic transducer driving circuitry

The +200V D.C. bias was derived from the microphone polarisation voltage output of the Brüel & Kjær 2607 microphone amplifier. The 470kΩ resistor increased the low impedance output of the bias voltage, so that it did not short circuit the output of the transformer, and also limited the current in case of a fault condition, or accidental electrocution. Zener diodes protected both the amplifier and the transducer from excessive voltages.

Transmitting probe

No attempt was made to equalise the termination impedance of the transmitting probe, since the probe tube did not operate in the plane wave region, and the dimensions of any elements would be too small to be practical. A schematic diagram is shown in Figure 5-17.

Particular care was taken to direct the flushing air away from the delicate face of the transducer, and the flow is kept as laminar as possible in order to reduce the generation of high frequency noise. The flushing air was metered into the probe using a 1.4 mm choke flow nozzle.

The thin membrane was also expected to make the transducer sensitive to static pressure differentials between the front and rear of the transducer. Equalisation was provided to rear of the transducer by mounting it on blobs of sealant, and allowing an annular gap of approximately 1mm around its periphery. The volume of the chamber at the rear was reduced and sealed by a conformable sealant. This combination of low flow resistivity and low compliance combines to ensure that the high pass characteristic could be expected to extend to medium audio frequencies, ensuring that any pressure differential is minimal.

The metal body of the transducer was isolated from the pipeline earth by making the mounting insert out of plastic: this reduced electrical noise by eliminating one possible earth-loop.

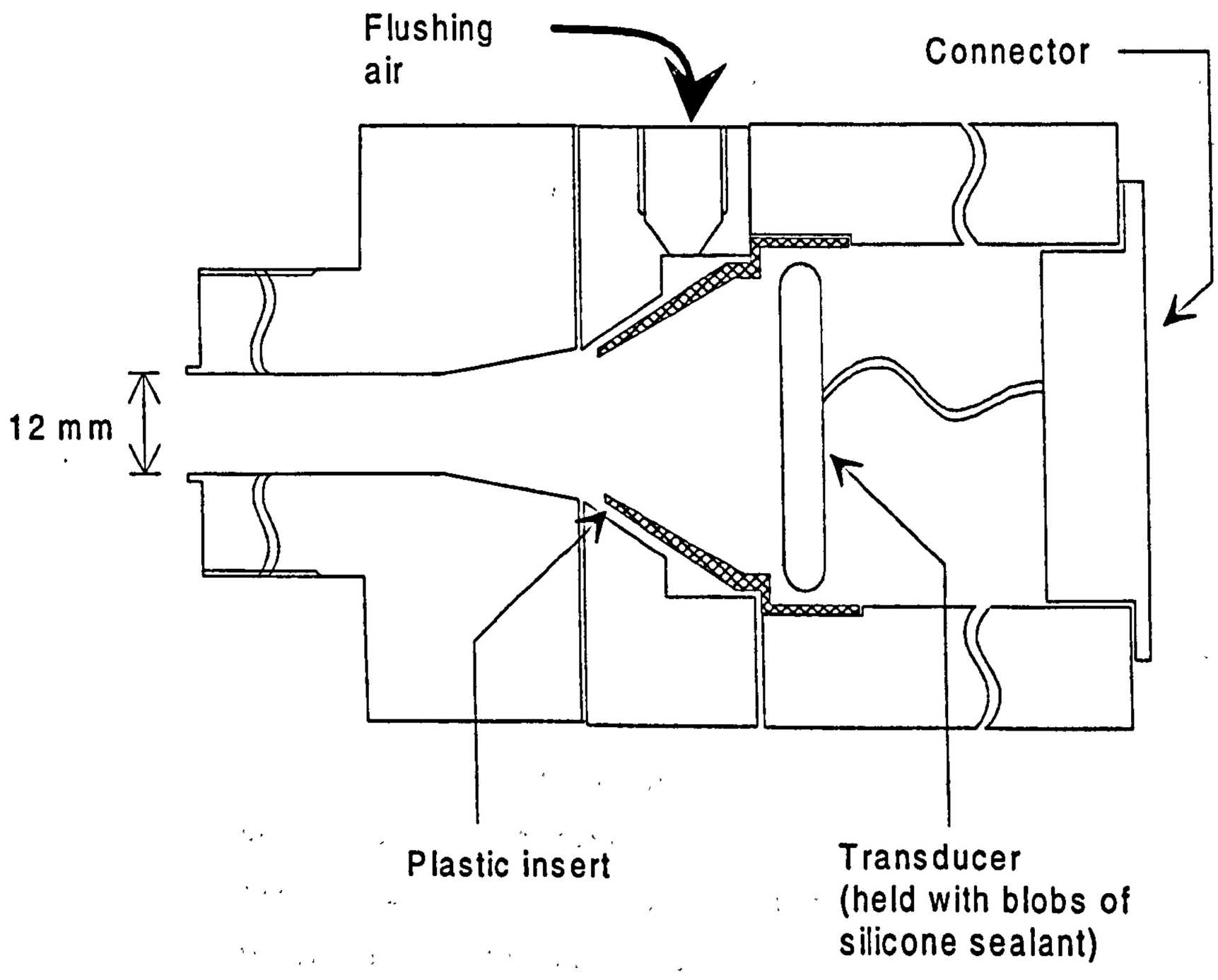

Figure 5-17 *Schematic diagram of the ultrasonic transducer probe*

5.6 MASS-CONCENTRATION MEASUREMENT

The measurement of mass-concentration in the dust flow-rig by non-acoustic means is pivotal to the success and validity of the project. Such a measurement provides the reference against which the acoustic technique is judged: both the absolute accuracy and repeatability.

As explained earlier, the non-acoustic method relies on measuring the gain-in-weight of the storage hopper, using a set of load cells. The gain-in-weight signal is recorded on a chart recorder. The mass flow rate of dust is found from the first derivative of this signal, ie. the gradient of the trace. The differentiation process tends to amplify short-term fluctuations, and to bury the long-term trend. Some short-term fluctuations will be physically valid; the feed rate of particulate into the venturi can be unsteady, according to the cohesiveness of the material and the degree of its consolidation in the feeder tank – indeed, the fluctuating concentration was sometimes audible. Other fluctuations in the differentiated signal (especially negative ones), will be due to electrical noise or physical causes; these include force pulses induced by decelerating dust as it falls into the storage hopper, and forces that are transmitted through the pipeline and incompletely isolated. For example, instantaneous jumps in the weight trace are often noticeable when the conveying conditions are changed.

In order to gain a good estimate of mass concentration, the gain-in-weight signal was recorded on the chart recorder at a slow paper speed (typically 0.5mm/s), and a straight line was fitted to a long record (typically several minutes). This yielded a long-term average value of mass flowrate. As the air mass flowrate was known from the calibrated nozzles, the mass concentration could therefore be found as the ratio of particle/air mass flow rate.

The acoustic measurements, by contrast, were each made over a period of several seconds. Such relatively "instantaneous" measurements could not validly be compared with the long term average of mass concentration, since the acoustic measurement could be sampling the flow at a moment of anomolously high or low concentration. To compare the results validly, the timescale over which the acoustic measurement was made should be the same as for the non-acoustic measurement.

This suggests two approaches:

- Time-Averaged measurements: many acoustic measurements are averaged over a period of several minutes. The average is compared to the long-term average that is measured graphically from the chart recorder. If the acoustic data require significant post-processing, then the averaging cannot be performed in real-time, and so large datasets must be collected and analysed off-line.
- "Instantaneous" measurements: individual acoustic measurements are compared to the local (short-term) gradient of the gain-in-weight signal at the moment that the acoustic measurement is made. Since the length of the time series is short, the estimation of

gradient is less accurate than the previous method. This method is also sensitive to errors in synchronisation between the acoustic and non-acoustic measurements.

The advantage of comparing instantaneous measurements is that they also would provide a measure of the repeatability of the acoustic technique through the scatter in measurements, in addition to the mean accuracy. However, the method of measuring the local gradient of the curve is so inaccurate, that it is impossible to separate errors in the acoustic signal from inaccuracies in the non-acoustic measurement. Therefore, the time-averaged method was used for most measurements, apart two datasets measured on flour, which appear in Chapters 6 and 7.

Most measurements on the Wolfson rig involved measuring an acoustic parameter, while the mass concentration was varied. The plots derived from such a dataset often show an uneven spread of concentration points. This is generally due to the lack of direct control over the concentration; some materials would flow smoothly over a variety of feed-rates, while others demonstrated an "all-or-nothing" flow, making it difficult to obtain low or intermediate concentrations.

Furthermore, there are often fewer concentration points than would be ideal. This was due to the time-pressure of working on a borrowed rig: all of the measurements on the rig took place over a total of 12 days.

5.7 BACKGROUND NOISE IN THE FLOW RIG

In order to understand the variation of background noise in the flow rig, long time sequences of the microphone signal (without any excitation) were recorded at a variety of conveying conditions. They were analysed by passing the samples through a bank of digital bandpass 1/2 octave filters, to yield the power spectral density. Appendix B gives the code listing to achieve $1/n$ octave analysis in accordance with IEC 225 [65].

5.7.1 Air-flow only

The airflow was varied between 0 to 42m/s, and a long time sequence of sound pressure was recorded at a bandwidth of 25kHz. The power spectral density is shown in Figure 5-18.

With no airflow, the background noise is mainly caused by the air flushing through the microphone probe. The PSD increases with speed, most markedly at the lowest frequencies, and hardly at all in the band around 380Hz, where it appears that a flow-induced resonance is being excited.

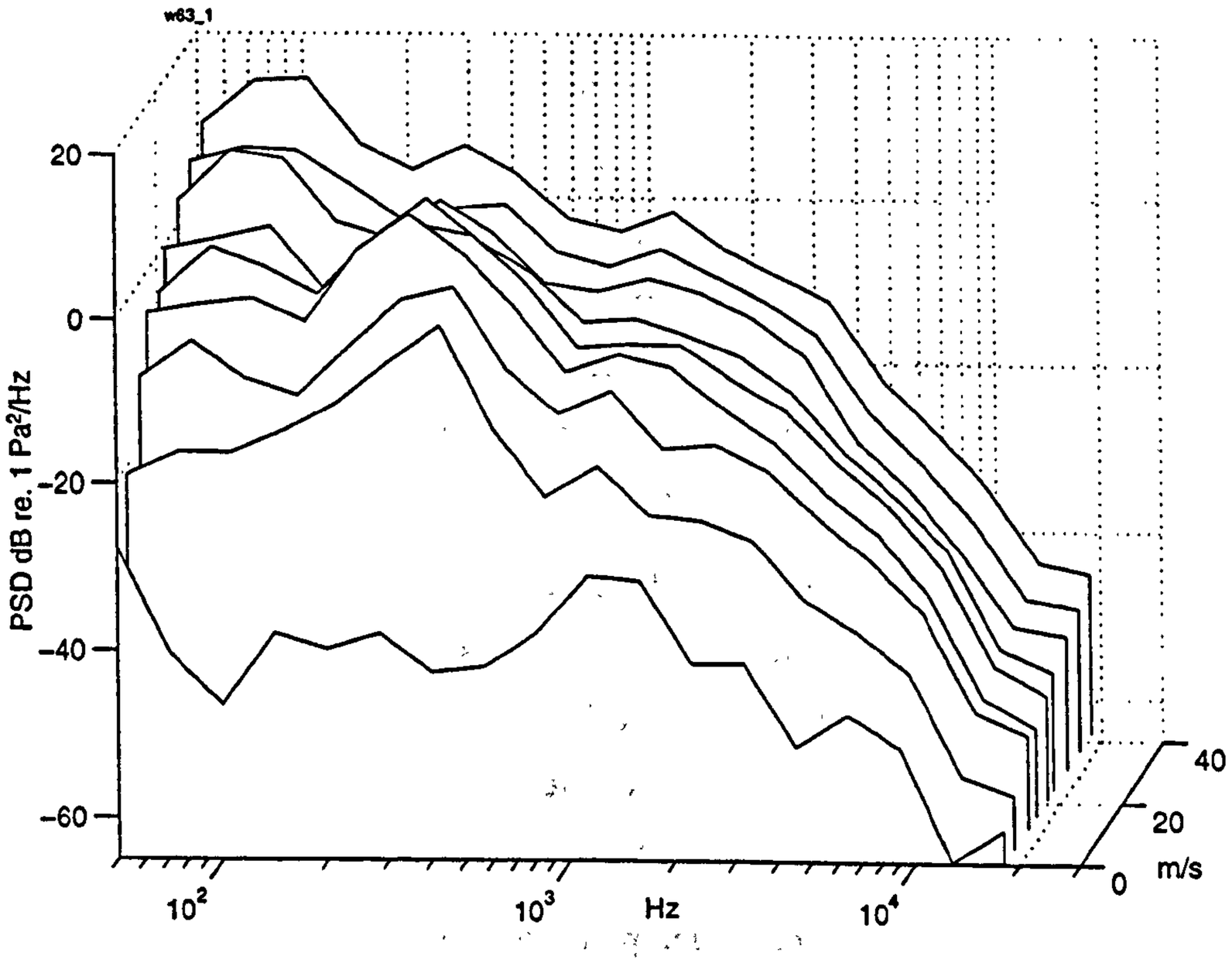

Figure 5-18 Power spectral density (PSD) of background noise SPL in 1/2 octaves, for different airflow rates (no dust); 100% supplementary airflow.

However, the flow noise also depends on the air split between supplementary and venturi nozzle banks. If more air flows through the venturi channel, then the noise level increases and the peak moves to a higher frequency, shown in Figure 5-19. This is probably due to the disruption of the flow regime as it passes through the venturi, which presents a severe constriction to the flow.

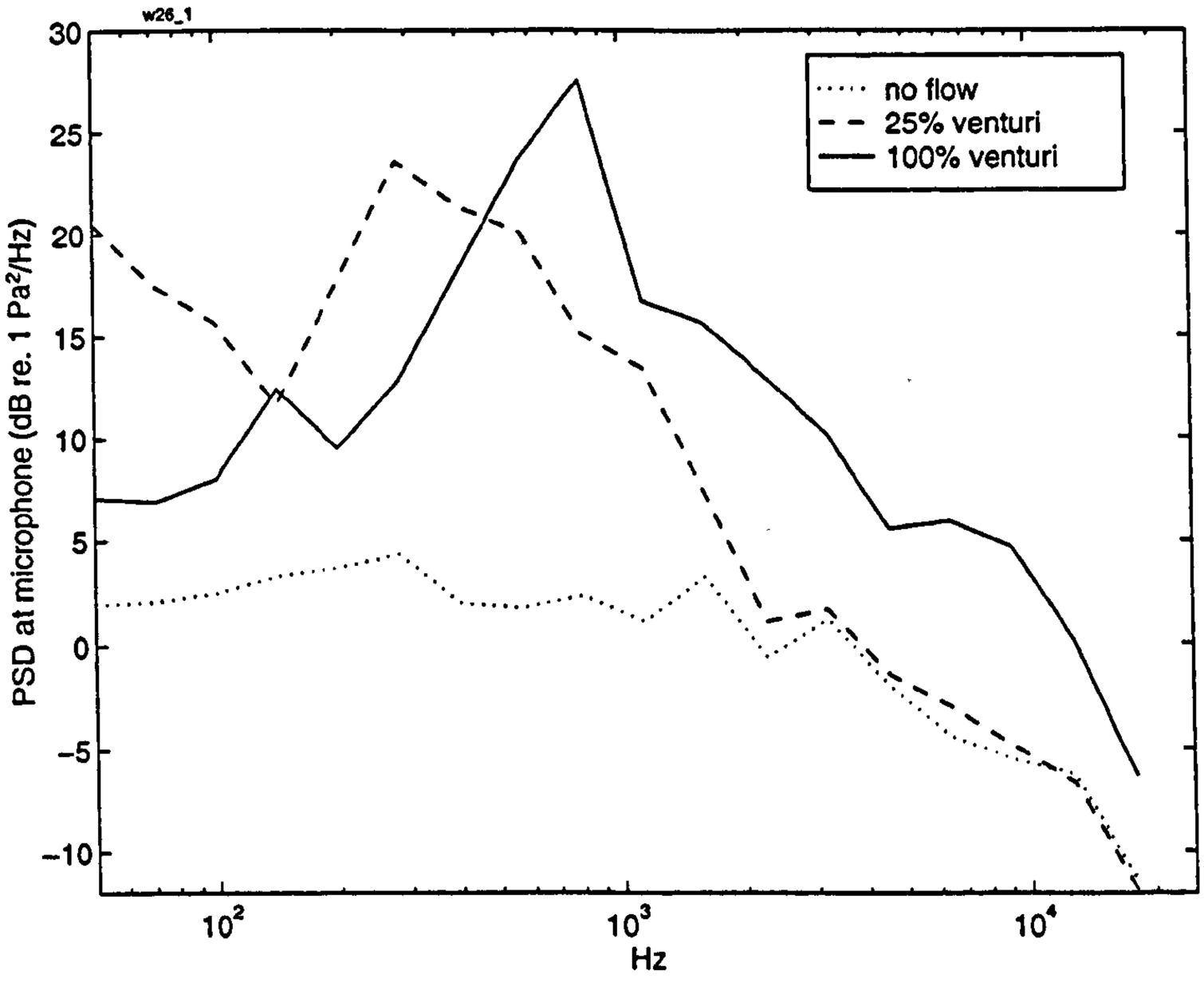

Figure 5-19 *Power spectral density (PSD) of background noise, with and without airflow at 20m/s, and with different proportions of venturi flow / total flow. 1/2 octave analysis.*

5.7.2 Suspension flow

Using a similar measurement technique, the superficial air velocity (S.A.V.) was kept constant at 20m/s, while the venturi / supplementary airflow split was changed to vary the concentration of the suspension. The particulate used was flour, with a mean diameter of 58μm (see Appendix F). The results are shown in Figure 5-20.

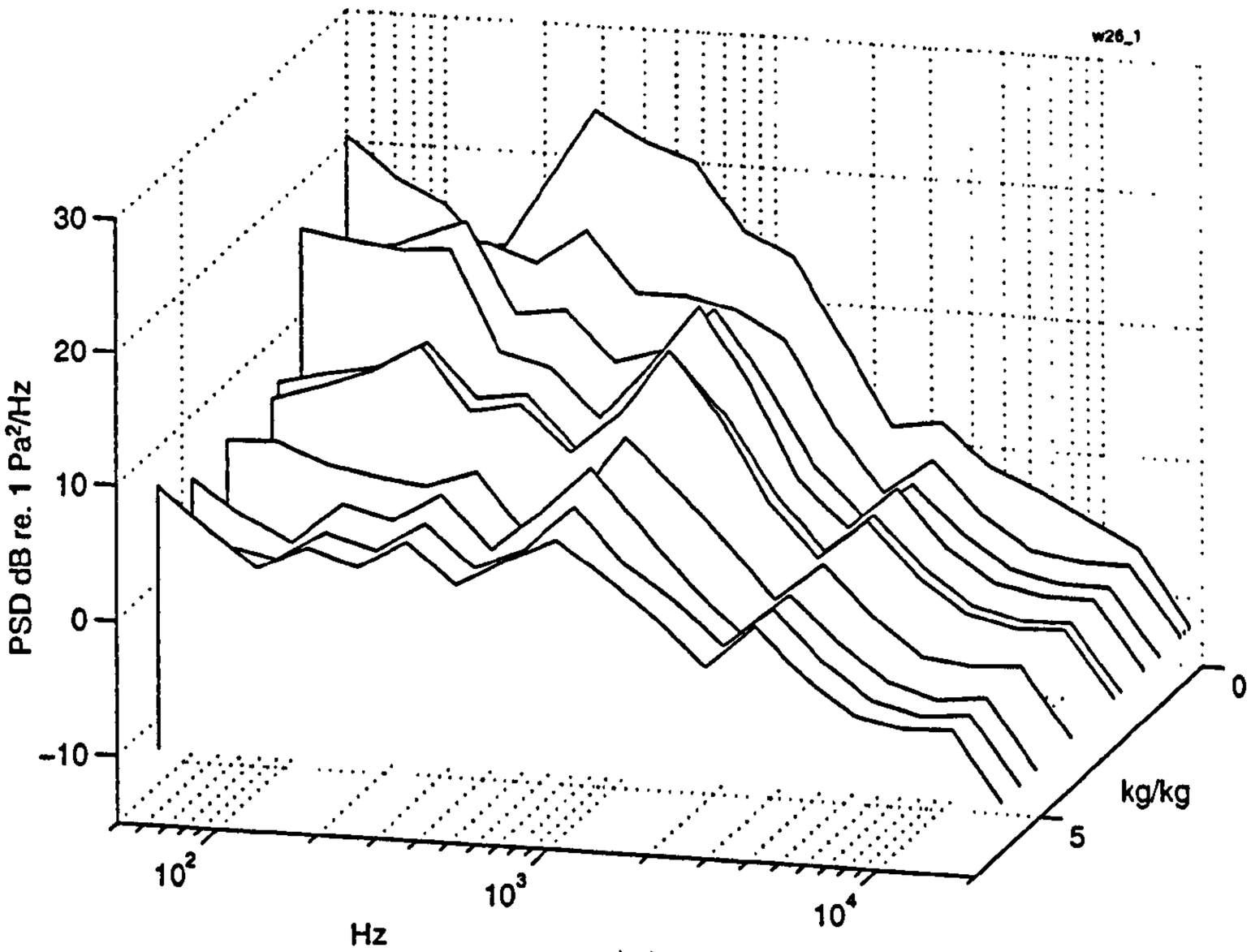

Figure 5-20 Power spectral density (PSD) of background noise for varying flour concentrations at 20m/s nominal S.A.V. 1/2 octave analysis.

Below 1kHz, the PSD falls steadily with increasing dust mass concentration, while above 1kHz, the levels drop abruptly for small dust levels, and reach a plateau level. Throughout the frequency range, it appears that the presence of dust attenuates the transmission of flow noise, and maybe also damps its generation. There is little evidence that the level rises due to particle collision noise. The greatest damping effect is at lower frequencies; at 280Hz, the level falls by 25dB over the flow range.

This result appears to be in contradiction to the findings of Sheen & Raptis [130] who found that the noise level increased by over 20dB when particles were flowing. However they were measuring at higher frequencies (up to 140kHz), and with much larger particles (1 mm limestone chips) that could be expected to create greater impact noise and to cause negligible attenuation of the noise. In contrast, Raptis & Lau [116] used the level of background noise to deduce the presence/absence of char (ash particles) in a flow of steam. In particular, they found that the presence of char in small (unspecified) concentrations *reduced* the sound level above 10 kHz by over 20 dB.

In the above experiments, it appears that background noise caused by the flushing air swamped any changes at high frequency due to the presence of particles. However, it can be concluded that the level of background noise varies in a complex manner according to the size of the particle, the flow rate, and the frequency range under consideration. It tends to increase with particle size and flow rate, and decrease with flow rate for small particles, but increase for large particles.

5.8 CONCLUSIONS

An existing rig was selected for experiments on flowing suspensions. The non-acoustic (gravimetric) technique of measuring the mass flow rate requires long averaging times to produce accurate results, and the implications for comparison with acoustic measurements has been discussed. A separate, air-only rig has been constructed to allow easy access to experimental facilities for measurements with clean- air flow.

To interface delicate acoustic transducers with harsh environment of the flowing suspension, special probes were developed. These were designed to protect the transducers, reduce the possibility of causing explosion, and minimise their acoustic influence. In particular, a continuously-flowing column of air was used as a buffer against contact with the suspension, and a technique of impedance matching improved the acoustic performance of the transducer/probe assemblies.

The background noise in the rig was measured while varying the air-speed and mass flow rate. In clean flow, the noise increased with velocity, especially at low frequencies, and also increased with the proportion of air-flow through the venturi. During suspension flow, this latter effect could be expected to contribute to an increasing noise generation level as concentration is increased. Nonetheless, the noise level was found to decrease with concentration across the frequency range, presumably because due to the attenuation of the suspension.

At higher frequencies (>10 kHz) the noise level generated by air flushing in the probe tended to mask any variations in the pipe-line. Further investigation would require the development of a quieter flushing system.

6

MEASUREMENTS OF PLANE WAVE PROPAGATION

This chapter presents measurements of plane wave propagation parameters. Wave propagation was constrained to the plane wave mode by the dimensions of the waveguide. Practically, the frequency range of measurement was selected to be below the cut-on frequency of the first transverse mode; this is calculated to be 2010 Hz for the 100mm tube, and 4020 Hz for the 50mm tube [41].

Measurements were performed on both quasi-static suspensions (section 6.1) and flowing suspensions (section 6.3). Section 6.2 presents measurements in varying flowrates of clean air, to assess the acoustic effect of the airflow, due to mechanisms such as turbulent loss and changes in orifice impedance.

The main aim of the measurements on quasi-static suspensions was to obtain low noise data on a well-characterised material, with which to assess the validity of theoretical formulations. The extension to flowing suspensions then gave an opportunity to see if correlations may be measured between acoustic measurements and suspension concentration, and to test the experimental equipment that was described in Chapter 5. Furthermore, measurements are compared with predictions wherever possible.

6.1 QUASI-STATIC SUSPENSIONS

The equipment described in Chapter 4 was used to measure the plane wave parameters of alumina powder (Al_2O_3). As a test material, it has several advantages: it is readily available in well-defined size distributions; it is non-toxic, and disperses well without particles adhering to each other significantly. This latter property was tested by visually inspecting samples of alumina that had settled out from suspension (using a scanning electron microscope). The relevant physical properties are listed in Appendix F.

6.1.1 Dependence on concentration

A total of 14 measurements were made at varying particle concentrations (by selecting different nozzle sizes in the blow gun). Initially a grade of alumina labelled F800 was used; this had a mean particle radius of 3.2μm. The volume concentration ranged from 0.22 – 9.8 ppm (0.66 - 31 g/kg mass fraction).

The specific attenuation and dispersion were calculated in the manner described in Chapter 4. The dependence of both parameters on concentration at several example frequencies is illustrated in Figure 6-1.

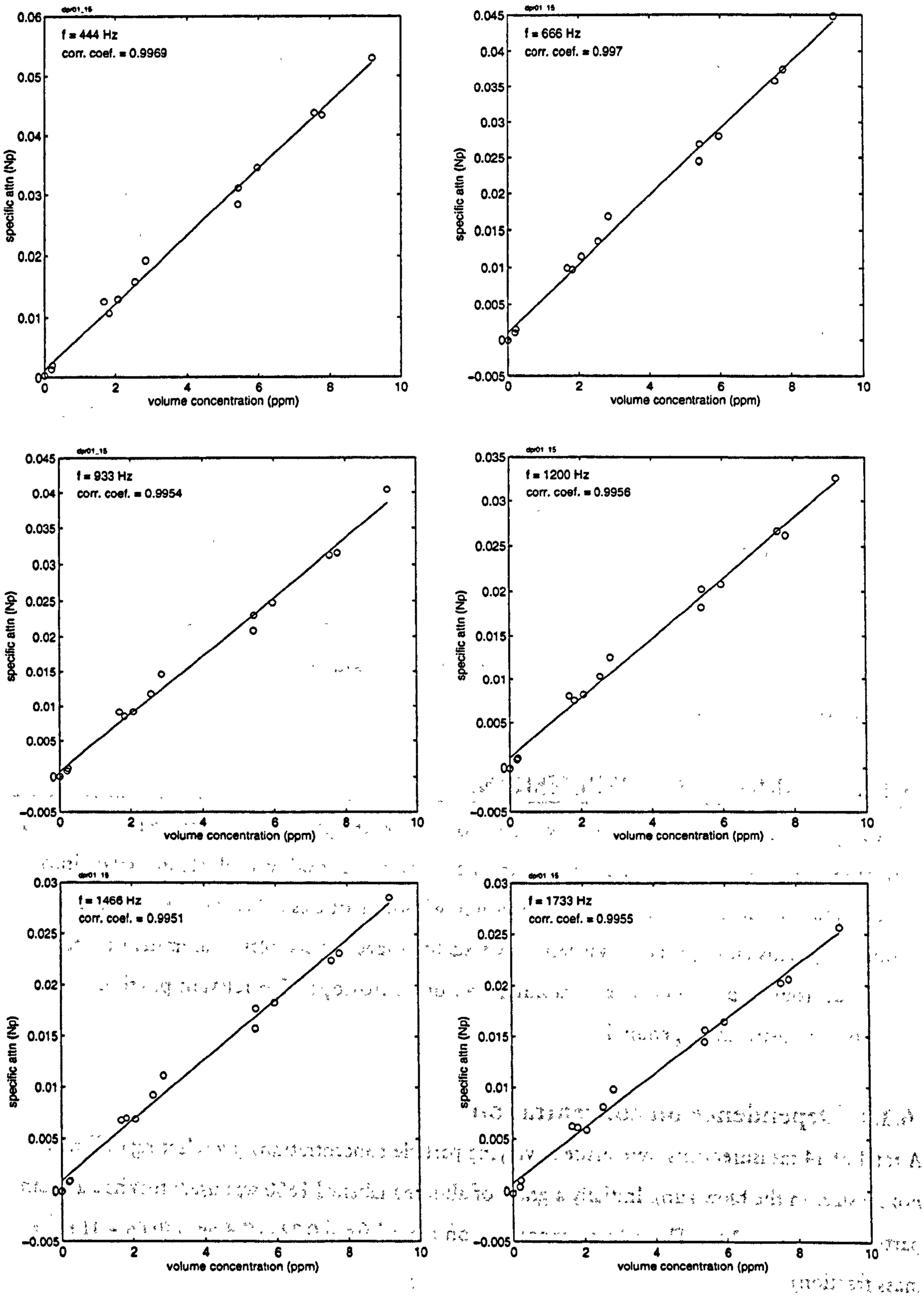

Figure 6-1 Example plots of specific attenuation as a function of volume concentration (measured in parts per million, ppm), for F800 grade alumina (mean radius 3.2μm). Best fit lines (solid) and correlation coefficients are also shown.

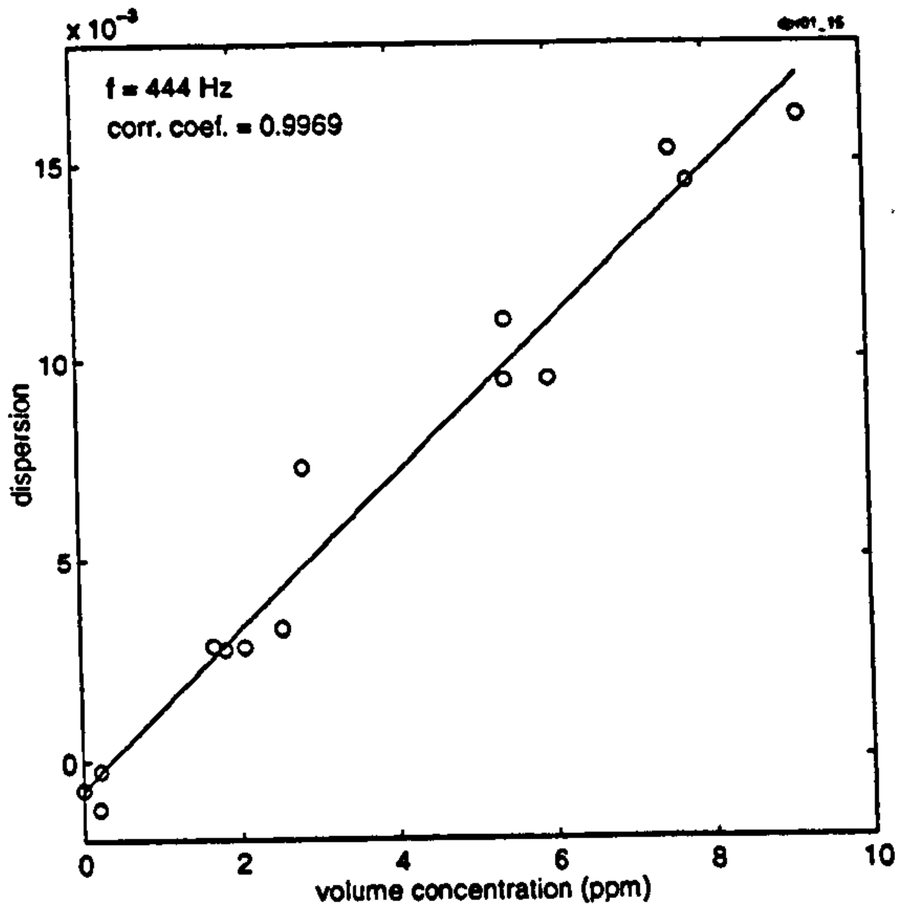

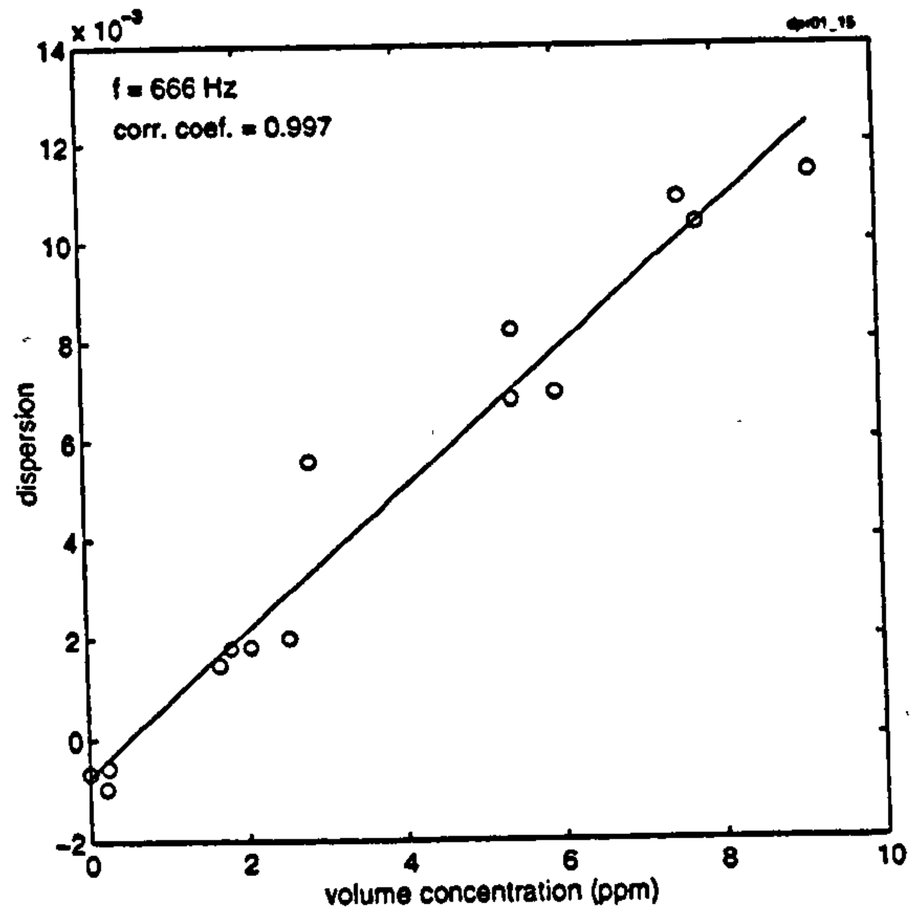

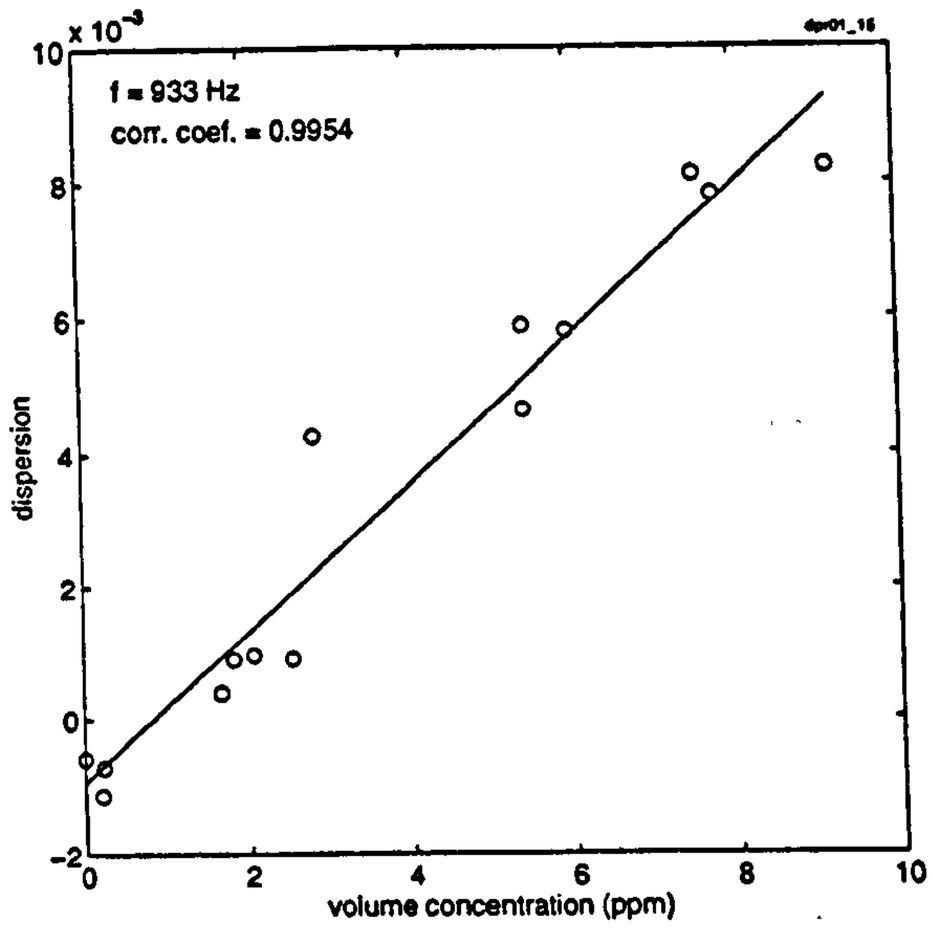

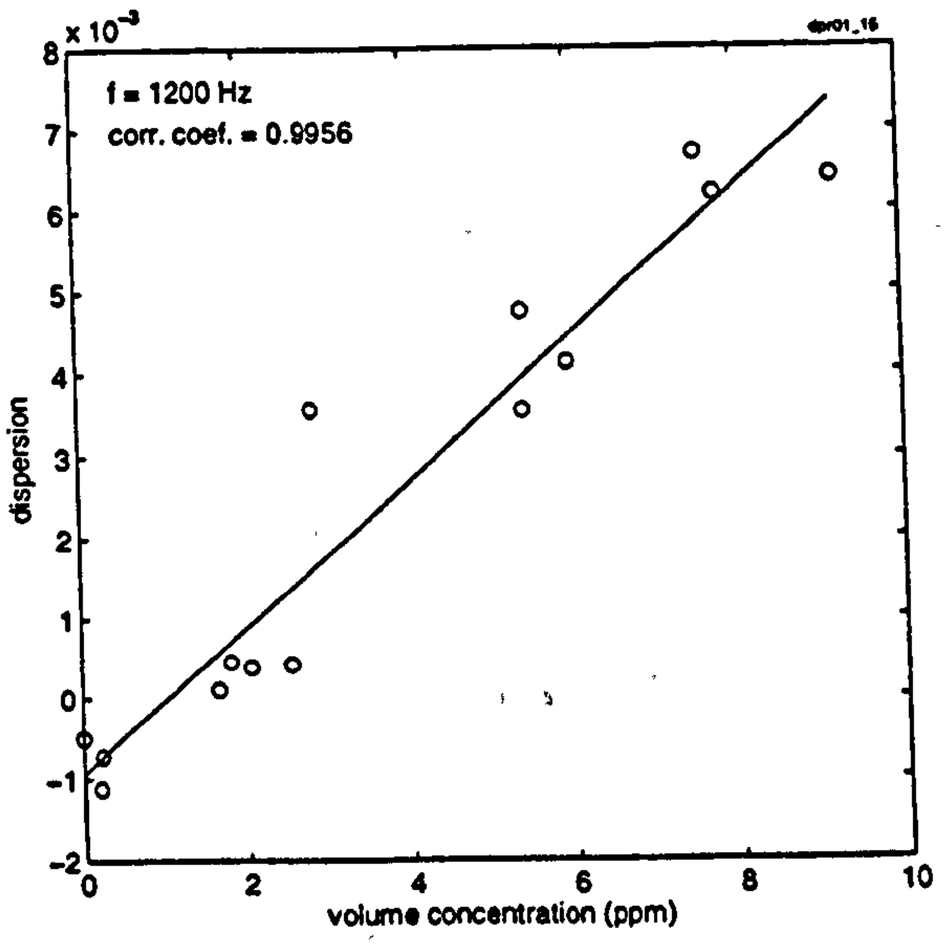

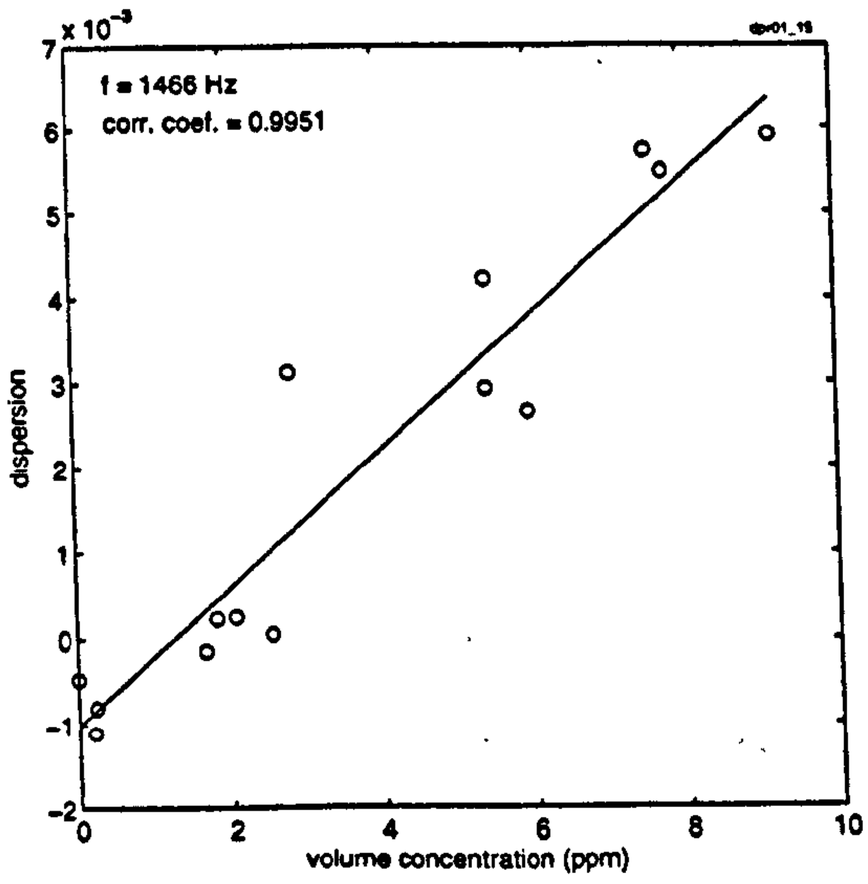

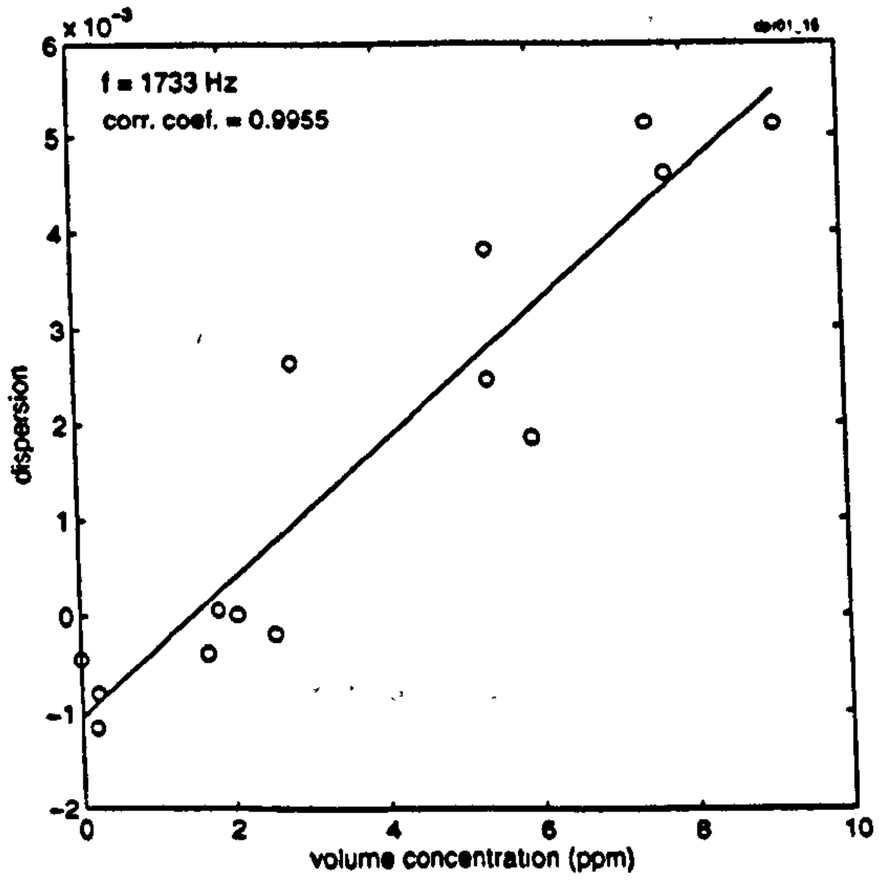

Figure 6-2 *Example plots of velocity dispersion as a function of volume concentration (measured in parts per million, ppm), for F800 grade alumina (mean radius 3.2μm). Best fit lines (solid) and correlation coefficients are also shown (solid).*

The plots of specific attenuation show little scatter and good linearity. Dispersion, however, shows greater point scatter, especially at higher frequency where the absolute phase difference being measured is very low.

The gradient of each plot yields the sensitivity of the variable to volume concentration [53], or, alternatively, the specific attenuation (or dispersion) at a value of 10^{-6} m^3/m^3; it will be referred to as the normalised specific attenuation or (dispersion). The method of calculating the uncertainty in these values is described below.

For a series of measured values, x_i, y_i, a line of best fit was found (using a least mean squares routine):

$$y_i^{fit} = \hat{m}x_i + \hat{c} \tag{6.1}$$

By assuming a Gaussian distribution of measurement errors, the uncertainty in the gradient was estimated by [112]:

$$m = \hat{m} \pm t(df,\%)\sqrt{\frac{\sum_i \left(y_i - y_i^{fit}\right)^2}{(n-2)\sum_i \left(x_i - \bar{x}\right)^2}}, \quad i = 1, 2,...n \tag{6.2}$$

where $\bar{x}$ is the mean value of x, and $t(df, \%)$ is the value of the t distribution for (n-2) degrees of freedom, and the desired confidence level; here, n = 14 and a confidence level of 90% was chosen.

6.1.2 Dependence on size

Alumina grade F800

The normalised parameters are plotted in Figure 6-3 and compared to the theoretical predictions of Lloyd & Berry [85].

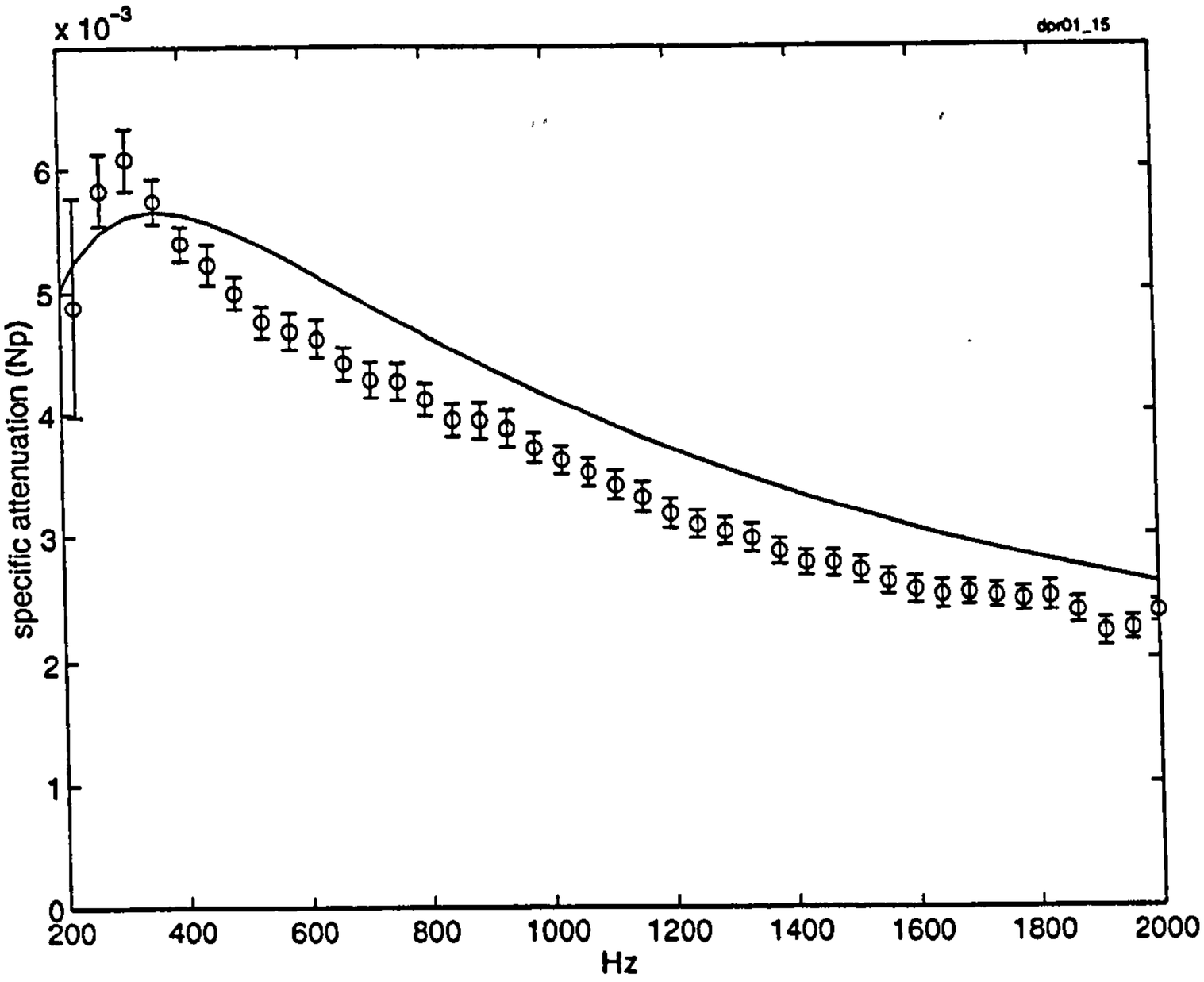

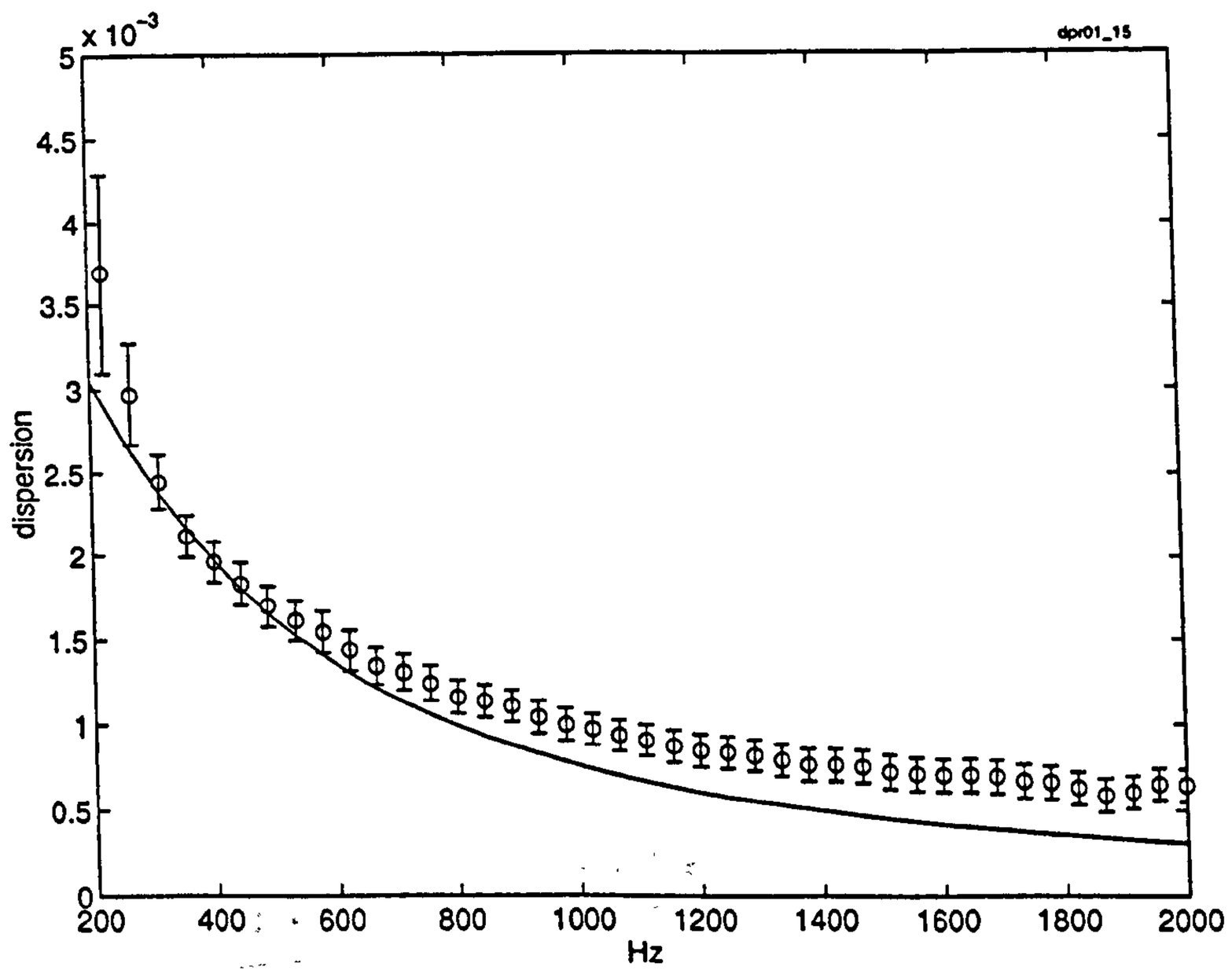

Figure 6-3 *Specific attenuation (top) and velocity dispersion (bottom) of alumina (grade F800, mean radius 3.2μm), normalised to $\phi_v=10^{-6}$ m^3/m^3, as a function of frequency. Circles are measured values with error bars marking 90% confidence limits; solid line is the theoretical prediction.*

Alumina grade F1000

Three measurements were taken with a finer grade of alumina (labelled F1000), which had a mean radius of 2.0μm. The curves were normalised by the volume fraction and averaged (see Figure 6-4).

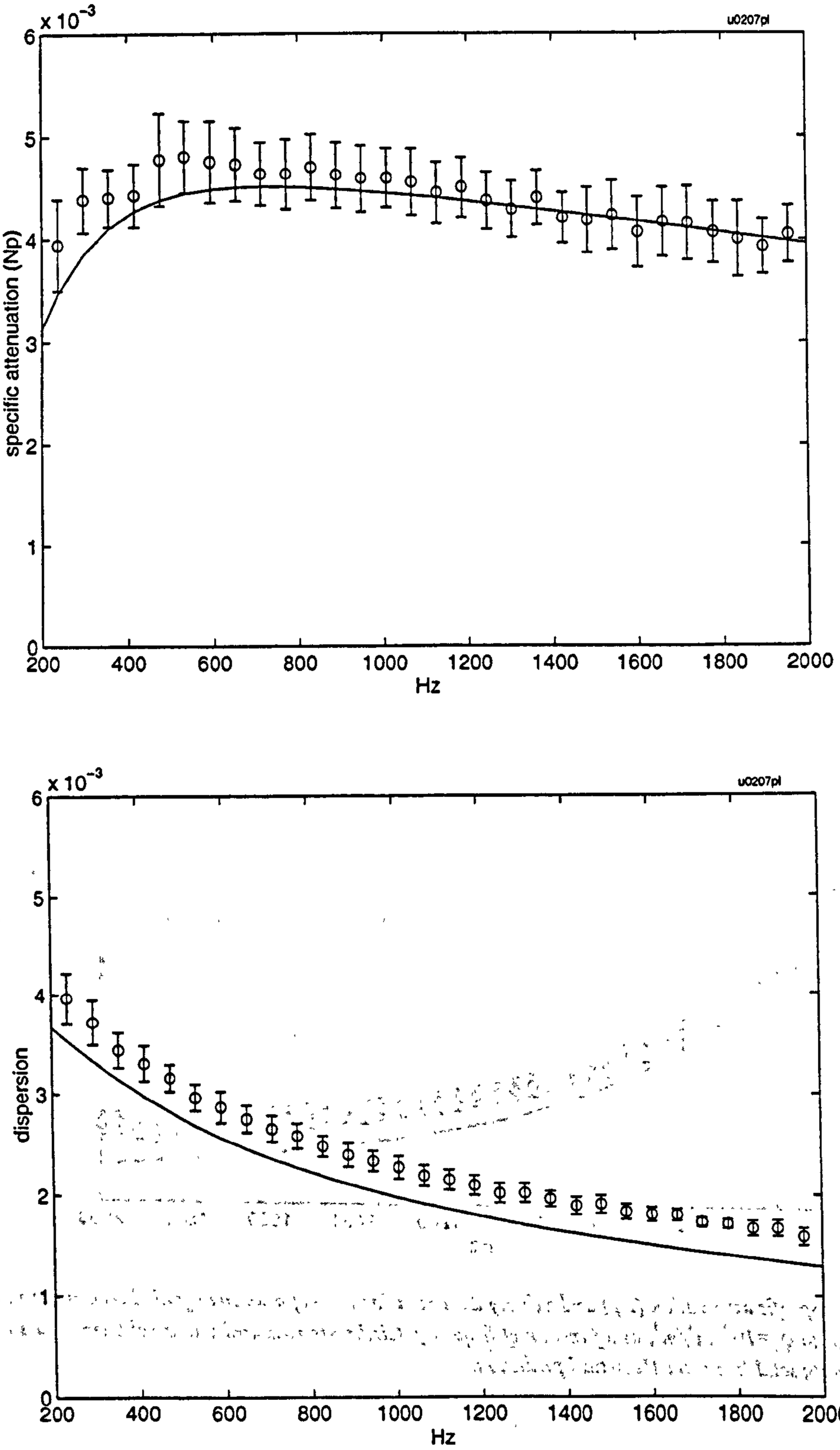

Figure 6-4 Specific attenuation and velocity dispersion of alumina (grade F1000, mean radius 2.0μm) normalised to $\phi_v = 10^{-6}$ m^3/m^3, as a function of frequency. Circles are measured values (mean of three datasets); solid line is the theoretical prediction; error bars indicate ± 1 standard deviation.

Alumina grade F1200

This grade has a similar mean size to F1000 grade (1.9μm), but with a greater skew in the PSD towards fine particles. Two measurements were made, and are presented in Figure 6-5.

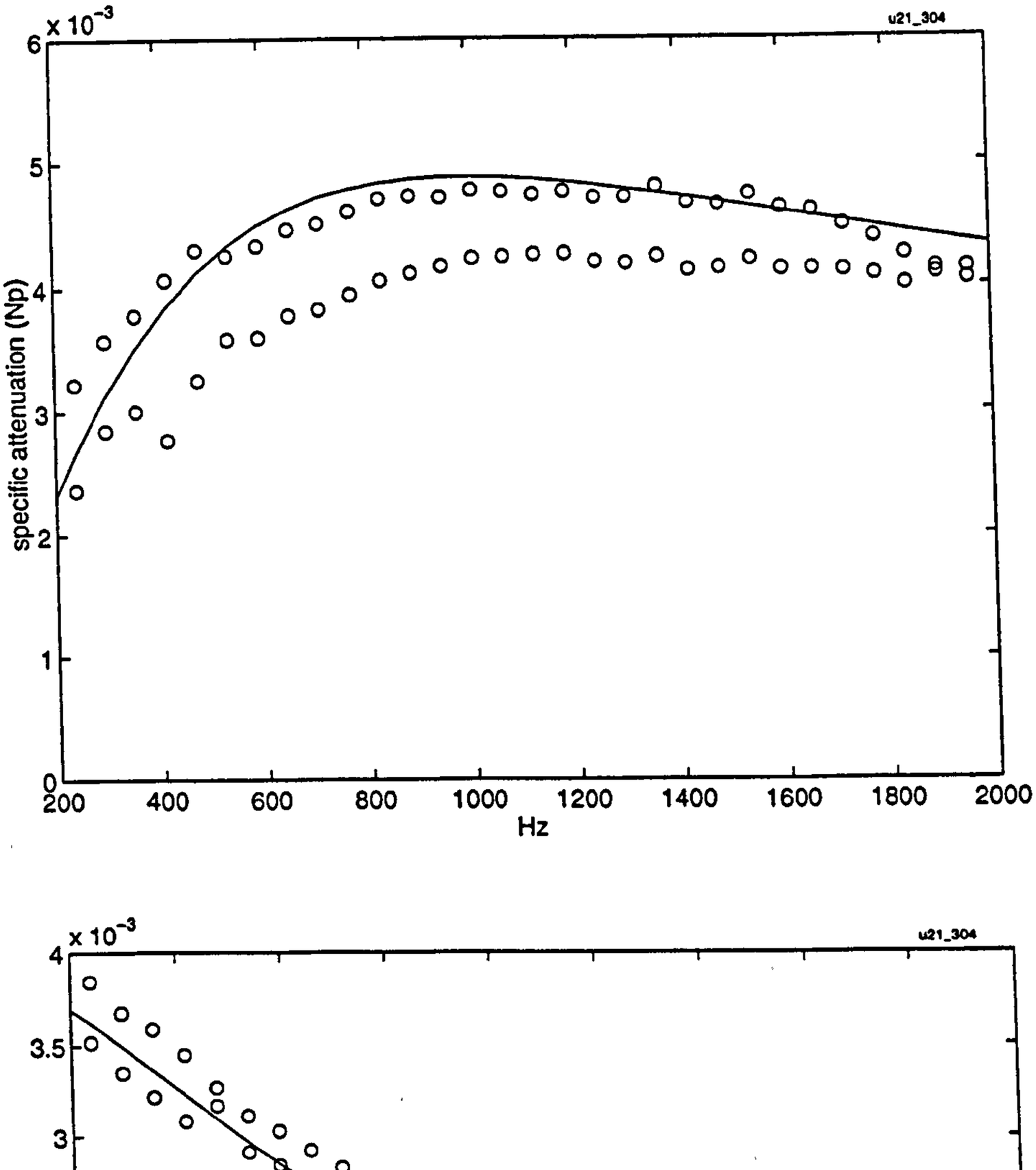

Figure 6-5 Specific attenuation and velocity dispersion of alumina (grade F1200, mean radius 1.9μm) normalised to $\phi_v = 10^{-6}$ m^3/m^3, as a function of frequency. Circles are measured values (two datasets); solid line is the theoretical prediction.

Discussion

We can make the following observations:

- The predicted variations with frequency correspond reasonably closely with the shape and magnitude of the measurements.
- The measured specific attenuation is generally lower, and the dispersion is higher than the predictions. This pattern could not be explained by systematic measurement errors in concentration or PSD.
- There is greater uncertainty in the measurements at low frequency. This could be due to the temporal truncation of the FFT window (12.4 ms, giving a minimum resolvable frequency of 80 Hz); or due to the finite length of the tube that limits the number of low frequency wavelengths (1.2 wavelengths at 200 Hz).
- The predicted peak in the specific attenuation (which marks the transition from the viscous to the inertial regimes) coincides closely with the measured position.

6.2 CLEAN AIR FLOW

Before making acoustic measurements in flowing suspensions, tests were made on clean airflow to check whether the presence of flow would have a significant acoustic effect. Several possible mechanisms were reviewed in Chapter 3: redistribution of the sound pressure field due to mean flow and flow profile; changes in the impedance of the entry and exit orifices; and reduction in the mean coherent field due to turbulent scattering.

Measurements were made initially in the air-only flow rig at the Open University , where greater control and reduced background noise maximise the accuracy of the measurement, and then in the Wolfson rig to check the results under realistic conditions.

6.2.1 OU Rig

Measurement method

Two excitation signals were used in two different experiments: single-tone bursts (2.5 ms gate length) and MLS excitation. Short duration signals were used so that the reflections from the end of the tube could be edited out in the time domain.

The signals were transmitted by the Fane driver (connected to a short threaded tube) through port D (see Figure 5.3) into the upstream portion of the fully developed flow. Due to the possible variation of orifice impedance with flow, the input sound power could not be assumed constant with flow, so two microphones (reference and receiver) recorded the resulting sound pressures at ports A and B respectively; they were mounted flush with the inside of the tube and separated by 1.3m. The air velocity at the tube axis was measured by a hot-wire anemometer mounted in port C.

The received acoustic waveforms were averaged synchronously (64 averages[1]) in the time domain to remove the large uncorrelated noise components due to flow-induced noise, and turbulent pressure fluctuations. Hence, the synchronously-averaged sound pressure approximated to the mean coherent sound field, defined in equation (3.18).

The experiment was performed in the plane wave frequency region, (at two frequencies 2500Hz and 3500Hz), so that changes in transverse modal shapes due to flow would not alter the measured insertion loss.

The transfer function, H, between the microphones was calculated with and without air flow, using two techniques: by calculating the D.F.T. of the received waveform, evaluated at the single frequency of transmission; and by calculating the envelope of the signal (using a Hilbert transform) and finding the maximum amplitude value. Both methods gave comparable results: the results from the envelope analysis are presented.

The insertion loss was calculated as the change in transfer function magnitude:

$$IL = 20\log_{10}\left(\frac{|H_{flow}|}{|H_{no\ flow}|}\right) \text{ dB} \tag{6.3}$$

Results

At a mean air speed of 29 m/s, the insertion loss was not measurable above experimental error, and was less than 0.5dB (see Figure 6-6). Amplitude drift in the equipment could have been responsible for the measured changes.

[1] The comparatively small number of averages, compared to measurements with pure impulses, reflects the noise rejection capabilites of MLSSA, and the high SNR of the measurement.

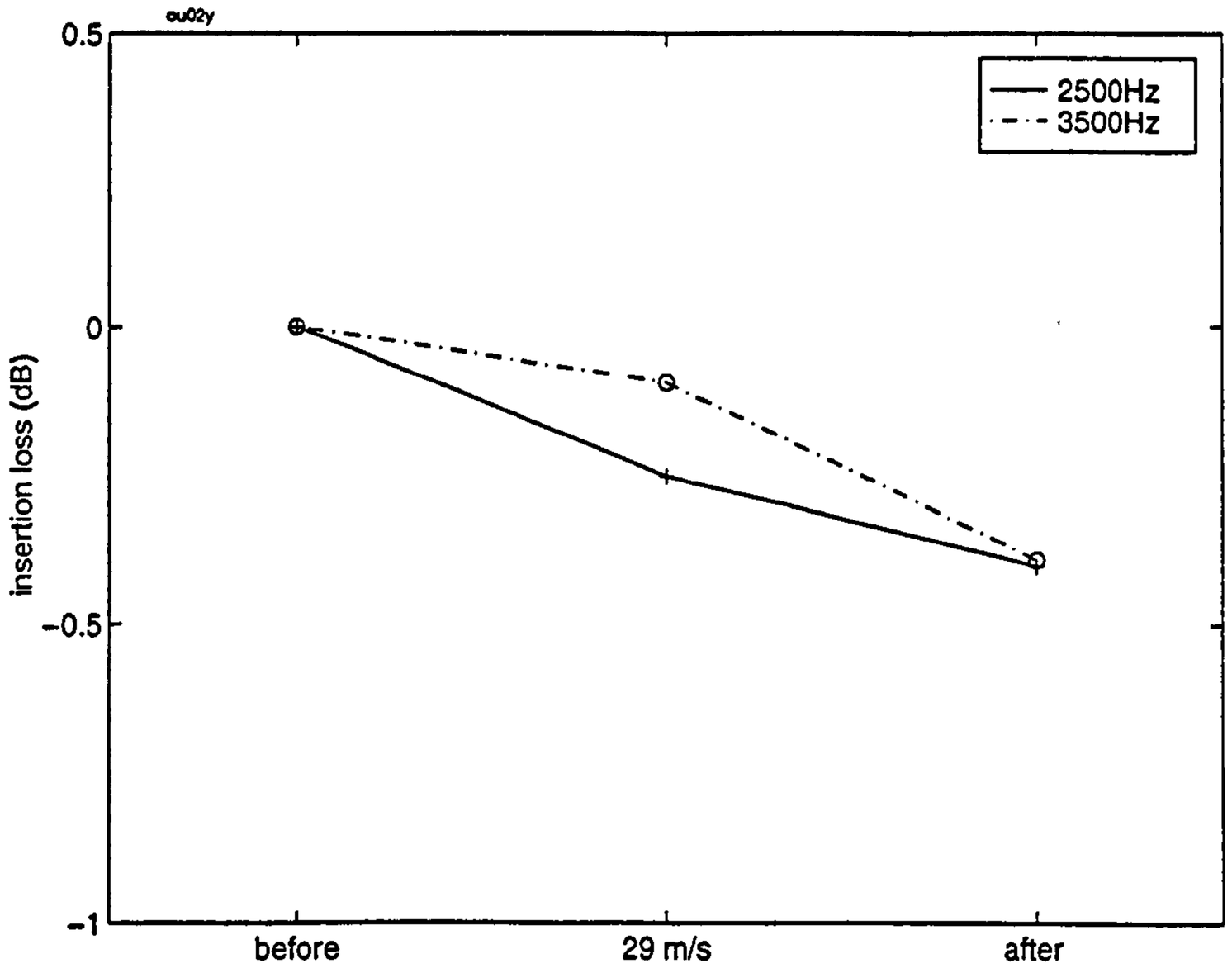

Figure 6-6 Insertion loss for tone bursts along 1.3m path, before, during and after airflow at 29m/s; referenced to value before flow.

The level of the reference signal (Figure 6-7) reduced very slightly (<0.5dB) with airflow; this small change suggests that the power radiated into the pipe is almost constant with flow velocity over the range considered, and that changes of the orifice impedance are not significant. This result is used to justify the use of a single receiving microphone in section 6.2.2.

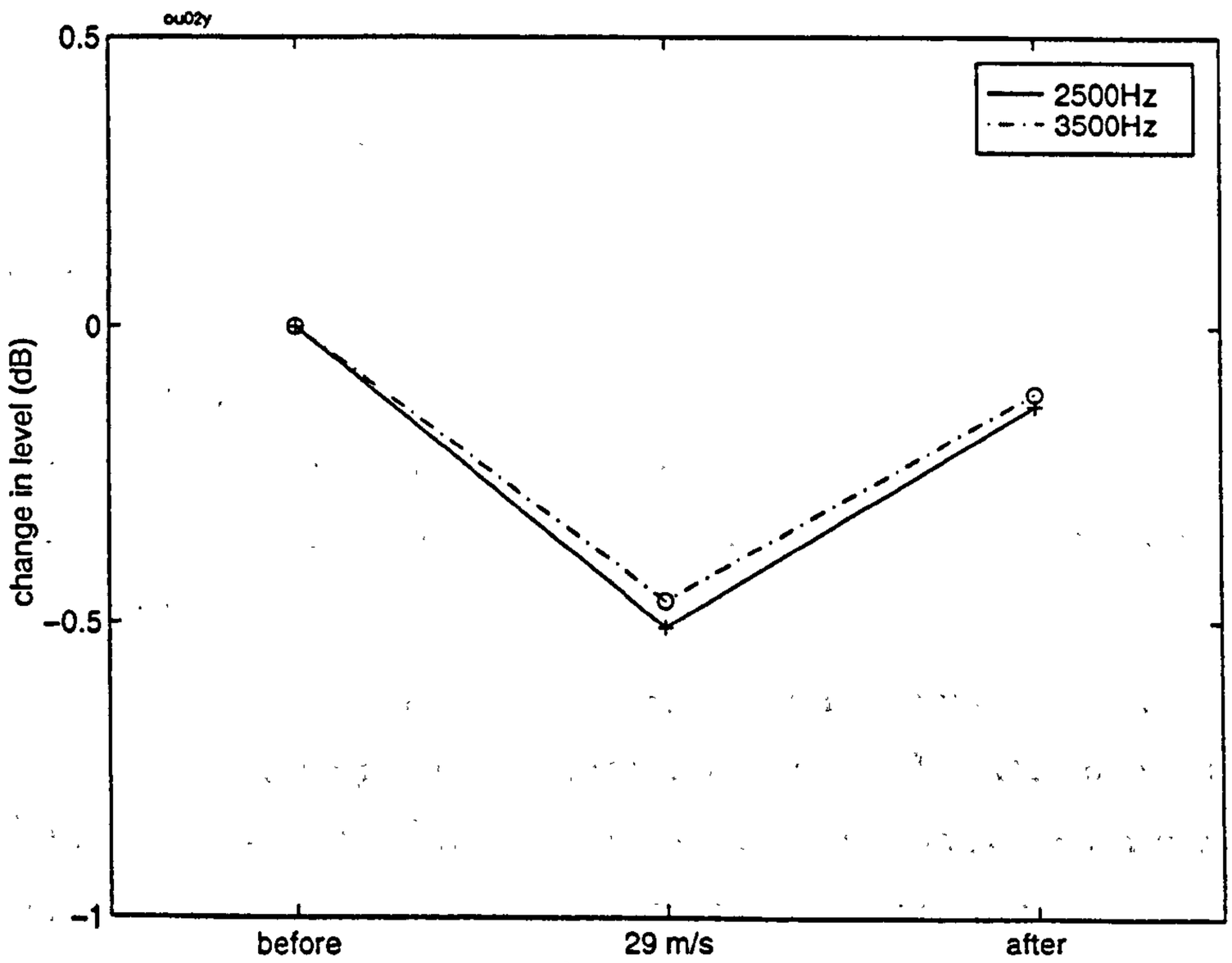

Figure 6-7 Change in reference SPL of tone bursts at 2.5 & 3.5kHz, before, during and after airflow at 29m/s; referenced to value before flow.

Wideband measurements were made also made with MLS excitation, by switching between the two microphones (as MLSSA is a single channel device). These measurements (Figure 6-8) show an insertion loss that decreases with frequency, and remains less than 1 dB over the most of the measured frequency and velocity range.

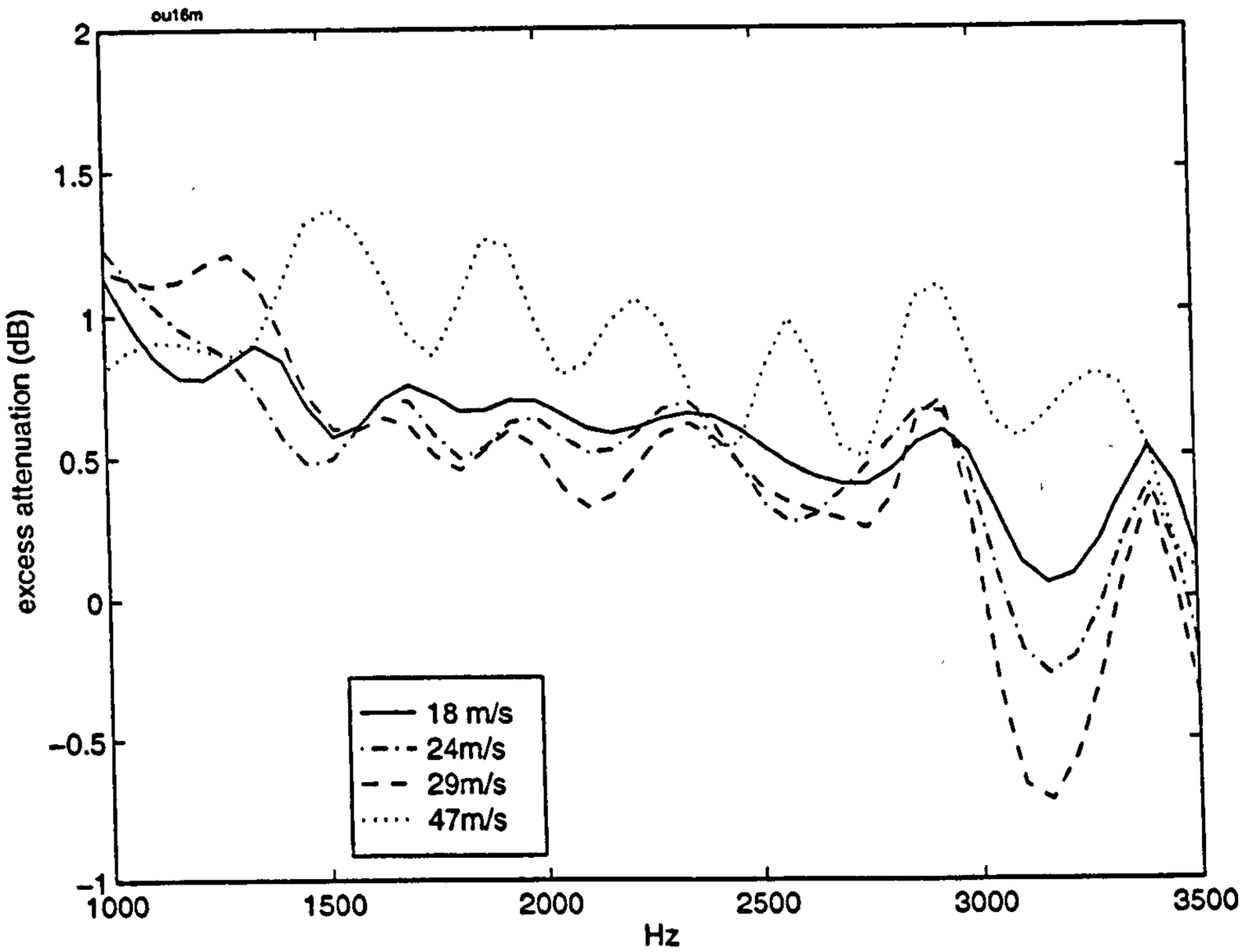

Figure 6-8 *Insertion loss over 1.3 m path due to airflow at varying speeds.*

6.2.2 Wolfson rig

Measurement Method

The experiment was repeated on the Wolfson rig. The main differences were that both the microphone and driver were contained in their respective probes[1], and that a single microphone was used, since the assumption was made (confirmed by the twin-microphone experiments) that the sound power level radiated into the pipe is independent of air-flow under these experimental conditions.

MLSSA was used to find the impulse response along the path length. The apparatus is shown in Figure 6-9.

[1] The driver probe at this stage had not had a modification to allow static pressure equalisation. This led to a peak in the response at 900Hz when it was subjected to an overpressure. Therefore, the SNR for these measurements is worse than for measurements after the modification.

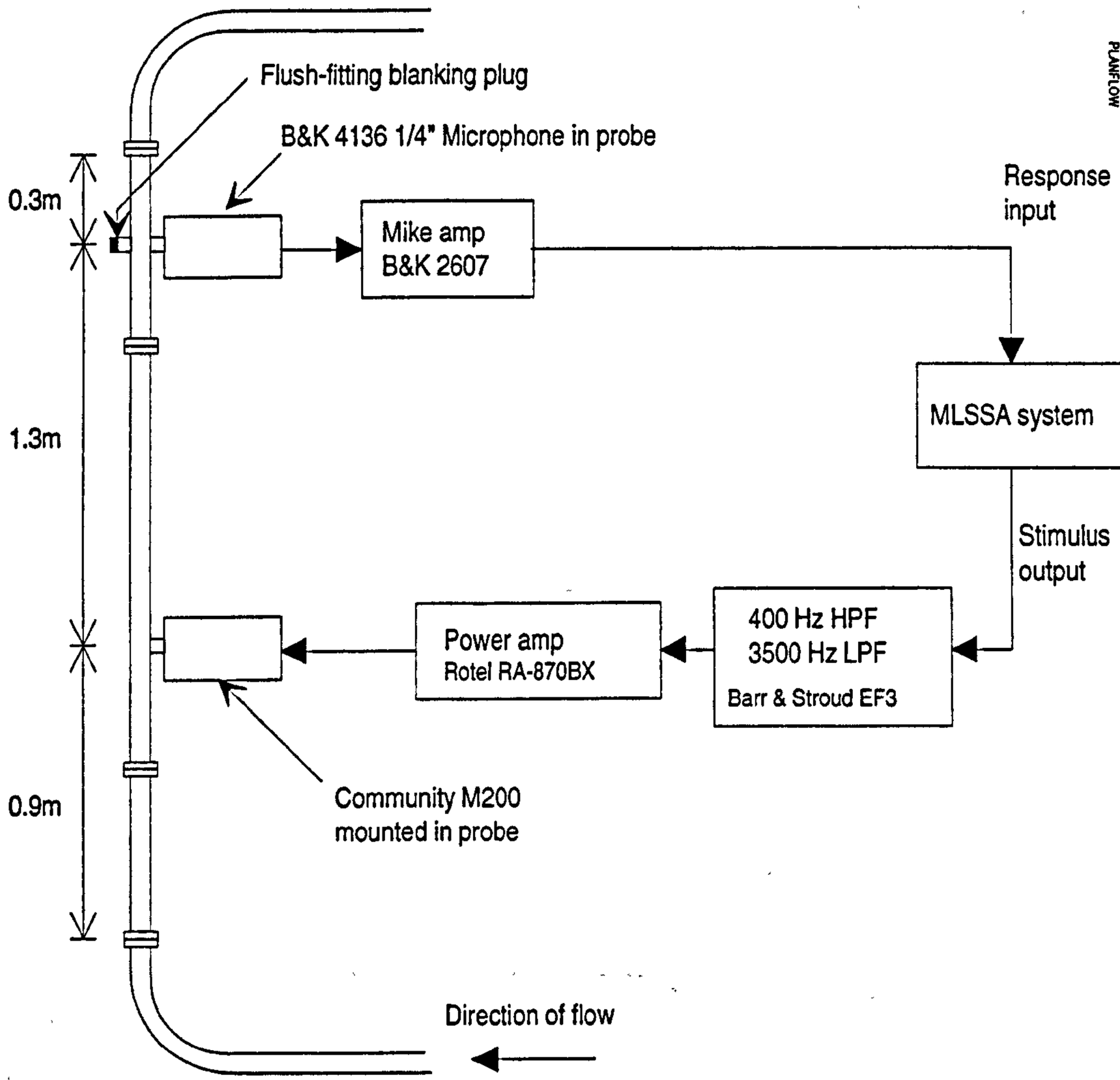

Figure 6-9 *Apparatus to measure the plane wave attenuation of air- and suspension flow.*

Results

The impulse response was measured for air speeds up to 40m/s. The results are plotted in Figure 6-10.

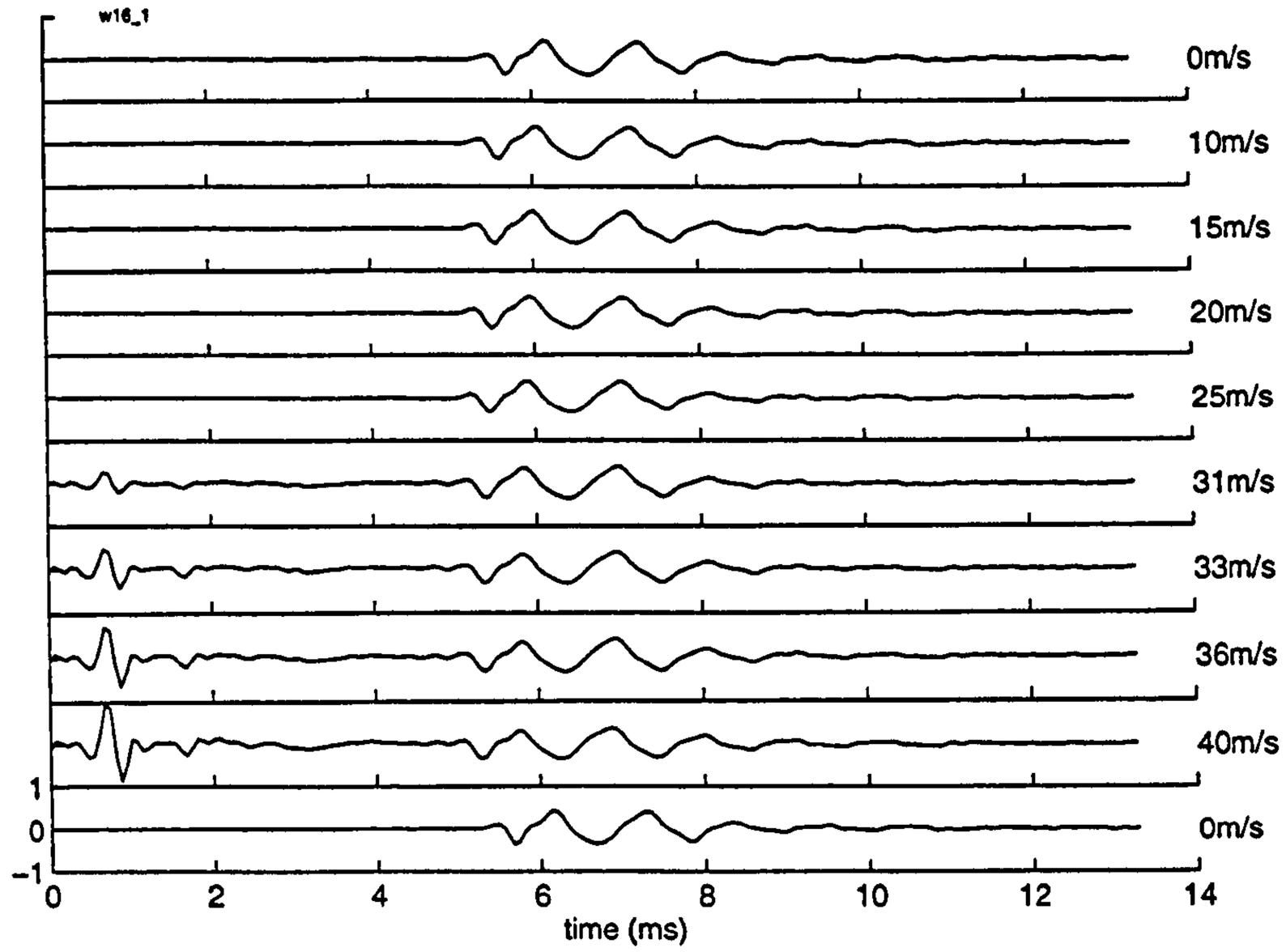

Figure 6-10 *Impulse response in air-only flow, for varying air speeds*

The most striking feature is the sudden appearance of a very high velocity wave (approximately 5000m/s) above an air speed of 30m/s, and disappearing when flow ceases.

The clear dependence on flow speed would tend to rule out it being a fixed-pattern non-linearity [122] or a bulk solid wave, being transmitted via a flanking path into the microphone body. One hypothesis is that it is a surface wave travelling along the tube wall/air boundary, and being recoupled into an acoustic compressional wave at the mike probe mouth. Surface waves are excited when source and receiver are close to the surface, as in this case. They are also encouraged by surface roughness (leading to a complex admittance) [13, 117] — possibly supplied by the welded seam that runs longitudinally along the inside wall. The speed would be approx. 90% of the speed of the slowest speed in the solid, again matching the observations. The abruptness of onset could be explained by a change in air flow regime that changes the flow gradient. This could, in turn, change the acoustic refraction towards the wall and might therefore increase the coupling into the surface wave, and/or increase the coupling from the surface wave back into an acoustic compressional wave in the probe tube.

The most important observation for this study is that it is well-separated from the plane wave pulse, and so, in later measurements, was excluded by the FFT window. A further concern was whether significant energy was being coupled from the plane wave into this spurious wave. The total energy in each was measured, and plotted in Figure 6-11 as a function of flow velocity.

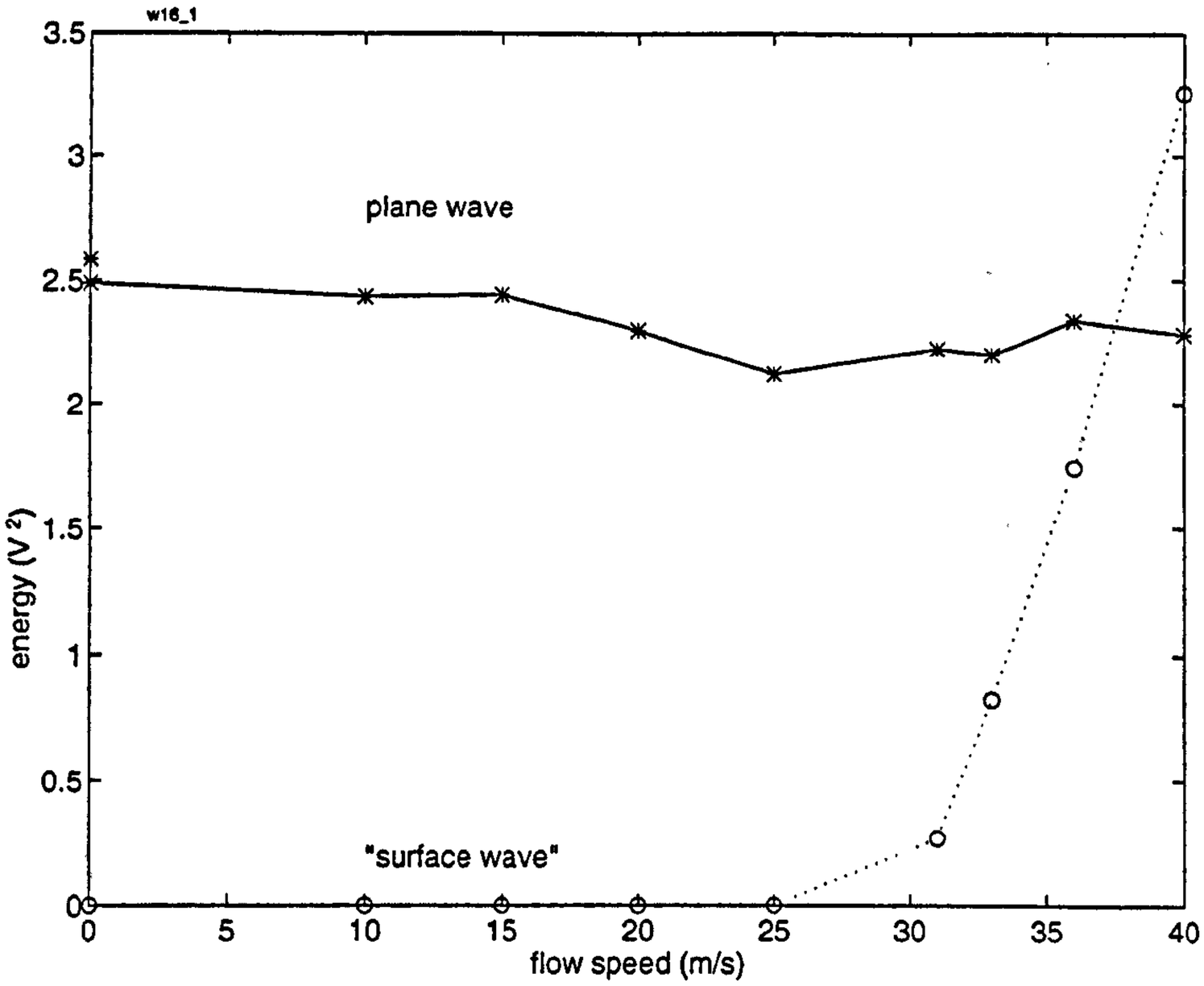

Figure 6-11 Energy in the plane wave, and the inferred "surface wave" as a function of flow speed, in clean air flow.

The dramatic onset of the "surface wave" is clear, even becoming more energetic than the plane wave at 40m/s. However, the energy of the plane wave decreased by only 8% over the range (-0.36dB), and was not considered significant.

The variation with frequency was also tested. The spectrum of the plane wave pulse was calculated from the windowed impulse response, and referenced to the spectrum for no flow, producing a value of insertion loss due to flow, shown in Figure 6-12

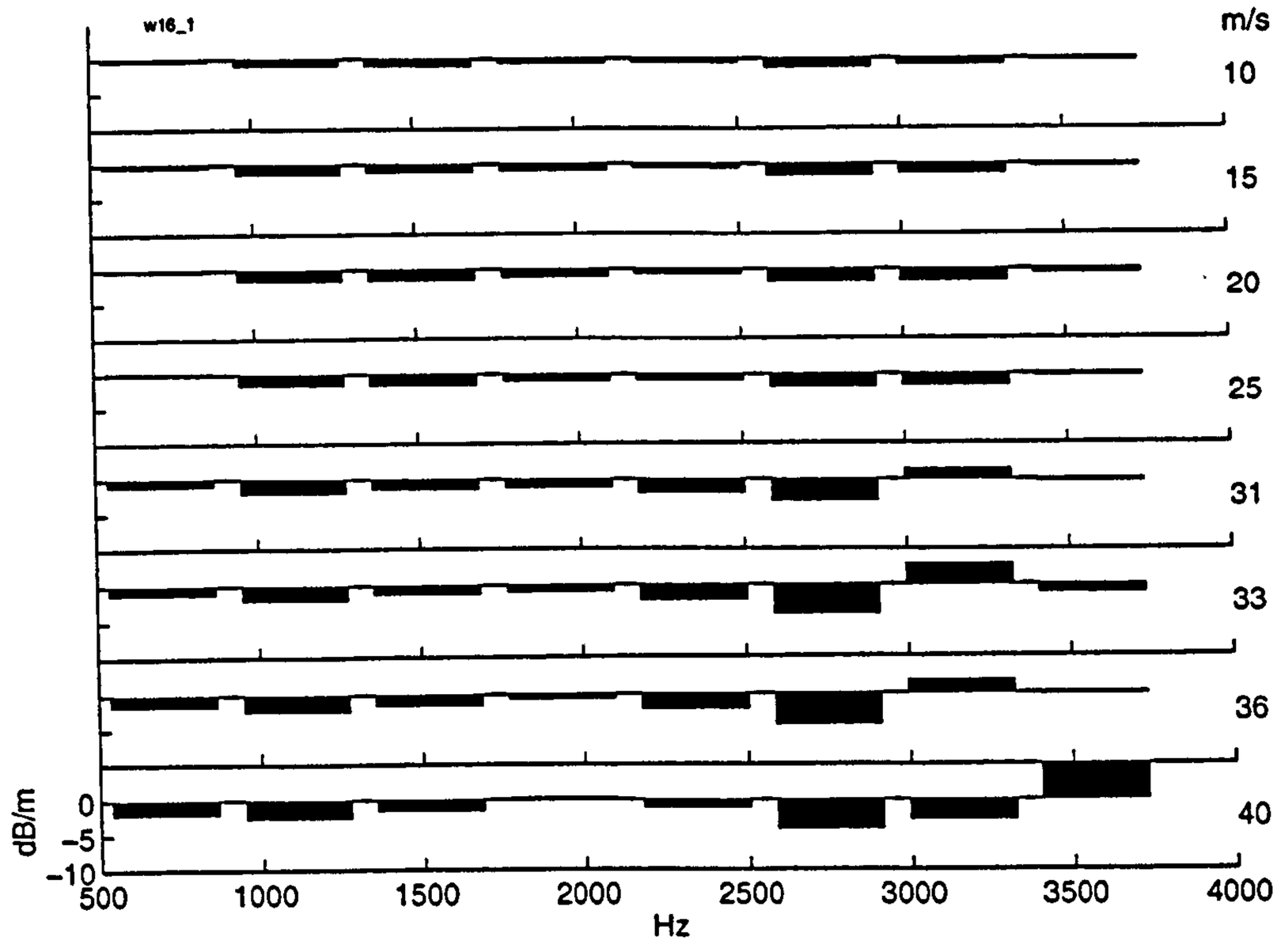

Figure 6-12 Insertion loss of plane waves due to air flow, for varying flow speeds; the frequency axis shows the complex mean of 7 FFT lines for clarity.

Most frequency bands show a negative insertion loss that increases with velocity. This can be expected from the observations of Ingard & Singhal [64] (see section 3.4.3). They found that the presence of mean flow caused a higher SPL upstream than downstream; at $M = 0.1$, the difference in the SPL equidistant up and downstream was approx. 3.5 dB. A quantitative comparison is not possible due to the different experimental configurations, but the magnitude of the change is similar. However, there is significant variation in both magnitude and trends between different frequency bands; the explanation is not clear.

The most important observation is that at 20m/s — the speed used for tests on suspensions — the magnitude of the insertion loss remains below -1.8dB. This suggests that turbulent losses are not significant for measurements made in the plane wave regime, and that the other mechanisms have only a small effect. Plane wave measurements on suspensions were measured at constant flow velocity, and referred to the values with clean airflow, and so changes in these mechanisms are expected to be small.

6.2.3 Conclusions

No insertion loss due to turbulence has been detected; in fact, an apparent gain in transfer function magnitude occurs as a result of flow (for downstream sound propagation). At speeds of 20m/s, the effect of flow will amount to less than 2dB in the plane wave region of this apparatus (<4000Hz).

There is no significant flow-induced change in signal power radiated into the pipe; hence the orifice impedance of the driving probe is deduced to remain constant within the measuring range.

A wave of very high velocity is detectable for air-speeds of above 25m/s. Since its amplitude appears to be related to flow speed, there is a remote possibility that it may be used to measure flow speed; more investigation is needed.

6.3 FLOWING SUSPENSIONS

Since it was found that a single microphone can be used to measure the insertion loss due to flow over a fixed pathlength, this same technique was used for flowing suspensions, and is described in section 6.3.1. The results of these experiments suggested that there is some merit in measuring the loss over two path lengths, to deduce the excess attenuation; these experiments are described in section 6.3.2. The effect of varying the air velocity, while keeping concentration constant was investigated in section 6.3.3.

Measurements of dispersion are not presented in this section, because they are so sensitive to air flow that the scatter is too great to be useful.

In section 6.1, the frequency range spanned the transition from the viscous to the inertial regimes, and so the specific attenuation was presented to illustrate the transition, which was marked by a maximum. In the following section, the particle size and frequency are higher, and so measurements occur in the inertial regime. Therefore, the attenuation coefficient will be presented instead of specific attenuation.

6.3.1 Single path

The apparatus shown in Figure 6-9 was used to measure the impulse response in flowing suspensions. The nominal flow rate was maintained constant at 20 m/s, while the concentration was varied. For each measurement, the plane wave pulse was transformed into the frequency domain, and the spectrum — after normalisation by the clean-airflow spectrum — was averaged for several minutes[1] so that a good non-acoustic estimation of concentration was achieved. Hence, the time average of insertion loss was compared with the time average of mass concentration over the same time duration.

Flour

Flour (mean diameter 27.3 μm) was the first material used[2]. Frequency spectra of the measured insertion loss (*I.L.*) are shown in Figure 6-13. There is a clear trend of increasing loss for increasing mass concentration, and, superimposed on top of ripples, for increasing frequency. The highest concentration curve appears to be approaching a ceiling to the insertion loss of around 40dB, which is imposed by the limited S.N.R. This dataset was not used in any subsequent curve-fitting.

[1] 20 frequency-domain averages were used, in addition to 3 time-domain pre-averages to improve SNR.
[2] See Appendix F for the physical properties of the flour sample.

In order to assess the function of loss vs. concentration at a given frequency, without undue influence of the frequency ripples, the complex mean of 21 lines was calculated, effectively increasing the line width to 307Hz. The effect of this operation is displayed in Figure 6-14.

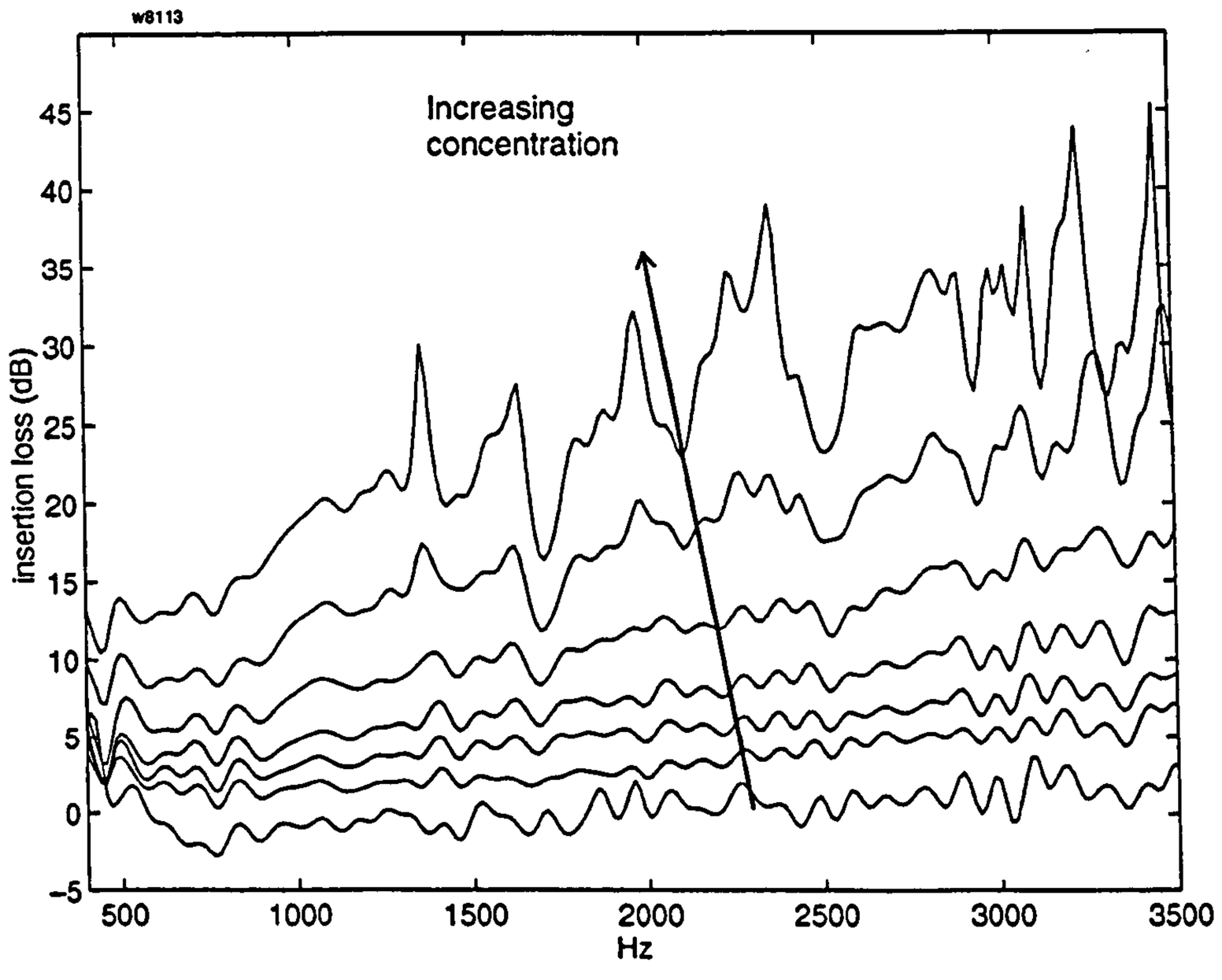

Figure 6-13 *Insertion loss of plane waves in flowing flour, along 1.3m path, with parametrically-varying mass concentration.*

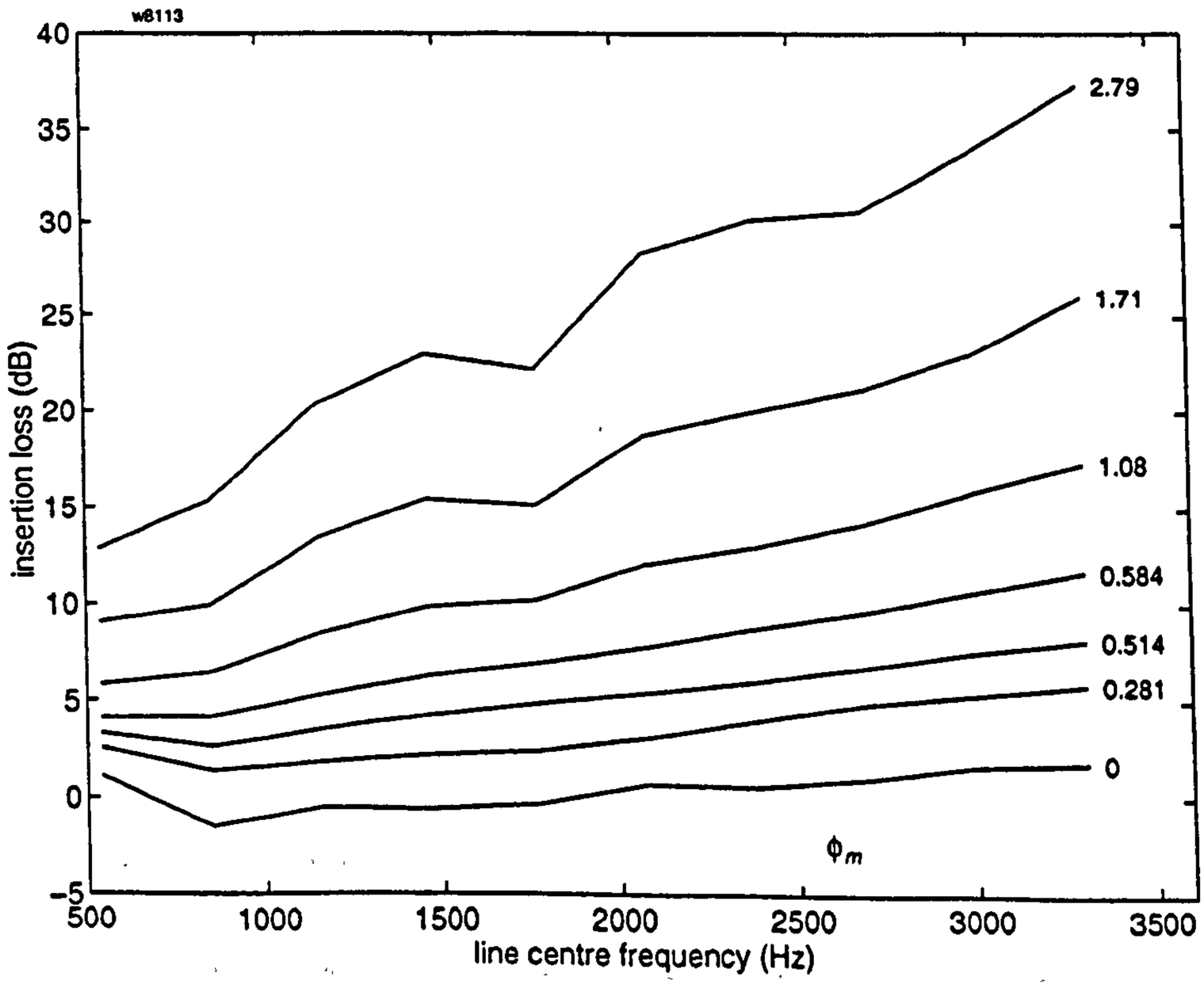

Figure 6-14 *Insertion loss of plane waves in flowing flour vs. complex mean of 21 FFT lines, along 1.3m path, in varying mass concentration.*

To assess the function between the measured insertion loss and mass flow rate at each frequency line, a series of example plots is shown in Figure 6-15. It can be seen that, except for the highest concentration point, the values lie on a good straight line, as exhibited by the correlation coefficients (all are >0.99). It is noticeable that the pattern of measured points is consistent throughout all frequencies, suggesting that the scatter is due to the directly-measured mass-flow rate.

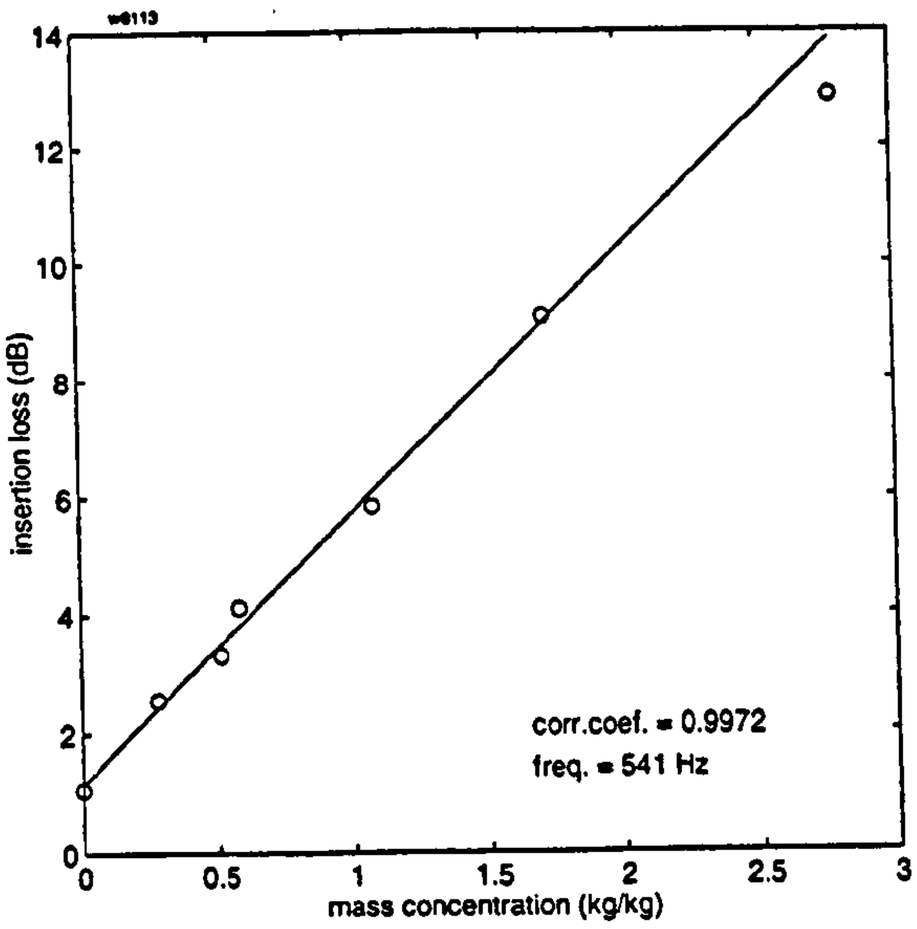

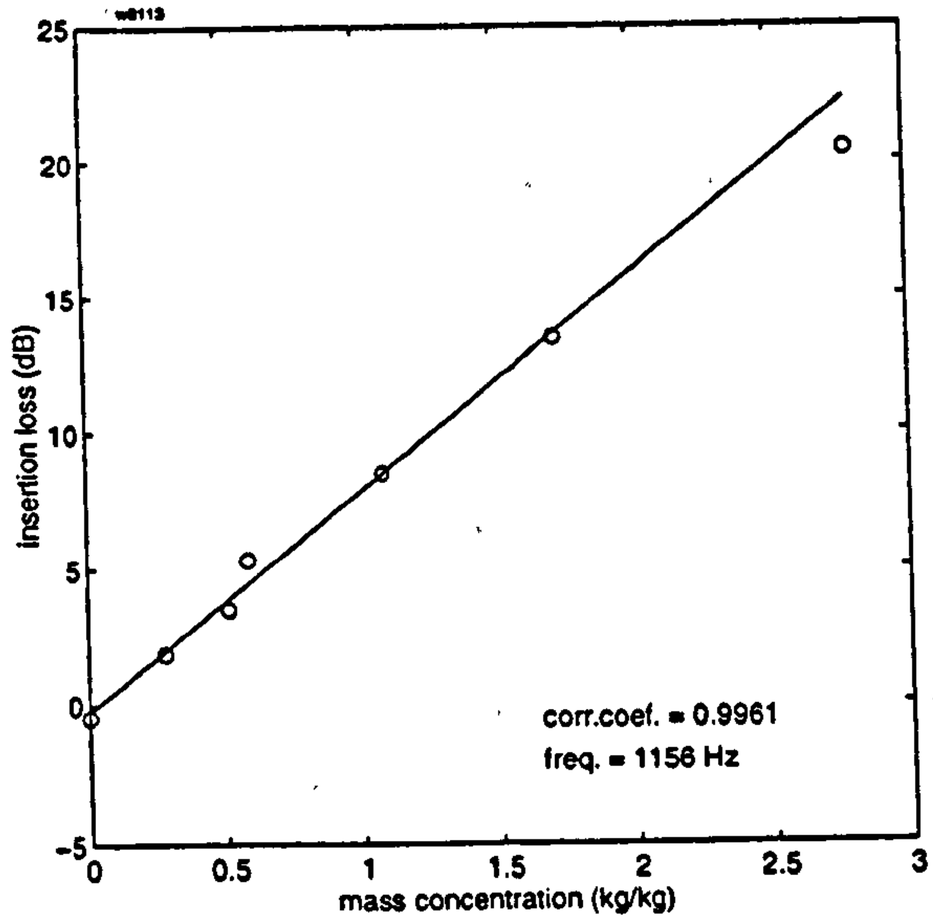

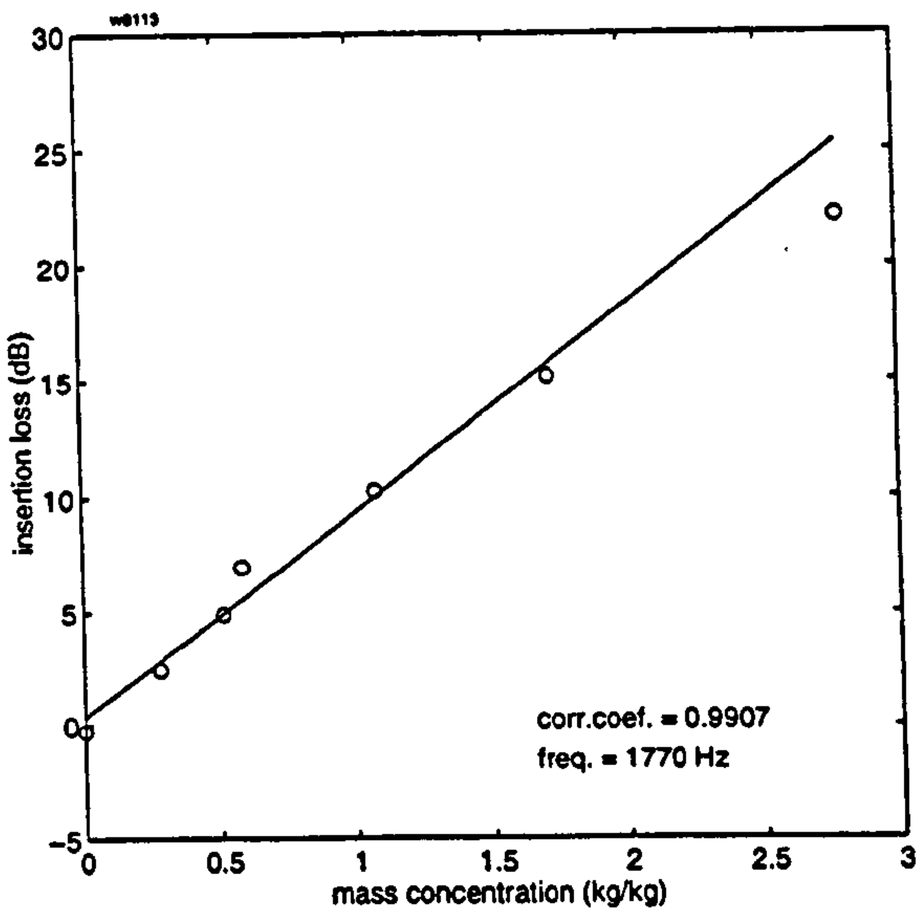

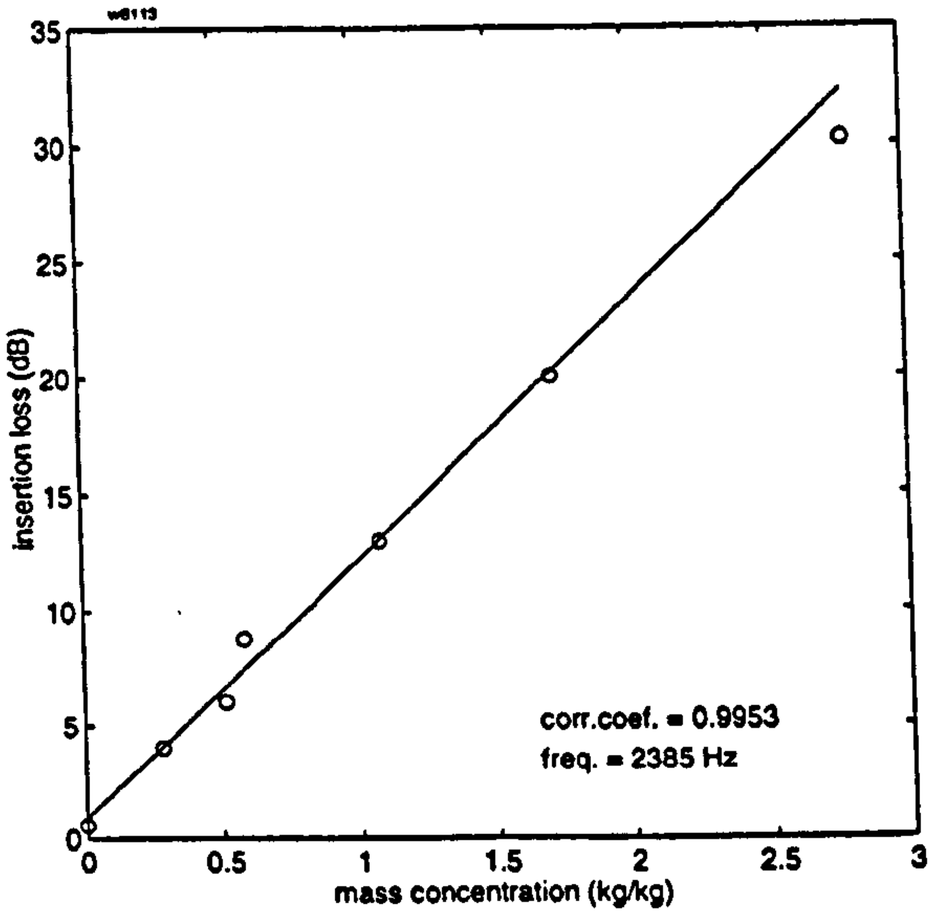

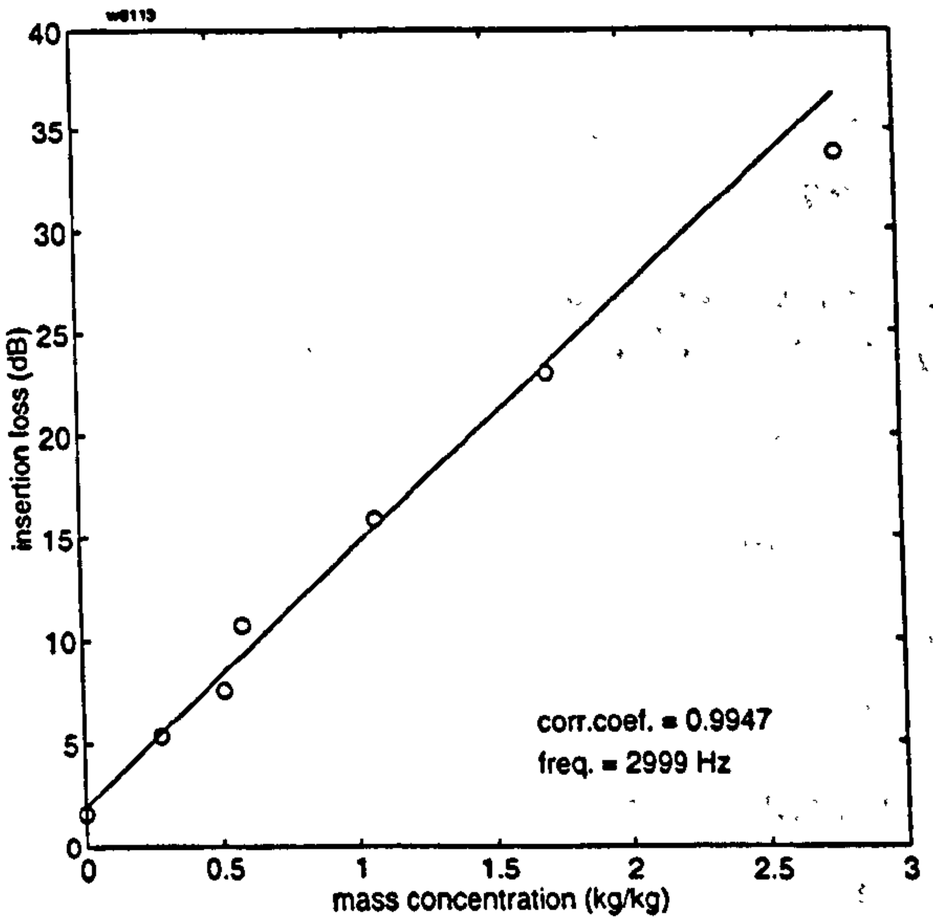

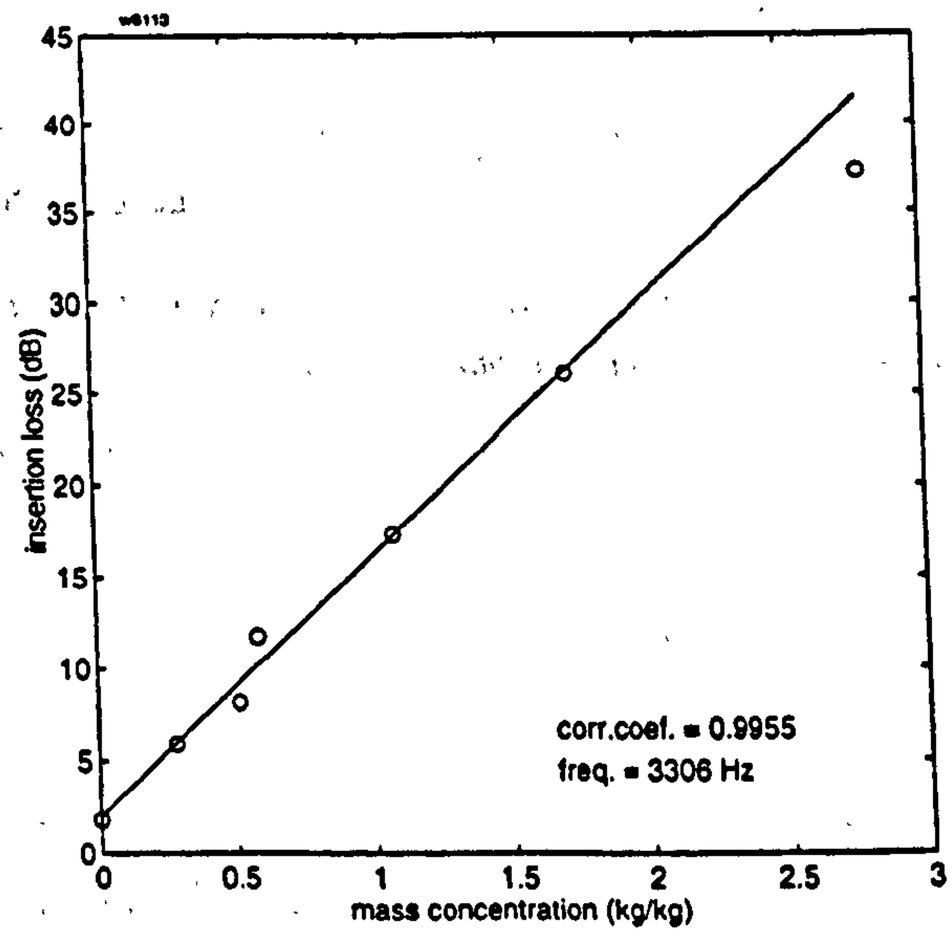

Figure 6-15 *Example plots of insertion loss vs. flour mass concentration, for various frequencies, with lines of best fit (not including the highest concentration point)*

We can compare these graphs with another dataset in which instantaneous attenuation measurements were plotted against locally-approximated ("instantaneous") mass concentration (as discussed in section 5.6). Figure 6-16 shows this data, which exhibited a better SNR that in Figure 6-15 [1], and so the measurements could be gathered up to the higher concentration of 4.5 kg/kg. The purpose of this plot is to show that the linearity appears to continue up to the higher concentration. The points are more scattered than time averaged readings due to the inherently less accurate non-acoustic measurement of mass concentration, and the difficulty of measuring the mass concentration at the instant of making the acoustic measurement. The greater scatter at higher concentrations is probably due to more pronounced fluctuations in the gain-in-weight trace as mass concentration is increased.

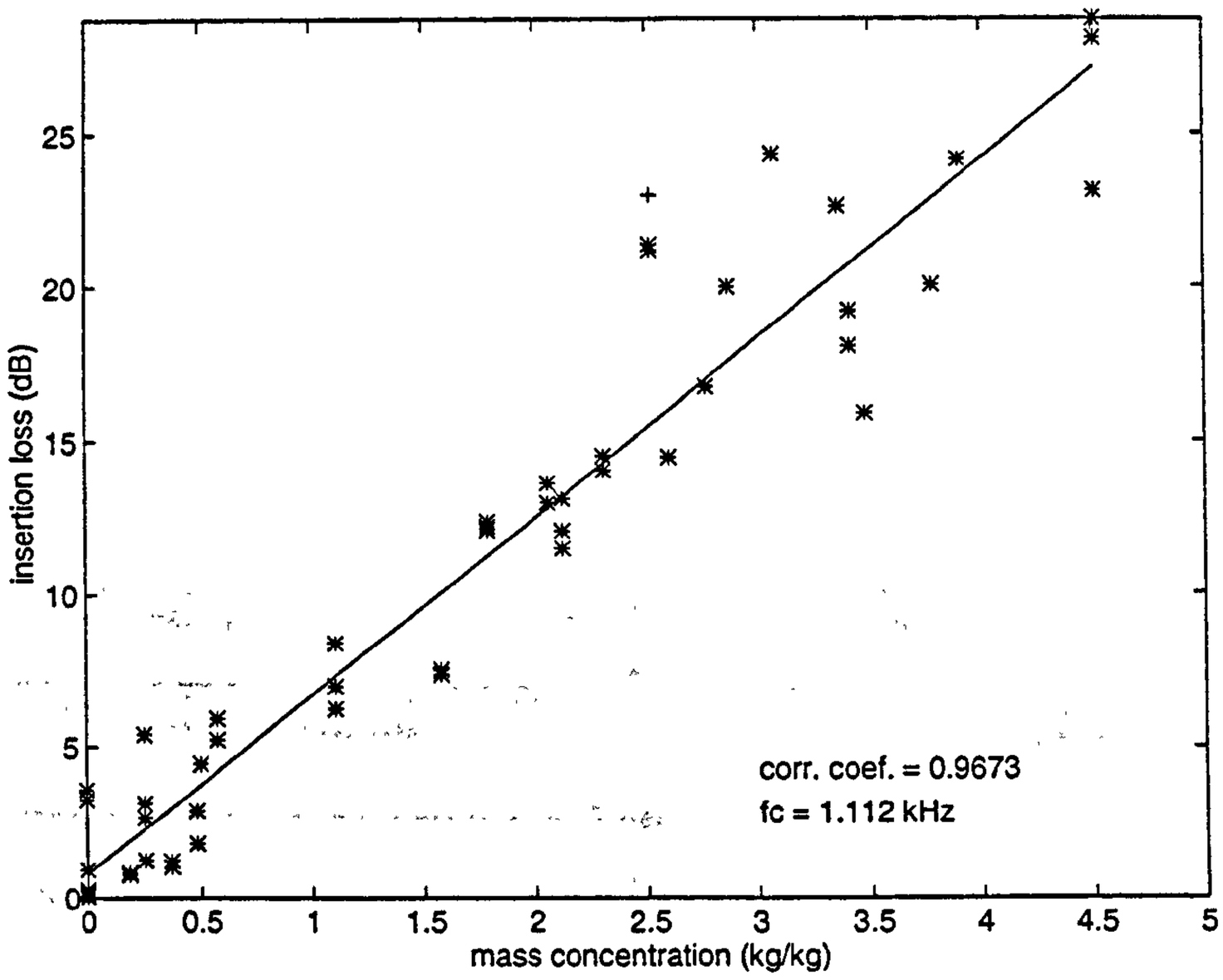

Figure 6-16 Measured insertion loss in flowing flour in the frequency range 910 - 1320 Hz; instantaneous measurements vs. instantaneous mass concentration. + is unfitted point (> 3 standard deviations from trend).

[1] The background noise in the rig was lower on this occasion. Also, the static pressure equalisation port had not been incorporated into the loudspeaker probe: the overpressure on the cone gave a more "peaky" response, which improved SNR at the frequency range shown, but reduced it at other frequencies.

Returning to the time-averaged data presented in Figure 6-13 to Figure 6-15, we can now calculate the attenuation coefficient, α, for each frequency point:

$$\alpha = \frac{IL}{20 \log_{10} e \cdot l}, \tag{6.4}$$

where l is the path length.

The normalised attenuation coefficient, and the uncertainty in this value, were calculated as described in section 6.1.1, and plotted in Figure 6-17, together with the predicted attenuation coefficient[1]. Also shown are the values of normalised attenuation coefficient that were calculated from the instantaneous measurements; these allow us to compare the repeatability of measurements over a period of time and using different techniques.

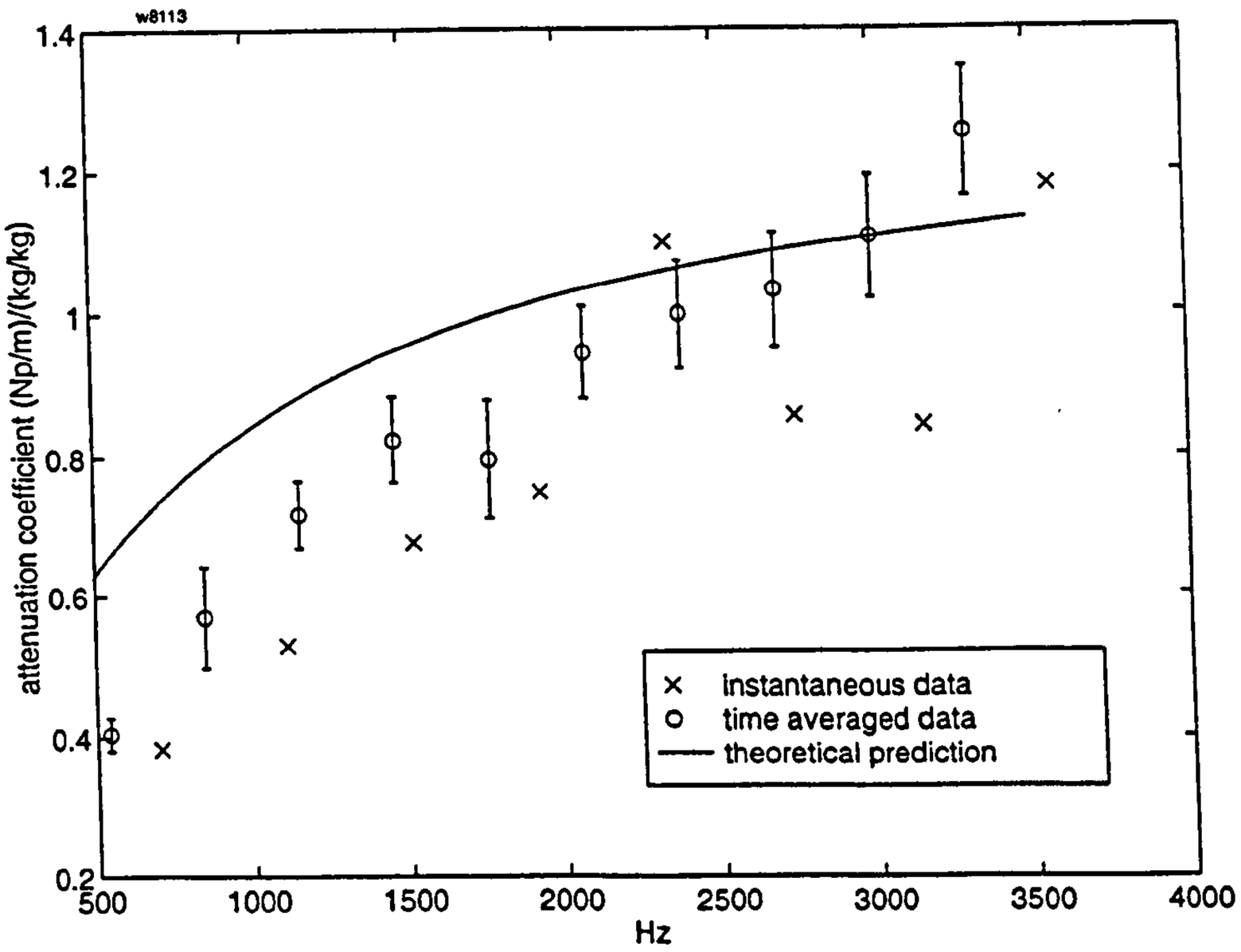

Figure 6-17 Attenuation coefficient per 1kg/kg: in flowing flour; predictions and measured values (using both the time averaged, and instantaneous data). Error bars indicate 90% confidence limits.

The predicted magnitudes agree reasonably well with the measured values. However, they differ in their frequency dependence; the measurements show a near-linear increase with frequency, which is the expected variation for a suspension with a wide PSD [162, 114]. The instantaneous measurements show greater scatter at high frequencies, where the SNR ratio was poor. Generally, they are based on a poorer dataset than the time-averaged data.

[1] The attenuation coefficient is calculated using Lloyd & Berry's theory and the material parameters listed in Appendix F.

Sand

A sample of olivine sand was measured using the same procedure and flow conditions as for flour. The particle size was much larger than that of flour – the mean radius was 278μm. Such a sample is predicted to have negligible attenuation at audio frequency, and it was used to check if any other mechanisms were creating loss or apparent loss.

To maintain reasonable accuracy with the lower insertion losses, a slight change was made in the processing of the data: the FFT line width was increased to 512Hz, by complex averaging of 35 adjacent lines resulting in 6 lines covering the range 400Hz - 3500Hz.

Individual plots of insertion loss against sand mass concentration are shown in Figure 6-18. The small insertion losses lead to greater point scatter, especially at low frequencies, and so the probability that the points are uncorrelated, p, is also shown. This is calculated [112] as:

$$p = erfc\left(|r|\sqrt{\frac{n}{2}}\right) \tag{5}$$

where r is the correlation coefficient of the points.

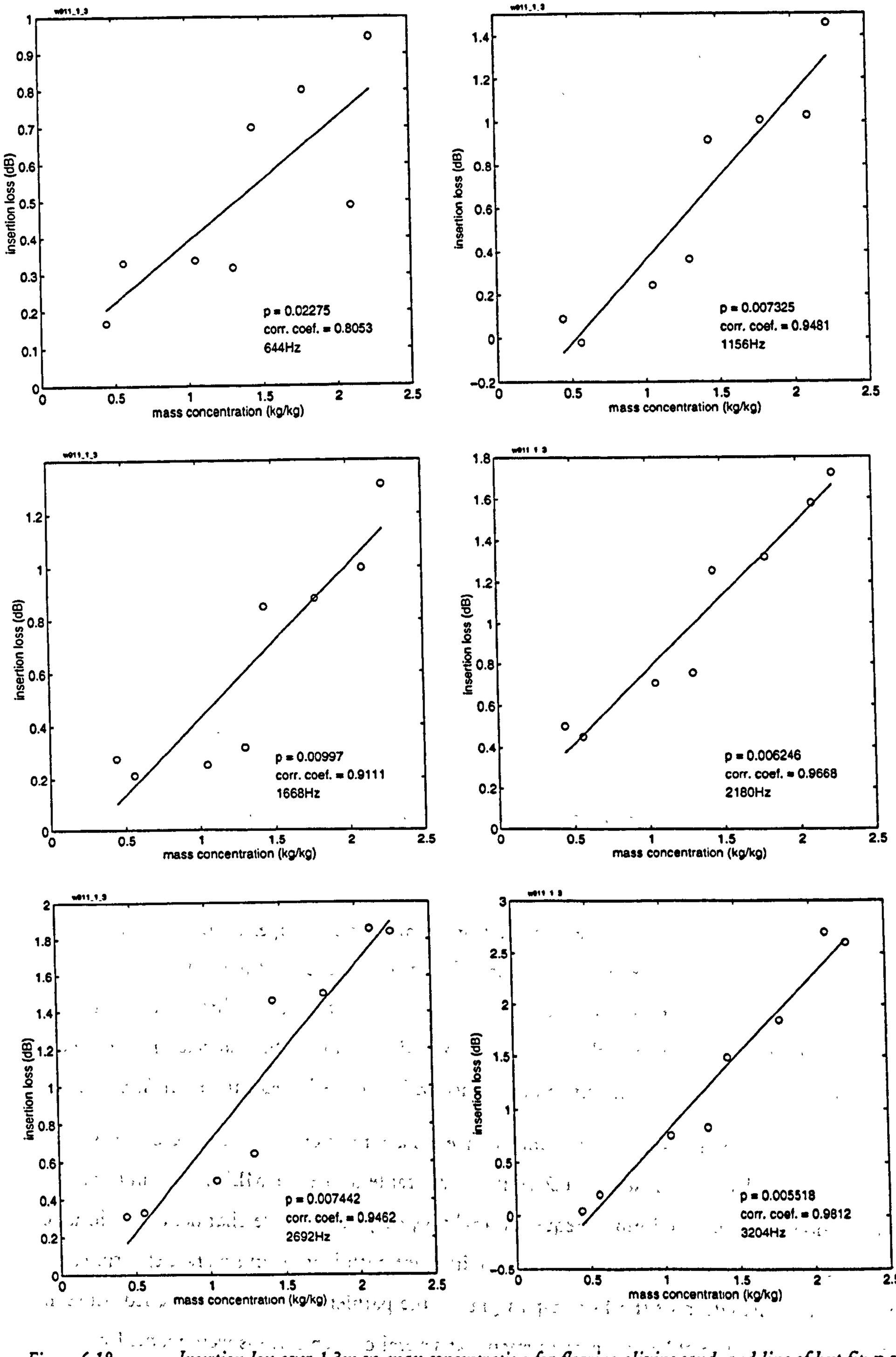

Figure 6-18 Insertion loss over 1.3m vs. mass concentration for flowing olivine sand, and line of best fit; p value shows the probability of the points being uncorrelated.

It can be seen that the measured insertion losses are approximately a factor of 10 lower than for flour, making them more susceptible to errors.

The normalised attenuation coefficient is plotted in Figure 6-19, together with the uncertainty limits, and a curve of predicted α. The measurements are considerably higher than the predictions, and we see once again the trend of measured attenuation coefficient to increase with frequency at a higher rate than is predicted.

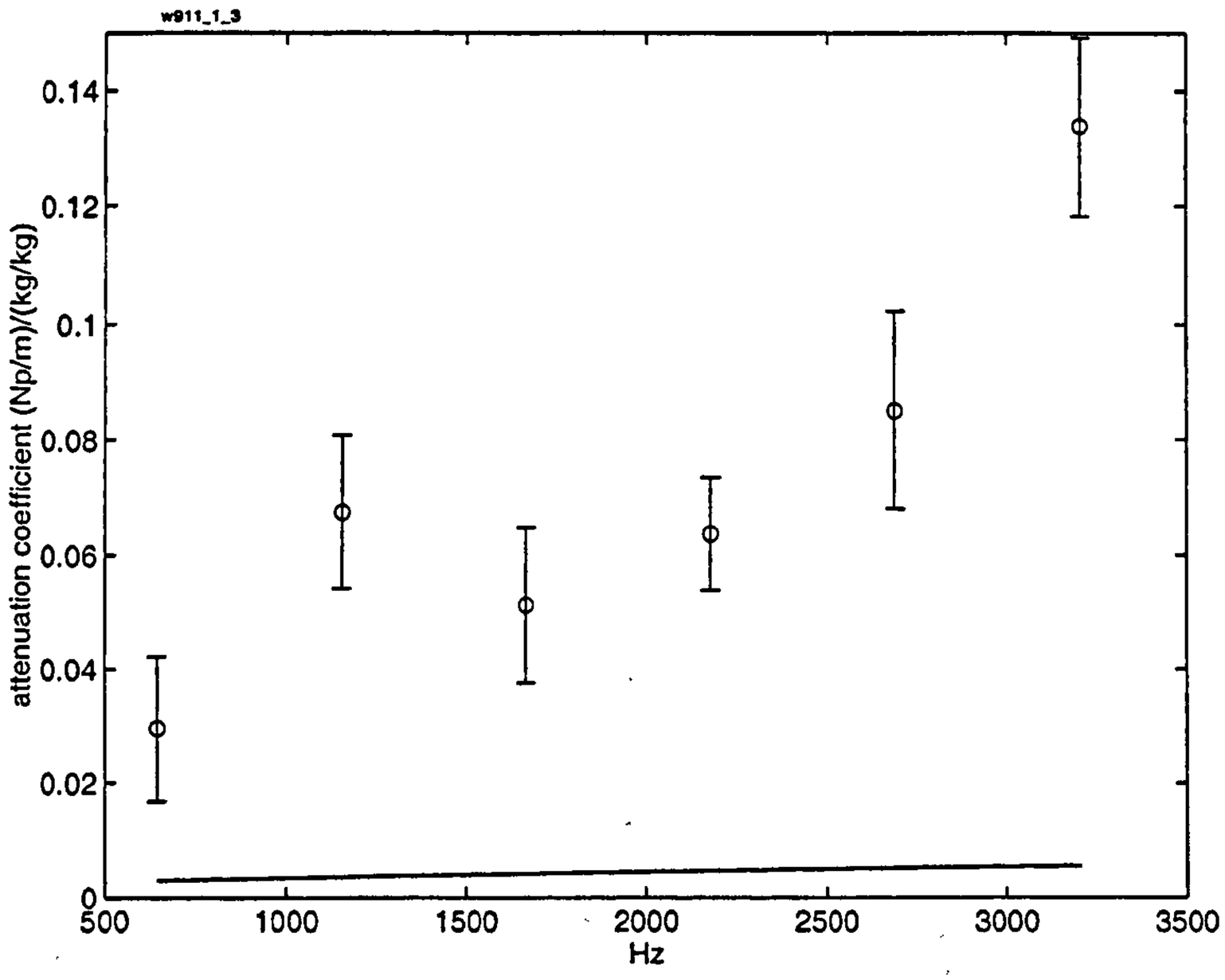

Figure 6-19 Attenuation coefficient per kg/kg of flowing sand; error bars indicate 90% confidence limits.

6.3.2 Double path

A possible explanation for the measured attenuation being so much larger than the predictions, is that the orifice impedance of the probes is being affected by presence of the sand, and hence changing the coupling into and out of the probe tubes. The effect could be direct, due to the varying characteristic impedance of the suspension, or indirect, due to the particles' influence on the boundary layer. The changes in orifice impedance will be investigated further in Appendix A.

To remove the effect of changes in orifice impedance, an arrangement using two receivers would be ideal (similar to that used in section 6.2.1). It was desirable to use the MLSSA system (since it offers good noise rejection and multi-frequency analysis), despite its single channel restriction. So, it was used to measure the insertion loss over two different path lengths in separate experiments. By reversing the orientation of the 1.4m pipe segment, the pathlength could be switched between 1.3m and 0.7m. At each pathlength, measurements at several concentrations were made. By subtracting the insertion loss at 0.7m from that at 1.3m (for each concentration point), the excess attenuation over 0.6m could be calculated.

Although it was not possible to reproduce the same concentration points in both configurations, by fitting a curve through the points measured over 0.7m, the insertion loss at the concentrations measured over 1.3m could be estimated.

When this procedure was applied to measurements using the same sample of olivine sand, the calculated excess attenuation was not reduced, suggesting that there is some real mechanism causing loss as the wave propagates through the pipe.

Barytes

The double path method was used to measure the excess attenuation of barytes (Ba_2SO_4). The sample had a small particle size (mean radius 0.8μm), with the intention that the same sample could also be tested in the static rig. A further attraction of the material is that its crystals are a regular cubic shape, as opposed to the irregular particle shapes tested so far.

However, the surface properties of the particles made them very cohesive, so the suspension consisted of large clumps instead of individually separated particles. Without knowing the size of the clumps, as generated in this particular rig, no comparison with theoretical predictions is possible. The results are presented in Figure 6-20 and Figure 6-21 because they show an interesting pattern.

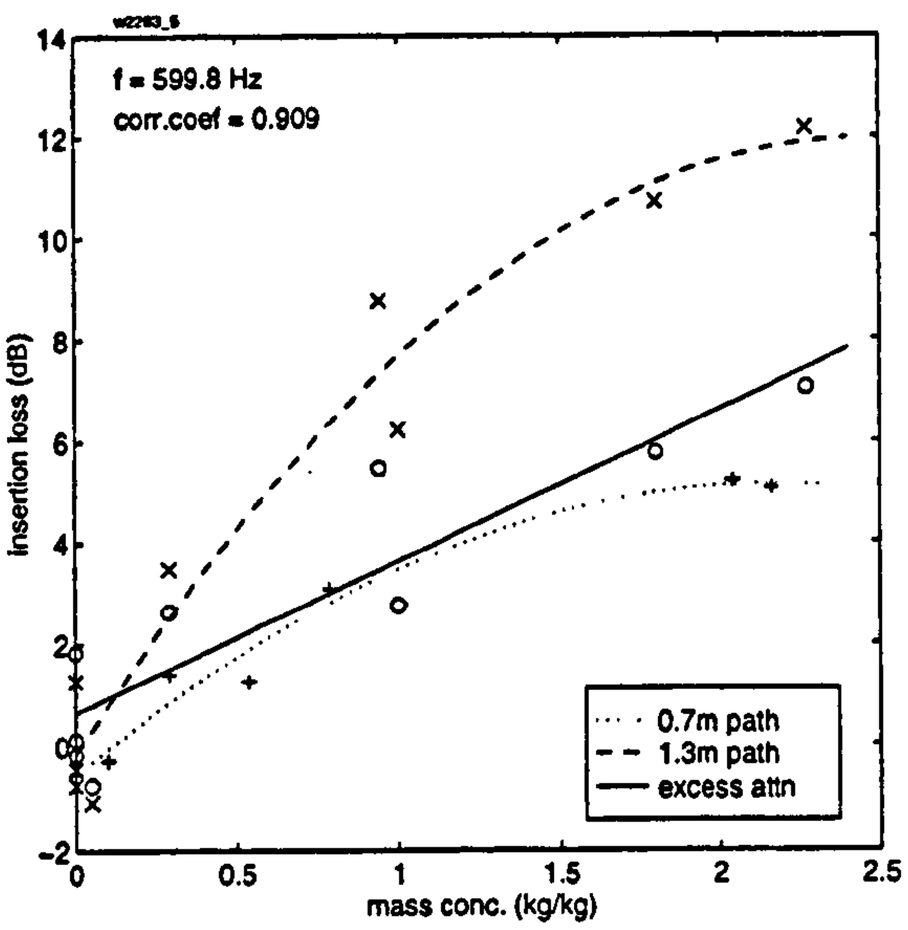

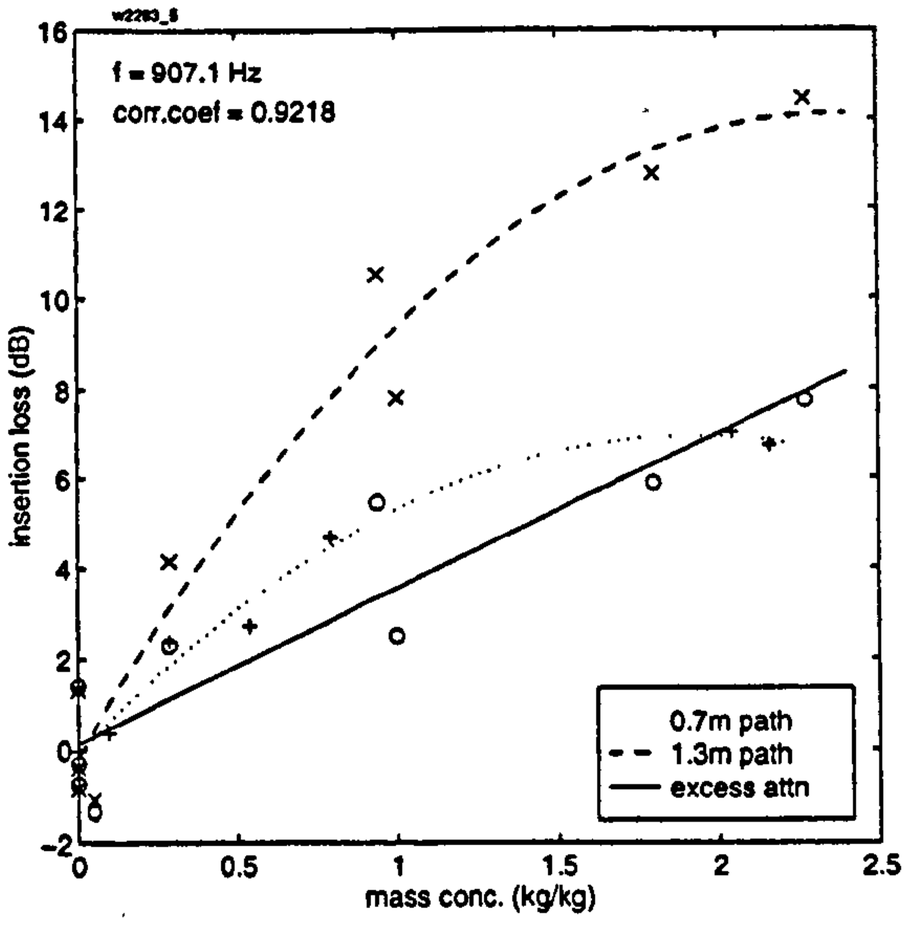

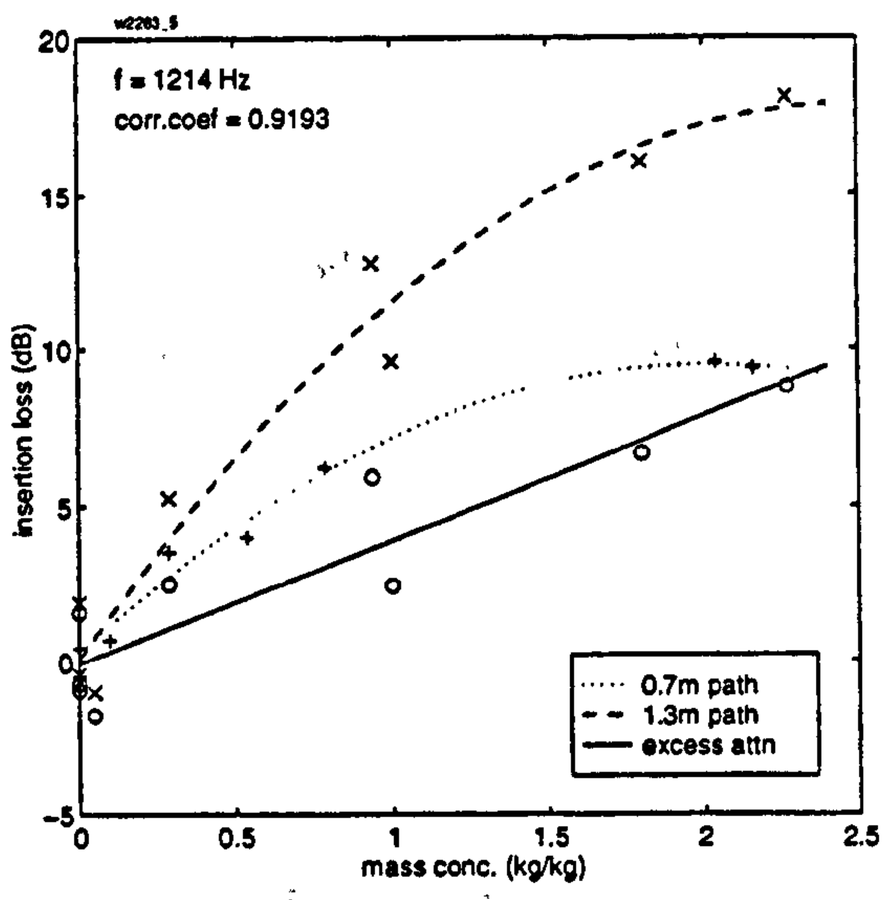

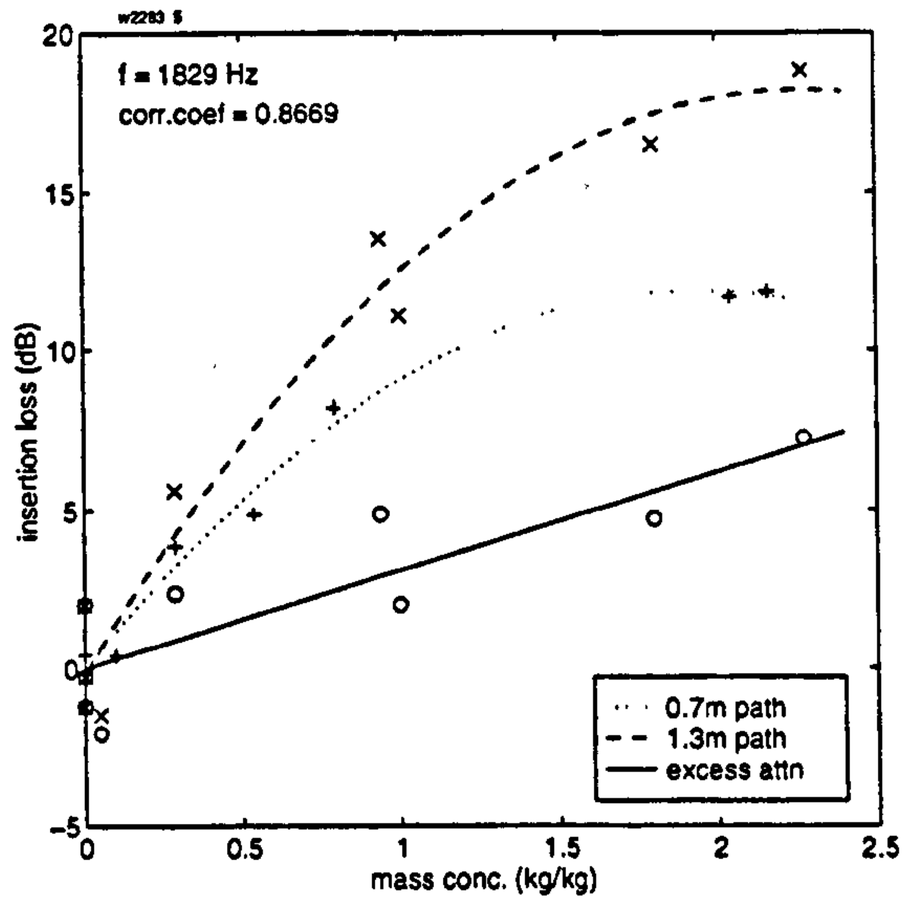

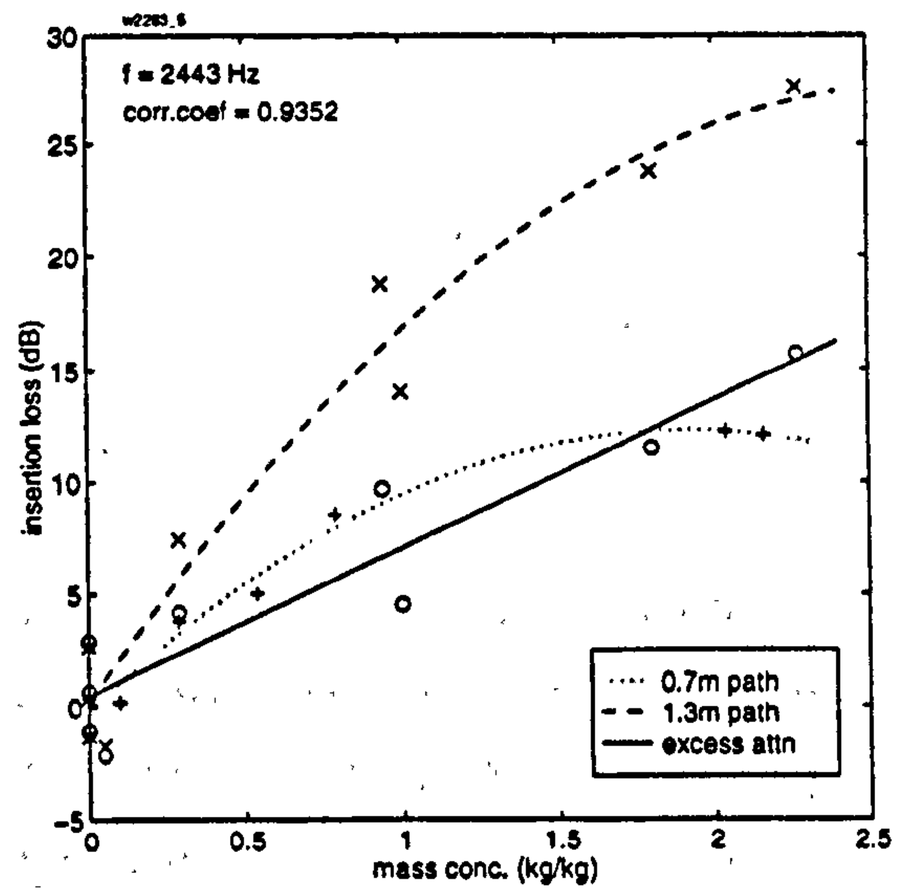

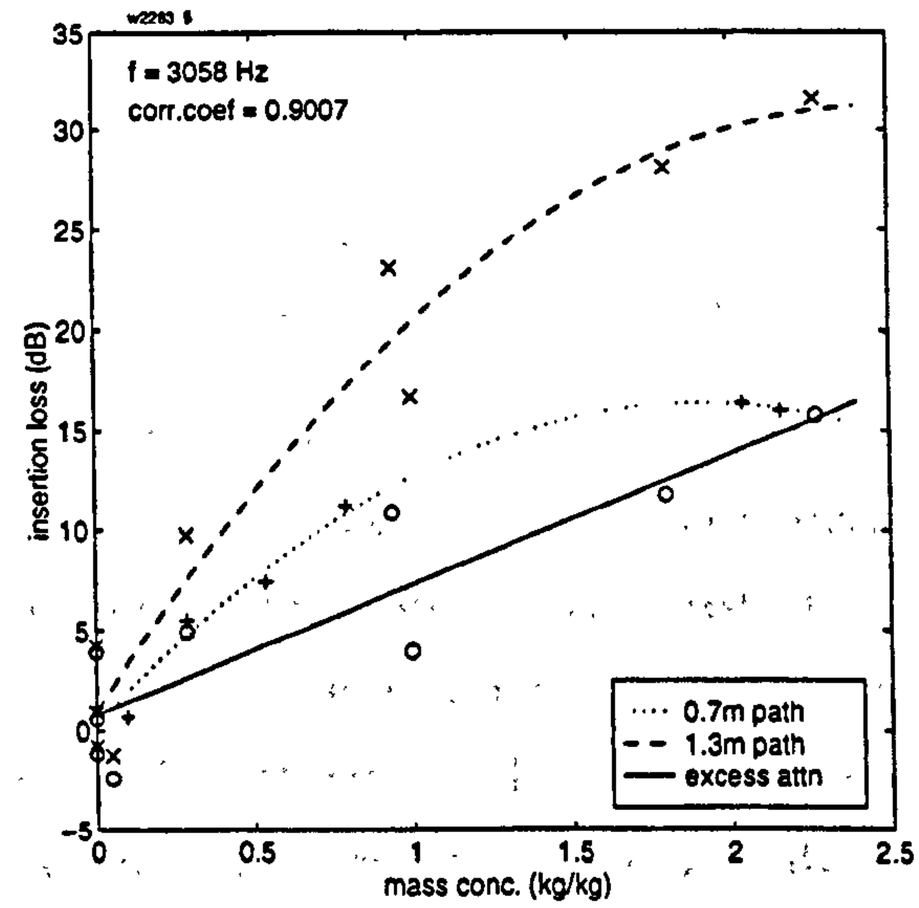

Figure 6-20 Insertion loss with fitted curves (path length 0.7 & 1.3m), and calculated excess attenuation for a flowing suspension of barytes. Example curves are shown at several frequencies. 'o' indicate measurements over 1.3m pathlength, '+' over 0.7m, and 'x' is the excess attenuation.

The insertion loss appears to be a non-linear function of concentration at both path lengths. Therefore quadratic curves have been used to fit the points, and to interpolate between concentration points for the 0.7m path. However, when the excess attenuation is calculated, it appears to be a linear function of concentration, suggesting that a non-linear mechanism is operating in addition to the attenuation due to particles. The attenuation coefficient, calculated from the gradient of the excess attenuation lines, is shown in Figure 6-21.

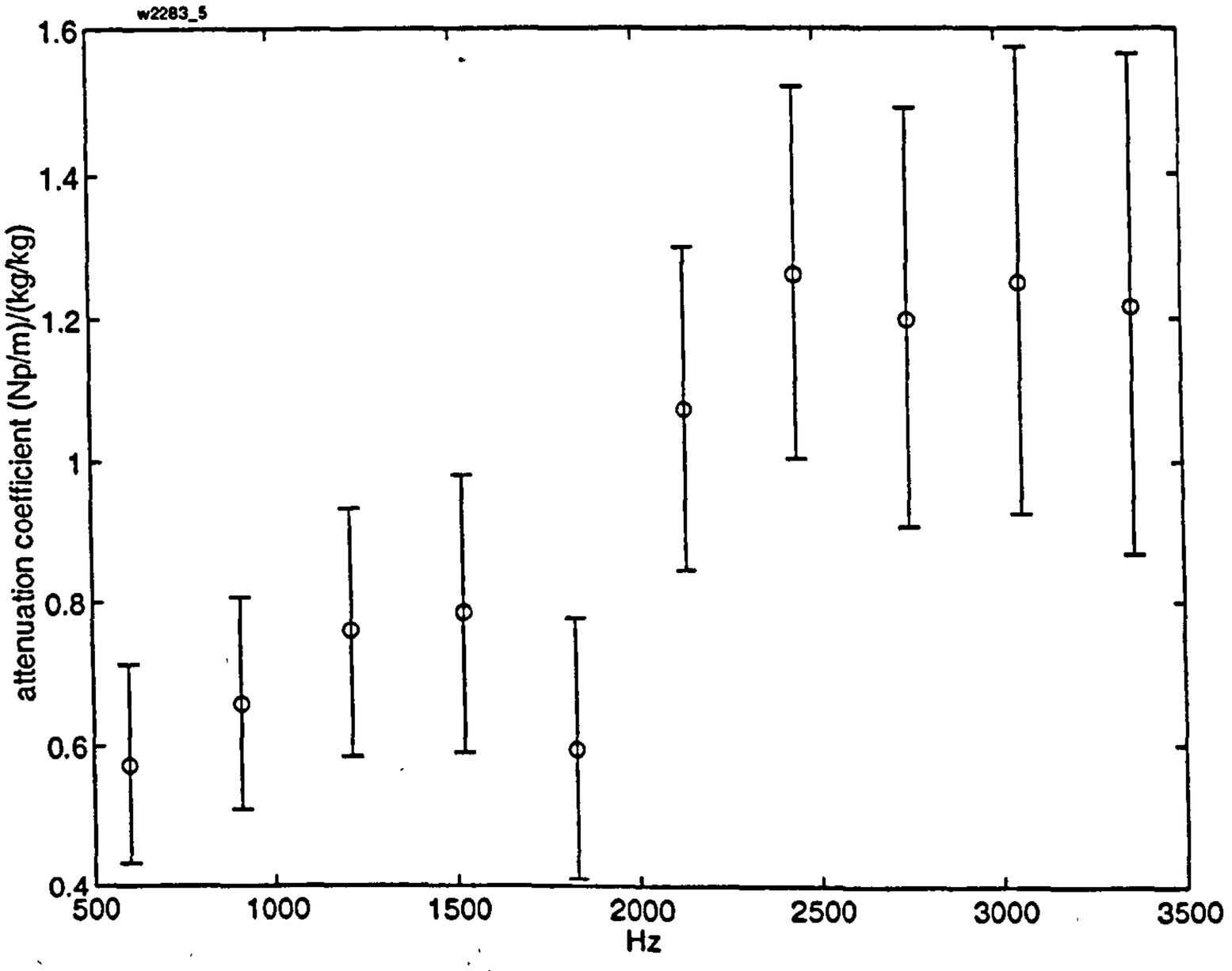

Figure 6-21 Attenuation coefficient per kg/kg of a flowing suspension of barytes; error bars indicate 90% confidence limits.

6.3.3 Varying air velocity

All the measurements taken on suspensions so far were made with a constant air velocity of 20m/s (nominally). One further set of measurements was made by keeping the mass concentration nominally constant [1], while varying the air velocity from 17 - 25 m/s. The material used was barytes, and the path length was 1.3m.

[1] The ratio between the venturi and supplementary airflow rates was maintained constant at 1:1, although the mass concentration still varied between 1.24 - 2.24 kg/kg.

The attenuation coefficient was calculated in the same way as in section 6.3.1, and plotted in Figure 6-22, with each curve normalised to 1 kg/kg to remove the effects of fluctuations in concentration.

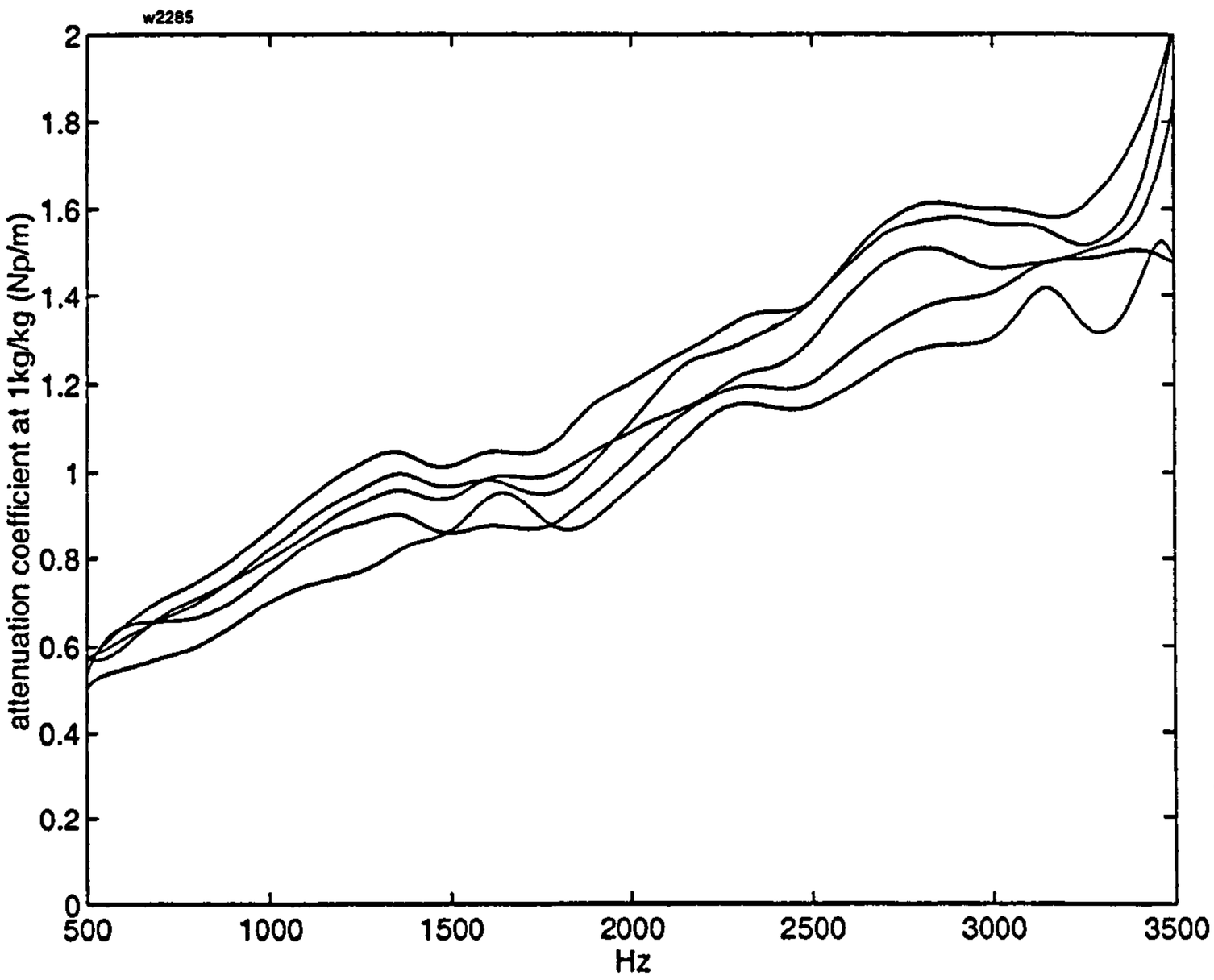

Figure 6-22 Attenuation coefficient of flowing barytes (normalised to 1kg/kg) for air velocities varying between 17 & 25 m/s.

There is a moderate spread in the curves, which is illustrated further in Figure 6-23 by plotting the relative change in attenuation coefficient (referred to the value at the lowest velocity), against air velocity, for three frequencies.

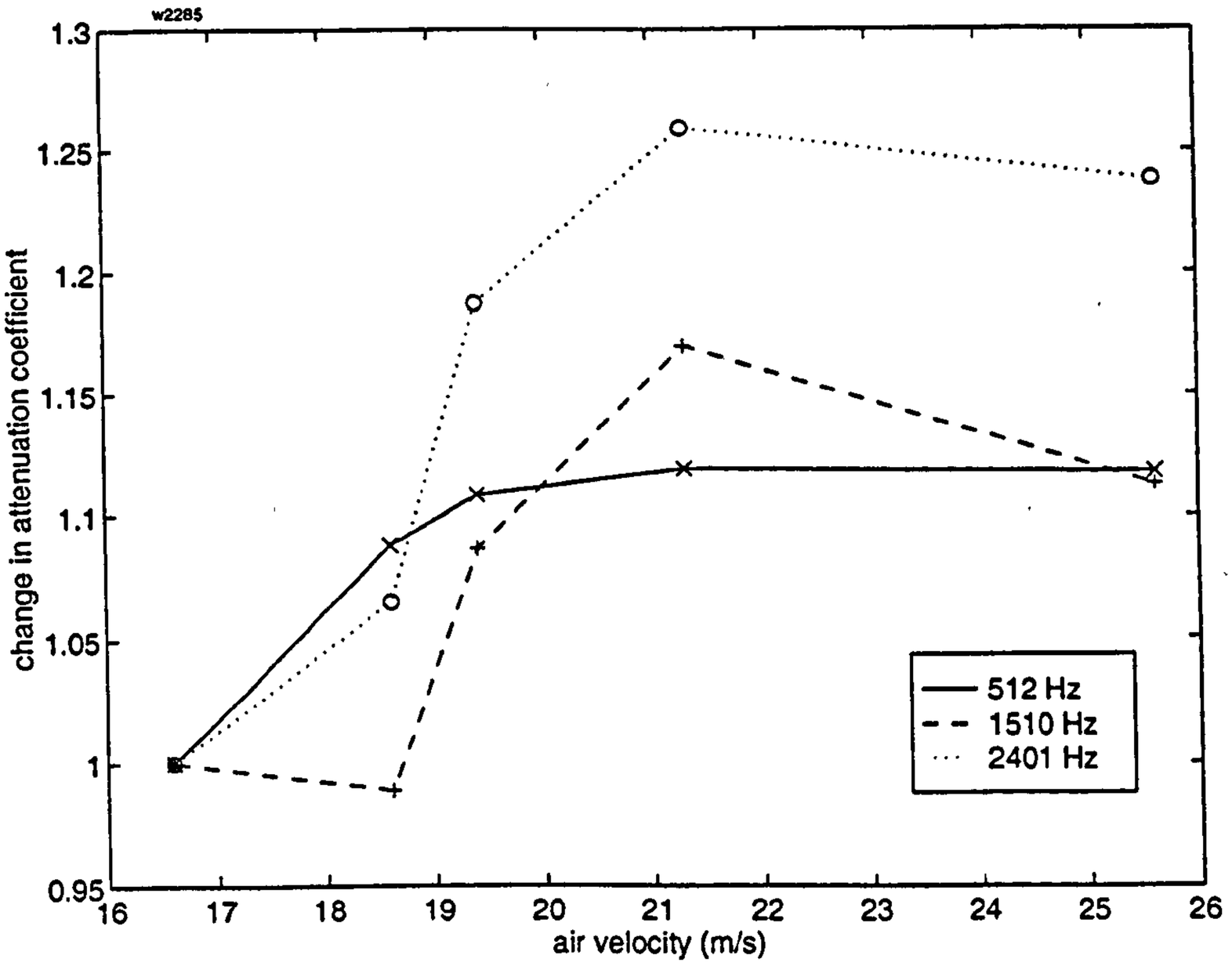

Figure 6-23 Fractional change in attenuation coefficient of flowing barytes (relative to value at 17 m/s) as a function of air velocity

There is a general trend for the measured attenuation coefficient to increased with velocity, although the sensitivity to velocity varies between frequency lines, apparently being more sensitive at higher frequencies. For this 63% increase in velocity, the measured attenuation rises by between 12 - 25 %.

6.4 DISCUSSION & CONCLUSIONS

Measurements on quasi-static suspensions of alumina confirmed the linearity of specific attenuation and dispersion with volume concentration (for $\phi_v < 10^{-5}$) that was predicted by multiple scattering theory. The shape and magnitude of the predicted dispersion and specific attenuation and curves agreed closely with the measured values. The measured dispersion was systematically higher than the predictions, while the measured specific attenuation tended to be lower: these discrepancies could not be explained by systematic errors in measured particle size or concentration.

Measurements on clean airflow showed only a small influence of airflow on the measured insertion loss below 4000 Hz (<2 dB change at 20m/s) which could be explained by the redistribution of sound pressure due to the flow velocity profile. This suggests that the effects of turbulent losses and changes in orifice impedance of the probes are small, at this air velocity and frequency range. This finding justified the use of a single receiver, since the power output of the transmitter was not apparently changed by airflow.

The insertion loss due to suspensions of flour, sand and barytes was measured for mass concentrations of 0 – 2.5 kg/kg (separate measurements for flour extend up to 4.5kg/kg).

The measured insertion loss of flour shows a linear dependence on concentration over the measured range. The predicted magnitude of the attenuation coefficient closely matches the measured values, although the measured increase as a function of frequency is more rapid than predicted, and the curve shape is less sigmoidal than predicted. This latter finding has been reported in several studies in which propagation through slurries was measured: for example, Holmes *el al* [62] measured suspensions of polystyrene beads in water; Urick [148] and Greenwood *et al* [53] measured kaolin-water slurries; Allegra & Hawley [6] measured suspensions of latex spheres in water.

The insertion loss of suspensions of olivine sand was on the limit of measurability given the current apparatus, in the frequency range of plane wave propagation. Nevertheless, correlations were found with concentration, and the attenuation coefficient deduced from measurements of insertion loss was one order of magnitude higher than predicted. Again, the measured rate of increase with frequency was higher than predicted.

The theoretical predictions are based on the assumption that the particles are spherical. For the particulates tested, this is poor approximation: alumina particles, imaged by a scanning electron microscope, vary between being needle-like to plate-like; flour particles consist of an aggregation of smaller (1– 5 μm) particles; olivine sand is crystalline, and barytes consists of cubic crystals, aggregated together. It is noticable that the measurements and predictions diverge as the mean particle size increases. One possible reason is that, as the particle size decreases, the viscous (or thermal) boundary layer thickness becomes larger compared to the particle dimensions; therefore roughness or non-sphericity become increasingly "invisible" to the viscous (or thermal) wave. The ratio of the particle radius to the viscous boundary layer thickness, $\frac{a}{\delta_v}$, is the Reynolds number (defined in equation (2.25)), and was called the viscous wavenumber by Wu *et al* [162]. They suggest that, when Re >> 1, the boundary layer is much smaller than the particle, and so roughness and non-sphericity of the particles become significant. Their measurements of attenuation of sand in water extended over the range $60 < Re < 240$, and were uniformly larger than the predictions (by a factor of 2 – 10). For the measurements on sand just presented, $Re \approx 6$, and it seems difficult to believe that the large discrepancies observed are solely due to roughness and non-sphericity.

A further point worth noting, is that the PSD of alumina was measured by the photosedimentometer method, whereas that of the other materials was measured by optical scattering. The photosedimentometer measures the (steady state) drag force on the particles, and converts it into an equivalent spherical particle size; the acoustic theory then converts this nominal figure back into a drag force (and less significant heat transfer terms). Therefore, this technique measures the particle size in a way that inherently compensates for roughness and non-

sphericity, provided that the *Re* of the test conditions is similar to that of the acoustic measurement. This is only true for acoustic measurements in the viscous and inertial regimes, where *Re* is the main governing parameter: as compressional wave scattering becomes significant, the geometrical scattering cross-section, as measured by an optical technique, is probably a more relevant measure.

The insertion loss of olivine sand was retested using the difference between loss over two path lengths, in an attempt to measure excess attenuation more directly. This did not reduce the measured attenuation coefficient. However, when a suspension of barytes was tested in this way, the insertion loss over both path lengths appeared to be a non-linear function of concentration. Even so, the difference between them — the excess attenuation — remained a linear function, suggesting that a non-linear mechanism is operating in addition to attenuation due to particles. Comparison with the theoretical attenuation coefficient was not possible, because the barytes particles were so cohesive that they could not be assumed to be suspended individually.

This result suggests that the coupling into and/or out of the probe tubes can be affected by the type of particulate. It should be noted, however, that the cohesiveness of the barytes particles led to a build-up around the orifice, which may have reduced the effective diameter of the orifice. The particles also adhered to the tube walls, which may have changed the surface roughness of the walls, and hence the flow velocity profile.

There is a further advantage to measuring excess attenuation rather than insertion loss: with the latter technique, the assumption is made that the path length is the distance between transmitter and receiver, and therefore that the wave converts into a plane wave at the point of entry into the tube. In fact this will take a finite distance — probably a few pipe diameters. By contrast, with the excess attenuation method, one can arrange for the conversion to a plane wave to be completed over the distance between the transmitter and the reference receiver.

Measurements of normalized attenuation coefficient for flowing flour were made with both short-term ("instantaneous") and long-term averaging. The results of both methods compare well, except for a small systematic offset (shown in Figure 6-17), although the scatter in the "instantaneous" measurements is greater than that of time-averaged data (Figure 6-15 compared to Figure 6-16).

Given the present non-acoustic method for measuring the mass concentration, for greatest accuracy the estimate should be measured over a long period, and the acoustic parameter also averaged over an equal period. If an "instantaneous" non-acoustic method of measuring the mass concentration (e.g. beta particle absorption [136]) were used to compare with the acoustic measurements, then an indication of the repeatability of acoustic measurements would be possible. However, because of the rapidly fluctuating density of the suspension, the measurement duration and synchronisation between the instruments would need to be closely matched.

The above measurements attempted to reduce the effect of flow, by maintaining flow velocity constant and referring insertion loss to the values with a flow of clean air. In further tests, the flow velocity was varied while maintaining constant concentration. These showed a slight dependence of measured insertion loss on flow velocity, ranging from a 12 - 25 % increase in loss for a 63 % increase in velocity.

7

MEASUREMENTS OF THE REVERBERANT FIELD

Measurements in the previous chapter used time-domain editing to remove unwanted reflections from the ends of the pipe. The path length over which acoustic properties could be measured was limited by the length of the test chamber, and the upper frequency range was limited by the cut-on frequency of the first transverse mode, which is inversely related to the pipe diameter. Chapter 8 will describe measurements across the pipe diameter, once again using time-domain editing. Due to the short path length, a short impulse is necessary to allow editing without inclusion of unwanted reflections, so restricting the technique to ultrasonic frequencies.

This chapter explores an alternative technique, in which the total reverberant field in the chamber is measured. Such measurements have the advantage that the path length can be effectively much larger, since a wavefront can make multiple traverses of the volume, and so this technique can be expected to be more sensitive to medium attenuation than the other two methods. Furthermore, measurements can be made at audio frequencies above the plane wave limit of the measuring tube, therefore providing data on an otherwise inaccessible frequency range.

The reverberant field is harder to quantify than a travelling plane or spherical wave, and it can be difficult to relate reverberation measurements to plane wave parameters — statistical methods are normally used. While some theoretical comparisons will be made in this chapter, the main aim is to find correlations between particle concentration and acoustic measurements.

This chapter will present measurement methods and results of three acoustic parameters:

- Narrow-band excess decay rate in quasi-static suspensions (section 7.2), and flowing suspensions (section 7.3).
- Modal frequency shift in flowing suspensions (section 7.4)
- Narrow-band steady-state sound pressure level (SPL) in flowing suspensions (section 7.5)

The theoretical basis of these measurements is presented below (section 7.1).

Specifications for the materials tested (alumina, flour and olivine sand) are presented in Appendix F.

7.1 THEORY

Theoretical descriptions of the reverberant field are usually based on statistical analysis using geometrical methods. Such an analysis is used to estimate the mean path length of rays between reflections. The major assumption is that the field is diffuse: that is, at any one measuring point, the sound is arriving from all directions uniformly. Furthermore, all wavefronts are assumed to be mutually incoherent, so that their intensities or energies may be summed, without consideration of interference phenomena.

7.1.1 Excess decay rate due to medium attenuation

Consider the case where a reverberant environment with finite medium attenuation is excited by a broadband signal to a steady state, and then the excitation is switched off at t = 0. Assume that the r.m.s. pressure in a given frequency range decays exponentially from p_0 to p at time t. Knudsen [75] first proposed that the decay could be represented by the sum of two decay constants: one constant, Γ, due to absorption at the enclosure walls, and the other due to the distance travelled, ct, through the medium of attenuation coefficient, α:

$$\frac{p}{p_0} = e^{-\Gamma t - \alpha c t} \tag{7.1}$$

Hence a decay rate, Q, measured in dB/s, may be defined by

$$Q \equiv -\frac{20}{\Delta t}\log_{10}\left(\frac{p_{\Delta t}}{p_0}\right) = 20\log_{10} e \cdot (\Gamma + \alpha c) \tag{7.2}$$

Suppose we have two measurements of Q in an enclosure, with and without a suspension of particles: Q_{dust} and Q_{air}. If the surface absorption remains constant then,

$$Q_{air} = 20\log_{10} e \cdot (\Gamma + c\alpha_{air}) \quad \text{and} \tag{7.3}$$

$$Q_{dust} = 20\log_{10} e \cdot \left[\Gamma + c(\alpha_{air} + \alpha_{dust})\right] \tag{7.4}$$

Here, α_{air} is the attenuation coefficient of air alone (at the prevailing conditions), and α_{dust} is defined as the excess attenuation coefficient of dusty air above that of air alone.

The excess decay rate may be defined:

$$\Delta Q \equiv Q_{dust} - Q_{air} \tag{7.5}$$

From equations (7.3) and (7.4):

$$\Delta Q = 20c\left(\log_{10} e\right)\alpha_{dust} \tag{7.6}$$

If the above assumptions are correct, then ΔQ should be proportional to α_{dust}. Furthermore, if α_{dust} is a linear function of dust volume concentration ϕ_v (which is predicted for small ϕ_v), then excess decay rate should be linearly related to dust concentration.

Experiments have been performed to investigate which frequency bands yield exponential decay, and how closely those bands show the postulated linear relationship between excess decay rate and dust concentration.

7.1.2 Modal structure of a cylinder

Consider a cylindrical tube of length l, radius R, in which the velocity of sound is c.

The characteristic frequencies, f_{mod}, for a cylindrical enclosure are found from the longitudinal and the transverse modal frequencies[1] [98]:

$$f_{\mathrm{mod}}^2 = f_{long}^2 + f_{trans}^2 \tag{7.7}$$

$$f_{long} = cn_z / 2l \quad \text{where } n_z = 0,1,2... \tag{7.8}$$

$$f_{trans} = c\varepsilon_{mn} / 2\pi R \quad \text{where } \varepsilon_{mn} \text{ is the } n\text{th solution of } \frac{dJ_m(\varepsilon)}{d\varepsilon} = 0 \tag{7.9}$$

and J_m is the cylindrical Bessel function of order m, (ε is a dummy variable).

Transverse modes are usually labelled (m,n), where m shows the number of nodal lines in the radial direction, and n shows the number of nodal circles (illustrated in Figure 7-1). Mode (0,0) represents the special case of plane wave propagation.

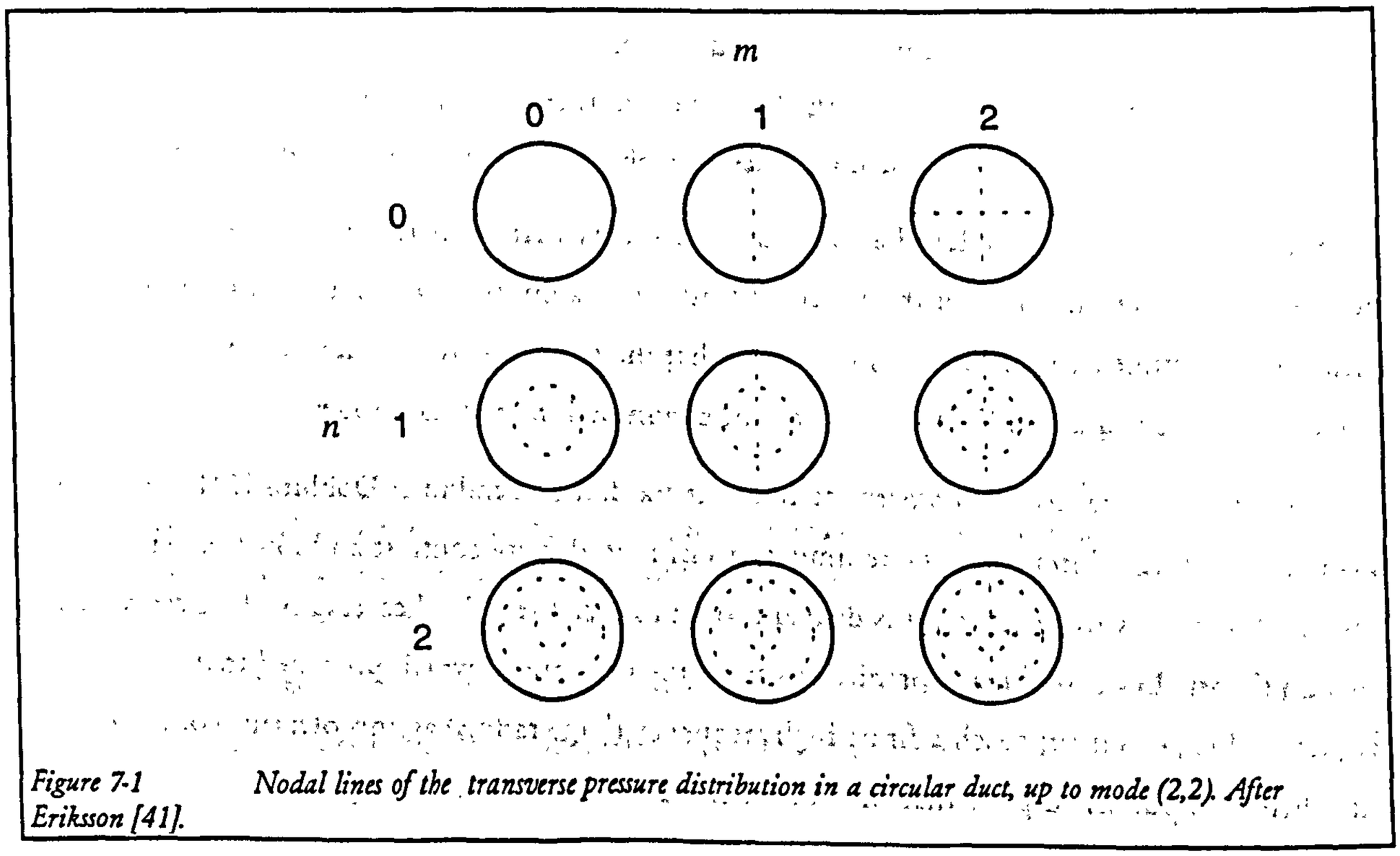

Figure 7-1 Nodal lines of the transverse pressure distribution in a circular duct, up to mode (2,2). After Eriksson [41].

[1] Programs that evaluate equations (7.7) & (7.9) are listed in Appendix B.

If $l>>R$, as is the case in this study, then the close spacing of longitudinal modes leads to large clusters of modes around the cut-on frequency of each transverse mode. The theoretical modal density is plotted in Figure 7-2 showing peaks where modes cluster around values of f_{trans}.

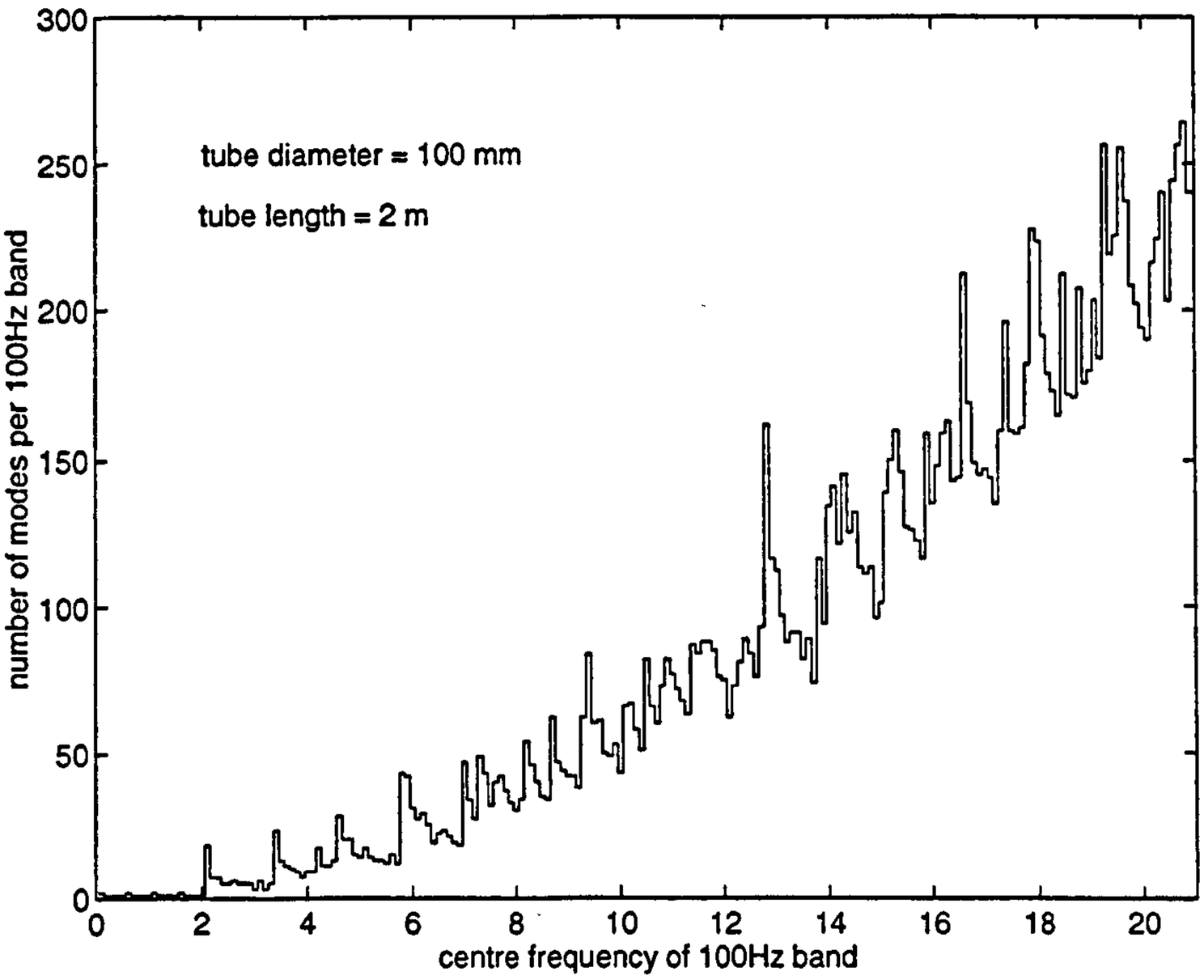

Figure 7-2 *Theoretical modal density of a cylinder, 2m × 100mm diameter*

7.1.3 Change in modal frequency

The cut-on frequency of a transverse mode is governed by the diameter of the duct and the wavelength. If the speed of sound in the enclosed medium changes, the cut-on frequency will change to maintain a constant wavelength. This gives another mechanism with which to measure the acoustic effect of a suspension, using the lesser-exploited parameter of velocity dispersion.

Vetter & Culick [151,150] produced a coupled-phase theory that predicted the change in modal frequency explicitly, allowing for the effects of finite wave amplitude, and sources within the enclosure. It assumed an infinitely long tube, so that the characteristic frequencies of the tube would be given by equation (7.9), without modification by longitudinal modes.

They used the same terms for momentum and heat transfer as Temkin & Dobbins [141], and their theory is therefore subject to the same limitations of high density contrast and low frequency (restricted to the viscous regime). It is difficult to reproduce the published results of Vetter & Culick's theory. Evans [43] made predictions from their equations which predicted that the frequency shift would approach a finite high frequency (large radius) asymptote; this conflicted with their own published plots that showed the frequency shift approaching zero.

A simpler prediction of frequency change can be made by predicting the sound velocity shift (using any conventional scattering or coupled-phase theory), and calculating the frequency change necessary to maintain constant wavelength. The fractional frequency change is:

$$\frac{\Delta f_{mn}}{f_{mn}} = \frac{f_{mn} - f'_{mn}}{f_{mn}} = 1 - \frac{c'(f'_{mn})}{c(f_{mn})} \tag{7.10}$$

where f_{mn} is the cut-on frequency of mode (m,n), and dashed variables refer to values when the suspension is present. Since calculation of f'_{mn} requires knowledge of f'_{mn} in order to calculate the sound speed at the new frequency, an iterative procedure is required: the sound speed is calculated at f_{mn}, giving an approximation to f'_{mn} which can be improved by recalculating the sound speed at f'_{mn}; and so on until the value for f'_{mn} converges.

This method was used (using Temkin & Dobbins' theory to predict the sound velocity) to compare with some of Vetter & Culick's own predictions [150, fig 18]. Predictions from both methods are shown in Figure 7-3.

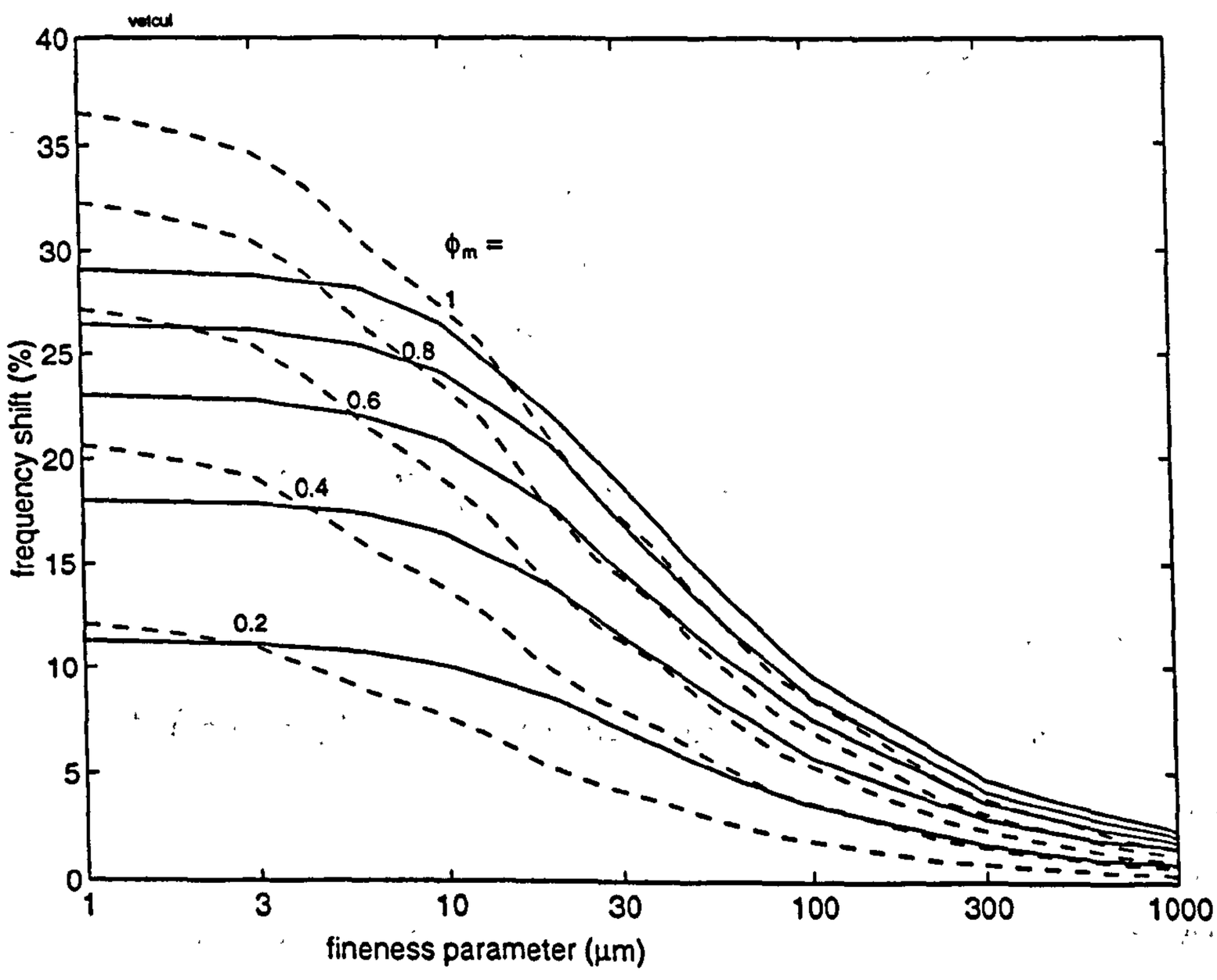

Figure 7-3 Predicted frequency shift of the (0,1)[1] mode in a 3m diameter pipe ($f_{0,1}$ = 67Hz), for coal with a Rosin-Rammler PSD. Dispersion parameter σ_{rr} = 0.8, variable fineness parameter $\bar{a}_{rr}$, and mass concentration ϕ_m varied parametrically. Solid line = prediction by Vetter & Culick (reproduced from [150]), dashed line = prediction using Temkin & Dobbins' theory iteratively applied to equation (7.10).

Equation (7.10) predicts higher shifts than Vetter & Culick's theory at small particle sizes (and low frequencies) and high concentration. If the theory of Lloyd & Berry were used instead of Temkin

[1] Note that this notation to label modes (from Erikson [41]) is different to that used by Vetter & Culick, who reverse the order of m & n.

& Dobbins', this tendency would be magnified, because the former theory predicts a higher low frequency asymptote of dispersion.

As one would expect, the fractional frequency shift is a function of both mass concentration, and the particle size (fineness parameter in this model). However, Vetter & Culick pointed to the use of a second parameter that used broader band information to resolve the ambiguity: the ratio of frequency shift of the first to second resonance frequencies was found to be almost independent of the mass concentration. It was still a function of the (Rosin Rammler) dispersion parameter, but they argued that in real PF distributions, the dispersion parameter remains roughly constant, while the fineness parameter varies. They further postulated using the ratio of the third to first resonance frequency shifts to calculate dispersion.

Although they suggest experimental apparatus, only one preliminary measurement (on a water aerosol of unspecified PSD) has been reported [149] . Section 7.4 presents some measurements of frequency shift for different particle concentrations, and assesses the practical feasibility of their technique.

7.1.4 Steady state amplitude of sound power

If an enclosed medium is insonified with a constant noise source, the sound energy will build up until an equilibrium situation is achieved where the power absorbed in the medium and at the walls is equal to the power injected by the source. The level of the steady state sound pressure may be related to the absorption of the walls and medium, as described below [79, with modification for medium loss].

We can write an expression for the sound energy in an enclosure with no source in a form similar to equation (7.1):

$$E(t) = E_0 \exp -2(\Gamma + \alpha c)t \tag{7.11}$$

The factor of 2 is due to the square relationship between energy and pressure. Differentiating this expression gives:

$$\frac{dE(t)}{dt} = -2E(\Gamma + \alpha c) \tag{7.12}$$

Now we add a source with sound power Λ:

$$\frac{dE(t)}{dt} = -2E(\Gamma + \alpha c) + \Lambda \tag{7.13}$$

In the steady state, $\frac{dE(t)}{dt} = 0$, and so we can write:

$$E = \frac{\Lambda}{2(\Gamma + \alpha c)} \tag{7.14}$$

Suppose we have two measurements of E, with and without suspension, and assume $\alpha_{air} = 0$:

$$\frac{E_{dust}}{E_{air}} = \frac{\Gamma}{\Gamma + \alpha c} \tag{7.15}$$

Equation (7.3) allows us to estimate Γ from the measured value of Q_{air}, which can be substituted into the expression above.

$$\frac{E_{dust}}{E_{air}} = \frac{Q_{air}}{Q_{air} + 20(\log_{10} e)\alpha c} \tag{7.16}$$

Invoking the power-of-two relationship between energy and r.m.s. sound pressure gives:

$$\frac{p_{dust}}{p_{air}} = \left(\frac{Q_{air}}{Q_{air} + 20(\log_{10} e)\alpha c} \right)^{\frac{1}{2}} \tag{7.17}$$

This gives us an expression which we can test experimentally, assuming a correct model to predict α from ϕ.

7.2 DECAY RATE IN QUASI-STATIC SUSPENSIONS[1]

7.2.1 Introduction

The method of measuring reverberant decay rate within an enclosure is used frequently to measure the absorption coefficient of sound absorbing materials [9], and also to measure the attenuation coefficient of the enclosed medium. For example, Knudsen used the technique to measure the attenuation due to fogs [76] and air humidity [75]. Usually the enclosure is designed to generate a diffuse sound field through the use of diffusers and carefully chosen dimensions that are large compared to the wavelength. The resulting reverberant decay may be filtered into $1/n^{th}$ octave bands to produce decay rate measurements as a function of frequency. Alternatively, the enclosure may be designed to encourage a non-diffuse field with a few well-separated modes: Harris [57] used a spherical enclosure to measure the acoustical properties of air.

This section describes a development of these methods. A regularly-shaped enclosure has been chosen (a cylinder with closed ends, or a pipeline) . It does not have well-separated modes; nonetheless, it will be shown that, by careful choice of frequency bands, decay curves with exponential portions can be observed, and their decay rate can be related to medium attenuation.

7.2.2 Measurement apparatus

To measure the reverberant decay rate in quasi-static suspensions, the lower tube of the static apparatus (described in Chapter 4) was used, with a heavy bung sealing the topmost end. The equipment is illustrated in Figure 7-4. Midway along the tube were two diametrically opposed

[1] This section is based on a paper published in J. Acoust. Soc. Am. [100]

ports that allowed the injection and reception of sound. The acoustic driver was a 70W titanium-dome tweeter coupled to the end of a 55 mm feed tube of 7 mm bore that was filled with light wadding to damp out standing waves. The impulse response of the system was measured by MLSSA. The microphone was mounted with the grid flush with the inside of the tube wall, and was supported, sealed and decoupled from structural vibrations by two O-rings. The diaphragm was protected from dust by a fine plastic gauze over the screen. The S.P.L. at the microphone was 104 dB re. 2×10^{-5} Pa.

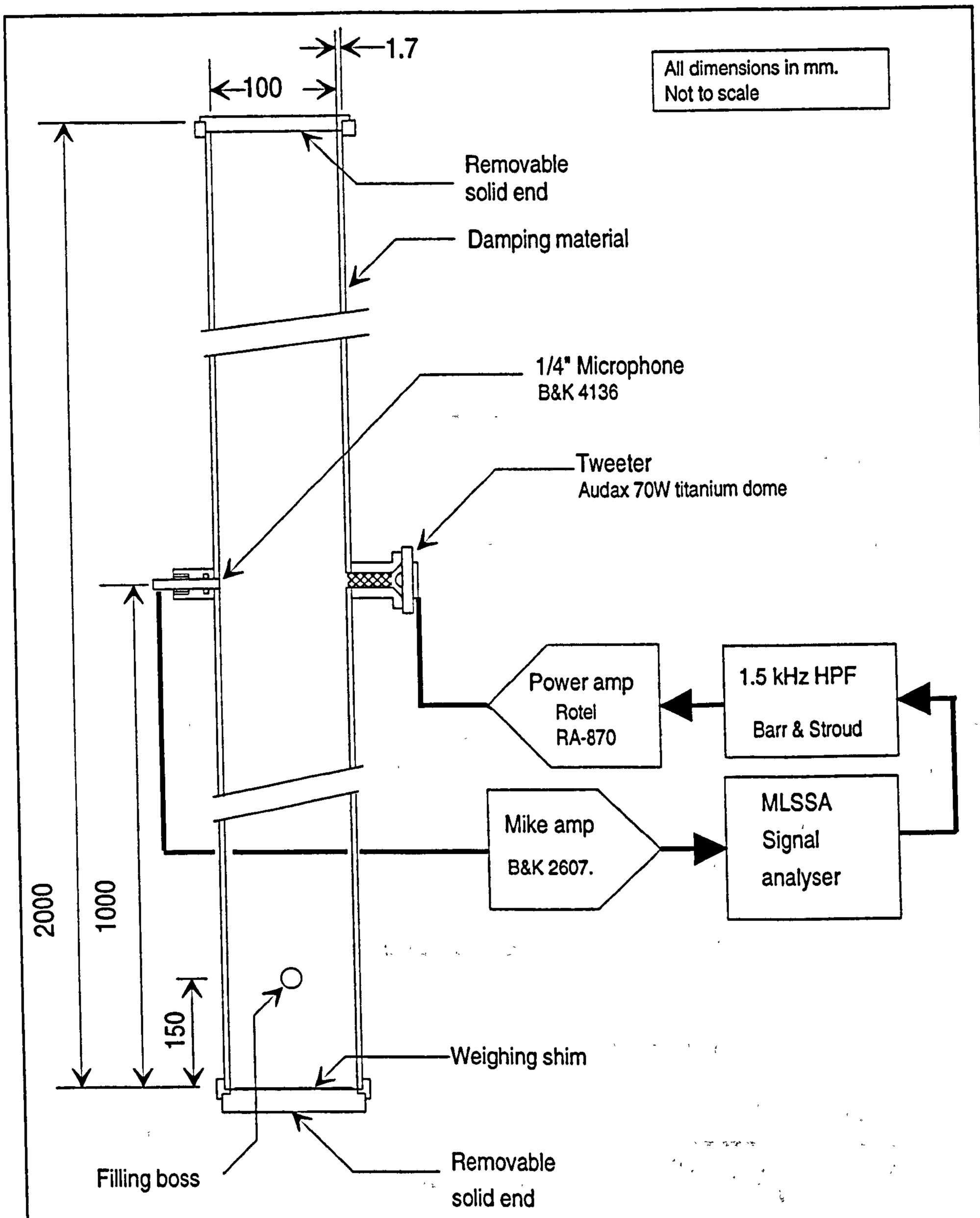

Figure 7-4 *Schematic diagram of apparatus for reverberation measurements on quasi-static suspensions.*

The tube was filled with dust and measurements taken in an identical manner to that described in Chapter 4 for plane wave measurements. Sixteen experiments were conducted, with varying concentrations of particulate. The particulate used was alumina dust, with a mean particle size of 3.1μm (F800 grade).

7.2.3 Signal Analysis

The signal was recorded at a sampling rate of 90.9 kHz.

The impulse response was filtered into a series of band-limited impulse responses, using a bank of digital band-pass filters; the selection of the filter characteristics will be explained in Section 7.2.4. The decay curve for each frequency band was calculated from the band-limited impulse response using Schroeder's [127] method of reverse integration[1], together with Chu's [32] noise subtraction technique, described in Chapter 3.

The advantage of the Schroeder technique, in conjunction with the M.L.S. method of measuring impulse response, is that, unlike the method of interrupted random noise, averaging is unnecessary. This made the measurement fast, which was essential given the changing nature of the suspension as it settles out (the acoustic conditions were assumed to be constant over the period of one measurement: approximately one second). The technique was also very repeatable, which was necessary for measuring small changes in decay rate.

Values of decay rate, Q, were calculated for each decay curve by fitting a straight line to the portion of the curve displaying linear decay. The iterative algorithm that was used is explained in Appendix H. Curves with less than 15 dB of decay range were rejected. This procedure was repeated for each frequency band of each dataset, with and without dust.

To assess how closely a decay record approximated to being exponential – and hence how valid a measure of excess decay rate would be for that record – a "straightness" parameter was calculated for the portion of the decay curve that was used. The parameter chosen was the linear correlation coefficient, r (also known as Pearson's r); this is similar to the inverse of Bodlund's [23] definition of decay curvature.

For N pairs of quantities (x_i, y_i), $i = 1,2,\ldots N$

$$r(x,y) = \frac{\sum_i (x_i - \bar{x})(y_i - \bar{y})}{\sqrt{\sum_i (x_i - \bar{x})^2}\sqrt{\sum_i (y_i - \bar{y})^2}} \qquad (7.18)$$

where $\bar{x}$ is the mean of the x_i's and $\bar{y}$ is the mean of the y_i's. The magnitude of the function varies between 0 for a set of completely uncorrelated points, up to 1 for points that lie exactly on a straight line; the sign of the function indicates whether the relationship has positive or negative gradient.

Hence the correlation coefficient r_{dec} of the decay curve segment is given by:

$$r_{dec} = |r(t_i, S_i)| \qquad (7.19)$$

[1] The upper integration limit was 200ms, chosen to be after the slowest decaying frequency band had decayed into the noise floor.

where i encompasses the range of time samples used for the straight line fit, and S_i is the value of $S(t)$ at time sample t_i .

In each frequency band there were 32 decay curves (with and without dust, for 16 different values of particle volume concentration, ϕ), and hence up to 32 values of r_{dec} To indicate the general decay linearity in a frequency band, the mean of the values, $<r_{dec}>$ will be presented.

Excess decay rate ΔQ was calculated using equation (7.5). If a measurement time scale t_m is defined such that $t_m = 0$ corresponds to the end of dust introduction, then values of Q_{dust} were calculated from the measurements taken at $t_m = +7$ s (the delay is due to the experimental method described in section 4.4.) Attempts were made to extrapolate the value of Q_{dust} back to $t_m = 0$, using another measurement at $t_m = 10$ s; however, this process seemed to make the processed results more erratic, possibly because random errors were amplified by the extrapolation process.

Values of Q_{air} were calculated either from the data taken before dust introduction, $Q_{-\infty} = Q(t_m = -\infty)$, or after the dust had settled out (30 minutes later), $Q_{+\infty}$. The former values were used except where mentioned otherwise.

For each frequency band, values of ΔQ were plotted against ϕ. A straight line was fitted through the points, and its gradient, referred to as the "decay sensitivity" ψ, measured the sensitivity of ΔQ to changes in ϕ. It also has units of dB/s, since ϕ is dimensionless. Hence:

$$\psi = \frac{\partial(\Delta Q)}{\partial \phi} \approx \frac{\Delta Q}{\phi} \quad \text{for a straight line.} \tag{7.20}$$

The correlation coefficient, r_ψ, of the straight line fit was calculated in a similar way to r_{dec} :

$$r_\psi = r(\phi_j, \Delta Q_j) \tag{7.21}$$

where ΔQ_j is the excess decay rate (of a given frequency band) at a concentration of ϕ_j , j = 1,2,....16.

r_ψ is used to assess the degree of linear dependence of ΔQ on ϕ, and hence the constancy of ψ for that frequency band. It was an aim of the experiment to find frequency bands in which the decays were tolerably exponential, giving acceptably high $<r_{dec}>$, and maximum linearity, r_ψ.

7.2.4 Results & discussion

Initially the data were processed without filtering into frequency bands; that is, the value of broadband ΔQ was measured. These values are plotted against ϕ in Figure 7-5, together with the best-fit linear curve.

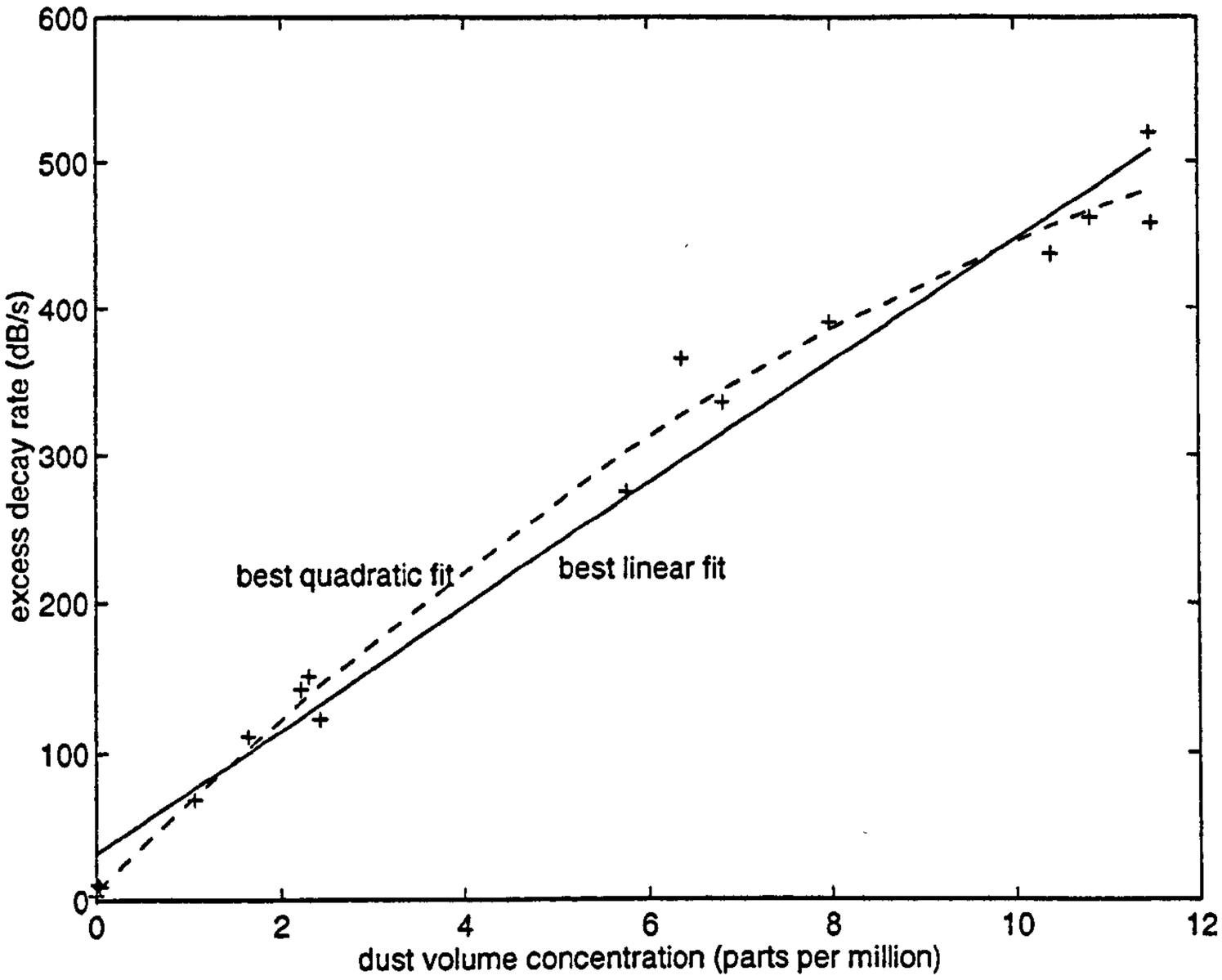

Figure 7-5 *Broadband excess decay rate ΔQ against ϕ: $r_{dec} = 0.998$, $r_{\psi} = 0.987$, $\psi = 41.5 \times 10^{6}$. R.M.S. value of residues: 28 for linear fit and 19 for quadratic fit.*

There is clearly a rather poor straight line fit, due to both point scatter and a degree of nonlinearity. This is demonstrated by the relatively low value of $r_{\psi} = 0.987$, despite the good value of $\langle r_{dec} \rangle = 0.998$. A quadratic fit is also shown to illustrate the curvature. It is this relatively poor broadband linearity that partly makes narrow band processing necessary.

For the initial narrow band investigation, the filter bank was chosen to give a series of 93 overlapping, 800 Hz bandwidth filters (Butterworth, 3rd order). Figure 7-6 shows the correlation coefficients and the decay sensitivity ψ, plotted against the centre frequency of each filter.

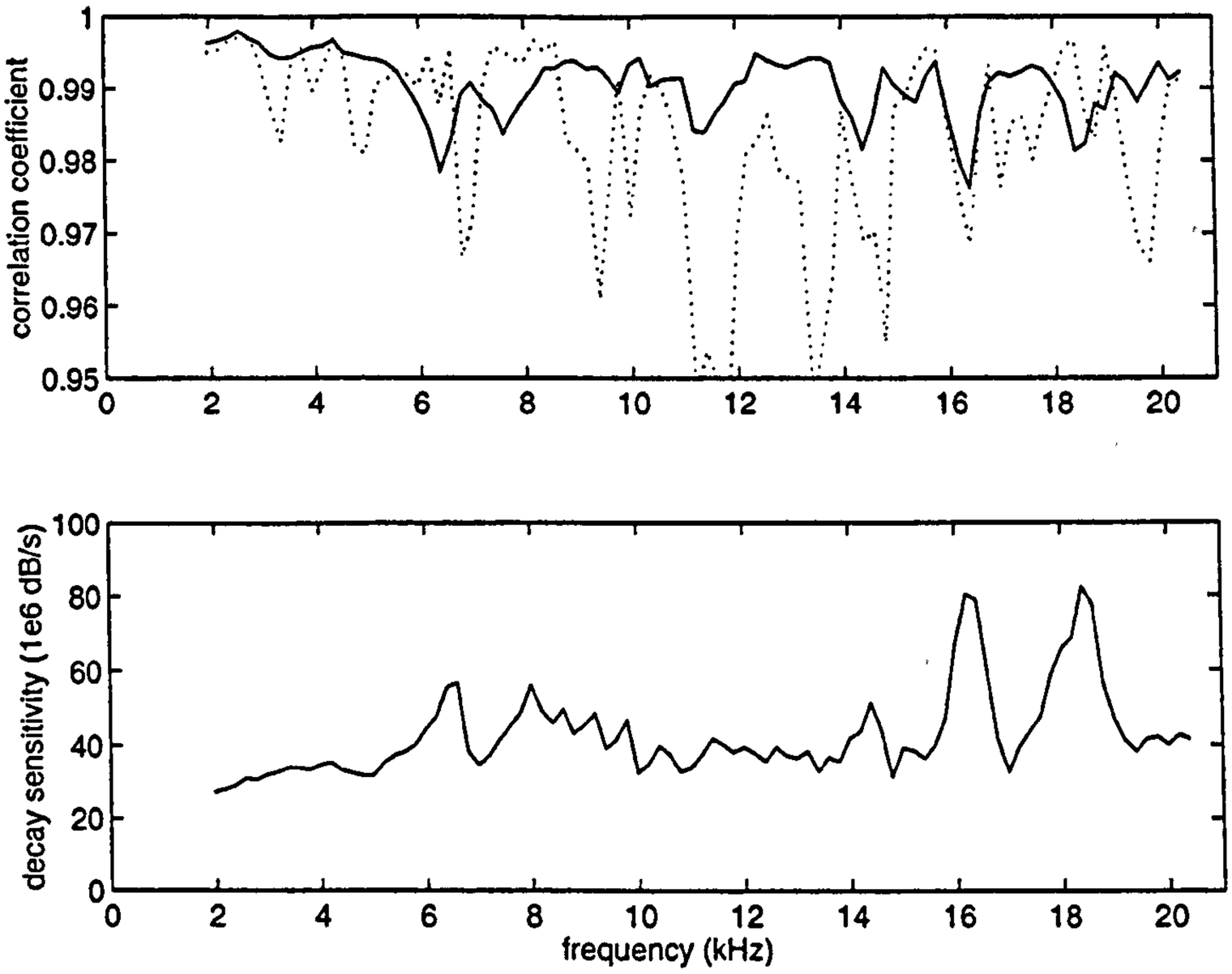

Figure 7-6 *93 filter bank results. Upper axis: r_{dec} (solid), r_ψ (dotted); lower axis: ψ.*

There appears to be little correlation between the *r* curves (in fact the correlation coefficient between $<r_{dec}>$ and r_ψ is +0.43, showing weak positive correlation), and therefore little correlation between a linear dependence of ΔQ on ϕ, and good exponential decay. There is, however, greater correlation between peaks in ψ, and dips in $<r_{dec}>$ (the *r* value between ψ and $<r_{dec}>$ is -0.72, indicating fairly strong negative correlation). It is not clear whether the dips in r_{dec} invalidate the calculated value of ψ, or whether the same mechanism that creates non-exponential decay also increases the decay sensitivity.

To emphasise the maxima in r_ψ, a "goodness of fit" parameter is defined as:

$$G = 1 / (1 - r_\psi) \qquad (7.22)$$

Figure 7-7 shows the relationship between *G* and the modal density (taken from Figure 7-2).

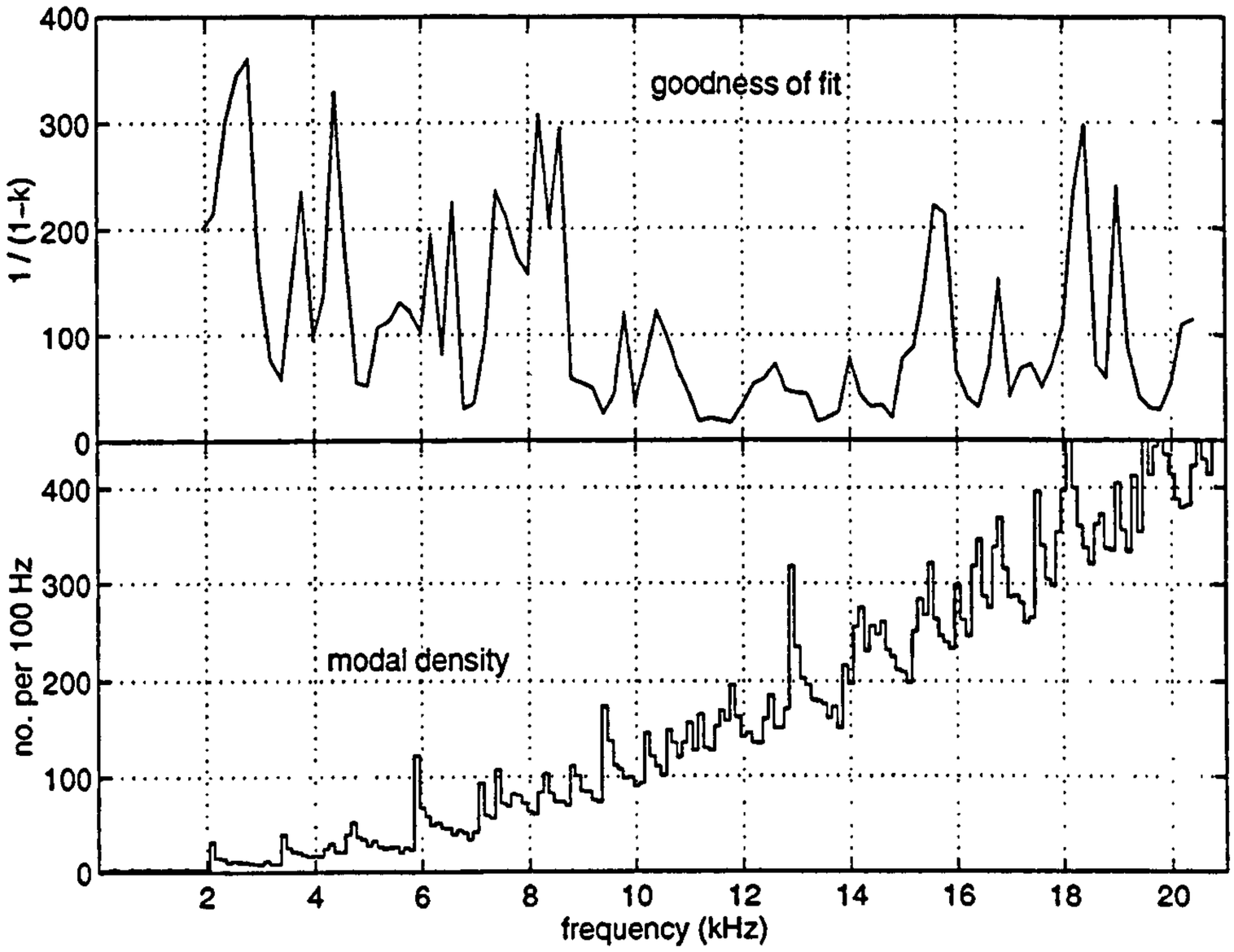

Figure 7-7 *Relationship between "Goodness of fit" G (from r_ψ) and modal density.*

There is a general tendency for the bands with the peaks in *G* to lie just above peaks in the modal density, particularly for the first few peaks; that is, just above the cut-on frequency of a transverse mode. There is also a tendency for dips in *G* (and $<r_{dec}>$) to occur <u>at</u> the cut-on frequency.

Next, a smaller bank of filters was designed to use this information to maximise both $<r_{dec}>$ and r_ψ, while spanning the useful frequency range. The filter shapes are shown in Figure 7-8.

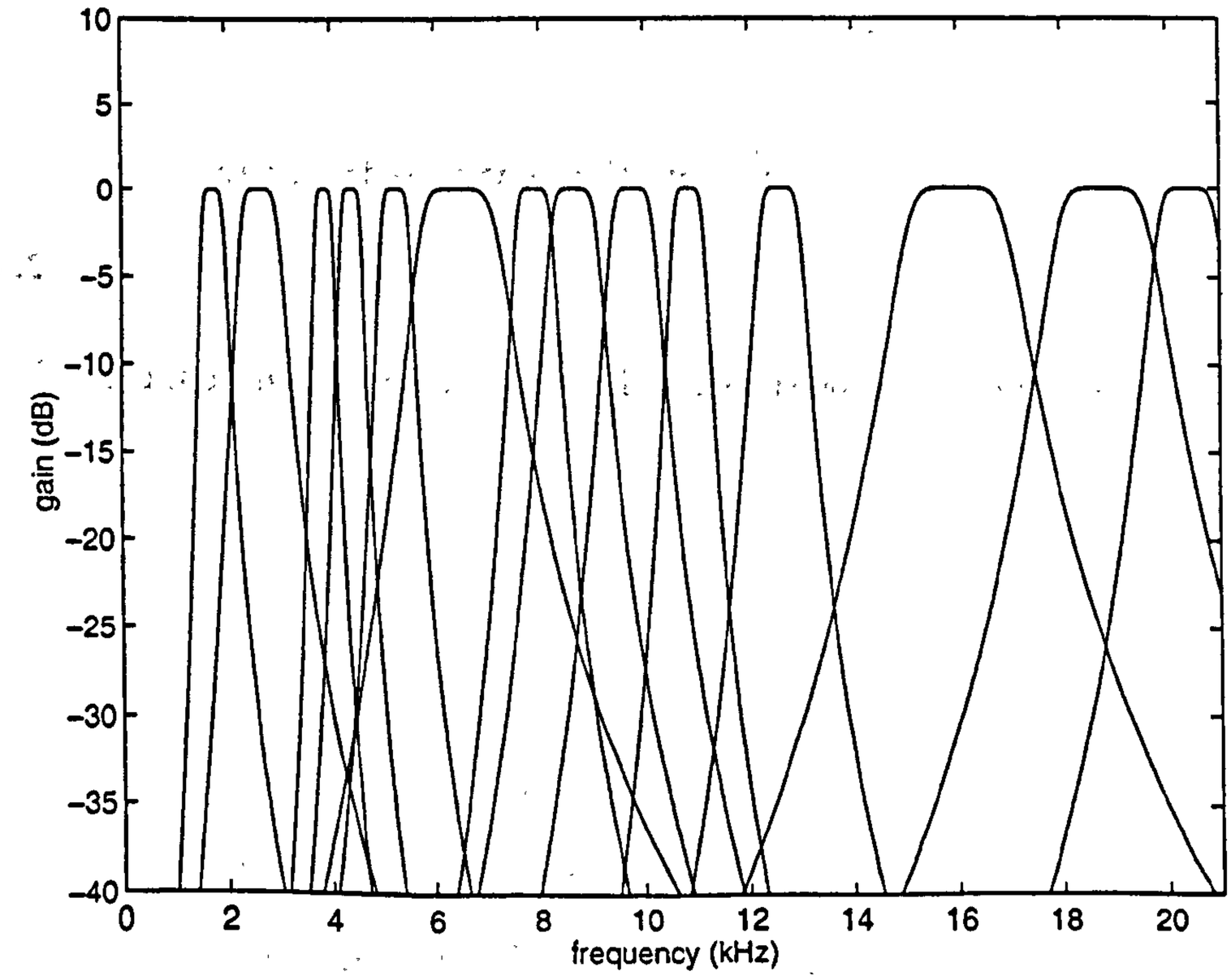

Figure 7-8 *Frequency response of "mode-picking" digital filter bank; all are 3rd order Butterworth.*

They are chosen to span peaks in r_ψ and avoid dips in $<r_{dec}>$. Lower frequency filters (< 8 kHz) predominantly pick out the frequency region above an individual transverse mode, while higher frequency filters span several transverse modes. Note that the lowest filter (centre frequency 1.74 kHz) samples the spectrum below the first transverse mode, and therefore measures the decay of plane wave "flutter" echoes propagating along the tube axis. For all filters, Jacobsen's [67] bandwidth criterion was met (BT_{60} > 16, where B is the filter bandwidth) to ensure negligible influence of the filters' own decay rate. Example curves of ΔQ as a function of ϕ are plotted in Figure 7-9, showing the approximately linear relationship and the corresponding value of r_ψ.

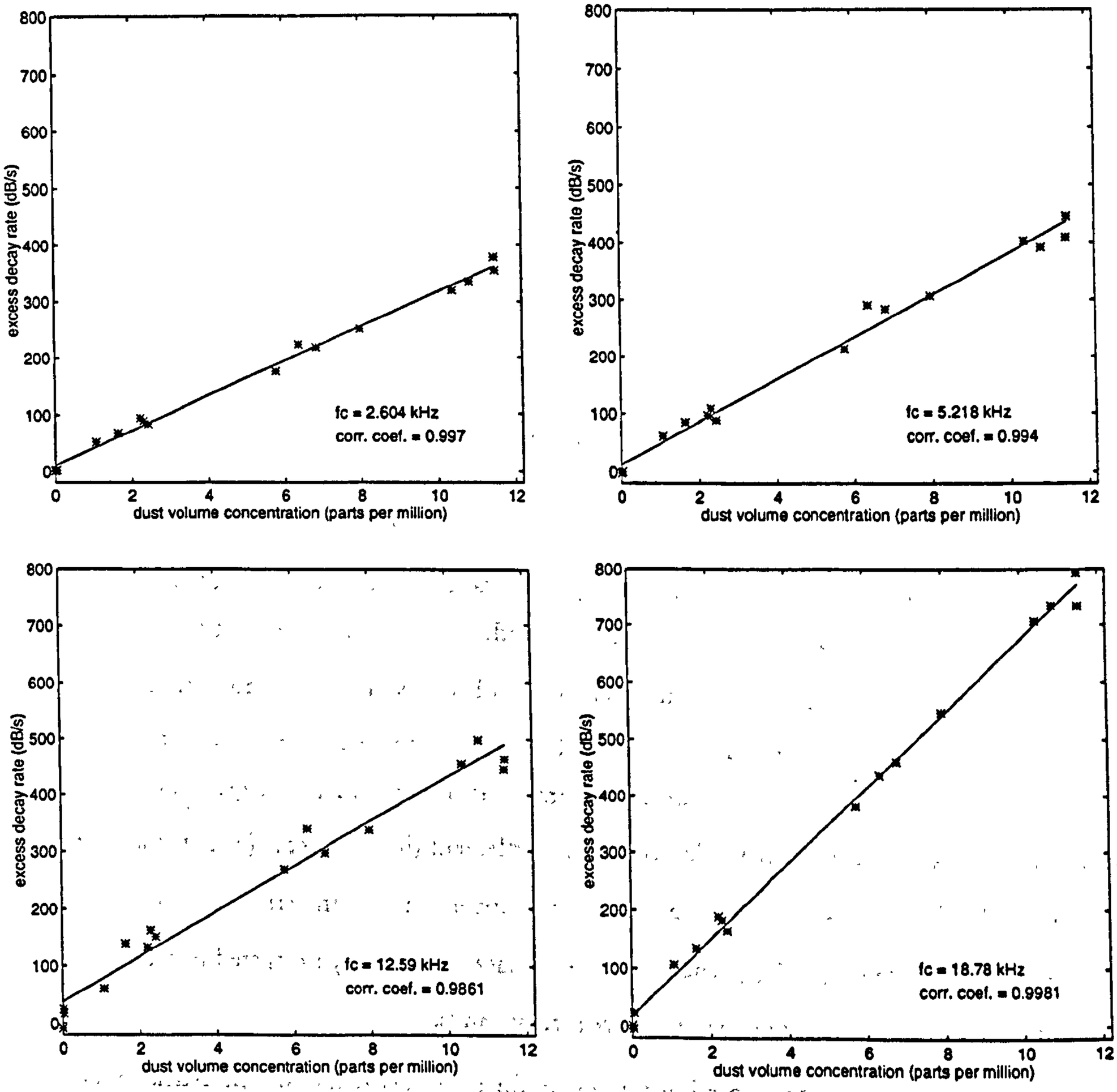

Figure 7-9 *Example plots of ψ against ϕ for some modal filters: r_ψ also shown.*

The frequency bands with the highest and lowest values of r_ψ are included. It can be seen that most curves show a high degree of linearity, and lower values of r_ψ are usually due to scatter in the points rather than non-linearity. Individual decay curves with r_{dec} < 0.98 (Bodlund's curvature >

20) were judged to be insufficiently exponential, and so their ΔQ values were rejected, and the corresponding points are missing from Figure 7-9.

The three parameters $\langle r_{dec} \rangle$, r_ψ and ψ, for this bank of filters, are shown in Figure 7-10.

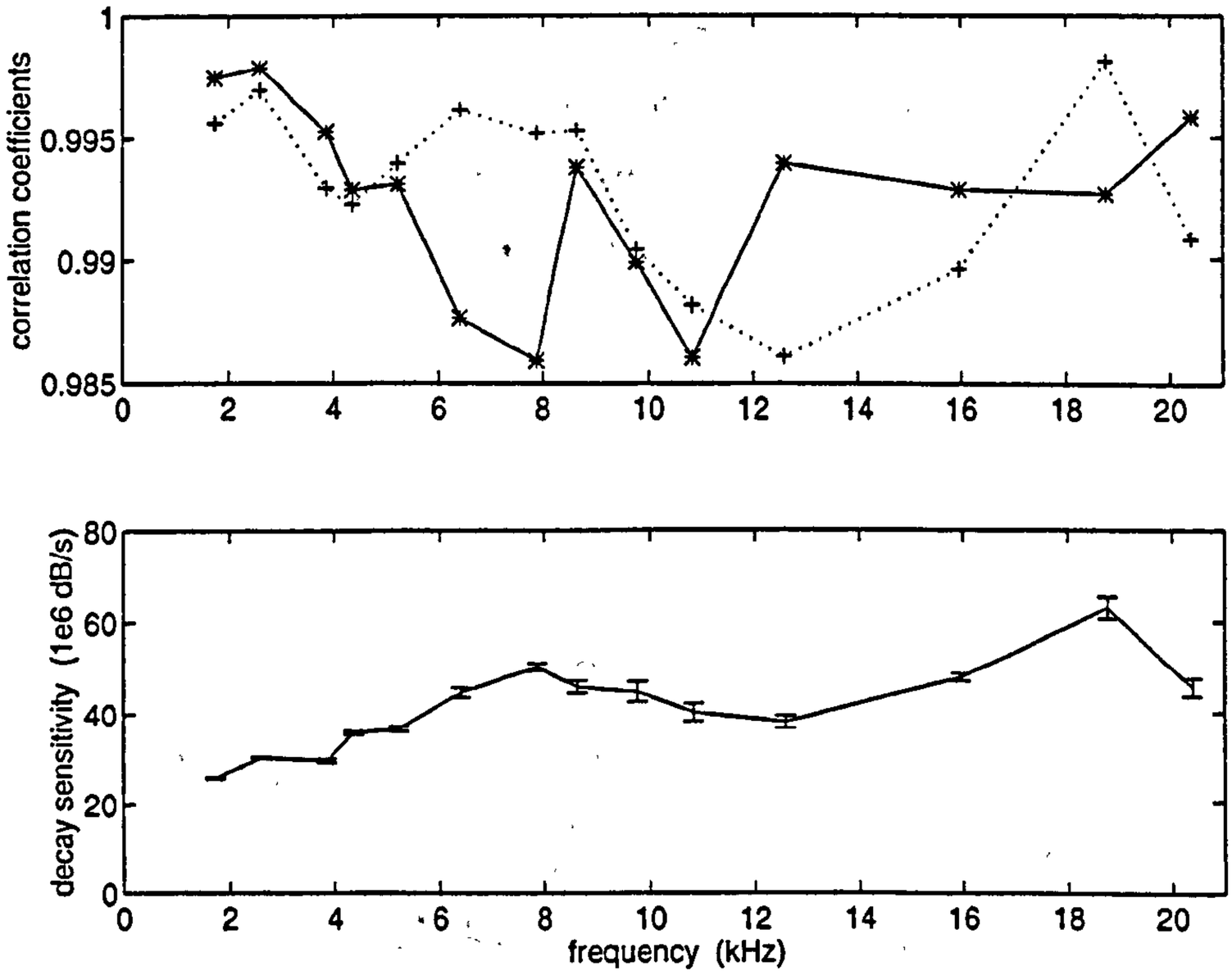

Figure 7-10 Mode-picking filter bank results. Upper axis: r_{dec} (solid), r_ψ (dotted); lower axis ψ.

Error bars are shown on the curve of ψ, to indicate the variation caused by using the two different measurement points of Q_{air} (before dust introduction, and after dust settlement). $Q_{+\infty}$ was generally larger than $Q_{-\infty}$ (resulting in lower ΔQ), probably because some dust still adhered to the tube wall after settlement, increasing the wall absorption coefficient, a. However, it is not clear whether the dust adhered to the walls during dust introduction (in which case $Q_{+\infty}$ would be the valid measure of Q_{air}) or whether it adhered during settlement (in which case $Q_{-\infty}$ would be more valid), or both. Hence ψ was calculated both ways: the upper limits of the error bars use $Q_{air} = Q_{-\infty}$, the lower limits use $Q_{air} = Q_{+\infty}$. The true values of ΔQ are probably bracketed between the bars. Little difference is noticeable over most frequency bands.

Finally, the applicability of the theoretical expression for excess decay rate was investigated. From (7.6) and (7.20) an expression for theoretical decay sensitivity can be found:

$$\psi = \frac{\partial}{\partial \phi}(\Delta Q) = 20c \log_{10} e \cdot \frac{d\alpha_{dust}(f)}{d\phi} \qquad (7.23).$$

The long wavelength model of Lloyd & Berry [85], described in Chapter 2, was used to predict $\frac{d\alpha_{dust}(f)}{d\phi}$, and hence $\psi(f)$.

This predicted value of decay sensitivity is independent of any geometrical considerations (modal structure etc.), and depends only on the variation of α_{dust} with frequency. It is plotted in Figure 7-11, together with the measured values of ψ.

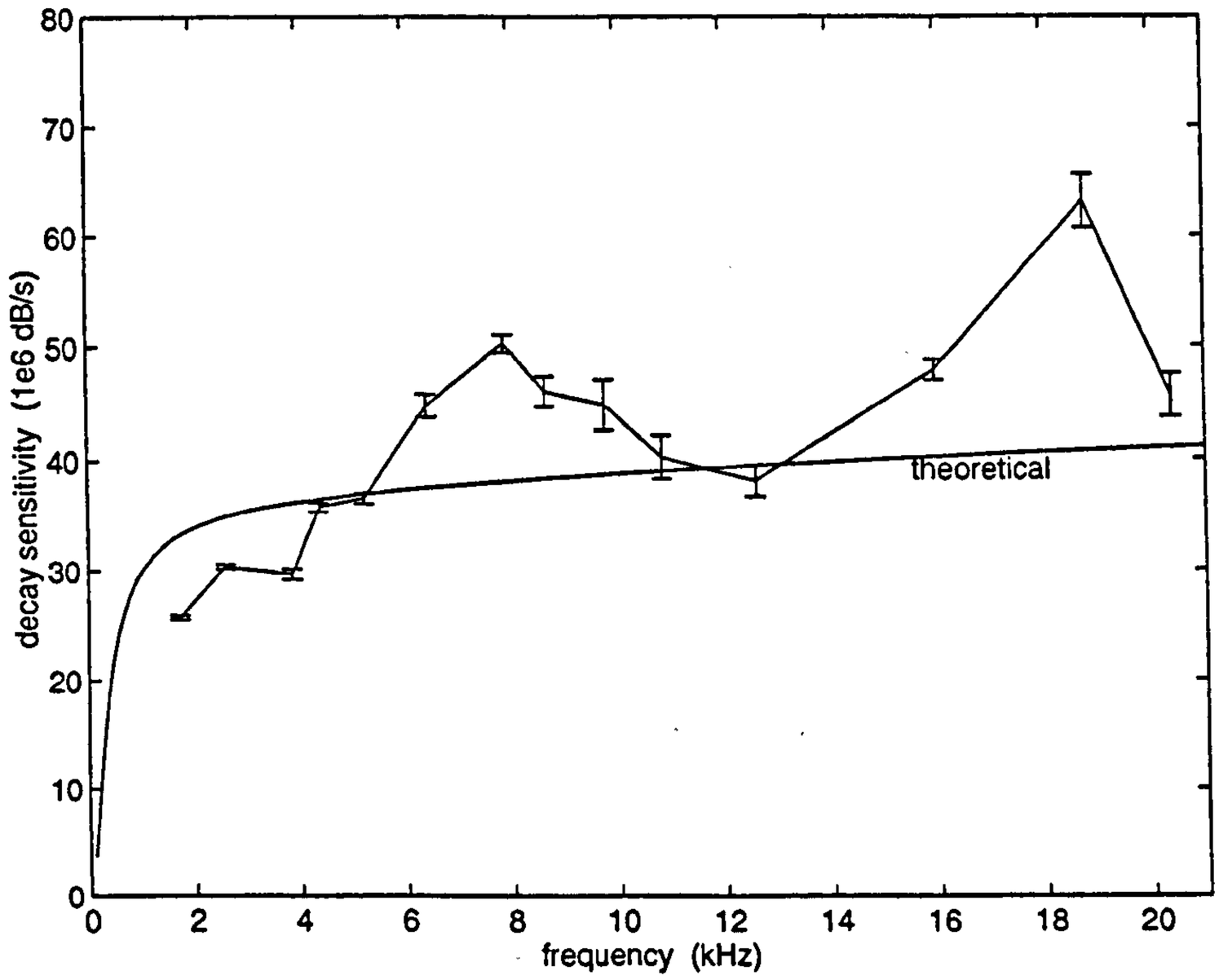

Figure 7-11 *Decay sensitivities: theoretical and mode-picking filter bank.*

Clearly, while the general scaling and trend of the theoretical curve are similar to that measured, there are some significant excursions. These excursions are predominantly positive, representing regions that are more sensitive to medium attenuation than predicted. The explanation for the excursions can probably be found in the initial assumption (of equation (7.1)) that the decay is exponential. This assumption will be correct if the sound field is fully diffuse; however, the geometry of the apparatus will create an ordered (non-diffuse) field, and so the assumption of exponential decay must be an approximation within a given segment of decay.

20) were judged to be insufficiently exponential, and so their ΔQ values were rejected, and the corresponding points are missing from Figure 7-9.

The three parameters $\langle r_{dec} \rangle$, r_ψ and ψ, for this bank of filters, are shown in Figure 7-10.

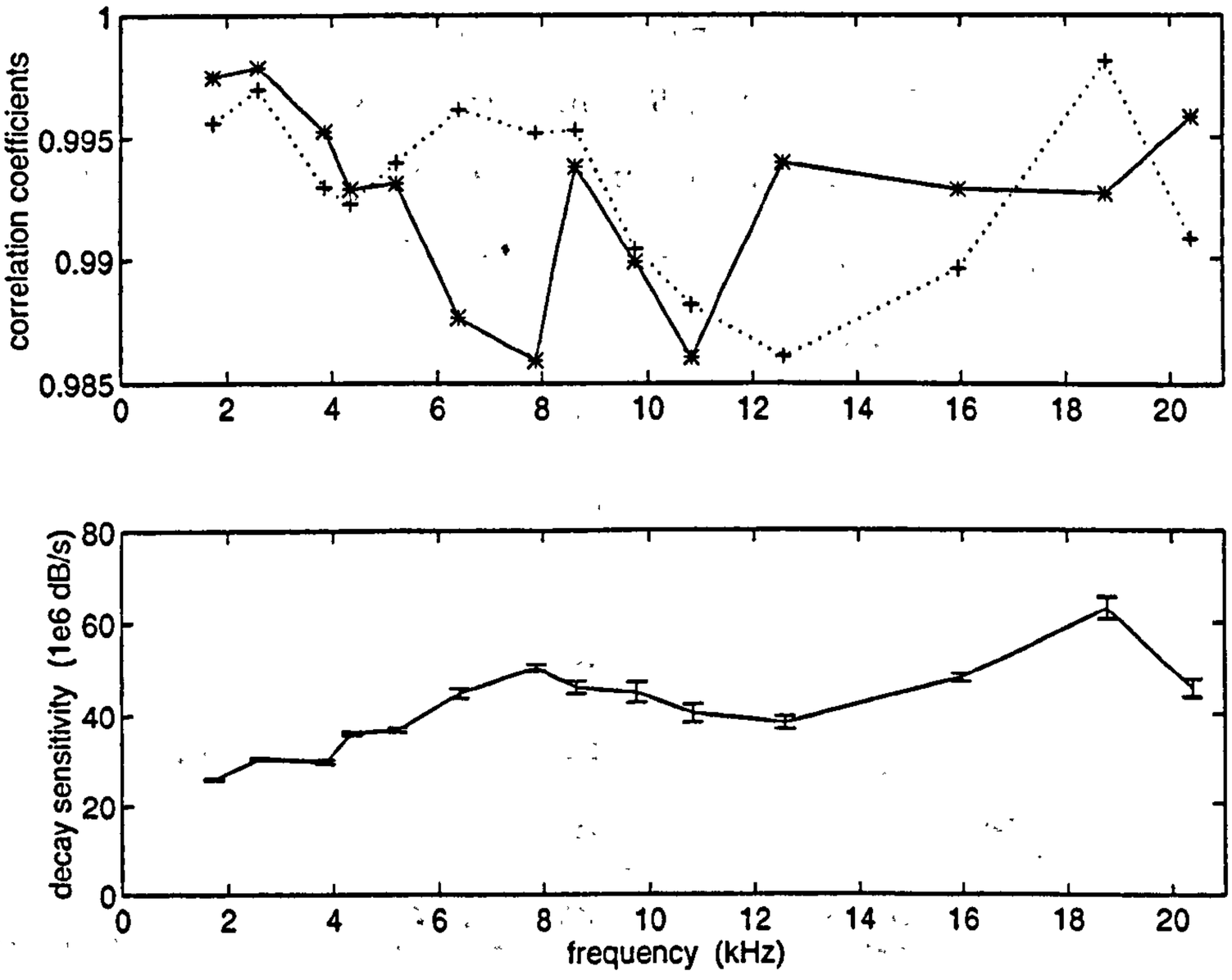

Figure 7-10 Mode-picking filter bank results. Upper axis: r_{dec} (solid), r_ψ (dotted); lower axis ψ.

Error bars are shown on the curve of ψ, to indicate the variation caused by using the two different measurement points of Q_{air} (before dust introduction, and after dust settlement). $Q_{+\infty}$ was generally larger than $Q_{-\infty}$ (resulting in lower ΔQ), probably because some dust still adhered to the tube wall after settlement, increasing the wall absorption coefficient, a. However, it is not clear whether the dust adhered to the walls during dust introduction (in which case $Q_{+\infty}$ would be the valid measure of Q_{air}) or whether it adhered during settlement (in which case $Q_{-\infty}$ would be more valid), or both. Hence ψ was calculated both ways: the upper limits of the error bars use $Q_{air} = Q_{-\infty}$, the lower limits use $Q_{air} = Q_{+\infty}$. The true values of ΔQ are probably bracketed between the bars. Little difference is noticeable over most frequency bands.

Finally, the applicability of the theoretical expression for excess decay rate was investigated. From (7.6) and (7.20) an expression for theoretical decay sensitivity can be found:

$$\psi = \frac{\partial}{\partial \phi}(\Delta Q) = 20c \log_{10} e \cdot \frac{d\alpha_{dust}(f)}{d\phi} \qquad (7.23).$$

The long wavelength model of Lloyd & Berry [85], described in Chapter 2, was used to predict $\frac{d\alpha_{dust}(f)}{d\phi}$, and hence $\psi(f)$.

This predicted value of decay sensitivity is independent of any geometrical considerations (modal structure etc.), and depends only on the variation of α_{dust} with frequency. It is plotted in Figure 7-11, together with the measured values of ψ.

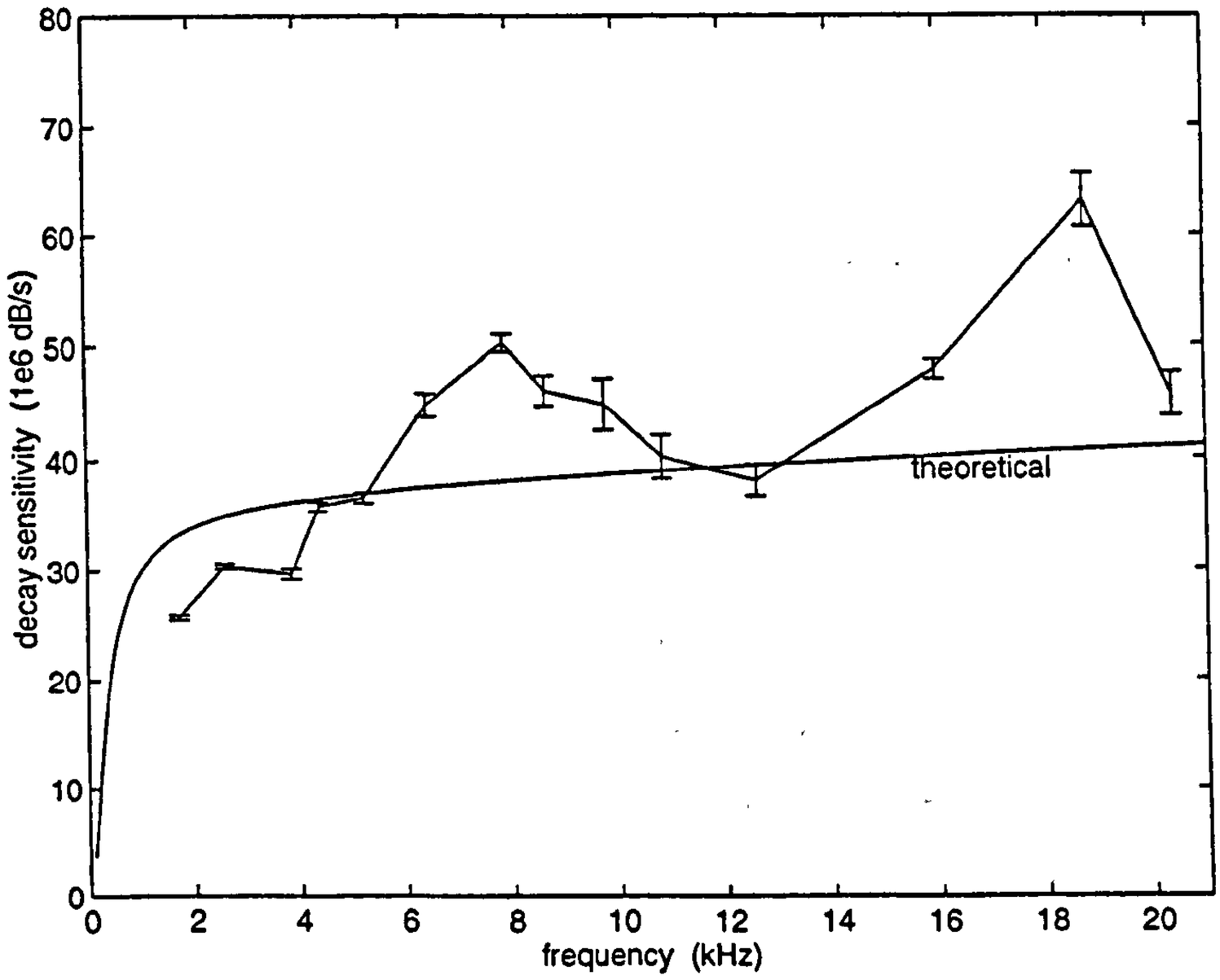

Figure 7-11 Decay sensitivities: theoretical and mode-picking filter bank.

Clearly, while the general scaling and trend of the theoretical curve are similar to that measured, there are some significant excursions. These excursions are predominantly positive, representing regions that are more sensitive to medium attenuation than predicted. The explanation for the excursions can probably be found in the initial assumption (of equation (7.1)) that the decay is exponential. This assumption will be correct if the sound field is fully diffuse; however, the geometry of the apparatus will create an ordered (non-diffuse) field, and so the assumption of exponential decay must be an approximation within a given segment of decay.

7.3 DECAY RATE IN FLOWING SUSPENSIONS

The technique described above in Section 7.2 was designed to measure small quantities of particulate in a static, enclosed suspension. The question then arose: will the same technique still be useful when applied to a flowing suspension? The main differences that indicate against its use are:

- The level of background noise is much higher, therefore reducing the range of decay curve, and hence the estimation accuracy of the decay rate.
- The longer, narrower tube approximates to an infinitely long tube, and so acoustic energy will tend to propagate away from the measuring volume – indeed, the concept of a measurement volume is less valid. The signal level will be comparatively lower and the reverberant field becomes even less diffuse. This will further compromise any theoretical predictions that rely on assumptions of diffusivity.
- Because of the open nature of the system, the decay rates will be larger, and therefore there will be a shorter segment of decay from which to measure the decay rate.
- The effects of flow on reverberant decay are unclear. The shift in modal frequency and change in modal shape have been mentioned in Chapter 3; in themselves, they should not appreciably affect the decay rate.

7.3.1 Experimental arrangement

The major difference from previous measurements of reverberant decay, was to offset the driver port from the microphone port by 0.7m, and the axial angle between the two ports was arranged to be 90°. This was done to reduce direct impingement of the signal on the microphone, and hence to reduce the proportion of the received signal that is due to the direct wave. This decreases the (anomalous) early decay portion and hence gives a longer decay curve from which to estimate the decay rate. The arrangement is illustrated in Figure 7-12.

The high frequency compression driver was used, with the MLS signal filtered by a 3000Hz high-pass filter to increase the maximum signal level obtainable in the frequency range of interest. The microphone in the probe arrangement was placed in a port downstream. The signal level received at the microphone was 130 dB; despite this high level, the signal/noise ratio still approached 0dB, while to extrapolate a reasonable decay curve, a S.N.R. of approximately 30dB is desirable (15dB is feasible). While the MLSSA system inherently increases the SNR, time domain averaging was additionally required to increase it sufficiently.

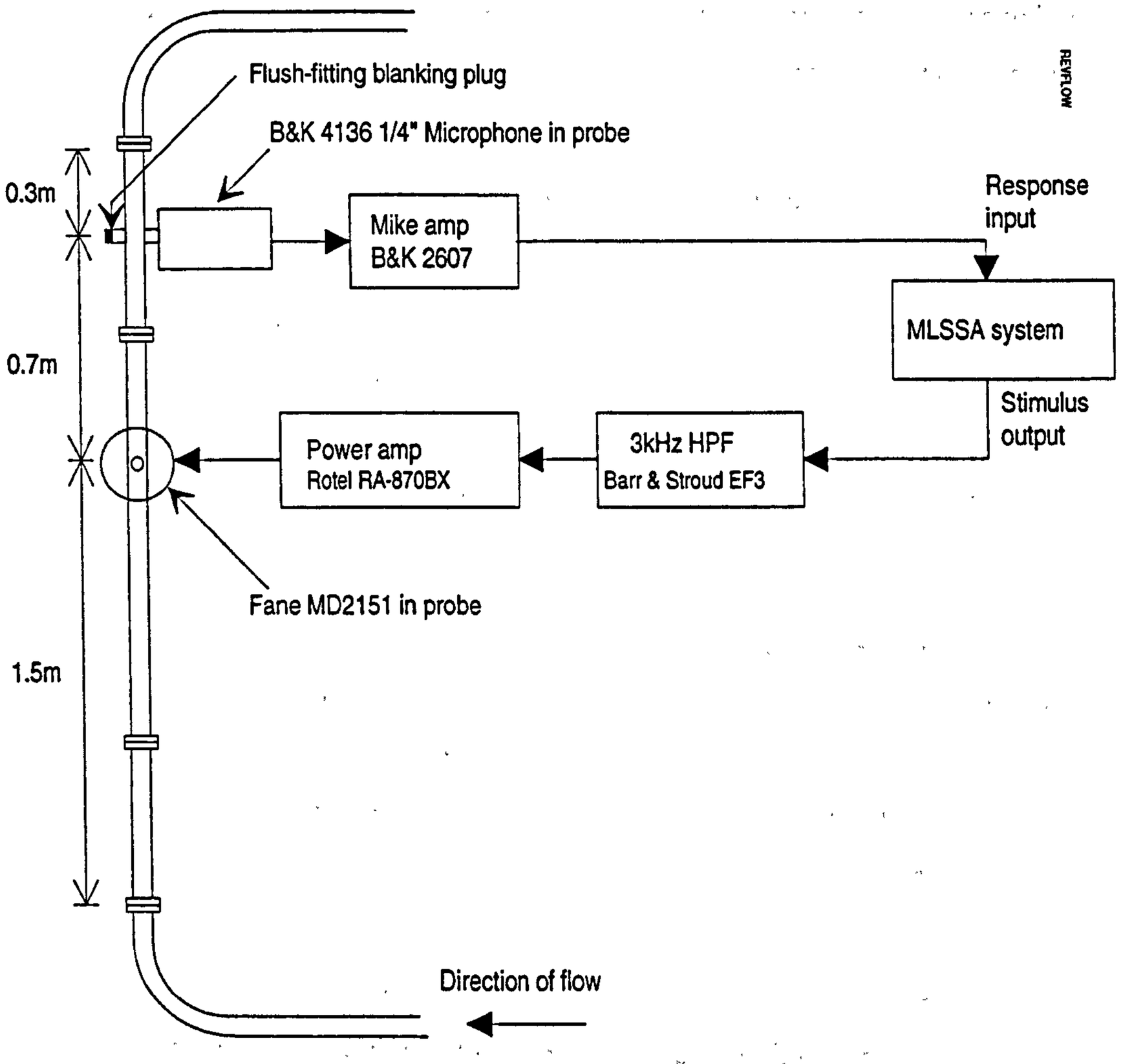

Figure 7-12 *Apparatus to measure the reverberant decay in flowing suspensions.*

Two sets of data were taken on different materials and using slightly different techniques to measure the particle concentration. As explained in Section 5.6, the mass flow rate can be calculated from either a long term average or a local estimate of the gradient of the gain-in-weight trace. The first dataset, measured on flour, used local estimates of the mass flow rate over the duration of each measurement and correlated instantaneous acoustic measurements with these local values; the second dataset, measured on olivine sand, used a long term average (of several minutes) measurement of mass flow rate, and consists of multiple acoustic measurements which were processed separately, and then the decay rates for each segment were averaged together to compare with the long term average for that segment. The two sets of data are presented in sections 7.3.3 and 7.3.4.

7.3.2 Analysis

The analysis method is similar to that performed on static suspensions, except that a different algorithmic method was used to calculate decay rates. The higher noise level in flowing suspensions and the reduced straight-line decay range made the linear fitting routine susceptible to error. The selected technique was the non-linear fitting routine devised by Xiang [163], which is

described in Appendix H[1]. Conversely, the non-linear fitting algorithm does require a moderate level of noise to operate correctly, and so was found to be unreliable on decay curves measured in quasi-static suspensions.

The major difference from measurements on enclosed, static suspensions is the presence of much higher decay rates. In the enclosed volume, the decay rates all satisfied Jacobsen's requirement

$BT_{60} > 16$, where T_{60} is the 60dB decay time of the system. In the unenclosed system, the T_{60} becomes small enough to violate this condition, and hence the impulse response of the filter would distort the measured decay rate. To reduce this source of error, the technique of reverse filtering is used. This reduces the inequality to the less stringent requirement,

$BT_{60} > 4$.

For high mass concentrations, however, this condition is still violated, and the decay rate approaches that of the {loudspeaker probe + microphone probe + filter} system (10000 dB/s wideband). The system decay rate imposes a ceiling level, and so when decay curves approach this ceiling, they are significantly influenced by that of the decay of the system. Such decay curves were rejected when decay rate is calculated.

A way to avoid discarding such decay curves was attempted: this relied on deconvolving the {loudspeaker probe + microphone probe + filter} impulse response from the measured decay curve, using an FFT division technique (numerical deconvolution was unstable, probably due the large number of zeros in the function). Resulting curves showed such fast decay that curve fitting was no longer accurate, due to the small number of points on the decay. It was concluded that the reverberant decay technique was no longer workable at such decay rates.

The filter bank was designed by reference to the measured and predicted modal structure; further heuristic iteration did not provide many improvements. Again, the filters were selected to span clusters of modal peaks, immediately above the cut-on frequency of a transverse mode. The relationship between the filters (top) and the tube modes (top: measured, and bottom: theoretical) is shown below:

[1] The programs that implements the algorithm (REV_MAIN & DECRAFIT.M) are listed in Appendix B

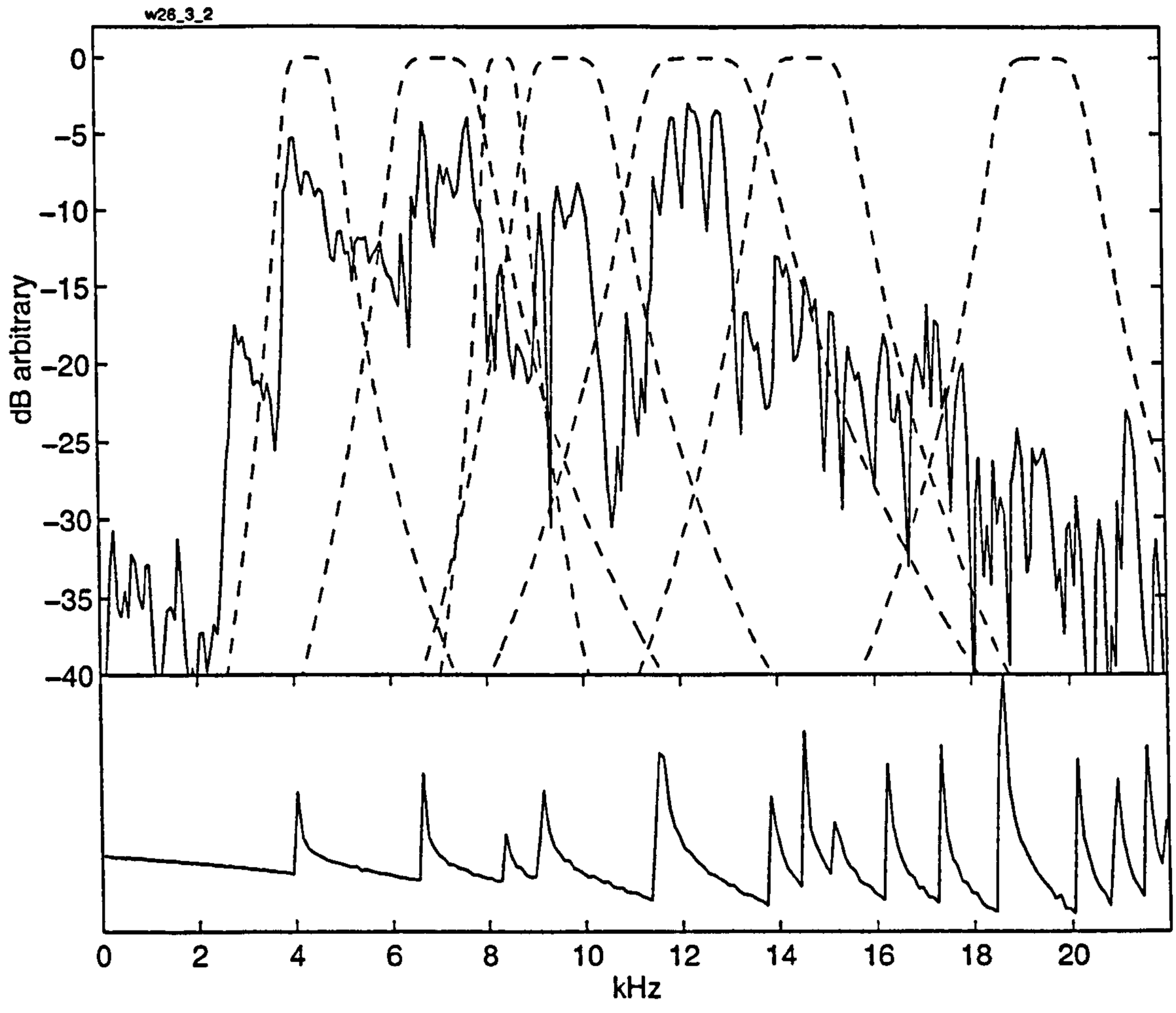

Figure 7-13 Top: Filter shapes, and spectrum of measured impulse response (top). Bottom: Theoretical modal density (arbitrary, detrended axis to remove f^2 dependence), assuming acoustic tube length of 11m

The analysis again uses the two correlation coefficients r_{dec} and r_{ψ} as benchmarks:

When calculating r_{ϕ}, decay curves with $r_{dec} < 0.96$ were rejected as being excessively curved.

7.3.3 Measurements on flowing flour

Each impulse response was measured using 10 time domain averages. This figure was found to give optimum SNR: more averages reduced S.N.R, possibly because the time duration of the measurement allowed significant variations in flow conditions.

A total of 28 measurements were taken at varying mass concentrations up to almost 2.5 kg/kg, and a constant superficial air-speed of 20 m/s nominal. However, the decay rate in suspensions above 1kg/kg was so high, that these data were discarded, reducing the useful data to 17 measurements.

To assess the necessity of performing narrow-band analysis, initially a broadband (unfiltered) analysis was made of the decay rate.

The decay curves were visually very curved, and had a mean value of r_{dec} of 0.969. This contrasts with the observed result in the enclosed volume, where the decay curves were very linear ($\langle r_{dec} \rangle$ = 0.998). In common with the enclosed volume, the correlation of excess decay rate with concentration is very poor (0.388). Clearly the measurement of wideband excess decay rate does

not provide much useful information about dust concentration, and so narrow band analysis was pursued.

The filter bank illustrated in Figure 7-13 was used to calculate excess decay rate in 7 frequency bands.[1] A straight line was fitted to points derived from reasonably linear decay curves (r_{dec} > 0.96), and the gradient of this line gave the decay sensitivity ψ.

The correlation coefficients $<r_{dec}>$ and r_{ψ} are shown in Figure 7-14. The mean correlation coefficient of the decay curves $<r_{dec}>$ is reasonably large (>0.97) at all except the band centred on 9.8 kHz. This latter band also appears to exhibit a weak negative correlation between ϕ and excess decay rate, (and hence a negative decay sensitivity); this is discussed in the next section.

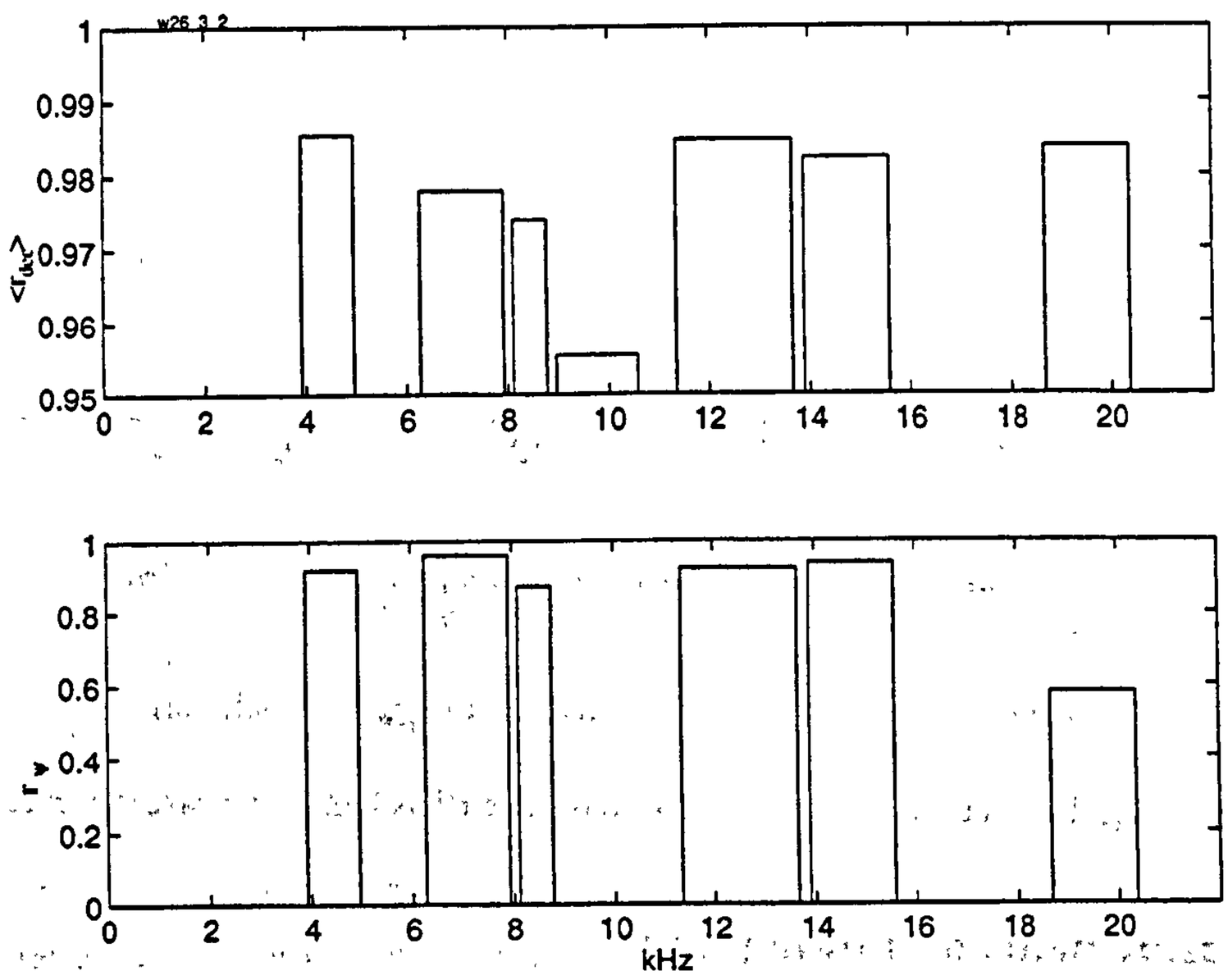

Figure 7-14 Correlation coefficients (in flowing flour) across frequency bands: $<r_{dec}>$ (top) and r_{ψ} (bottom). Width of bars corresponds to the -3dB width of the filters.

[1] It could be argued that the filters should track the change in modal frequency as the solids loading changes. However, it will be shown in section 7.4 that the frequency shift is negligible (<20Hz).

The decay sensitivity, measured in (dB/s)/(kg/kg) is plotted in Figure 7-15, together with the theoretical prediction, made by evaluating equation (7.6) for the theoretical attenuation coefficient at a concentration of 1kg/kg.

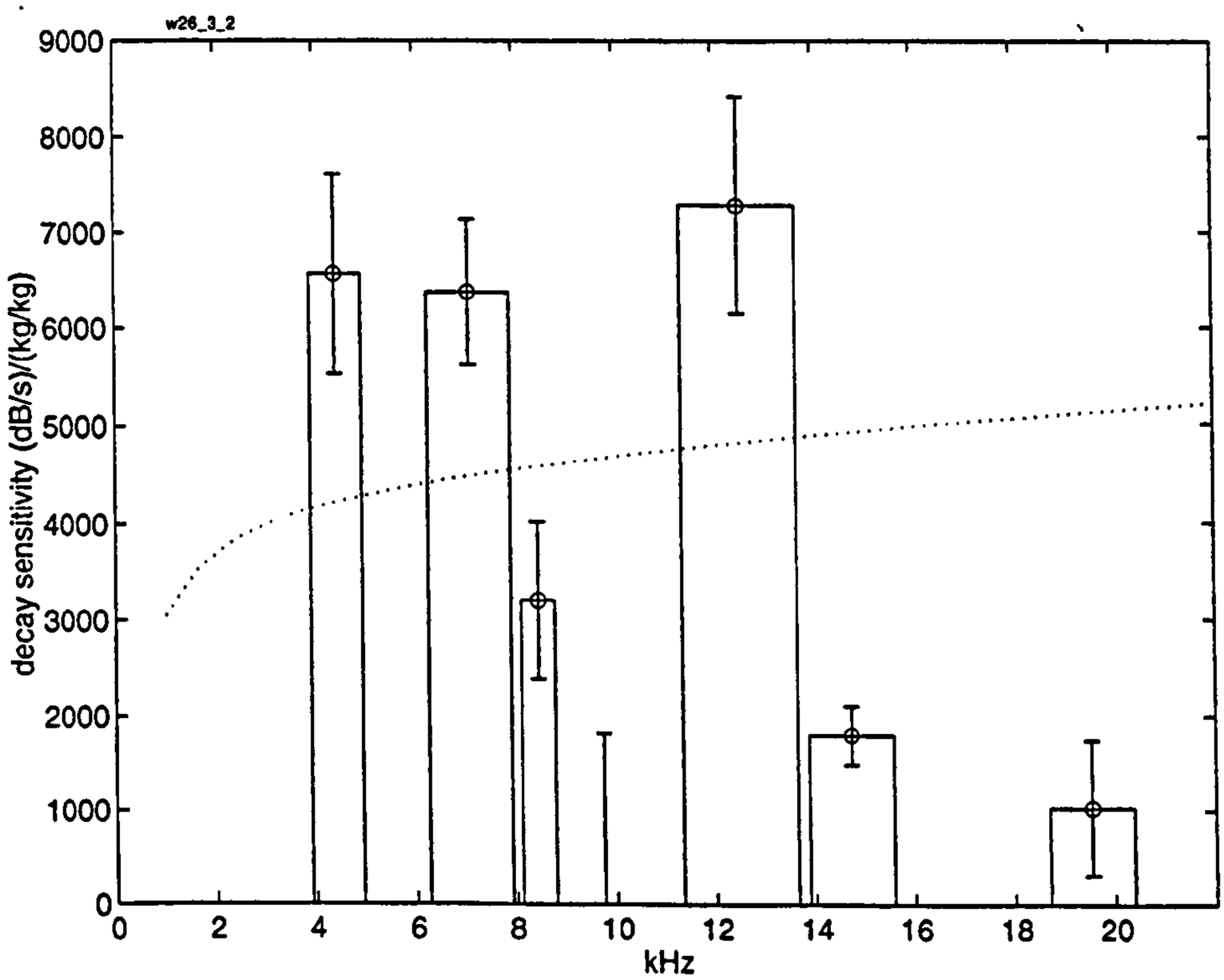

Figure 7-15 Decay sensitivity , ψ, in flowing flour for each frequency band. Error bars indicate the 90% confidence interval. Theoretical ψ (dotted line) is also shown.

7.3.4 Measurements on flowing sand

This dataset consists of 75 separate measurements (using 5 time domain averages each) at 9 concentrations of flowing olivine sand. Due to the sensitivity of the technique, this study was restricted to concentrations below 0.7 kg/kg. The individual impulse responses were processed to yield narrow-band excess decay rate, using the same filter bank as section 7.3.3, and then the decay rates for each concentration were averaged together and compared with the long term concentration measured using the gain-in-weight signal.

The averaged excess decay rates in each band are plotted against the mass concentration of sand in Figure 7-16; before averaging, decay curves with $r_{det} < 0.96$ were rejected as being excessively curved.

The correlation coefficients $\langle r_{det} \rangle$ and r_{ψ} are shown in Figure 7-17; the decay sensitivities of each frequency band are shown in Figure 7-18.

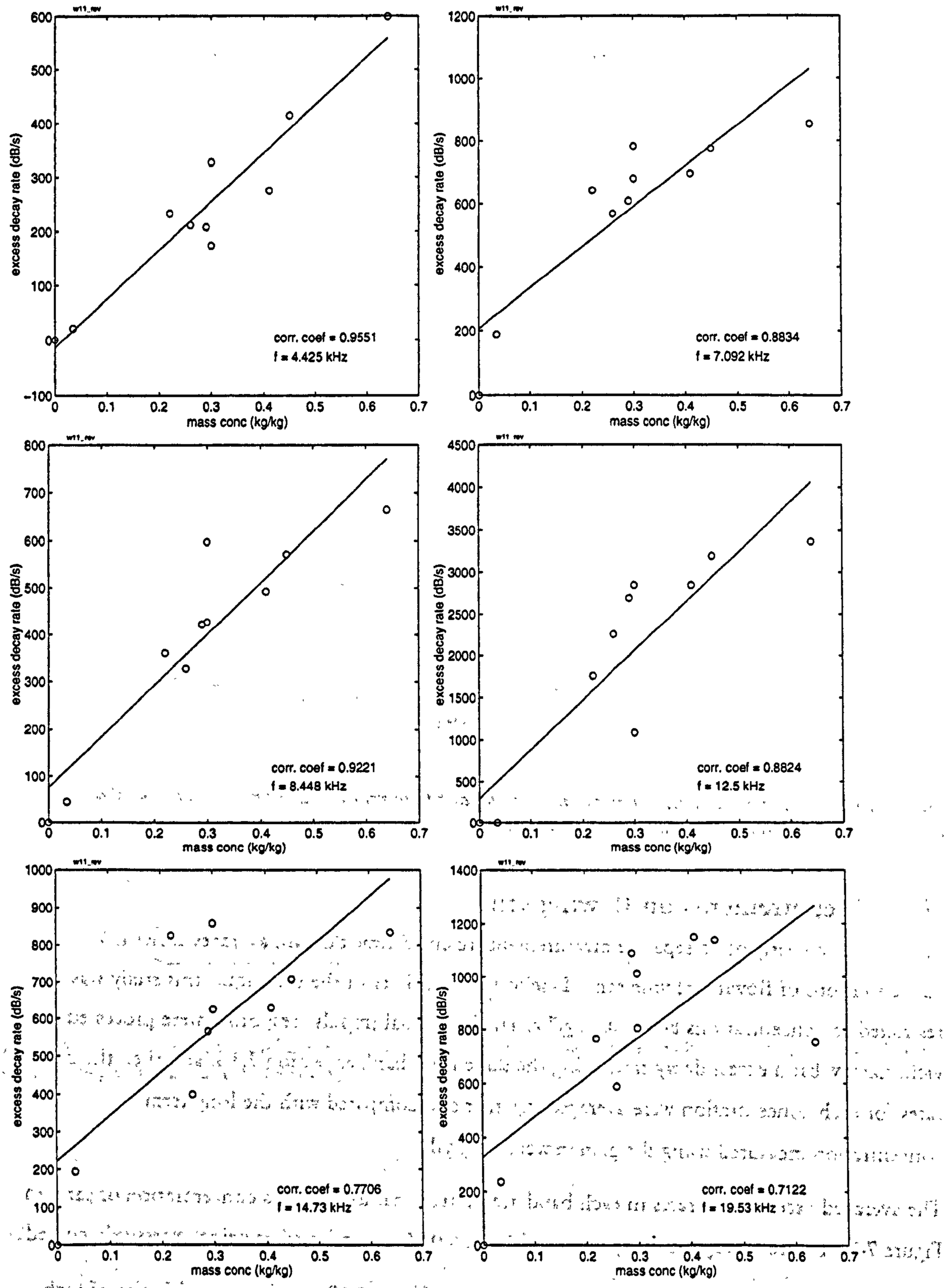

Figure 7-16 Example plots of narrow-band excess decay rates against mass concentration ϕ_m of flowing sand against: r_ψ of the straight line fit (solid line) is also shown.

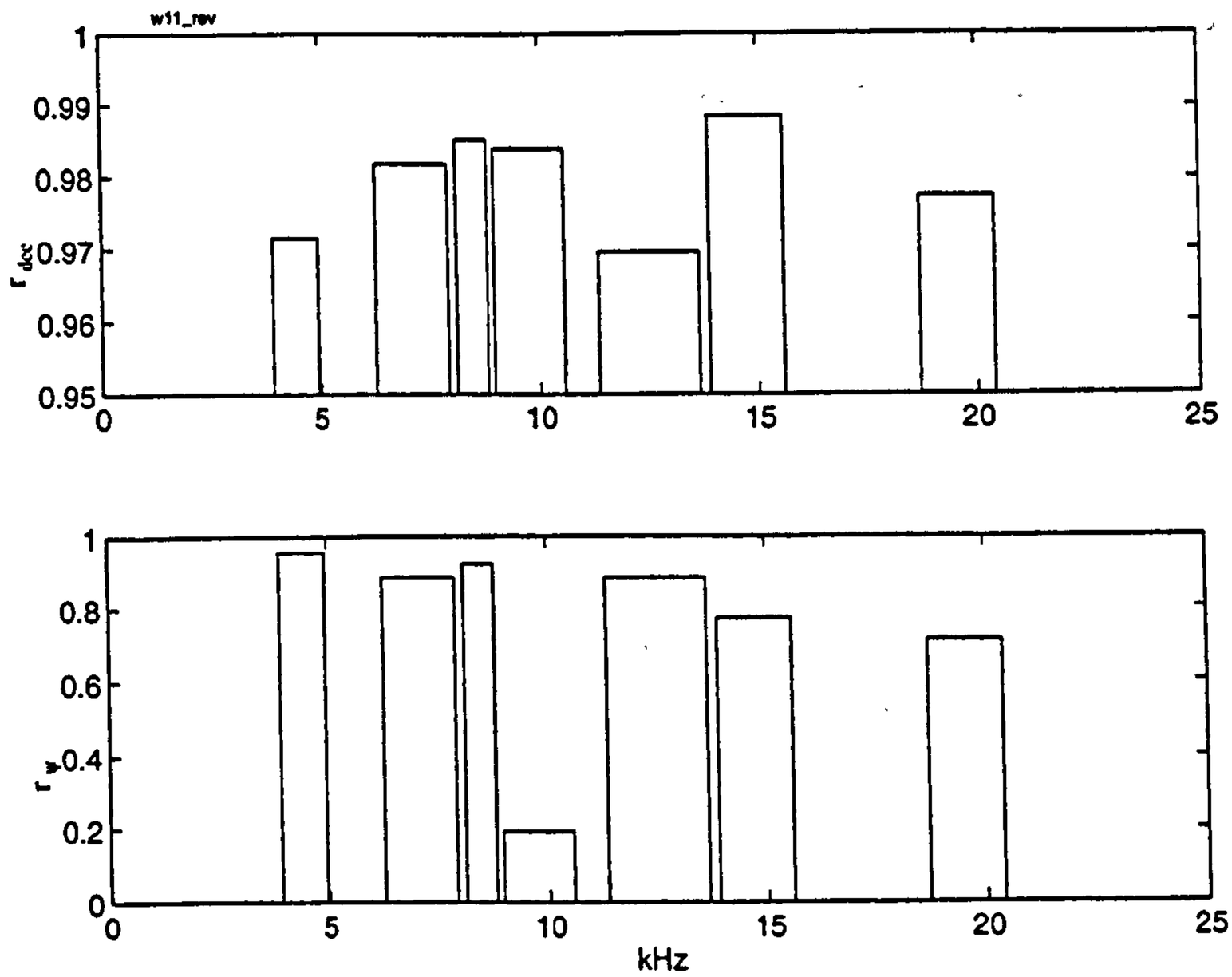

Figure 7-17 *Correlation coefficients of decay in flowing sand : $\langle r_{dcc} \rangle$ (top) and r_ψ (bottom). Width of bars indicates the -3dB width of the filters.*

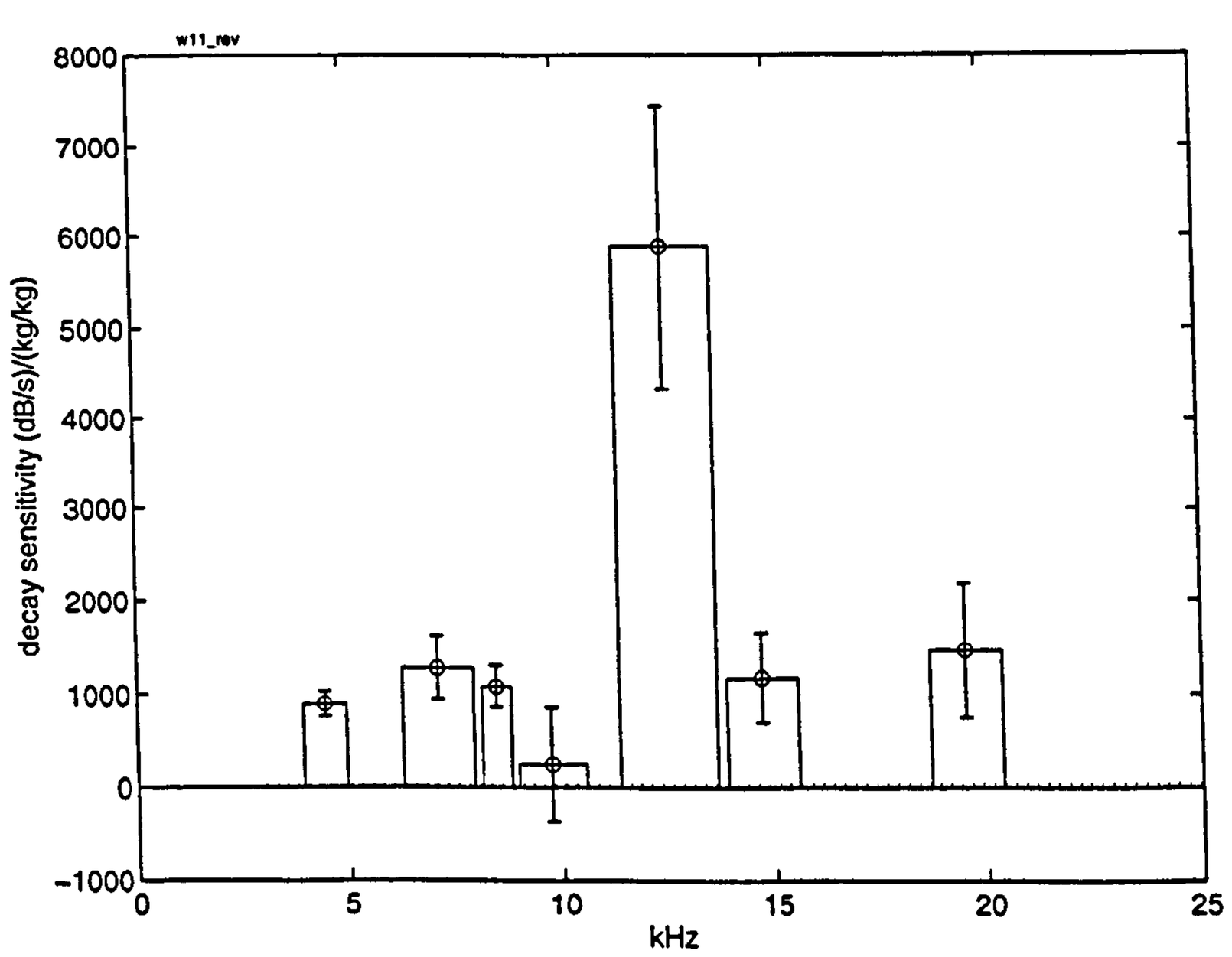

Figure 7-18 *Decay sensitivity ψ for flowing olivine sand in selected frequency bands. Error bars indicate the 90% confidence limits. The theoretically predicted curve is indistinguishable from the x-axis, rising from 16 to 45 dB/s.*

7.3.5 Discussion

The correlation coefficients r_{der} and r_{ψ} are generally lower than those in the quasi-static case, due to the higher noise levels and faster decay rates. It is nonetheless still possible to extract reasonable linear correlations between excess decay rate and concentration in some frequency bands. There appears to be little similarity between the patterns of decay sensitivity in the three cases. However, the band centred on 12.5 kHz shows an anomalously high decay sensitivity in both flour and sand. We may observe that this band encompasses the first occurrence of two closely-spaced ("degenerate") transverse modes: the (0,4) mode at 11.5 kHz and the (1,1) mode at 11.6 kHz, which are visible on the modal density plot (Figure 7-13) as a large peak. The peak is also well isolated from surrounding clusters. However, the filter centred on 19.5 kHz, which also encompasses two degenerate modes (18.5 & 18.6 kHz) shows a low decay sensitivity.

The filter centred on 9.8 kHz produced decays that showed little correlation between ΔQ and ϕ: indeed, it exhibits a negative correlation in the measurements on flour. In the latter case, the decays were significantly curved, with $r_{der} = 0.95$, although this was not the case with sand.

The decay sensitivity of reverberant sound in a flow of flour, while varying widely between different bands, generally encompassed the predicted curve. That of flowing sand, however, was several orders of magnitude higher than the prediction, with even greater variation between the bands.

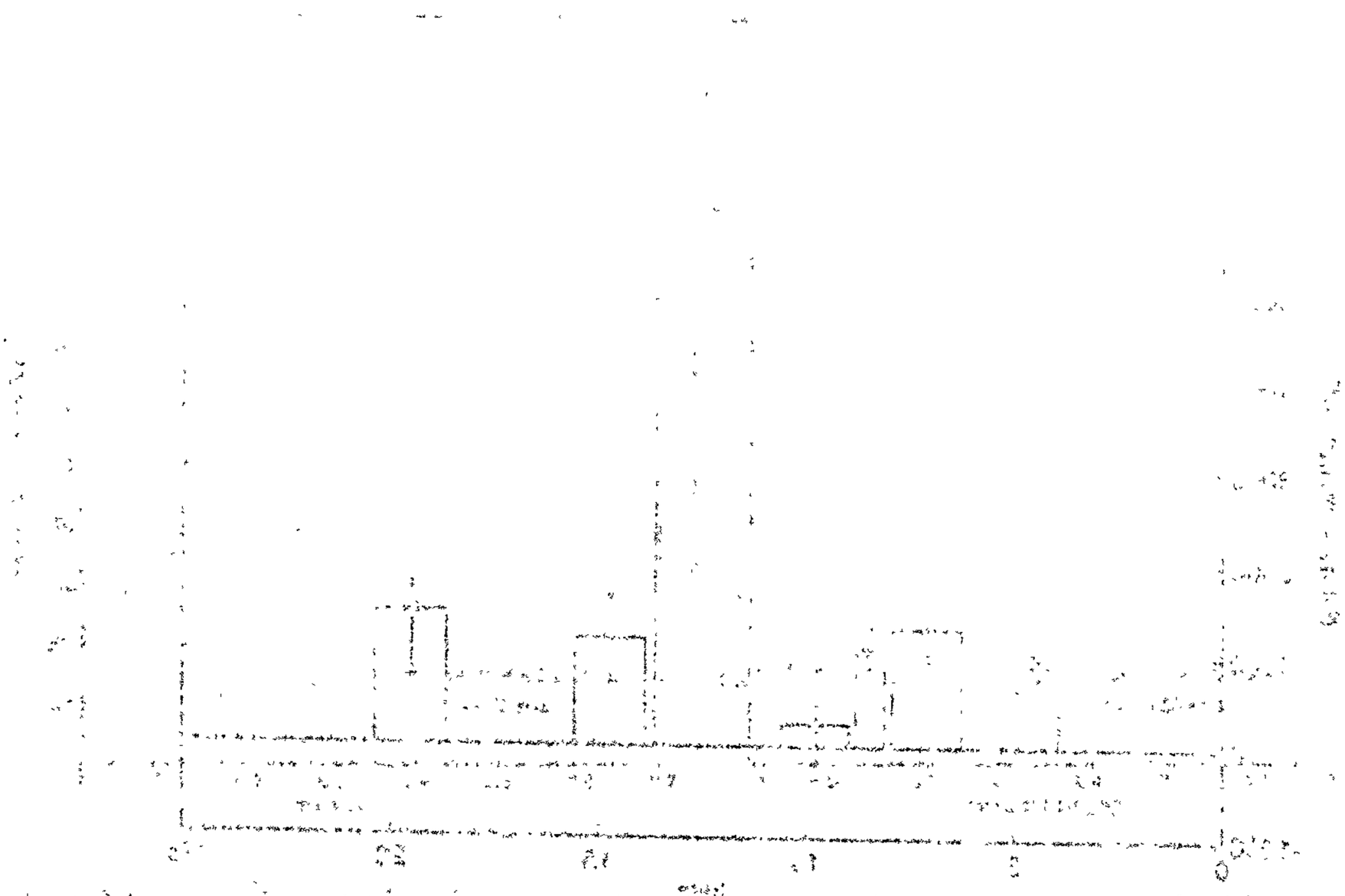

7.4 MODAL FREQUENCY SHIFT

Vetter & Culick's theory to predict modal frequency shift assumed that the tube is infinitely long. In this case, the transverse modes exist in isolation, unmodified by longitudinal modes, and therefore the frequency of individual modes may be tracked. Due to the finite tube length, we have observed both theoretically (Figure 7-2) and experimentally (Figure 7-13) that measured spectra do not exhibit isolated peaks, but rather complex clusters of modes that cut on above a reasonably well-defined frequency. Therefore, there are practical problems in trying to track the frequency of single mode; for example, it may be impossible to tell the difference between a modal frequency shift, and the change in relative amplitude between two closely spaced modes. This problem is further exacerbated at high concentrations, where the modal peaks are broadened and attenuated, until they become buried in the surrounding noise spectrum.

7.4.1 Frequency shift in flowing flour — from impulse response

To make an assessment of the actual modal frequency shift, impulse response data was used from the previous reverberation measurements on flowing flour. Each impulse response was Fourier transformed with a very high frequency resolution (4.5Hz)[1]. The lowest transverse mode (0,1) was inspected, since this has the largest separation from adjacent modes, and is quite prominent. Furthermore, in contrast to attenuation coefficient, the sound velocity change decreases with increasing frequency, and so the largest frequency shift should be observed at the lowest modal frequency.

Initially, the shift due to airflow alone was investigated. Figure 7-19 shows that clean air-flow at 20m/s reduces the cut-on frequency of the (0,1) mode by approximately 18 Hz (the spectrum is repeatable before and after dust flow).

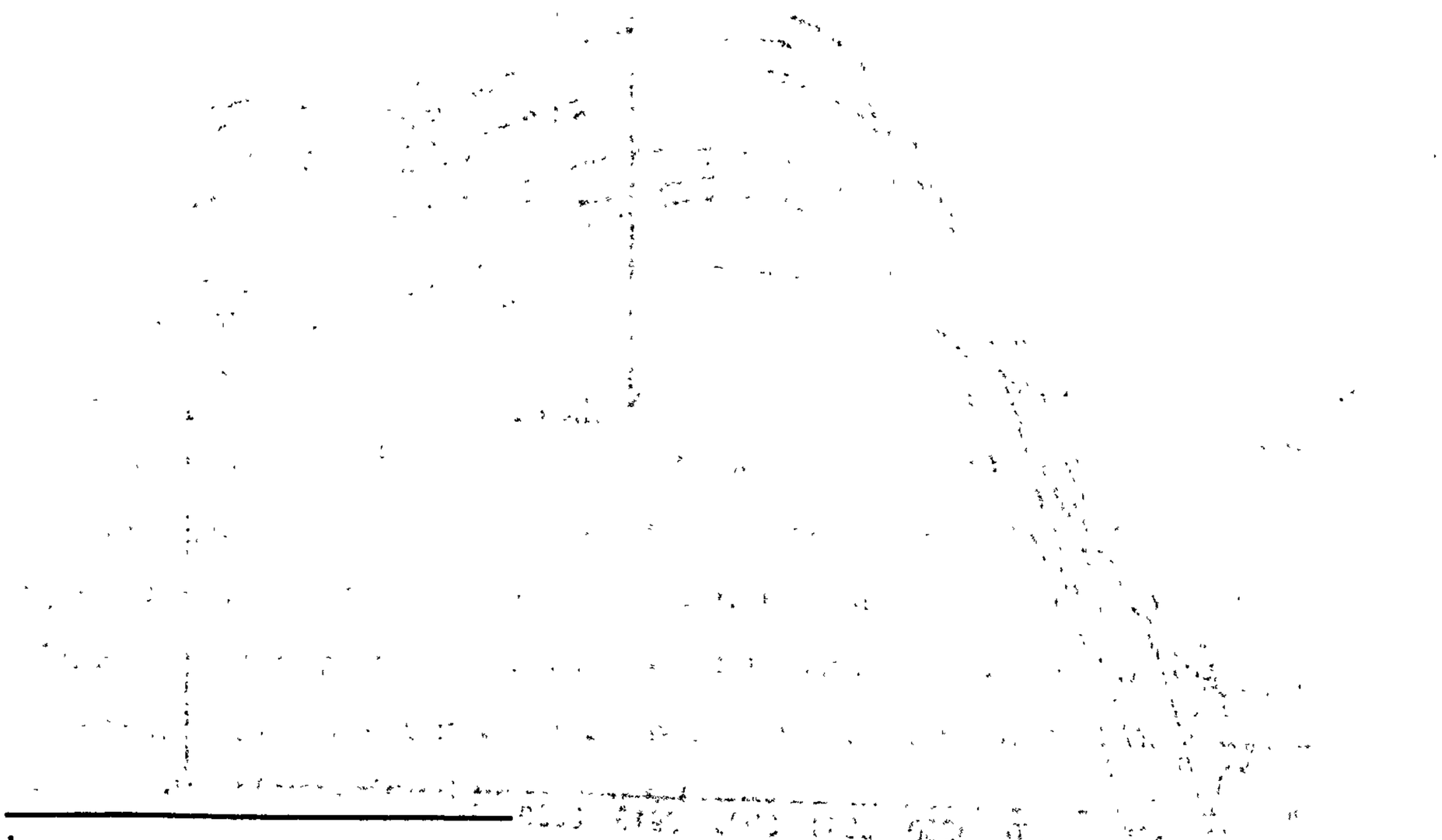

[1] The segment of data (4000 samples) was zero-padded to give a 16 k sample FFT. This method can give a modest increase in the frequency resolution over, say, a 4k sample transform [72].

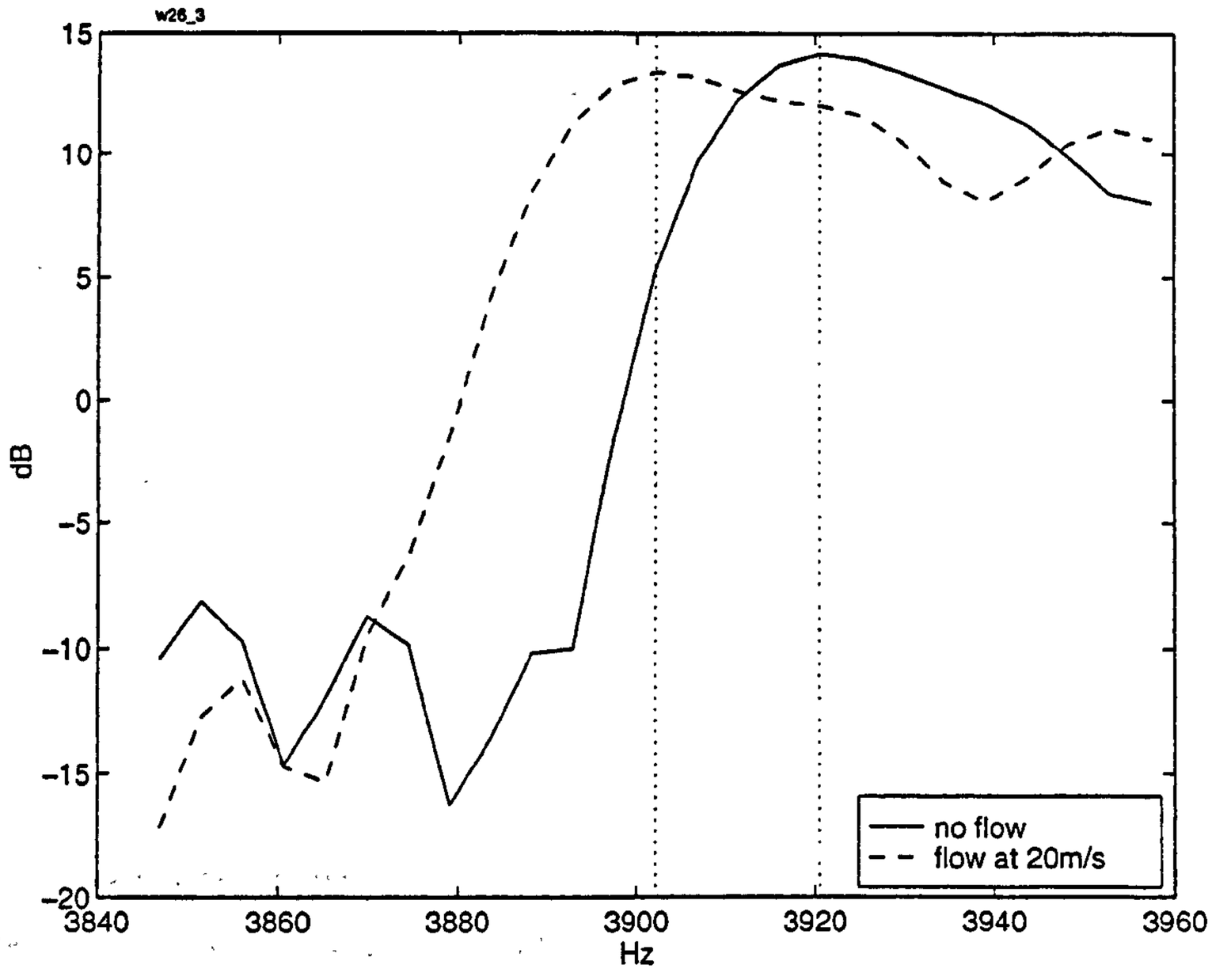

Figure 7-19 *Spectrum of transverse mode (0,1) with and without airflow at 20m/s.*

The expected shift due to airflow can be predicted using equation 3.14 [49]. Substituting a value of $M = 20/340$ gives a value of $f'_{m,n} - f_{m,n} = 7$ Hz.

In the following measurements with varying levels of suspension loading, all the zero-loading reference spectra are measured with clean air flow at the nominal rate of 20m/s. Therefore, changes in spectra due to the presence of a suspension are additional to the shift due to flow alone.

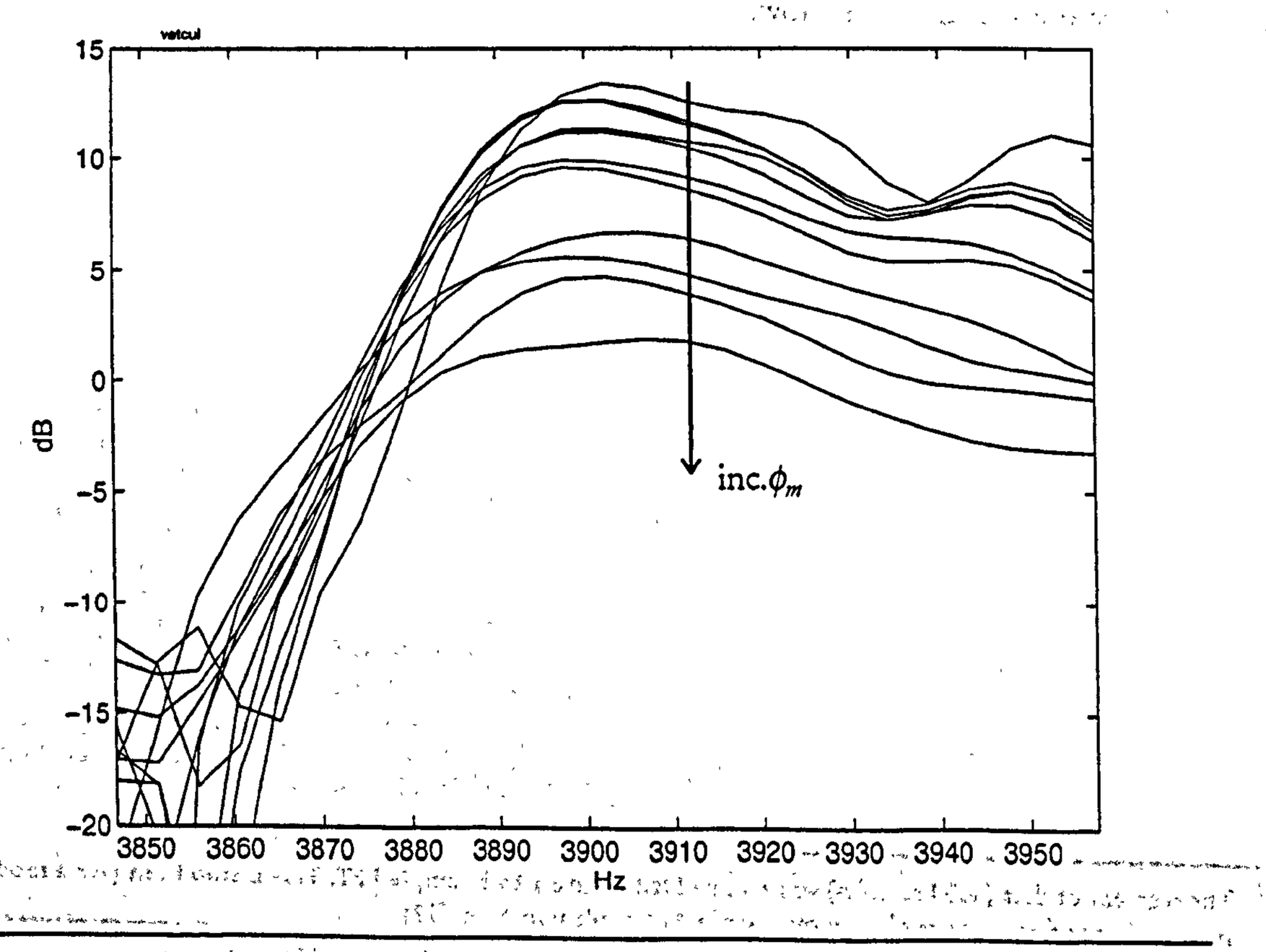

Figure 7-20 High resolution spectrum around the (0,1) mode cut-on frequency, with parametrically varied mass concentration of flour ϕ_m = 0 to 0.45 kg/kg.

Figure 7-20 shows spectra around the (0,1) mode with suspension flow up to a concentration of 0.45 kg/kg (above this concentration, the (0,1) cluster is obscured by noise, or attenuated strongly, and an adjacent resonance becomes dominant.) The most noticeable effect is the decrease in amplitude of the peak; the frequency of the maximum does not show any consistent shift, although there does appear to be a decrease in the frequency of first cut-on. This latter effect is demonstrated by taking a horizontal section through the curves at a heuristically chosen value of -10dB. The frequency at which each spectrum crosses this value was calculated (using interpolation to increase the frequency resolution), and displayed in Figure 7-21 as a function of mass concentration.

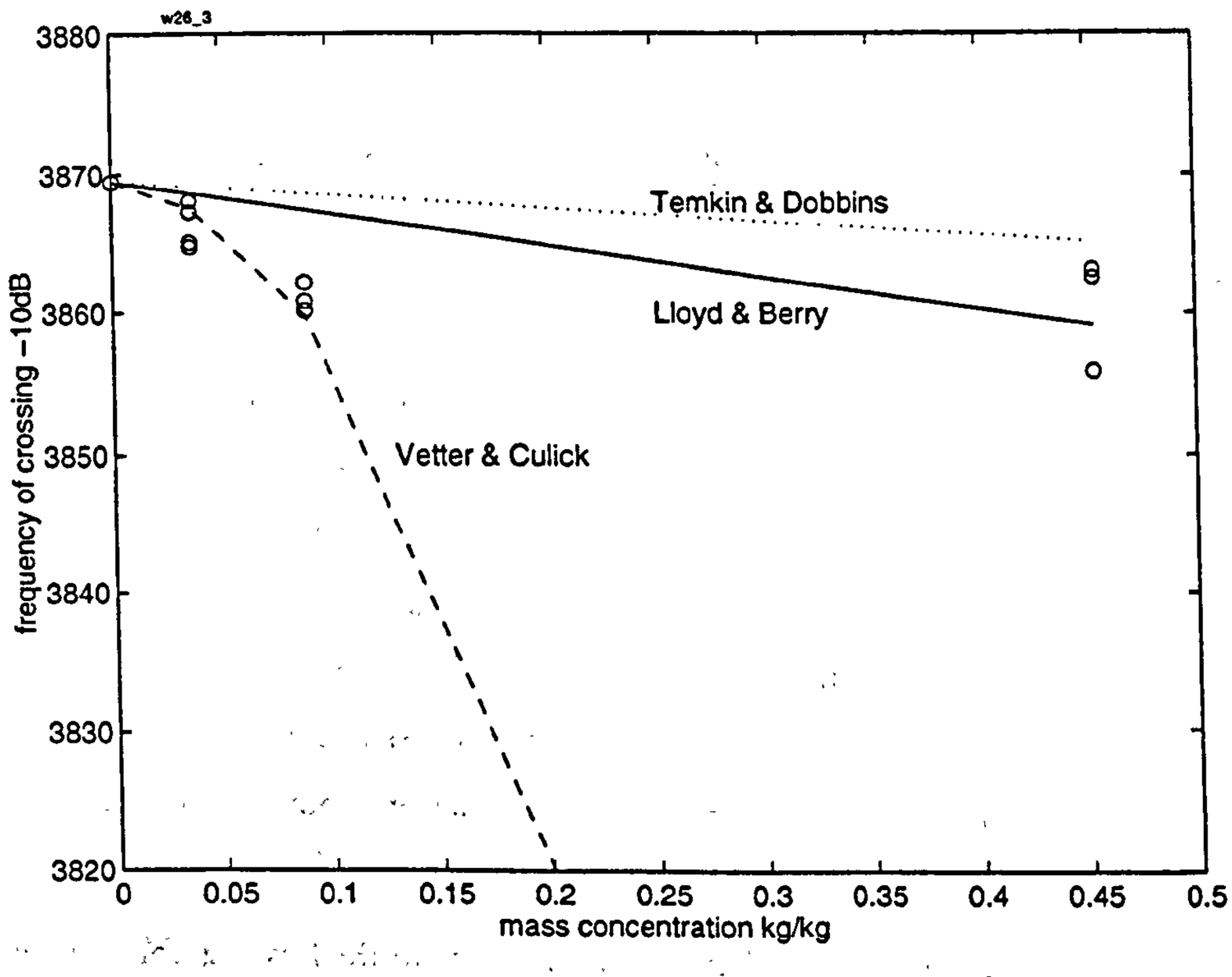

Figure 7-21 Nominal cut-on frequency of (0,1) mode (circles) as a function of mass concentration, compared with theoretical curves. Solid (Lloyd & Berry) and dotted (Temkin & Dobbins) curves were calculated using the respective theory in equation (7.10); dashed curve uses Evans' [43] algorithm to evaluate the theory of Vetter & Culick [150].

7.4.2 Discussion

A small frequency reduction of up to 10 Hz (0.25%) is noticeable. The theoretical predictions of Lloyd & Berry appear to be the best fit to the limited data. Such a small shift is not large enough to measure with great confidence; at higher concentration the shift might be larger, but the amplitude reduction of the peak would make tracking the shift troublesome. The theory of Vetter & Culick appears to predict very much larger shifts, although this could be due to the implementation of the algorithm, which gives larger predictions at large values of radius or frequency than those published by Vetter & Culick.

It should be noted that this method depends closely upon the pipe diameter, and therefore the small scale rig (pipe diameter of 50mm) used for these measurements is not necessarily a good guide to potential performance. By increasing the diameter to the more realistic size of 0.5m, the predicted frequency shift of the first mode (440 Hz) increases to 3%, although the magnitude of the shift increases only to 13Hz.

The technique is limited due to the small velocity change that occurs for frequencies above the viscous regime. For a particle radius of 10 μm, the viscous regime ends at approximately 100Hz; for 100μm particles the corresponding frequency is 1 Hz. So, suspensions with a PSD between these typical values will only produce a significant frequency shift below 100Hz. This, in turn, suggests that the method will only work in pipes of diameter above 2m. Even so, the small changes of absolute frequency will be difficult to measure, and the measurement time required to resolve them with sufficient accuracy will be significant.

7.5 STEADY-STATE SOUND PRESSURE LEVEL (SPL)

7.5.1 Passive monitoring of SPL

Section 7.1.4 showed theoretically how the steady state SPL, under excitation by a source of constant power, was related to the medium attenuation. Some attempts have been made in the literature to measure variations in the background noise, relying on the flow-generated noise and/or the prime mover to act as a noise source. If the background SPL is correlated with mass concentration [eg. 140], then this method relies on the noise source having constant power and spectral content. Alternatively, if attenuation of the medium is ignored, the variation is attributed to changes in the sound generating mechanism (such as particle size and flow speed [131, 132, 42].) The number of interacting mechanisms make any such correlations complicated (see section 3.2.5 for a discussion).

Section 5.7 described measurements of background noise made in the flow rig, for varying airflow rates and mass concentration of flour. As could be expected if the dominant effect were medium loss, the low frequency noise showed a reduction with increasing mass concentration. Above 1kHz, any change was negligible – this was attributed to the noise generated within the microphone probe by the flushing air. It was further shown how, for this flow rig in particular, the spectrum of the *generated* background noise varied with mass concentration due to the varying proportion of air-flow through the (noise generating) venturi. Hence, the assumption of constant noise power and spectral content could not be made.

For these reasons, passive monitoring of background noise was not pursued further, and the experiments below describe measurements in which a known, repeatable excitation signal was introduced and monitored.

7.5.2 Monitoring of steady state SPL with active excitation

The measurements of impulse response already presented can be reprocessed to yield the narrow band rms. level of the IR. This does not satisfy the condition of steady state excitation, and so any results are to be considered heuristic correlations. Section 7.5.4 presents measurements gained using continuous excitation, and so conform to the condition of steady state.

Referring to Figure 7-20, we noted the clear reduction in the peak amplitude of the spectrum. This is demonstrated in Figure 7-22 by plotting the amplitude of the spectral line at 3910 Hz against the mass concentration.

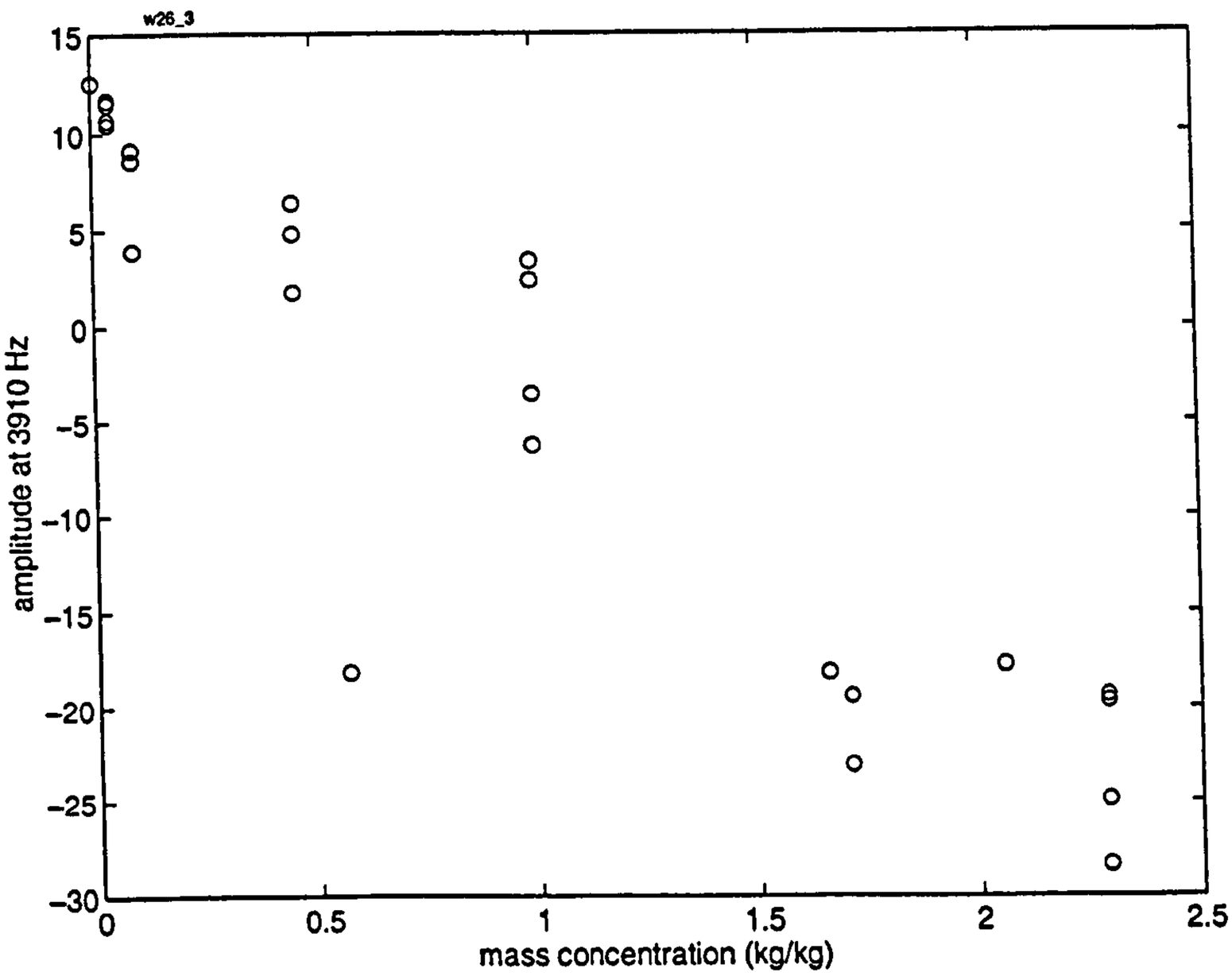

Figure 7-22 *Amplitude of the spectrum at 3910Hz for varying mass concentration of flour.*

There is a large and clear reduction in the amplitude of the frequency line as the mass concentration increases. Measurements are included up to a concentration of 2.5 kg/kg, showing that the method is useful up to higher concentrations than the frequency shift method.

These measurements are not compared to predictions according to equation (7.17), since it was not possible to calculate the decay rate at a single FFT line[1] to give a value for Q_{air}.

In order to compare measurements with predictions, two methods were used to measure the reduction in modal power.

[1] A Short Time Fourier Transform (STFT) method was attempted, which used a short sliding time window, and measured the decay rate from the decay of the relevant spectral line. However, the decay was very irregular, and did not yield consistent results.

7.5.3 Modal SPL in flowing flour — using the filtered impulse response

The impulse responses that were used to measure reverberant decay were re-processed to measure the change in narrow band level. The IRs were filtered using the modal filters described in section 7.3.2., and the rms. level in each band was calculated.

The theoretical attenuation coefficient was calculated for each frequency and mass concentration, using the theory of Lloyd & Berry; the values of Q_{air} at each frequency had already been measured. Therefore a prediction for the reduction in sound pressure as a function of mass concentration could be made with equation (7.17). Results are shown for 2 frequency bands (the lowest and the highest that were calculated) in Figure 7-23 and Figure 7-24 respectively.

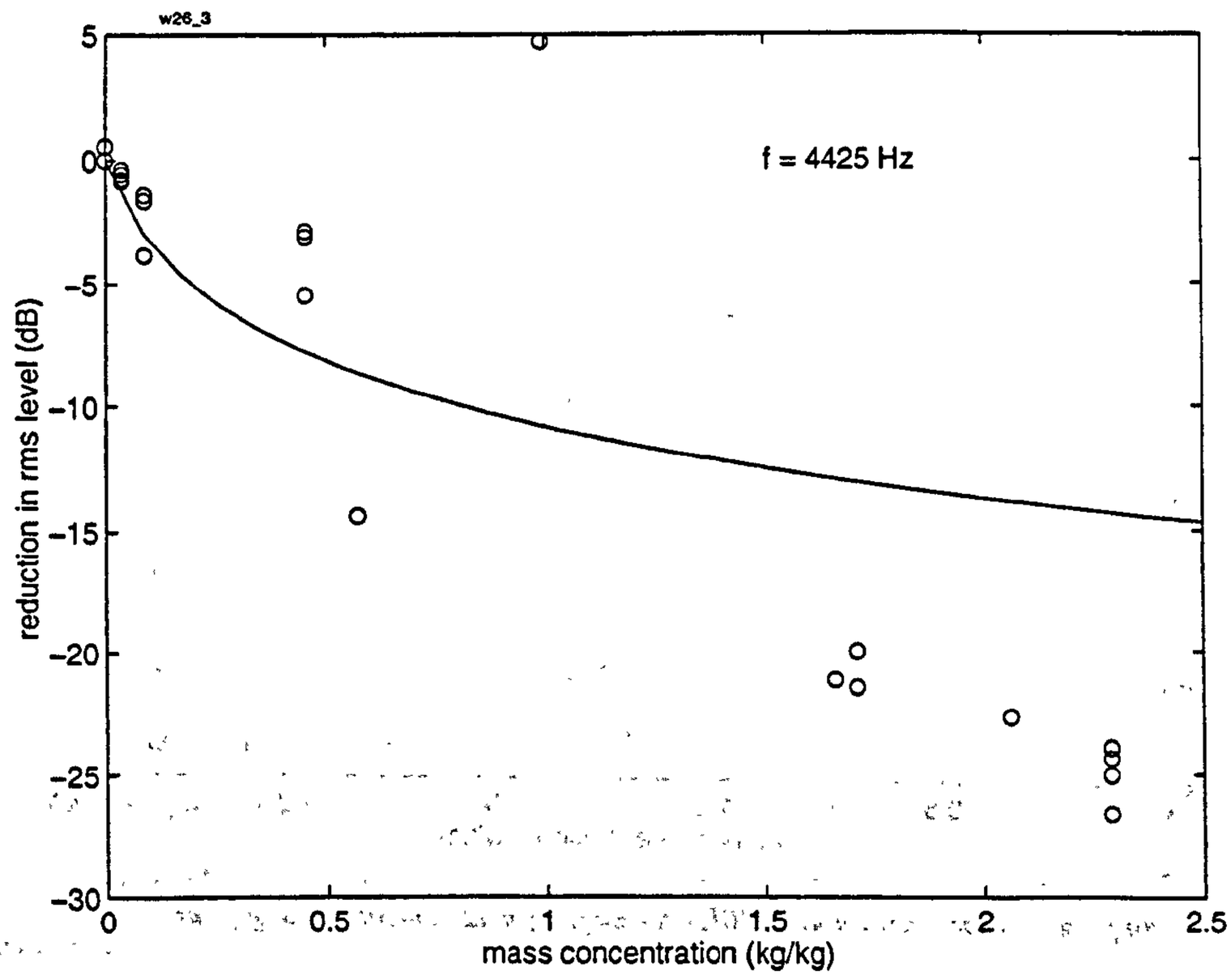

Figure 7-23 Change in SPL in the first modal band (f_c = 4.425 kHz) as a function of mass concentration of flowing flour: measurements (circles) and predictions (solid line).

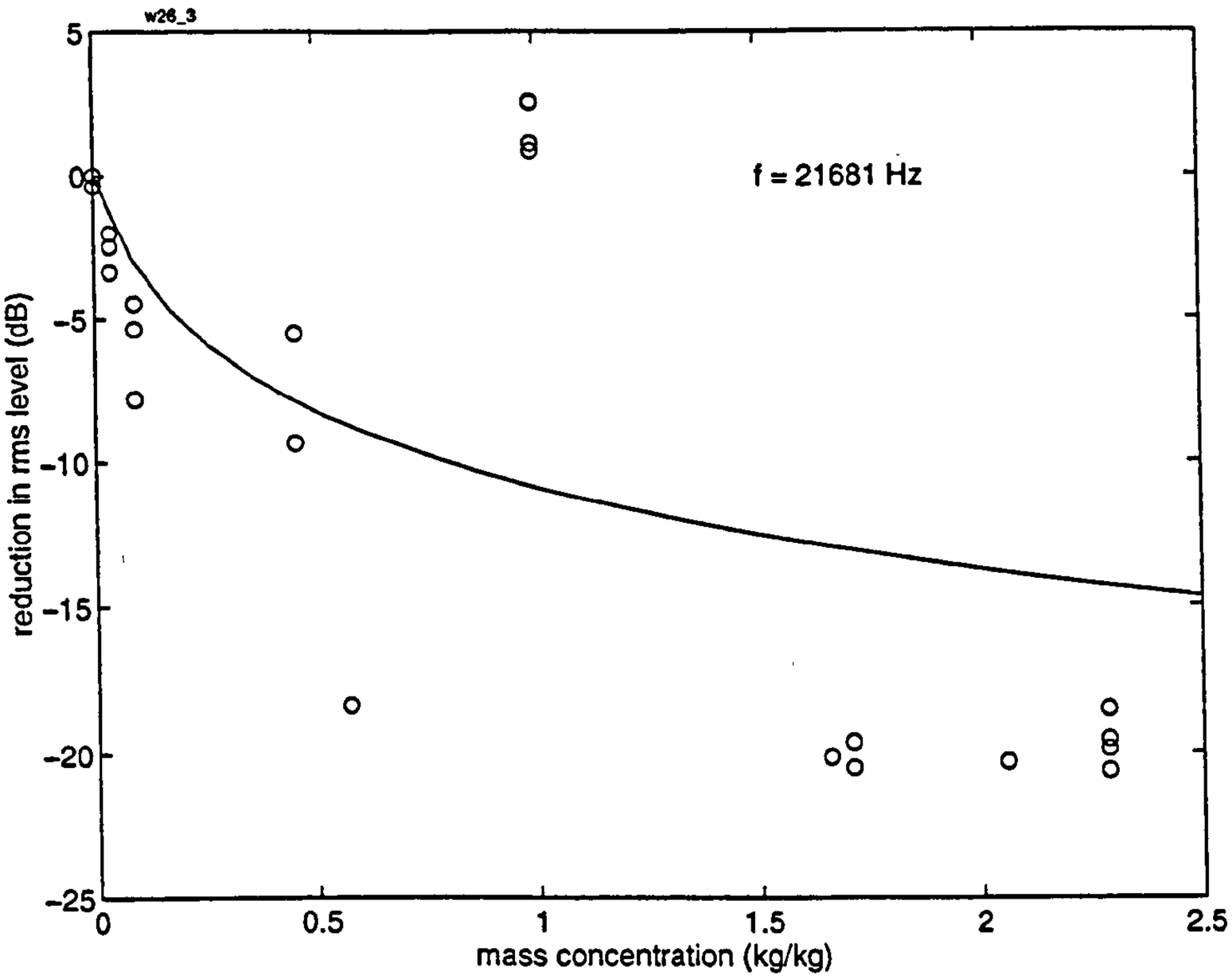

Figure 7-24 Change in SPL in the highest measured modal band (f_r = 21.68 kHz) as a function of mass concentration of flowing flour: measurements (circles) and predictions (solid line).

The measurements show a clear reduction in the narrow band SPL (with an outlier at 1kg/kg). The trend and shape of this reduction are predicted surprisingly well by the theory (given its simplicity), but underestimated at high mass concentrations.

7.5.4 Modal SPL in flowing olivine sand — using continuous excitation

This technique also insonified the environment with MLS noise (16 order), but the received 64k sample time sequence was used "raw" instead of cross-correlating to deduce the impulse response. Ten time domain averages were used to reduce background noise, and to form an average signal over a 2 min period – long enough to compare reasonably with the non-acoustic measurement of mass concentration. In effect, the repetitive property of the MLS signal was being used to allow synchronous averaging. The time sequence of received noise was then filtered and processed as before. The change in SPL in the first four modal bands is shown in Figure 7-25.

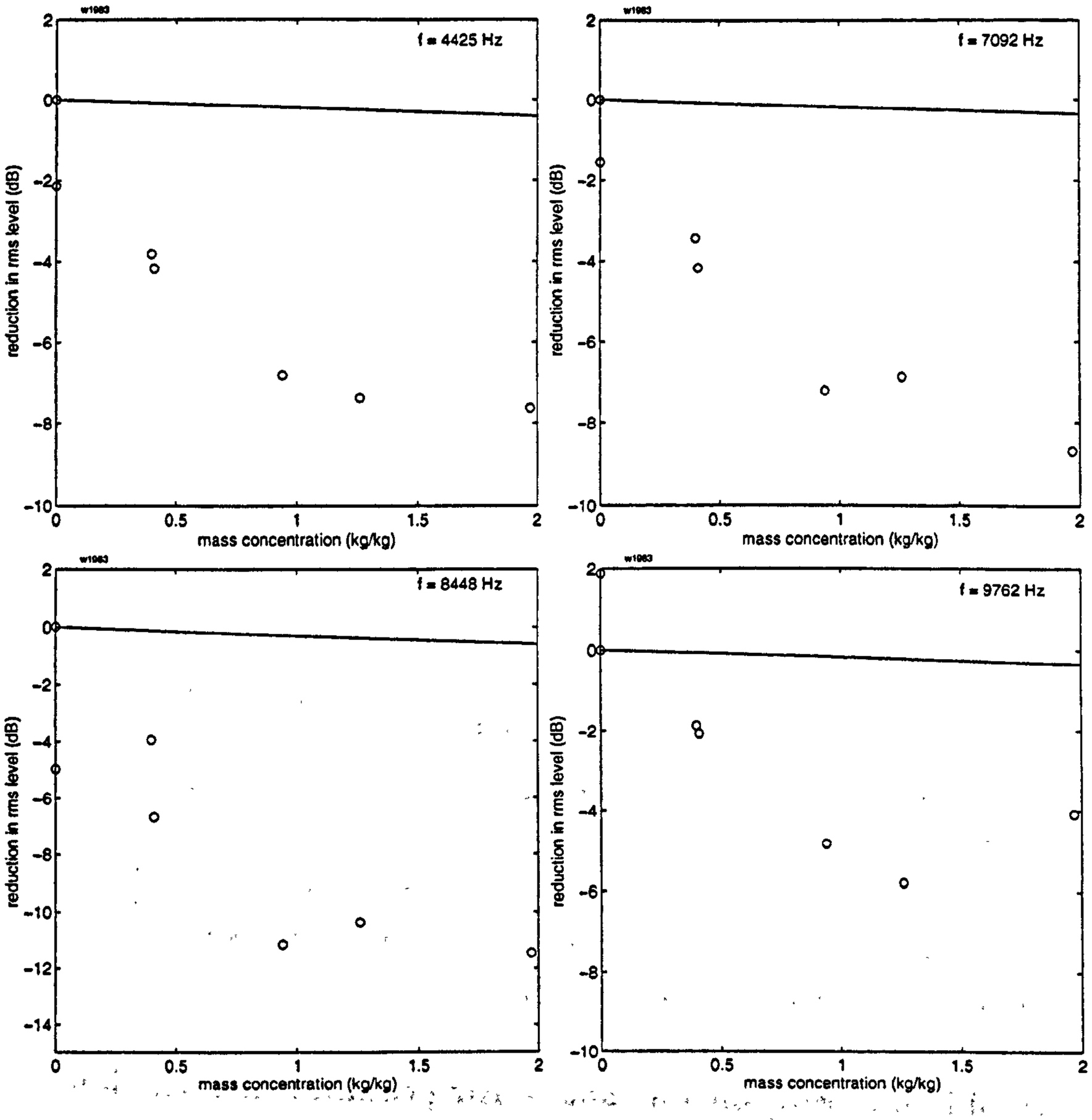

Figure 7-25 Change in SPL in flowing olivine sand in four modal bands as a function of mass concentration: measurements (circles) and predictions (solid line).

7.5.5 Discussion

The trend and shape of the curves are similar to those measured with flour, but with a lower magnitude due to the larger particle size. The reduced scatter of the points presumably indicates that measurement technique is more robust than the impulse response method. In common with measurements of plane wave attenuation and reverberant decay of sand, the change in SPL is significantly larger than the predictions.

Tallon & Davies [140] found a similarly high change in SPL when they made passive measurements of flow noise in a suspension of coarse, flowing sand (see section 3.1.2).

7.6 CONCLUSIONS

The reverberant sound field has been measured, and derived parameters were correlated with the concentration of solids. Three methods of measuring and deriving data have been described.

7.6.1 Reverberant excess decay rate

The reverberant excess decay rate was measured in quasi-static suspensions of fine alumina, and flowing suspensions of flour and sand. It was found to be a very sensitive measurement, and unsuitable for strongly attenuating flows.

Narrow band values of excess decay rate showed a linear relationship to ϕ, if frequency bands were selected according to the modal structure of the pipe. This is presumably because the decay rate and sensitivity are uniform within a cluster associated with a single transverse frequency. The frequency bands yielding the least curved decays and most linear relationship to concentration were just above the cut-on frequency of transverse modes of the cylindrical enclosure. It is not clear why. One observation is that this frequency region contains modes with a moderately high longitudinal component ($n_z >> 1$, see equation (7.8)). There will therefore be a greater degree of spatial averaging within the volume of the tube compared with modes close to the cut-on frequency (n_z small), which may reduce random errors due to inhomogeneous dust distribution, and short-term fluctuations.

The results measured in the quasi-static suspension indicate that narrow-band excess decay rate in a cylindrical enclosure could be used as an indirect measure of the volume concentration of a dust of known physical characteristics (and hence known $\frac{d\alpha_{dust}(f)}{d\phi}$).

Measurements in a flowing suspension were compromised by the high level of background noise. This was partly mitigated by synchronous (time-domain) averaging; however, such a technique can be expected to increase the curvature of the decays if there are short-term fluctuations of concentration, that would lead to curves with different decay rates being averaged. The averaging process is also time-consuming, and may be a problem in a real application.

Knudsen's formulation [75] for the effect of finite medium attenuation was used to derive an average indication of decay sensitivity, ψ, although the measured ψ showed large excursions around these values without any clear trend. The measurements on flowing sand showed much greater sensitivity than predicted, with a single, highly sensitive frequency band.

An advantage of this measurement method (over measuring the transmission loss directly), is that absolute and stable calibration of transducers is not required. Additionally, it should be insensitive to variations in orifice impedance, assuming that the impedance remains constant throughout the duration of a measurement.

It is not practically possible to isolate decay of a single mode, so the narrow band decay curve will be a composite of decays of a number of closely spaced modes. If the modes have a similar (exponential) decay rate, then the resulting decay curve can be expected to be exponential. If, however, there is a spread in decay rates, then a curved decay will result.

The broadband decay was very curved in flowing suspensions. Furthermore, the broadband excess decay rate measured in a static suspension appears to have a non-linear relationship to dust volume concentration, ϕ. Both the decay rate and decay sensitivity varied with frequency to a larger degree than predicted: these observations would explain the curved decays and non-linear relationship, respectively, of the broadband decays, since the latter are a summation of decays across a wide range of frequencies.

7.6.2 Modal frequency shift

The change in cut-on frequency of the first transverse mode has been estimated in flowing flour. The measured shift was very small (< 10Hz at ϕ_m = 0.45 kg/kg). This corresponded with the value predicted by an "intuitive" approach, which used the theory of Lloyd & Berry to predict the change in sound velocity. The theory of Vetter & Culick appeared to overpredict the change, but a definitive comparison is hampered by an inability to reproduce their own published predictions.

This method is likely to be most useful where the particle size is small and the pipe diameter large so that the lowest transverse resonance is at low frequency; that is, $a\sqrt{f}$ is small, so that the Reynolds number remains in the viscous regime (see section 2.4.1). In this regime, the frequency shift will be at an asymptotic maximum, while the attenuation will be comparatively low, therefore allowing the modal peaks to be prominent and easily tracked, without excessive damping due to attenuation. Above the viscous regime, the frequency shift will only be significant if the particle concentration is very high, in which case the attenuation will be correspondingly high. If one can operate well below the viscous-to-inertial transition, there will be the additional bonus that the shift should be relatively insensitive to particle size (due to the asymptotic equilibrium sound speed), and therefore be a function predominantly of concentration.

Alternatively, if an estimation of particle size is required, the frequency (and hence pipe diameter) should be chosen to encompass the transition region for the particle size range of interest. In this case, the relative shift between several low order modes should be significant, because of the rapidly changing sound speed (as a function of $a\sqrt{f}$). As suggested by Vetter & Culick, the relative shift(s) should then provide an estimate of the location of the transition, and hence of the Sauter mean particle size (see section 2.5.1).

7.6.3 Steady state SPL

It was concluded that passive monitoring of background noise in the pipeline would not yield useful data in this particular flow rig, due to the changing noise generation mechanism. In general, the technique is simple, and does yield extra data, even though interpreting the data and finding valid correlations is more complex. If a microphone were already installed in a plant for active measurements, then passive measurements could be interlaced with active ones, and the additional information comes essentially "free-of-charge".

Measurements of SPL were made under active insonification, and the received signal was processed into modal bands. The advantage of this technique (over passive monitoring) is that it is less sensitive to variations in flow- and system-generated noise.

Measurements on both flowing flour and sand showed the expected decrease in SPL with increasing solids concentration. The pattern of the measurements corresponded with the predicted function, but the reduction in SPL was greater than predicted: the difference was very great in the case of flowing sand. The theoretical predictions relied on an experimental measurement of the decay rate in the absence of suspension, in order to estimate the power loss due to wall absorption and sound propagation away from the measuring volume.

8

MEASUREMENTS OF ULTRASONIC ATTENUATION

This chapter describes measurements of the insertion loss of flowing suspensions at low ultrasonic frequencies (40 – 75 kHz). Measurements in this frequency range are desirable for the following reasons:

- To extend the frequency range of attenuation measurements; previous researchers [55, 136] have concentrated on the range above 200kHz. As mentioned previously, higher frequency measurements in flows suffer from complications due to turbulent loss, beam drift, and restricted bandwidth. The further practical value of measuring in the low ultrasonic region will be mentioned further in section 9.3.
- To extend the range of measurement techniques; in particular, to measure the attenuation across the pipe diameter. This requires the transmitting and receiving transducers to exhibit a short impulse response, so that the directly received signal can be separated from multiply reflected signals: a short impulse response implies an extended high frequency response.

No measurements are reported on the quasi-static rig: even with the highest achievable concentration of 10^{-5} m^3/m^3, and the finest alumina grade (F1200), no significant attenuation was measured, due to the short "cross pipe" path length of 0.1m. The attenuation is predicted to be < 0.3 dB. While the path length in the flow rig is even shorter (0.053 m), the concentrations that are achievable are so much higher, that significant attenuation can be measured.

Section 8.1 presents a justification for the method of using insertion loss to calculate the plane wave attenuation coefficient, even where the wavefront is not planar, as is the case for the following reported experiments.

Section 8.2 describes an experimental technique used to make preliminary measurements of the insertion loss of flowing flour at 40 kHz, and reports the results. These measurements did not use air-flushed transducers, and so they avoided the uncertainties associated with the coupling ratio of the probe orifices.

The remainder of the chapter reports on a more sophisticated apparatus, that derives the attenuation coefficient with greater validity, due to its shorter impulse response. Section 8.3 describes the equipment and signal processing, while section 8.4 describes the measurements on flowing flour, olivine sand, and barytes.

8.1 THEORY – SPHERICAL SPREADING

In Chapter 6 the frequency range of measurements was restricted so that propagation in the pipe was confined to the plane wave mode and the plane wave attenuation coefficient could be measured directly. However, when analysing ultrasonic measurements across the tube diameter, the same assumption cannot be made. The simplest approximation is that the wavefront spreads spherically.

In this case, the field p, at a distance r from the transmitter is [73]:

$$p = \frac{1}{r}\exp(ikr - i\omega t) \tag{8.1}$$

where $k = \frac{\omega}{c} + i\alpha$ is the wavenumber.

If we make two measurements of p across the pipe diameter D, one with clean airflow and one with suspension flow, then (ignoring the time varying component):

$$p_{air} = \frac{1}{D}\exp\left(i\frac{\omega}{c}D - \alpha_{air}D\right) \tag{8.2}$$

$$p_{dust} = \frac{1}{D}\exp\left[i\frac{\omega}{c}D - (\alpha_{air} + \alpha_{dust})D\right] \tag{8.3}$$

So, the insertion loss IL, in dB:

$$IL = 20\log_{10}\left(\frac{p_{dust}}{p_{air}}\right) = 20\log_{10} e \cdot \alpha_{dust} D \tag{8.4}$$

Hence, the insertion loss can be used to measure the attenuation coefficient for both plane wave and spherical propagation.

Spherical spreading can only be assumed outside the near field of the transducers. The near field distance, r_{NF} is given by [106]:

$$r_{NF} = \frac{d_x^2 f}{4c} \tag{8.5}$$

where d_x is the diameter of the transducer. If d_x is taken as the size of the orifice, 12mm, then, for the frequency range 40 – 80 kHz, the near field distance varies between 4 – 8 mm, which represents 7 – 15% of the path length. This limitation on the use of equation (8.4) to deduce attenuation coefficient has been observed in the subsequent analysis.

8.2 PRELIMINARY MEASUREMENTS[1]

These experiments represent an initial investigation into the feasibility of measuring the ultrasonic insertion loss across the pipe diameter. Flour was used as the test material.

8.2.1 Equipment

Sealed ultrasonic transducers were chosen so that they could be exposed to the suspension flow[2]. The transducers were a resonant piezoelectric pair, operating at 40 kHz (nominal), consisting of a transmitter and a receiver[3]. They were mounted into plastic inserts that screwed into ports B & C in the pipe segment, so that the path was the internal diameter across the pipe cross section (see Figure 8-1)

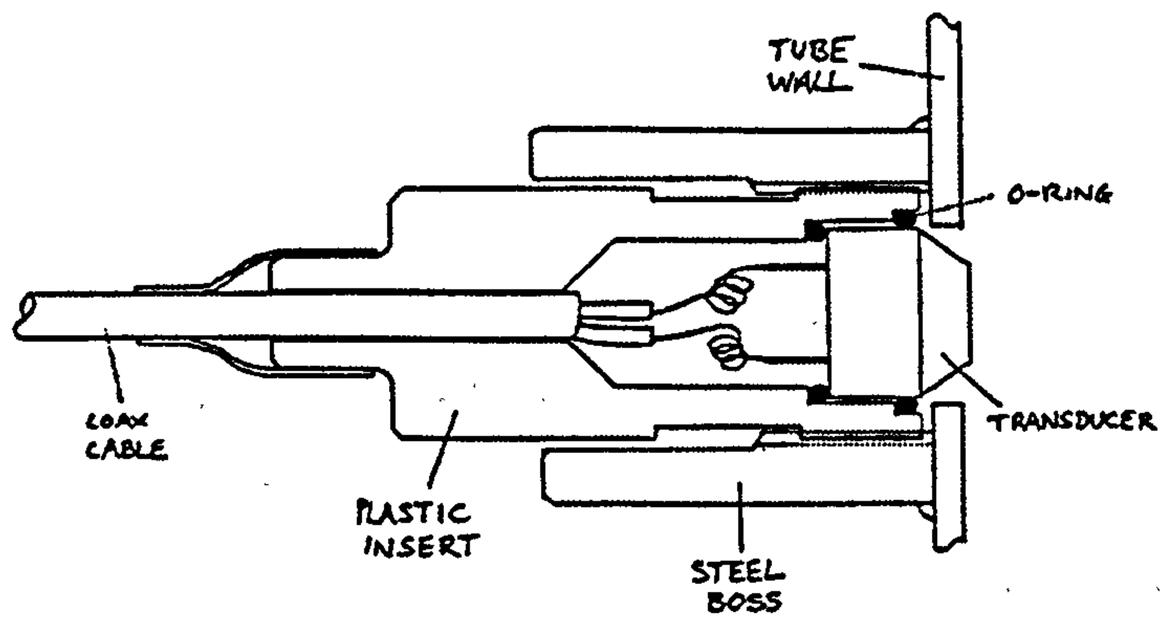

Figure 8-1 Diagram of an ultrasonic transducer, insert, and threaded boss of the pipe segment.

Mechanical flanking paths were attenuated by making the transducer inserts out of plastic (which also provided electrical isolation, thereby eliminating earth loops) and by supporting the receiver inside two O-rings (which also provided the air tight seal). To further reduce structural transmission, it was found necessary to back off the inserts by 1/8 turn so that their end faces did not seat on the tube wall. Initially the transducers were recessed slightly into the tube walls, but this led to rapid build-up on the transducer faces, reducing their sensitivity significantly. To keep the face of the transducer free of particulate build-up, it was found necessary for them to protrude slightly (≈ 1mm) into the flow, thus producing a self-cleaning action. However, this would not be a practical solution for long term monitoring because of the erosive nature of a flowing suspension.

The measurement system was built around an Ono Sokki twin channel FFT analyser, and is shown in Figure 8-2. The analyser generated a continuous sine wave at 40.250 kHz, which was gated to a

---

[1] These were the first set of data that were collected from the Wolfson Centre rig, before the experimental programme was fully devised.

[2] The experience of these tests led to the decision to use a flushing arrangement for the acoustic probes.

[3] Types: Murata MA40E1S and MA40E1R, respectively. Supplier: Murata Electronics (UK) Ltd, Oak House, Ancells Business Park, Aldershot, Hampshire, GU13 8UN.

1.65 ms duration. This signal was amplified to 30V peak-peak, and passed through a power-limiting resistor to the transmitting transducer.

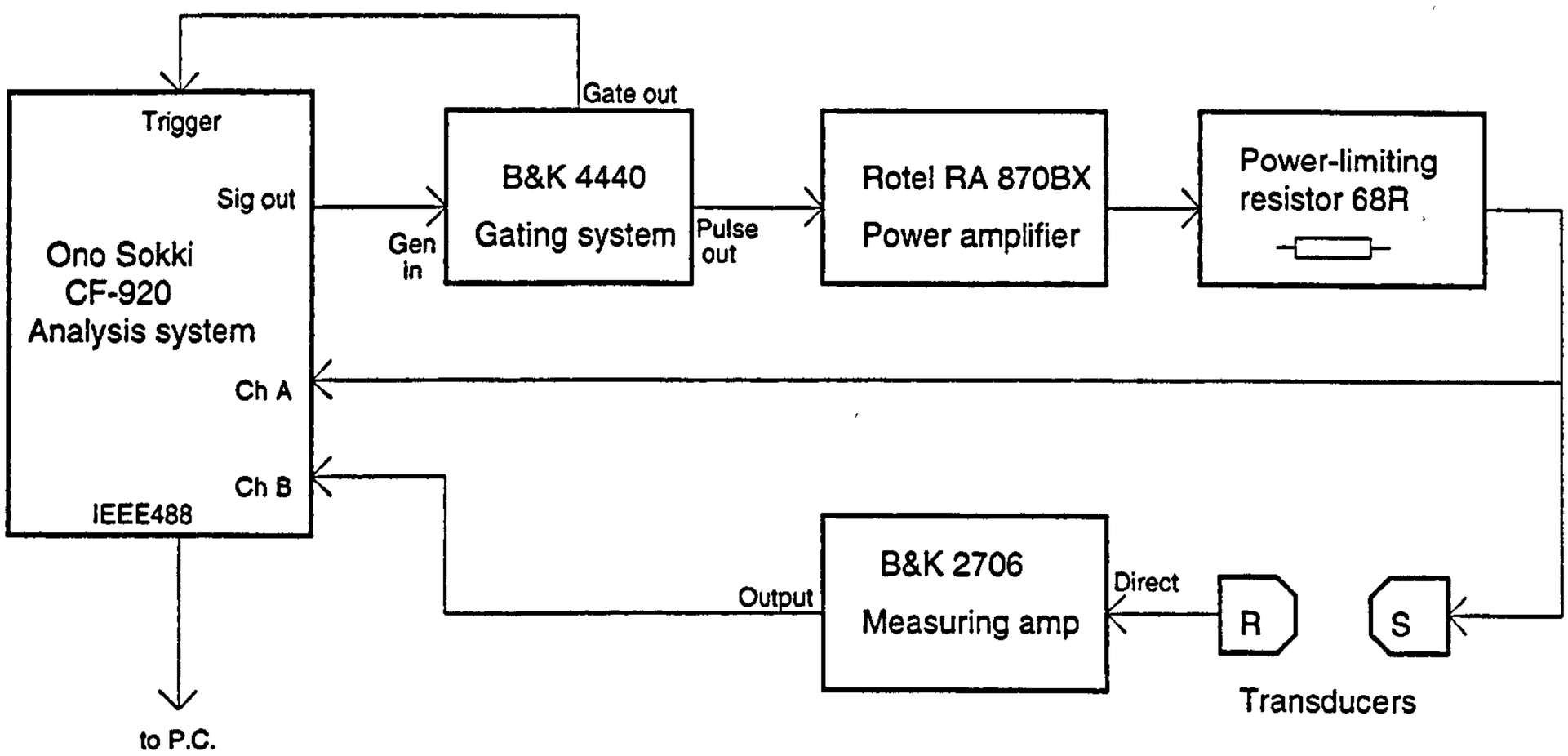

Figure 8-2 *Block diagram of the ultrasonic sensing system*

The resistor served to limit the failure-mode power dissipated in the transmitter to a worst case value of 3W, sufficiently low to ensure intrinsic safety (that is, the potential power dissipation in case of failure would not be able to ignite the flour). This was necessary due to the potentially explosive nature of the flour suspension, and the direct contact between the transducer and suspension.

The analyser calculated the received signal energy at the transmitting frequency, with and without suspension flowing in the pipeline. However, because the transducers had a long impulse response (approx. 4ms) compared to the time-of-flight of the path (0.16ms), the direct wave was inseparable from several reflected waves. It is therefore impossible to calculate a true value of attenuation coefficient from these measurements; nonetheless, the value should be correct to within a few dBs, and useful correlations may still be found with the mass concentration.

Further measurements were taken with no excitation signal; these values were subtracted from the signal levels with excitation to correct for the background noise. The insertion loss was calculated as the ratio of the noise-corrected levels with and without suspension flow. Instantaneous measurements were averaged 48 times to reduce uncertainty and provide a reasonable duration over which to estimate the mass concentration.

8.2.2 Results

The mass concentration varied between 0.6 - 16.5 kg/kg. The upper limit was much higher than measurements in previous chapters, because the flow rig was operated with a "blow tank" feeder configuration [158] instead of the venturi feeder; the disadvantage of this arrangement was that the concentration varied considerably over time, with both short term oscillations, and a long term decreasing trend as the blow tank emptied. Datapoints taken with this configuration are shown with errorbars on the abscissa, to indicate the range of concentration values that could be sensibly interpreted from the gain-in-weight trace.

The insertion loss is plotted as a function of mass concentration in Figure 8-3.

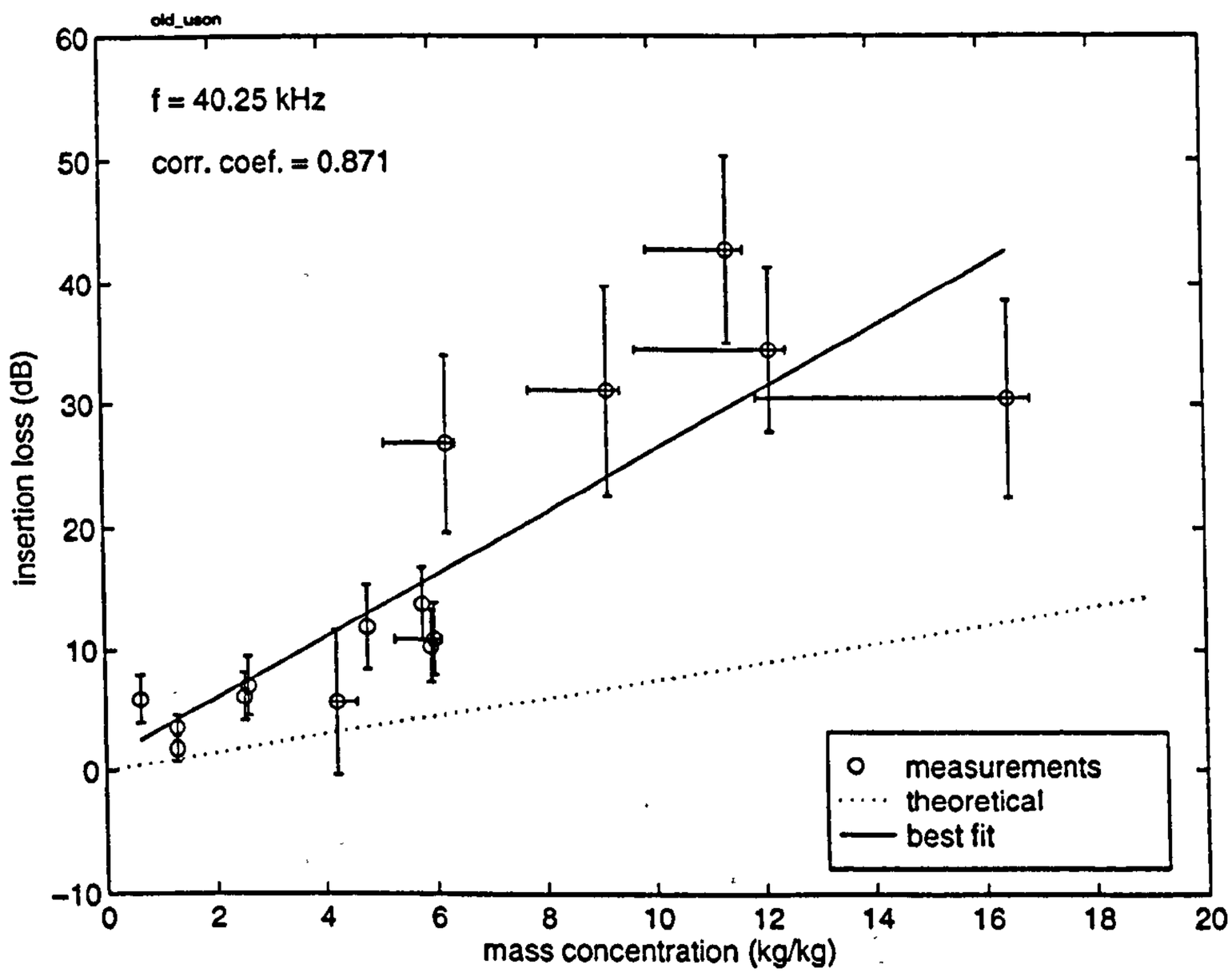

Figure 8-3 Insertion loss of a suspension of flowing flour across 53mm diameter: measured values (circles) with vertical error bars showing ±1 standard deviation, and horizontal error bars on points with a wide variation in concentration over the measuring period ; predicted insertion loss (dotted line, assuming a single transit of the pipe diameter) and line of best fit (solid line).

While there is a fair degree of scatter in the data, there is nonetheless a clear relationship between insertion loss and mass concentration. Although the measurements are not strictly comparable with the theoretical predictions, the difference between them seems too large to be explained by the existence of multiple path lengths in the measurements. The size of the vertical errorbars is largely due to scatter in the insertion loss caused by real fluctuations in the mass concentration – oscillations in the value of instantaneous insertion loss were found to correlate with oscillations in the gain-in-weight trace. The straight line fit is not convincing, and is included for comparison with results in section 8.4.2.

These preliminary measurements proved the feasibility of making low frequency ultrasonic measurements across this short path length, and so a more sophisticated apparatus was built that would allow time-domain editing to remove the internal reflections.

8.3 DRIVING AND ANALYSIS EQUIPMENT

The selection of the ultrasonic transmitter and design of its probe were described in Chapter 5. The microphone probe was found adequate to act as the receiver (this is checked in section 8.4.2). The overall block diagram is shown in Figure 8-4.

Most aspects of signal generation and acquisition, and all analysis algorithms were handled by the National Instruments AT-MIO-16E2 A/D, D/A board coupled with the LABVIEW programming environment. The software was written using LABVIEW to produce a "virtual instrument" (V.I.) (see Figure 8-6) which performed the three main tasks, listed individually in the following sections.

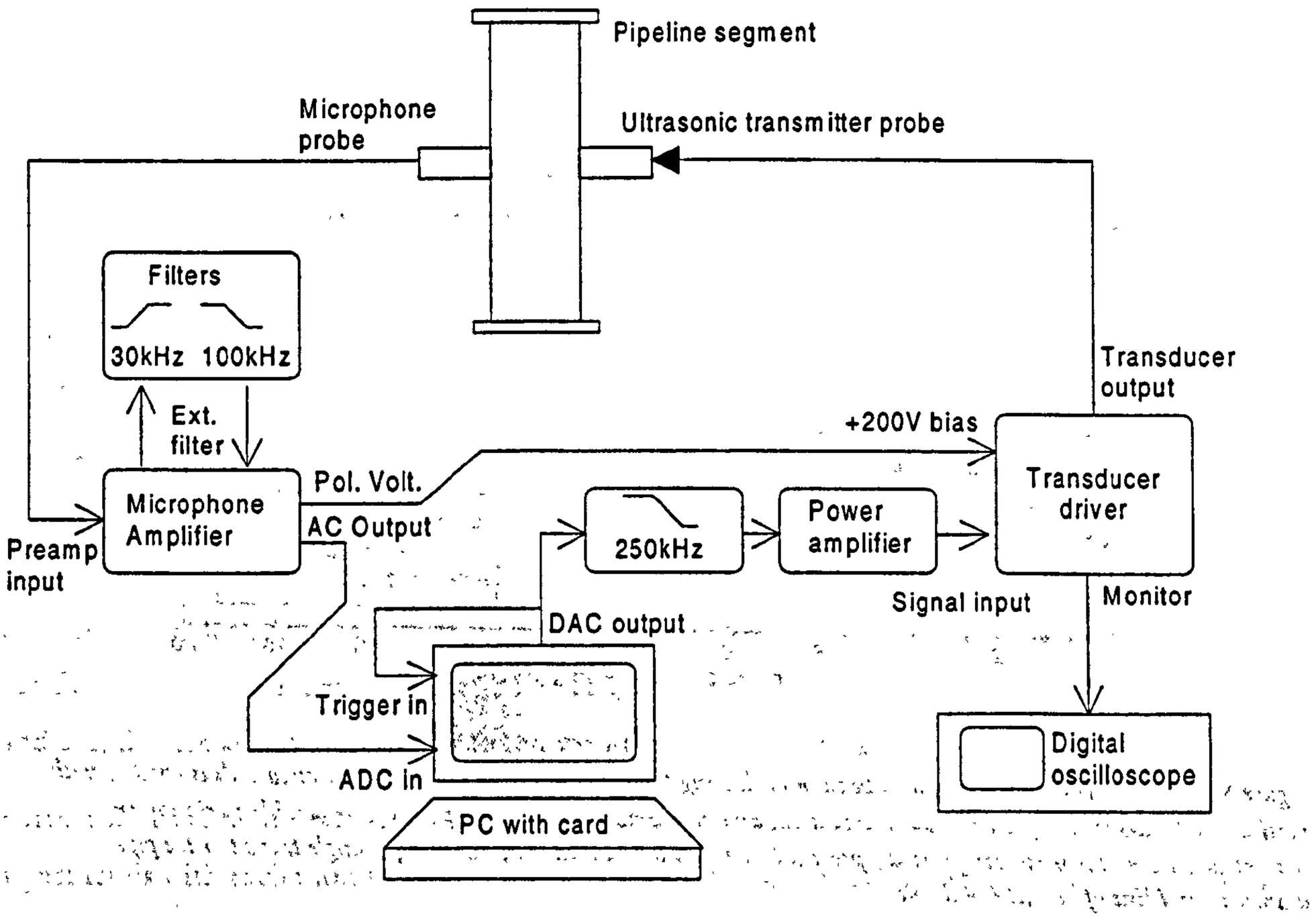

Figure 8-4 Block diagram of apparatus to measure ultrasonic insertion-loss.

8.3.1 Signal Generation

The "multiple sine source generator" V.I. allows the user to design a stimulus waveform containing up to three sinusoidal components. The amplitude and phase of each component are variable, together with the overall record length, to produce a data block that contains an integer number of cycles of each component, and that starts and finishes from zero. Furthermore, the crest factor of the waveform may be optimised for maximum S.N.R. by adjusting the relative phases. The front panel of the V.I. , and an example stimulus waveform, is shown in Figure 8-5.

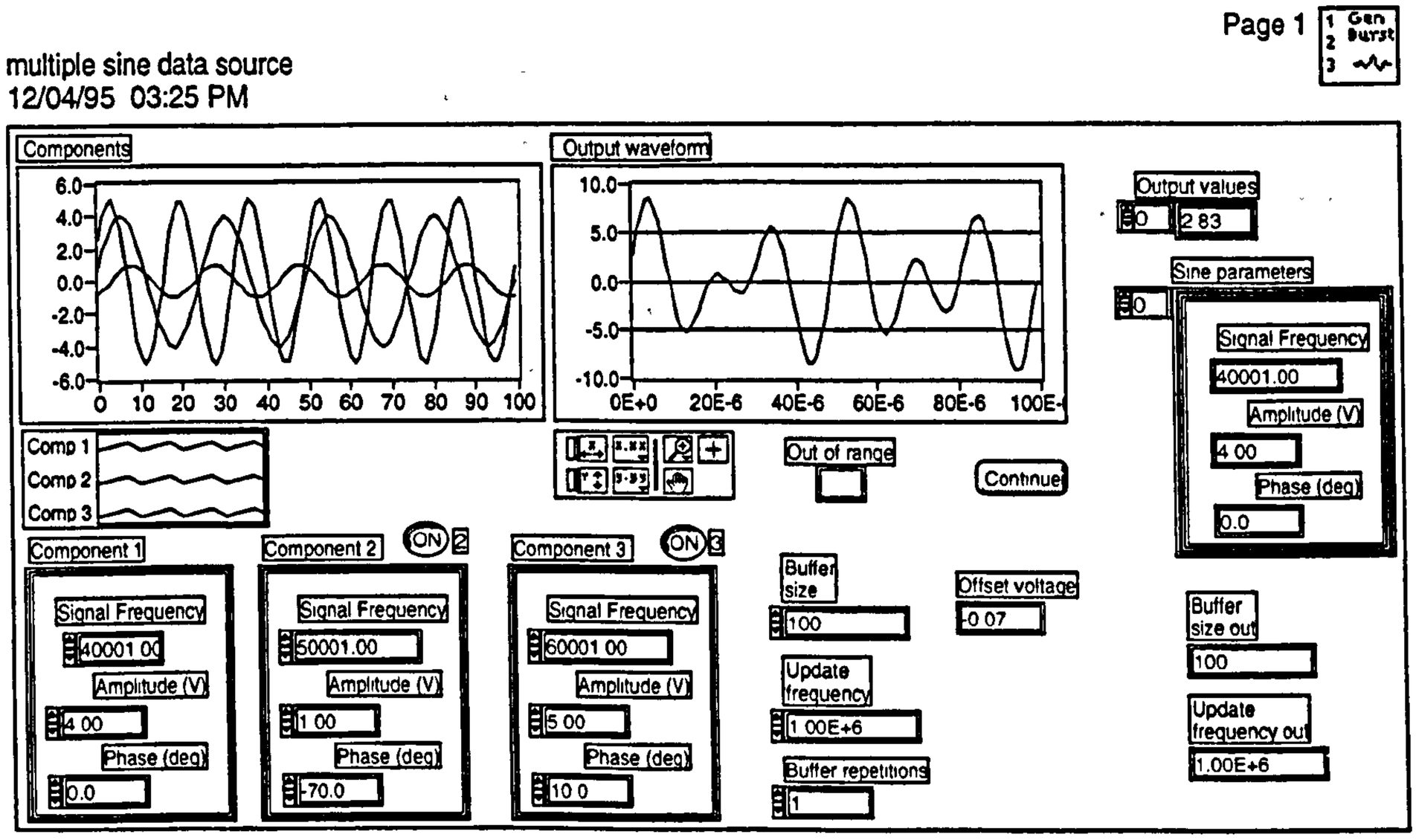

Figure 8-5 *Front panel of multiple sine source generator VI, and an example stimulus waveform.*

The data block is sent to the hardware card, where it is converted into an analogue waveform at a rate of 10^6 samples/second. This waveform was passed through a reconstruction filter to remove glitches and quantisation steps, before being amplified; the filter was a 250kHz low-pass 4th order Butterworth passive filter. It incorporated a 20dB attenuator to prevent the high DAC signal level (10Vpp) from overloading the amplifier input.

The power amplifier provides the power gain necessary to operate the transducer driver. The gain of the power amplifier was set such that the transducer voltage peaked at +400V (under load), as measured by a digitising storage oscilloscope (with a +10 probe).

8.3.2 Data acquisition

The microphone signal was amplified by the B&K 2607, and filtered by high and low pass filters at 30kHz and 100kHz respectively, to improve the SNR by optimising the ADC input range.

This high level signal was digitised by the hardware card at a rate of 500 ksamples/s, controlled by the main VI, whose front panel is shown in Figure 8-6. The trigger to capture the waveform was derived from the DAC output, to ensure jitter-free recording.

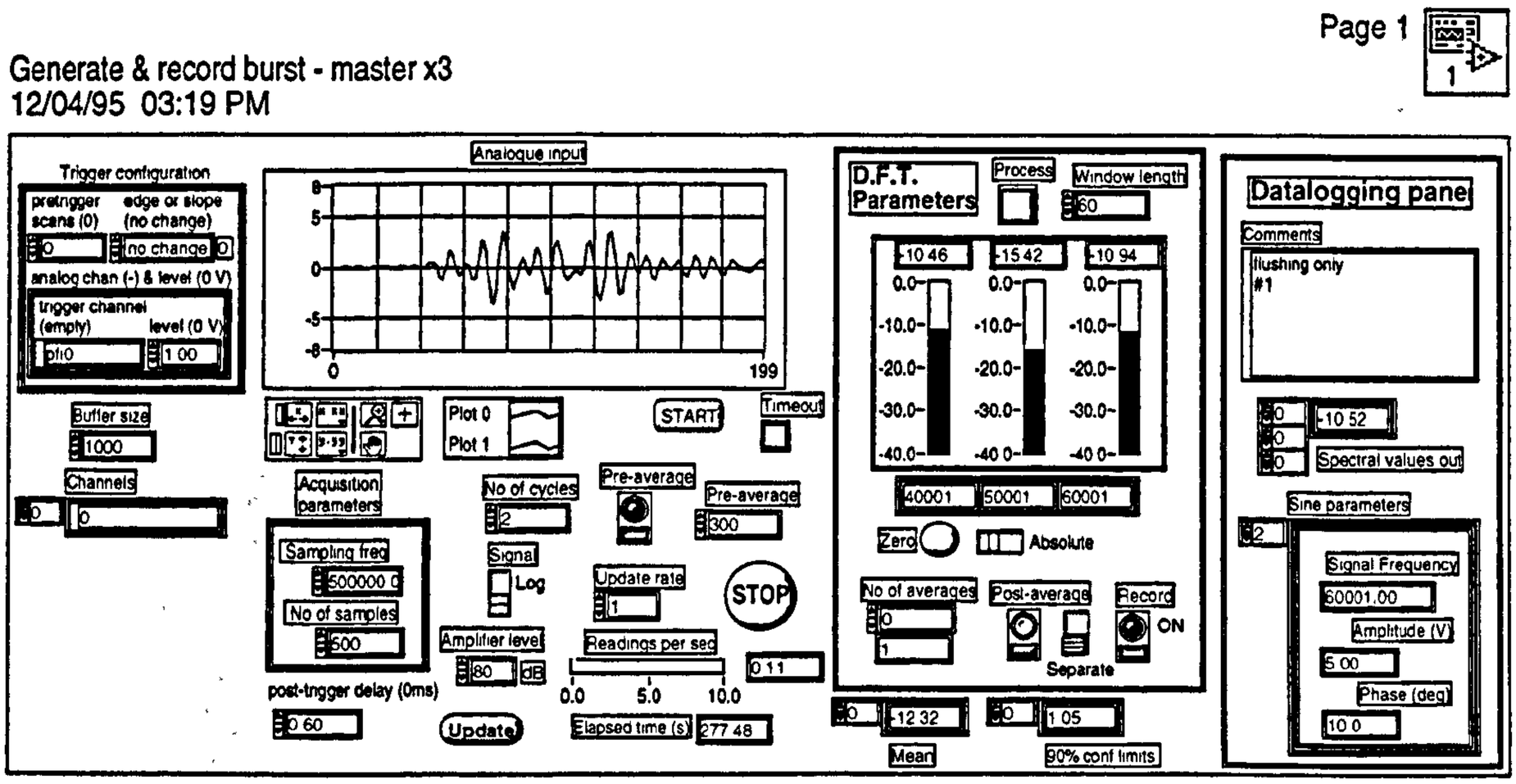

Figure 8-6 Front panel of transmitting, receiving and processing virtual instrument, showing an example of a received waveform. The x-axis on the graph indicates sample number, taken at a rate of 500 ksamples/s: so the 200 sample interval corresponds to 0.4 ms.

8.3.3 Data processing and analysis

Synchronous averaging of time data $x(n\Delta t)$, was employed to reduce uncorrelated noise. 300 blocks of time data were averaged to produce a single block of averaged data, $\langle x(n\Delta t)\rangle$. Here, n is the sample number, and Δt is the sample interval, 2μs.

A discrete Fourier transform (D.F.T.) was performed at each selected frequency component. For each component ω_k, the magnitude of the D.F.T. line was calculated as:

$$Z_k = \frac{1}{w}\sum_{n=n_0}^{n_0+w} \langle x(n\Delta t)\rangle \cdot \exp(j\omega_k n\Delta t) \qquad (8.6)$$

Instead of integrating over the entire record length of 200 samples, a rectangular window of length w=60 samples (120μs) was swept across the block by incrementing n_0, and the maximum value of $|Z_k|$ was found. The window length was chosen as being slightly longer than the transmitted block length (100μs), and its purpose was to record the energy of the incident received pulse, while excluding that of any reflections. The values of $|Z_k|$ were then post-averaged over the time duration of the specific experiment. The operation is shown diagrammatically in Figure 8-7.

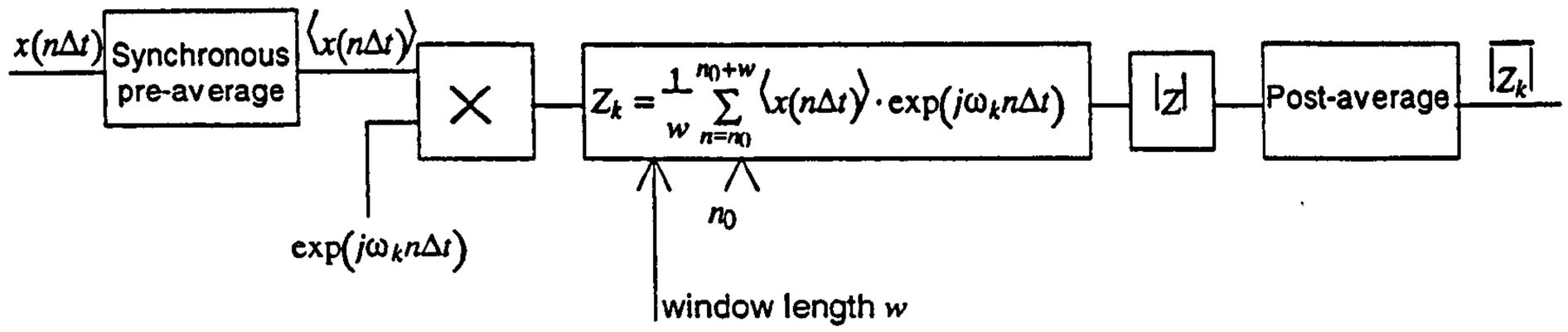

Figure 8-7 *Block diagram of data processing: pre-average, D.F.T., post-average (shown for one DFT line only, ω)*

Furthermore, the confidence interval of $\overline{|Z_k|}$ was calculated using [78]:

$$\Delta\overline{|Z_k|} = \frac{c\sigma}{\sqrt{N}} \tag{8.7}$$

where c = 1.645 for 90% confidence limits, σ is the standard deviation of $|Z_k|$, and N is the number of averages.

A value of $\overline{|Z_k|}$ was measured with clean air-flow, and then with suspension flow. The insertion loss in dB was calculated (for each component) as the ratio of the measured values.

8.4 MEASUREMENTS

8.4.1 Technique

Initially the stability of the system was measured to ascertain if significant drift of received signal level would occur during the duration of a measurement, due to amplifier gain drift, transducer sensitivity etc. Over a period of 30mins, the drift was measured at < 0.1dB, with no flushing air.

However, the addition of flushing air significantly increased the background noise level across the frequency spectrum. After the addition of external 30kHz high-pass and 100kHz low-pass filters to reduce out-of-band noise, the level in the frequency range of interest was such that the SNR was only 6dB (118dB signal, 112dB noise, re. 20μPa) . While some of the ultrasonic noise was due to noise generated by the choke flow nozzles that were used to meter flushing air, the majority was generated at the point at which the air entered the probe tube, in both the transmitter and receiver. Little could be done to reduce the latter source without a complete redesign of the probe system; some foam and wadding were deployed in the plenum chamber after the choke flow nozzles to reduce this source of noise.

To improve the accuracy of the readings, 300 synchronous preaverages were taken. Each preaveraged data block took 10s to acquire (at 30 excitations per second).

Readings were taken over a concentration range of 0 - 2.3 kg/kg. For each concentration value, acoustic measurements were averaged over a period of approx. 500s, to reduce the uncertainty both in the mean value of acoustic insertion loss, and the directly-measured concentration value.
Insertion loss was defined as

$$IL(f) = \frac{|\overline{Z}(f)|_{dust}}{|\overline{Z}(f)|_{air}} \tag{8.8}$$

where f = 40, 50, 60 kHz. The attenuation coefficient, α, was calculated as:

$$\alpha(f) = \frac{IL(f)}{20\log_{10} e \cdot D} \tag{8.9}$$

where D is the pipe diameter. Reference measurements, subscripted $_{air}$, were measured with flushing air and nominal air velocity in the pipe, but without the dust feed valve opened.

8.4.2 Results

Calibration check

In order to check the accuracy of the equipment, the insertion loss of a test material was measured. A material with a low acoustic impedance was required; if, for example, glass beads were chosen, less of the incident waveform would couple into the beads compared to a suspension, and so the

insertion loss would be overestimated. A polyester fibre with a very loose structure was chosen[4]; a 5cm block was inserted into the pipe segment, and its insertion loss was measured at 8 frequencies individually, in three ways:

1. The microphone was flush with the inside wall; the DFT analysis window was the same length as the transmitted burst (140μs).
2. As 1. but with a longer window, the length of the main body of the direct pulse (335μs)
3. As 1. but with the microphone held in its probe.

For each case, the transmitting transducer was held in its probe, and no air was flushing or flowing. The insertion loss for each case is plotted in Figure 8-8.

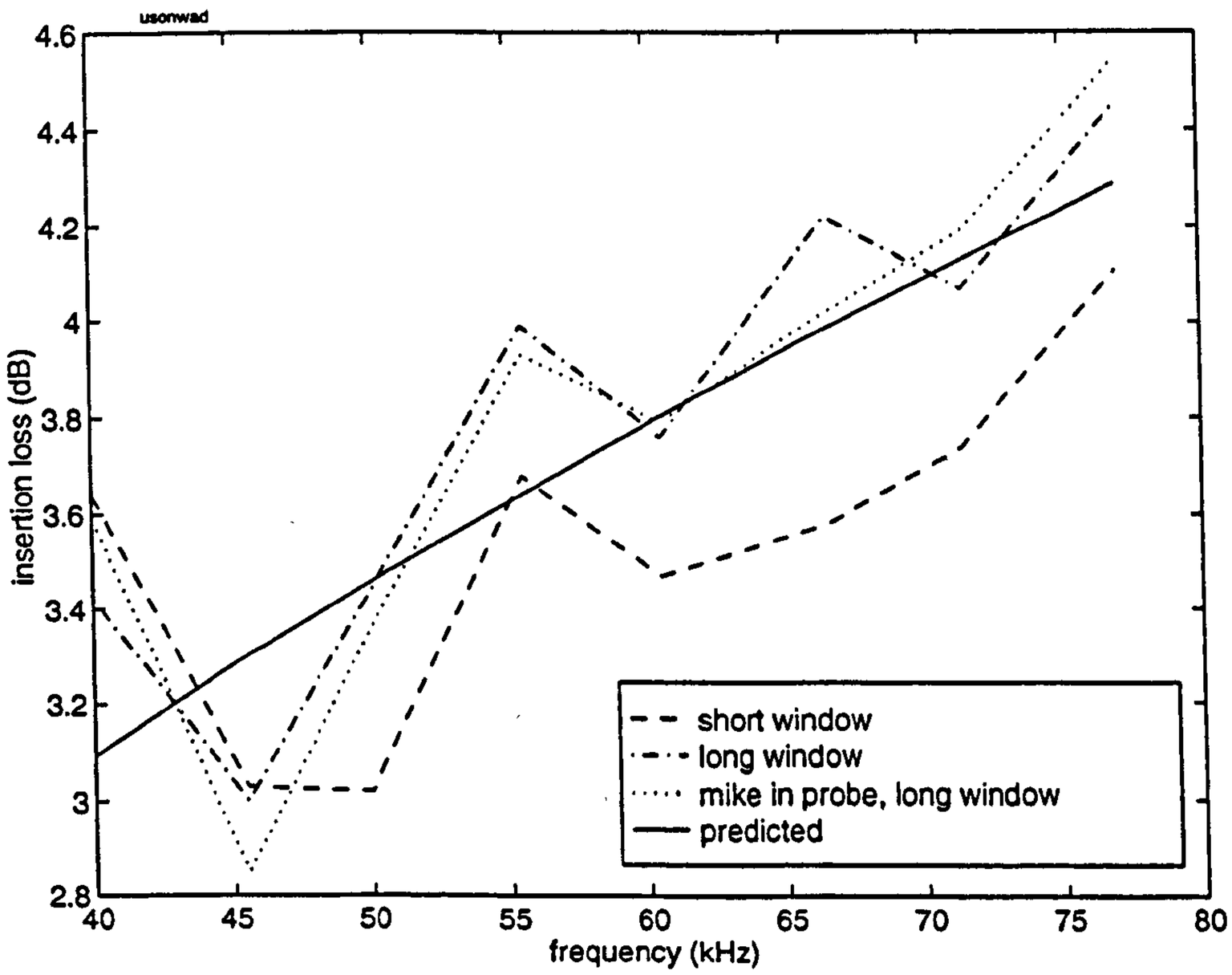

Figure 8-8 The insertion loss of a sample of 15 oz polyester fibre, measured in three ways (see text), compared to predictions of the Rayleigh-Attenborough four parameter model [14]: δ = 90 MKS Rayls, Ω = 1, S_p = 0.5, n_p = 0.5.

The acoustic properties of the fibre were calculated using the Rayleigh-Attenborough four parameter [14] model, and a directly-measured flow resistivity. There is very good agreement between the measured and predicted values. The presence of the microphone probe housing has negligible effect, suggesting that its useful frequency range extends up to 75kHz; the different window lengths have a small effect (< 0.5dB).

[4] Its characteristic impedance was predicted to be <15% higher than that of air (using the Rayleigh-Attenborough 4 parameter model — parameters as listed in Figure 8-8).

Flour

The system was used to measure the insertion loss of flowing flour at 40, 50 & 60 kHz simultaneously. The measurements are plotted in Figure 8-9 – Figure 8-11, for each of the 3 frequency components. The error bars indicate the 90% confidence limits, defined by equation (8.7).

It can be seen that the overall values of insertion loss are low (< 7dB), and, surprisingly, decrease with increasing frequency, contrary to the monotonic increase that is predicted.

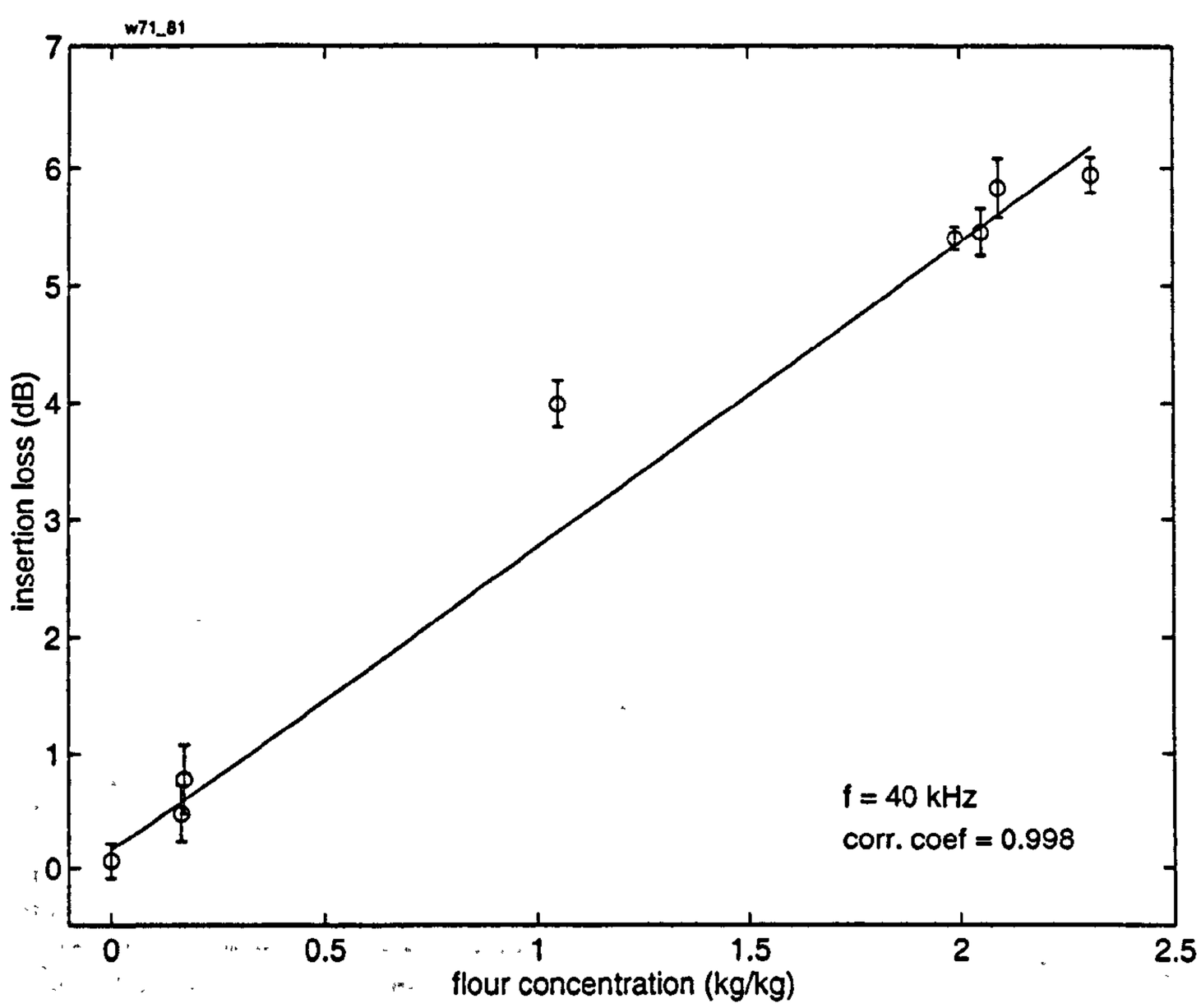

Figure 8-9 *Insertion loss of flowing flour at 40kHz, and line of best fit.*

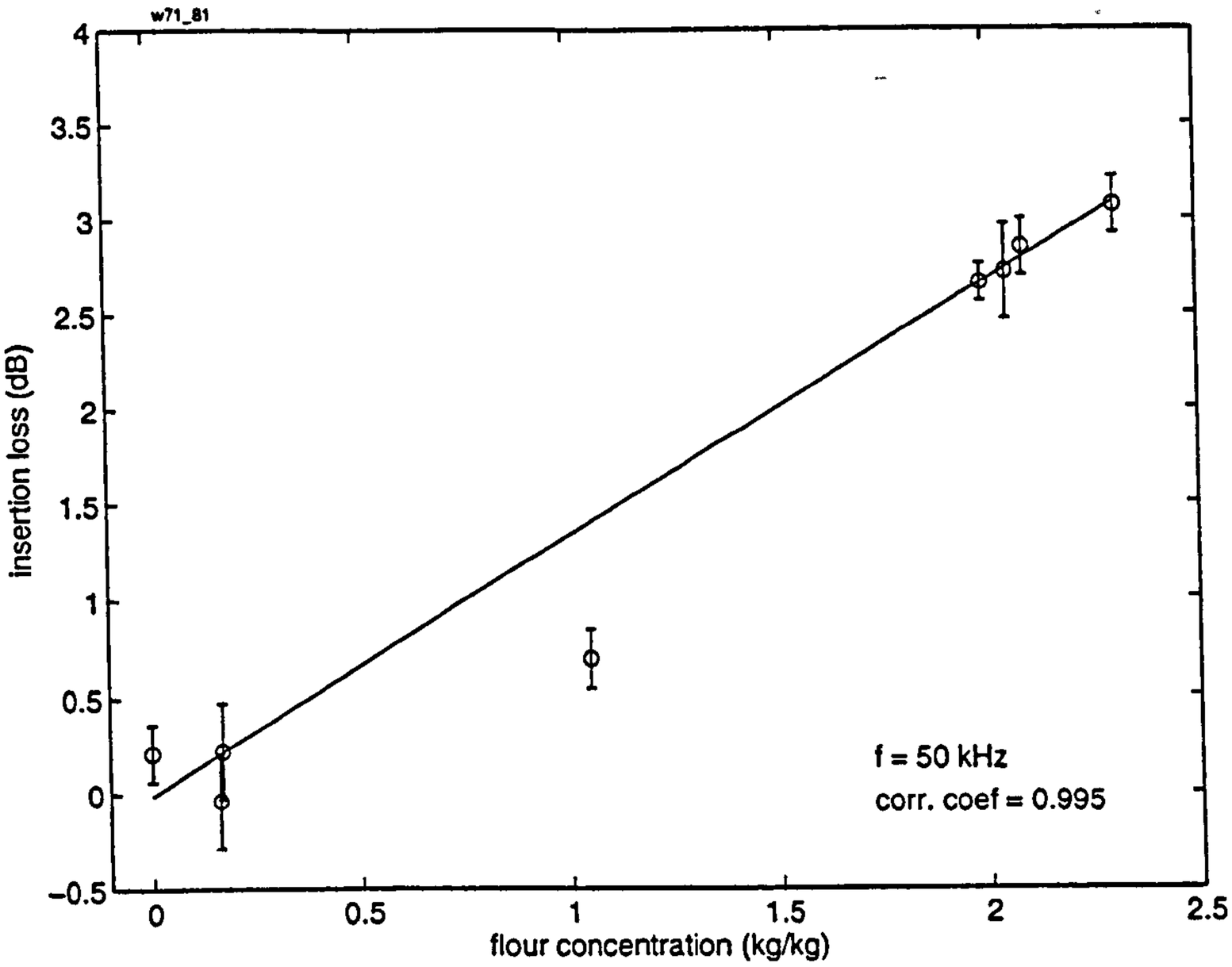

Figure 8-10 *Insertion loss of flowing flour at 50kHz, and line of best fit.*

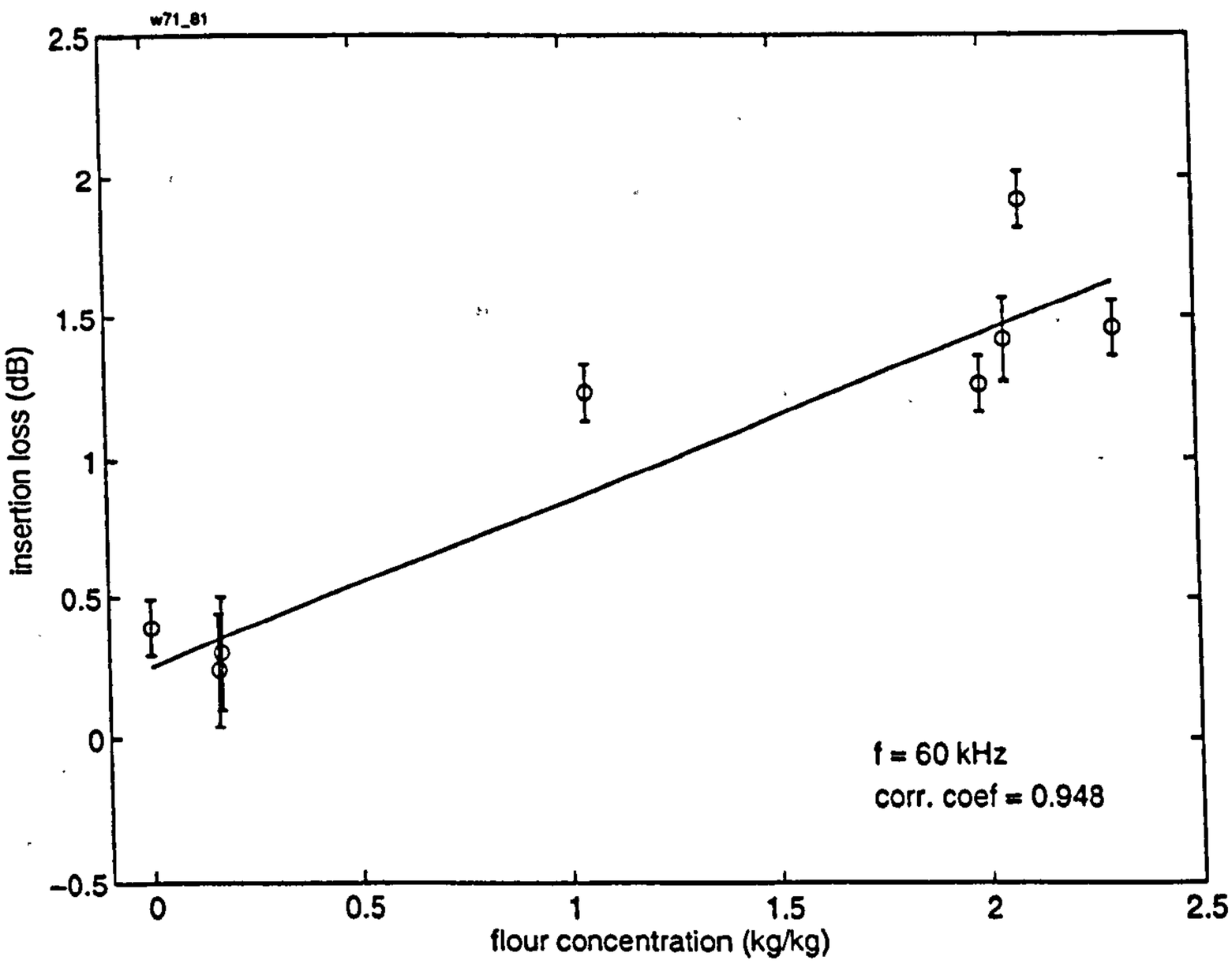

Figure 8-11 *Insertion loss of flowing flour at 60kHz, and line of best fit.*

The attenuation coefficient normalised to 1kg/kg of flour is plotted as a function of frequency in Figure 8-12. The decrease of attenuation with frequency is most remarkable.

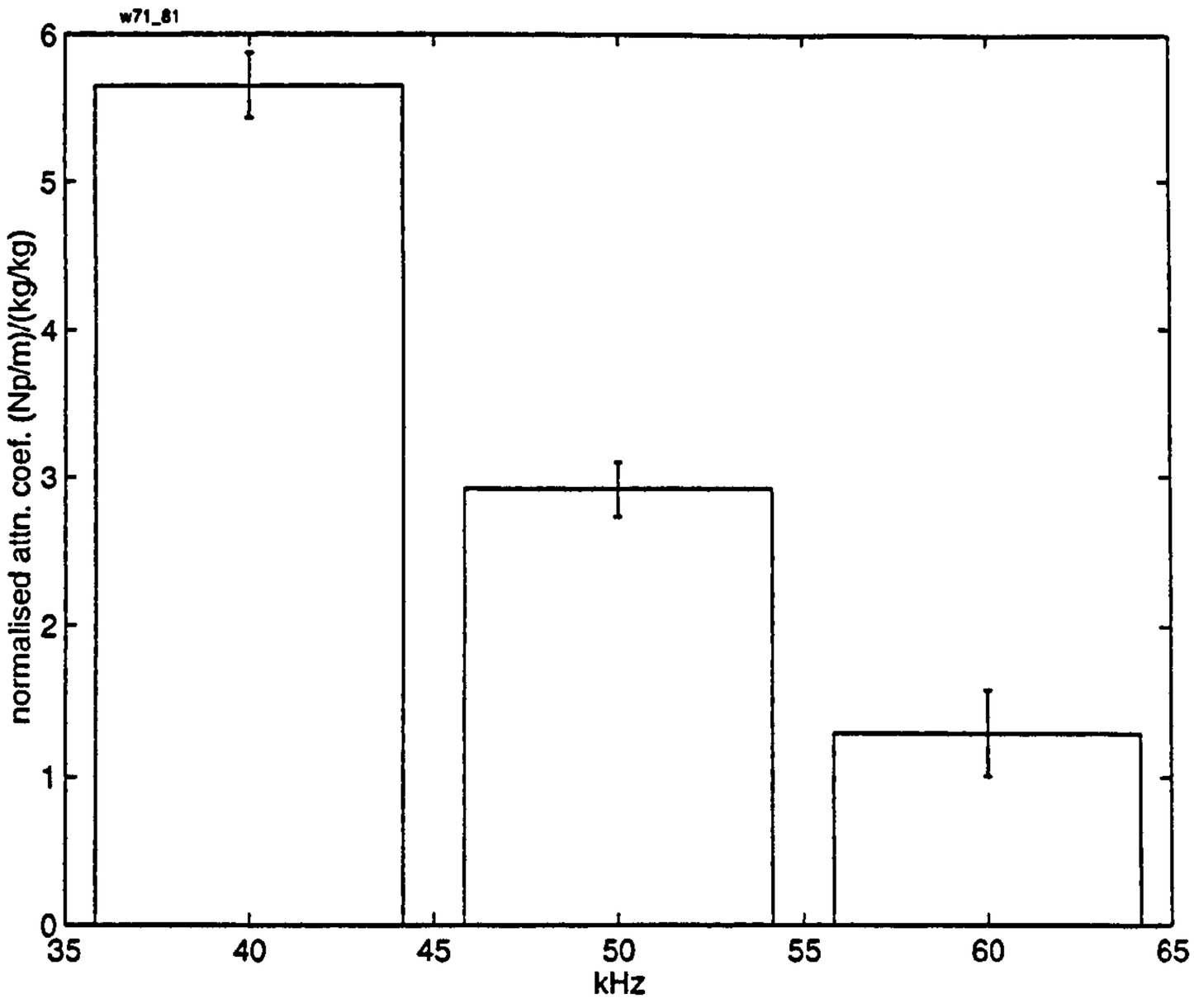

Figure 8-12 Attenuation coefficient per kg/kg of flowing flour ; error bars indicate 90% confidence limits, bar width indicates the inverse of the window length.

To compare the values of attenuation coefficient measured with this ultrasonic method, with the value deduced from Figure 8-3, and those previously presented for the plane wave method, the measurements are plotted on the same axis in Figure 8-12. Curves are also shown, calculated using both theories of both Lloyd & Berry and Ma, Ma & Varadan (with lossy scatterers); the latter theory, which includes low-order terms for compressional wave scattering, is shown since the value of *ka* approaches 0.3 for the higher frequency and larger particles, and so Rayleigh scattering could begin to be important.

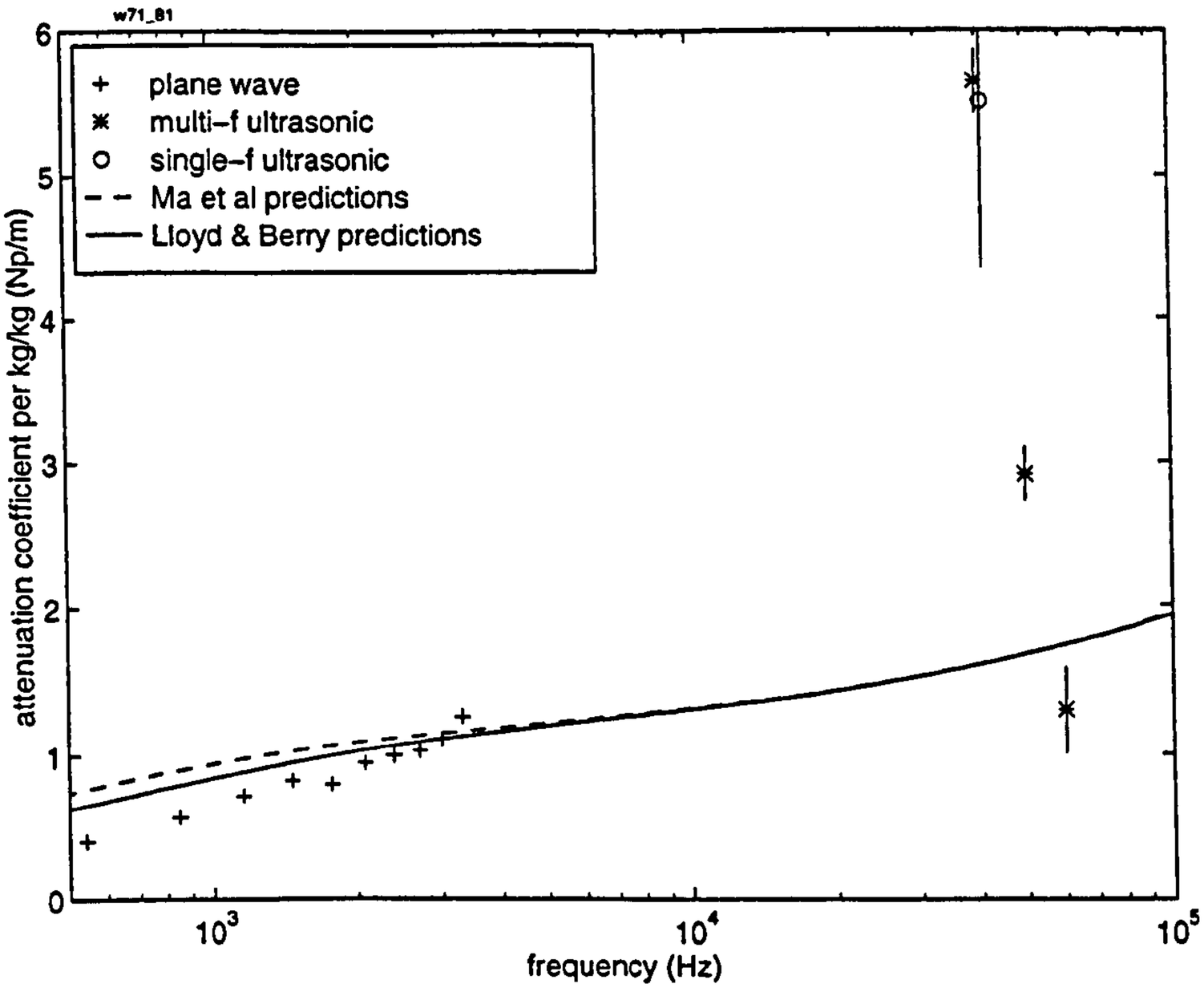

Figure 8-13 Attenuation coefficient per kg/kg, for flowing flour; plane wave (axial) and ultrasonic (diametrical) measurement techniques (two methods). Theoretical curves are calculated using Lloyd & Berry and Ma et al (with lossy scatterers).

The measured frequency dependence in the ultrasonic range is completely unlike the predictions, although of the same order of magnitude. The measured attenuation coefficient at 40 kHz is almost identical to the value measured (by a very different method) in section 8.2.2, giving some confidence in the unexpectedly high figures. Compressional wave scattering is not predicted to cause a significant effect. The divergence between the theories at low frequency could be explained by an approximation in the evaluation of the theory of Ma *et al.* Since this theory does not include the effects due to particle size distribution, to account for the wide PSD of flour, the effect of each size fraction was weighted and summed; this is effectively a single scattering approximation, and so is less valid at lower frequencies, due to the larger viscous and thermal boundary layers.

Olivine Sand

To investigate the possible causes of the unusual behaviour just mentioned, the measurement technique was changed slightly. Single tone bursts were used instead of measuring at three frequencies simultaneously, to ensure that no non-linear interference could occur between frequencies. Furthermore, the position of the DFT window was maintained constant, around the main incident wave, with a length of 290 μs.

Olivine sand was used as the test material (the flour sample was not available for testing). Its larger particle size was predicted to cause negligible attenuation over the path length, except at values of $ka > \pi/10$. Therefore the upper frequency was increased to 75kHz (at which $ka = 0.38$), to investigate whether compressional scattering becomes significant.

The insertion loss at 40, 50 and 75 kHz is shown in Figure 8-14 to Figure 8-16.

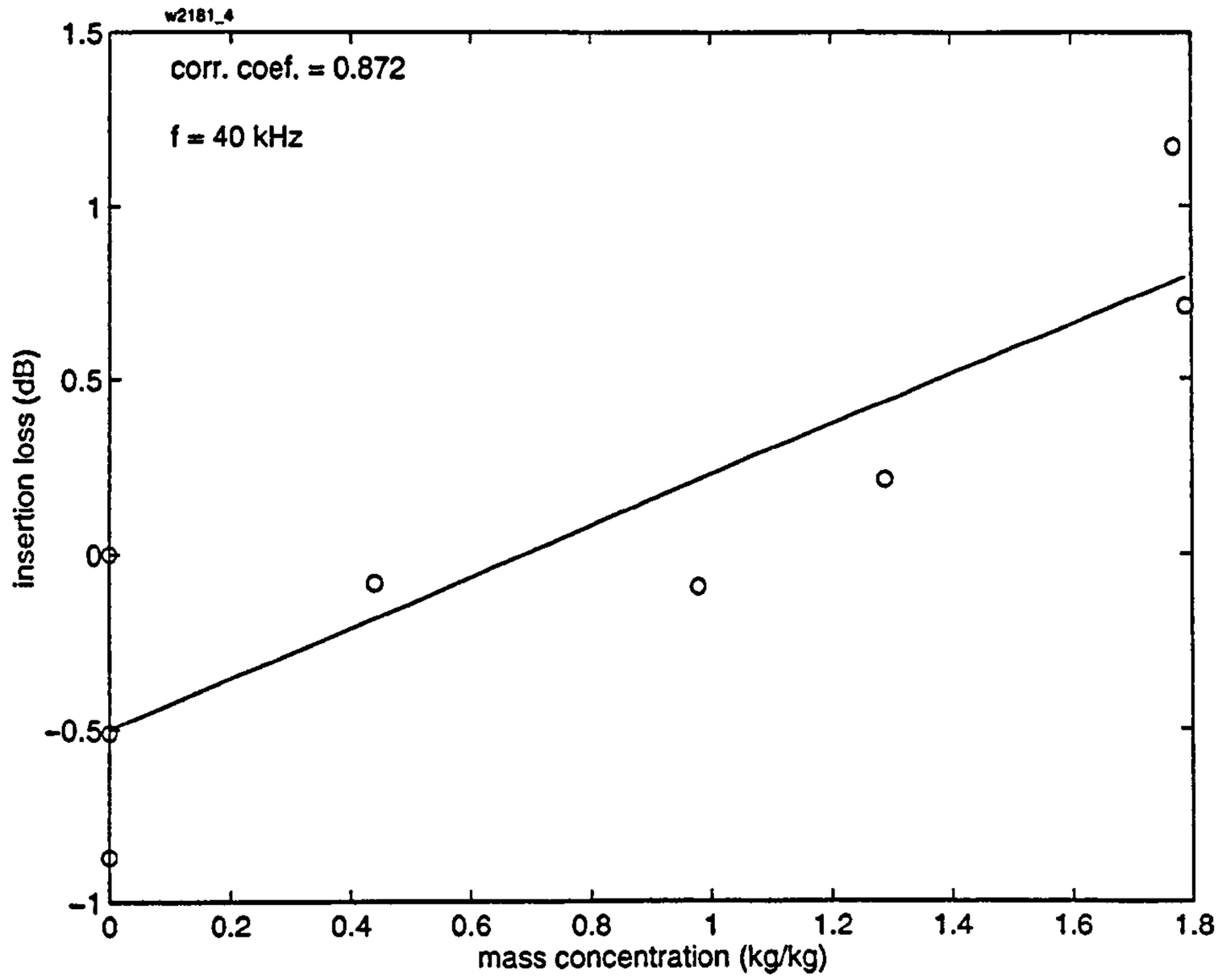

Figure 8-14 *Insertion loss of flowing sand at 40kHz over 1.3 m path, and line of best fit.*

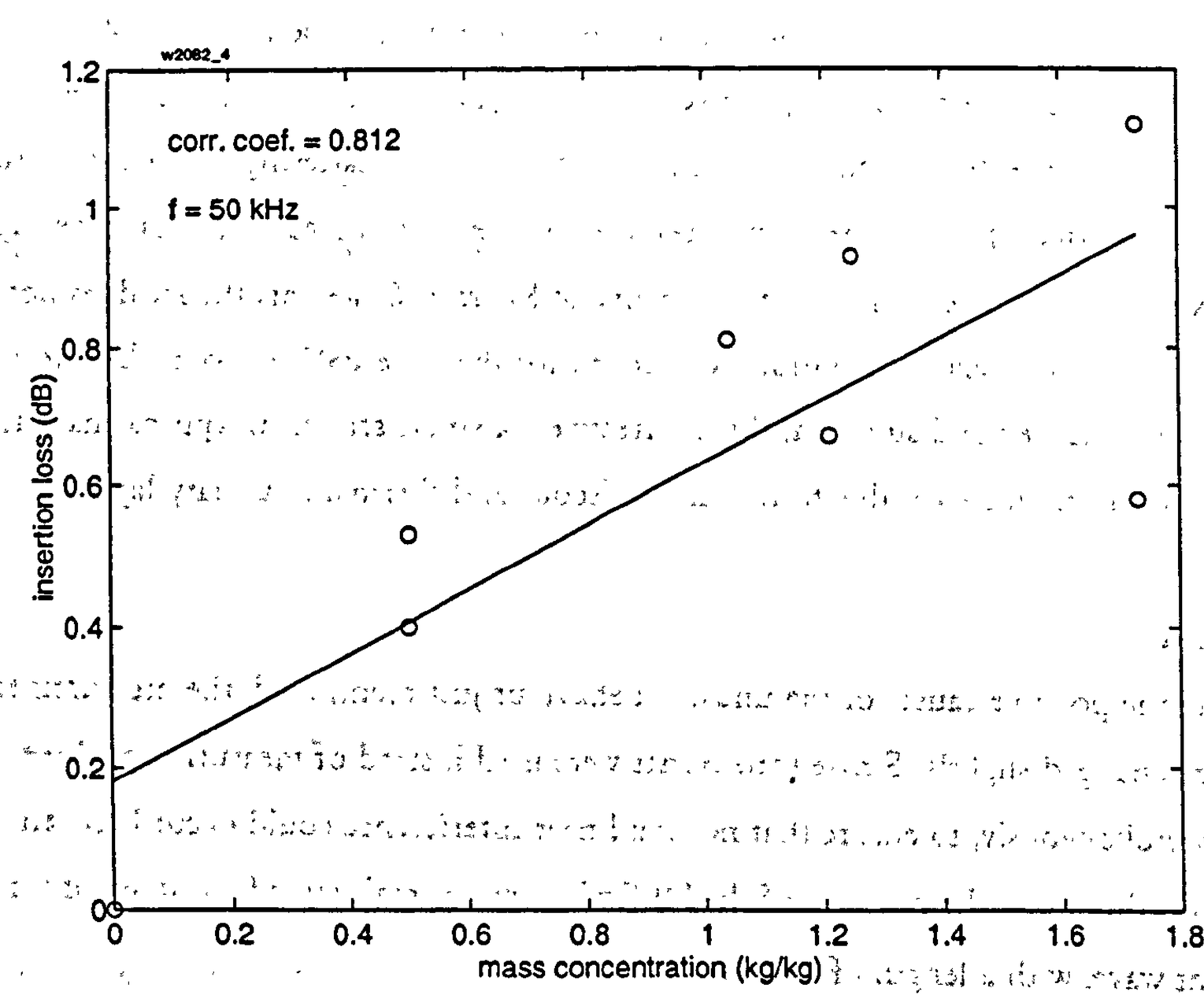

Figure 8-15 *Insertion loss of flowing sand at 50kHz over 1.3 m path, and line of best fit.*

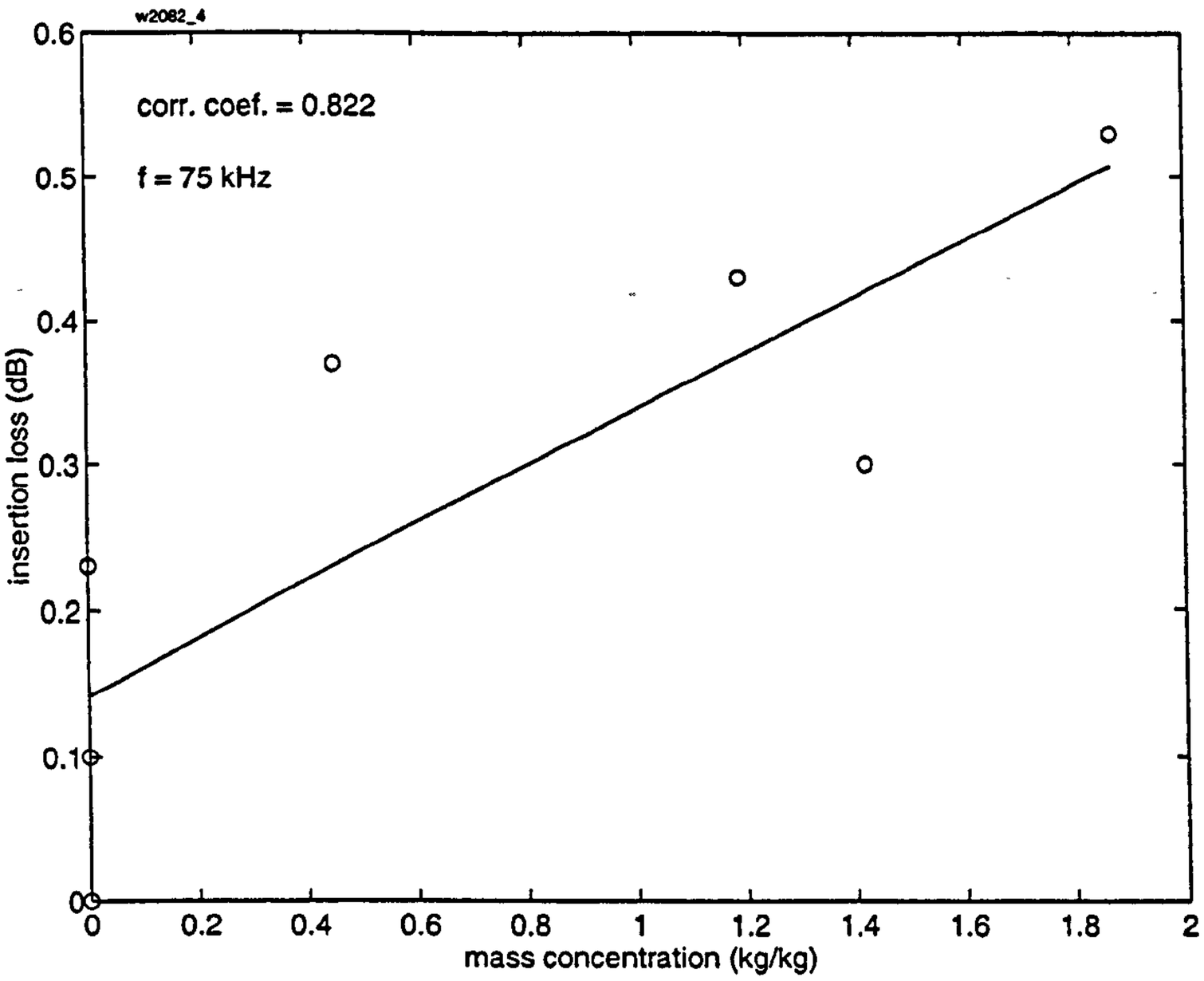

Figure 8-16 *Insertion loss of flowing sand at 75kHz over 1.3 m path, and line of best fit.*

It can be seen that the insertion loss remains below 1.5 dB, and so the accuracy of the measurements is limited by the repeatability of the measuring system. There does appear to be a positive correlation between concentration and insertion loss (with a correlation coefficient > 0.8). The normalised attenuation coefficients, calculated from the gradients of the best fit lines, are shown in Figure 8-17.

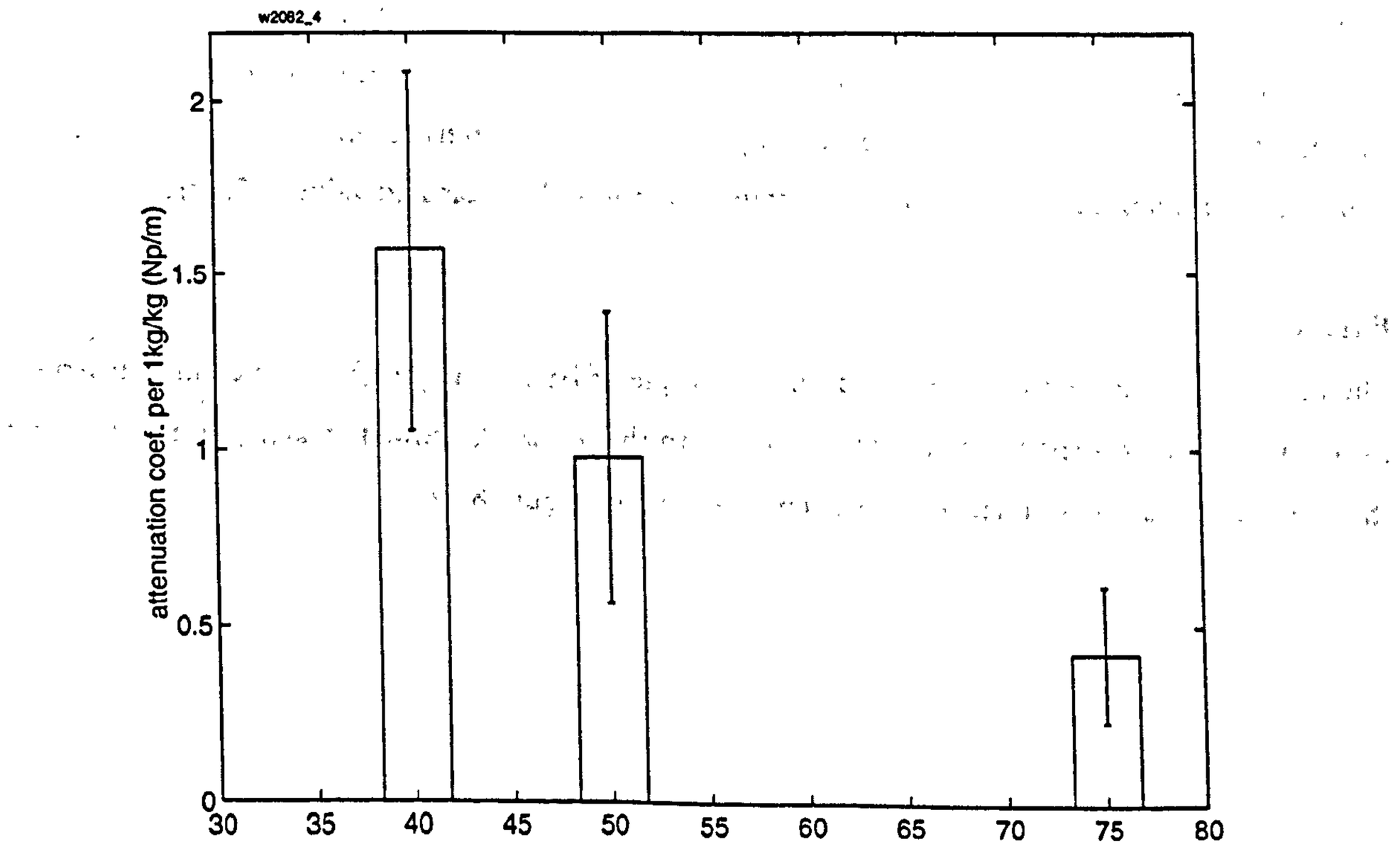

Figure 8-17 *Attenuation coefficient per kg/kg of flowing sand ; error bars indicate 90% confidence limits, bar width indicates the inverse of the window length.*

Once again, we note the decreasing attenuation coefficient as a function of frequency, although the confidence intervals are large, and little can be deduced with certainty. Figure 8-18 shows these values of attenuation coefficient plotted together with the values deduced from the plane wave measurements in section 6.3.1, and the predictions of the two theories.

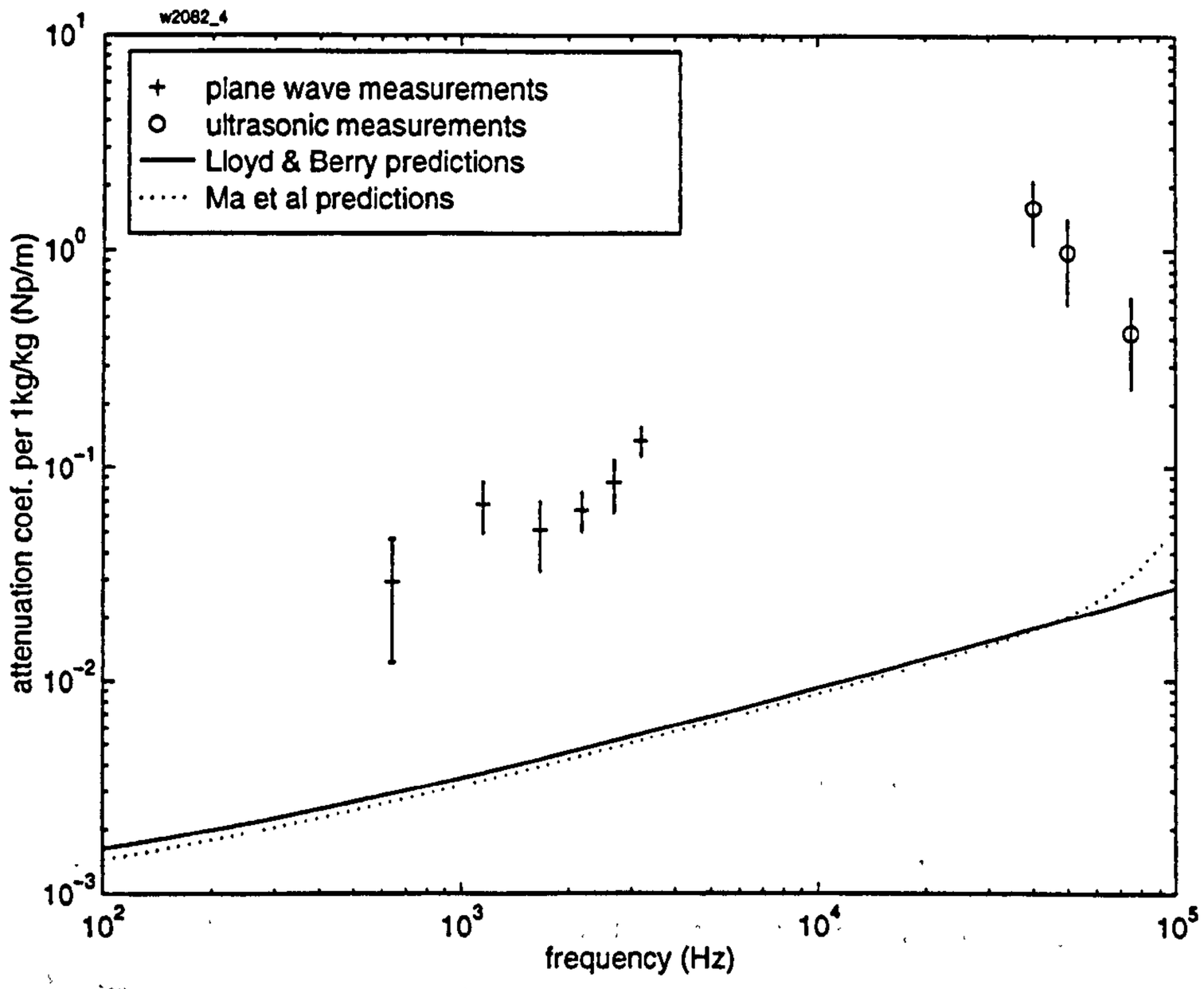

Figure 8-18 Attenuation coefficient per kg/kg, for flowing sand; plane wave (axial) and ultrasonic (diametrical) measurement techniques. Theoretical curves are calculated using Lloyd & Berry and Ma et al (with lossy scatterers).

The measured ultrasonic attenuation is consistent with the scaling of the plane wave measurements and both sets are far in excess of the predictions (note the logarithmic y-axis). The overall pattern is very similar to that measured with flour. The predictions of Ma *et al* show the expected transition to the higher power scaling of compressional wave scattering (above 60 kHz), but the magnitude of attenuation still remains substantially below the measured value at 75 kHz.

Barytes

The measurement method was repeated on the sample of barytes (Ba_2SO_4). The measured insertion losses, while having a slightly larger magnitude than that of sand, showed greater point scatter (not shown). The deduced attenuation coefficient is shown in Figure 8-19.

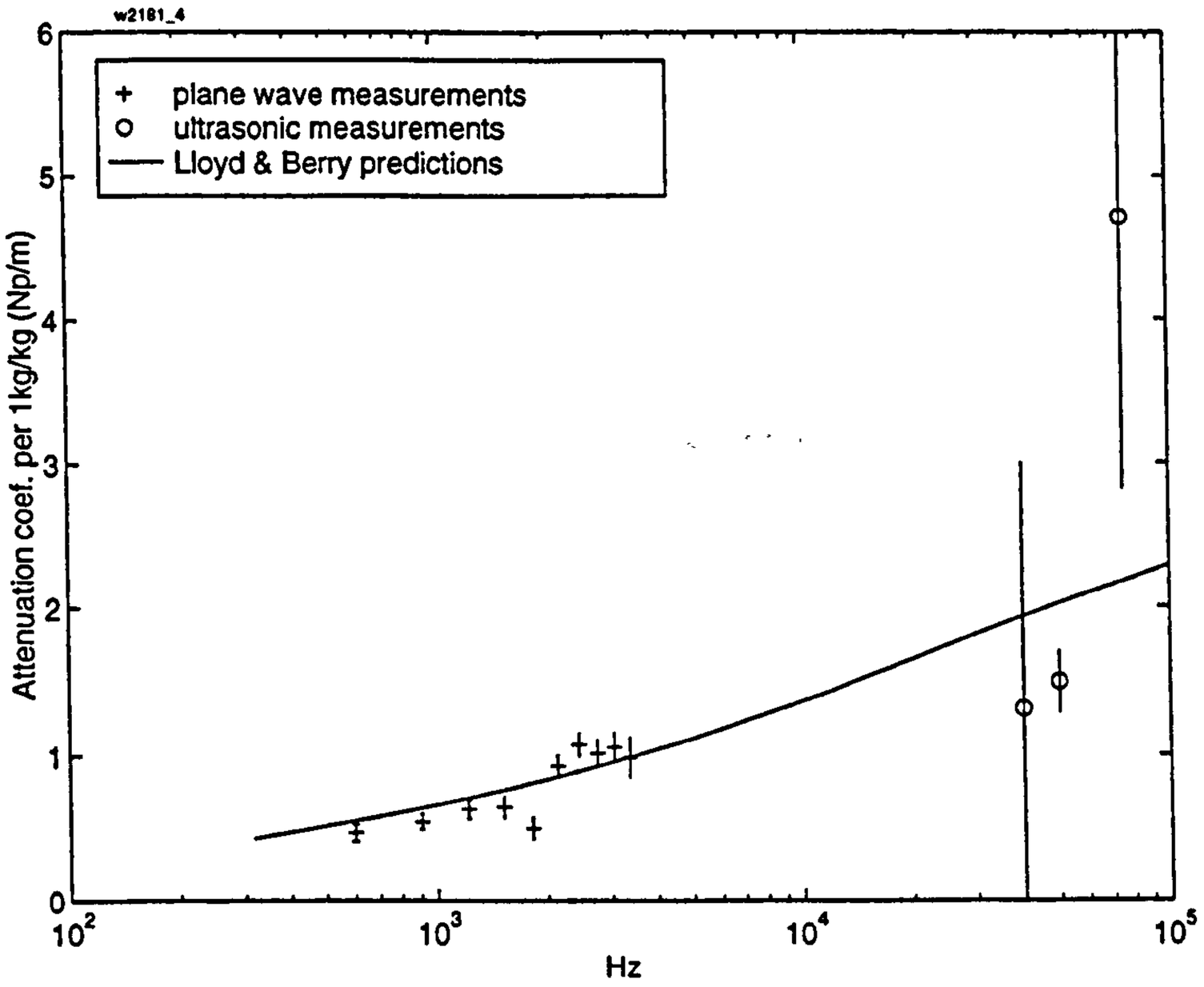

Figure 8-19 Attenuation coefficient per kg/kg, for flowing barytes; plane wave (axial) and ultrasonic (diametrical) measurement techniques. Theoretical curve is calculated using Lloyd & Berry, and fitted Rosin Rammler distribution: fineness = 18μm, dispersion = 1.7.

The point scatter is reflected in the large confidence limits – except at the 50 kHz point. Nonetheless, the data are interesting since the attenuation appears to show the expected increase with frequency, and is of the same order as the plane wave measurements. A theoretical curve is shown to assess whether the overall scaling of the curve is reasonable: the PSD was chosen to give a best fit to the plane wave measurements.

Due to its cohesive nature, this sample of barytes was not a good material with which to obtain repeatable results. The repeatability of the reference (clean air) measurements were poor; the airflow could never be assumed to be "clean", because, even with the feed valve closed, particles would be picked up from the tube walls and carried in suspension. Furthermore, since the very fine particles aggregated into clumps, the acoustic properties of the suspension were strongly dependent on the size of the clumps, which could change over time. Therefore, the suspension could not be assumed to maintain a constant PSD.

8.5 CONCLUSIONS

The insertion loss caused by flowing suspensions of flour, sand and barytes has been measured using an ultrasonic cross-pipe technique, covering the range 40 - 75 kHz.

Single frequency (40 kHz) measurements were made on flour, in which a pair of sealed resonant piezoelectric transducers were exposed directly to the flow, and kept clear of dust build-up by the flow itself. The temporary nature of this solution led to the development of the air-flushed probes, that were described in Chapter 5. These measurements extended up to a concentration of 16 kg/kg, and so large insertion losses were measured (up to 43 dB). Correlation of the insertion loss with concentration was fairly poor (see Figure 8-3): this could be due to the very unsteady flow conditions that prevailed at high concentrations, and possibly because of the received acoustic signal, that included multiply reflected signals. The attenuation coefficient that was deduced from this method was approximately a factor of 5 higher than predicted. Even attributing the whole of the measured insertion loss to the first reflection – with a path length three times longer than the direct wave – would not account for such a difference.

Broadband electrostatic transducers[5] were chosen for further measurements, and were incorporated in air-flushed probes. A system was devised that could measure the insertion loss at several frequencies simultaneously, and which could edit out unwanted reflections from the received signal. Concentrations up to 2.3 kg/kg were measured.

The attenuation coefficients of flour, sand and barytes, estimated from the insertion loss, are the same order of magnitude as that expected by extrapolating plane wave measurements. The magnitude of the insertion loss is lower than that using a plane wave technique, because the path length is 25 times shorter; this makes the technique susceptible to noise. The measurements on sand, especially, show very small insertion losses (< 1.5 dB, Figure 8-14 - Figure 8-16). The main limitation is the pipe diameter; the insertion loss is predicted to scale linearly with the diameter, and so the method becomes more practical for full scale pipelines: PF feed pipes are typically around 0.5 m diameter, and so would produce insertion losses one order of magnitude higher than measured here.

The measured attenuation coefficient of flour and sand was observed to fall steeply with frequency between 40 and 75 kHz (Figure 8-13 & Figure 8-18). This trend can not be explained theoretically, unless the resonant scattering regime is being entered at very much lower frequency than predicted: this seems unlikely. The 40 kHz measurement on flour is supported by a very similar figure measured using the earlier, different technique. Furthermore, the accuracy of the equipment was supported by the very good agreement with theoretical predictions of the attenuation coefficient of polyester fibre (Figure 8-8). This latter experiment did not, however, include any flow, and so further mechanisms due to flow could be responsible. The pattern of reducing

[5] - The microphone is also an electrostatic device.

attenuation coefficient with frequency has not been found in a suspension of barytes (Figure 8-19), and so is not an inherent characteristic of the equipment; however, the underlying dataset was poor due to the unpredictable nature of the material.

The measured attenuation coefficient of olivine sand at ultrasonic frequencies was over one order of magnitude higher than predicted. The values are, however, consistent with those found from the plane wave measurements, suggesting that a real physical mechanism is operating. The measurements on barytes can not be compared with predictions, due to the unknown particle size. Divergences from theoretical predictions can be expected at these high values of *Re* (up to 35 for sand), since the viscous boundary layer is very small compared to the particle size, and so effects of non-sphericity and roughness become more significant. It does not seem likely, however, that such effects could account for all of the disagreement.

A source of error in these measurements is the unstability of the reference levels, which are measured with clean airflow. One possible reason for the drift (which was not found on the OU airflow rig) is the variable static pressure in the pipeline, which may be affecting the sensitivity of the transmitter. While the transducer mounting arrangement included a static pressure equalisation to the rear of the transducer with a low flow resistance, the internal path within the transducer to the rear of the membrane is not well defined, and is likely to be through joints in the casing. This high flow resistance would cause a comparatively low -3dB point, therefore causing short term sensitivity variations as the pressure in the pipeline varies — due to varying quantities of particulate in suspension, for example. One solution may be to modify the transducer by drilling holes in its rear cover; however, this may not be possible without destroying it. A further option would be to use piezoelectric transducers, which are not sensitive to static pressure variations, as they react against a seismic mass rather than an acoustic compliance.

The noise created by the probe flushing arrangement is the greatest source of background noise, and necessitates many pre-averages to increase the S.N.R. to a useable level. Future probe design could reduce this noise level.

9

CONCLUSIONS AND SUGGESTIONS FOR FURTHER WORK

This thesis has described the development of experimental techniques that, in combination, allow measurement of acoustic properties of aerosols over a wide range of frequencies and concentrations. The frequency range spanned more than 9 octaves, from 200 to 75000 Hz with few gaps, while the acoustic techniques were tested on concentrations that varied over more than 4 decades, from 0.6 g/kg to 20kg/kg. Several novel measurement techniques have been developed. The purpose of this work is to find techniques that are suitable in a range of different operational conditions, and which convey sufficient information about the acoustic properties of the suspension to enable deduction of useful physical information. In particular, the deduction of suspension concentration while the particle size distribution (PSD) is also varying, requires measurements at several well-chosen frequencies. This will be discussed further in section 9.3.

There are three sections to this final chapter:

- Section 9.1 summarises the main conclusions from each chapter (and Appendix A)
- Section 9.2 highlights the main questions raised in this work, and suggests ways in which they may be answered; it also suggests general improvements to the methods presented, and further methods that may be developed.
- Section 9.3 presents some conclusions of this work from the viewpoint of someone designing an acoustic instrument to measure the mass flow rate of an aerosol. It advises on the choice of frequency range and measurement technique for different operational parameters.

9.1 CONCLUSIONS[1]

Three main frequency regions were investigated. In the plane wave region, the wavelength was somewhat larger than the pipe diameter, so that only a single acoustic mode — the plane wave mode — could propagate. The measurement path was along the tube axis. In the ultrasonic region, the wavelength was small compared to the tube diameter, allowing measurement across the width of the pipe. In the reverberant region, the wavelength was small enough for the propagation of many different modes, but too large to permit the identification of a signal path, and so the propagation constant could not be measured directly: statistical techniques were more appropriate.

9.1.1 Plane wave region (Chapter 6)

The impulse response between an axially-separated transmitter and receiver was used to measure propagation along the tube axis. The length of the pipe allowed isolation of a single, direct pulse, and since the path of this packet of energy was known, the attenuation coefficient could be found. The method assumes that the coupling of energy into and out of the probe tube remains constant over varying flow conditions. This was found to be approximately correct for varying air velocity.

Measurements were made on low concentration (0.6 - 32 g/kg), quasi-static aerosols of three grades of fine alumina particles (<10μm radius). The theoretical predictions of Lloyd & Berry (with a long wavelength approximation [93]) showed good agreement with the measurements. In particular, the predicted linearity of attenuation and dispersion as a function of concentration was shown convincingly, and the predicted variation of these quantities as a function of frequency was demonstrated by the data.

Using specially-designed equipment, measurements were made on more concentrated (up to 20 kg/kg), flowing suspensions of larger particles. These measurements showed less agreement with the predictions. While some of the difference is likely to be due to the more complex and noisy acoustic environment, there appear to be systematic differences that can not be dismissed so easily. Measurements on flour, with a mean particle radius of 29μm, showed the predicted linearity of attenuation coefficient as a function of concentration; but the frequency dependence also appeared nearly linear, rather than the predicted dependence which was more sigmoidal. Such a pattern is characteristic of a particulate with a wide PSD, and it has been observed by several experimenters [53, 62, 6, 148] all of whom measured propagation in slurries. The difference between theoretical predictions and measurements might be explained by the non-sphericity of the particles. Photomicrographs of flour particles, for example, reveal that they consist of clusters of smaller particles (1 - 5 μm in radius). It is unclear how such a structure should be modelled; intuitively one may expect it to create effects similar to a suspension of a wider PSD. However, Allegra & Hawley [6], made their observations on polystyrene microspheres, which should be a

[1] More detailed conclusions are given at the end of each chapter.

good approximation to spheres, and they still found the unpredicted linear frequency dependence of attenuation coefficient.

The acoustic effects of flowing olivine sand were predicted to be negligible, because of the larger particle size (mean radius of 278μm). Nevertheless, small but measurable insertion losses were found, and they appeared to be proportional to the mass concentration. The deduced attenuation coefficient was considerably higher than predicted, and also showed a higher rate of increase as a function of frequency than predicted.

The excess attenuation of a flowing suspension of barytes was found by measuring the difference in attenuation coefficient over two path lengths. Unlike measurements on flour and sand, the insertion loss at both path lengths was found to be a non-linear function of mass concentration. Even so, when the excess attenuation was found by taking the difference of the insertion losses, the function appeared linear. This suggests that, for this material, a non-linear mechanism is operating in addition to the medium attenuation. One hypothesis is that the boundary layer parameters at the orifice are affected by the properties and concentration of the particulate, hence changing the coupling ratio of the probe tubes into the pipeline.

9.1.2 Reverberant region (Chapter 7)

Measurements in the plane wave and ultrasonic regions attempted to reproduce the free field (in which the direct wave only is received) by editing out reflections. In the reverberant region, the sound field is approximately diffuse (sound arrives at the receiver equally from all directions). This assumption is implicit in the theories that are used to model the reverberant field. For the case of a semi-infinite tube, it is a poor assumption, but it was made to allow some crude comparison of measurements with theory.

Three types of acoustic measurements were made: excess decay rate, shift of modal frequencies, and steady state sound level.

Excess decay rate (sections 7.2 & 7.3)

Measurements of the excess decay rate in enclosed, quasi-static suspensions showed a close proportionality to concentration, provided that analysis was carried out in narrow frequency bands. To achieve the best correlation of excess decay rate with concentration, the bands should be chosen to lie just above the cut-on frequency of the transverse modes of the cylindrical enclosure.

Measurements on flowing suspensions were complicated by a faster decay rate, so giving fewer samples from which to deduce the decay rate. The higher rate was due to the unbounded nature of the pipeline, allowing propagation of sound away from the measuring volume. Measurements were also hampered by background noise, and required much averaging to attain a sufficient signal/noise ratio (SNR). Nevertheless, the measured decay rates were found to correlate with concentration, provided the concentration was kept sufficiently low to ensure a good SNR. The

order of magnitude of the measurements was consistent with the predictions for alumina and flour, although there was considerably more structure to the frequency dependence than predicted. Measurements on flowing olivine sand – in common with measurements across the other two frequency regions – showed considerably greater acoustic effect than predicted.

The measurement of excess decay rate has the advantage that absolute or stable calibrations of the transducers are not required. Similarly, such measurements should be insensitive to variations of the orifice impedance (provided that conditions remain stable over the duration of each measurement). As each decay is measured over a much longer duration than plane wave or ultrasonic measurements, the path length is effectively very long, giving a high sensitivity to the presence of the suspension. Equally, due to the reverberant sound field, one can expect the measurement to provide good volume averaging of the pipe interior, and so to compensate automatically for inhomogeneously distributed flows.

The technique is unlikely to be practical for real applications since, in a semi-infinite pipe, most energy propagates away from the transmitter instead of creating a diffuse reverberant field, leading to a decay that rapidly descends into the noise floor. The method also requires fairly intensive signal-processing, although this could be mitigated with dedicated equipment.

Modal frequency shift (section 7.4)

A theoretical method (proposed by Vetter & Culick [151]) of measuring the change in resonant frequency of transverse modes has been assessed experimentally. The method relies on being able to track the frequency of a single mode. It was found that a real (finite length) pipeline does not display individually separable modes, but rather that they cluster about the cut-on frequency of each transverse mode. As the attenuation of the suspension increases, the sharpness of the resonance deteriorates, since the Q-factor decreases and the peak becomes less distinct above the surrounding spectral components. A small frequency shift of <0.25 % in the first transverse mode (3870 Hz) was noticeable at a concentration of 0.5kg/kg of flour. This is less than that predicted by Vetter & Culick, but consistent with a simplified theory based on the sound speed change predicted by Lloyd & Berry.

The greatest modal shift is predicted to occur at low frequencies – in the viscous regime. Since the lowest frequency of operation is inversely dependent on pipe diameter, this means that the method would work best on large pipes, and with small-sized particles. However, while the percentage frequency change increases as the frequency decreases, the absolute change remains fairly small, so that the accurate resolution of the change will require a lengthy measurement time.

Steady state sound level (section 7.5)

The background noise level of the flowing suspension was measured, and found to decrease with increasing frequency, and tended to decrease with increasing concentration of particulate (when

tested on flour). Measurements were hampered by the flushing noise of the microphone probe, and attempts to find correlations with flow parameters were complicated by a feature specific to the flow rig being used: namely, that the noise spectrum of the flow was dependent on the valve settings that controlled the suspension density. Although this problem may be specific to the rig, it indicates the likelihood that any such measurements in the field will be complicated by uncontrolled changes in plant operating conditions.

In order to reduce the masking effect of flushing noise, and to decouple the measured signal from changes in rig settings, "active" monitoring of steady state noise was attempted: this entailed transmitting a pseudo-random signal, and synchronously-averaging the response to reduce uncorrelated noise components. The received signal was filtered into the same modal bands as used for measurements of reverberant decay. The resulting sound pressure level (SPL) was found to decrease with increasing concentration. A simple theory was proposed to predict the decrease. The measurements on flour agreed with the predictions reasonably well, although the acoustic effect of sand was, as usual, far in excess of predictions; the shape of the measured dependence on concentration corresponded to that predicted.

9.1.3 Ultrasonic region (Chapter 8)

Measurements were made of the propagation of ultrasonic signals across the width of a pipe, to find the insertion loss due to flowing suspensions, over the range 40 - 75 kHz. The values of insertion loss were towards the bottom of the measurable range, due to the short path length through the suspension (equal to the pipe diameter, 53mm), and so the values of attenuation coefficient that were deduced from these measurements were susceptible to error. The magnitude of attenuation coefficient for all three test materials (flour, olivine sand and barytes) was consistent with measurements made over the plane wave region. Measurements on flour and sand show a steeply decreasing attenuation coefficient as a function of frequency, which is significantly different to the predictions of a monotonic increase; measurements on barytes, however, show the expected increase. The acoustic effect of sand was over one order of magnitude higher than predicted.

These unexpected results were checked by using the equipment to measure the insertion loss of a sample of fibrous material, without any airflow. The measurements closely matched predictions by a porous material theory. Furthermore, the measured attenuation coefficient of flour at 40kHz was nearly identical to the value measured using a different set of transducers that did not require air flushing, and used a different signal processing method.

The diameter of the flow pipeline was too small to make accurate measurements of insertion loss (unless the suspension was more dense, or composed of finer particles). The attempt to create a suspension of higher attenuation properties by testing a sample of fine barytes particles was not successful, because the particles agglomerated into much larger particles. A pipeline in a real PF

application would have a diameter approximately 10 times larger, and the insertion losses (in dBs) would be proportionally higher.

9.1.4 Characteristic impedance (Appendix A)

Changes in the terminal impedance of a low frequency loudspeaker, coupled to the pipeline via a probe tube, were measured as it was continuously excited at a single frequency. The change in the radiation loading of the driver was predicted to be reflected in the terminal impedance, and therefore it was expected that changes in the acoustic properties of the flow may be detected in this way. Measurements were not calibrated in terms of impedance, but the relative direction of changes in the resistive and reactive parts of the impedance could be detected.

The impedance change was found to be closely related to the air flow velocity in the main pipeline, and also in the probe tube. For both experiments, the change was in qualitative agreement with findings of other researchers. For the case of pipeline flow, the results are explained by variations in orifice impedance; for the case of probe tube flow, the results are explained by variations in the reflection coefficient at the orifice.

Little clear correlation was found with the concentration of either barytes or olivine sand particles. However, the presence of particles was found to have a noticeable effect compared with clean air. A possible explanation for such a non-linear mechanism is that the largest influence is that of particles on the orifice impedance, due to changes in the boundary layer at the pipe wall.

9.2 SUGGESTIONS FOR FURTHER WORK

9.2.1 General

The main questions that arise from this work are:

- What is causing the attenuation coefficient to show linear dependence on frequency (in the plane wave measurements)?
- What acoustic effect will different levels of particle agglomeration have, and how should agglomerated particles be modelled?
- What causes the acoustic effect of olivine sand to be uniformly higher than predictions, in all experiments ? Are we measuring a real loss mechanism; or is some other mechanism – eg. the coupling into/out of the transducer orifices – being affected by the particle concentration?
- How is the coupling into/out of the transducer orifices affected by flow speed and particle concentration?
- What is causing the attenuation coefficient to fall with frequency in the ultrasonic region? Is it the effect real or an artifact ?

9.2.2 Equipment (Chapters 4 & 5)

There are many incremental improvements that could be made to the equipment. A major improvement in the microphone performance would be achieved if the background noise due to flushing could be reduced. This will require a detailed redesign of the internal airways, to increase the hole area through which the air enters the probe tube (and a consequent increase in the resistance of the compensation material). A further, slight improvement, could probably be achieved by relocating the choke flow nozzle that supplies the flushing air, away from the probe, and inserting reactive and resistive silencing elements in the supply channel[1].

Some of the fundamental questions could be best resolved in laboratory conditions with static suspensions. The operation of the quasi-static rig is limited to diffuse suspensions of fine particles. Since it is not possible to suspend higher densities of larger particles without flow, such apparatus will probably produce "suspensions" by creating a falling column of particles, moving through still air. This will require a feeder mechanism that will supply into the top of an air column, a controllable, stable flow of particles; this can be done readily by a vibratory feeder. To ensure that particles are individually separated (a process normally achieved by the shear force of the

[1] The reason that this was not done in the original design, was the desire to reduce as far as possible the volume (and hence compliance) of air after the regulating nozzle, so that the flow rate of flushing air remained closely constant, regardless of pressure pulses in the main pipeline.

perpendicular airflow that entrains the particles), an acoustic excitation method may be feasible [125].

More specific modifications to equipment will be addressed under the relevant heading.

9.2.3 Plane wave measurements (Chapter 6)

To remove the uncertain variations of the orifice coupling ratio, more experiments could be attempted with twin receivers, to find the excess attenuation between them. The measurement would ideally be performed with a dual-input MLSSA-type system.

The frequency dependence of different materials would be investigated. In particular, the effects of particle agglomeration and non-sphericity would be tested to see if these factors could explain the divergence between theory and measurements. The materials could be chosen to display the characteristics required; eg. fine glass beads should approximate to spheres.

9.2.4 Reverberation measurements (Chapter 7)

If the background noise of the microphone flushing system can be reduced sufficiently, then passive monitoring of flow noise can be attempted, to see whether useful correlation with flow parameters can be found.

There is an experimental method that may be able to combine measurements both of steady state SPL and modal frequency shift. The marginal oscillator is an elegant and computationally simple method that has been used in several different fields [143, 48, 144]. The principle is to connect the amplified, received signal to the acoustic driver. The resulting feedback will, at certain frequencies have the correct phase relationship to create oscillations that would, unless otherwise controlled, increase in level until some part of the signal chain limits the amplitude by saturating. However, if the gain stage is arranged to control the signal gain to maintain oscillations at a certain reference level (using a form of automatic gain control, AGC) then stable, unsaturated, oscillations will result. The system will require a band-pass filter to restrict oscillations to only the mode desired, and possibly a phase shift network to ensure that the feedback signal has the correct phase. Figure 9-1 shows one such possible system. Any changes of modal frequency could be tracked by using a voltage controlled oscillator to lock onto a fixed phase of the signal.

The loop gain of the system is $G_{loop} = G_1 . G_2 . G_m . G_a$

As the automatic gain control keeps oscillations at a constant level, the loop gain remains constant, with the amplifier gain G_a increasing as the medium gain G_m decreases. Therefore, G_a, as measured by the gain control voltage, is inversely related to the gain of the acoustic medium:

Medium gain $G_m \propto 1 / G_a$.

Unlike the reverberant decay technique, however, this system is sensitive to changes in transducer gains, G_1 and G_2, however they may be caused.

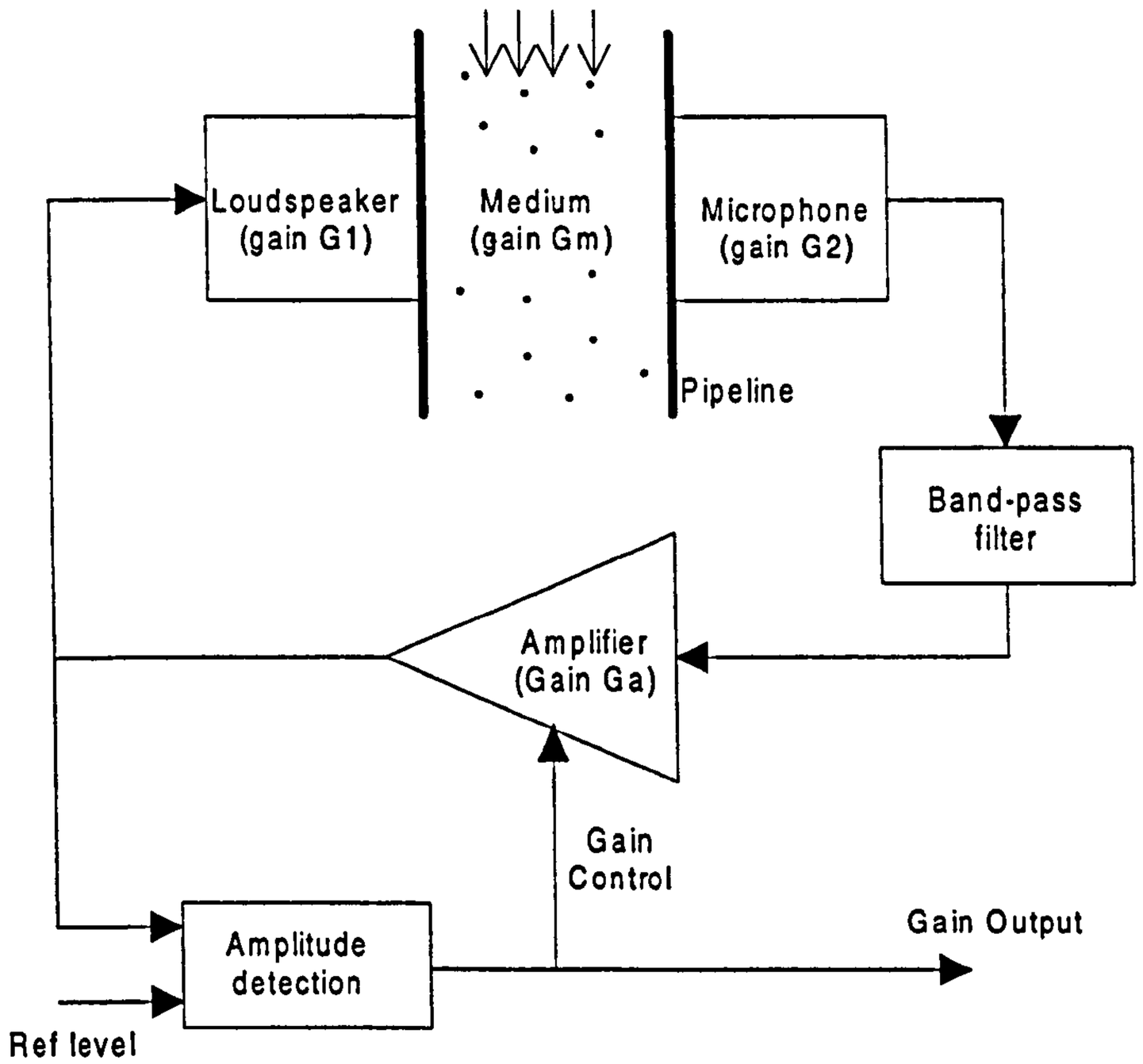

Figure 9-1 Schematic diagram of marginal oscillator system for measuring suspension "gain".

9.2.5 Ultrasonic measurements (Chapter 8)

The SNR of ultrasonic measurements could be improved significantly if the probes are redesigned to reduce the flushing noise. Alternatively, the electrostatic transducers could be replaced by piezoelectric types; these have a higher acoustic impedance, and can drive a layer of rubber that is inserted flush into the wall of the flow tube, removing the necessity for flushing air. This is the approach taken by Sowerby *et al* [136]; it is uncertain what the long term resistance or stability of such a rubber facing would be, although Burnett [29] has shown that rubber can be quite resistant to abrasion by flow.

Using a piezoelectric transducer would also reduce one postulated cause of drift: the sensitivity of electrostatic transducers to pressure fluctuations in the pipeline. Alternatively, suggestions have been made of ways in which the transducer may be modified to provide better pressure equalisation.

A disadvantage of piezoelectric transducers, is that their bandwidth is usually narrower than electrostatic transducers: their impedance mismatch with air is so great, that rubber matching layers are often used to increase coupling, but these are usually only effective over a narrow frequency range. Furthermore, the lower frequency range of piezoelectric transducers is higher

than that of electrostatic transducers, so that measurements with a piezoelectric transducer will probably not be able to reproduce the measurements over the range tested in this work.

This would be unfortunate, because there is a clear need for further testing to investigate the cause of the anomalous frequency dependence. The accuracy could be increased by testing in a larger diameter pipeline, with higher concentrations and/or smaller particles, so that measuring errors constitute a smaller proportion of the insertion loss.

The acoustic effects at the orifice are very uncertain in this frequency range. The orifice impedance is not likely to have a large effect on the transmitted power, because the reflection coefficient of the expansion into the pipeline is small at high frequencies. Effects of refraction and reduction in coherence due to the shear layer at the orifice are likely to be more significant [27]. If the probe tube method is pursued further, then investigations into these phenomena would be valuable.

A possible method to eliminate these effects, would be to use the same transducer as a transmitter and receiver (a monostatic arrangement), and measure the amplitude difference between successive reflected signals. This is a standard technique in ultrasonic thickness measurement of solids, but will be complicated in the case of flow, because the (necessarily tight) beam will drift downstream.

Even more speculative is the idea of creating a phased-array transmitter or transceiver: this would probably entail an electrostatic transducer with multiple electrodes, so that the wavefront of the signal can be shaped and steered. With such an arrangement, the beam could be automatically steered to give the largest received response, and hence eliminate effects due to flow-induced beam drift.

9.2.6 Impedance measurements (Appendix A)

The impedance measuring technique used continuous wave excitation so that a very sensitive detection method — the impedance bridge — could be used. However, since the acoustic system reaches a steady state, the whole insonified volume is effectively part of the radiation load, and it is not possible to know where the measured effects are occurring.

It could be possible to restrict analysis to a certain spatial volume if a short-duration excitation signal were used, so that the impedance signal could be edited in the time domain. Attempts were made to use burst sine waves. An alternative would be to use the MLSSA system in impedance measuring mode (see reference [122] and Figure 9-2).

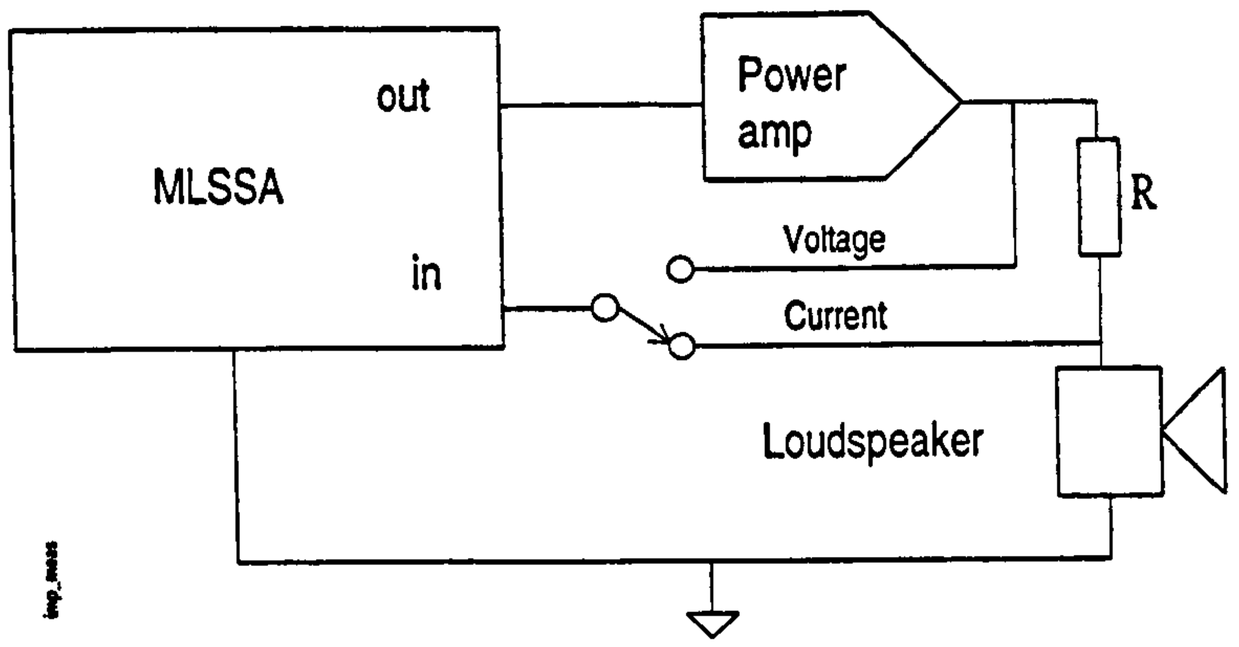

Figure 9-2 *Method of measuring the electrical impedance of a loudspeaker using MLSSA.*

Here, the voltage drop across the series resistor is measured, and used to calculate the current through the driver. The voltage output of the amplifier is also measured, and so the impedance of the driver can be calculated. Since the results will be presented as a time-varying impedance, the time segment corresponding to a particular volume of space can be extracted, and transformed to the frequency domain, if necessary, to give a wideband impedance measurement.

In order to calibrate the electrical impedance in terms of acoustic impedance, measurements may be made of the transduction coefficients of the driver in its probe assembly (see reference [73], chapter 14). Alternatively, a calibrated impedance change could be inserted into the acoustic path: for example, a step change in cross section. The signal resulting from this would give a reference against which the later signal from the suspension could be compared.

If the measurements resulting from loudspeaker impedance were found to be too inaccurate (too sensitive to pressure variations, for example), then a more conventional impedance tube arrangement could be used. For example, the driver and orifice would be at opposite ends of the tube, as before, but microphones in the side of the tube would be used to monitor the internal sound field, and deduce the termination impedance directly [eg. 52].

There is scope to redesign the probe tube specifically to optimise it for impedance measurements. The probe arrangement was designed for a short impulse response, by shunting the loudspeaker acoustic impedance with a parallel acoustic load. This reduced the reflection coefficient from the diaphragm, but also reduced the influence of the acoustic load on the loudspeaker electrical impedance, and so this design feature was counterproductive for the measurement of acoustic impedance. Furthermore, there are ways of optimising the probe design that would maximise the sensitivity of the loudspeaker impedance to changes in the termination impedance of the probe tube [47].

Further measurements of acoustic impedance could be used either as another means to characterise the suspension, or alternatively, to research into the impedance variations at the end of the probe tube, that are caused by mechanisms other than changes in the specific impedance of the suspension.

9.3 REGIMES OF USE & RECOMMENDATIONS FOR INSTRUMENT DESIGN

This section aims to present conclusions and recommendations from the viewpoint of someone designing an instrument based on this technology, for a given application. The models and conclusions of Chapter 2 are illustrated with examples.

Firstly, a distinction must be drawn between an instrument that is designed to measure absolute values of mass flowrate/concentration, and one that is required solely to measure relative differences between two flows of the same composition. For the target application of measuring the imbalance of pulverised fuel (PF) concentration between pipes after a bifurcation, it could be argued that a relative measure of concentration only is required. In such a case, if the composition and particle size of the material in both pipes can be assumed identical, then a single frequency measurement of attenuation is all that is required. The selected frequency is determined by the need for a measurable acoustic effect, and experimental considerations such as transducer choice.

Such technology has already been demonstrated by Abernethy *et al* [2] with their ultrasonic cross-pipe attenuation measurements at 215 kHz (reviewed in section 3.1.2). This approach would work, provided that the concentration is the only variable that changes between the pipelines. However, if there is an aerodynamic imbalance between the pipes that causes a concentration difference, it would seem feasible that a difference in PSD could also occur, and cause an uncorrected concentration reading to be erroneous.

9.3.1 Scaling regimes (section 2.4)

For an instrument to be insensitive to changes in PSD, then a multi-frequency measurement must be made (unless some non-acoustic compensation is applied). Furthermore, the selection of frequencies must be made such that a change in PSD causes a relative change between the frequency points that is different to that caused by a change in concentration. This is achieved by ensuring that the frequency points lie in different scaling regimes (see section 2.4) so that the relative frequency scaling is sensitive to particle size. These regimes are mapped as a function of frequency and particle radius in Figure 9-3.

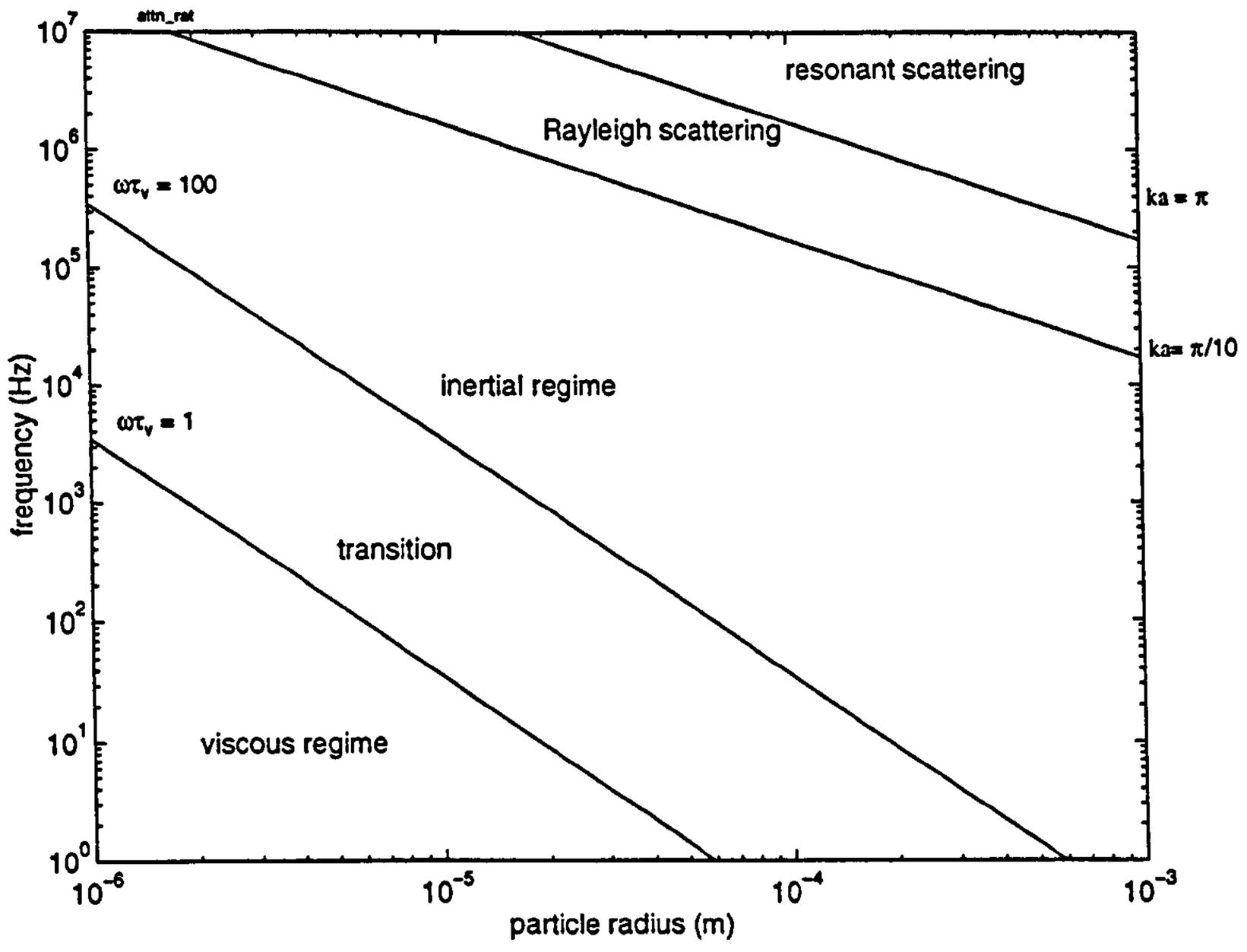

Figure 9-3 *Regime map for a suspension of alumina spheres in air. The viscous regime is shown as the area for which* $\omega\tau_v \leq 1$, *the inertial regime as* $\omega\tau_v > 100$, *with a transition region between them. The transition to domination by Rayleigh scattering starts at* $ka \approx \frac{\pi}{10}$, *and the transition to resonant scattering happens at* $ka \approx \pi$.

Detecting changes in PSD could be achieved simply by making a dual frequency measurement, with the frequency points lying in different regimes. The ratio of the two measurements would be insensitive to changes in concentration, since the attenuation at both frequencies is proportional to concentration, but sensitive to changes in PSD. This principle is illustrated in the next section.

9.3.2 Example: dual frequency analysis of coal grades.

For an example, we can take three grades of PF, measured by Woodhead [158]. They are labelled fine, medium and coarse, with mean particle radii of 10.5, 33 and 46 μm respectively[1]. Initially, we choose two frequencies that lie in the same regime for all the radii; say 20 kHz and 200 kHz, both of which lie in the inertial regime for each mean particle size (though not for every particle size, it should be noted). Now, the ratio of the acoustic attenuation at 200 kHz to that at 20 kHz can be calculated, and is plotted in Figure 9-4.

[1] Their PSDs are plotted in Appendix F.

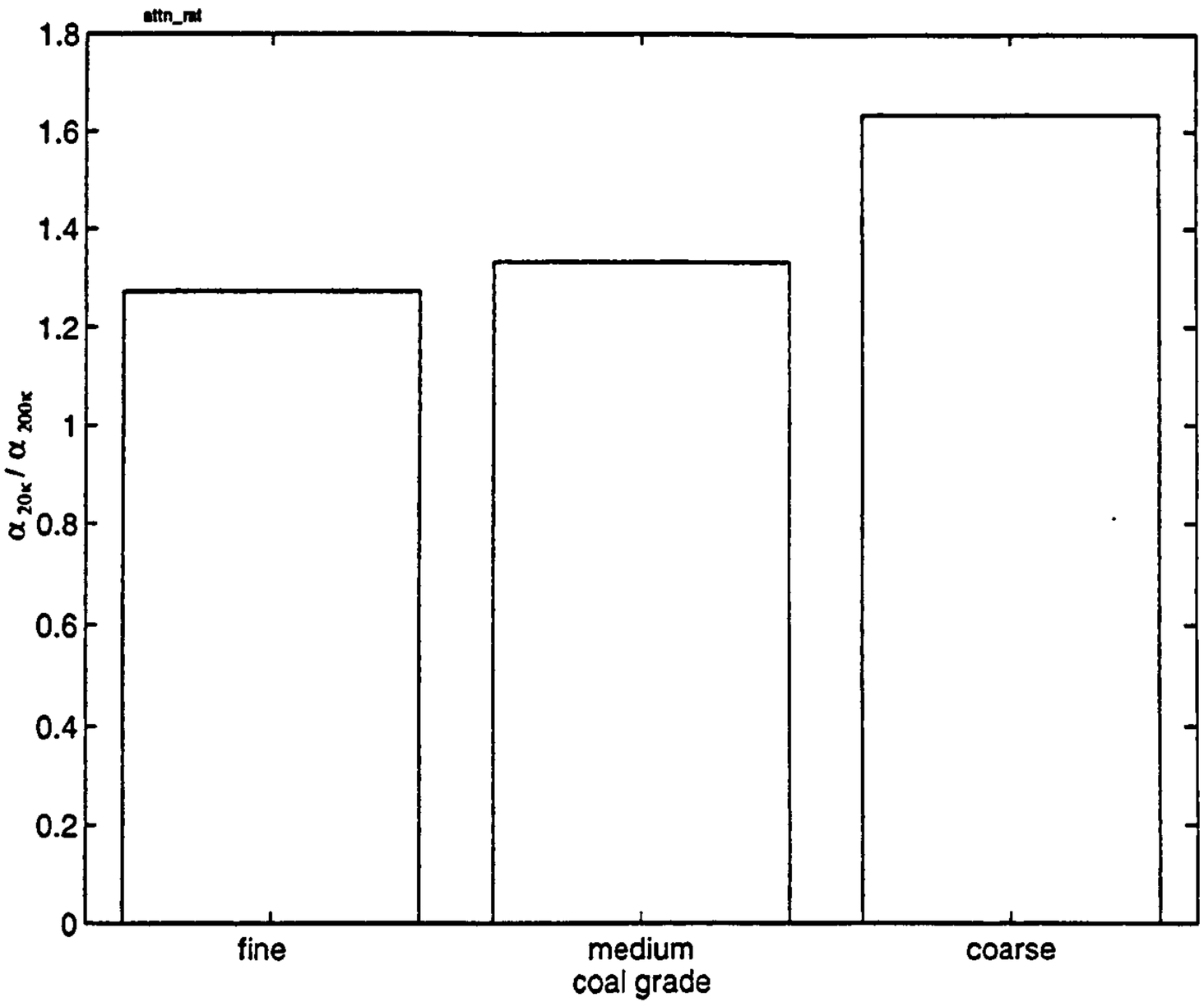

Figure 9-4 *Ratio of attenuation at 200 kHz to 20 kHz, for three grades of PF (using parameters for alumina).*

The difference in the ratio between fine and medium grades is negligible, while the ratio for the coarse grade is just 23% higher than that for the fine grade; this finite difference is caused by the wide spread of PSD, such that some particle sizes will be lying in a transition region.

Now, frequency points are chosen to lie in different scaling regimes: Figure 9-5 shows the case when the 50 kHz point still lies in the inertial regime, while the 200 Hz point is in the transition from viscous to inertial regimes.

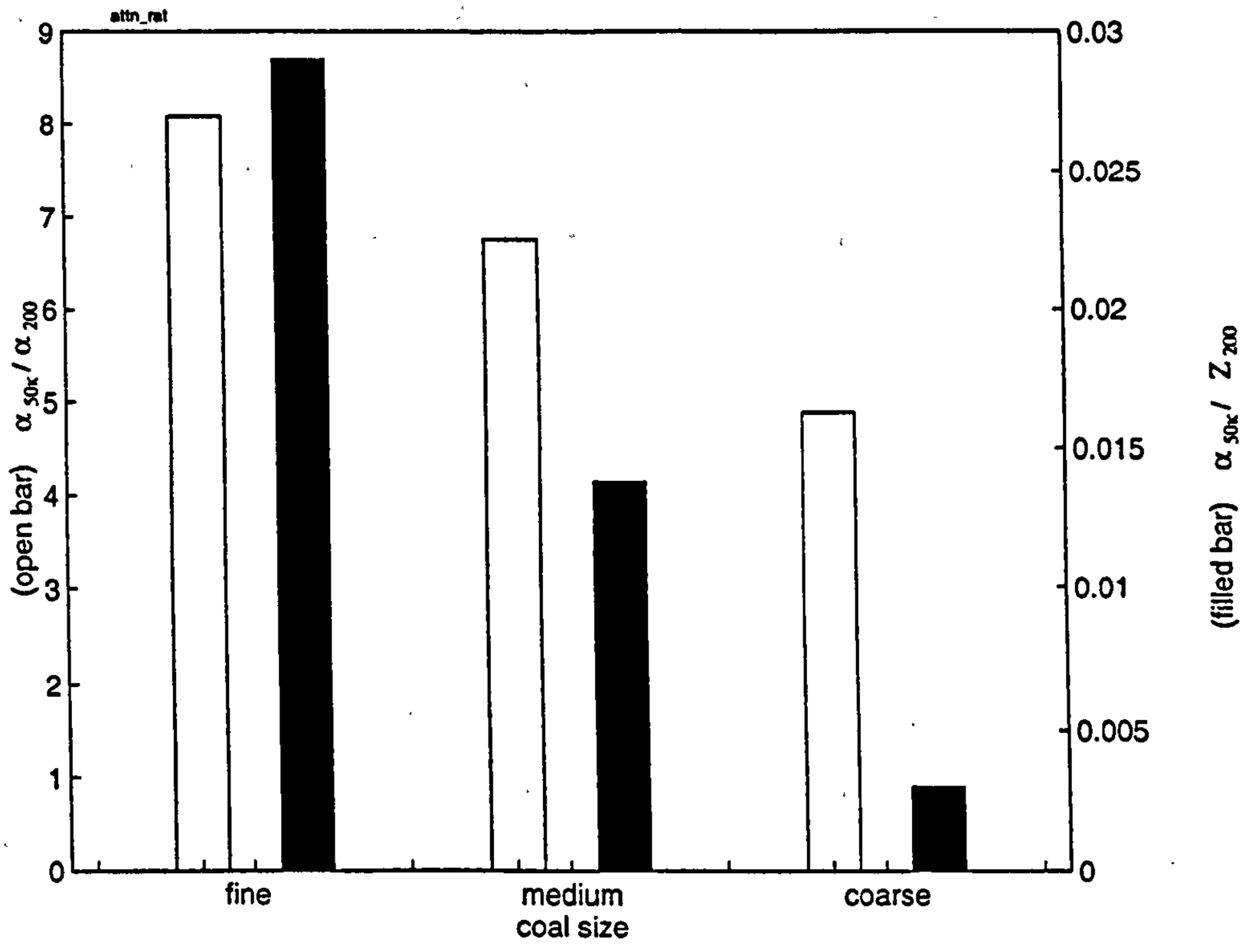

Figure 9-5 Ratio of attenuation at 50 kHz to 200 Hz (open bar) and of attenuation at 50 kHz to impedance at 200 Hz (filled bar), for three grades of PF (using parameters for alumina).

Now we notice a larger difference in the ratio between different size fractions, with a 47% decrease from the fine to the coarse grades. Even more noticeable is the change in the ratio for which the specific impedance at 200 Hz is used as the reference; this ratio decreases by nearly one decade between fine and coarse grades, and shows the potential of using a single frequency impedance measurement in combination with, say, an attenuation measurement at a single ultrasonic frequency.

These short examples have shown that the ratio of measurements at two frequencies can be used to detect variations in PSD, independently of variations in concentration. There is a possibility that this variable may be then used to correct the measurement of concentration for the shift in PSD, although this would need further investigation.

Such limited measurements can only be expected to provide immunity to changes in PSD over a narrow excursion. To provide a more robust measurement in the face of greater uncertainty of PSD would almost certainly require measurements across a frequency spectrum.

9.3.3 Example: wideband frequency analysis to infer PSD (section 2.4.4)

Some attempts to infer the PSD from spectroscopic measurements of attenuation have been reviewed in section 2.5.3. It was implied that the selection of frequency range of the measurement should be made with regard to the range of particle size that will be analysed. It was postulated that for each particle size of interest, the frequency range should encompass a region of varying scaling, so that a unique solution for the PSD may be found, without knowledge of concentration.

This principle is illustrated with the technique of Beckord & Höfelmann [17], which is based on a kernel function that uses the coupled-phase theory of Temkin & Dobbins [141].

As an example, consider a suspension of alumina spheres in air, with a mean particle radius of 6 μm, and a log-normal PSD with standard deviation $\sigma = 0.5$. The predicted attenuation was calculated using the theory of Temkin & Dobbins, and the attenuation at each frequency point had a random error added to it to simulate the effect of experimental error[1]. This simulated attenuation measurement was fed into the iterative algorithm of Beckord & Höfelmann to infer the PSD; the result could then be compared with the original PSD to assess the accuracy of the method. The purpose is to illustrate how the selected frequency range affects the accuracy of the result.

Two frequency ranges were selected: 0.2 - 20 kHz, and 4 - 400 kHz. Both span two decades, but the former was chosen to span the viscous-inertial transition for the whole particle radius range (1.3 - 27 μm), whereas the latter range lies entirely in the inertial regime for particles above 10μm. This is illustrated in Figure 9-6, which repeats the regime map of Figure 9-3 and marks the radius-frequency regions spanned by both simulated measurements.

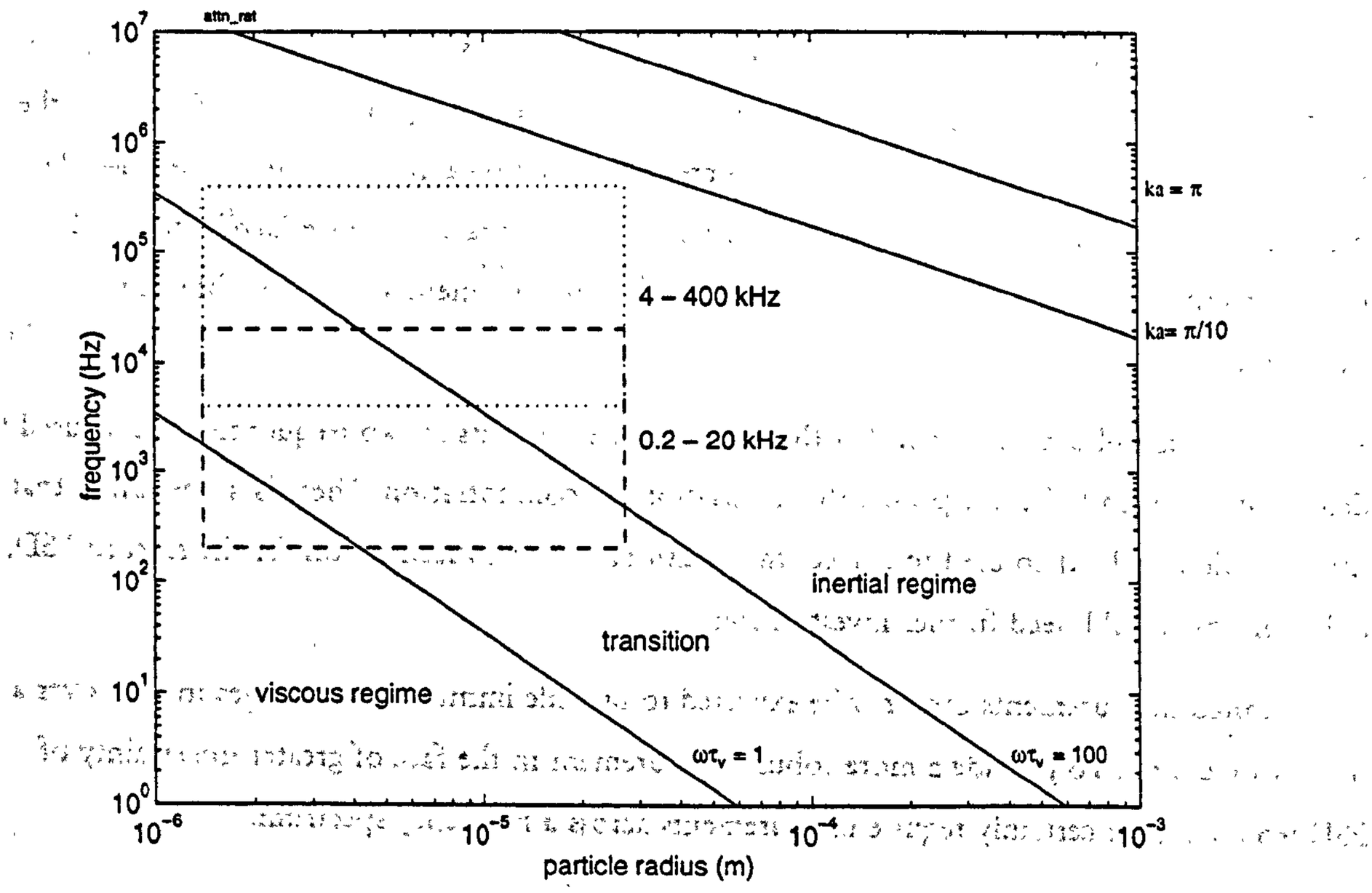

Figure 9-6 Regime map for a suspension of alumina spheres in air (repeated from Figure 9-3). The regions spanned by the two simulated measurements are marked in dashed (0.2 - 20 kHz) and dotted (4 - 400 kHz) boxes.

The actual and inferred PSDs are plotted in Figure 9-7 for the two frequency ranges.

[1] The noise had a Gaussian distribution, with a mean amplitude of 2% of the predicted attenuation.

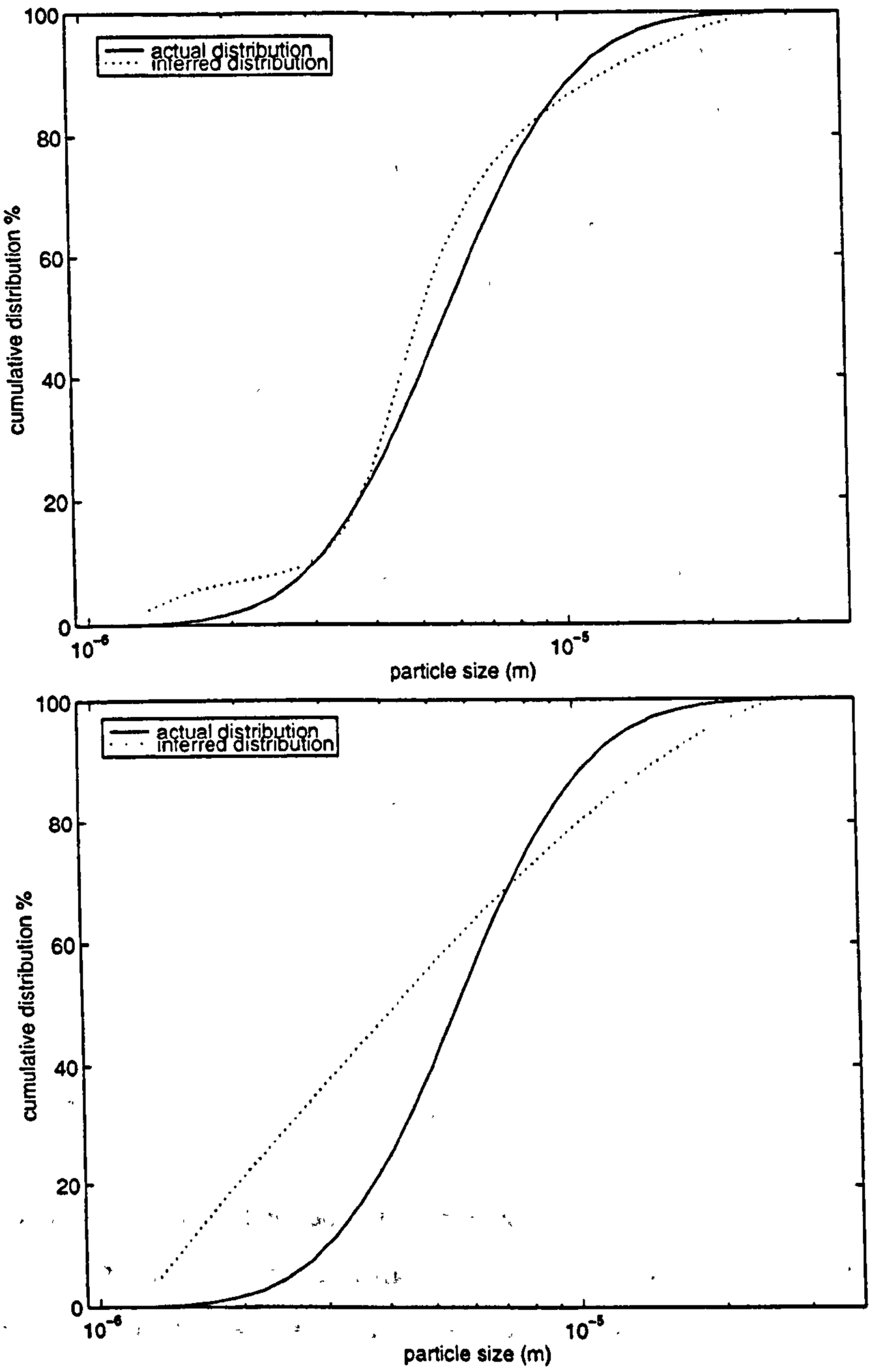

Figure 9-7 *Cumulative distribution of alumina particles, $\bar{a}$ = 6μm, σ = 0.5. Actual (solid line) and inferred (dotted line) when measured with two frequency ranges. Top: 0.2 - 20 kHz; bottom: 4 - 400 kHz. Both inferred plots are the result of 5000 iterations.*

It can be seen that the PSD resulting from the 0.2 - 20 kHz range gives a very much better fit to the actual PSD, albeit with some discrepancy due to the random error imposed on the simulated measurement (if no error was imposed, the fit was perfect). By contrast, the PSD resulting from the 4 - 400 kHz range is grossly incorrect, but was a stable solution to the problem: ie. the predicted attenuation resulting from the inferred PSD matched the simulated attenuation, so that the solution did not converge further. This demonstrates the assertion that, if the frequency range of measurement does not straddle a change in scaling for all particle sizes, then an accurate inference of PSD is not possible, because there will not be a unique solution to the problem.

9.3.4 Final recommendations

In designing an acoustic instrument to meet a given application, the parameters that need to be considered are: pipe diameter D, range of concentration ϕ_m, and particle size distribution $\Phi(a)$. From these, an appropriate frequency or frequency range may be selected, to give a range of attenuation that is within a measurable range for an instrument, and which, if necessary, meets the criteria given above to provide correction for changes in PSD. This frequency range will dictate the measurement method to be used: plane wave measurement along the tube axis; measurement of the reverberant field; ultrasonic measurement across the tube axis; or measurement of the characteristic impedance.

It is instructive to note how the different parameters of the application affect the selection of the frequency range and measurement method.

Influence of the pipe diameter D

As the pipe diameter increases, the cut-on frequency of the first transverse mode (0,1) decreases, and so the upper frequency limit of the plane wave region decreases. A convenient expression to calculate the cut-on frequency of the (0,1) mode is [41]:

$$f_{(0,1)} = \frac{0.586c}{D} \tag{9.1}$$

The lower frequency limit of plane wave measurements is likely to be limited by the SNR, as it was found (section 5.7) that the background noise is greatest at low frequency; furthermore, it is problematic to couple significant acoustic energy into the pipeline below 200 Hz, possibly requiring a positive displacement transducer instead of an electrodynamic loudspeaker. Therefore, the available range of plane wave measurements becomes narrowed with increasing pipe diameter. Nonetheless, it has been shown that measurements in the viscous-inertial transition regime are valuable in providing some immunity to changes in PSD, and for particles larger than $a = 2\mu m$, this will require measurement at frequencies below 1 kHz.

By contrast, ultrasonic measurements generally become more feasible with increasing diameter, since the cross-pipe path length becomes longer, which increases the total attenuation and alleviates the problem of internal reflections.

Particle size and concentration

To a good approximation, the acoustic effects of a suspension (attenuation, dispersion and impedance) may be assumed to scale proportionally to the mass or volume concentration. The behaviour as a function of particle radius has been seen to be more complicated. The attenuation increases with radius in the viscous regime, decreases in the transition and inertial regimes, and increases very rapidly in the Rayleigh scattering regime (see Figure 2.6). The dispersion is at an

asymptotic maximum in the viscous regime, and rapidly decreases to zero in the transition region (see Figure 2.3); the specific characteristic impedance also follows this pattern (decreasing to unity, see Figure A-1).

Achieving the correct dynamic range

To achieve reasonable accuracy in an instrument, the measured quantity must lie within a range that can be resolved with the desired accuracy. For the case of measuring acoustic attenuation, the lowest resolvable value of loss will be set by random fluctuations in the signal level, and the highest value of loss will be set by the level of background noise, above which the desired signal is not resolvable. For example, we can estimate the dynamic range of measurement to be 5 - 45 dB of loss. By knowing the pipe diameter, and the range of particle sizes and concentrations, we can use theoretical formulations to calculate the frequency range that will give attenuation values within this range.

Figure 9-8 and Figure 9-9 demonstrate the selection of frequency range to achieve a measurable value of loss, in the plane wave and ultrasonic regions, respectively. From these graphs, the insertion loss, *IL*, may be calculated as:

$$IL = 8.69 \alpha L \, \phi_m \quad \text{(dB)}$$

where ϕ_m is the mass concentration, α is the attenuation coefficient at $\phi_m = 1$ kg/kg, L is the path length, and 8.69 is a factor that converts from Np/m to dB/m.

For example, consider a pipe diameter of 0.3m, carrying an aerosol of alumina particles of 33 μm radius (the same mean size as the medium grade coal considered earlier). Figure 9-8 shows that the plane wave region is restricted to frequencies below 700Hz, in which the attenuation will be between approximately 0.04 - 0.06 Np/m . To achieve a minimum loss of 5 dB at the minimum expected concentration of 2kg/kg (say), will therefore require a path length of 5 / (0.06 * 2 * 8.69) = 4.8 m . This will require a pipe segment approx. 15m long with no substantial internal reflections (eg. bifurcations, constrictions or side arms). However, an ultrasonic cross-pipe measurement has the path length limited to 0.3m, and so the frequency must be elevated to 1 MHz (see Figure 9-9), to achieve an attenuation coefficient of 5 / (0.3 * 8.69 * 2) ≈ 1 Np/m. Above this frequency, Rayleigh scattering becomes significant, and the attenuation increases rapidly. However, measurements at such high frequencies in air are fraught with problems already mentioned (section 3.4).

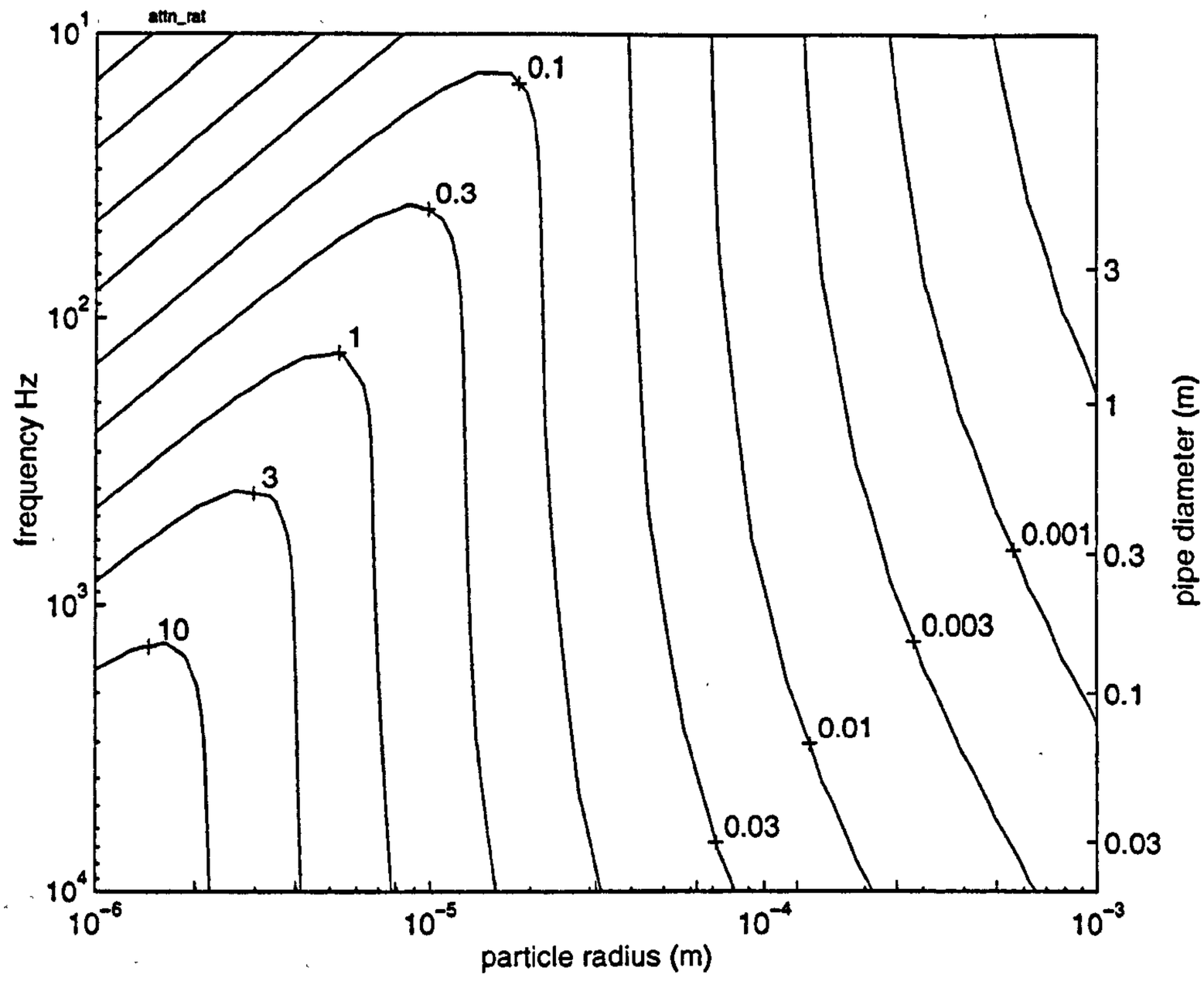

Figure 9-8 *Contour map of constant attenuation coefficient in Np/m (for monodispersed alumina spheres), for mass concentration of 1 kg/kg, as predicted by the theory of Lloyd & Berry. Propagation along the pipe axis is restricted to the plane wave mode above a horizontal line of given pipe diameter (right hand axis). Note the reverse direction of the frequency axis.*

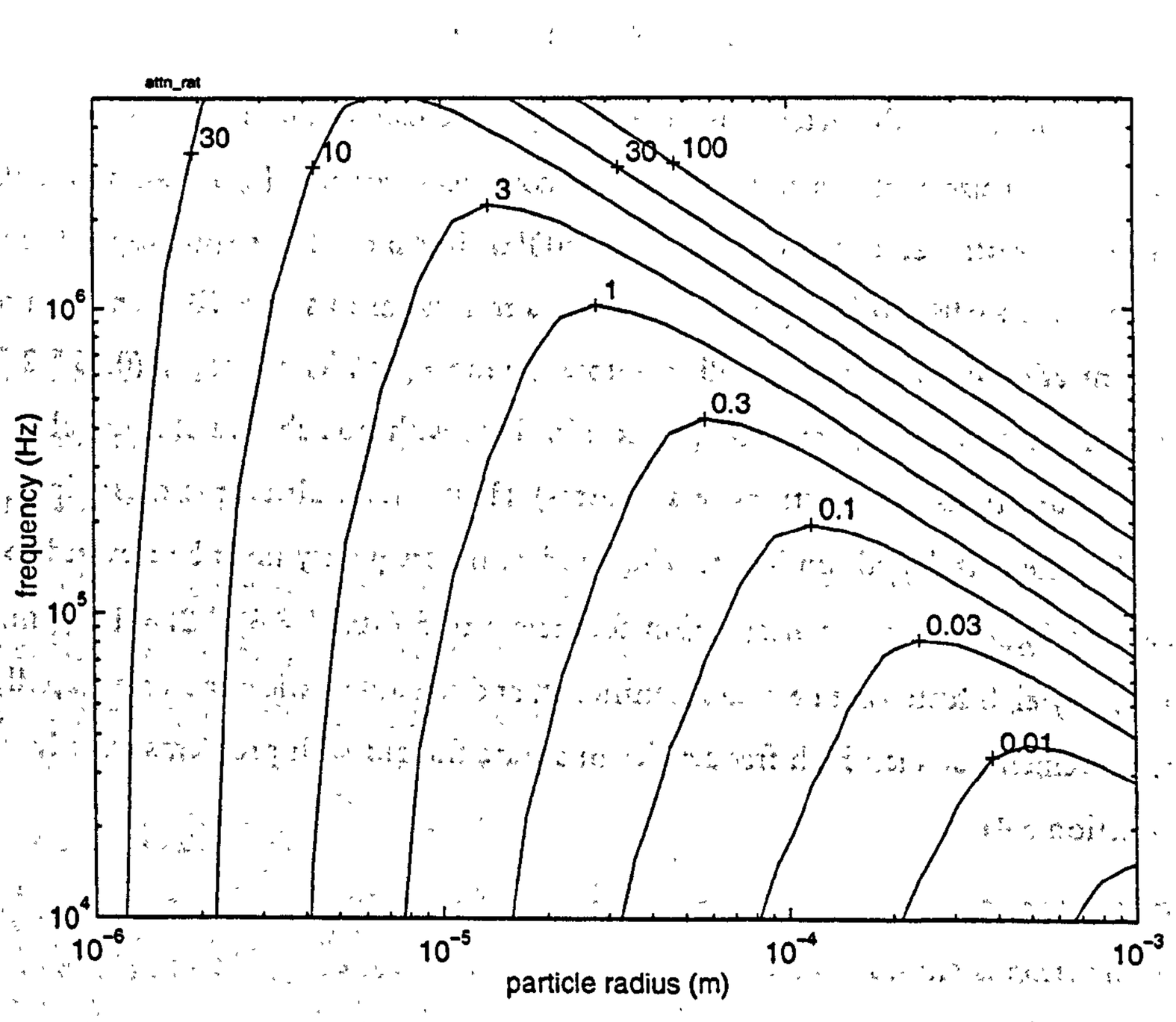

Figure 9-9 *Contour map of constant attenuation coefficient in Np/m (for monodispersed alumina spheres), for mass concentration of 1 kg/kg, in the ultrasonic frequency range, as predicted by the theory of Ma et al [89].*

While the examples above illustrate attempts to achieve significantly large acoustic effects, there could also be applications where the attenuation is so high that detecting a measurable signal is the problem; for example, a large pipeline carrying a very concentrated flow of fine particles. In such an application, the measurement of characteristic impedance could be the best technique, since there is no need to detect the transmitted signal.

It should be noted that these graphs are based on theoretical predictions; however, the accuracy of these predictions, especially for larger particles, is somewhat uncertain following the results presented in this work.

Measuring inhomogeneous flows

The particle velocity and density across the section of a conveying line have been found to vary considerably, especially after a bend in the pipeline [95]. Some acoustic techniques are more susceptible than others to errors in the presence of inhomogeneous flows. Velocity meters based on ultrasonic cross correlation were found most sensitive to the particle velocity near the tube wall, and hence underread the mean velocity [130, 132]. Ultrasonic cross-pipe measurements, in general, tend to interrogate a comparatively small volume of the flow; one approach to provide greater volume-averaging is to use multiple transducer pairs interrogating different chords of the pipe section [25].

Plane wave measurements along the pipe axis may be expected to provide good volume averaging, since the whole section of the pipe along the path length is interrogated by the wavefront. However, it has been pointed out [140] that in cases of extreme inhomogeneity – such as in horizontal pipes, where the suspension has settled out into a bed flow regime – the acoustic medium is so inhomogeneous that the acoustic wavefront may not be assumed to be planar: the propagation path is effectively "short-circuited" by the clean air path, bypassing the high concentration bed.

It would seem likely that measurements of the reverberant field provide the best volume averaging, due to the large volume of space and complex paths that are interrogated by a nominally diffuse field. The modal pattern will introduce some bias into the sensitivity, with nodal points being a "blind spot", but if a range of frequencies (and modal shapes) is measured, then this bias will be reduced.

REFERENCES

[1] Abernethy D.A., Cutmore N.G., Evans T.G., Millen M.J. & Sowerby B.D., "On-line determination of pulverised coal mass flow", CSIRO Division of Minerals Report DM-R262 (Jan 96)

[2] Abernethy D.A., Millen M.J. & Sowerby B.D., "Plant trial of an ultrasonic gauge for the on-line measurement of pulverised coal mass flow", IEEE Instrumentation and Measurement Technology Conference, Brussels, Belgium, 667 - 670, (June 96)

[3] Agarwal N.K. & Bull M.K. "Acoustic wave propagation in a pipe with fully developed turbulent flow", J. Sound Vib. 132 (2), 275 - 298 (1989)

[4] Ahuja A.S. & Hendee W.R., "Effects of particle shape and orientation on propagation of sound in suspensions", J. Acoust. Soc. Am. 63(4) 1074 - 1080 (1978)

[5] Alig I. & Lellinger D., "Frequency dependence of ultrasonic velocity and attenuation in two-phase composite systems with spherical scatterers", J. Appl. Phys. 72 (12) 5565 - 5570 (1992)

[6] Allegra J.R. & Hawley S.A., "Attenuation of sound in suspensions and emulsions: theory and experiments", J. Acoust. Soc. Am. 51, 1545 (1971)

[7] Alrutz H. & Schroeder M.R. "A fast Hadamard transform method for the evaluation of measurements using pseudorandom test signals", Proc. 11th Congress Acoust., Paris (GALF France, 1983), 6, 235 - 238 (1983)

[8] American Society for Testing Materials, ASTM C384-58, "Standard test method for impedance and absorption of acoustical materials by the tube method", (1958)

[9] American Society for Testing Materials, ASTM C423-84A, "Standard test method for sound absorption and sound absorption coefficients by the reverberation room method", (1984)

[10] Anonymous, "Pneumatic Conveying of Bulk Materials", course notes, Wolfson Centre for Bulk Solids Handling Technology, University of Greenwich, London, U.K.,15 - 17 Nov (1994)

[11] Aoshima N. "New method of measuring reverberation time by Fourier transforms", J. Acoust. Soc. Am. 67(5) 1816 - 1817 (1980)

[12] Attenborough K."Models for the acoustical characteristics of air-filled granular materials" Acta Acustica 1993

[13] Attenborough K., S.I. Hayek and J.M.Lawther, "Propagation of sound above a porous half-space", J. Acoust. Soc. Am., 68, 1493-1501, (1980)

[14] Attenborough K., "Acoustical characteristics of rigid fibrous absorbents and granular materials", J. Acoust. Soc. Am. 73 (3), 785 - 799 (1983)

[15] Baerg W. & Schwartz W. H. "Measurements of the scattering of sound from turbulence", J. Acoust. Soc. Am. 39 (6), 1125 -1132 (1965)

[16] Bartel T.W. & Yaniv S.L. "Curvature of sound decays in partially reverberant rooms", J. Acoust. Soc. Am. 72(6), 1838 - 1844 (1982)

[17] Beckord P., Luck H.O. & Höfelmann G. "Fast determination of the particle size of aerosols and hydrosols by measuring the attenuation of sonic waves", J. Aerosol Sci. 23, Suppl. 1, S317 - 320 (1992)

[18] Beltran N., Haindl C. & Taylor E. "Design of low cost instrumentation to measure flow and concentration of a copper metallurgical slurry", IEEE Trans. on Instrumentaion & Measurement, 38(6) 1127 - 1131 (1989)

[19] Bentley J.P. "Principles of measurement Systems", Longman, New York, (1983)

[20] Birdsall T.G. "Signals and signal processing for acoustic monitoring of ocean processes", Proceedings of IEEE International Conference on Acoustics, Speech and Signal Processing, Detroit, MI, USA, May 1995, 5, 2767-2770 (1995)

[21] Bobis J.P., Porges K.G.A. & Raptis A.C. "Particle velocity and solid volume fraction measurements with a new capacitative flowmeter at the solid-gas flow test facility", AAIA/ASME 4th Fluid Mechanics, Plasma Dynamics & Lasers conference, May 1986, 35, 79 - 86 (1986).

[22] Bodlund K. "On the use of the integrated impulse response method for laboratory reverberation measurements", J. Sound Vib. 56, 341 - 362 (1978)

[23] Bodlund K., "Monotonic curvature of low frequency decay records in reverberation chambers", J. Sound Vib. 73(1), 19 - 29 (1980)

[24] Bradley M.S.A. PhD Thesis, Thames Polytechnic, UK (1990)

[25] Bragg M.I. & Lynnworth L.C. "Internally-nonprotruding one-port ultrasonic flow sensor for air and some other gases", 4th European conference on Control 94, IEE 2 (389), 1241 - 1247, Coventry, UK (March 1994)

[26] Brain T.J.S. & Reid J. "Performance of small diameter cylindrical critical-flow nozzles", N.E.L. Report no 546, Glasgow (June 1973)

[27] Brown E.H. & Clifford S.F. "On the attenuation of sound by turbulence", J. Acoust. Soc. Am. 60(4) 788 - 794 (1976)

[28] British Standards Institution, BS1042 "Measurement of fluid flow in closed conduits", Section 3.1, "Method of measurement of gas flow by means of critical flow Venturi nozzles" (1991)

[29] Burnett A.J, de Silva S.R. & Reed A.R., The Solid Particle Impact Erosion of a Range of Materials Commonly used in the Construction of Pneumatic Conveyors using Two Forms of Erosion Testing Device", Proc. 5th International Conference on Bulk Materials Handling, Storage and Transportation, Newcastle, NSW, Australia, (July 1995).

[30] Challis R.E., Harrison J.A., Holmes A.K. & Cocker R.P. "A wide bandwidth spectrometer for rapid ultrasonic absorption measurement in liquids", J. Acoust. Soc. Am. 90 (2) Pt. 1, 730 - 740 (1991)

[31] Chen Z.X. & Sanderson M.L. "Ultrasonic tomography for process measurements", IEEE Instrumentation and Measurement Technology conference, 659 - 662, Brussels, Belgium, June 4 - 6 (1996)

[32] Chu W.T., "Comparison of reverberation measurements using Schroeder's impulse method and decay-curve averaging method", J. Acoust. Soc. Am. 63, 1444 - 1450 (1978)

[33] Chu W.T. "A deterministic broad-band signal for acoustical measurements", Proc. Internoise 87, 1199- 1202 (1987)

[34] Chu W.T. "Impulse-response and reverberation-decay measurements made by using a periodic pseudorandom sequence", Applied Acoustics 29, 193 - 205 (1990)

[35] Crowe C.T. "Review – numerical models for dilute gas-particle flows", J. Fluids Eng. 104, 297 - 303 (1982)

[36] Cummings A. "The effect of grazing incidence turbulent pipe-flow on the impedance of an orifice", Acustica 61 234-242 (1986)

[37] Davidson G.A. "A Burgers' equation for finite amplitude acoustics in fog", J. Sound Vib. 45, 473 - 485 (1976)

[38] Davies P.O.A.L. "Practical flow duct acoustics", J. Sound Vib 124 (1), 91 - 115 (1988)

[39] Davy J.L., Dunn I.P. & Dubout P. "The variance of decay rates in reverberation rooms", Acustica 43 12 - 25 (1979)

[40] Epstein P.S. & Carhart R.R., "The absorption of sound in suspensions and emulsions. I. Water fog in air", J. Acoust. Soc. Am. 25, 553 - 564 (1953)

[41] Eriksson L.J. "Higher order mode effects in circular ducts and expansion chambers", J. Acoust. Soc. Am. 68 (2) 545 - 550 (1980)

[42] European Patents EP 0 309 155 A2 "Method for determining physical properties", and EP 0 317 322 A2 "Method for monitoring acoustic emissions".

[43] Evans J. "Models for sound propagation in suspensions and emulsions", PhD dissertation, The Open University, Milton Keynes, UK (1996)

[44] Fasman G.D. "Handbook of biochemistry and molecular biology: Physical and chemical data, Vol 1", 3rd ed.

[45] Fay R.D. & Hall W.M. "The determination of the acoustical output of a telephone receiver from input measurements", J. Acoust. Soc. Am. 5, 46 - 56 (1933)

[46] Fay R.D. & White J.E. "Acoustic impedance from motional impedance diagrams", J. Acoust. Soc. Am. 20 (2) 98 -107 (1948)

[47] Finch R.D. & Higgins P.W. "Optimizing the monotone performance of electrodynamic drivers using tubular couplers", J. Acoust. Soc. Am. 60 (4) 937 - 941 (1976)

[48] Flanagan I.M., Jordan J.R. & Whittington H.W. "An inductive method for estimating the composition and size of metal particles", Meas. Sci. Technol. 1, 381 - 384 (1990)

[49] Fuller C.R. & Bies D.A. "The effects of flow on the performance of a reactive acoustic attenuator", J. Sound Vib. 62(1) 73 - 92 (1979)

[50] Garai M. "Measurement of the sound-absorption coefficient *in situ*: the reflection method using periodic pseudo-random sequences of maximum length", Appl. Acoust. 39, 119 - 139 (1993)

[51] Garwood M. PowerGen, personal communication (95)

[52] Gibiat V. & Laloë F. "Acoustical impedance measurements by the two-microphone three calibration (TMTC) method", J. Acoust. Soc. Am. 88 (6) 2533 (1990)

[53] Greenwood M.S., Mai J.S., Good M.S., "Attenuation measurements of ultrasound in a kaolin-water slurry: a linear dependence on frequency", J. Acoust. Soc. Am. 94 (2) Pt. 1, 908 - 916 (1993)

[54] Gumerov N. A., Ivandaev A. I. & Nigmatulin R.I. "Sound waves in monodisperse gas-particle or vapour-droplet mixtures", J. Fluid Mech. 193, 53 - 74 (1988)

[55] Hamade T.A. "Ultrasound attenuation in pipe flow of turbulent gas and suspended solids", PhD dissertation, Wayne State University (1982)

[56] Harker A.H. & Temple J.A.G. "Velocity and attenuation of ultrasound in suspensions of particles in fluids", J. Phys. D: Appl. Phys. 21, 1576 - 1588 (1988)

[57] Harris C.M., "Absorption of sound in air in the audio-frequency range", J. Acoust. Soc. Am. 35, 11 - 17 (1963)

[58] Hayman A.J., "Ultrasonic properties of oil-well drilling muds", Proc. IEEE, 327 - 332, Ultrasonics Symposium (1989)

[59] Henley D.C. & Hoidale G.B. "Attenuation and dispersion of acoustic energy by atmospheric dust", J. Acoust. Soc. Am. 54, 437 - 445 (1973)

[60] Höfelmann G. & Beckord P., "On-line determination of aerosol parameters by means of mechanical interactions", J. Aerosol Sci. 21 (S1), S601 - S604 (1990)

[61] Höfelmann G., Luck H.O. & Beckord P., "Reconstruction of temperature and velocity flow fields of aerosols", J. Aerosol Sci. 23 (S1), S51 - S54 (1992)

[62] Holmes A.K., Challis R.E., Wedlock D.J., "A wide bandwidth study of ultrasound velocity and attenuation in suspensions: comparison of theory with experimental measurements", J. Colloid & Interface Science, 156, 261 - 268 (1993)

[63] Howard A.V. "Development of techniques for the measurement of concentration and mass flow rate of pneumatically conveyed coal dust", Internal report, C.E.G.B. North Region (1980)

[64] Ingard U. & Singhal V.K. "Upstream and downstream propagation into a moving fluid", J. Acoust. Soc. Am. 54 (5) 1343 - 1346 (1973)

[65] International Electrotechnical Commission, IEC 225 "Octave, half-octave and third-octave band filters intended for the analysis of sounds and vibrations", (1966)

[66] International Organisation for Standardisation, ISO 354-1985(E), "Acoustics — measurement of sound absorption in a reverberation room" (1985)

[67] Jacobsen F., "A note on acoustic decay measurements", J. Sound Vib. 115(1), 163 - 170 (1987)

[68] Jacobsen F. "Time reversed decay measurements", J. Sound Vib. 117(1), 187 - 190 (1987)

[69] Jansen D.P., Hutchins D.A. & Young R.P. "Ultrasonic Tomography using scanned contact transducers", J. Acoust. Soc. Am. 93(6) 3242 - 3249 (1993)

[70] Jiang P. "Characterizing tissue phantoms via measurements of multiple acoustic parameters", PhD Dissertation, Yale University, U.S.A. (1993)

[71] Kaye G.W.C. & Laby, "Tables of Physical & Chemical Constants", 14th ed. (1973)

[72] Kaye S.M., Marple S.L. "Spectrum analysis — a modern perspective", Proc. IEEE 69 (11) 1380 - 1419 (1981)

[73] Kinsler L.E., Frey A.R., Coppens A.B. & Sanders J.V. "Fundamentals of Acoustics", 3rd ed. Wiley, New York (1982)

[74] Kleizen H.H. & Van Brakel J. "On-line measurement techniques in coal-handling systems", Powder Tech. 40, 113 - 128 (1984).

[75] Knudsen V.O., "The effect of humidity upon the absorption of sound in a room, and a determination of the coefficients of absorption of sound in air", J. Acoust. Soc. Am. 3, 126 - 138 (1931)

[76] Knudsen V.O., Wilson J.V., & Anderson N.S., "The Attenuation of Audible Sound in Fog and Smoke", J. Acoust. Soc. Am. 20, 849 (1948)

[77] Kolansky, M.S., Weinbaum S. & Pfeffer R. "Drag reduction in dilute gas solid suspension flow: gas and particle velocity profiles", 3rd International conference on the pneumatic transport of solids in pipes, Bath, UK, April 1976, pp. C1-1 - C1-20, (1976)

[78] Kreysig E. "Advanced engineering mechanics", 5th ed. Wiley, New York, (1983)

[79] Kuttruff H., "Room Acoustics", Wiley, New York, (1973)

[80] Kytömaa H.K. "Theory of sound propagation in suspensions: a guide to particle size and concentration characterization", Powder Technology 82, 115 - 121 (1995).

[81] Laidler T.J. & Richardson E.G., "The absorption of supersonics in smokes", J. Acoust. Soc. Am. 9, 217 - 223 (1938)

[82] Lamb H., Hydrodynamics, 6th Edition, Dover Publ., New York (1945)

[83] Leach M.F. & Rubin G.A. "An acoustic method for the continuous determination of particle size", Prepr. Int. Symp. In-stream measurements of particulate solid properties, II (1978).

[84] Leffert C.B., Hamade T.A., Barry R.E., Weisman L.H., "Mass flow rate measurements in coal-air ducts", Conference on recent developments in elctrical utility research, Chicago, Illinois, USA, April 1984, 247 - 256

[85] Lloyd P. & Berry M.V., "Wave propagation through an assembly of spheres", Proc. Phys. Soc. London 91, 678 - 688 (1967)

[86] Loosmore R.M. "Evaluation of BCURA pulverized fuel mass flow meter", CEGB report SSD/SW/R139 (Sept. 1972).

[87] Lynnworth L.C., "Ultrasonic measurements for process control", Academic Press Inc, London, (1989)

[88] Lyons M.L.G., Smith P.E., Moser H.G. "comparison of cross-shelf trends in acoustic doppler current profiler: amplitude and zooplankton displacement volume in southern California", California Cooperative Oceanic Fisheries Investigations Reports,35, 240 - 245 (1994)

[89] Ma Y., Varadan V.K. & Varadan V.V. "Comments on ultrasonic propagation in suspensions", J. Acoust. Soc. Am. 87 (6), 2779 - 2782 (1990)

[90] Matts D. National Power, personal communication (95)

[91] Matts D. National Power, personal communication (96)

[92] McClements D.J. & Povey M.J.W., "Scattering of ultrasound by emulsions", J. Phys. D: Appl. Phys. 22, 38 - 47 (1989)

[93] McClements D.J., "Comparison of multiple scattering theories with experimental measurements in emulsions", J. Acoust. Soc. Am. 91, 849 (1992)

[94] McClements D.J., Advances in the application of ultrasound in food analysis and processing", Trends In Food Science & Technology, 6 (9), 293-299 (1995)

[95] McCluskey D.R, Easson W.J., Greated C.A., Glass D.H., "The use of particle image velocimetry to study roping in pneumatic conveyance", Part. Part. Syst. Charact. 6 129 - 132 (1989)

[96] Mecredy R.C.& Hamilton L.J. "The effects of nonequilibrium heat, mass and momentum transfer on two-phase sound speed", Int. J. Heat Transfer 15, 61 - 72 (1972)

[97] Mednikov E.P. Soviet Phys. Acoust. 15, 507 (1977)

[98] Morse P.M., "Vibration and Sound", (McGraw-Hill, New York, 1948), Chapter 8.

[99] Moss S. & Attenborough K., "Measurements of attenuation and dispersion in an airborne suspension of dust", Applied Acoustics, 42, 187 - 196 (1994).

[100] Moss S.H.O.and Attenborough K. "Measurements of the narrow-band decay rates of a gas/particle suspension confined in a cylindrical tube: relationship to particle concentration", J. Acoust. Soc. Am 100 (4) 1992 - 2001 (1996)

[101] Müller E. & Matschat K.R. "The scattering of sound by a single vortex and by turbulence", Max Planck Inst. Strömforschung, Göttingen, Germany, ASTIA AD 213658, AFSOR 1666 (1959)

[102] Mungur P. & Gladwell G.M.L "Acoustic wave propagation in a sheared fluid contained in a duct", J. Sound Vib. 9(1) 28 - 48 (1969)

[103] Nagel R.T. & Brand R.S. "Boundary layer effects on sound in a circular duct", J. Sound Vib. 85 (1) 19 - 29 (1982)

[104] Ogushwitz P.R. "Measurement of acoustical scattering from plumes of sediment suspended in open waters", J. Marine Env. Eng. 1, 119 - 130 (1994)

[105] Ostashev V.E, "Sound propagation and scattering in media with random inhomogeneities of sound speed, density and medium velocity", Waves in Random Media 4, 403-428 (1994)

[106] Panametrics, Technical Notes (1993)

[107] Parkinson M.J. "Measurement of the mass flow rate of airborne powdered material in a duct", J. Sci. Inst. (J. Phys. E) Series 2, vol 1, 823 - 824 (1968)

[108] Parkinson M.J. & Hiorns F.J. "Mass flowmeter for gas-borne powder", Instrument Practice 23 (3) p.197 (1969)

[109] Penner S.S., Wang C.P. & Bahadori M.Y. "Nonintrusive diagnostic techniques for measurements on coal-combustion systems", Prog. Energy Combust. Sci. 10, 209 - 212 (1984).

[110] Pendse H.P. & Sharma A. "Particle size distribution analysis of industrial colloidal slurries using ultrasonic spectroscopy", Part. Part. Syst. Charact. 10, 229 - 233 (1993)

[111] Pickering A.R., Pope C.W. & James K. "Performance of BCURA pulverized fuel mass flow meter at Aberthaw 'B' Power Station", CEGB Report SSD/SW.H.533 (March 1973).

[112] Press W.H., Teukolsky S.A., Vetterling W.T. & Flannery B.P., "Numerical recipes in Fortran", 2nd Edition, Cambridge University Press, UK (1992)

[113] Pridmore-Brown D.C. "Sound propagation in a fluid flowing through an attenuating duct", J. Fluid Mech. 4, 393 - 406 (1958)

[114] Qian Z.W. "Concentrated suspension theory of sound attenuation in marine sediments – linear dependence of absorption coefficient on frequency", J. Sound Vib 103 (3), 427 - 436 (1985)

[115] Randall R.B., "Frequency Analysis", pub. Brüel & Kjær, 3rd ed, Denmark, 1987

[116] Raptis A.C. & Lau T.K. "State of the art acoustic instrumentation for coal conversion plants", Argonne National Laboratory report, ANL/FE-49628-TM04 (Oct 1981)

[117] Raspet R. and Baird G.E., "The acoustic surface wave above a complex impedance boundary", J. Acoust. Soc. Am., 85, 638-640, (1989)

[118] Reichel G, Nachtnebel H.P.,"Suspended sediment monitoring in a fluvial environment - advantages and limitations applying an acoustic-doppler-current-profiler", Water Research, 28 (4) 751-761 (1994)

[119] Richards S.D., Heathershaw A.D., Thorne P.D.," The effect of suspended particulate matter on sound-attenuation in seawater", J. Acoust. Soc. Am. 100 (3), 1447-1450 (1996)

[120] Riebel U. & Löffler F., "On-line measurement of particle size distribution and particle concentration in suspensions by ultrasonic spectrometry", Chem. Eng. Technol. 12, 433 - 438 (1989)

[121] Rife D.D. & Vanderkooy J., "Transfer-Function Measurement with Maximum-Length Sequences", J. Audio Eng. Soc. 37, 419 (1989)

[122] Rife D.D. "MLSSA Reference Manual, v 9.0", DRA Laboratories (1994)

[123] Roberts D. "Ultrasound analysis of particle size distribution", Materials World 4 (1) 12 - 14 (1996)

[124] Roberts W.L. "Encyclopaedia of Minerals" (1974)

[125] Russo P., Chirone R., Massimilla L. & Russo S. "The influence of the frequency of acoustic waves on sound-assisted fluidization of beds of fine particles", Powder Technology 82, 219 - 230 (1995)

[126] Schroeder M.R., "Integrated-impulse method measuring sound decay without using impulses", J. Acoust. Soc. Am. 66(2), 497 - 500 (1979)

[127] Schroeder M.R., "New method of measuring reverberation time", J. Acoust. Soc. Am. 37, 409 - 412 (1965)

[128] Selves T.P., Barnes R.N., and Reed A.R., "The control of splitting ratios at Bifurcations in Pneumatic Conveying Pipelines" Proc.Intl.Symposium *Reliable Flow of Particulate Solids II*, Oslo,Norway, August 1993

[129] Sewell C.J.T., "The extinction of sound in a viscous atmosphere by small obstacles of cylindrical and spherical form", Phil. Trans. Roy. Soc. 210A, 269 (1910)

[130] Sheen S.H. & Raptis A.C. "Potential acoustic techniques for monitoring mass flowrate in coal-air ducts", Trends in Electricity Utility Research, conference on Recent Developments in Electrical Utility Research, 277 - 285, Chicago (1984).

[131] Sheen S.H. & Raptis A.C. "Development of acoustic flow instruments for solid/gas pipe flows", Comp. Tech. Div., Argonne National Laboratory, IL, USA, May 1986.

[132] Sheen S.H. & Raptis A.C. "Acoustic flow instruments for gas/solid flows", Particulate Sci. & Tech. 5, 219 - 234 (1987).

[133] Shotts R.Q., Ch. 8 in "Coal Preparation", Leonard J.W. & D.R. Mitchell (eds), 3rd ed. American Institute of Mining, Metallurgical and Petroleum Engineers, New York, (1968)

[134] Shung K.K., Yuan Y.W. & Fei D.Y. "Effect of flow disturbance on ultrasonic backscatter from blood", J. Acoust. Soc. Am. **75**, 1265 - 1272 (1984)

[135] Soo S.L., Slaughter M.C. & Plumpe J.G. "Instrumentation for flow properties of gas-solid suspensions and recent advances", Part. Sci. Tech. 12 ,1 - 12 (1994)

[136] Sowerby B.D., Millen M.J., Abernethy D.A. & Wagner S. "On-line determination of pulverised coal mass flow using an ultrasonic technique", IEEE Ultrasonics Symposium, Florida, USA (December 1991)

[137] Stanton T.K. "Simple approximate formulas for backscattering of sound by spherical and elongated objects", J. Acoust. Soc. Am. 86 (4) 1499 - 1510 (1989)

[138] Steen B. "An acoustic method of measuring particle mass concentrations in gases", J. Aerosol Sci. 17(3), 485 - 488 (1986)

[139] Strout T.A. " Attenuation of sound in high concentration suspensions: development and application of an oscillatory cell model", PhD Thesis, University of Maine, U.S.A. (1991)

[140] Tallon S. & C.E. Davies, "Velocity and attenuation of sound: application to flow rate measurement in pneumatic conveying", Powder Handling and Processing 8 (4) 329 - 336 (1996)

[141] Temkin S. & Dobbins R.A. "Attenuation and dispersion of sound by particle-relaxation processes", J. Acoust. Soc. Am. 40(2), 317 - 324 (1966)

[142] Temkin S. & Dobbins R.A., "Measurements of Attenuation and Dispersion of Sound by an Aerosol", J. Acoust. Soc. Am. 40 (5), 1016 - 1024 (1966)

[143] Thomas L.J. "Use of marginal oscillator for acoustic monitoring of curing of epoxy resin", Rev. Progress in Quantitative Non-destructive Evaluation, 7B, 1555 - 1562 (1988)

[144] Thompson M., Arthur C.L., Dhaliwal G.K. "Liquid-phase piezoelectric and acoustic transmission studies of interfacial immunochemistry", Anal. Chem. 58, 1206 - 1209 (1986)

[145] Tsuji Y. & Morikawa Y. "L.D.V. measurements of an air-solid two-phase flow in a horizontal pipe", J. Fluid Mech. 120, 385 - 409 (1982)

[146] Tsang L., Kong J.A. & Habashy T. "Multiple scattering of acoustic waves by random distribution of discrete spherical scatterers with the quasicrystalline and Percus-Yevick approximation", J. Acoust. Soc. Am. 71, 552 - 558 (1982)

[147] Twersky V. "Acoustic bulk parameters in distributions of pair-correlated scatterers", J. Acoust. Soc. Am. 64, 1710 - 1719 (1978)

[148] Urick R.J. "The absorption of sound in suspensions of irregular particles", J. Acoust. Soc. Am. 20, 283 - 289 (1948)

[149] Vetter A.A. & Vetter R.S., "Balancing pulverized coal flows in parallel piping", J. Engineering for Gas Turbines & Power 107 679 - 684 (1985)

[150] Vetter A.A & Culick F.E.C., "Evaluation of the acoustical resonance measurement of particle loading in two-phase flow", U.S. Dept of Energy report DOE/ER/80193-1, (1985)

[151] Vetter A.A. & Culick F.E.C. "Acoustical resonance measurement of particle loading in gas-solids flow", Trans. ASME, J. of Eng'g for Gas Turb. & Power 109, 331-335 (1987)

[152] Vetter A.A. "Sensitivity of the acoustical resonance measurement of particle loading in gas-solids flow", Trans. ASME, J. of Eng'g for Gas Turb. & Power 110, 197-200 (1988)

[153] Vörlander M. & Kob M. "Practical aspects of MLS measurements in building acoustics", submitted to Appl. Acoust. (1996)

[154] Waterman P.C. & Truell R. "Multiple scattering of waves", J. Math. Phys. 2, 512 - 537 (1962)

[155] Warnock A.C.C. "Some practical aspects of absorption measurements in reverberation rooms", J. Acoust. Soc. Am. 74 (5), 1422 - 1432 (1983)

[156] Williams R.A., Xie C.G., Dickin F.J., Simons S.J.R., Beck M.S. "Multi-phase flow measurements in powder processing", Powder Technology 66, 203 - 224 (1991)

[157] Williams R.G. "Current monitoring for environmental pollution studies by acoustic Doppler profiling", J. Acoust. Soc. Am. 95 (5 Pt. 2), p. 2801 127th Meeting A.S.A. Cambridge, MA, U.S.A. (1994)

[158] Woodhead S.R. "The measurement of particle velocity and suspension density in pneumatic coal injection systems", PhD dissertation, University of Greenwich, UK (1992).

[159] Woodhead S.R., Barnes R.N., and Reed A.R., "On-line mass flow rate measurement in Pulverised Coal Injection Systems", Powder Handling and Processing 2 (2) 123-127 (1990)

[160] Woodhead S.R., Pittman A.N. & Ashenden. S.J. "Results of On-Line Mass Flow Rate Measurement Tests in a Pilot Pneumatic Coal Injection System Using an Electrostatic Measurement Technique", Proc. 20th International Conference on Coal Unilisation and Fuel Systems, Florida, USA, March 1995.

[161] Woodhead S.R., Pittman A.N., Ashenden S.J. "Laser doppler velocimetry measurements of particle velocity profiles in gas-solid two-phase flows", IEEE Instrumentation and Measurement Technology Conference, Proceedings of the 1995 IEEE Instrumentation and Measurement Technology Conference, Naltham, MA, USA, pp 770-773, Apr 1995

[162] Wu D., Qian Z.W. & Shao D. "Sound attenuation in a coarse granular medium", J. Sound Vib. 162 (3), 529 - 535 (1993)

[163] Xiang N. "Evaluation of reverberation times using a nonlinear regression approach", J. Acoust. Soc. Am. 98 (4), 2112 - 2121 (1995)

[164] Ye Z. & Ding L. "Acoustic dispersion and attenuation relations in bubbly mixtures", J. Acoust. Soc. Am. 98 1629 - 1636 (1995)

[165] Zink J.W. "Attenuation and Dispersion of Sound by Solid Particles suspended in a Gas", PhD Dissertaion, University of California, Los Angeles, USA (1957)

[166] Zink J.W. & Delsasso L.P., "Attenuation and Dispersion of Sound by Solid Particles suspended in a Gas", J. Acoust. Soc. Am. 30, 765 (1958)

[167] Zuber N. "On the dispersed two-phase flow in the laminar flow regime", Chem. Eng. Sci. 19, 897 - 917 (1964)

[168] Whelan P.M. & Hodgson M.J. "Essential Principles of Physics", 2nd ed. pub. John Murray, London (1978)

APPENDIX A

MEASUREMENT OF ACOUSTIC IMPEDANCE

It was stated in section 2.6 that the characteristic impedance of the suspension is a further variable that depends on the suspension properties, in addition to the attenuation and sound velocity. Expressions were given (equations (2.34) to (2.36)) to calculate the characteristic impedance from the usual suspension variables.

This appendix presents a preliminary study to assess whether the characteristic impedance of flowing suspensions may be measured using only a single transducer: a low frequency loudspeaker. The reported data are largely qualitative, since the full range of necessary calibration measurements on the equipment was not attempted.

- Section 1 sets out the predicted impedance of various suspensions, and assesses the feasibility of the method. The theoretical background of the chosen method is described briefly.
- Section 2 surveys the small number of previous studies that have attempted similar measurements, or used similar techniques on different problems.
- Section 3 describes the equipment that was used to make the measurements, while the results are presented in Section 4.

A.1 THEORY

A.1.1 Theoretical predictions of specific acoustic impedance

The real part of the predicted characteristic impedance for suspensions of three substances — flour, olivine sand and F800 grade alumina — was evaluated using (2.34), normalised by the value of clean air to yield the specific characteristic impedance, and is shown in Figure A-1.

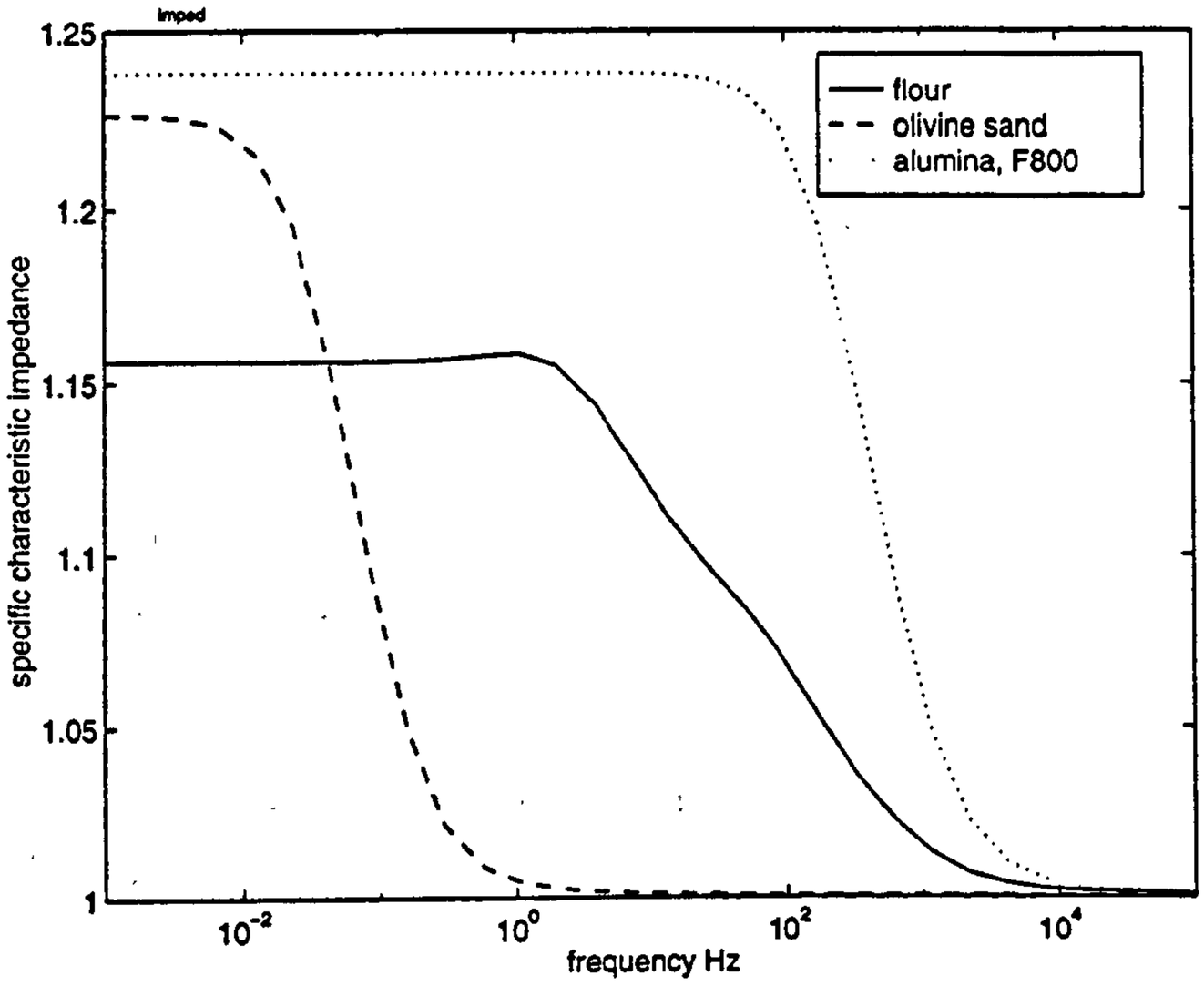

Figure A-1 Predicted specific characteristic impedance (real part) for sand, flour and F800 alumina, at a suspension density of 1kg/kg.

It can be seen that there is a low frequency asymptote (in the viscous regime) of maximum impedance, and a high frequency asymptote (in the inertial regime) where the impedance is unaffected by the particles. Therefore any useful measurements of suspension impedance must be made in the viscous regime, or the transition to the inertial regime. The frequency of this transition point is inversely related to the square of the particle size; materials with a large particle size therefore need to be tested at very low frequencies. The sand sample ($\overline{a}$ =278 μm) shows negligible predicted effect above 1 Hz, and will be unsuitable for this form of measurement.

As the curves were calculated for a mass concentration of 1kg/kg (corresponding to a doubling of volume-averaged density), if the impedance were controlled only by the suspension density, we could expect the specific impedance to show a low frequency asymptote of 2. However, we notice figures lie considerably below this; the reduction is caused by an additional effect due to the increased effective compressibility. To illustrate this point, the effective density and compressibility for flour are shown in Figure A-2.

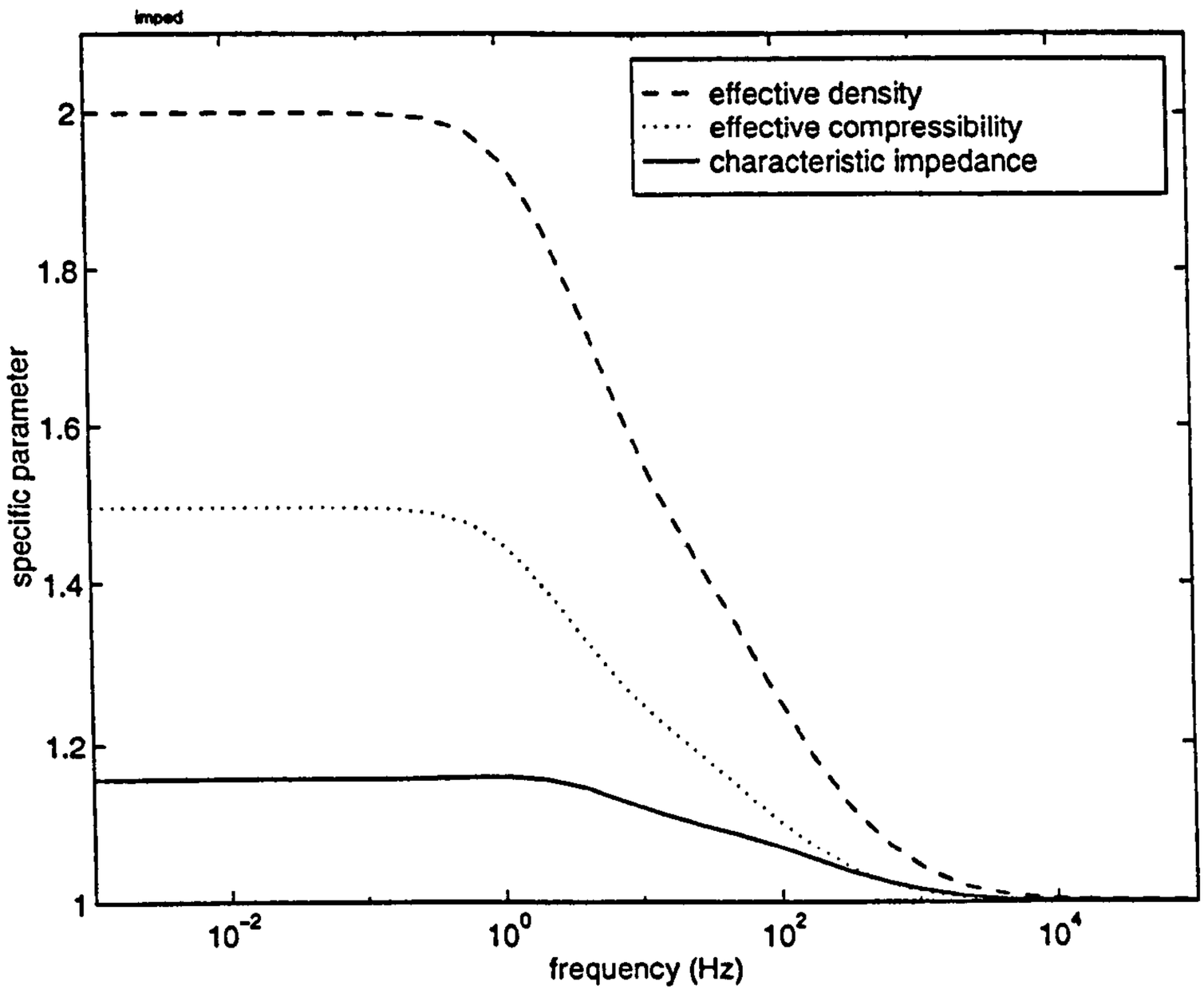

Figure A-2 Effective density and compressibility for flour (real parts), at a mass concentration of 1kg/kg, normalised to values for air.

While the effective density has the expected asymptote of 2, the compressibility has an asymptote of 1.47, representing the effect of heat transfer between air and particles, thus reducing the specific impedance to 1.16.

To assess the feasibility of measuring the impedance of suspensions at practical concentrations, Figure A-3 shows the specific impedance over a range of concentration values, at a fixed frequency. A frequency of 400Hz was chosen as the low frequency rating of the Community M200 driver used in the transmitting probe.

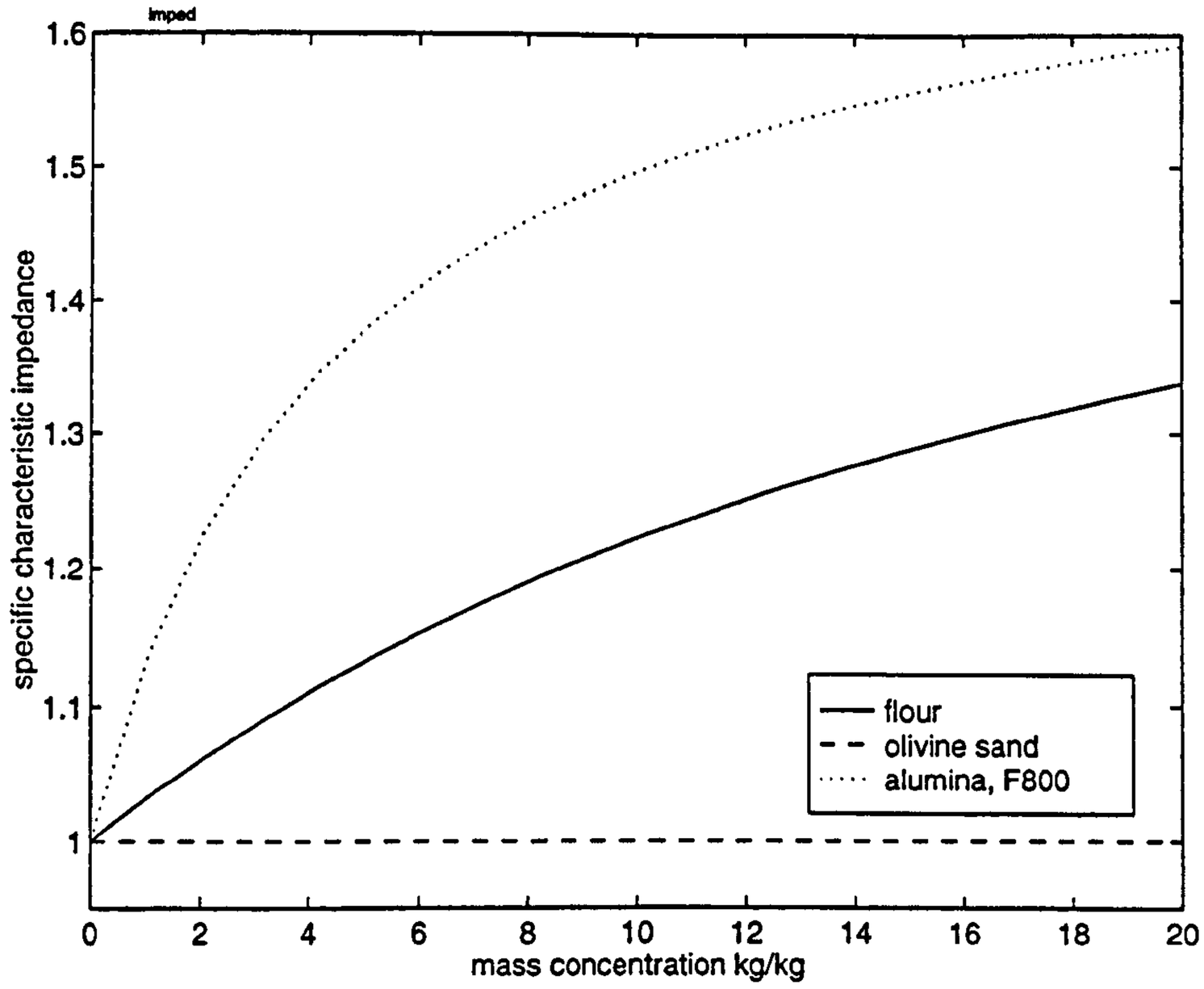

Figure A-3 Predicted specific characteristic impedance (real part) at 400Hz, for sand, flour and F800 grade alumina, as function of mass concentration.

It can be seen that, at a mass concentration of 5kg/kg, there is a 10% increase in impedance for flour, and 35% increase for alumina, while any change due to sand remains insignificant.

A.1.2 Predictions of reflection coefficient

One way of measuring the change in characteristic impedance due to the suspension, is to detect the change in reflection coefficient at the orifice between the probe tube and pipeline. The reflection coefficient is governed by the impedances of both environments, as well as the dimensions of both the tubes. If we use the naive simplification that the two pipes are axially aligned, instead of their axes being orthogonal, then calculation of the reflection coefficient is simplified[1].

The plane wave impedance of a pipe is simply Z / A , where Z is the characteristic impedance of the enclosed fluid, and A is the cross-sectional area. The impedances of the pipeline and probe tube are therefore:

$$Z_1 = Z_s / A_1 \qquad \text{(A.1)}$$

$$Z_2 = Z_0 / A_2 \qquad \text{(A.2)}$$

where subscript $_s$ refers to the suspension, $_0$ to air, $_1$ to the pipeline and $_2$ to the probe tube. The probe tube has diameter 12mm, and the pipeline 53mm.

The sound power reflection coefficient is [73]:

[1] This simplification is used for the purpose of evaluating the order of magnitude of the quantities; modelling the situation with orthogonal axes is very much more complicated.

$$R = \frac{(Z_1 - Z_2)^2}{(Z_1 + Z_2)^2} \qquad (A.3)$$

This is shown evaluated in Figure A-4, for the three materials, as a function of mass concentration.

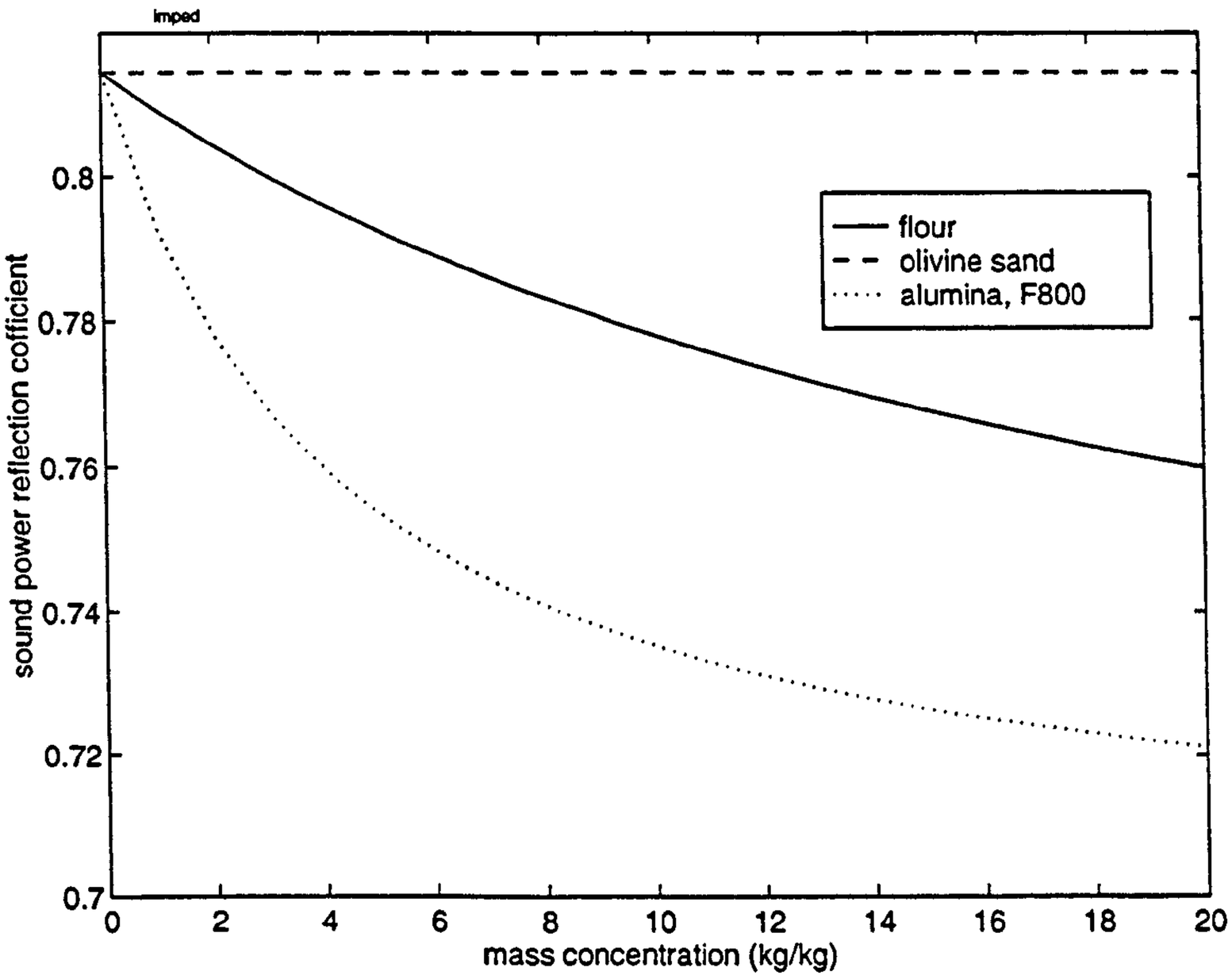

Figure A-4 Sound power reflection coefficient (predicted) for 12mm to 53mm pipe expansion, with a suspension of varying concentration in the 53mm diameter pipe. Frequency is 400Hz.

The reduction in the reflection coefficient should be measurable for flour at high concentrations (above approximately 5kg/kg); alumina should be easier to measure in this way, although its very fine particle size and abrasive qualities make it less suitable for dynamic testing.

A.1.3 Method — Electrical analogue of loudspeakers

The method of detecting changes in reflection coefficient described here was selected for its elegance and simplicity; a more rigorous and accurate method is outlined in Chapter 9. The technique relies on measuring the electrical impedance of an acoustic driver at the end of the probe tube.

Changes in the reflection coefficient at the orifice will, by definition, change the magnitude of the wave reflected back down the probe tube, and so will affect the radiation load on the loudspeaker. This change in radiation impedance is, in turn, propagated through into a change in electrical impedance. The reason for this becomes clear if one examines the electrical analogue of a loudspeaker, in which mechanical stiffnesses, masses and resistances are transformed into capacitors, inductors and resistors, respectively. The transformation of the variables requires a knowledge of the transformation factor, which links mechanical to electrical units (and vice versa). In the case of a moving coil loudspeaker, this factor is Bl, where B is the magnetic field

encompassing the voice coil, and l is the length of the wire in the voice coil. The transformation between the two sets of variables is often represented by a transformer. The loudspeaker can then be represented by a circuit that includes both electrical and mechanical elements, linked by the transformer. The mechanical elements include: the mass of the cone; stiffness and resistance of the suspension mechanism; the acoustical stiffness of the enclosed volume of air to the rear of the diaphragm; any losses in this volume; and the radiation impedance experienced by the loudspeaker (see Figure A-5).

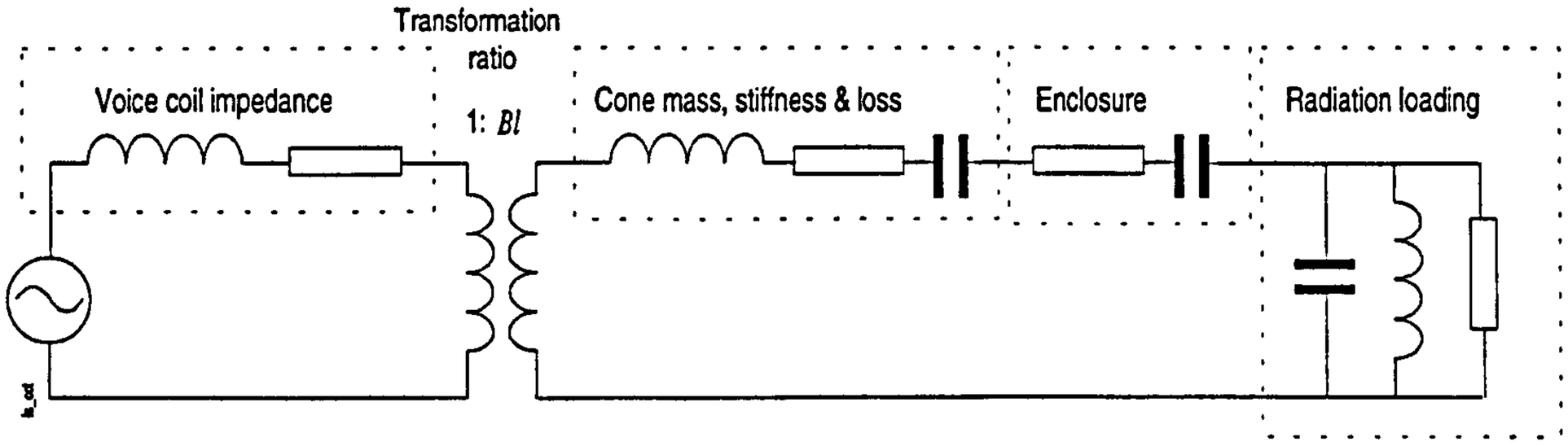

Figure A-5 *Electrical analogue of a moving coil loudspeaker*

Therefore, changes in the reflection coefficient, which affect the radiation loading, should be detectable by measuring changes in the electrical impedance of the loudspeaker. The challenge is to separate the small changes in impedance due to changes in the suspension, from the large steady-state electrical and mechanical impedance.

A.1.4 Method — Bridge measurement of impedance

A bridge arrangement [19] was chosen to subtract the steady-state impedance from the loudspeaker impedance, to allow sensitive detection of variations in the radiation impedance. The bridge technique[1] is often used to measure unknown impedances or small variations in impedance (e.g. strain gauges). The method (illustrated in Figure A-6) uses two voltage dividers ("arms"), one containing the test impedance Z_x, and the other containing a manually variable impedance Z_v. The variable impedance can be adjusted until the voltage differential, V_x, between the arms is zero, at which point the variable and test impedances are equal. Now the differential voltage is very sensitive to a slight imbalance caused by a change in the test impedance.

[1] When the impedances are purely resistive, it is commonly known as a "Wheatstone" bridge.

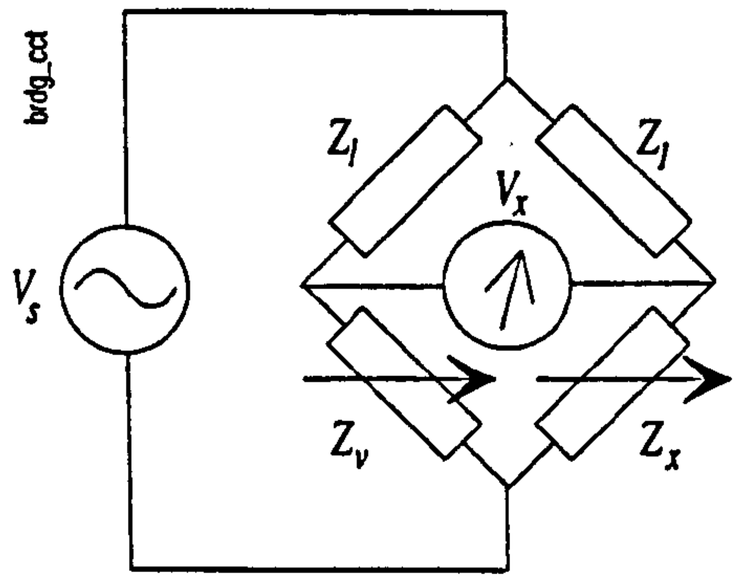

Figure A-6 *Circuit diagram of a general bridge: variable, known impedance Z_v is adjusted until bridge output voltage V_x is zero. Then the test impedance $Z_x = Z_v$. The impedances Z_1 are fixed.*

The bridge imbalance voltage can therefore be recorded to detect variations in Z_x. However, it can be readily shown V_x is a non-linear function of Z_x (although it may be linearised for small variations of V_x).

A.2 LITERATURE SURVEY

Almost all studies of suspensions have concentrated on measuring propagation parameters rather than characteristic impedance. The only exception that I am aware of, is the work of Hayman [58], who measured the impedance of oil-well drilling muds (which are slurries of solid particles in a viscous, non-Newtonian liquid). The mud was contained in a thick-walled measuring cell. Two ultrasonic transducers (bandwidth 200 – 700 kHz), opposed each other and were coupled to the walls. The impedance was found by measuring the amplitude of the reflection from the interface between the cell wall and mud at the transmitting transducer. The thick cell walls (45mm) provided sufficient time separation of the transmitted pulse, and the first reflection, so that the latter could be analysed. The receiving transducer was used to measure the attenuation and sound speed. This method illustrates the "free" information that may be gleaned when measuring the propagation parameters, by using data from the transmitting transducer.

The method of measuring the reaction on the transmitter was exploited very early (1938) by Laidler & Richardson [81]. They measured the ultrasonic attenuation of lycopodium "smokes", by observing the current drawn by the oscillator that powered the transducer (described further in section 3.1.1).

Earlier, in 1933, Fay & Hall [45] used a bridge circuit to measure the impedance of a telephone receiver that was loaded by a variable-length waveguide. From these measurements, they used a graphical technique to deduce surprisingly many characteristics of the transducer: for example, the sound power output, and acoustic output impedance. In a later paper, Fay & White [46] elaborated on the technique to measure the impedance of a solid sample that terminated the waveguide. They also showed that there was an optimal length of waveguide, that provided maximum change in electrical impedance for a given change in acoustic impedance. Such knowledge could be used to optimise the equipment described here.

A.3 EQUIPMENT

The measurement system was built around a PC-based A/D card, so that signal processing could occur in real time within the LABVIEW environment. A block diagram of the overall system is shown in Figure A-7; the front panel of the LABVIEW virtual instrument (VI) is shown in Figure A-8, and the circuit diagram of the bridge is given in Figure A-9.

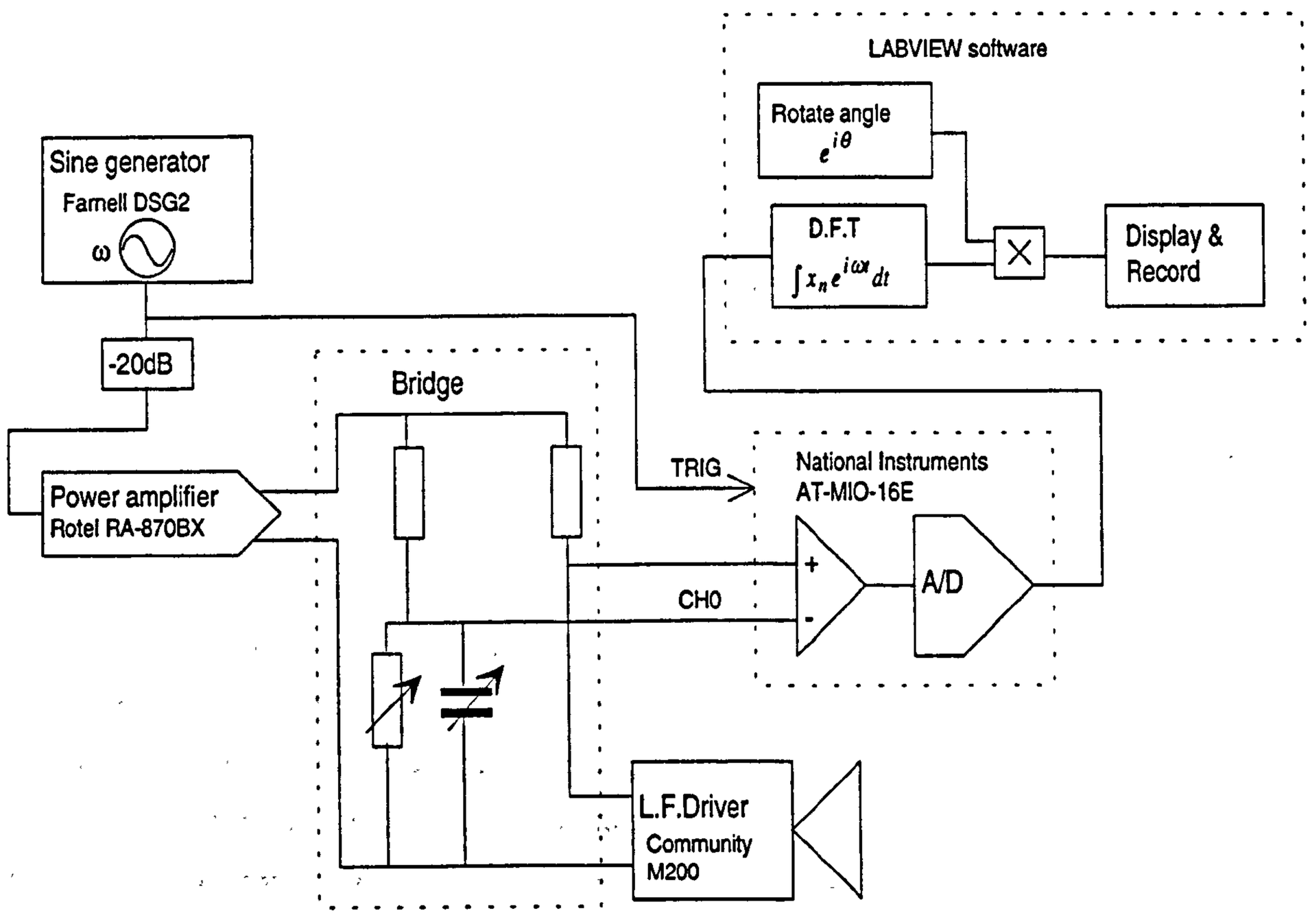

Figure A-7 *Simplified block diagram of loudspeaker impedance measuring system*

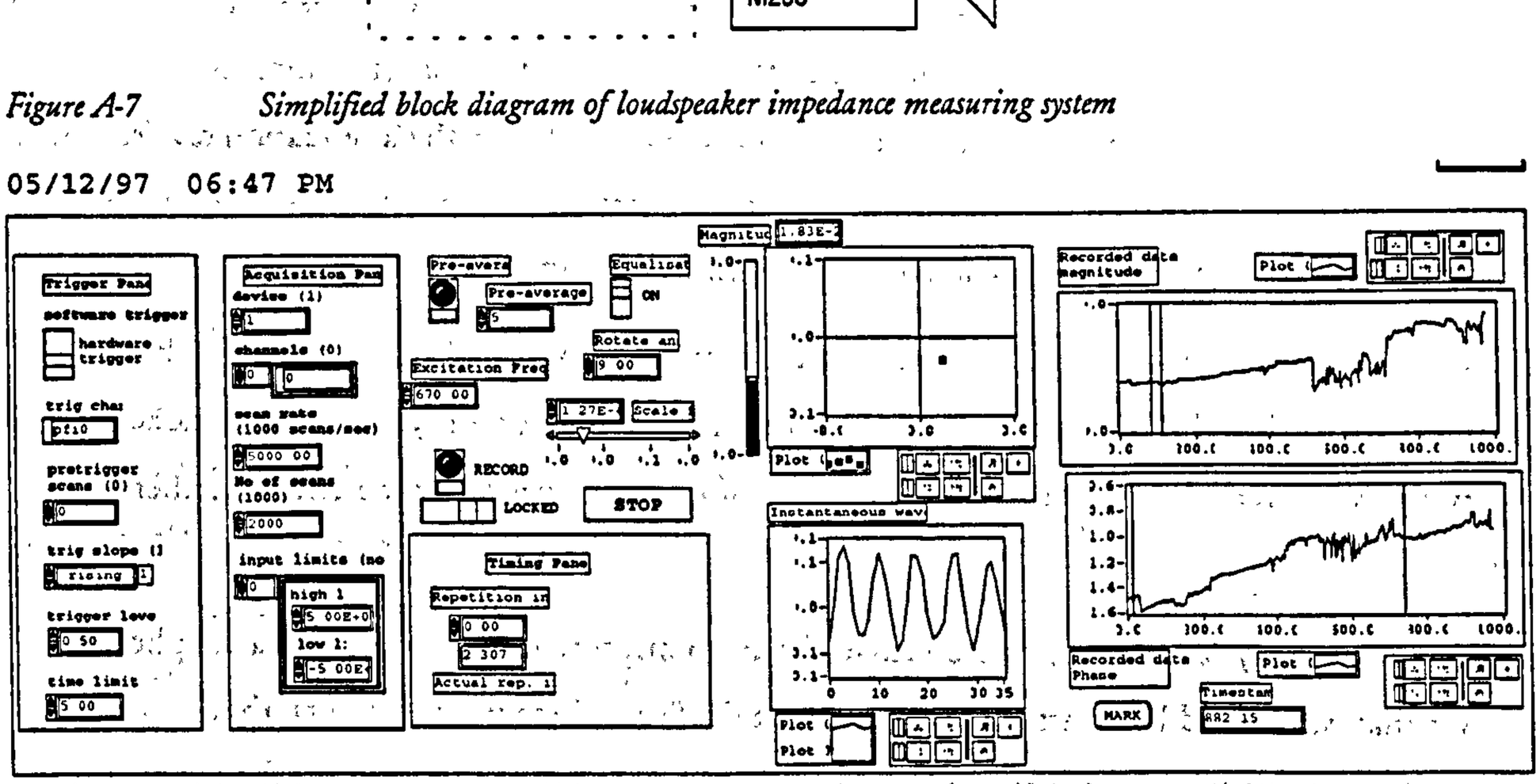

Figure A-8 *Front panel of the loudspeaker impedance measuring VI. The time trend of the bridge voltage is shown in the charts right top & bottom (magnitude & phase, respectively); a single block of measured voltage is shown bottom centre, and its resolved phasor at the measurement frequency appears above it (indicated by a dot on the Argand diagram).*

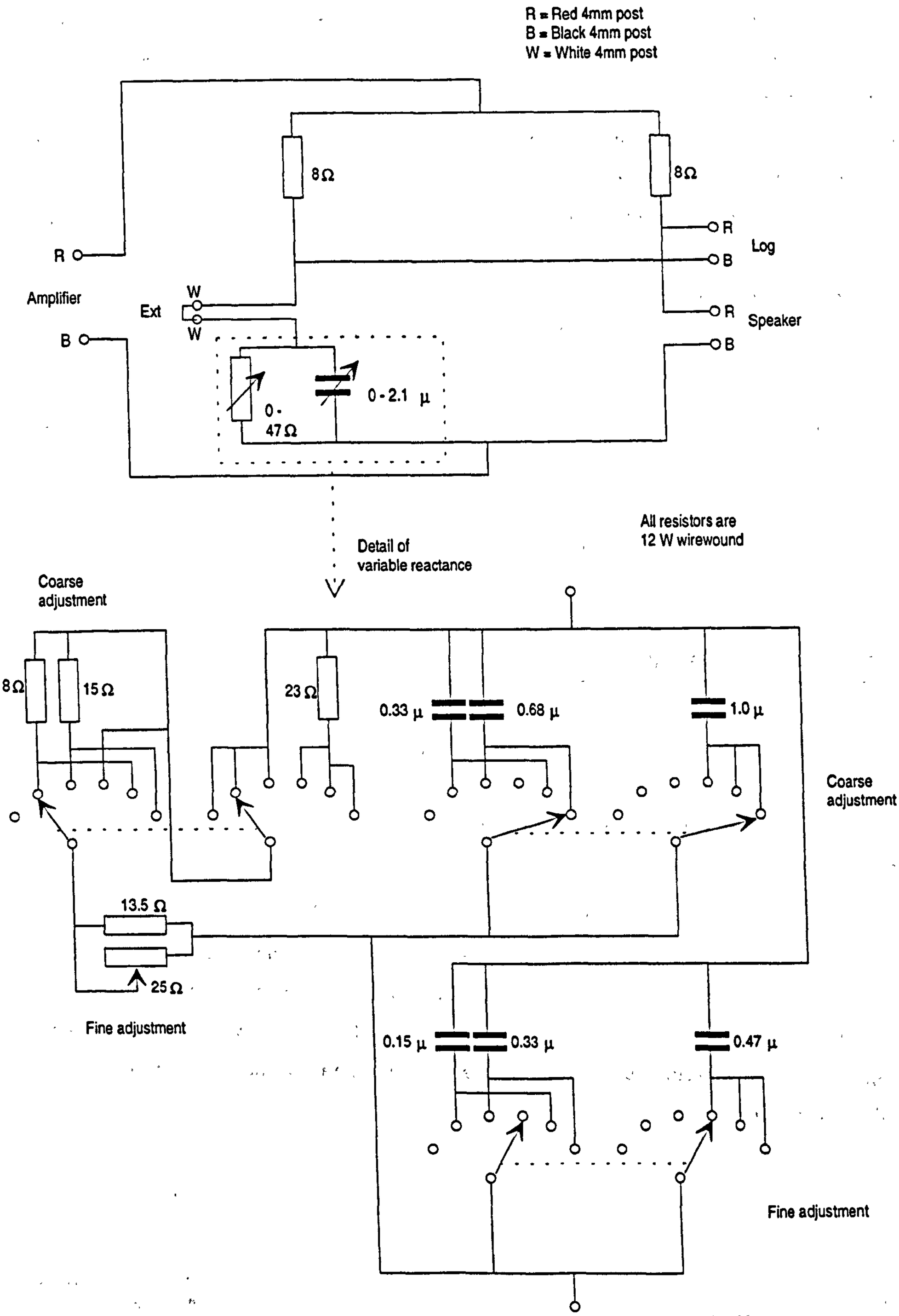

Figure A-9 *Circuit diagram of the loudspeaker impedance bridge*

For a loudspeaker, the Community M200 driver was used, mounted in its probe arrangement unchanged[1], so that no additional transducers or modifications to the probe were required. A synthesized signal generator excited it, through a power amplifier, at a single continuous frequency. The variable impedance in the bridge was adjusted to have the same impedance as the loudspeaker at the particular frequency: this was indicated by a null output from the bridge. The bridge output, after being digitised, was processed by a DFT at the single frequency of excitation. The DFT produced the phasor that represented the unbalanced voltage output of the bridge (data recording was synchronised with the signal generator, maintaining a fixed phase relationship between them); it also reduced the influence of noise and harmonics – the latter dominated the bridge output at a null since the bridge is unbalanced at these higher frequencies.

The voltage phasor resulting from the DFT was rotated so that an unbalanced resistive component produced a purely real voltage, and a reactive component produced an imaginary voltage. By observing the voltage phasor on an Argand diagram, one could therefore have a visual indication of the change of impedance. This also simplified the process of adjusting the variable impedance to null the voltage.

A.4 MEASUREMENTS

The variable impedance did not include any inductors[2], and so it could not be used to balance the reactance of the loudspeaker when it had a net inductive component. Consequently the frequency of operation was chosen so that the impedance of the loudspeaker was restricted to a region where a null could be found with the variable impedance in its mid-range. Two frequencies were selected for analysis: 670 Hz and 1050 Hz.

The variable impedance was adjusted to provide the closest possible null[3], with clean air flowing in the pipe, and the flushing air turned on. Five waveforms were synchronously preaveraged before being processed, to improve SNR. The resulting voltage phasor was recorded every two seconds (approx.) for a period of 2 - 3 minutes for each flow setting. The time series for each setting was averaged to produce a mean figure, and the standard deviation was calculated to indicate the variability within the dataset.

---

[1] The probe arrangement was optimised to *reduce* the sensitivity of the transducer to the orifice impedance; futhermore, the length of the probe tube could be optimised using the analysis of reference [46].

[2] Inductors are more likely to drift with temperature, more cumbersome when required to handle large currents and have high inductance, and also have a small resistance which, when switching between different value inductors, would tend to unbalance the resistive component.

[3] It was usually possible to null the resistive component, because the resistance was continuously-variable ; however, discrete switchable capacitors were used to null the reactive component, and so there remained a residual out-of-balance imaginary component of the voltage. The equipment could usefully be modified to give smaller steps between capacitance settings, giving more complete nulling of the reactive component, and therefore increasing the sensitivity.

A.4.1 Clean Airflow

Initially, the effect of clean airflow was tested. The bridge was nulled with only flushing air flowing, and then the main airflow was increased in steps up to 42 m/s. The bridge output voltage is plotted in Figure A-10, both in complex format, to show the trajectory, and separated into components as a function of velocity.

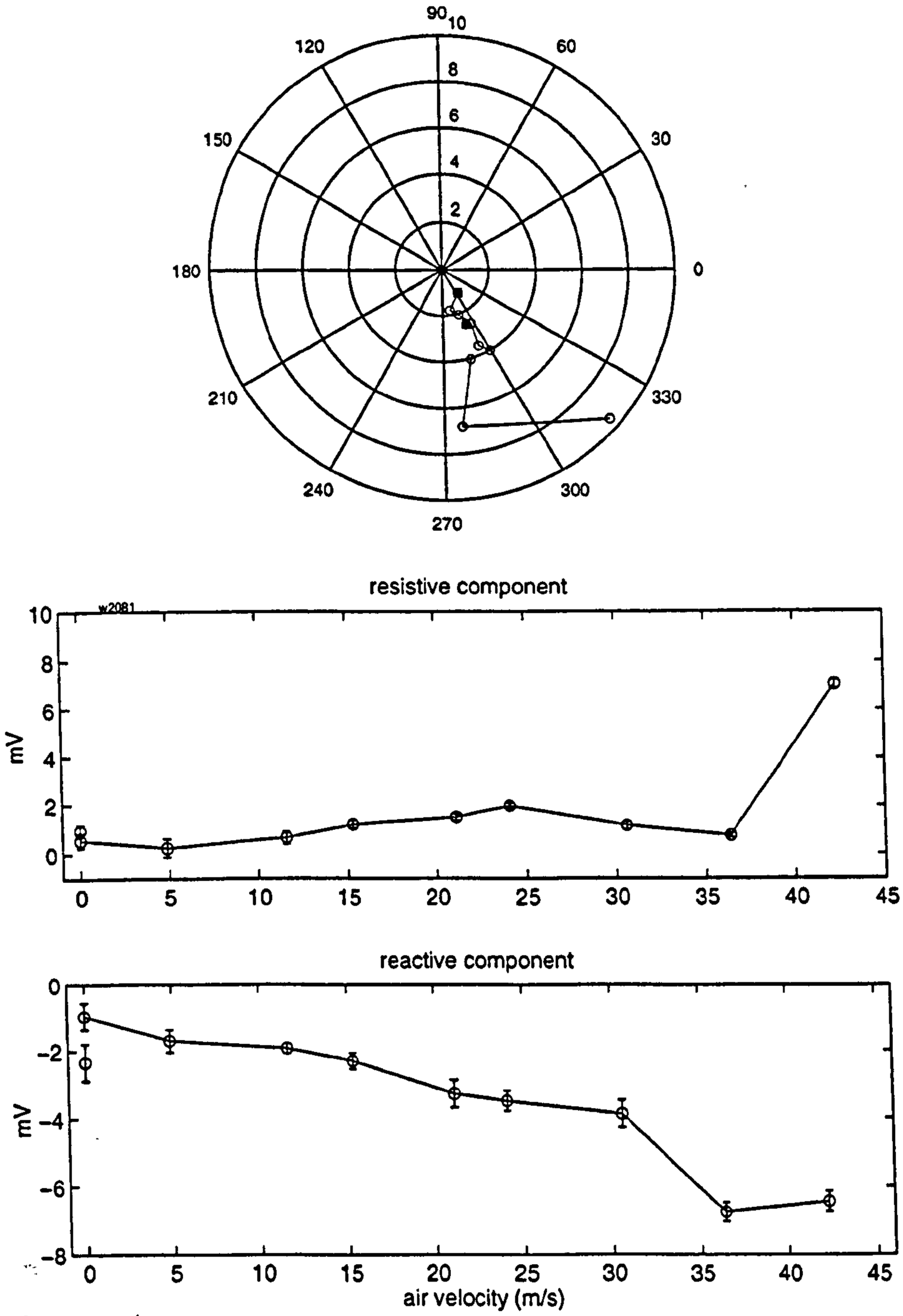

Figure A-10 Bridge output voltage for varying clean air velocity in the pipeline. Frequency = 1050 Hz. Top: Argand diagram with parametrically-varied velocity (filled circles represents no-flow points); middle & bottom: resistive and reactive components. A positive resistive imbalance represents an increase in resistance; a positive reactive imbalance represents a decrease in capacitance or an increase in inductance. Error bars represent ± 1 standard deviation.

The unbalanced voltage at 42m/s was re-nulled by changing the variable impedance from (18 - 3i) Ω to (20 - 4.1i) Ω at 1050 Hz. It is not possible to deduce quantitative figures for reflection coefficient or orifice impedance, without more involved measurements on the loudspeaker/probe

to find the transduction coefficients. Nonetheless, we can observe that the impedance experienced by the loudspeaker increases in resistive and negative reactive (capacitative) components as the air velocity increases, and most sharply above 30 m/s. This result is qualitatively in agreement with measurements of Cummings [36], who found that the orifice resistance increases as a linear function of friction velocity (related to flow speed), and that the mass end correction of the orifice (an "inductive", or positive reactive, component) fell with friction velocity.

A.4.2 Flushing airflow

The dependence on the flowrate of the probe flushing air was also investigated. The flowrate was normally held constant by maintaining a constant air pressure (4.0 bar) to the choke flow nozzle that supplied the flushing air. However, by varying the supply air pressure, the air mass flowrate is predicted to vary in direct proportion [26]. In this experiment, the bridge was nulled with a supply air pressure of 4.0 bar, and then the pressure was reduced in steps to 2.0 bar. The resulting bridge output is shown in Figure A-11.

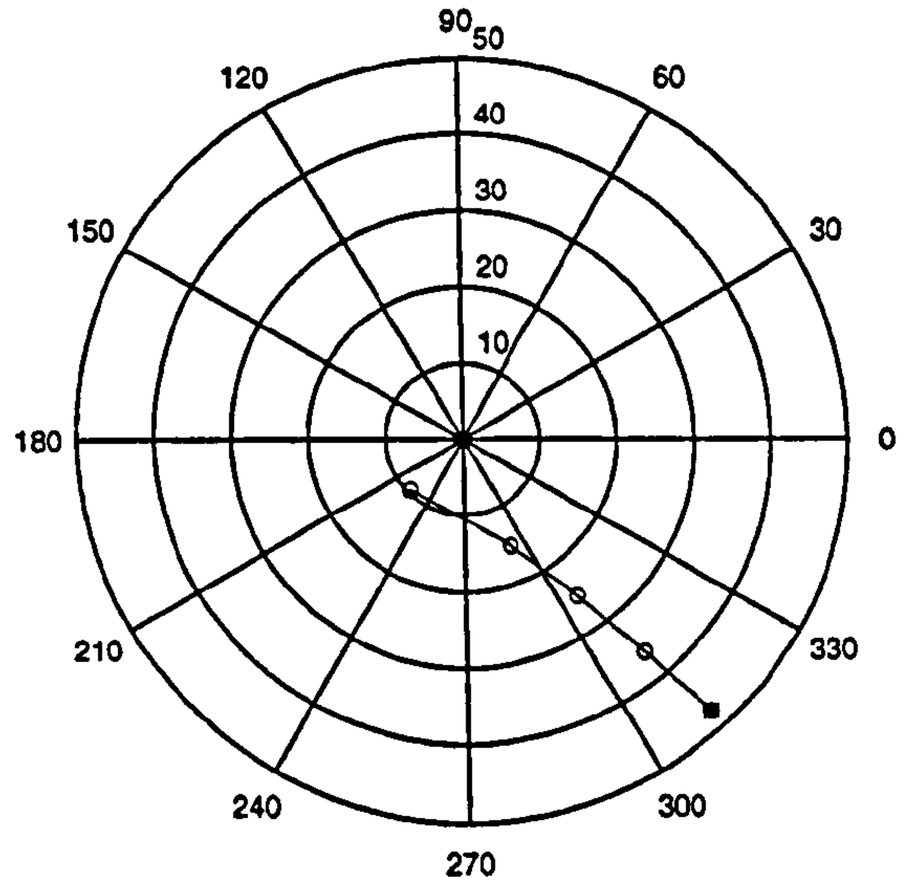

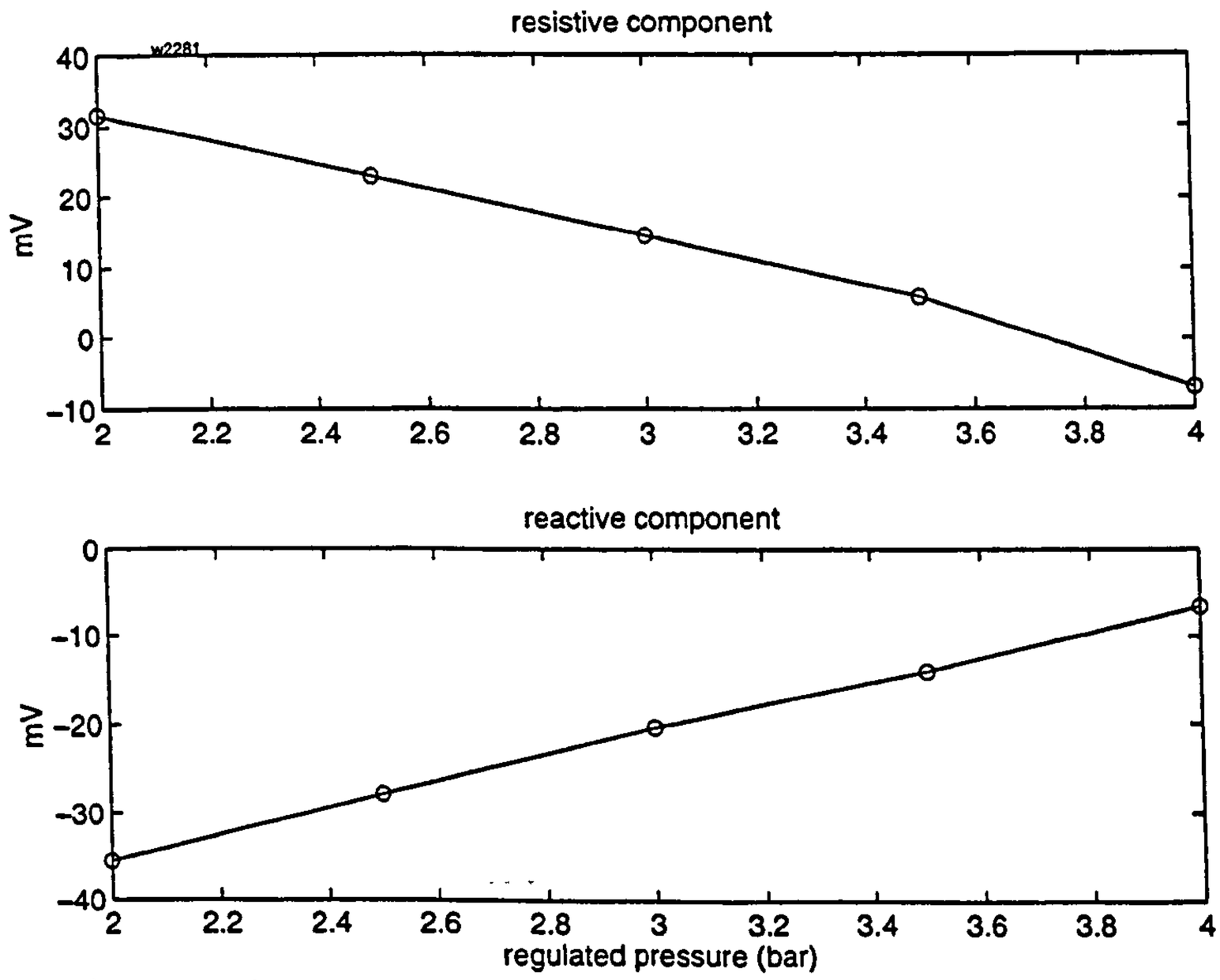

Figure A-11 *Bridge output voltage for variable flowrate through the probe tube, governed by varying the supply air pressure to the choke flow nozzle. Frequency = 1050Hz. Top: Argand diagram (filled circle represents value at 2.0 bar); middle & bottom: resistive and reactive components. A positive resistive imbalance represents an increase in resistance; a positive reactive imbalance represents a decrease in capacitance or an increase in inductance. Error bars are too small to be shown.*

Error bars are not shown on the graphs because the measurements showed no significant scatter. There is a very clear trend for a reduction in resistive and negative-reactive components with increasing flowrate. This also agrees with experimental and theoretical findings, summarised by Davies [38], who showed that the modulus of reflection coefficient of an open-ended tube with outflow decreases with increasing Mach number. The magnitude of the changes are very much larger than that measured with pipeline airflow, and larger than any measurements reported later.

A.4.3 Olivine Sand

Olivine sand was measured in this way over a concentration range of 0 - 2 kg/kg (approx.) The clean airflow (reference) measurement was taken at the start and end of the measurement series, to assess its repeatability.

Due to its large particle size, the sand was predicted (Figure A-4) to have no significant effect on the reflection coefficient, and so could be used to assess other influences on the measurement.

The bridge output voltage is plotted in Figure A-12 (1050 Hz) and Figure A-13 (670 Hz).

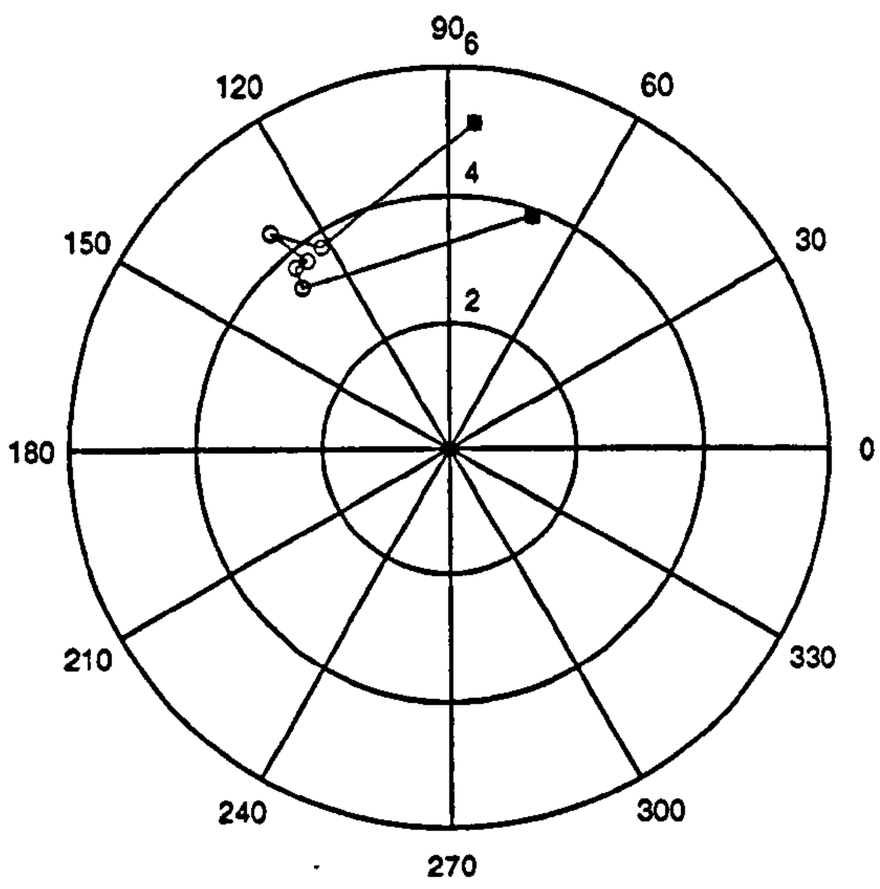

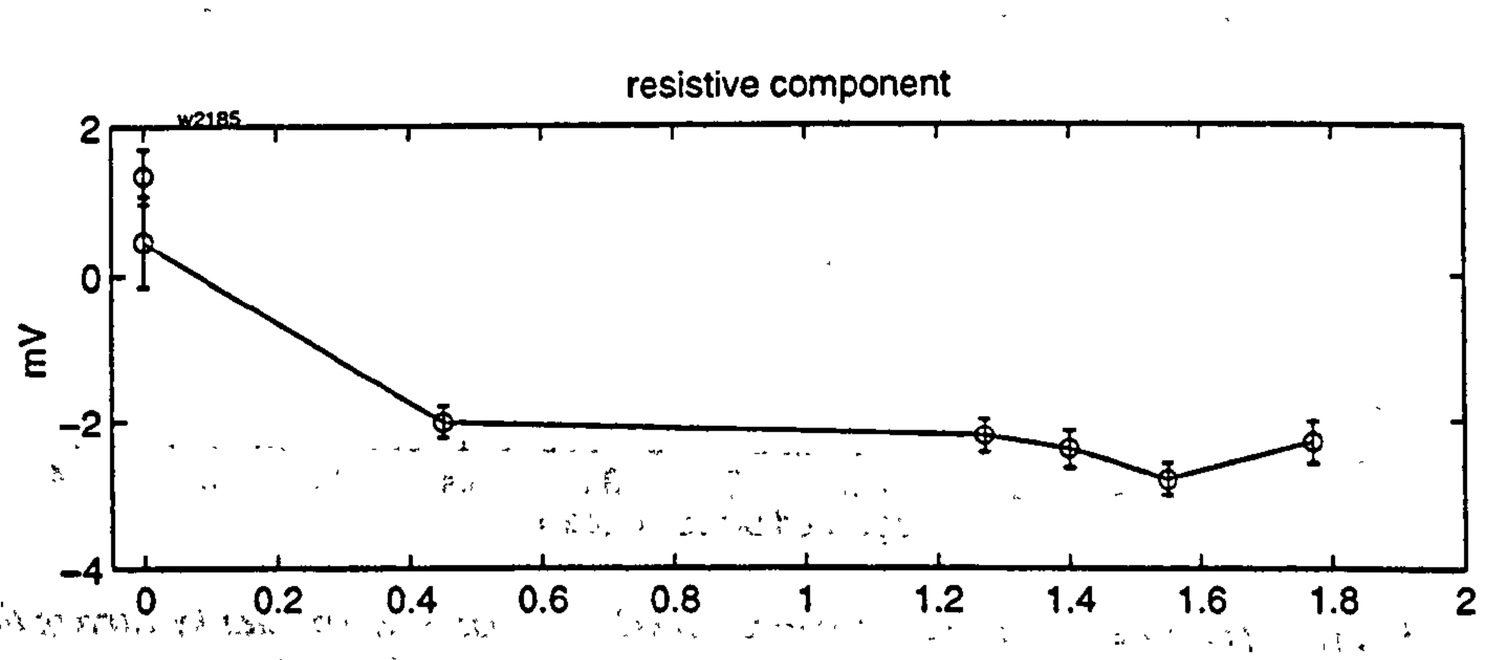

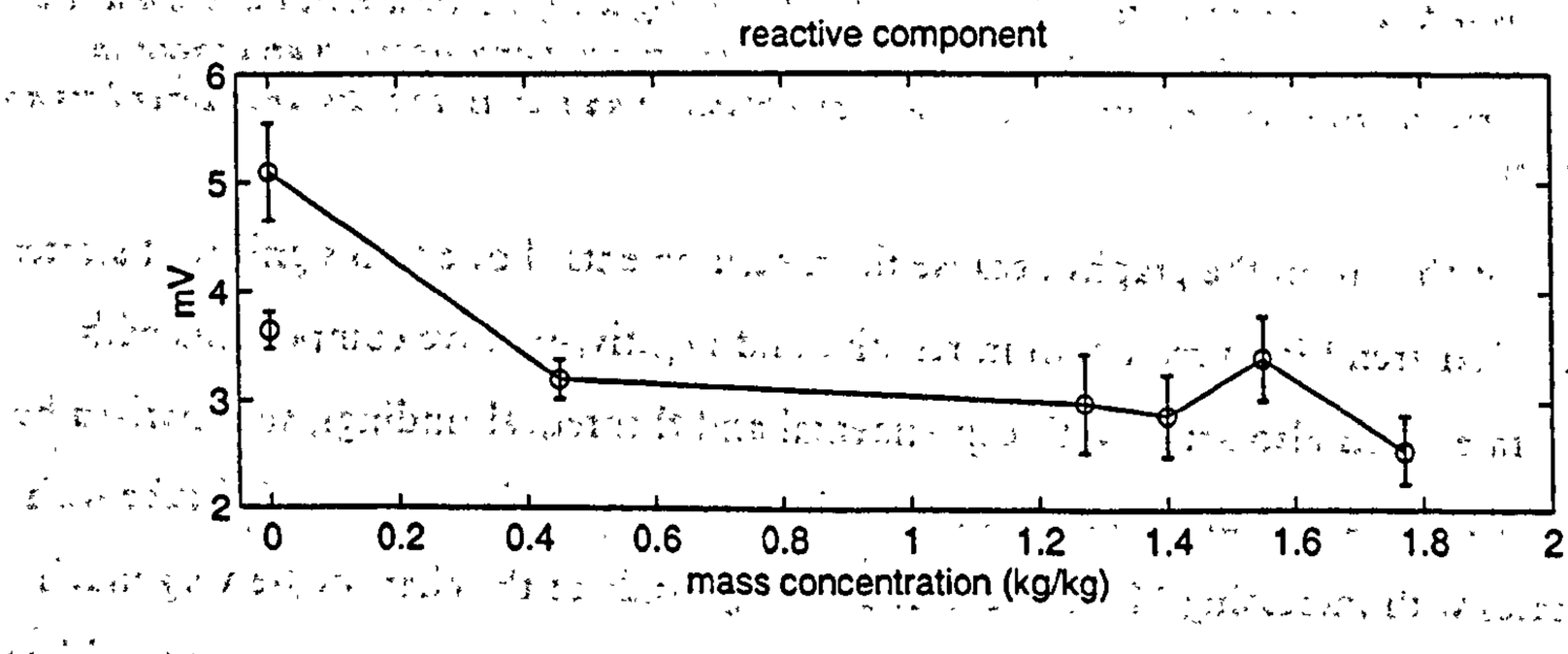

Figure A-12 Bridge output voltage for flowing olivine sand; frequency = 1050 Hz. Top: Argand diagram (filled circles = clean airflow points, $\phi_m = 0$); middle & bottom: resistive and reactive components.

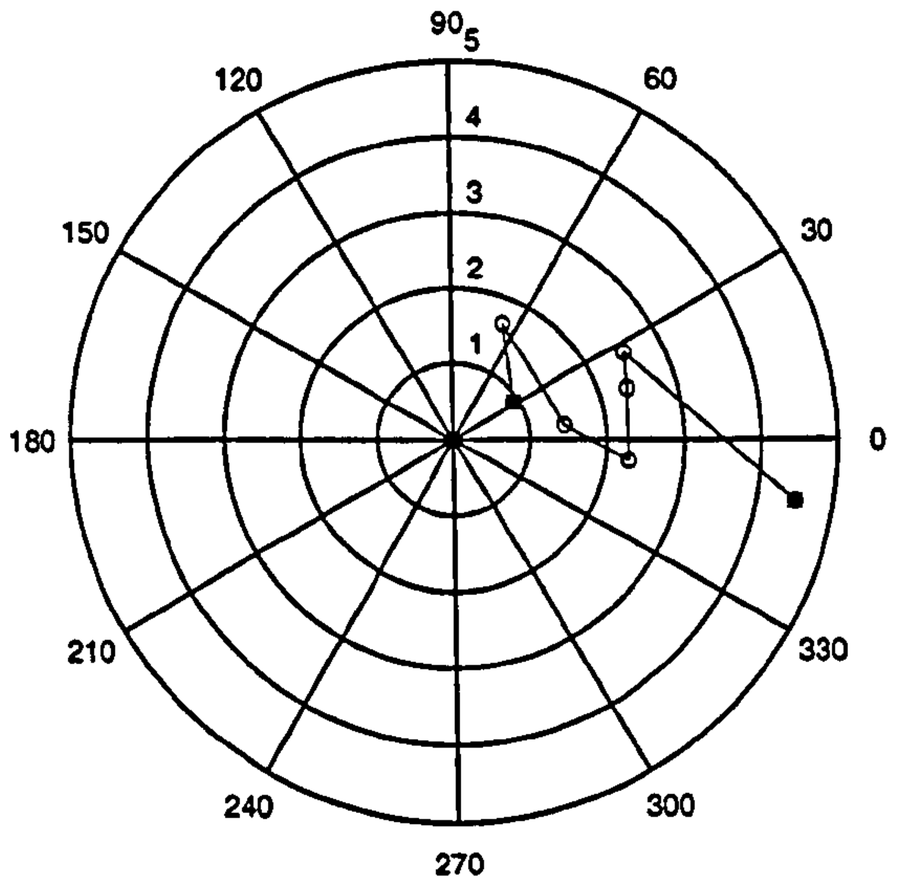

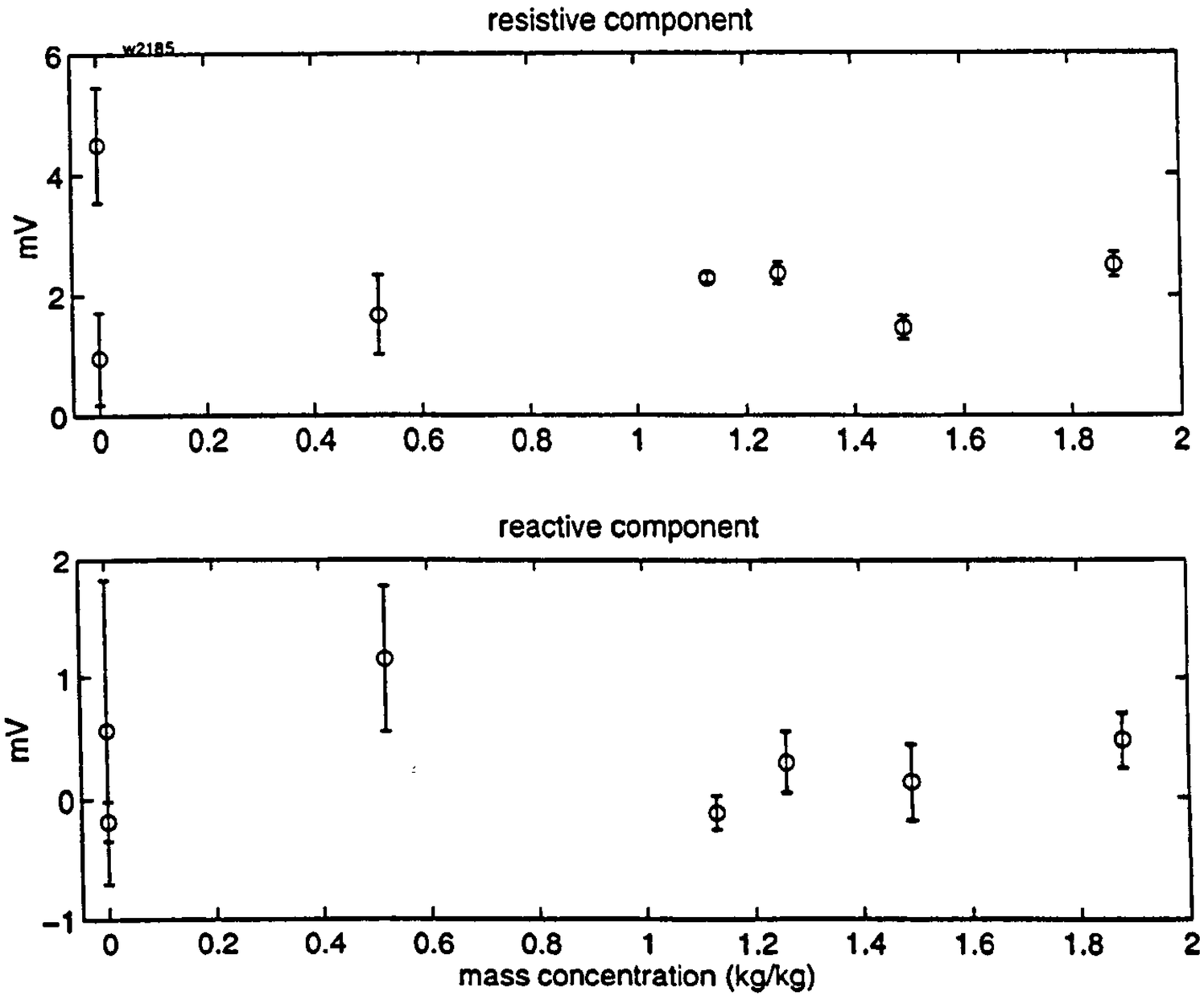

Figure A-13 Bridge output voltage for flowing olivine sand; frequency = 670 Hz. Top: Argand diagram (filled circles = clean airflow points, $\phi_m = 0$); middle & bottom: resistive and reactive components.

The largest effect at 1050 Hz is due to the presence or absence of sand suspension; there appears to be little correlation with concentration. The presence of sand suspension leads to a reduction in the resistive and reactive components, with a very clear clustering of points on the Argand diagram. The results at 670 Hz show a less consistent trend. The clean airflow point at the end of the experiment shows poor repeatability with the initial value. There is a slight possibility that this caused by a hole in the conveying line that developed towards the end of the measurement series.

A.4.4 Barytes

The same measurement method was used on the sample of barytes. This had been found to be very cohesive, and to produce much less acoustic effect than would be predicted from its fine particle size – in Chapter 6, it was found to have approximately the same attenuation coefficient as the flour sample. The measurements of bridge voltage are plotted in Figure A-14 (1050 Hz) and Figure A-15 (670 Hz).

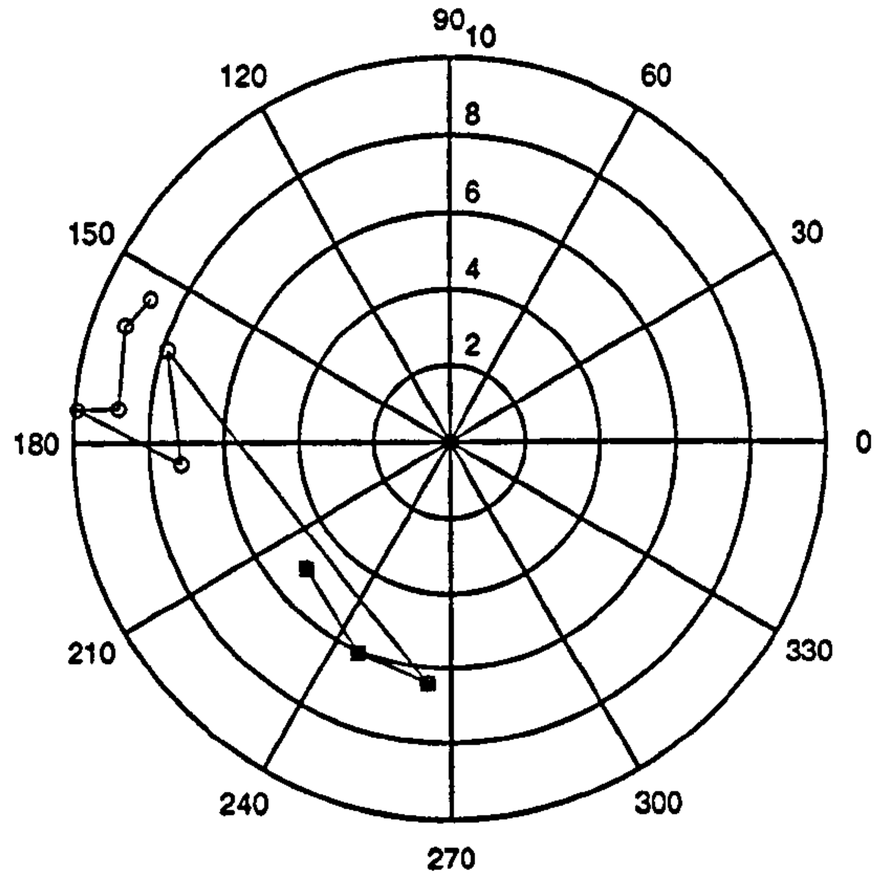

Figure A-14 *Bridge output voltage for flowing barytes; frequency = 1050 Hz. Top: Argand diagram (filled circles = clean airflow points, $\phi_m = 0$); middle & bottom: resistive and reactive components.*

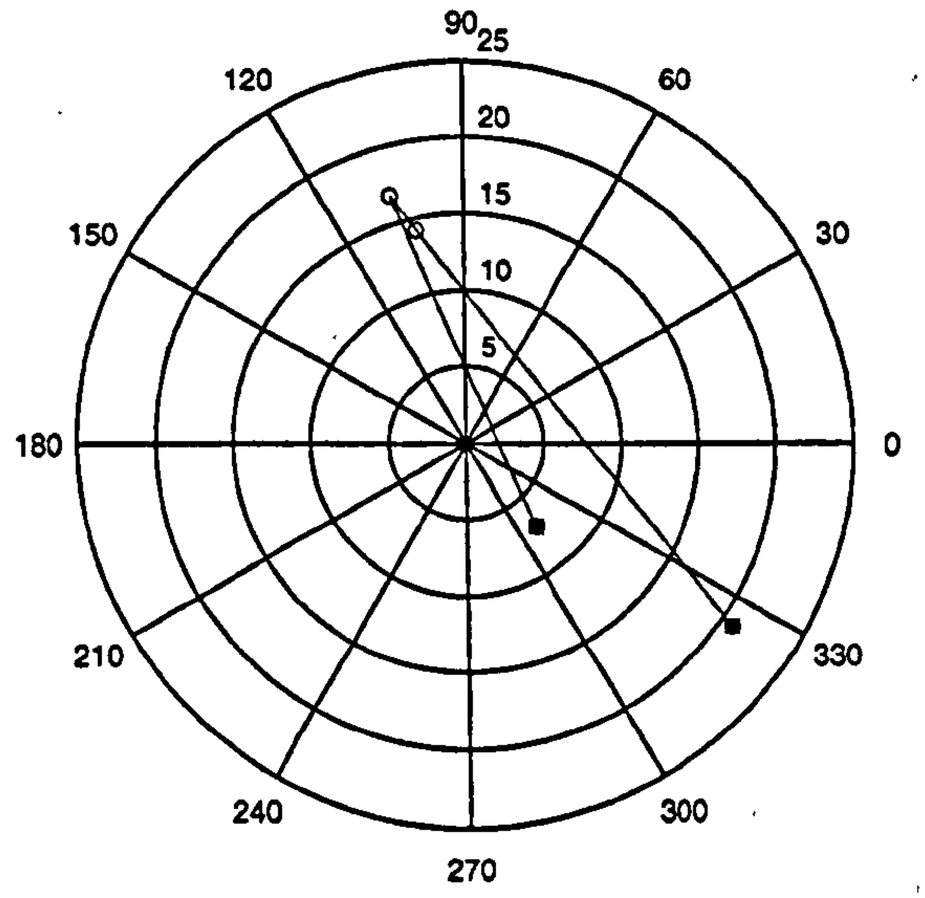

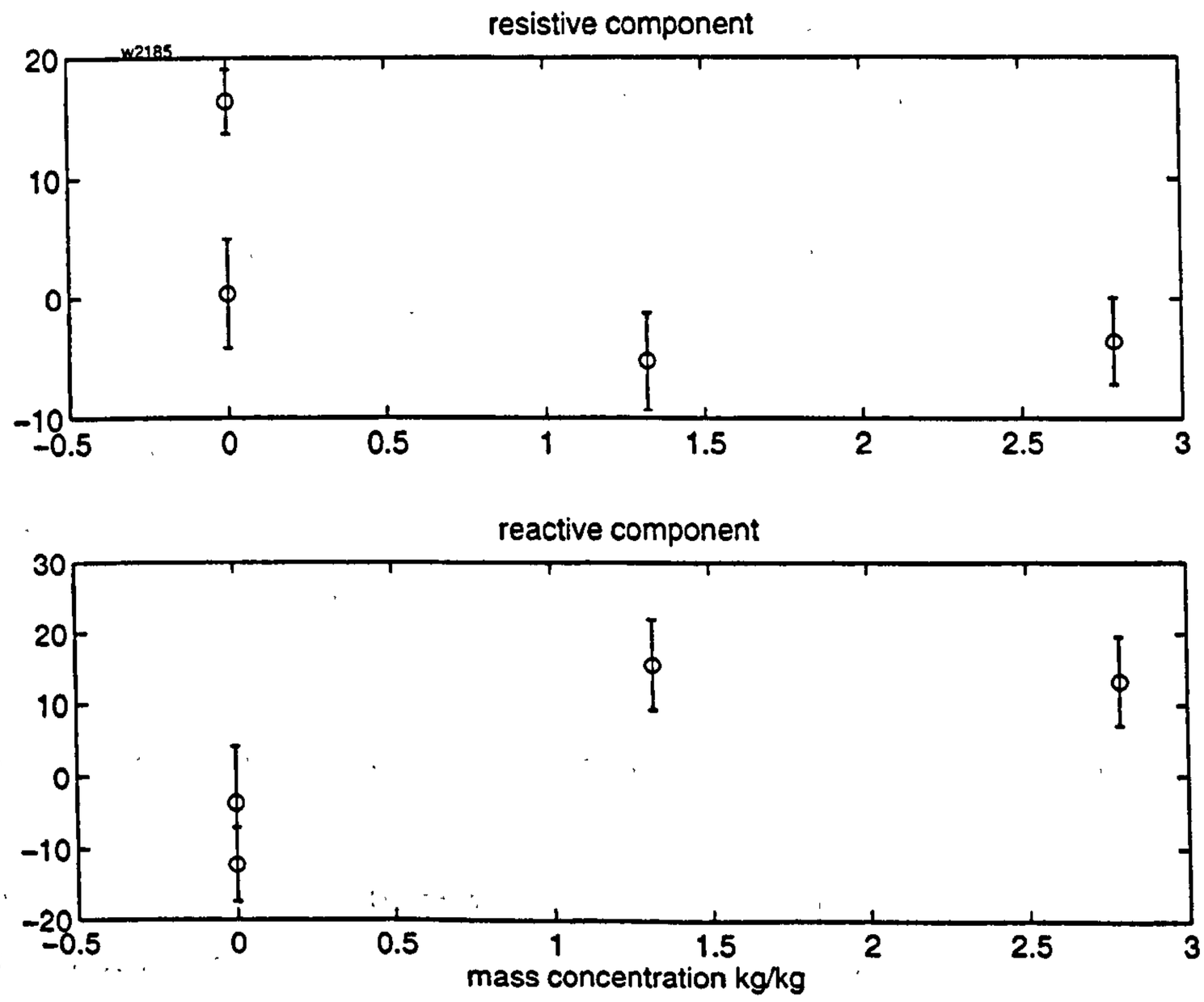

Figure A-15 Bridge output voltage for flowing barytes; frequency = 670 Hz. Top: Argand diagram (filled circles = clean airflow points, $\phi_m = 0$); middle & bottom: resistive and reactive components.

The patterns at both 1050 Hz and 670 Hz (albeit with fewer points) are mutually consistent, and are fairly similar to that of sand: the presence of barytes causes a reduction in the resistive component, but an increase in the reactive component, with clear clustering between the measurements with and without suspension flow. There is a slight trend for an increasing reactive component with concentration. Both components appear very sensitive to small concentrations of suspension, with less sensitivity to subsequent increases.

A.5 DISCUSSION AND CONCLUSIONS

The output of an impedance bridge was recorded to measure changes in the impedance of a loudspeaker coupled to a probe tube, and hence to detect variations in the boundary conditions at the orifice between the probe tube and the flow pipeline. While the intention was to detect changes in the specific impedance of the flowing medium in the pipeline (due to suspended particles), the boundary conditions may also be affected by changes in the orifice impedance. This is expected to be affected by the boundary layer parameters in the main pipeline, which, in turn, are predicted to depend on the flow velocity and the presence of particles.

The bridge voltage was found to be well correlated with the air flow velocity in the main pipeline, and also in the probe tube. The inferred impedance change for both experiments was in qualitative agreement with findings of other researchers. For the case of pipeline flow, the results are explained by variations in orifice impedance; for the case of probe tube flow, the results are explained by variations in the reflection coefficient at the orifice.

Little clear correlation has been found between the bridge voltage and the concentration of either barytes or olivine sand particles. However, the presence of particles was found to have a noticeable effect on the measured voltage. This suggests that the largest influence is that of particles on the orifice impedance, due to changes in the boundary layer at the pipe wall [36]. Particles have been found to affect the boundary layer by either creating [77, 160] or damping [145] turbulence in the flow, and therefore affecting momentum diffusion into the boundary layer.

The technique described here used continuous excitation of the loudspeaker. This gave a measurement system that was very sensitive to changes in the environment (it could readily detect a 10 mg piece of polyester fibre inside the pipeline). However, since the entire environment is insonified, it does not give any spatial information about where the changes are occurring. It is conceivable, for example, that a time trend could be caused by the bag filters becoming steadily more clogged during a test run. Preliminary tests were also conducted with burst sine waves, so that the reflection from the orifice could be separated from other reflections signals from elsewhere in the pipeline. The results of such a measurement are more involved to analyse, but should convey useful information; this is discussed further in Chapter 9.

A further potential cause of error is the variation of pipeline pressure. The loudspeaker was modified to include a pressure equalisation channel (chapter 5). This forms a first-order system with a time constant governed by the flow resistivity of the channel and the volume of air behind the diaphragm, and so a step increase in pipeline pressure will produce an exponentially-decaying differential pressure across the diaphragm. Such a differential pressure is likely to be experienced by the loudspeaker as a change in impedance. This conjecture is supported by the appearance on the bridge voltage - time trace of spikes with fast attack and slower decay, which coincided with changes in conveying conditions. To reduce the effect of these, and of the transition between

conditions, the trace from 2 seconds before, to 5 seconds after a setting change was disregarded in calculating the mean and standard deviation of the voltage for a given setting.

It appears that this method could serve two purposes: it could detect variations in the orifice impedance, either for further research into this phenomenon, or to provide a very sensitive measure of low particle concentrations, that appear to affect the boundary layer at the tube wall; alternatively it may be able to quantify the suspension density for very concentrated suspensions of fine particles, by detecting variations in specific impedance of the suspension. As such, it is another technique that may be applied to a particular regime, ie. strongly attenuating suspensions, where the transmission loss may be too high to be measured accurately. It has the advantage of being only a single port measurement, and the technique described here uses only minimal equipment.

APPENDIX
B
PROGRAM LISTINGS

B.1 THEORETICAL PREDICTION PROGRAMS

B.1.1 Lloyd & Berry with long wavelength approximation

```
function [alpha, beta, attn, phasevel] = scatlbp3 (freq, r, v, phi, param);

% syntax:  [alpha, beta, attn, phasevel] = scatlbp3 (freq, r, v, phi, param);
% applies Lloyd & Berry's multiple scattering theory to distribution of particle sizes
% freq is row vector of frequencies at which to evaluate alpha & beta
% r is column vector of  radii,
% v is column vector of associated particle volume fraction distribution [sum(v)=1]
% param is the row vector of particle parameters

% 0-suffixed variables apply to continuous (fluid) phase
% p-suffixed variables apply to solid (particle) phase

% Simon Moss, 15-10-93
% rev. 2        25-3-94  corrected calculation for dispersion
%                      before was:  beta = 1 - (phasevel / c0) .^ 2
% rev 4-8-95 from SCATLB, but passing parameter vector, using MAT_PARA
%               bug fix to handle monodispersed distn without using dummy sizes
% 15-3-95 from SCATLBP, but using corrected for the the volume fraction: do not convert
values
% 21-1-96 from SCATLBP2, modified so tan(z) / (z - tan(z)) term doesn't break down at high
f or a


% Extract particle & gas parameters from param vector

rhop = param(1);        rho0 = param(2);
shcp = param(3);        shc0 = param(4);
gamma = param(5);       mu0 = param(6);
cp = param(7);                  c0 = param(8);
condp=param(9);         cond0 = param(10);
betap = param(11);

radno = length (r);
freqno = length (freq);

frac=v;                                         % NB NO CONVERSION -> volfrac

r = r(:,ones (1, freqno));                      % create matrix from r
frac = frac(:, ones (1, freqno));               % create matrix from frac

t = 293.15;                                     % temperature in K

w = 2 * pi * ones (radno,1) * freq;             % create matrix of w

therm = (1 / (t * rho0 * shc0)  -  betap / (rhop * shcp)) ^2;

deltv0 = sqrt (2 * mu0 ./ (w * rho0));                  % viscous skin depth of fluid
deltt0 = sqrt (2 * cond0 ./ (w * rho0 * shc0));         % thermal skin depth of fluid
delttp = sqrt (2 * condp ./ (w * rhop * shcp));         % thermal skin depth of solid

k0 = w / c0;
kp = w / cp;

z0 = (1 + i) * r ./ deltt0;
zp = (1 + i) * r ./ delttp;

% 3 cases:      large z ->      tan(z) = i
%               med z   ->      normal trig expansion
%               small z ->      Taylor expansion

if real(zp) > 40
        zpt = i;
        zp2 = zpt ./ (zpt -zp);
```

```
elseif real(zp) > 6e-2
        zpt = tan(zp);
        zp2 = zpt ./ (zpt -zp);
else
        zp2 = (zp.^2)/3 + 2/15 * zp.^4 + 17/315 * zp.^6;
        zp2 = 1 + 1./zp2;
end

h = 1 ./ (1 ./ (1 - i * z0) - (cond0 / condp * zp2));
therm =  therm * c0 * t * rho0 * cond0 * h;

kr3 = (r(:,1) * k0(1,:)) .^ 3;

% Allegra & Hawley single sphere scattering coefficients, long wavelength

A0 = i/3 * kr3 .* (rho0 * kp .^2 ./ (rhop * k0 .^2) - 1);
A0 = A0 - ((r(:,1) * k0(1,:) .^2) .* therm);

A1 = 1 + 3*(1 + i) * (deltv0 ./ (2*r)) + 3*i * (deltv0 .^ 2 ./ (2*r.^2));
A1 = -i/3 * kr3 .* (rho0 - rhop) ./ (3*rho0 + 2*(rhop - rho0) ./ A1);


% if particle size distribution, sum over all radii
if radno ~= 1
        a = -3*i* sum (A0 .* frac ./ kr3);
        b = 3*i* sum(A1 .* frac ./ kr3);
else
        a = -3*i* A0 ./ kr3;
        b = 3*i * A1 ./ kr3;
end


% Lloyd & Berry (67) multiple scattering complex wavenumber

K = k0 (1,:) .* sqrt ((1 + phi * a) .* (1 - 3*phi * b) + 6*phi*phi * b .^2);

% find attenuation & dispersion from wavenumber
attn = imag (K);
phasevel =  w (1,:) ./ real (K);

alpha = attn ./ freq * c0;              % attenuation / wavelength
                                        % NB no factor of pi
beta = ((c0 ./ phasevel) .^ 2) - 1;     % dispersion
end
```

B.1.2 Acoustic impedance

From McClements & Povey [92].

```
function [Z, rho, kappa] = scatlbpz (freq, r, v, phi, param);

% syntax:  [Z, rho, kappa] = scatlbpz (freq, r, v, phi, param);
% calculates specific impedance of a suspension, using expressions for rho & kappa
% in McClements & Povey 1989
% adapted from scatlbp2

% freq is row vector of frequencies at which to evaluate alpha & beta
% r is column vector of radii,
% v is column vector of associated particle volume fraction distribution [sum(v)=1]
% param is the row vector of particle parameters

% 0-suffixed variables apply to continuous (fluid) phase
% p-suffixed variables apply to solid (particle) phase
% Simon Moss, 15-10-93
% rev. 2        25-3-94  corrected calculation for dispersion
%                        before was: beta = 1 - (phasevel / c0) .^ 2
% rev 4-8-95 from SCATLB, but passing parameter vector, using MAT_PARA
%               bug fix to handle monodispersed distn without using dummy sizes
% 15-3-95 from SCATLBP, but using corrected for the the volume fraction: do not convert
values
% from SCATLBP2, modified to calculate characteristic impedance Z, as well as
% complex density rho & compressibility kappa

rhop = param(1);        rho0 = param(2);
shcp = param(3);        shc0 = param(4);
gamma = param(5);       mu0 = param(6);
cp = param(7);                  c0 = param(8);
condp=param(9);         cond0 = param(10);
betap = param(11);

radno = length (r);
freqno = length (freq);
```

```
frac=v;                                          % NB NO CONVERSION -> volfrac

r = r(:,ones (1, freqno));                       % create matrix from r
frac = frac(:, ones (1, freqno));                % create matrix from frac

t = 293.15;                                      % temperature in K

w = 2 * pi * ones (radno,1) * freq;              % create matrix of w

therm = (1 / (t * rho0 * shc0)  -  betap / (rhop * shcp)) ^2;

deltv0 = sqrt (2 * mu0 ./ (w * rho0));                % viscous skin depth of fluid
deltt0 = sqrt (2 * cond0 ./ (w * rho0 * shc0));       % thermal skin depth of fluid
delttp = sqrt (2 * condp ./ (w * rhop * shcp));       % thermal skin depth of solid

k0 = w / c0;
kp = w / cp;

z0 = (1 + i) * r ./ deltt0;
zp = (1 + i) * r ./ delttp;
zp2 = tan (zp) ./ (tan (zp) - zp);    % doesn't seem to need Taylor approx
                                      % for small zp - but beware

h = 1 ./ (1 ./ (1 - i * z0) - (cond0 / condp * zp2));
therm =  therm * c0 * t * rho0 * cond0 * h;

kr3 = (r(:,1) * k0(1,:)) .^ 3;
A0 = i/3 * kr3 .* (rho0 * kp .^2 ./ (rhop * k0 .^2) - 1);
A0 = A0 - ((r(:,1) * k0(1,:) .^2) .* therm);

A1 = 1 + 3*(1 + i) * (deltv0 ./ (2*r)) + 3*i * (deltv0 .^ 2 ./ (2*r.^2));
A1 = -i/3 * kr3 .* (rho0 - rhop) ./ (3*rho0 + 2*(rhop - rho0) ./ A1);

% if distribution, sum over all radii
if radno ~= 1
        a =  sum (A0 .* frac ./ kr3);
        b =  sum(A1 .* frac ./ kr3);
else
        a =  A0 ./ kr3;
        b =  A1 ./ kr3;
end

kappa0 = 1 / (rho0 * c0^2);
kappa = kappa0 * real (ones(size(a)) - 3*i*phi*a);
rho = rho0 *  real (ones(size(a)) - 9*i*phi*b);
Z = (sqrt (rho ./ kappa));
```

B.1.3 Predict effects due to inhomogeneity in static rig

Vertical stratification of particle size

```
function [alpha, beta, attn, cs]=strat (f,r,v,phi,para);

% syntax:[alpha beta attn cs]=strat (f,r,v,phi,para);
% revised version of SQ_MAIN to fix the number/volume bug
% divides the column into segments according to number of radius bins
% & segregates each radius to one segment.

% S. Moss 30-10-96

1 = 1.918;
nsegs = length(r);
dl = 2*1 / nsegs;
c0 = para(8);

a = ones(1,length(f));
et = zeros(1,length(f));

for seg = 1:nsegs
        [du du atts css]= scatlbp3(f, r(seg), 1, phi*v(seg)*nsegs, para);
        a = a .* exp (-atts*dl);
        et = et + dl ./ css;
end

attn = -log(a) / (2*1);
cs = (2*1) ./ et;
alpha = attn * c0 ./f;
beta = (c0 ./ cs).^2 -1;
```

Vertical particle concentration gradient

```
function [alpha, beta, attn, cs]=ver_inh (f,r,v,phi,para,nsegs,tilt);

% syntax:[alpha beta attn cs]=strat (f,r,v,phi,para,nsegs);
% revised version of SQ_MAIN to fix the number/volume bug
% divides the column into nsegs segments
% redistributes the phi according to tilt (<1, >-1)

% S. Moss 30-10-96

l = 1.918;
dl = 2*l / nsegs;
c0 = para(8);

a = ones(1,length(f));
et = zeros(1,length(f));
weight = linspace (1-tilt,1+tilt, nsegs)';
phi_inh = phi * ones(nsegs,1) .* weight;

for seg = 1:nsegs
        [du du atts css]= scatlbp3(f, r, v, phi_inh(seg), para);
        a = a .* exp (-atts*dl);
        et = et + dl ./ css;
end

attn = -log(a) / (2*l);
cs = (2*l) ./ et;
alpha = attn * c0 ./f;
beta = (c0 ./ cs).^2 -1;
```

B.1.4 Simulate PSD measurement of Höfelmann & Beckord [17]

```
%PSD_MAIN
% Script file
% Initialise parameter row vector

param = zeros(1,7);
rho0 = 1.2; c0 = 343; gamma0 = 1.4; Pr = 0.71;
mu0 = 1.85e-5; shc0 = 1005;
rhop = 3800;  shcp = 769;
param(1) = rhop; param(2)=rho0;
param(3)=shcp/shc0; param(4) = Pr;
param(5) = gamma0-1; param(6) = mu0; param(7) = c0;
%clear rho0 rhop shc0 shcp Pr gamma0 c0 mu0

%-------------------------------------------------
% Program parameters
%-------------------------------------------------

nbins = 26;                     % number of particle & freq bins
rm = 6e-6;                      % actual mean radius
sd = 0.5;                             % actual standard deviation
phiv = 1e-4;                    % actual volume concn
phim=phiv*rhop/rho0;
fhi = 400e3;                    % upper frequency limit
flo = 4e3;                      % lower frequency limit
rep=200;                              % drawing repetition rate


f=logspace (log10(flo), log10(fhi), nbins);
w = 2*pi*f;
[ract nact]=lognorm(rm,sd,nbins);
%ract=r*.6; nact = n;  !!
N0 = sum (dis2num(phiv, nact, ract)); % total particle number

%-----------------------------------------
% Generate pseudo measured results
%-----------------------------------------

Kwr_act = kernal(w, ract, N0, param);
att_act = attn_co (nact, Kwr_act);
nois = randn(1,nbins) * 0.02; % 2% error
att_meas = att_act .* (1+nois);                 % add gaussian noise
%att_meas = att_meas * 1.02;            % add systematic 2% offset
%att_meas = att_act;                    % no error
%semilogx (f, att_act, f, att_meas)
%break

%-----------------------------------------
% Starting distribution
%-----------------------------------------

ni1 = ones (nbins,1) / nbins; ni2 = ni1;
%rp=sqrt (9*mu0./(4*pi*fliplr(f)*rhop))';    % size range of relaxation freqs
rp = ract;                      % adopt same radius bins as generated
```

```
%rp=r;
%rp=logspace(-7,-5,nbins)';   % 0.1 - 10 microns as Beckord
Kwr = kernal(w, rp, N0, param);       % kernal function constant
q=0;

% ITERATION STARTS HERE
%_____________________________________________

while q<5000
q=q+1;
atti1 = attn_co(ni1,Kwr);
atti2 = attn_co(ni2, Kwr);
corri1 = att_meas ./ atti1 -1;
corri2 = att_meas ./ atti2 -1;
if sum (abs(corri1))< sum(abs(corri2))
        ni = ni1; corri = corri1; atti=atti1;
else
        ni = ni2; corri = corri2; atti = atti2;
end

theta = max(corri(find(corri<0)));
if theta ~=[]
         theta = -1/theta;
else
        theta = 1;
end

corri1 = corri;
corri2 = corri * theta;

hi1 = sum ((1 + corri1(ones(nbins,1),:).* Kwr)')';
hi1 = hi1 ./ sum(hi1.*ni);
hi2 = sum ((1 + corri2(ones(nbins,1),:).* Kwr)')';
hi2 = hi2 ./ sum(hi2.*ni);

ni1 = ni.* hi1;
ni2 = ni.* hi2;
if q/rep == round(q/rep)
        subplot (2,2,1)
        loglog (f, atti, f, att_meas,'r'); set (gca,'XLim',[flo*.8 fhi/.8]);
        subplot (2,2,3);
        semilogx (f, corri1);set(gca,'XLim',[flo*.8 fhi/.8]);
        subplot (2,2,2)
        semilogx (rp,hi1); axis([min(rp)*.7 max(rp)/.7 .999 1.001]);grid
        subplot (2,2,4)
        semilogx(ract, cumsum(nact),'r',rp,cumsum(ni),':')%,ract,nact,'r+',rp,ni,'yo')
        set(gca,'XLim',[min(rp)*.7 max(rp)/.7]);
        text (min(rp)*.72,0.95,['iter=' int2str(q)])
        drawnow
        end
end
end


function Kwr = kernal(w,r,N,param);

% syntax: Kwr = kernal(w,r,N,param);
% solves the kernal function of Temkin & Dobbins
% w angular frequency (row vector), r particle radius bins (column)
% param, physical parameters (row vector)
%       (rhop, rho0, shcrat, Pr, gammadif, mu0, c0)
% where shcrat = shcp/shc0, gammadif = gamma0 - 1

rhop=param(1); rho0=param(2);
shcrat=param(3); Pr=param(4);
gammadif=param(5); mu0=param(6);
c0=param(7);

w2 = w.^2;
td = 2 * rhop / (9*mu0) * r.^2;
tt = td * 1.5 * shcrat * Pr;

Kwr = td*w2 ./ (1+ td.^2 * w2);
Kwr = Kwr + gammadif*shcrat* tt*w2 ./ (1 + tt.^2 * w2);
Kwr = N/2*4/3*pi*rhop/rho0/c0 * r(:,ones(1,length(w))).^3 .* Kwr;


function att = attn_co (n, Kwr);

%syntax: att = attn_co (n, Kwr);
% uses kernal function of T & D to calculate attenuation coefficient
% see kernal.m for details
% for PSD_FIT suite of programs

% S. Moss 28-7-95
```

```
[p q]=size (Kwr);

att = sum (n(:,ones(1,q)) .* Kwr);

%NB converted to amplitude attn coef
```

B.1.5 Calculate modal frequencies of a cylinder

Transverse modes of infinitely-long cylinder

```
function [Jmm, xsort]=tubemod3(maxx,show)

% syntax: [Jmm, xsort]=tubemod3(maxx,show)
% Calculate modes of infinite cylindrical waveguide
% up to maximum value of x maxx
% frequency related by f = Jmm * c /(pi * D)
% Matrix of x values returned in Jmm (m,n)
% m = Bessel order, m=0 gives axisymmetric modes
% Ordered & restricted values in xsort
% plots operation if show=1;

% Written by Simon Moss 15-9-93
% Sums by Jon Evans
% revised 14-6-94 to turn it into function from script
% revised 21-10-96 to lose fminmax function & segment function by zero crossings
% gives greater precision, adjustable by prec

nm = 30;                        % no. of m modes
nn = 10;                        % no. of n modes
prec = 150;                     % no of grid points per half cycle

if nargin < 2, show=0; end

xcoar=[0:.15:maxx];                     % coarse grid
lenxc = length(xcoar);

jmm = zeros (nm, nn);

for ord = 0:nm-1
       J = bessel (ord, xcoar);
       if show, hold off; plot (xcoar, J,'r'); hold on; end
       indlo=1;
                                        % find zero crossing points
       cross=abs(diff(sign(J)));
       cross(1)=0; cross=[0 cross];  % tidy up boundaries
       cross = find(cross>0);
                                        % repeat for each max/min
       indlo=1; n=0;
       while  n <= nn & length(cross)>0
              indhi = cross(1);
              xfin = linspace ( xcoar(indlo), xcoar(indhi), prec);
              Jfin = bessel(ord, xfin);
              [Jmax indm] = max (abs(Jfin));
              Jmm (ord+1, n+1) = xfin(indm);
              if show, plot (xfin, Jfin,'y',xfin(indm),Jfin(indm),'wo'); drawnow; end
              cross = cross(2:length(cross));              % strip off next zero crossing
point
              n=n+1;
              indlo=indhi;
       end
end

xsort = sort(Jmm(:));
xsort = xsort(find((xsort>0)& (xsort < maxx)));
```

Characteristic frequencies of finite length cylinder

```
function [fcell, densy] = modensy (fxsym, fxasym, fup, l);

%  syntax:  [fcell, densy] = modensy (fxsym, fxasym, fup, l);
% calculates the modal density of a cylinder of length l
% input the symettric (m=0) and asymettric (m>0) modal frequencies
% in fxsym & fxasym.
% returns      number of modes per 100Hz in densy;
%              centre freq of 100Hz band in fcell
% calculates up to maximum freq of fup.

% S. Moss, 9/5/94
nfcell = ceil (fup/100);
densy = zeros (nfcell,1);
flong = 335 / (l * 2)                   % fundamental longitudinal mode
```

```
for xv = 1 : length (fxsym)
        disp ('radially symmetric modes (m=0)')
%       disp (['radially sym transverse mode no. ' int2str(xv)])
        lmod = 0;                       % harmonic of long'l mode
        fmod = sqrt (fxsym(xv) ^ 2 + (flong * lmod) ^ 2);
        while (fmod < fup)
                ind = ceil (fmod / 100);        % appropriate 100Hz cell
                if ind == 0 , ind = 1; end
                template = zeros (nfcell,1);
                template (ind) = 1;
                densy = densy + template;
                lmod = lmod + 1;
                fmod = sqrt (fxsym(xv) ^ 2 + (flong * lmod) ^ 2);
        end
end
for xv = 1 : length (fxasym)
        disp ('radially asymmetric modes (m>0)')
%       disp ([' transverse mode no. ' int2str(xv)])
        lmod = 0;                       % harmonic of long'l mode
        fmod = sqrt (fxasym(xv) ^ 2 + (flong * lmod) ^ 2);
        while (fmod < fup)
                ind = ceil (fmod / 100);        % appropriate 100Hz cell
                template = zeros (nfcell,1);
                template (ind) = 2;             % doubly degenerate
                densy = densy + template;
                lmod = lmod + 1;
                fmod = sqrt (fxasym(xv) ^ 2 + (flong * lmod) ^ 2);
        end
end

fcell = [50:100:fup-50];
```

B.2 DATA PROCESSING PROGRAMS

B.2.1 Plane wave processing

```
function [f,alpha,betauc,betatc,segs,anecsp] =  plan7mc (raw, ny, order,refind,segs);

% syntax: [f,alpha,betauc,betatc,segs,anecsp] =  plan7mc (raw, ny, order,refind,segs);
% order is optional: if present, allows you to chose higher order reflection

% rev.15-4-94 can input window start & finish in segs, then not chosen manually
%             and refind (vector or scalar) is passed as argument, default=[1]
% rev. 19-4-94 calculates c0 from time of flight of pulses, instead of temp or
%             fixed value
%             and factor of 8.9 dB/m = 1 Np/m corrected to 8.69
% rev. 9-8-94 for MATLAB4.2
% rev 25-6-96 from PLAN5MUL, to include temperature compensation
% rev 27-6-96 from PLAN6MCX to include temp compensation and phase drift

%load testco                            % load filter coefs alp etc
%load planco10
%y=fildatpl (raw, alp, blp, ahp, bhp);
y=raw;
[n,m] = size (raw);

if nargin < 5
        manual=1;
        segs = zeros (1,4);
else
        manual=0;
end
if nargin < 4, refind = 1; end
if nargin < 3, order = 1; end

c0=335;                                 % approx velocity (calculated later)
fs = 2*ny;                              % sampling frequency
fmin = 200;                             % minimum displayed frequency
fmax = 2500;                            % maximum displayed frequency
l1 = 2.082;                             % distance from speaker to mike
l2 = 1.918;                             % distance from mike to reflective end

margin = l1 / 3;                        % plotting overlap margin

ordmax = floor ((c0*n/fs - l1) / (2*(l1+l2)));
disp (['maximum order <= ' int2str(ordmax)])
if order > ordmax, disp ('WARNING order probably too high'); end

% calculate actual c0 from time of flight using unfiltered data

ordc = round (ordmax / 2);              % order of reflection to use
[dum,ind0] = max(raw(:,1));             % position of direct pulse
```

```
pathl = 2 * (12 + (ordc-1) * (11 + 12));
tmin = (pathl - margin) / c0;
tmax = (pathl + margin) / c0;
indmin = ind0 + tmin*fs;
indmax = ind0 + tmax*fs;
[dum, ind1] = max(raw(indmin:indmax,1));
ind1 = ind1 - 1 + indmin;
dt = (ind1 - ind0) / fs;                    % time of flight
c0 = pathl / dt;                            % corrected c0
disp (['calculated velocity of sound = ' num2str(c0)])

if manual
%  chose anechoic & reflected pulses manually
   clf; hold off; fullfig;
   ymax = max (abs(y(:,1)));                          % find peak value of ir
   tmax1 = (3*11 + 2*12 + margin) / c0;                     % plot to end of first refl

   plot ([y zeros(n,1)])
   axis ([1 tmax1*fs -ymax/2 ymax/2]);
  if order == 1
        [axsch, txth] =textsc (0.1,0.95,'click at end of direct pulse & end of first
refl');
        [segs (3:4) du] = ginput (2);
        segs (3:4) = round (segs(3:4))
        segs(2) = segs (3);
  else
        [axsch, txth]=textsc (0.1,0.95,'click at end of direct pulse');
        [segs(2) du] = ginput (1);
        segs(2) = round (segs(2));
        tmin2 = ((2*(order-1) + 1)*11 + 2*order*12 - margin) / c0;
        tmax2 = ((2*order + 1)*11 + 2*order*12 + margin*order) / c0;
        plot ([y zeros(n,1)]);
        axis ([tmin2*fs tmax2*fs -ymax/2 ymax/2])
        set (txth,'string','click at beginning & end of reflected pulse');
        [segs(3:4) du] = ginput (2);
        segs (3:4) = round (segs(3:4));
  end

  l=segs(4)-segs(3);                              % length of blocks
  segs(1)=segs(2)-l;
else
  l=segs(4)-segs(3);
end

pad = round(2^ceil(log(l)/log(2)));          % round up size to power of 2
disp (['segment size = ' int2str(l) '  FFT size = ' int2str(pad)])

% initialize arrays

range = ceil (pad * fmax / (2*ny));          % range of frequency cells calculated
anecsp=zeros(pad,m); reflsp=anecsp;
xfer = zeros (range,m); dust=zeros(range-1,m);
alpha = dust; beta = dust;

[anecy, refly] = window (y, segs, pad);
if manual
   plot ([anecy refly])
   axis ([1 pad -ymax ymax]);
end

for j=1:m
   anecsp(:,j)=(fft(anecy(:,j)));
   reflsp(:,j)=(fft(refly(:,j)));
   xfer(:,j) = reflsp(1:range,j) ./ anecsp(1:range,j);      %eq wrt anechoic
end

f=linspace (0, ny, pad/2);
f = f (2:range);

% calculate reference spectrum: mean of several if refind is vector
if (length(refind)==1)
        refspec = xfer (:,refind);
else
        refspec = mean (xfer(:,refind)')';
end

for j=1:m
   dust(:,j) = xfer(2:range,j) ./ refspec(2:range); % equalize wrt no dust
   tempdis (:,j) = anecsp (2:range,j) ./ anecsp (2:range,refind);  % form temperature
comp'n
   phasdis (:,j) = reflsp (2:range,j) ./ reflsp (2:range,refind);  % form phase comp'n
end

% post process transfer function into alpha & beta
```

```
lamda(:) = c0 ./ f;

for j=1:m
        alpha(:,j) = -20* log10 (abs (dust (:,j))) / (8.69 * 12 * 2 * order);
        alpha(:,j) = alpha (:,j) .* lamda;
        betauc(:,j) = angle(dust(:,j)) .* lamda;
        betauc (:,j) = (( 1.0 - betauc (:,j) / (4*pi*12*order)) .^ 2 - 1.0) ;
end

% compensation
w = f * 2*pi;
Y = angle(dust);
P0 = angle (tempdis);
P1 = angle (phasdis);

for j = 1 : m

Qy (:,j) = 1 ./ (1 - c0 * (P1(:,j)-P0(:,j)) ./ (w' * 2*12));
Q0 (:,j) = 1 ./ (1 - c0 * (P1(:,j)-Y(:,j)) ./ (w'* 11));
Qy2 (:,j) = 1 ./ (1 - c0 * (Y(:,j)) ./ (w' * 2*12));
Q02 (:,j) = 1 ./ (1 - c0 * (P0(:,j)) ./ (w'* 11));
betatc (:,j) = (1 ./ (1 + Qy(:,j) - Q0(:,j))) .^ 2  - 1;

end

% plot results
clf
%subplot (2,1,1)
%plot (f,betatc)
%set (gca, 'XLim', [fmin fmax])
%subplot (2,1,2)
%plot (f,betauc)
plot (f, (Qy-Qy2)./Qy2,'o',f,(Q0-Q02)./Q02,'+')
set (gca, 'XLim', [fmin fmax])


function [anecy, refly] = window (y, segs, pad)
% truncates IR at positions in segs
% windows data segment y with leading & trailing cosine taper
% length of taper set internal to program
% pads with zeros to length in pad
% syntax:  [anecy, refly] = window (y, segs, pad);
% rev 2.  28-3-94  allows for gap between end of 1st seg & start of 2nd seg
% by having length (segs) = 4

[n,m]=size(y);
l=segs(2)-segs(1)+1;
anecy=zeros(pad,m);
refly = anecy;
nlead = 15;
ntrail = 40;

%!!!!!!!!!!!!!!!!!!!!!
nlead = round (1/100)
ntrail= round (1/2)
%!!!!!!!!!!!!!!!!!!!!!


pi2=pi/2.0;
win = ones (1,1);

w = -pi2: pi / (nlead-1) : pi2;
win (1:nlead) = (1+sin (w)) / 2;
w = -pi2: pi / (ntrail-1) : pi2;
win (1-ntrail+1 : 1) = (1-sin(w)) / 2;

anecy (1:1,:) = y(segs(1):segs(2),:);
if length (segs) == 3
        refly (1:1,:) = y(segs(2):segs(3),:);
else if length (segs) == 4
        refly (1:1,:) = y(segs(3):segs(4),:);
else error ('incorrect size of segs')
end

j=0;
for j=1:m
anecy(1:1,j) = anecy(1:1,j) .* win(:);
refly(1:1,j) = refly(1:1,j) .* win(:);
end

end
```

```
function [alp, blp, ahp, bhp] = planefil (ny, mname)

% function to design filter coefficients to equalize raw MLS signal
% convert to form suitable for plane wave calculations
% stores them in MAT file mname if specified
% syntax:  [alp, blp, ahp, bhp] = planefil (ny, mname);

wlp = 2200;
ordlp=8;
whp = 400;
ordhp=1;

% design 2.2kHz LPF
[blp,alp]=butter(ordlp, wlp/ny);
[hlp,w]=freqz(blp,alp,1024);
f=w/pi*ny;

% design 500Hz HPF to flatten spectrum, shorten IR
[bhp,ahp]=butter (ordhp, whp/ny, 'high');
[hhp, w]=freqz (bhp, ahp, 1024);

hold off
hlp=20*log10(abs(hlp));
hhp=20*log10(abs(hhp));

plot (f,hlp, f, hhp)
axis([100 5000 -60 10])

if nargin == 2
       eval (['save ' mname ' alp blp ahp bhp wlp ordlp whp ordhp'])
end

end
```

B.2.2 Reverberant decay

Curve fitting method of Xiang [163]

```
function [rate, corco] = rev_main (raw,a,b,ny,params, manual);

% syntax:   [rate, corco]= rev_main (raw,a,b,ny,params,manual);
% calculates dB/s decay rate of 1/n octave analysis of raw
% all manual picking for decay range
% raw is array of amplitude time-series: columns successive data points
%                                        rows are different data sets
% rate is array of decay rates; columns are 1/n octaves,
%                               rows are different datasets
% a,b contain filter coefficients for 1/n octave bank - see noctfil.m
% ny is Nyquist frequency,
% flight is time of flight in samples
%              - if omitted, or if negative, prompted manually
% if reverse = 1, data is reverse filtered

% Simon Moss 2-12-93
% rev. 18-1-93 account for decimation in Schroeder algorithm & change to decay rate
% rev. 1-4-94  allow iterative decay rate determination
% rev 5-4-94 to allow parameter passing of flight
% rev 5-5-94 to allow reverse filtering of data to reduce filter IR distortion
% rev 16-5-94 to return correlation coefficient for each decay curve fit
% rev 20-5-94 to use DECRATI4, hence ignore early decay - range set in earlydec
% from NOCTRAT4, but to use DECRATI5, hence also return confidence interval & not
%              reject outliers
% rev 14-6-95 from NOCTRAT6, but using manual picking of decay range, no conf lims
% rev 6-3-97   correct for decimation in Schroeder plot

tstart = clock;
[nfil,dum] = size (a);
[nsamp, nset] = size (raw);

rate = zeros (nfil, nset);
corco = rate;

if nargin < 6, manual = 0; end

% unpack parameters from params vector
flight = params(6);
reverse = params(7);
noisfrac = params(8);

hold off;clg
t = mkbase(zeros(ceil(nsamp/10),1),5/ny);    % create timebase, correct for decimation

for set = 1: nset
```

```
if (set==1 & min(flight) < 0)
     plot (raw(1:nsamp/10,1))
     flight = ginput(1);                          % input time of flight
end

for oct = 1:nfil
   if all(a==0) & all(b==0)
     rawfil=raw(:,set);
   else
     if reverse
            rawfil = filter (b(oct,:),a(oct,:),flipud(raw(:,set)));
            rawfil = flipud (rawfil);
     else
            rawfil = filter (b(oct,:),a(oct,:),raw(:,set));
     end
   end
   [d, n2] = schrofit(rawfil,flight,noisfrac);
   [rate(oct,set) corco(oct,set) dummy errmsg manual] = decrafit(d,t,n2,manual,params);
     if errmsg~=''
       disp (['set ' int2str(set) ' , filter ' int2str(oct) ' message = ' errmsg])
     end
  end
  if manual, beep(1); end
end

disp (['elapsed time ' num2str(etime(clock,tstart))])



function [Q, corco, x, errmsg, manual] = decrafit (d, t, n2, manual, params);

% syntax:  [Q, corco, x, errmsg, manual] = decrafit (d, t, n2, manual,params);
% finds coefficient x1,x2,x3 of Schroeder decay curve, according
% to N.Xiang, JASA 98(4),'95
% d is integrated and normalised decay curve, without full noise reduction
%       or logs taken.
% t is timebase for d; n2 is mean square normalised noise of IR
% optional params sets the accuracy parameters
% returns decay rate Q dB/s, and coefficient vector x
% also returns cor. coef. of portion of curve, with noise subtracted
% over range til noise=decay
% manual output allows manual input on to be cancel by right button click
% subroutine of rev_main

nd = length (d);
if (length (t)~= nd)
       error ('DECRAFIT: d & t vectors are not same size')
end
if nargin < 4, manual = 0; end

% Initialise variables

L = t(nd);                % time length of dataset
A = zeros (3,3);
b = zeros (3,1); x = b;
itn = 1;
errmsg='';                % error message and flag
errx = [NaN;NaN;NaN];  % value of x in case of error
dx = [9; 9; 9];                  % dummy starting values to force first itn.
sch = 10*log10(d);     % log decay curve

if manual
       clg
       plot (t,sch)
end

% Initialise parameters
if nargin<5
       hival = -6;             % higher value """, and initial t point
       loval = -12;            % lower value over which to estimate x2
       tol = 0.002;            % proportional total change in x vector for finish
       maxitn = 20;            % bailout value
       xovermin = 4;           % min. length of decay over which to fit
else
       hival = params(1); loval = params(2);
       tol = params(3); maxitn = params(4);
       xovermin= params(5);
end

% Estimate initial parameters

x(3) = n2;                % noise estimate
indhi = firstval (sch,hival);
indlo = firstval (sch, loval);
if indlo==NaN
       errmsg = ['less than ' int2str(loval) 'dB of decay'];
```

```
        x=errx; coco = NaN; Q=NaN;
        return;
end

T60 = (t(indlo) - t(indhi))*60/(hival-loval);
x(2) = 13.8 / T60;
x(1) = d(1) - x(3) * nd;
dFdx3 = ones(nd,1)*L - t;
k=[indhi:nd];          % index range, starting from initial -hival dB point

% START ITERATION

while (sum((dx./x).^2) > tol)

% select summation length m
        m=nd;
        tk = t(k)-t(k(1));     % offset time base
        dFdx1 = exp (-x(2) * tk);
        dFdx2 = -x(1) * tk .* dFdx1;

% Assemble A matrix
        A(1,1) = sum (dFdx1 .^ 2);
        A(1,2) = sum (dFdx1 .* dFdx2);
        A(1,3) = sum (dFdx1 .* dFdx3(k));
        A(2,1) = A(1,2);
        A(2,2) = sum (dFdx2 .^2);
        A(2,3) = sum (dFdx2 .* dFdx3(k));
        A(3,1) = A(1,3);
        A(3,2) = A(2,3);
        A(3,3) = sum (dFdx3 .^ 2);

% Calculate model curve & error
        dec = x(1) * dFdx1;
        noise = x(3) * dFdx3(k);
        F =  dec + noise;
        E = d(k) - F;

% Assemble b vector
        b(1) = sum (E .* dFdx1);
        b(2) = sum (E .* dFdx2);
        b(3) = sum (E .* dFdx3(k));

% Solve for dx + update x
        dx = A\b;
        x = x + dx;
%       if x(3)<=0, x(3) = 1e-15; end                  % no negative noise

% Too many iterations?
        itn = itn + 1;
        if itn > maxitn
                errmsg=[errmsg 'Too many iterations in DECRAFIT:bailed out'];
                break
        end
end

if manual
        plot (t,sch,t(k),db(noise+1e-10)/2,'r:',t(k), db(dec+1e-10)/2,'r:')
end

% Find crossover point of decay & noise
xover = firstval(dec-noise,0);

if isnan(xover) & all(noise>dec)
        errmsg = [errmsg 'No crossover of noise & decay'];
elseif all(dec > noise)
        xover = (nd-indhi)*.8;          % catch case of negligible noise
elseif (xover < xovermin)
        errmsg = [errmsg 'Insufficient no. of points for decay portion'];
end

if finite (xover)
        dxnoise = d(k) - noise;

        % set min value so can log
        neg=find(dxnoise<=0); lneg=length(neg);
        if lneg ~= 0, dxnoise(neg) = 1e-8 * ones(lneg,1); end

% find corr. coef over usable portion
        schxnoise = db(dxnoise)/2;
        fit = corrcoef(tk(1:xover),schxnoise(1:xover));
        if all(isnan(fit)), x=errx; Q=NaN; corco=NaN; errmsg=[errmsg 'Biggy'];return;end
        corco = fit (1,2);

% find decay rate (my JASA paper, eqn5, factor of 10 since measured from
% energy decay rather than pressure
```

```
        Q = 10*log10(exp(1))*x(2);
end


if manual

        hold on; plot (t(k),db(F)/2,'c')
        plot (t(k),db(noise)/2,'r:',t(k), db(dec)/2,'r:')
        axis ([0 L -40 0]);
        if errmsg==''
                plot (tk+t(k(1)), schxnoise,'g')
                text (L*.7,-10,['rate = ' num2str(Q) ' dB/s']);
                text (L*.7,-8,['cor.co. = ' num2str(corco)]);
                text (-L*.1,-45,'click here to wipe');
        else
                text (0,-35,errmsg)
        end
        text (L*.7,-6,['fitted points = ' int2str(xover)])
        [dux,duy,button] = ginput(1);
        if (dux<0.1 & duy<-40), errmsg = [errmsg 'manually wiped']; end
        if button > 1,  manual = 0; end
        hold off
end

if errmsg~=''
        x=errx; Q=NaN; corco=NaN;
        if manual~=1, disp (errmsg); end
end

function [y, n2] = schrofit(x,flight, noisfrac)

% syntax: [d, n2] = schrofit(x,flight,noisfrac)
% only good for x as column vector

% makes Schroeder curve of array in x, without noise subtraction
% returns log & normalised curves, & mean noise level in t.o.f
% decimates number of samples.
% noisfrac subtracts portion of noise, to increase decay range without inducing -ve terms
% reverse integrates square of the elements

% Simon Moss   9-9-93
% as SCHROED4.M, but cuts off noise data at end of dataset, (also eliminate reverse)
%15-6-94 from SCHROED5, but for manual range picking with NOCTRATM
% 16-6-95 to allow range of time-of-flight indices
% 7-12-95 from SCHROEDM, remove noise sub, & output noise & un-logged

n = length (x);
if nargin < 3, noisfrac=0; end

x = x .* x;                     % square all data values

% calculate mean square noise level in flight time
if flight == 0
   noise = 0;
   flight = 1;
elseif length(flight)==1
   noise = mean (x(1:flight));
   noise2=mean(x((n*.9):n));
   noise = min([noise noise2]);        % find minimum noise from beg or end

else
   noise = mean (x(flight(1):flight(2)));
end

x = x - noise*noisfrac;                 % subtract proportion of noise only

x2 = flipud (x);
y = cumsum (x2);                % reverse integration
y = flipud (y(1:10:n));                 % decimate
n2 = length (y);
ref = y(1);
y = y / ref;                    % normalize to total
n2 = noise / ref;               % noise value for SCHROFIT

function params = rev_para(params)

varnam=['hival    ';...
        'loval    ';...
        'tol      ';...
        'maxitn   ';...
        'xovermin ';...
        'flight   ';...
        'reverse  ';...
        'noisfrac '];
nvar=8;
```

```
if nargin < 1
        hival = -6;             % higher value """, and initial t point
        loval = -12;            % lower value over which to estimate x2
        tol = 0.002;            % proportional total change in x vector for finish
        maxitn = 20;            % bailout value
        xovermin = 4;           % min. length of decay over which to fit
        flight = 2000;          % flight & pre-trigger in samples
        reverse = 0;            % set to 1 for reverse filtering
        noisfrac = 0.4;                 % proportion of noise to subtract pre-integration

        params(1) = hival; params(2) = loval;
        params(3) = tol; params(4) = maxitn;
        params(5) = xovermin; params(6) = flight;
        params(7) = reverse; params(8) = noisfrac;

elseif length(params)==nvar
        for varno=1:nvar
                disp([varnam(varno,:) ' = ' num2str(params(varno))])
        end

else error('params is wrong size')
end
```

Iterative straight line fitting

```
function [rate, conlim,corco] = decrati7 (x, manual,range,rangehi)

% function to calculate decay rate from Schroeder decay arrays
% syntax:  [rate conlim corco] = decrati7 (x, manual, range,rangehi);

% input array of spectra, x(freq, seg)
% output vector of decay times  rate (m), x axis in segment no.
% fitted for linear decay (of log curve) over dynamic range
% determined from first & last bracket samples
% iterates until gradient changes converges to <tol
% for manual operation, manual = 1, default auto = 0
% for Schroeder plots, include decay range (+ve, in dB)
% also returns confidence interval the fit

% S. Moss 18-3-94
% rev. 1-4-94 to accomodate manual input of decay range (from SCHROED4.M)
% 16-5 94 as DECRATI2, but returns correlation coefficient of fit
% 17-5-94 as DECRATI3, but can specify starting point rangehi, for removal
%                      of nonlinear "early decay" for Schroeder plots
% 27-5-94 from DECRATI4, but returns confidence interval as well as corr. coef
%                      and doesn't reject outliers - mainly for Schroeder
% 16-8-94 from DECRATI6, for MATLAB4.2; uses SCHROED5

[n m] = size (x);
rate = zeros (1, m);
conlim = zeros (1,m);
corco = conlim;

tol = .01;                      % fractional tolerance for change in grad
lolevmin = -10;                         % signal level difference to bailout at
bracket = round (n / 15);       % number of lines to compare at beginnning & end
itmax = 20;                     % max number of iterations
margin = 5;                     % dB increment to lolev to speed convergence
tval = 1;                       % from t-tables, depending on confidence limit
                                % if unity its unscaled
                                % tval = 1.645 for 90% limits
                                %      = 1.96 for 95% limits
if nargin == 1, manual = 0; end
if nargin < 3
        ref = mean (x(1:bracket,:));
        x = x - ones(n,1)*ref;
        lolev =  mean (x(n-bracket:n,:));
else
        % assume Schroeder plot so initial value = 0dB
        lolev = 5 - range;      % deduct 5db to speed up convergence
end
if nargin < 4, rangehi = 0; end

lolev = lolev + margin;

for q = 1:m;

% reject lines with minimal decay (ie. insufficient signal)

        if lolev(q) > lolevmin
                rate (q) = 0;
        else
                if manual
                        clf;fullfig;hold off
```

```
        plot ([1:n], ones(n,1)*lolev(q))
        hold on;plot (x(:,q))
        axis ([1 n -60 5])
end
invalid = 0;
it = 1;
indmax = n;
indlo = firstval (x(:,q), rangehi);
graddif = 1; gradnew = 100;   % force first iteration
while (abs (graddif) > tol & it < itmax & ~ invalid)
        ind = [indlo:indmax]';
        if length (ind) < n/100
           invalid = 1;
        else
           x2 = x (ind,q);
           p = polyfit(ind, x2, 1);
           gradold = gradnew;
           gradnew = p(1);
           graddif = (gradnew - gradold) / gradold;
           if manual plot (ind,polyval(p, ind),'g'); end
           indmax = round ((lolev(q) - p(2)) / gradnew);
           if indmax > n indmax = n; end
           if indmax < indlo indmax = indlo; end
           it = it + 1;
        end
    end
    if invalid
        rate(q) = 0;
    else
        xfit = polyval(p,ind);
        if manual plot (ind,xfit); end
        rate (q) = p(1);
        fit = corrcoef (ind, x2);
        corco (q) = fit (1,2);

% calculate error margins
        ssr = sum ((x2 -xfit).^2);
        indmn = mean (ind);
        cind = sum ((ind - indmn).^2);
        conlim (q) = sqrt(ssr/(cind*(length(ind)-2)));
        if manual
            txh=textsc (.6,.8,['no. of iterations = ' int2str(it)]);
            textsc (.6,.75,['rate = ' num2str(rate(q)) ' +- '
num2str(conlim(q))],txh);
            textsc (.6,.7,['index = ' int2str(q)],txh);
            textsc (.6,.65,['r = ' num2str(corco(q))],txh);
            textsc (.6,.6,'click right button for auto',txh);
            textsc (0,0.02,'click here to wipe',txh);
            [dux,duy,button] = ginput(1);
            if (dux<0.1 & duy<.1), rate(q) = 0; end
            if button > 1,  manual = 0; end
        end
    end
  end
end

conlim = conlim * tval;
hold off;

function [sch, range] = schroed6(x,flight)

% syntax:  [sch, range] = schroed6 (x, flight);
% makes Schroeder curve of array in x
% flight is length (in samples) of flight time (=0 default for noise noise sub)
% decimates number of samples.

% reverse integrates square of the elements
% returns answer in dB format, normalized to total square of values
% compensates for noise by subtracting mean square noise level from
% each individual sample (squared).
% as SCHROED3.M, but also outputs approx. range of decay in dB

% Simon Moss   9-8-93
% as SCHROED4.M, but cuts off noise data at end of dataset, (also eliminate reverse)
% as SCHROED5.M but uses mean square raw values for range, not integrated
% rev 12-10-94 to correct error condition for flight = 0;

[n,m]= size(x);

if nargin < 2, flight = 0; end

bracket = round(n/30);          % no. of points at beg & end to calculate range

x = x .* x;                     % square all data values

% calculate mean square noise level in flight time
```

```
if flight == 0
   noise = zeros (1,m);
   flight = 1;
else
   noise = mean (x(1:flight,:));
end

% subtract mean square noise from each individual sample
for j=1:m
   x(:,j) = x(:,j) - noise(j);
end

% find negative values (due to noise sub) and set them to 0
minus = find (x < 0);
under = length (minus);
if under > 0
   x(minus) = zeros (under,1);
end
bracket;
% calculate decay range
hilev = mean (x((flight:flight+bracket),:));
lolev = mean (x((n-bracket:n),:));
range = lolev ./ hilev

x2 = flipud (x);
y = cumsum (x2);                    % reverse integration
y = flipud (y(1:10:n,:));           % decimate
n2 = length (y);
ref = ones (n2,1) * y(1,:);
y = y ./ ref;                       % normalize to total

minus = find (y <= 0);              % offset any zero points
under = length (minus);                     % to allow logs
if under > 0
   y(minus) = ones (under,1) * 1e-6;
end


% repeat, but with zero padding to reject noisey tails
ind =firstval(y,range);
if  any(ind < 0.9 * n2);
  disp ('RECALC')
  for set = 1:m
       if ind(set)~=NaN
            lpad = n - ind(set)*10;
            x2 (1:lpad,set) = zeros(lpad,1);
       end
  end
  y = cumsum (x2);                  % reverse integration
  y = flipud (y(1:10:n,:));         % decimate
  ref = ones (n2,1) * y(1,:);
  y = y ./ ref;                                 % renormalize to total

  for j=1:m;
       y(:,j) = y(:,j) / y(1,j);    % normalize to total
  end

  minus = find (y <= 0);            % offset any zero points
  under = length (minus);           % to allow logs
  if under > 0
       y(minus) = ones (under,1) * 1e-6;
  end
end
range = -10 * log10 (range)
sch = 10 * log10(y);
```

B.2.3 1/n octave analysis

Design of digital filter defined by coefficients a & b, that complies with IEC 225 [65].

```
function [a,b, enbw, fc] = noctfil (nyqf,n,flo,fcup,noplot);

% syntax:   [a,b, enbw, fc] = noctfil (nyqf,n,flo,fcup,noplot);
%
% function to produce filter coefficients for 1/n octave analyser
% use with noctany.m
% pass nyquist freq of data, 1/n fraction, lowest frequency & highest freq
% if noplot=1 then the resulting curves are not plotted
% outputs filter coefficients in a & b
%         equivalent noise bandwidth of each filter in enbw
%         centre frequency of each filter in fc

% S.Moss
%  10-3-95 from noctfil, adapted so all parameters are passed
% 8-1-97 from noctfil, adapted to comply with IEC 225

fc(1) = flo;

%  Centre frequencies
ind = 1;
while fc(ind) < fcup
        ind=ind + 1;
        fc(ind) = fc(1) * exp ((ind-1) / n * log(2));
end


% Break frequencies
ind2 = 2;
while ind2 <= ind
        fb (ind2) = sqrt (fc(ind2) * fc(ind2 - 1));
        ind2 = ind2 + 1;
end

filtno = ind-1;                                 % number of parallel filters
fb(1) = fc(1)*fc(1)/fb(2);                % break freq of lowest filter
fc = fc(1:filtno);
enbw = zeros (filtno,1);

% Design filters

nlines=4096;
a=zeros (filtno, 21); b=a;                % pad out coefficient matrix to n=10
h= zeros (nlines,filtno);
maxord=1;

stopmul = 2^(1/n);

for fil = 1:filtno

        pass = [fb(fil) fb(fil+1)];
        stop = [fb(fil)/stopmul fb(fil+1)*stopmul];
        stop = stop / nyqf;
        pass = pass / nyqf;
        [n, wn]=buttord (pass, stop, 5, 35);
        [btemp, atemp] = butter (n,pass);
        ord = length (atemp);
        if ord > maxord
                maxord = ord; end
        b(fil, 1:ord) = btemp;
        a(fil, 1:ord) = atemp;
        [h(:,fil), w] = freqz(btemp, atemp, nlines);

end

f = w / pi * nyqf ;
hdb=db(h);

% Check out worst case values:

        % set starting points
ibtolworst=0; corntolworst = 0; stoptolworst = -999; fartolworst = -999;

ibmul = 2^(1/(n*4));            % in-band multiplier

for fil = 1:filtno
        indup = findval(fc(fil) * ibmul,f); indlo = findval(fc(fil) / ibmul,f);
        ibtol = min([hdb(indup,fil) hdb(indlo,fil)]);
        if ibtol < ibtolworst, ibtolworst = ibtol; end
```

```
        indup = findval(fb(fil),f); indlo = findval(fb(fil+1),f);
        corntol = min([hdb(indup,fil) hdb(indlo,fil)]);
        if corntol < corntolworst, corntolworst = corntol; end

        indup = findval(fc(fil)*stopmul,f); indlo = findval(fc(fil)/stopmul,f);
        stoptol = min([hdb(indup,fil) hdb(indlo,fil)]);
        if stoptol > stoptolworst, stoptolworst = stoptol; end

        if fc(filtno)*4 > nyqf
                fartolworst=0;                  % insufficiently high freq range
        else
                indup = findval(fc(fil)*4,f); indlo = findval(fc(fil)/4,f);
                fartol = min([hdb(indup,fil) hdb(indlo,fil)]);
                if fartol > fartolworst, fartolworst = fartol; end
        end
end

if n<1.5
        skirttolallow = -18; stoptolallow = -40;
elseif n<2.5
        skirttolallow = -18; stoptolallow = -50;
else
        skirttolallow = -13; stoptolallow = -50;
end
skirttolallow=num2str(skirttolallow); stoptolallow=num2str(stoptolallow);
disp(['in band  (min allowable = -1 dB):              ' num2str(ibtolworst)])
disp(['corner   (min allowable = -6 dB):              ' num2str(corntolworst)])
disp(['skirts   (max allowable = ' skirttolallow 'db):                '
num2str(stoptolworst)])
disp(['stopband (max allowable = ' stoptolallow 'db);                 '
num2str(fartolworst)])


%       Calculate Equivalent Noise Bandwidth ENBW by integrating |H(f)|^2
        enbw  = sum (abs(h) .^2) * (f(2) - f(1));

a = a(:, 1:maxord);             % shave off excess zeros
b = b(:, 1:maxord);

if nargin>=5
  if noplot ==1, return
  end
end
h= abs(h(2:nlines,:)); f=f(2:nlines);
htot = 20 * log10(sum (h'));

semilogx (f,db(h), f, htot)
axis ([fc(1)/2 fcup*2 -40 10])
```

B.2.4 Settled mass device

```
function [dm, r2] = weigh (x,x0, Q, m0);

% syntax: dm = weigh (x,x0, Q, m0);
% analyses data from settled mass detector; x is time domain trace of resonant response
% x0 is original response (dm=0), Q is Q factor of system
% infers the additional mass dm above m0

% S. Moss 22-4-96

b2 = 1/Q^2;                             % normalised half power bandwidth squared
xrat = ((ones(size(x)) * x0) ./ x) .^2;

dum = (b2 - 2)^2 - 4*(1 - b2 * xrat);
r2 = ( (2 - b2) + sqrt(dum) ) /2;

dm = m0 * r2 - m0;


function x = weighresp(f,fn,Q);
% subroutine of weigh.m

b=1/Q;
r2 = (f/fn).^2;

dum = (1 - r2).^2 + b^2*r2;
x = 1./sqrt(dum);
```

B.2.5 Wide angle scanning photosedimentometer (WASP) processing algorithms

```
function [r,n,ncum,tscan,Vdcal,tstart,h0,param]=wasp(t,Vd,tscan,Vdcal,tstart,h0,param);
%syntax: [r,n,ncum,tscan,Vdcal,tstart,h0,param]=wasp(t,Vd,tscan,Vdcal,tstart,h0,param);
%
%runs the function wasp_ana when scanning is used
% input time t and voltage Vd vectors only => prompts for calibration data, working
section,
% descending portion, & uses default parameters; outputs all chosen values
%
% or input Vdcal[zero inf], tstart, & h0 (param still optional) & algorithm works on
entire
% dataset, so truncate if necessary before passing.

argno = 7;
if nargin < argno, param=[3800 1000 1e-3];   end                    % parameters for
alumina in water
if nargin < argno-1, h0=[]; end
if nargin < argno-2, tstart = []; end
if nargin < argno-3, Vdcal = []; end
if nargin < argno-4, tscan = []; end
if nargin < argno-5, error ('insufficent input arguments'); end


clf;
slim=0;
scanrate = 0.01 / 60;                    % scanning rate in m/s

if tscan == []
        tscan = input ('enter time (s) after which scanning started ');
end

if h0 == [];
        plot (Vd)
        title ('select scan end point')
        [indtop du]=ginput(1);
        slim = 1;
end

if Vdcal ==[];
        plot (Vd)
        title ('select infinity & zero portion')
        [indcal du]=ginput(2);
        Vdcal= smothval([1:length(Vd)]',Vd, indcal, 3,3);
        slim = 1;
        hold on; plot (indcal, Vdcal, 'r*'); hold off; pause(2)
end

if slim ==1
        plot (Vd)
        title ('select working portion')
        [indwk du]=ginput(2);
        t2=t(indwk(1):indwk(2))-t(indwk(1));
        Vd2=Vd(indwk(1):indwk(2));
else
        Vd2 = Vd;
        t2=t;
end

if tstart == [];
        plot (t2, Vd2)
        title ('select start of descending portion')
        [tstart du] = ginput (1);
end

if h0 ==[]
        indtop2 = indtop-indwk(1)+1;
        if indtop2 > length(t2), indtop2 = length(t2); end
        scandur = t2 (indtop2) - tscan;
        h0 = scandur * scanrate
end

D = v2dconv (Vd2, Vdcal(2), Vdcal(1));

nr=20;

[r,n,ncum]=wasp_ana(t2,D,h0,param,nr,tscan,tstart);


function [r,n,ncum, Vdcal, tstart, h0,param ]=wap(t,Vd, Vdcal, tstart, h0,param);
%syntax: [r,n,ncum, Vdcal, tstart, h0,param ]=wap(t,Vd, Vdcal, tstart, h0,param);
%
%runs the function wasp_ana for no scanning
```

```
% input time t and voltage Vd vectors only => prompts for calibration data, working
section,
% descending portion, & uses default parameters; outputs all chosen values
%
% or input Vdcal[zero inf], tstart, & h0 (param still optional) & algorithm works on
entire
% dataset, so truncate if necessary before passing.

if nargin < 6
        htot = input ('enter total height of water column (mm) ');
        h0 = (htot - 34)/1000;                                          % convert to m

        clf;plot (Vd)
        title ('select infinity & zero portion')
        [indcal du]=ginput(2);
        beep(1); title ('select working portion')
        [indwk du]=ginput(2);
        t2=t(indwk(1):indwk(2))-t(indwk(1));
        Vd2=Vd(indwk(1):indwk(2));
        plot (t2, Vd2)
        title ('select start of descending portion')
        [tstart du] = ginput (1);
        Vdcal= smothval([1:length(Vd)]',Vd, indcal, 2,10);
else
        Vd2 = Vd;
        t2=t;
end


D = v2dconv (Vd2, Vdcal(2), Vdcal(1));

if nargin <7, param=[3800 1000 1e-3]; end           % parameters for alumina in water
nr=20;
tscan=-1;

[r,n,ncum]=wasp_ana(t2,D,h0,param,nr,tscan,tstart);



function [r,n,ncum]=wasp_ana(t,D,h0,param,nr,tscan,tstart);

%syntax:  [r,n,ncum]=wasp_ana(t,D,h0,param,nr,tscan,tstart);
%Converts data gathered in Wide Angle Photosedimentometer into particle size distribution
%t is time vector in secs, not necessarily equispaced
%D is optical density read from WASP
%h0 is height of fall at start of experiment
%param is vector containing: density of material, density of liquid, viscosity of liquid
%nr is number of radius bins (def. 15)
%tscan is time (s) at which scan starts (def. no scan, or tscan=-1)
%tstart is time at which trace starts descending (def. manually chosen, or tstart=-1)

% Simon Moss 27-2-96


% INITIALISE
%_____________________________________________________

% set defaults
if nargin < 7, tstart = -1; end
if nargin < 6, tscan = -1; end
if nargin < 5, nr = 15; end
scanvel = 1.67e-4;                          % scanning velocity in m/s
trat = 1.15;                                % ratio for first time point after start

% manually pick start of descending slope
if tstart < 0
        clg; plot (t, D)
        set(gca,'YLim',[max(D)*.9 max(D)*1.05])
        title ('select start of descending portion')
        [tstart du]=ginput(1);
end

% ensure column vectors
t = t(:);
D = D(:);
smoothno = 20;                                  % no of samples over which to interpolate

% SAMPLE THE TIME AXIS
%_____________________________________________________

% generate time axis for evaluation
if tscan < 0            % log axis
        tn = logspace (log10(trat*tstart), log10(max(t)), nr);
else
        tn = linspace (trat*tstart, max(t), nr+1)';
        tn = tn (1:nr);                                 % throw away h=0 point
```

```
end

% find mean values of D at these times
Dn = smothval (t, D, tn, 2, smoothno);

% find the h at these times for scanning operation
hn = ones(size(tn)) * h0;
if tscan >0
        ind = find (tn > tscan);
        if length (ind) > 0
                hn(ind) = hn(ind) - (tn(ind)-tscan)*scanvel;
        end
end

% find Stokes diameters corresponding to these times
dstoke = t2dstoke (tn, hn, param);

%_____________________________________________________

% SORT OUT END VALUES
%_____________________________________________________


% find Dmax, at start of descending trace, & add to Dn
Dnmax = smothval(t,D,tstart, 2,smoothno);
Dn = [Dnmax;Dn;0];

% find upper size limit from start of descending trace
dstokemax = t2dstoke (tstart, h0, param)
dstoke = [dstokemax; dstoke];

%_____________________________________________________

% CALCULATE DIFFERENCES
%_____________________________________________________

Ddif = -diff(Dn);

% find arithmetic mean size between bins
dmean = filter ([1 1],2,flipud(dstoke));
Ddif = flipud(Ddif);

Ddifdmean = Ddif .* dmean;

Ddifdmeancum = cumsum (Ddifdmean);
ncum = flipud(Ddifdmeancum / Ddifdmeancum(length(Ddifdmeancum)) * 100);
r = flipud(dmean / 2);
n=-[diff(ncum);0];


function dstoke = t2dstoke (t, h, param);

%syntax: dstoke = t2dstoke (t, h, param);
% converts the time taken to fall a given distance into Stoke's diameter of sphere
%param: rhop, rhof, visc

% S. Moss 25-4-97 from t2dstoke, with correction factor for small particles

rhop = param(1);
rhof = param(2);
visc = param(3);
K = (0.83e-7)*2;                        % correction factor for small particles

inter = 18/9.81 * visc * h ./ ((rhop - rhof)* t);

dstoke = sqrt(inter)

small = find (dstoke < 2e-6)  % correct for small particles with Cunninghams factor
if length(small)>0
        dstoke(small) = (sqrt(K^2 + 4*inter(small)) - K)/2;
end
```

APPENDIX

C

DYNAMIC DUST WEIGHING DEVICE

The volume concentration of dust in the static rig is measured by weighing the settled-out dust at the end of the experiment. For this to give a true representation of the actual volume fraction during the acoustic measurement, we need to be sure that the quantity of dust that settles before or during the acoustic measurement is negligible; any such premature settlement would tend to lead to an overestimation of the volume fraction.

Hence it was necessary to measure the weight of dust as it settled in real time, with a time resolution of < 1 second. This had to be accomplished with as little modification to filling airflow as possible.

C.1 TECHNIQUE

A device was designed which would dynamically measure the mass of dust as it settled onto the lower end-cap.

The physical principle used was to measure the resonant response of a lightly damped mass-spring system, in which the resonant frequency is dependent on the value of the mass.

A special lower end-cap was devised, with a thin brass shim suspended above the surface of the cap. The shim was excited to vibrate at resonance by insonifying it from below, via a hole in the end cap which was coupled through a plastic tube to a low frequency compression driver.

The displacement of the shim was measured by treating it as the diaphragm of an electrostatic microphone; insulating posts maintained an airgap between the shim and metal end cap, and hence oscillations of the shim resulted in a change of capacitance of the shim/cap system. This system was wired to a microphone preamplifier and measuring amplifier in the usual way, so that the shim was maintained with a polarisation voltage of 200V.

The shim has a complex set of resonances, some of which are extremely lightly damped ($Q > 100$). By exciting the shim to a low-order, lightly-damped resonance, and measuring its vibration amplitude as a function of time, very small quantities of dust settling on the shim may be detected. This is because the dust affects the resonant system in two ways:

- The resonant freqeuncy is lowered, because the mass of the system is increased.
- The Q of the resonance is reduced.

These mechanisms both lead to a reduction in vibration amplitude, provided the same excitation frequency is maintained. The higher the Q, the more sensitive is the system to added weight.

C.2 THEORY

Let us assume that, in the vicinity of a resonance, the shim acts as a second-order linear mass-spring system, in which the mass and stiffness are distributed over the area of the shim.

The amplitude response of such a system is:

$$x = \frac{F}{k} \frac{1}{\sqrt{\left[\left(1-\left(\frac{\omega}{\omega_n}\right)^2\right)^2 + b^2\left(\frac{\omega}{\omega_n}\right)^2\right]}} \qquad \text{(C.1)}$$

where F is the amplitude of the exciting force, k is the spring constant, $b = 1/Q$, and $Q = \frac{\omega_n}{\Delta\omega_3}$,

$\Delta\omega_3$ being the width of the resonance between -3dB points.

ω_n is the natural resonant frequency (in the absence of damping), which is given by

$$\omega_n = \sqrt{\frac{k}{m}}, \qquad \text{(C.2)}$$

where m is the mass.

Suppose we have one measurement of x at the resonance, so that $\frac{\omega}{\omega_n} = 1$, and another measurement, x', at the same frequency, but with the resonant frequency reduced to ω_n' due to an increase in mass Δm. Assume that the Q factor of the system remains constant and high, so that the (lightly) damped resonant frequency may be approximated by ω_n.

For clarity, define $r = \frac{\omega}{\omega_n}$. (C.3)

Hence:

$$\left(\frac{x}{x'}\right) = \frac{\left(1-r^2\right)^2 + b^2 r^2}{b^2} \qquad \text{(C.4)}$$

$$r^4 + \left(b^2 - 2\right)r^2 + \left[1 - b^2\left(\frac{x}{x'}\right)^2\right] = 0 \qquad \text{(C.5)}$$

Solving for r^2 gives:

$$r^2 = \frac{1}{2}\left[\left(2-b^2\right) + \sqrt{\left(b^2-2\right)^2 - 4\left(1-b^2\left(\frac{x}{x'}\right)^2\right)}\right] \qquad \text{(C.6)}$$

And, since we maintain the frequency constant at $\omega = \omega_n$, we can say that

$$r^2 = \left(\frac{\omega}{\omega_n'}\right)^2 = \left(\frac{\omega_n}{\omega_n'}\right)^2 \tag{C.7}$$

And, from equation (C.2):

$$\left(\frac{\omega_n}{\omega_n'}\right)^2 = \frac{m + \Delta m}{m} \tag{C.8}$$

So, for a time series of values of x', we can calculate r^2, and hence the added mass thus:

$$\Delta m = mr^2 - m \tag{C.9}$$

To demonstate the principle, Figure C-1 shows the 30% change in amplitude which results from a 1% change in mass.

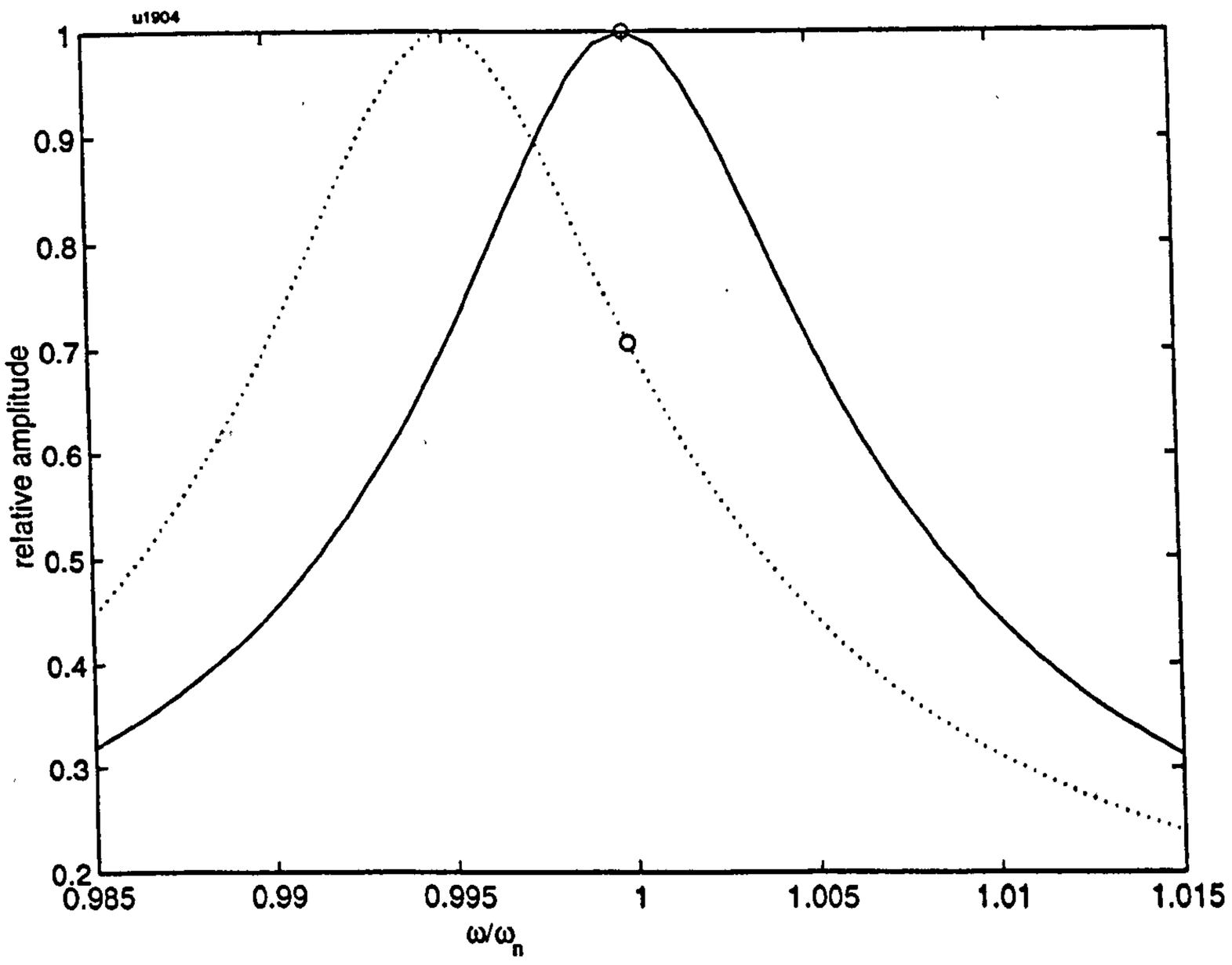

Figure C-1 *Response curves before (solid line) and after 1% increase in mass (dotted line) predicted for 2nd order mass-spring system with* Q=100. *Circles show the resulting amplitudes when excited at the original resonant frequency.*

C.3 VALIDATION OF DEVICE

The system was assembled as shown in Figure C-2. A resonance peak at approximately 250 Hz was chosen because of its very high Q (between 50 and 250, depending on the mounting of the shim), and because it was a low order mode; ideally one would chose the lowest mode, so that the only nodal points would be at the mounting points, hence minimising the area of shim which is insensitive to added dust.

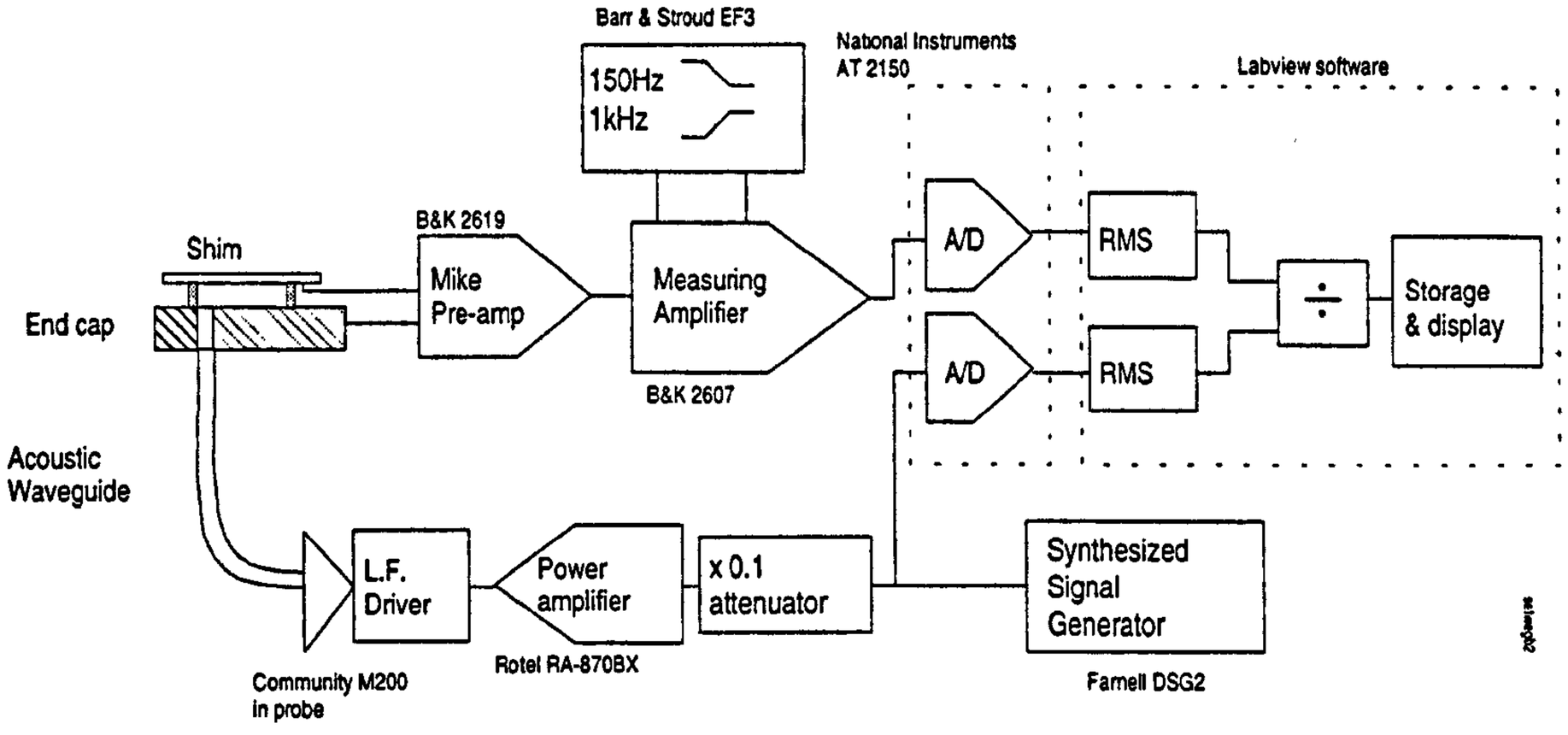

Figure C-2 *Block diagram of dynamic weighing device*

In order to check the hypothesis that the resonant response can be approximated by a 2nd order system, an actual frequency response was measured and compared to the prediction of equation (C.1); the results are plotted in Figure C-3.

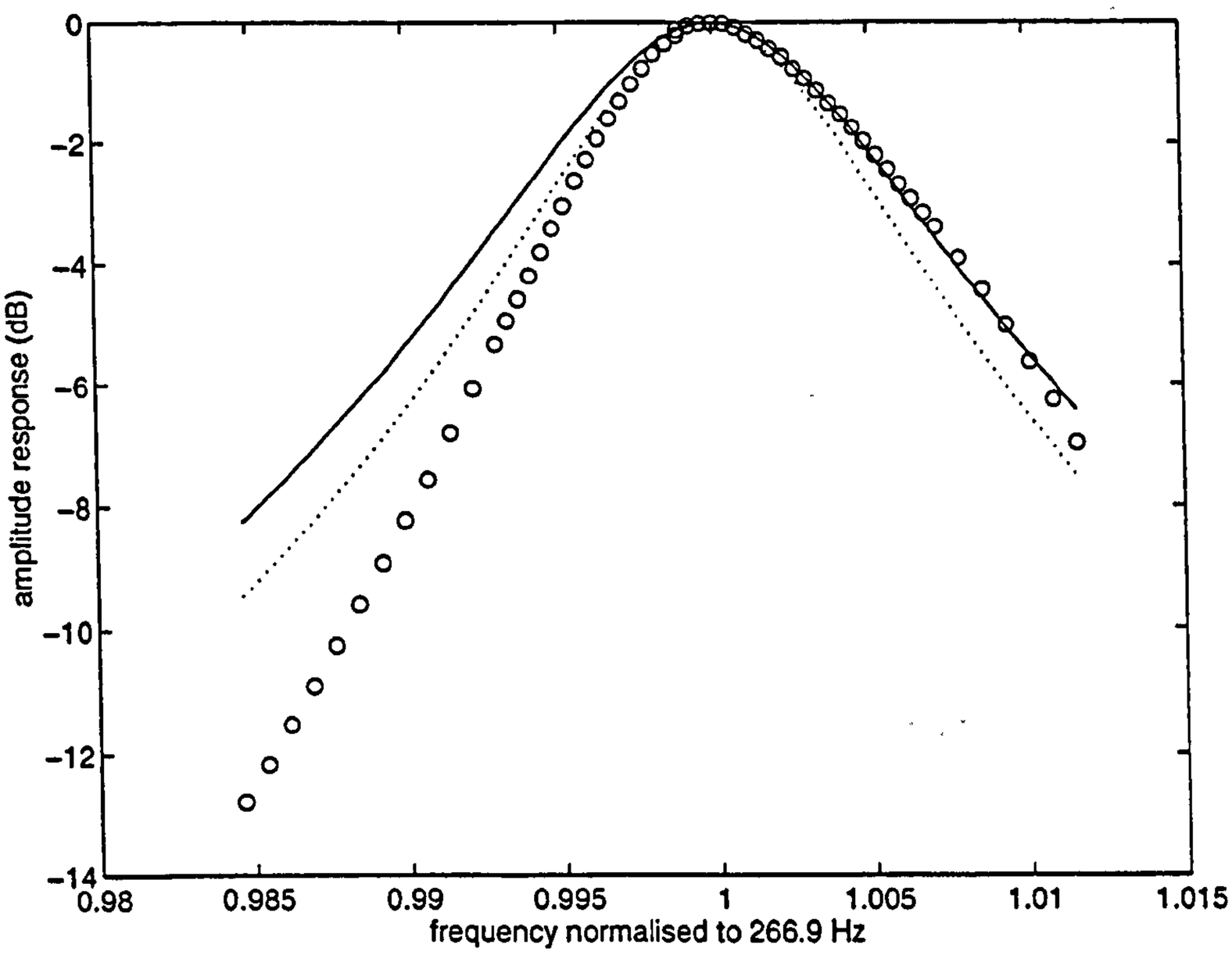

Figure C-3 Measured frequency response of a resonance at 266.9 Hz (circles), and predicted response; Q = 92 measured from -3dB bandwidth (dotted line), and Q=78 from upper -3dB point only (solid line).

The predicted curve was obtained initially by measuring the Q from the -3dB width of the peak (ie. frequency width between -3dB points). However, it is clear that the response is not symmetric about the resonant frequency, and that this prediction is not a good fit above the resonance, which is the region in which accuracy is required (as seen in Figure C-1). So a second value of Q was calculated, by doubling the width from the peak to the upper -3dB point. The resulting prediction (dotted line) fits the measured data well, down to approximately -6dB.

The calibration of the device was tested as follows. The end cap was inserted into the lower end of the 4m high vertical tube, excited to a resonance, and the response was recorded. Then a small quantity of talc was dropped into the top opening of the tube (in several bursts), until the response of the system had dropped to approximately -3dB. The change in response was converted into added mass using equations (C.9) & (C.6), and plotted in Figure C-4 . The shim was removed and weighed to assess the actual settled mass of talc; this was found to be 25mg, compared to a final value of approx. 34 - 38mg measured using the dynamic weigher. The overprediction of the apparatus is due to the decrease in Q caused by the settled dust. Hence the dynamic weighing apparatus will give an upper bound for the actual settled weight

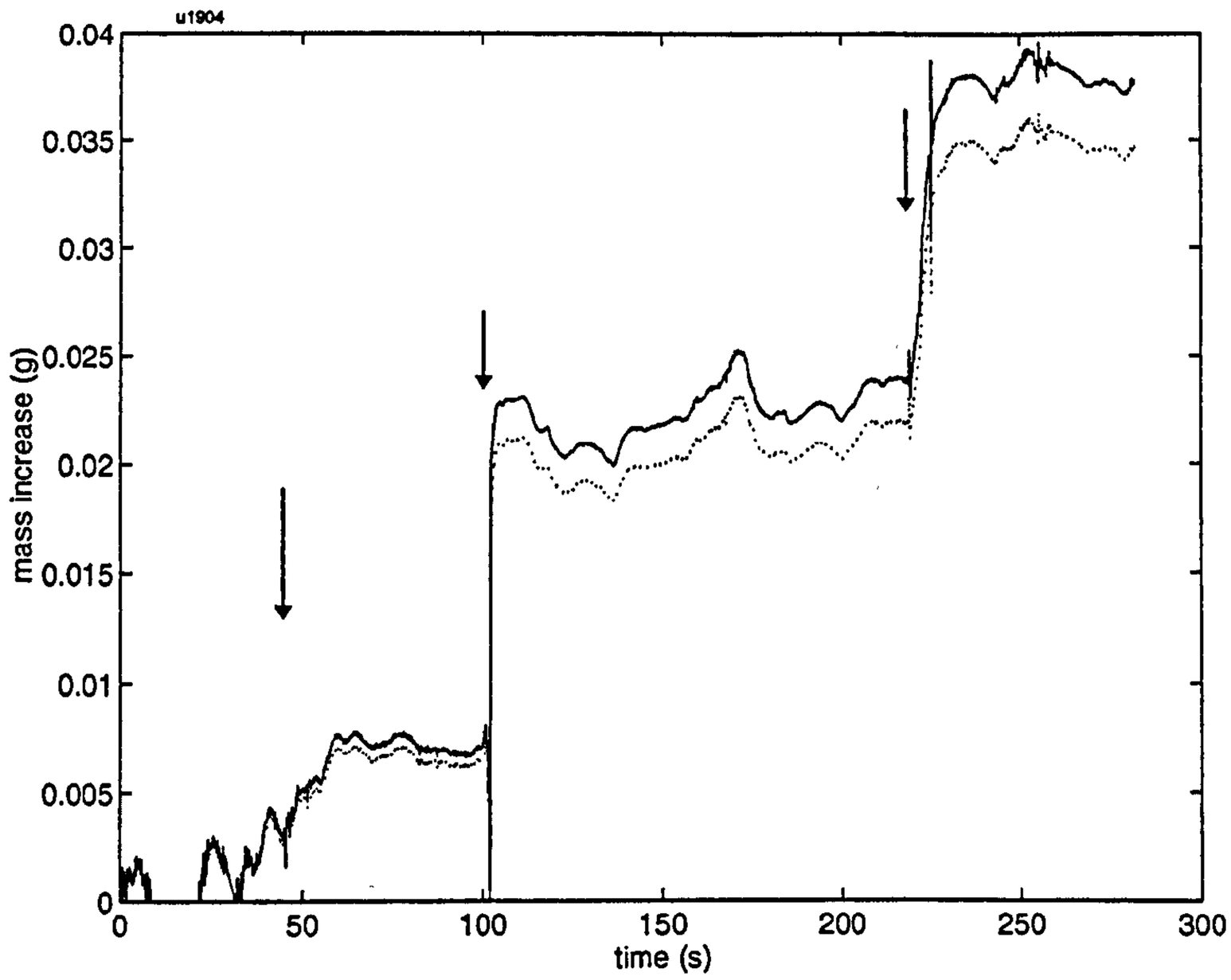

Figure C-4 Curve of added mass of talc, calculated from change in resonant response. Weight of settled talc measured using balance = 0.025g. Arrows show points at which talc was dropped into the tube. Dotted line uses Q = 116 measured from -3dB width, solid line Q = 106 from upper -3dB point.

It is clear that the apparatus can provide a very sensitive measure of settled weight. To illustrate, Figure C-5 shows the detected mass that is calculated for a given change in measured amplitude, for Q = 100. Amounts of 5mg are quite easily measured, corresponding to an amplitude change of just under 1%. If a lighter vibrating element can be found (the one used weighed 4.7g), then the apparatus becomes even more sensitive.

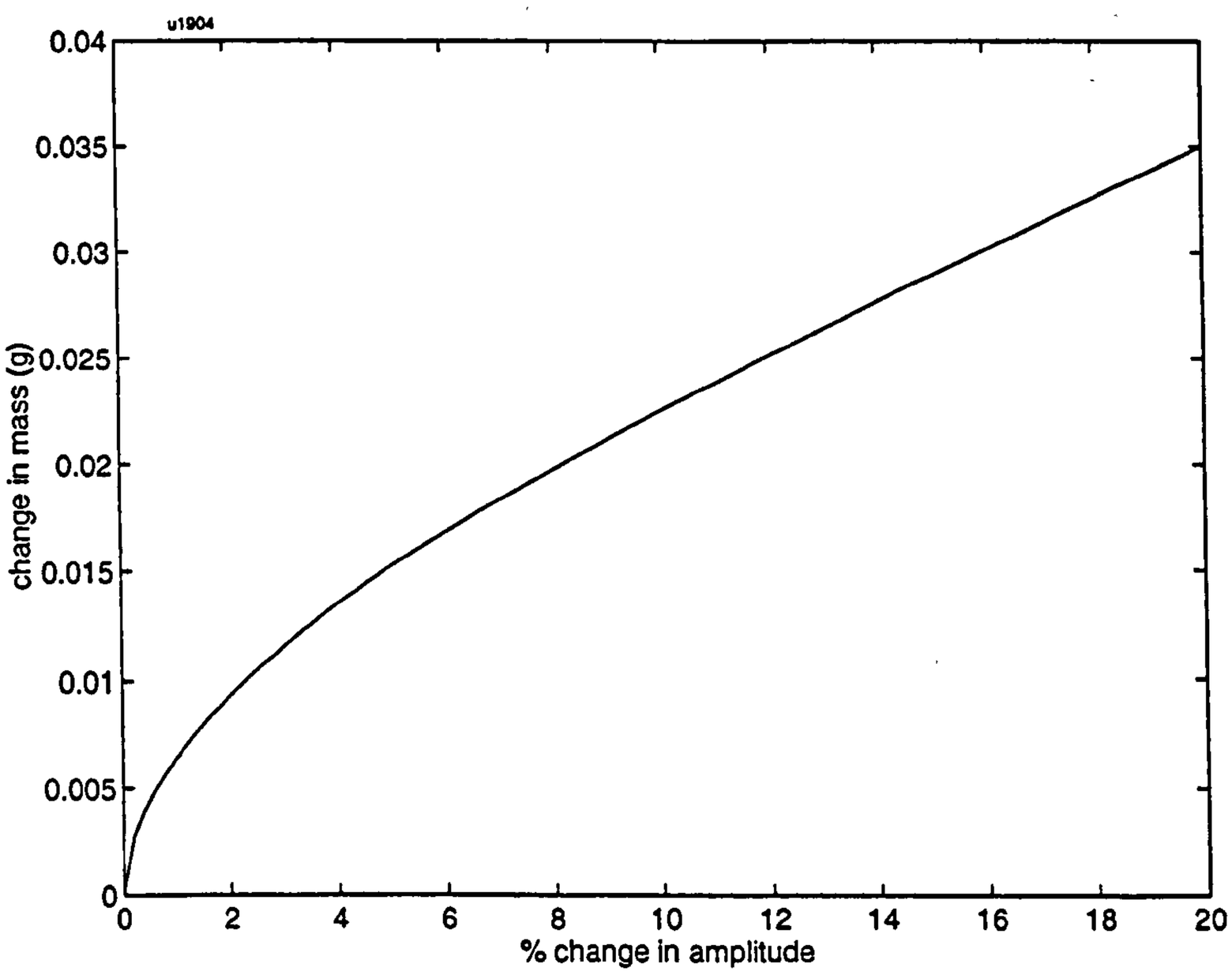

Figure C-5 *Theoretical sensitivity of the dynamic weighing device: detected mass vs. change in amplitude response. $Q = 100$.*

C.4 FURTHER DEVELOPMENT

The dynamic weighing device was devised in order to estimate error margins, not to make absolute measurements, and hence many potential developments have been ignored. However, its sensitivity and simplicity make it a device that may be of use in other circumstances, and so the potential improvements are listed below.

1. The mounting of the shim was very crude, being clamped by two nuts, and the tension being maintained by the spring inherent in the plastic support pillars (whose separation was slightly less than the hole spacing in the shim). A much better mounting system would clamp the shim along its width (instead of at a point), and would be able to introduce adjustable tension into the shim. This could shift the resonance to a higher frequency, thereby further increasing the accuracy and speed of response.
2. Given such a tension system, a much thinner shim could be used (since it would not need the stiffness to support its own weight). In the extreme, aluminised mylar film may be used, having negligible mass, and therefore being very much more sensitive to added weight.

The system measured the change in amplitude due to a change in resonant frequency. However this technique is very sensitive to changes in Q, and to the exact shape of the response curve in the vicinity of the resonance. A better technique would be to track the resonant frequency directly, with a resonance dwell system. This is a phase-locked loop, which works on the principle that the

phase angle of the response voltage changes very steeply around the resonance. A phase-detector controls the frequency of sine excitation using a voltage-controlled oscillator within a feedback loop.

APPENDIX
D
EXPERIMENTAL TECHNIQUES

This appendix lists the procedures for several different experimental techniques. It is aimed at people who are trying to repeat experiments using the original equipment.

D.1 EXPERIMENTAL PROCEDURE: PLANE WAVE MEASUREMENT OF DUST SUSPENSIONS

This section describes the experimental procedure to measure the attenuation and dispersion caused by a suspension of dust in air. The apparatus used is a double-length vertical tube. Two operatives are required.

D.1.1 Apparatus and consumables

Hardware

Both halves of vertical tube affixed to wall
Lower tube cap, with magnetic clamp and steel shim
Lower tube end strap
1/4" hole blanking plug with thermocouple hole
Dome tweeter on threaded insert, or blanking plug to fit
Filling boss blanking plug
Probe mike port boss, bunged with blu-tak
Short length of 2" diameter perspex tube
Dust blow gun with nozzles
Foam cleaning pull-through

Instrumentation

PC with MLSSA card
1/2 " Brüel & Kjær 4133 microphone and 2639 preamp
Goodmans loudspeaker on wooden surround
Rotel RA-870BX amplifier
Series capacitor box (16μF)
Brüel & Kjær 2607 measuring amplifier
Balance: 0.1g resolution
Balance: 0.1 mg resolution
Thermocouple & thermocouple amplifier (eg.Comark 6600)
Optional - chart recorder (eg. J-J Instruments)

Consumables

Dust masks
Supply of relevant dust (alumina or otherwise)
Fine plastic mesh (100μm or finer)
Double sided tape
Vaseline

Plenty of paper towels
Blu-tak
Plastic bin-liner and elastic band

Tools

Step-ladder
Forceps
Flat-headed screwdriver
Stopwatch

Leads

Phono-phono
Banana-banana (approx. 4.5m)
B&K "banana" - phono
if chart recorder used: 3.5 mm jack - banana
Mains leads to suit
Mains extension lead and rubber anti-trip cover

D.1.2 Procedure

Initially...

1. Ensure compressed air supply is available. Feed air-hose through holes in wall and connect to gun, securing connection with a Jubilee clip. Set regulator pressure to 55 psi when the gun button is pressed.
2. Clean lower tube using paper towel wrapped around pull-through. Couple together upper and lower tubes.
3. Clean inside of filling boss and lubricate stopper O-ring with Vaseline.
4. Affix square of mesh over 1/2" mike port on interior of tube, using ring of double-sided tape.
5. Insert blanked probe-mike boss in threaded hole, loudspeaker in open end of top tube and blanking plugs in mid-way ports of lower tube.
6. Insert microphone into 1/2" mike port: use steady, moderate pressure to push grid past both the O-rings. Leave front face flush with inner wall of tube.
7. Insert thermocouple through hole in 1/4" port bung, so that the bead is roughly at the tube axis. Secure with Blu-tak at outer end of bung. Connect to, say, input 1 of thermocouple amplifier. If desired, connect thermocouple amplifier to chart recorder.
8. Set Rotel amplifier switches: tone off, volume fully down, CD direct off, Monitor source, Function CD.
9. Set B&K 2607 switches: Gain control cal, Input preamp, 22.4Hz filter on, other switches off, output attenuator ×1, meter function RMS Log., averaging time fast, output AC.
10. Set thermocouple amplifier by pressing number of the channel, say, 1.
11. Connect instrumentation as shown in Figure D-1, turn on and allow all (including mike preamp) to warm up for one hour. Cover mains lead with rubber anti-trip cover. Ensure all cables are strain-relieved.
12. Ensure both balances are level and zeroed.
13. Weigh steel shim on 0.1 mg resolution balance (see *Box 1*). Record m_{shim}.
14. Centre steel shim within scribed marks on end cap; ensure it is clamped down evenly by the magnet in cap.
15. Insert end cap squarely into lower end; ensure it is well-seated (not skew), and clamp in with the end strap.
16. Ensure dust hopper is clean and dry; insert required nozzle, ensuring hole is clear.
17. Wearing dust mask, fill hopper with required grade of dust. Try to keep dust as loosely packed as possible (tapping hopper minimally or not at all) while eliminating

gross air pockets. Keep the hopper at a shallow angle during filling to reduce compaction and the generation of dust plumes.

18. Weigh the hopper on 0.1 g resolution balance; record m_{hopper}

Box 1 Notes on using the Balance

- Ensure balance is level by adjusting feet.
- Remove gross contamination from weighing pan.
- Do not lean or place any additional weight on the bench: even the weight of the end cap on the bench can affect the measurement.
- Zero the balance before each measurement, and recheck zero after measurement: repeat the measurement if necessary.

When instruments have warmed for one hour...

1. Launch MLSSA using: `cd\mls`
   `mlssa`
   `sl{name of setup file}`

Box 2 MLSSA Setup suitable for test

```
Acquisition                                  Stimulus
   mode: Cross-correlation                      Burst MLS
   length: 10000 samples (332.5 msec)           amplitude: 0.4922 V
   sample rate: 30.08 kHz (33.25 µsecs)         period: 16383 samples
   Concurrent pre-average cycles: 2             544.7 msec
   Autorange: enabled                        FFT
Antialiasing filter                             window: rectangular
   type: Chebyshev                              size: 1024 points
   bandwidth: 10 kHz                            best resolution: 29.37 Hz
   gain: 0.5 (* 10 volts range)                 Normal reference: 1
Trigger                                         min phs accuracy: High
   type: Stimulus trigger                       mode: Transfer Function
   delay: 0 samples (0 msec)
Units                                       Cumulative Spectral Decay
   acquisition: 1 volts/volt                    fftsize: 1024
   stimulus: 1 volts/volt                    cycles: 50 (0.65 msec)
Digital Filter                               shift: 1 pts (0.01 msec)
   center: 1000 Hz                           window: Blackman-Harris
   width: 1.000 octave                       0.15 msec risetime
Directory: C:\USERS\MLSSA                    range: 0.000 - 15.000 kHz
Last setup file: C:\USERS\MLSSA\DDT.SET      linear frequency axis
   modified: 9-7-93 11:32 AM                 6 dB/div, Auto floor
```

A suitable setup file is shown in *Box 2*.

2. Start stimulus by pressing {DELETE}. Adjust level by slowly turning up volume control on Rotel amplifier, until meter on 2607 reads 105 dBV. Turn off stimulus by pressing {DELETE}.
3. Choose a filename root: `tar{5 letter root name}`
   `talc{ENTER}{description}`
4. Remove loudspeaker, remove filling-port bung, insert dust gun without hopper attached and with Blu-tak bung over the dust feed-hole. Make note of initial temperature, then flush tube for 3 mins with compressed air, or until the tube temperature stabilizes.
5. Replace loudspeaker and filling-port bung, and take a reading, using: {ALT-F1}. At each reading, record the temperature.
6. Decouple the two tubes, secure bin liner over top of lower tube with elastic band, insert gun (with hopper attached) in filling port. Don face masks.
7. Operative 1 starts stopwatch & dust blowing simultaneously.
8. 5 s later: Operative 1 stops dust blowing, removes gun, replaces bung.
   Operative 2 removes bag, recouples tubes.
9. Asap, Operative 1 takes two consecutive measurements noting the elapsed time and temperature.
10. Weigh dust hopper with remaining dust, noting m'_{hopper}

Allow the dust to settle

(eg. 30 mins for F800 grade alumina).

1. Take measurement (noting time and temperature).
2. Carefully remove end cap, being careful not to knock the tube. Transport the dust-covered end to the balance, shielding dust layer with perspex tube.
3. Unscrew magnet assembly and carefully lift off the shim. Weigh and make note of m'_{shim}
4. Clean equipment and tube as above. Dispose of any hazardous dust and contaminated towels in the correct fashion. Ensure the (mild) steel shim is not left damp. Park the computer hard disk before transporting.

D.1.3 Data processing

Data are recorded in files named {*fileroot*}-nn.TIM where nn are two digits counted sequentially from 01, and incremented each time a measurement is taken.

1. To allow further processing by MATLAB, the data must be recorded in ACSII format. This is done within MLSSA for each dataset as follows:
   `tl-{nn}`
   `ted{`*`filename`*`.DAT}`
   where *filename* is *filerootnn*, that is, the existing filename with the hyphen removed, and a `.DAT` extension.
   The raw data are returned as an array in variable `raw` in the format `raw(sample:dataset)`. The Nyquist frequency (= ½ × sampling frequency) is returned in `ny`.
2. Launch MATLAB, and load the datasets using:
   `[raw,ny]=filnamx(fileroot,[nstart:nfinish]);`
   where `fileroot` is a string containing the fileroot, and `nstart & nfinish` are integers specifying the start and finish values of nn. Use the highest version number `x` of function file `filnamx.m`
3. Calculate dust volume concentration using:
   `phi = phical (mshim1 - mshim0);`
   where `mshim1`, `mshim0` are variables holding m'_{shim} and m_{shim} respectively.

Further data processing is performed by the latest version of the processing function file, currently `plan5mul`. See the help for the function.

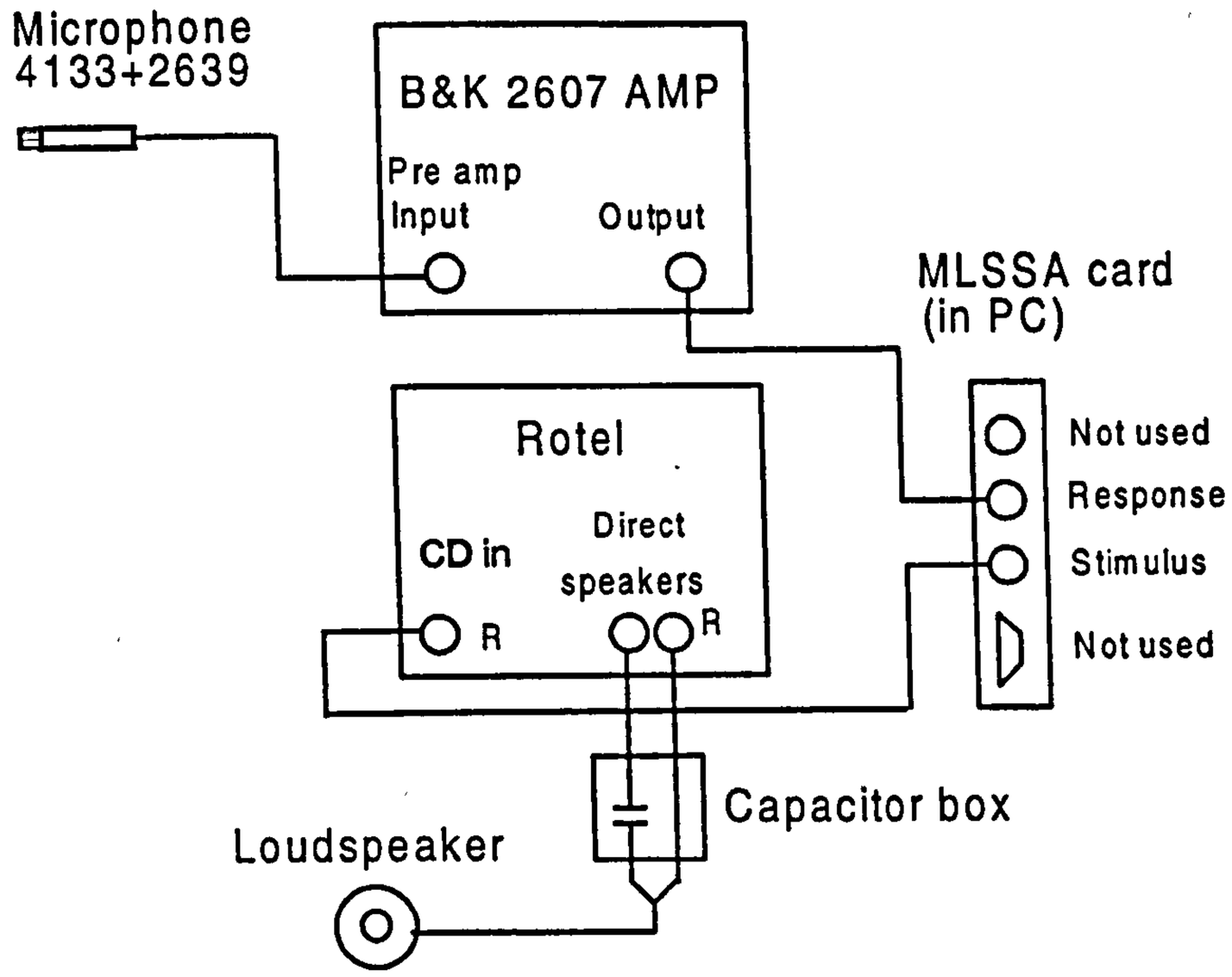

Figure D-1 *Schematic wiring diagram for instrumentation.*

D.2 OPERATION OF WOLFSON CENTRE FLOW RIG

This section describes procedures to operate the dust/air flow rig at the Wolfson Centre for Bulk Solids Handling. The rig will produce particulate flows of known mass concentration and flow speed in a pipe of 2" bore.

D.2.1 Overview of the rig

The rig is an open loop device: that is, the dust is picked up from one hopper (the blow tank) by clean air, conveyed through the test section, and then separated out by bag filters to drop into a receiving hopper. When the blow tank is emptied, then a procedure must be followed (§5) to re-charge it with material from the receiving hopper.

Instrumentation

The air source at 4bar is metered through choke-flow nozzles into two separate streams: the supplementary & blow tank streams. Blow-tank air picks up the dust from the blow-tank, and is then mixed with supplementary air. Two banks of switches inside the control room control the mass flow rates of air in both streams. The flow rate of blow tank air controls the mass flow rate of dust (in no fixed relation); the ratio of blow-tank to supplementary air controls the mass fraction of dust (in no fixed relation). The total mass flow rate of air controls the superficial air velocity.

A bank of load cells support the receiving hopper; the signal from these is recorded on a chart recorder, and indicates the weight of material in the receiving hopper. The gradient of the line – the rate of change of weight – indicates the mass flow rate of dust.

The choke flow nozzles are calibrated in terms of air mass flow rate; hence by knowing which nozzles valves are open, and the gradient of the gain-in-weight trace, the mass concentration of the flow may be calculated.

Configurations

The dust-feed arrangement may operate in two main configurations: venturi or blow-tank. Venturi feed – the usual arrangement – is where the blow-tank air passes through a venturi; dust is sucked from the blow-tank into the throat of the venturi. This arrangement provides smooth dust feed up to a mass concentration of approximately 5kg/kg.

The blow tank configuration provides higher concentrations, but in very irregular flows. The air is blown directly into the blow tank through annular nozzles around the base of the tank, carries dust out into the pipe. Thus the tank is pressurized; the operating instructions specified here are not sufficient for blow-tank operation.

D.2.2 Controls

Inside the control room, there is a panel of dials to the right, and, straight ahead, a panel of numbered switches in several banks.

Nozzle switches

The left hand switch bank controls the choke-flow nozzle valves, and the adjacent bank control various other valves. Nozzle switches 0 – 7 control the supplementary air; 8 – 15 control the venturi air. They are arranged in a binary sequence, with the smaller number providing the smaller flow, and the next higher number providing double the flow (nominally). The bottom switch "Enable" makes the valve switches active. With enable switched off, the valve switches may be changed, but the valves will only be affected when "Enable" is switched on. The LEDs to the left of the switches echo the current value of the control.

The air flow-rates and velocities are shown in Table D-I

	Switch #	Mass flow rate kg/s	Free air volume m^3/s	Superficial air velocity m/s
Supple-mentary air	0	0.00131	0.00111	0.502
	1	0.00260	0.00220	0.995
	2	0.00494	0.00417	1.891
	3	0.01010	0.00853	3.867
	4	0.02027	0.01712	7.761
	5	0.04000	0.03378	15.32
	6	0.08000	0.06757	30.63
	7	0.1482	0.1252	56.74
Blow tank air	8	0.00155	0.00131	0.594
	9	0.00260	0.00220	0.995
	10	0.00503	0.00425	1.926
	11	0.01060	0.00895	4.058
	12	0.02034	0.01718	7.787
	13	0.04007	0.03384	15.34
	14	0.07999	0.06756	30.62
	15	0.1485	0.1254	56.85

Table D-I Nozzle bank mass flow rates. Operating conditions: 53mm pipeline bore,; 4.0 barG upstream pressure; 1.0 barG pipeline pressure; 20°C upstream temperature

A chart recorder is connected to the gain-in-weight signal.

Dials

These are arranged as shown in Figure D-2. If the low- pressure dial goes out of range, then isolate it with the brass valve and read from the upper one.

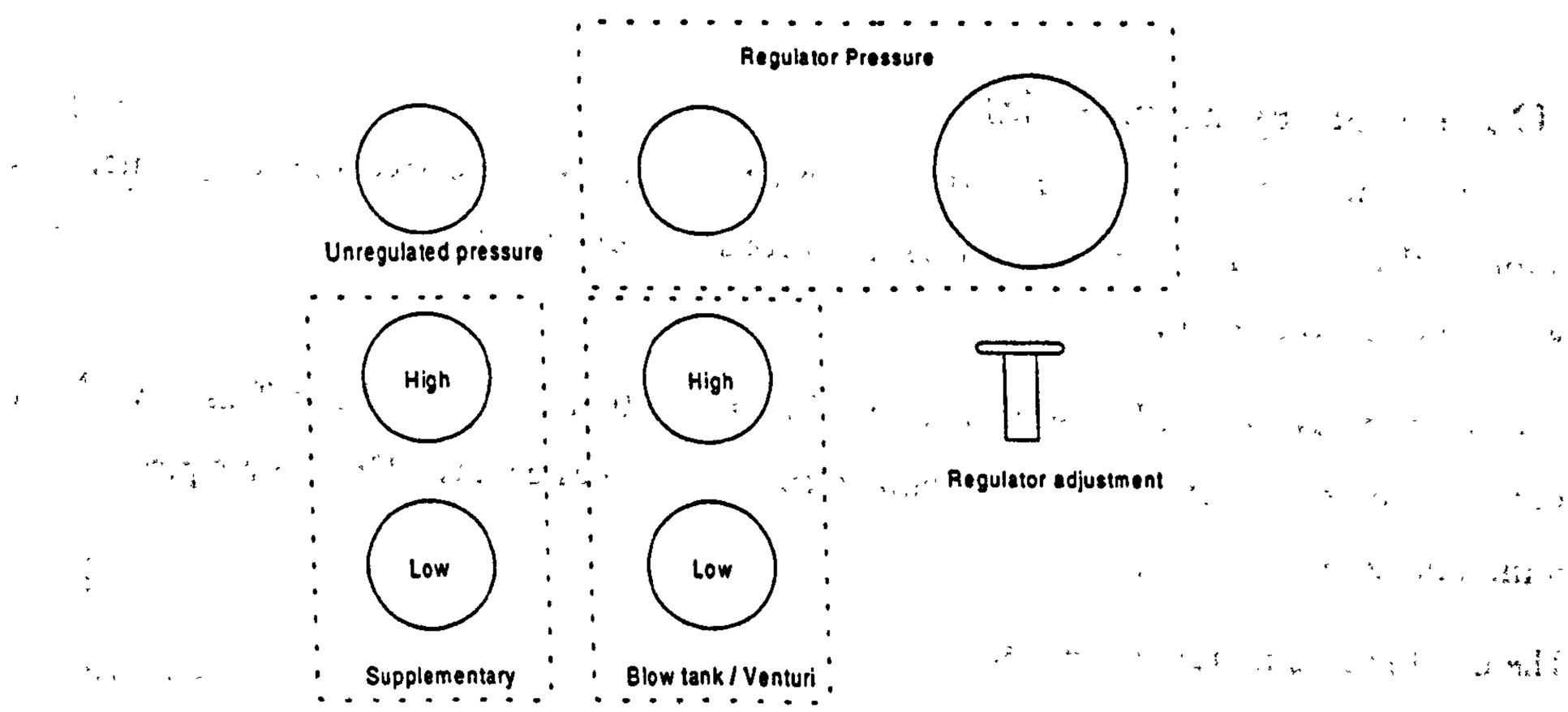

Figure D-2 Layout of pressure dials in control room

D.2.3 Preparing the rig

Outside the control room

1. Ensure the correct compressors are turned on, and various valves route the air to the rig – ask.
2. Open the valves to the regulator, nozzle bank, the supplementary circuit and the blow tank circuit. If any valves from after the regulator to other equipment are open, then ask. (Other rigs may cause drops in regulated pressure and send the rig out of calibration).
3. Turn on the power to the nozzle bank at the switch above the perspex plate.

Inside the control room

1. Press the reset switch on the black safety interlock box on the shelf. The green LED should light.

Set the nozzle bank pressure to 4 bar.

2. Turn on nozzle switches 10 & 12 to provide some air flow.
3. Set the regulator pressure to 4.0 bar using the adjuster below the large dial gauge.

Calibrate the gain-in-weight trace

4. Turn on the chart recorder, pen down, maximum sensitivity and record a short trace.
5. A string with a hook hangs down from one corner of the upper hopper. Attach a calibrated mass to this (a weight hanger of 20kg is often available nearby).
6. Record a further trace. The height of the trace's step provides the calibration.
7. Material should have been left in the top hopper. Transfer this to the blow tank by the method listed in section D.5.
8. It is initially worth conveying one blow-tank load of material (see section D.4), and then re-charging the blow-tank, in order to aerate the material and arrive at stable conveying conditions.

D.2.4 Conveying material

Before making a test-run, plan the switch settings to use to give the correct operating conditions.

Table D-II gives a series of nozzle settings for a constant superficial air velocity of 20m/s, and variable mass concentration.

A valve at the base of the blow-tank is controlled by Sw #0 of the second bank. This valve should not be open unless sufficient air is flowing to convey the released dust; 20m/s is a typical minimum conveying speed.

The usual procedure for any test is:

With all switches off, make no-flow measurements

1. Switch on nozzle valves required; make any air flow / no dust measurements

2. Start chart recorder at typ. 0.5mm/s (unless working at very low flows); record the speed and experiment number on chart.
3. Turn on Sw #0 of second bank to open dust valve.
4. Make tests and record dataset number on chart. Continue as necessary, or until have sufficient length of trace to deduce gradient.
5. With Enable switch off, change nozzle switches to next set-point; when ready, toggle Enable; simultaneously change range on chart recorder to mark change in set-point;
6. Repeat steps 4 & 5 as necessary according to programme.
7. When finished, or material is exhausted, close the dust valve (turn off Sw #0 on second bank); stop chart recorder.
8. Turn off nozzle switches & toggle Enable.

Notes:

- At the end of the day or test, leave all material in the receiving hopper: it is easier to transfer consolidated material down under gravity than to convey it.
- Operating limits: for venturi operation, the pipeline pressure (indicated by the supplementary pressure dials) should remain under 0.2 bar. The venturi pressure will usually be less than 0.85 bar; as long as it remains under 2.5 bar, then the choke flow nozzles will remain within calibration.

Supplem'y switches	Blow tank switches	air-flow mass proportion blow tank / supplementary	total mass airflow kg/s	approx. mass conc'n kg/kg
3,5	9	0.0493	0.05270	0.03
2,5	9,10	0.1451	0.05257	0.2
1,5	8,9,10	0.1773	0.05178	0.5
5	8,11	0.2320	0.05215	1.1
2,3,4	8,10,11	0.3273	0.05249	1.9
1,3,4	8,9,10,11	0.3750	0.05275	2.1
1,2,4	10,12	0.4771	0.05318	2.1
4	11,12	0.6042	0.05121	2.5
1,3	9,10,11,12	0.7523	0.05127	3.0
1,2	10,13	0.8568	0.05264	4.2
1	11,13	0.9512	0.05327	5.0
–	9,11,13	1.0	0.05327	5.1

Table D-II Example switch settings for 20m/s nominal set-point, variable mass concentration of flour (deduced from earlier experiments)

D.2.5 Re-charging the blow-tank

When the gain-in-weight trace shows that no further material is being transported despite the dust feed valve being open, then the blow-tank probably needs to be recharged.

The operation is mostly controlled by the switch bank adjacent to the nozzle bank; the switch numbers below refer to this bank.

1.	Ensure all nozzle valves are closed (left hand bank).	
2.	Open tank vent (usual for venturi operation)	Sw # 3 off
3.	Open lower butterfly valve	Sw #1 on
4.	Open upper butterfly valve – Pull orange lever out, move it from 9 o'clock to 6 o'clock position	Performed manually on rig.
5.	Open louvres	Sw # 4 on
6.	Shake filter bags	Sw # 5 on then off one minute later
7.	Shake centre coupling	Sw # 6 on intermittently for a few seconds several times
8.	Close louvres	Sw # 4 off
9.	Close upper butterfly	Manually, reverse of step 4.
10.	Close lower butterfly	Sw # 1 off

D.2.6 Changing the particulate material

To change the material in the rig – ask.

D.3 P.S.D. MEASUREMENT USING THE W.A.S.P.

This document describes the experimental procedure to measure the particle size distribution (PSD) of powders.

The principle is to measure the settling rate of the powder suspensed in a fluid, and to calculate the effective Stokes radius of the particles from the falling velocity.

The properties of the suspending fluid should be:

- Non-reactive (with solid powder of interest).
- Not a solvent of the powder of interest.
- Will not be absorbed inside the powder particles.
- Is significantly less dense than the powder, and has a well-known or measurable viscosity.

For the following, the use of distilled water with 0.1% sodium hexametaphospate is described.

D.3.1 Apparatus and consumables

WASP apparatus, including square section tank
200ml Pyrex beaker
500ml measuring jar
Stirring rod
Magnetic stirrer and magnet
Data acquisition system
Balance: 0.1g resolution
Ultrasonic cleaning bath
25ml pipette

Supply of relevant dust (alumina or otherwise)
600ml Distilled water
0.6g Sodium hexametaphosphate
Paper towels

D.3.2 Introduction

The WASP can be used to measure the particle size distribution of a powder. It works by dispersing the powder in a liquid dispersant, and measuring the projected area frequency as a function of terminal settling velocity. This can be processed to yield the weight frequency as a function of Stokes' diameter (ie. the diameter of the sphere which falls at the same speed of the particle of interest).

The optical density towards the bottom of the suspension tank is measured using a parallel light beam falling onto a large photocell. A decrease in light intensity at any one time corresponds to particles falling from the surface of the fluid; if the height of the fluid is known, then the settling speed of the particles crossing the beam can be found from the time at which it happens.

D.3.3 Procedure

1. Clean and dry the glass ware
2. Decide on quantity of dispersant to use - enough to almost fill the tank for dust with a significant large fraction, half a tank for smaller dust. Dissolve 0.1% by mass of sodium hexametaphosphate in the water, and place in tank.
3. Dial in scan delay onto timer if scanning is to be used. Note the delay.
4. Start the computerised logging system: select LABVIEW VI "Chart recorder with block average & save".
5. Take the electrical signal from across the 1.8 kΩ resistor on the left hand photocell, and feed it into the differential input on the A/D card.

Calibration

1. Ensure the tank platform is at the top of its travel, place tank on it, and cover with the lid.
2. Start recording data.

3. Rotate the filter wheel so the clear filter (hole) is in the light path. Adjust the zeroing knob to minimize output, and record this voltage for D=0

4. Rotate the filter wheel so that the light is completely blocked and record this voltage for D = ∞. Turn back to the clear hole.

Form suspension & measure

1. Place dust sample in beaker, mix to a thick paste with dispersant, then dilute in plenty of water. Place in ultrasonic bath and insonify for several minutes to shatter agglomerated particles.

2. Remove beaker from bath, and stir continuously with magnetic stirrer, to keep the particles in suspension.

3. Remove tank, turn off stirring and, using the pipette, add a little concentrated suspension. Before drawing up suspension, agitate it by bubbling some air through it using pipette bulb.

4. Agitate the tank by inverting it several times. Add suspension until its optical density D is approximately 0.5 - 0.7 (voltage is approx. 0.7 - 0.8 mV). This can be done roughly by eye, otherwise it needs several iterations of removing and replacing the tank in the instrument.

5. With the tank in the measuring cell and the lid replaced, the analysis starts here. Switch on the scanning switch if scanning is to be used.

6. When scanning has finished, or, if scanning is not used, the value of *D* has decreased to approx. 0, the recording can be stopped and the data saved. Measure the distance from the bottom edge of the glass base of the tank, to the bottom of the liquid meniscus: this is required in the analysis.

Analyse the data using Matlab programs WASP or WAP (with and without scanning, respectively), following the instructions given.

APPENDIX

E

REPRODUCTION OF PUBLICATION [99][1]

Applied Acoustics **42** (1994) 187–196

Technical Note

Measurements of Attenuation and Dispersion in an Airborne Suspension of Dust†

S. Moss & K. Attenborough

Department of Engineering Mechanics, The Open University, Walton Hall, Milton Keynes, UK, MK7 6AA

(Received 7 July 1993; accepted 3 August 1993)

ABSTRACT

A suspension of alumina particles in air has been created inside a cylindrical tube. The attenuation and dispersion characteristics of the mixture have been calculated from the impulse response of the tube, with and without the dust suspension. Results are presented for three dust sizes with mean radius 2·0, 3·1 and 6·7 μm, over the frequency range 200 Hz to 2 kHz. Dust concentrations varied between 6 and 18 ppm by volume. Results are compared with predictions of a multiple scattering model. Agreement is reasonable for larger particle sizes, while the smallest particle distribution showed higher than predicted dispersion. The measurements show larger discrimination in acoustical effects between different mean particle sizes than predicted.

1 INTRODUCTION

There is a need for a robust technology to monitor the level of industrial dust emissions. Most current devices, which are generally based on optical scattering techniques, require regular maintenance and ancillary equipment that continuously cleans the optical components. This paper

† Based on a paper presented at the IoA/SFA Acoustics 1993 Conference, Southampton, UK.

[1] Reference [100] is not reproduced, since its content appears in Chapter 7.

describes a first step in establishing the feasibility of an acoustic alternative to optical measurement devices, especially in areas of high dust concentration.

The goal of this study was to create a controlled atmosphere of airborne dust, and to measure the resultant effects on sound propagation at low frequencies—between 200 Hz and 2 kHz. At these frequencies, the wavelength of the sound is very much larger than the size of particles, and so the main effects are viscous and thermal losses at the particle/air interface. Rayleigh scattering is negligible. These loss mechanisms are predicted to introduce excess attenuation, and a frequency-dependent phase velocity that leads to dispersion.

By measuring a pulse before and after transmission through the dust suspension, the attenuation and dispersion of sound by the suspension may be derived.

2 APPARATUS

2.1 Dust suspension

Alumina particles (Al_2O_3) have been used at the test dust, since they are available in measured distributions of fairly small standard deviation. The three distributions used have mean radii of 2·0, 3·1 and 6·7 μm. The suspension was blown into a vertical steel tube by directing a stream of compressed air past a 3-mm diameter orifice, using the apparatus shown in Fig. 1(a), and feeding alumina into the orifice through a vibrating hopper.

2.2 Measurement tube

Sound was introduced into the top of the steel tube by a length of plastic tube, at the end of which was a mid-range acoustic driver (see Fig. 1(b)). Since the plastic and steel tubes were of different diameters (150 mm and 120 mm, respectively), they were joined by a coupler which was tapered to minimise reflections from the change in section. A probe microphone sampled the sound pressure half-way down the taper on the central axis of this coupler.

The PC software (MLSSA) excited the system with a 'maximum-length sequence' signal, and processed the measured steady-state response to yield the system impulse response.[1] Henceforth, the excitation will be discussed as though it were a delta impulse.

The microphone initially registered the downwards-travelling 'direct'

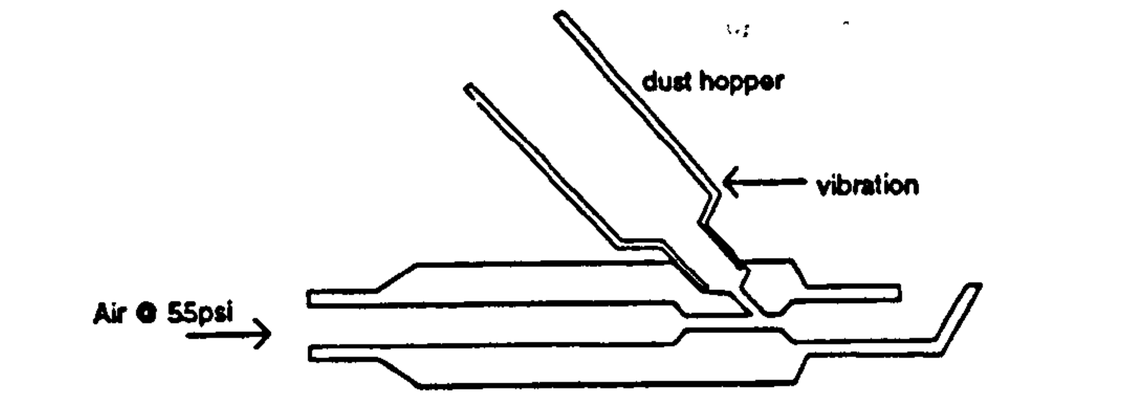

(a)

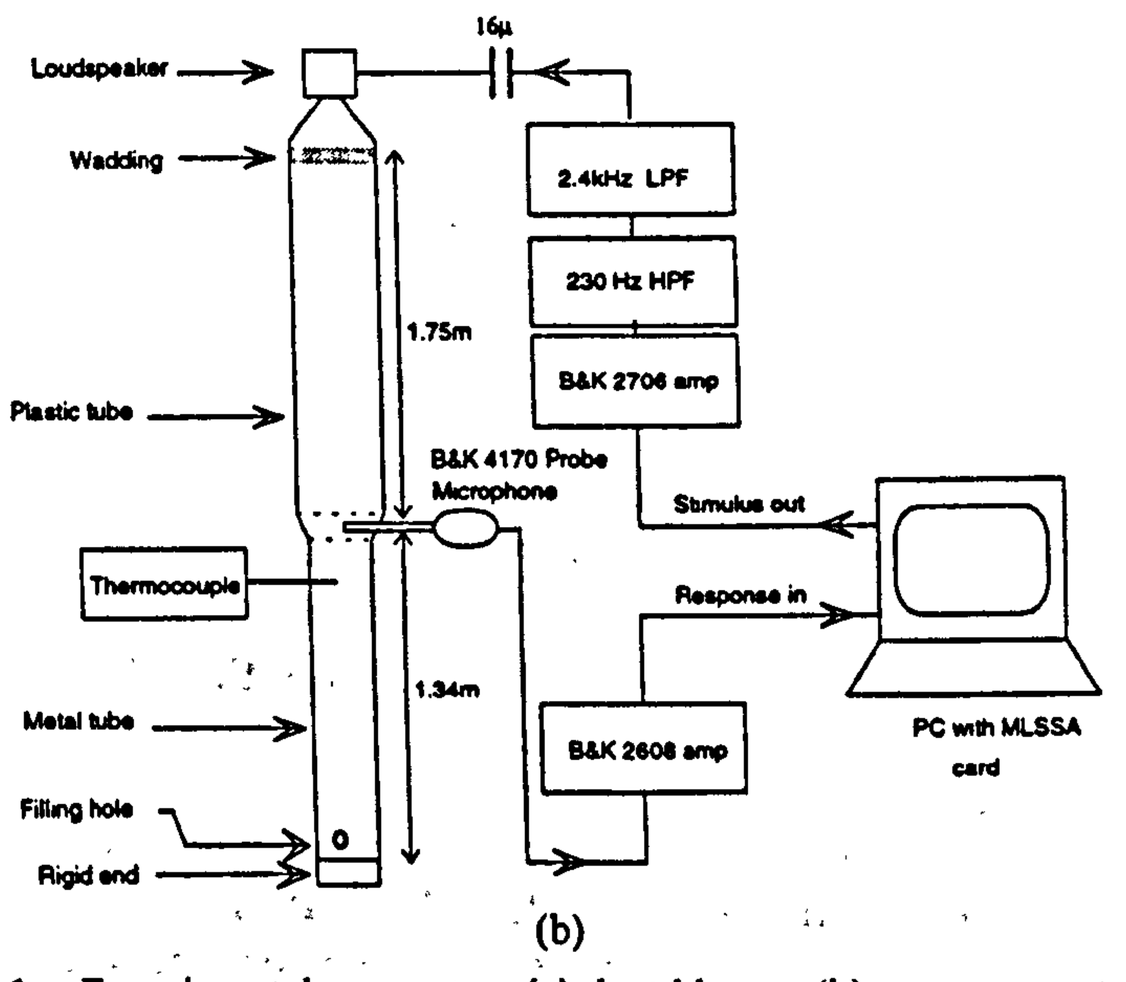

(b)

Fig. 1. Experimental apparatus: (a) dust blower; (b) measurement tube.

pulse. Next, 8 ms later, it registered the upwards-travelling pulse ('1st reflection') that had passed through the suspension, had been reflected from the rigid end, and had passed back through the suspension. These primary pulses were followed by multiple reflections from the loudspeaker cone and rigid end, and also lower amplitude reflections from the change in section at the coupler. Wadding near the loudspeaker attenuated the unwanted end-reflections, and so shortened the overall impulse response. This increased the signal/noise ratio in the measuring electronics, and reduced the tendency of the MLSSA system to suffer from time-aliasing.

The purpose of the upper tube was to increase the path length between loudspeaker and microphone, and hence increase the time gap between the first reflected pulse and the reflection from the loudspeaker cone. A

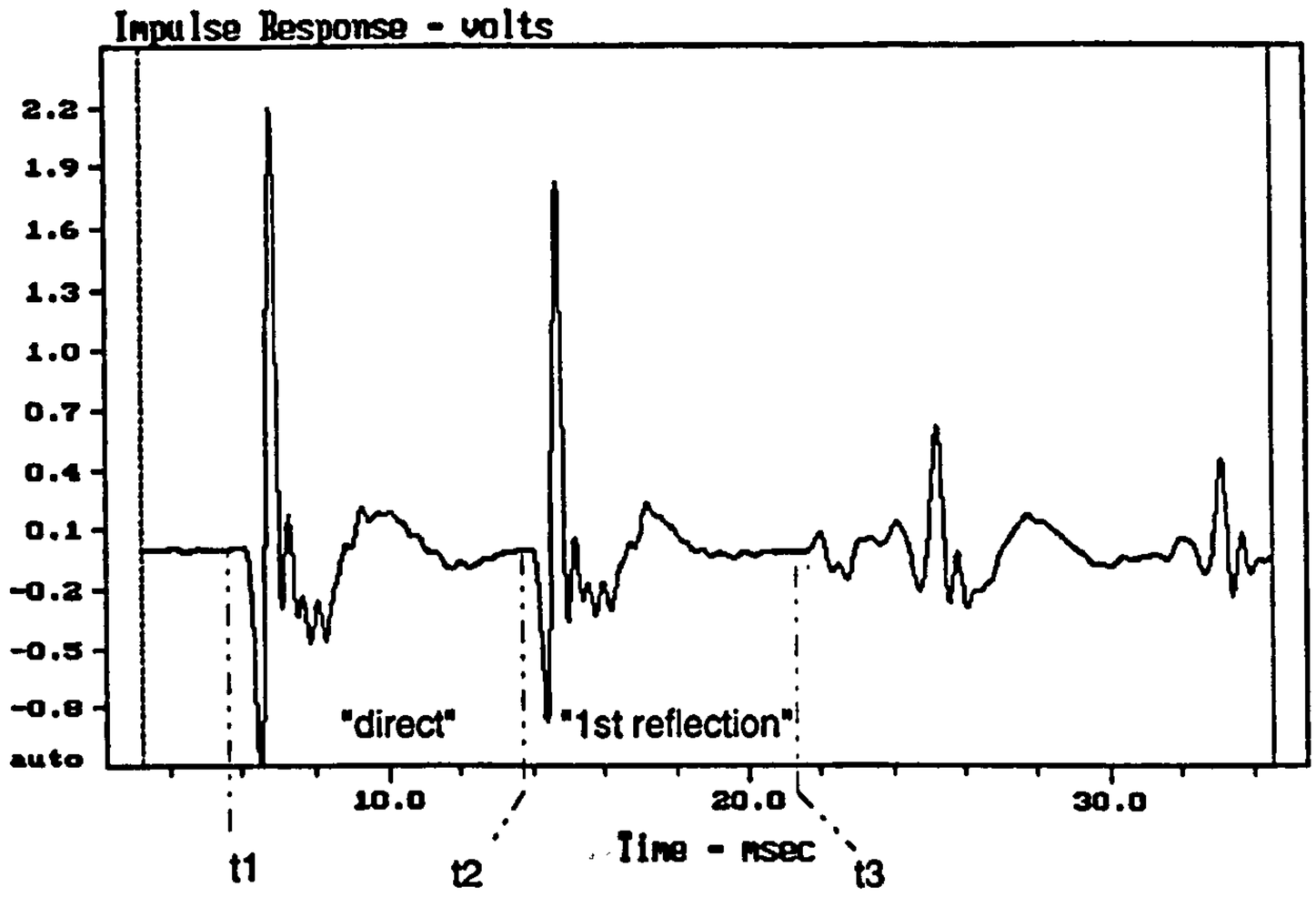

Fig. 2. Typical impulse response of system. The first loudspeaker reflection is visible at approx, $t = 24$ ms.

typical impulse response is shown in Fig. 2. Note that the first two pulses rise and fall virtually to zero, and are clearly separated, the importance of which is explained in the next section.

The excitation signal was high-pass filtered to increase the decay rate of the direct pulse, and low-pass filtered to attenuate frequencies that would have excited axial cross-modes in the tube and created a poorly damped high-frequency ripple on the measured impulses, thus reducing their separability.

3 EXPERIMENTAL PROCEDURE

The tube was flushed with compressed air for a few minutes to create a uniform air temperature. A measurement of impulse response was then taken in a dust-free system. The upper tube and coupler were removed, a large plastic collecting bag was sealed over the top of the metal tube, and the suspension was blown in through the filling hole for approximately 5 s with an air pressure of 3·7 bar; this was sufficient to change the air in the metal tube, and vent excess suspension into the collecting bag. The bag was removed, the upper tube was replaced, the filling hole was plugged, and a series of measurements was taken as soon as possible

after the end of the filling—usually about 8 s—so that minimal settling occurred. Each measurement took about 5 s. The tube temperature was measured on a thermocouple thermometer reading to 0·1°C.

After the suspension had completely settled out, the rigid end was removed and the weight of settled dust was measured. In advance of the experiment, a circular thin polythene membrane had been weighed and coupled to the rigid end by a film of oil; at the end of the experiment it was removed and weighed. A balance with 0·1 mg resolution was used. Typically, between 0·3 and 0·8 g of dust was collected, representing about 5% of the dust introduced into the tube; the rest either vented into the bag or adhered to the tube walls.

4 COMPUTATIONAL PROCEDURE

The measured impulse response of the system included the effect of amplifiers, filters, microphone and loudspeaker, as well as the dust-air-tube-end system. Consider two measurements of system impulse response: without dust (air-filled tube) $x_a(t)$, and immediately after the introduction of dust (suspension-filled tube), $x_s(t)$.

Let the direct pulse, extracted from $x_a(t)$ by a rectangular window between t_1 and t_2, be represented by $x_a^0(t)$:

$$x_a^0(t) = \begin{cases} x_a(t) & \text{for } t_1 \le t \le t_2 \\ 0 & \text{otherwise} \end{cases} \tag{1}$$

Similarly, let the first reflection, between t_2 and t_3, be represented by $x_a^1(t)$.

These pulses may be transformed to the frequency domain:

$$\begin{aligned} x_a^0(t) &\xrightarrow{\mathcal{F}} X_a^0(f) \\ x_a^1(t) &\xrightarrow{\mathcal{F}} X_a^1(f) \end{aligned} \tag{2}$$

This gives the spectral content of the incident pulse, and the pulse modified by two passes of the air column and a reflection from a rigid boundary.

The transfer function of the dust-free system may be calculated from:

$$H_a = \frac{X_a^1}{X_a^0} \tag{3}$$

In this way, the effects of amplifiers, speaker, microphone and filters are cancelled.

The process of windowing and forming spectra, may be repeated on the impulse response of the dust-filled tube, $x_s(t)$:

$$x_s^0(t) \xrightarrow{\mathcal{F}} X_s^0(f)$$
$$x_s^1(t) \xrightarrow{\mathcal{F}} X_s^1(f) \tag{4}$$

to give the transfer function of the dust-filled system:

$$H_s = \frac{X_s^1}{X_s^0} \tag{5}$$

The transfer function of the dust suspension alone, $Y(f)$, may be formed by equalising the transfer function of the dust-air-tube-end system with respect to the air-tube-end system:

$$Y = \frac{H_s}{H_a} \tag{6}$$

The result in eqn (6) is the complex transfer function for a path length, l, of dust suspension. As long as the tube is acting as a waveguide propagating plane waves, which should be the case if it is operated below its upper cut-off frequency, the excess attenuation per unit length and change in phase velocity may be calculated.

Excess attenuation is usually expressed as the dimensionless quantity, specific attenuation $\bar{\alpha}$, which is the attenuation over one wavelength, λ. This quantity was calculated from:

$$\bar{\alpha} = \frac{|Y|}{8{\cdot}9l} \cdot \lambda \qquad \text{if } |Y| \text{ is in dB} \tag{7}$$

Dispersion, β, may be defined, also in a dimensionless manner, as:

$$\beta = \left(\frac{c_a}{c_s}\right)^2 - 1 \tag{8}$$

where c_a and c_s are phase velocities in air and dust suspension, respectively. This difference in phase velocity results in the measured phase, arg (Y), of the transfer function.

Dispersion was computed from:

$$\beta = \left(1 - \frac{c_a \cdot \arg(Y)}{2\pi f l}\right)^2 - 1 \tag{9}$$

The value of c_a was estimated either from the measured air temperature, or from the time-of-flight of pulses over the known tube length.

Finally, the values of $\bar{\alpha}$ and β were calculated for three time series points, about 10, 15 and 20 s after the process of dust introduction on

each occasion had finished (defined as $t = 0$ s), and values were extrapolated back to $t = 0$ s, thus compensating for settling of dust during the delay before the first measurement.

The volume concentration, ϕ, was calculated from the mass of settled dust, m:

$$\phi = \frac{m}{\rho V} \tag{10}$$

where V is the volume of the metal tube, and ρ is density of the alumina used (3800 kg m^{-3}).

4.1 A note on windowing

The windowing stage (eqn (1)), represents a deconvolution in the time domain. Extracting the direct pulse yields the impulse response of the electronic system, and is viewed as the 'input' to the dust-air-tube system. The windowed first reflection is viewed as the modified impulse response i.e. the 'output' of the latter system. To achieve a valid deconvolution, it is necessary that each of the pulses ('input' and 'output') rise from and fall to zero within its own window, and does not contain other reflections. Hence it is important that the pulses are clearly separated.

In fact, the window used was a half Blackman-Harris window (not rectangular): this window is unity at $t = 0$, and tapers to zero at the record end. It has a broad main lobe, which filters the frequency spectrum slightly. Despite the 2·4 kHz low-pass filter, some ripple on the impulse response was noticeable, and tended to increase the spectral noise: windowing helped to reduce the noise.

The start and end points (t_1, t_2 and t_3, see Fig. 2) of the direct and reflected pulse windows must remain constant for a given dataset, to preserve the correct energy content and phase relationships.

5 RESULTS AND DISCUSSION

Five measurements were made with each of the three dust sizes in suspension. The concentration of each suspension was measured, and the results normalised to a value of volume fraction of 10 ppm; assuming a linear dependence on concentration. Measured values ranged from 6 to 18 ppm.

Figures 3(a) and (b) show the mean values of the measured specific attenuation and dispersion, respectively. Figures 4(a) and (b) show the corresponding curves predicted using a multiple scattering model.[2] This model is valid for spherical particles with radius ≪ wavelength.

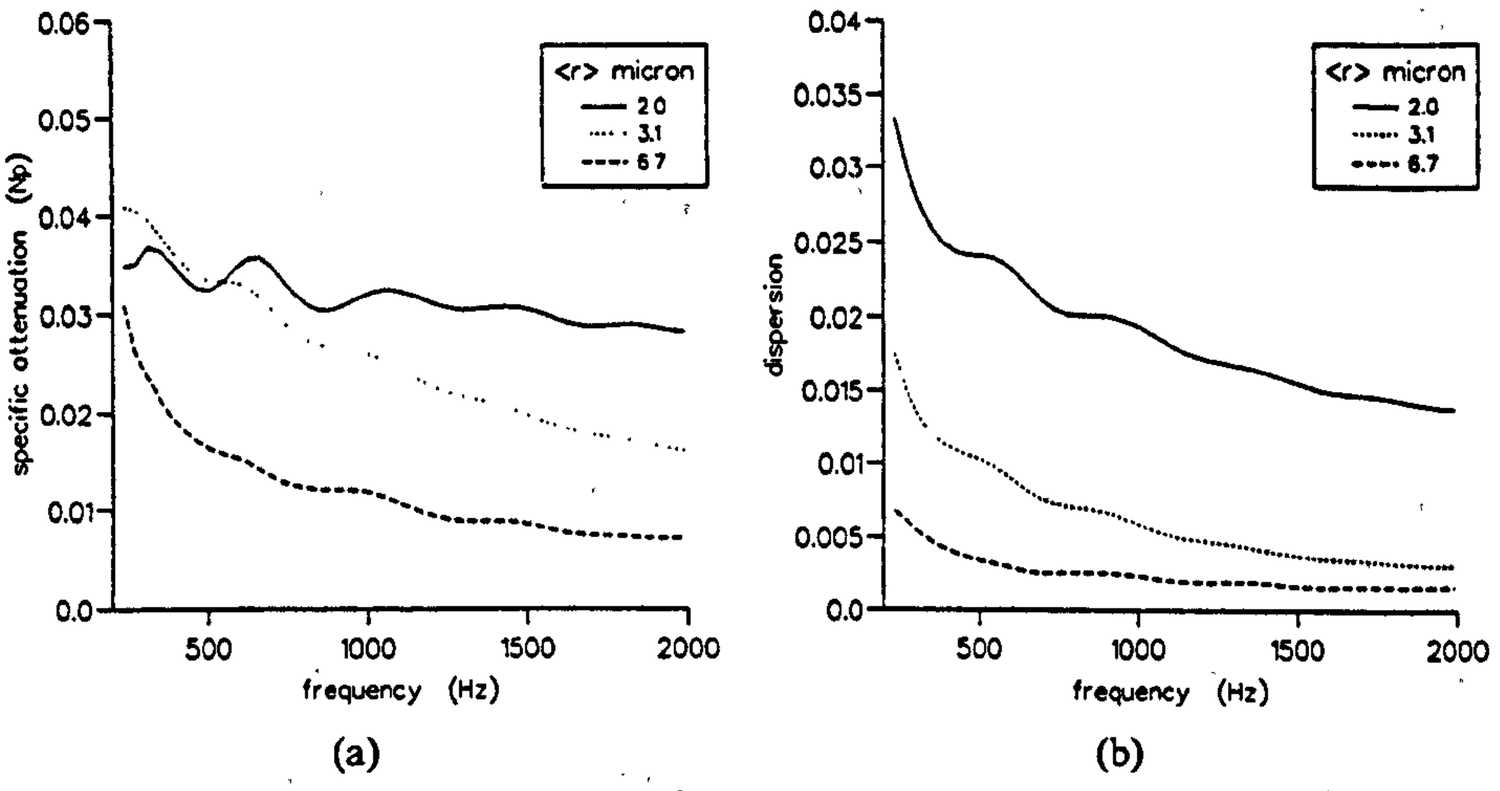

Fig. 3. Mean of measured values: (a) specific attenuation; (b) dispersion.

The measurements show less frequency-dependence than predicted. This is especially the case for the smaller particle sizes. The 2·0 μm dust shows very much larger dispersion values than predicted. It is thought that this is due to non-sphericity of the alumina particles: cleavage surfaces are clearly visible through a scanning electron microscope, and the presence of these surfaces is likely to mean that non-sphericity is more pronounced at smaller radii.

Little difference is predicted between the acoustical effects of the 2·0 and 3·1 μm distributions; this is because, despite the different values of mean radius, the 2·0 μm distribution has a larger standard deviation.

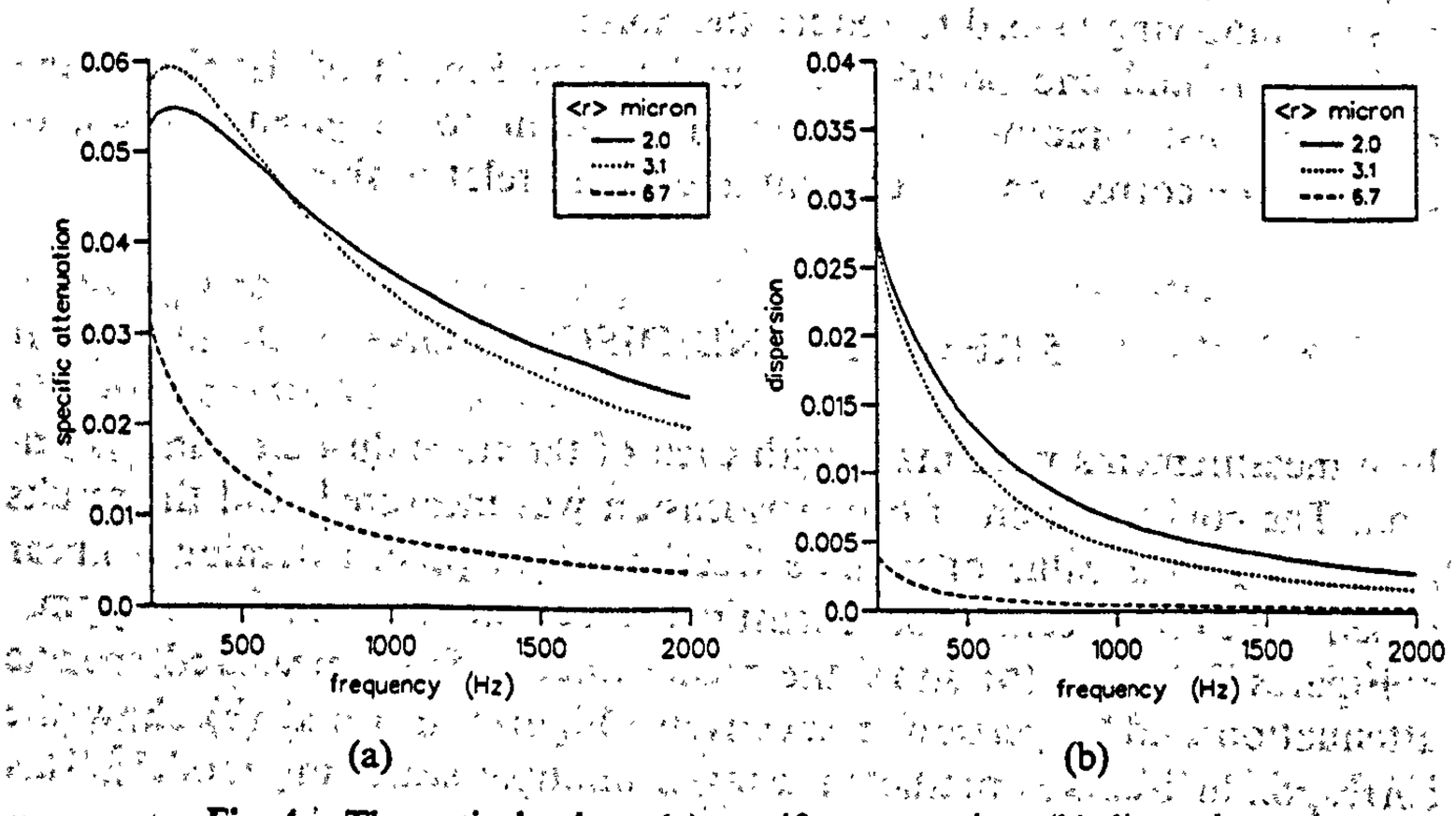

Fig. 4. Theoretical values: (a) specific attenuation; (b) dispersion.

However, the measured attenuations and dispersions show much greater divergence than predicted.

The model assumes a uniform concentration of particles. However, the concentration in the tube will be non-uniform, with a larger concentration towards the base of the tube; the measured concentration will be a mean value for the tube volume. Since attenuation and dispersion are integrated over the path length of the first reflection then, as long as they are both linearly related to concentration, the measured values will depend only on the mean value of concentration. Indeed, a simpler model based on relaxation theory[3] predicts that, at these low concentrations, there is a linear dependence on concentration.

Measured specific attenuation values for the two smaller dusts are lower than predicted at frequencies below 1000 Hz, and exhibit a periodic ripple. It is possible that the ripple is due to a reflection caused by the change in section. A new apparatus is being constructed with uniform section to eliminate this effect.

6 CONCLUSIONS

An apparatus has been designed to measure low frequency attenuation and dispersion of sound waves in a suspension of dust in air. The measured values are in general agreement with theoretical predictions. These measurements have shown that an acoustical technique is able to discriminate between different particle size distributions. The measured differences in attenuation and dispersion between distributions are larger than predicted. This is thought to be due to non-sphericity of the particles.

ACKNOWLEDGEMENTS

This work is supported by S.E.R.C. The authors would like to express their gratitude to Dr A. Watson for his invaluable advice, and to Mr P. Seabrook for his practical advice and help.

REFERENCES

1. Vanderkooy, D. D., 'Transfer-function measurement with maximum-length sequences'. *J. Audio Eng. Soc.*, 37(6) (1989) 419–43.
2. McClements, D. J., 'Comparison of multiple scattering theories with experi-

mental measurements in emulsions'. *J. Acoust. Soc. Am.*, 91(2) (1992) 849–53. McClements' modified form of the Waterman & Truell model is used.

3. Temkin, S. & Dobbins, R. A., 'Attenuation and Dispersion of Sound by Particulate-Relaxation Processes'. *J. Acoust. Soc. Am.*, 40(2) (1966) 317–24.

APPENDIX F

MATERIAL PROPERTIES

F.1 PHYSICAL PROPERTIES

To enable predictions to be made about the acoustic effect of the suspended materials, some knowledge is needed about the physical properties of the solid and suspending fluid. In decreasing order of importance, the properties required for scattering theory are:

- Particle radius (a) distribution
- Gas & particle density ρ (not bulk density)
- Specific heat capacity C_p
- Thermal conductivity κ
- Thermal expansion coefficient Θ
- Speed of sound c (compressional waves in solid).

The physical properties that were used in theoretical models are tabulated in Table F-I.

	ρ (kg m^{-3})	c (m s^{-1})	C_p (J kg^{-1} K^{-1})	Θ (K^{-1})	κ (J s^{-1} K^{-1} m^{-1})	μ (N s m^{-2})
Air	1.2	343	1005	3.33×10^{-3}	0.024	1.85×10^{-5}
Alumina [1]	3800	5000	769	2.65×10^{-5}	20.0	–
Flour	1500†	2080[2]	1250[3]	2.65×10^{-5} ‡	20.0 ‡	–
Olivine sand[4]	3200†	5660 [5]	830 [6]	5.4×10^{-6} [5]	6.92 [5]	–

Table F-I Physical properties of relevant materials.

F.2 PARTICLE SIZE DISTRIBUTION (PSD)

F.2.1 Alumina

Although the manufacturer supplied a measured PSD for each alumina sample (measured using a photosedimentometer), the figures presented here were measured from samples collected after settling out in the quasi-static rig. This was done because the process of filling the tube involves venting the excess suspension, and so there is the potential to change the PSD away from that which was supplied.

The measurement was performed on a wide-angle scanning photosedimentometer (WASP). To test the accuracy of the device, and the analysis software that was written for it, a sample from the manufacturer was tested (without first settling in the tube). The measured PSD is compared to the manufacturer's data in Figure F-1.

---

[1] All figures for alumina are from the suppliers: Washington Mills Electro Minerals Ltd, Mosely Road, Trafford Park, Manchester, M17 1NR

† Measured values

[2] This is the value for cellulose acetate butyrate [44]

[3] The thermal properties of flour are not well characterised. This figure is an average for various proteins [44]

‡ In the absence of any available data, the figures for alumina have been arbitrarily substituted.

[4] Olivine describes a family of minerals with the composition Mg_2SiO_2-Fe_2SiO_4 [124]. Consequently, data for silica sand SiO_2 may not be strictly applicable.

[5] This figure is that of crown glass [71]

[6] These figures are those of $MgSiO_4$

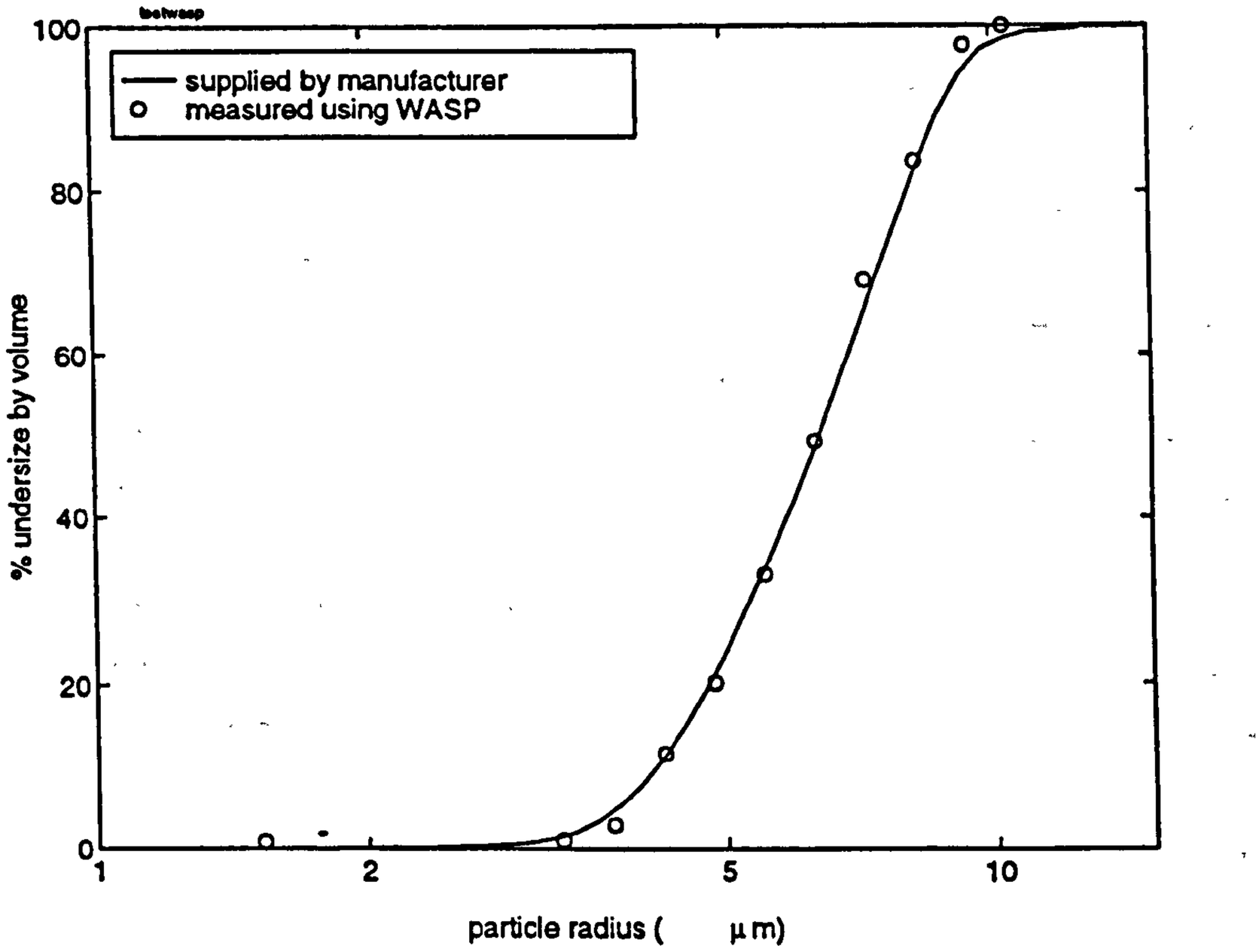

Figure F-1 *Measured PSD (using the WASP) of F500 grade alumina, compared to the manufacturer's supplied data.*

The two measurements are very close, giving confidence in the measurements from the WASP. The measured PSDs for the settled samples are tabulated (where appropriate) below, and plotted together in Figure F-2.

The measured PSD of F800 grade alumina was found to be fitted well by a Rosin-Rammler distribution (see Figure 4-7). The parameters were:

Fineness $\overline{a}_{rr} = 3.4\,\mu m$, dispersion $\sigma_{rr} = 4.5$.

The PSDs of F1000 and F1200 grades were too skewed to be approximated by a Rosin-Rammler distribution, and so the figures are tabulated in Table F-II and Table F-III.

Radius (μm)	% by volume	Radius (μm)	% by volume
0.30	0	1.59	3.65
0.633	5.42	1.76	7.00
0.701	1.10	1.95	4.97
0.777	3.36	2.16	3.85
0.861	1.84	2.39	3.71
0.953	1.62	2.65	5.32
1.06	1.77	2.94	9.21
1.17	5.96	3.25	19.00
1.30	8.64	3.60	7.77
1.44	5.19	3.99	0.776

Table F-II *Measured PSD of settled F1000 alumina*

Radius (μm)	% by volume	Radius (μm)	% by volume
3.90	0.5250	1.48	3.43
3.58	0.9710	1.34	5.10
3.25	0.3620	1.21	2.74
2.94	4.66	1.10	4.04
2.67	4.40	0.9740	2.63
2.42	0.8150	0.86	3.35
2.19	29.10	0.7760	2.58
1.98	12.10	0.6990	2.40
1.80	9.50	0.63	1.84
1.63	2.60	0.5670	1.40

Table F-III *Measured PSD of settled F1200 alumina*

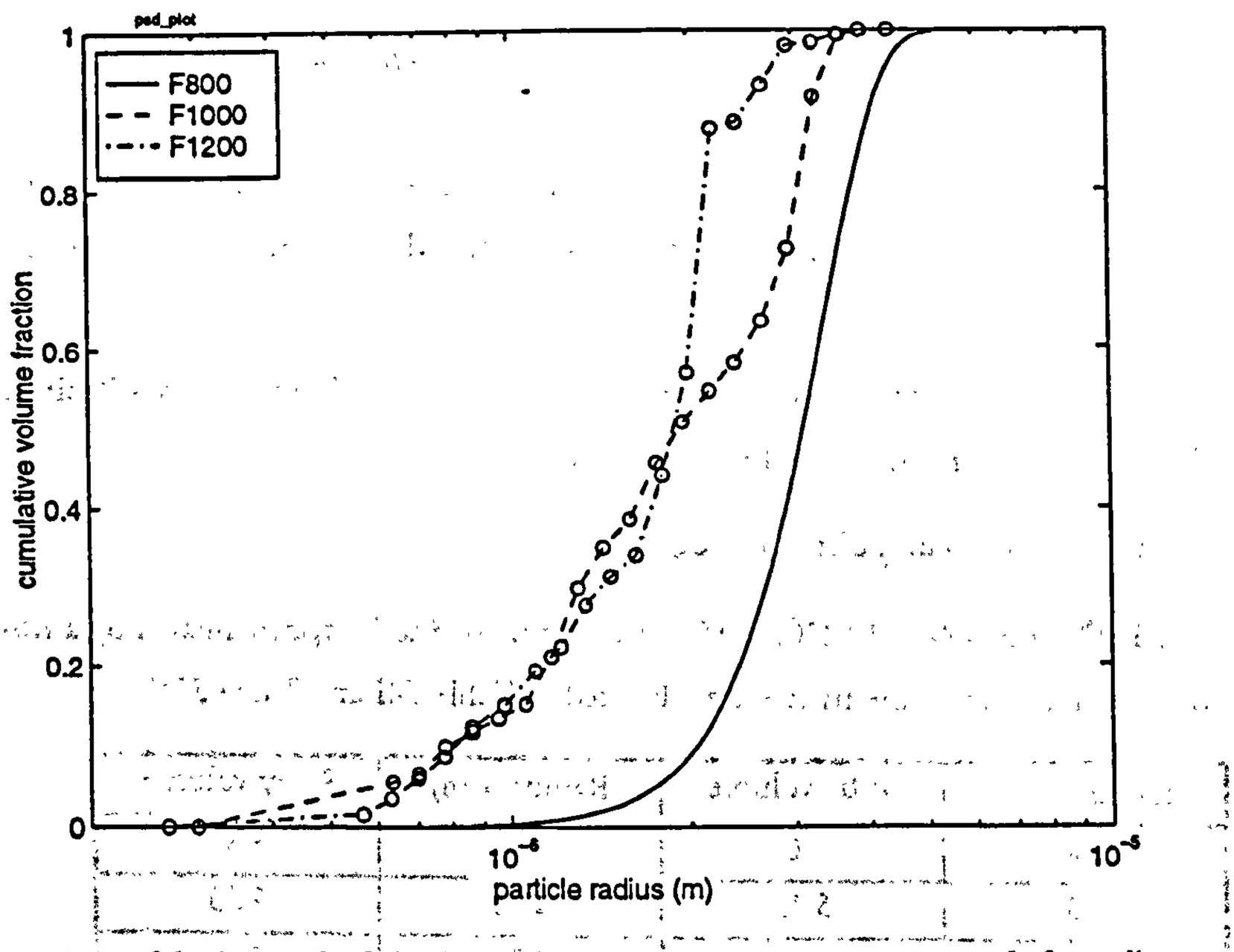

Figure F-2 *PSDs of the three grade of alumina used in quasi-static measurements: measured after settling.*

F.2.2 Flour

A sample of flour, measured early in its "life", had its PSD measured on a laser diffraction particle sizer. The results are tabulated in Table F-IV and plotted in Figure F-3. However, a sample taken soon after an experiment appeared to contain a significant fraction of olivine sand. The sample was sieved, to separate out the much larger sand particles, and the fractions were weighed. The

sand comprised approximately 18% by weight of the sample. Therefore, when predictions are for the effects of flour, the prediction uses the sum of effects of 82% flour, and 18% sand.

Radius (μm)	% by volume	Radius (μm)	% by volume
2.2000	0.3000	14.9000	3.5000
2.5250	0.9000	17.2750	2.8000
2.9250	1.1000	20.0000	2.1000
3.4000	1.8000	23.1750	2.3000
3.9500	1.9000	26.8750	3.6000
4.5750	1.6000	31.1500	5.3000
5.3000	1.8000	36.1000	6.7000
6.1500	2.8000	41.8500	7.9000
7.1250	4.4000	48.4750	8.3000
8.2500	5.0000	56.2500	8.4000
9.5500	5.0000	65.2500	6.9000
11.0750	4.7000	75.5000	4.9000
12.8500	4.1000	87.5000	1.9000

Table F-IV *The PSD of a flour sample, taken from the flow rig, measured by a Malvern Mastersizer.*

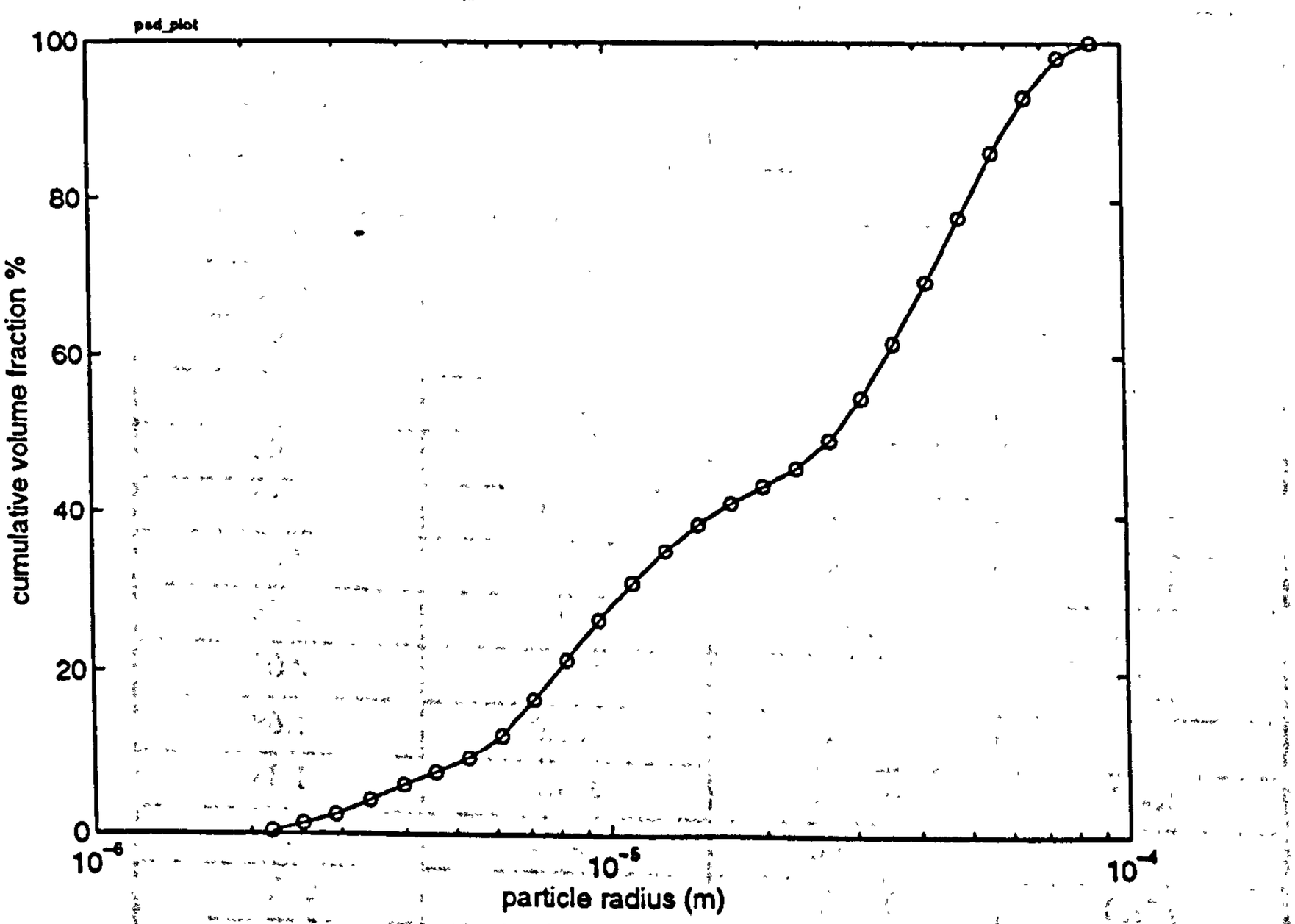

Figure F-3 *The PSD of a flour sample, taken from the flow rig, measured by a Malvern Mastersizer.*

F.2.3 Olivine sand

The measured PSD is tabulated in Table F-V and plotted in Figure F-4.

Radius (μm)	% by volume	Radius (μm)	% by volume
86.3	0.0118	195.0	0.95
88.1	0.0132	199.0	1.05
89.9	0.0148	203.0	1.16
91.8	0.0165	207.0	1.28
93.6	0.0185	211.0	1.41
95.6	0.0207	216.0	1.55
97.5	0.0231	220.0	1.70
99.5	0.0259	225.0	1.86
102.0	0.0289	229.0	2.03
104.0	0.0323	234.0	2.21
106.0	0.0362	239.0	2.40
108.0	0.0404	244.0	2.59
110.0	0.0452	249.0	2.79
112.0	0.0505	254.0	2.99
115.0	0.0565	259.0	3.19
117.0	0.0631	264.0	3.39
120.0	0.0705	270.0	3.57
122.0	0.0788	275.0	3.74
124.0	0.0881	281.0	3.88
127.0	0.0984	287.0	4.0
130.0	0.1100	293.0	4.08
132.0	0.1230	299.0	4.11
135.0	0.1370	305.0	4.1
138.0	0.1530	311.0	4.03
141.0	0.1710	317.0	3.90
144.0	0.1910	324.0	3.71
147.0	0.2130	331.0	3.46
150.0	0.2380	337.0	3.17
153.0	0.2650	344.0	2.83
156.0	0.2960	351.0	2.46
159.0	0.3300	359.0	2.07
162.0	0.3680	366.0	1.69
166.0	0.4090	374.0	1.33
169.0	0.4560	381.0	1.00
172.0	0.5070	389.0	0.721
176.0	0.5640	397.0	0.492
180.0	0.6270	405.0	0.317
183.0	0.6960	413.0	0.192
187.0	0.7720	422.0	0.108
191.0	0.8560		

Table F-V *PSD of a sample of olivine sand, taken from the flow rig, measured by a Malvern Mastersizer.*

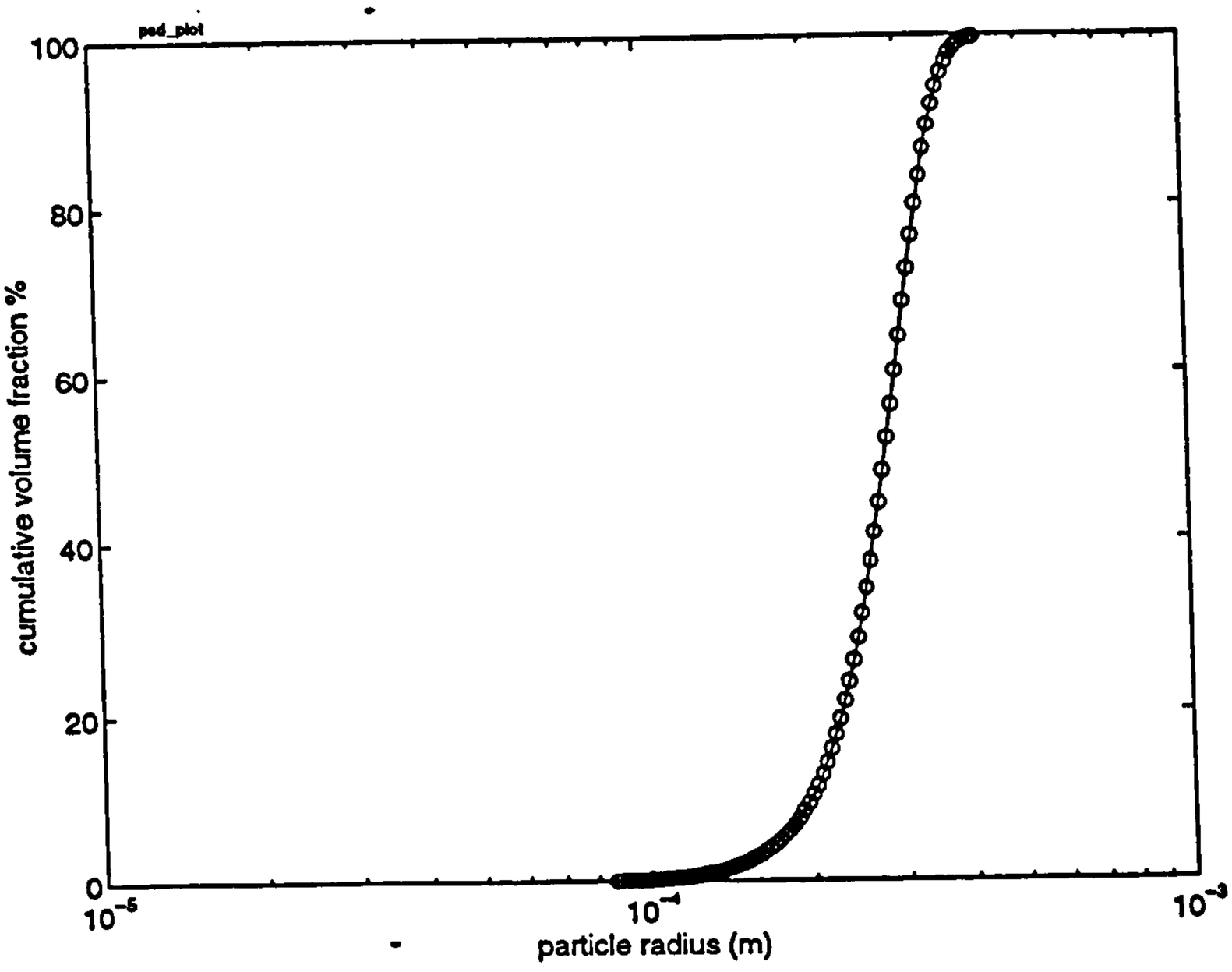

Figure F-4 *The PSD of a sample of olivine sand, taken from the flow rig, measured by a Malvern Mastersizer.*

F.2.4 Pulverised fuel (PF)

The PSDs of three grades of PF were measured by Woodhead [158], and are referred to in this work. They are plotted together in Figure F-5.

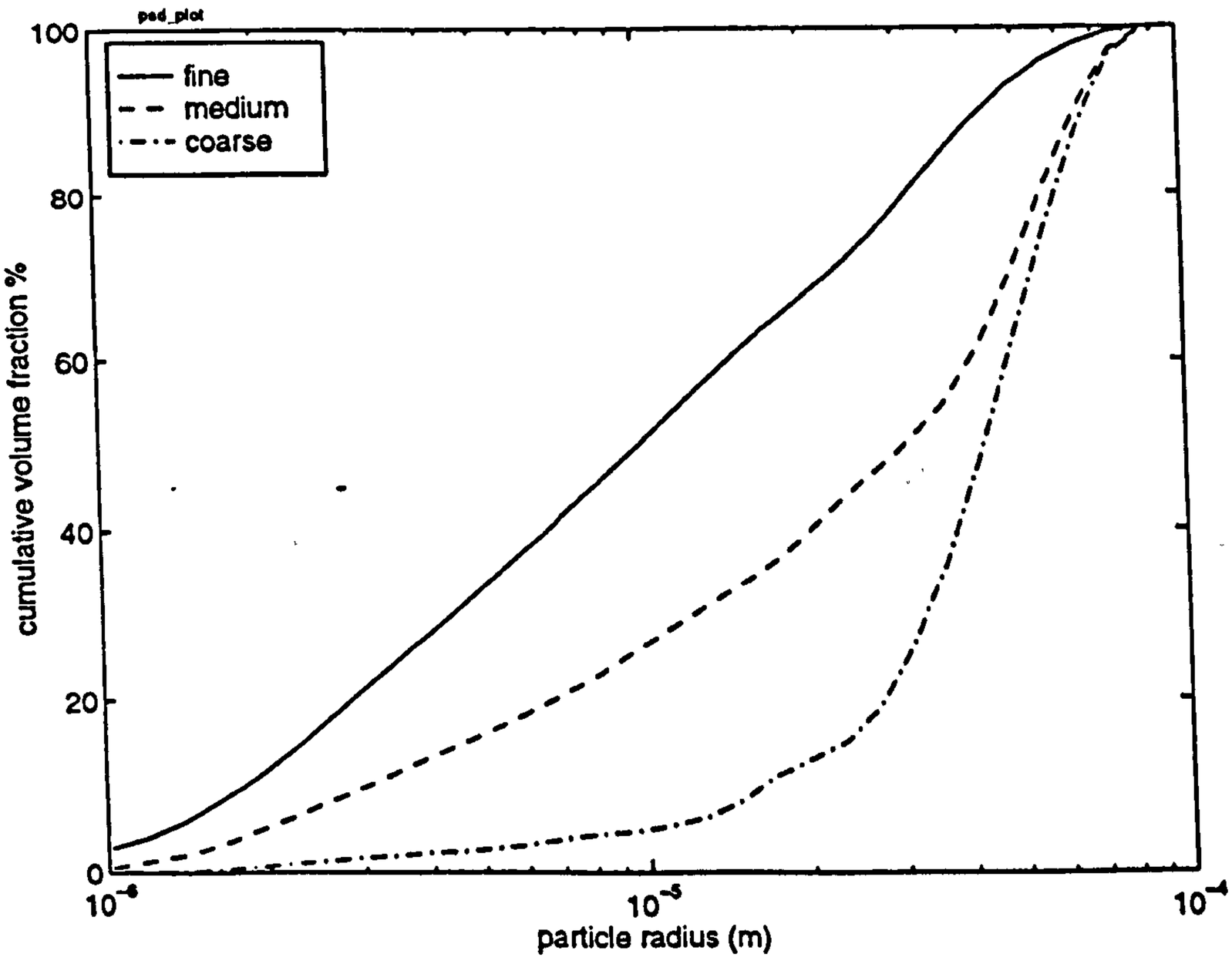

Figure F-5 *The PSD of three grades of pulverised fuel: fine, medium and coarse. Reproduced from Woodhead [158].*

APPENDIX
G
PHASE ACCURACY OF
DISPERSION MEASUREMENTS

This appendix is a justification of the experimental technique used in Chapter 6 to measure sound speed dispersion.

G.1 INTRODUCTION

If a pulse is transmitted through a suspension, the time of arrival of the pulse will be delayed (relative to clean air), and the pulse shape will change due to the frequency-dependent sound velocity. There are two main ways of characterising the velocity:

- The frequency domain method uses the change in spectrum of the pulse due to the suspension. The phase angle of the spectrum with the suspension, relative to the spectrum with clean air, can yield the frequency-dependent phase velocity in the suspension.
- The time-domain method measures the time of arrival of the pulse: this corresponds to measuring the group velocity of the pulse. This is the technique adopted, for example, by Steen [138] and Zink & Delsasso [166]. Group velocity is a concept which is only valid for pulses of comparatively narrow bandwidth, since it is assumed to be independent of frequency. Practically, it can be difficult to measure (see Lynnworth [87] p.189 for a discussion).

In section 2, a simple theoretical development will shown that, if the data are recorded by a sampled data system (that is, an A/D converter) then the quantisation effects in both time and amplitude will always be expected to make the frequency domain approach more sensitive and accurate.

In section 3, results of a model of a sampled data system demonstrate graphically the advantages of using the frequency domain approach, providing that the data is recorded digitally.

G.2 THEORETICAL TIME RESOLUTION OF SAMPLED DATA SYSTEMS

The following simple theory aims to show, non-rigorously, the minimum time resolution which is achievable by both time and frequency domain approaches.

Consider the leading edge of a signal $v_1(t)$, such that:

$$\begin{aligned} v_1(t) &= 0 \qquad t \le 0 \\ v_1(t) &= v' t \qquad t > 0 \end{aligned} \tag{G.1}$$

where v' is the voltage slew rate, in V/s. A second identical signal $v_2(t)$ is delayed by Δt with respect to the first,

$$\begin{aligned} v_2(t) &= 0 \qquad t \le \Delta t \\ v_2(t) &= v'(t - \Delta t) \qquad t > \Delta t \end{aligned} \tag{G.2}$$

They are sampled at a sampling frequency of f, by an A/D converter with N bits effective resolution (ie. N bits span the amplitude of the signal).

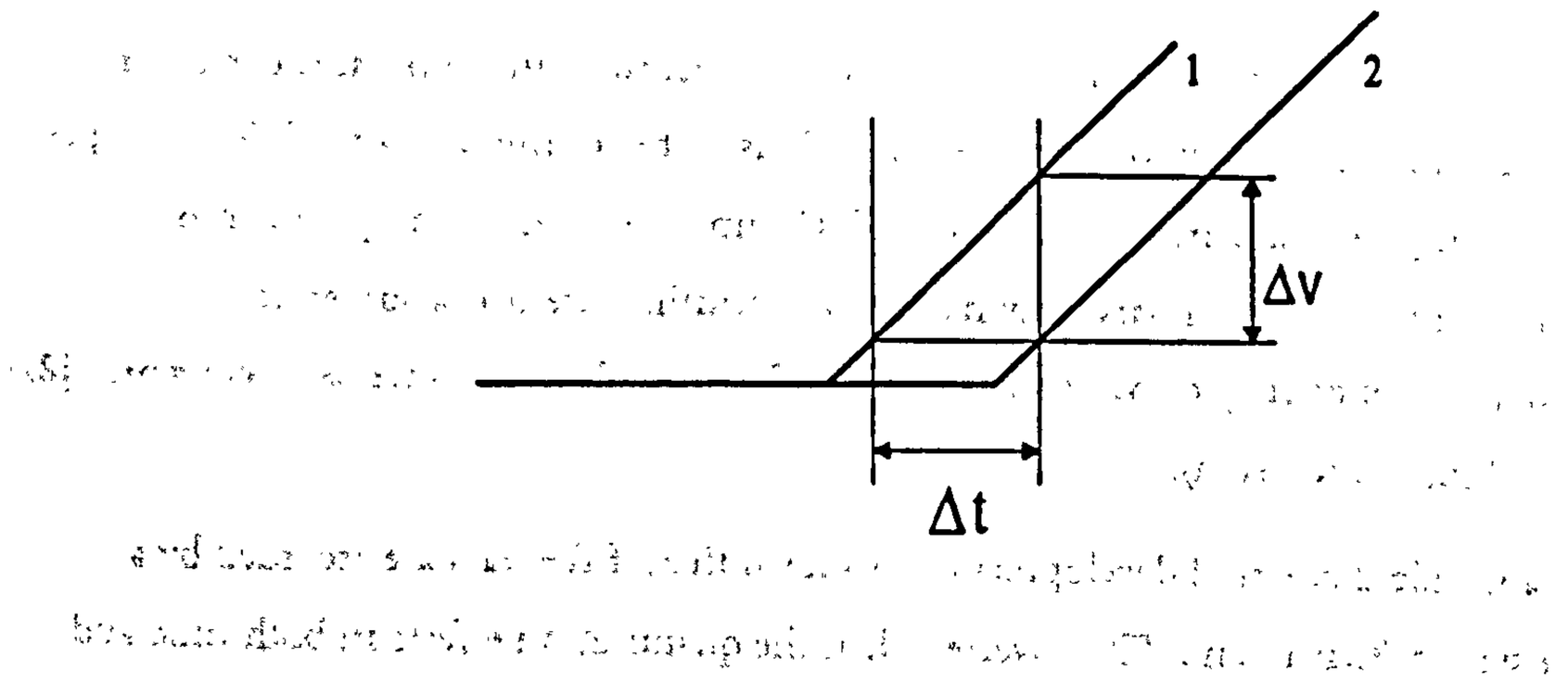

After quantisation, a small time lag may be detected by differences in the phase alone (Figure G-1), or in the amplitude alone (Figure G-2), or in both phase and amplitude.

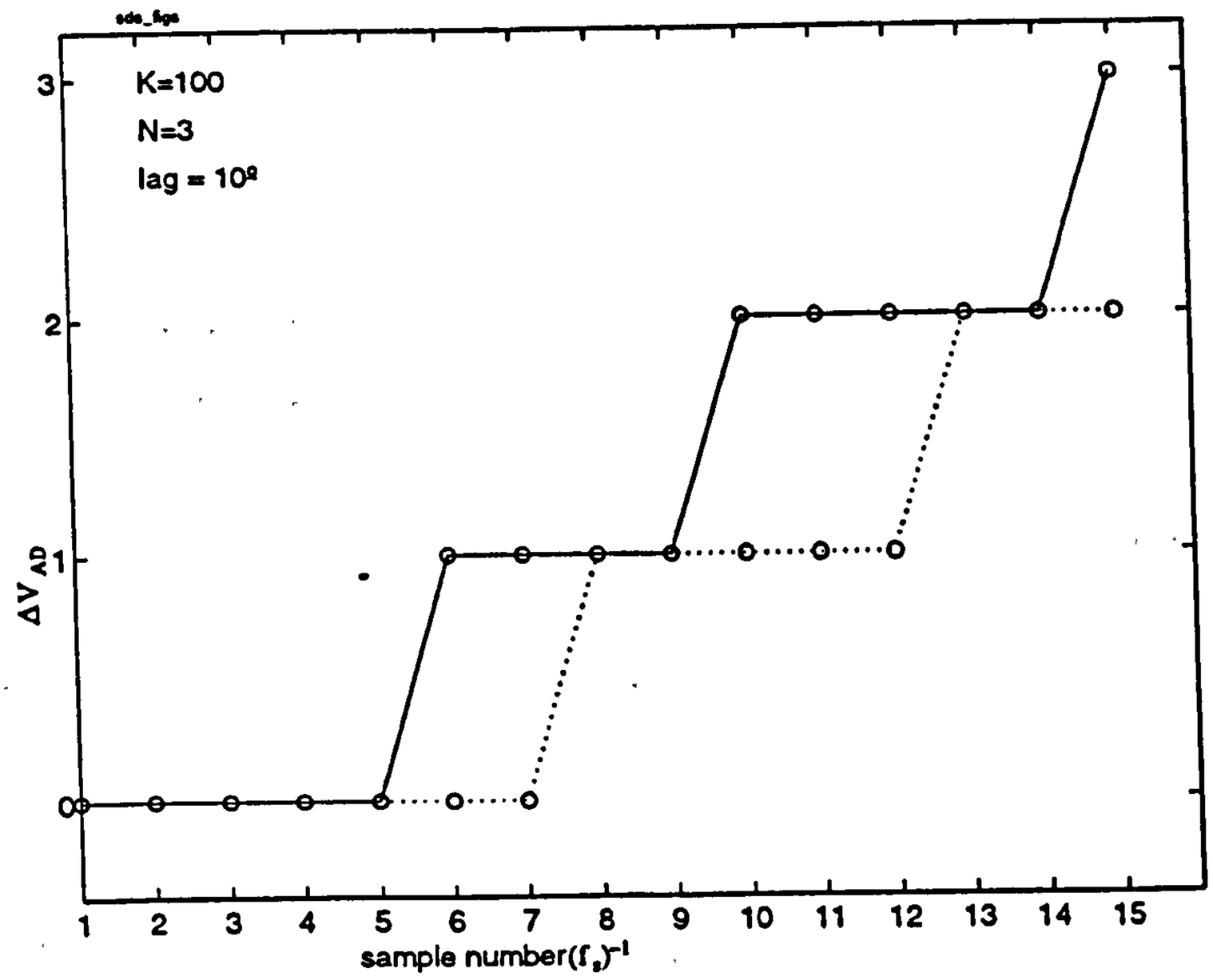

Figure G-1 *Quantised waveform, with phase detection through phase shift only.*

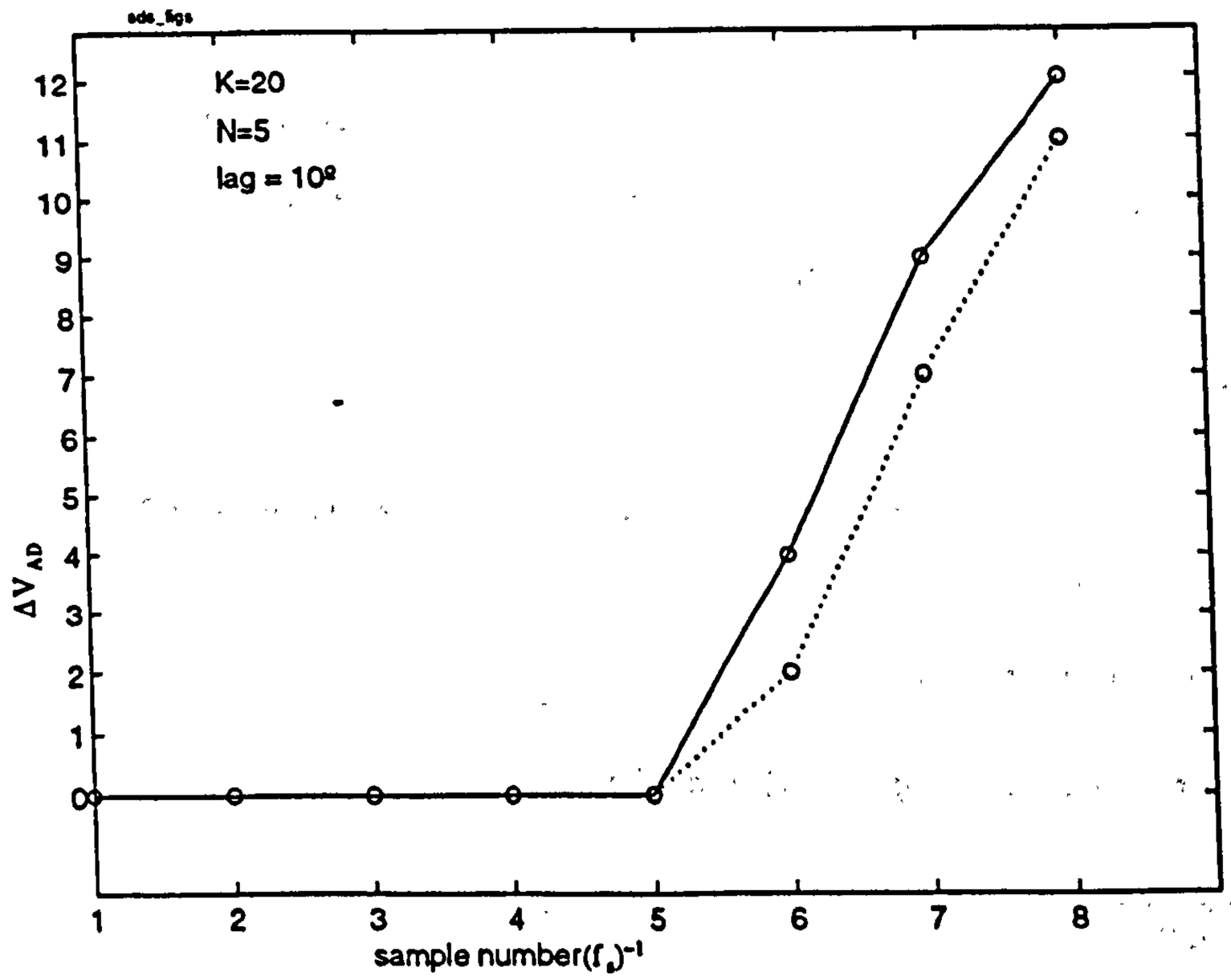

Figure G-2 *Quantised waveform, with phase detection through amplitude shift only*

It can be seen that there is a symmetry between time and amplitude quantisation, and that the relative resolution of time and amplitude sampling will determine which is the limiting factor.

G.2.1 Phase shift detection

The criterion for the guaranteed detection of the time delay due to phase shift is simply,

$$\Delta t_\phi \geq 1/f_s \tag{G.3}$$

Note that it is possible that the shift could be detected with a smaller delay than Δt_ϕ, depending on the relative phase of the sampling clock with respect to the timebase t.

G.2.2 Amplitude shift detection

The criterion to ensure the guaranteed detection due to an amplitude shift is that the voltage difference Δv at a given sample equals or exceeds the voltage resolution Δv_{AD} of the A/D converter,

$$\Delta v \geq \Delta v_{AD} \tag{G.4}$$

Knowing the voltage slew rate, we can calculate the minimum guaranteed time shift which can be detected,

$$\Delta t_a \geq \frac{\Delta v_{AD}}{v'} \tag{G.5}$$

Consider the case where the signal is a burst of sinewaves, of amplitude A, angular frequency $\omega=2\pi f$. If the A/D converter spans the full voltage range of $2A$, then we can calculate the voltage resolution, knowing that an N bit A/D converter has 2^N levels,

$$\Delta v_{AD} = \frac{2A}{2^N} = A \cdot 2^{-(N-1)} \tag{G.6}$$

Furthermore, we know the maximum slew rate of the sine wave, and so we choose this point for the best case detection,

$$v' = \max\left[\frac{d}{dt}(A\sin\omega t)\right] = A\omega \tag{G.7}$$

Substituting equations (G.6) & (G.7) into (G.5):

$$\Delta t_a \geq \frac{1}{\omega 2^{N-1}} \tag{G.8}$$

G.2.3 Comparison of techniques

The time domain measurement of time lag relies on the detection of phase shift, and so its detection limit is bound by equation (G.3). In addition, its resolution is poor, since it can only measure time shift as an integer multiple of sample intervals (unless interpolation is used).

The frequency domain technique involves Fourier transforming the entire record. It is therefore postulated that a time lag will be detected if either phase or amplitude shift is detected (as will be demonstrated in section 3). Hence the method will be superior to time domain measurement if,

$$\Delta t_a < \Delta t_\vartheta \tag{G.9}$$

Substituting equations (G.8) & (G.3),

$$\frac{1}{\omega 2^{N-1}} < \frac{1}{f_s}$$

$$K < \pi 2^N \tag{G.10}$$

where $K = \frac{f_s}{f}$, the oversampling ratio (ie. the number of samples per cycle).

To take an example, if N = 10 bits, then the sensitivity of time domain measurement will only match that of the frequency domain if $K > 3200$; so if the frequency of interest is 2kHz, then it must be sampled at $f_s > 6.4$ MHz. This is well above the limit of affordable PC-based A/D converters.

Clearly, if this analysis is correct, then the sensitivity of frequency domain measurement is superior in almost every conceivable instance, and it is never inferior. Furthermore, its resolution is higher due to the analysis of a greater quantity of data.

Note that both phase and amplitude shift are affected by changes in signal amplitude – leading to time measurement errors if uncorrected. Time domain measurement usually relies on setting the detection threshold either at a zero-crossing point, or where the voltage slew rate is high, to try to minimize this source of error.

The frequency domain technique is insensitive to amplitude changes since the Fourier spectrum separates out amplitude and phase differences.

G.3 DEMONSTRATION OF PHASE ACCURACY

A program[1] was written in MATLAB to simulate the effects of time and amplitude quantisation. The test signals used were two bursts of 2 sine wave cycles with a relative phase shift of $\Delta\Theta$ between them. The phase shift was measured using both the time domain $\Delta\Theta_t$ and the frequency domain $\Delta\Theta_f$ methods . Measured values were plotted against actual values, for various values of N and K. The modeled measurements are calculated for values of N & K typical for MLSSA measurements. The results are shown in Figure G-3 for two different values of oversampling.

[1] The program suite (PUL_LAG, PUL_NOI & PULSE) is listed in Appendix B.

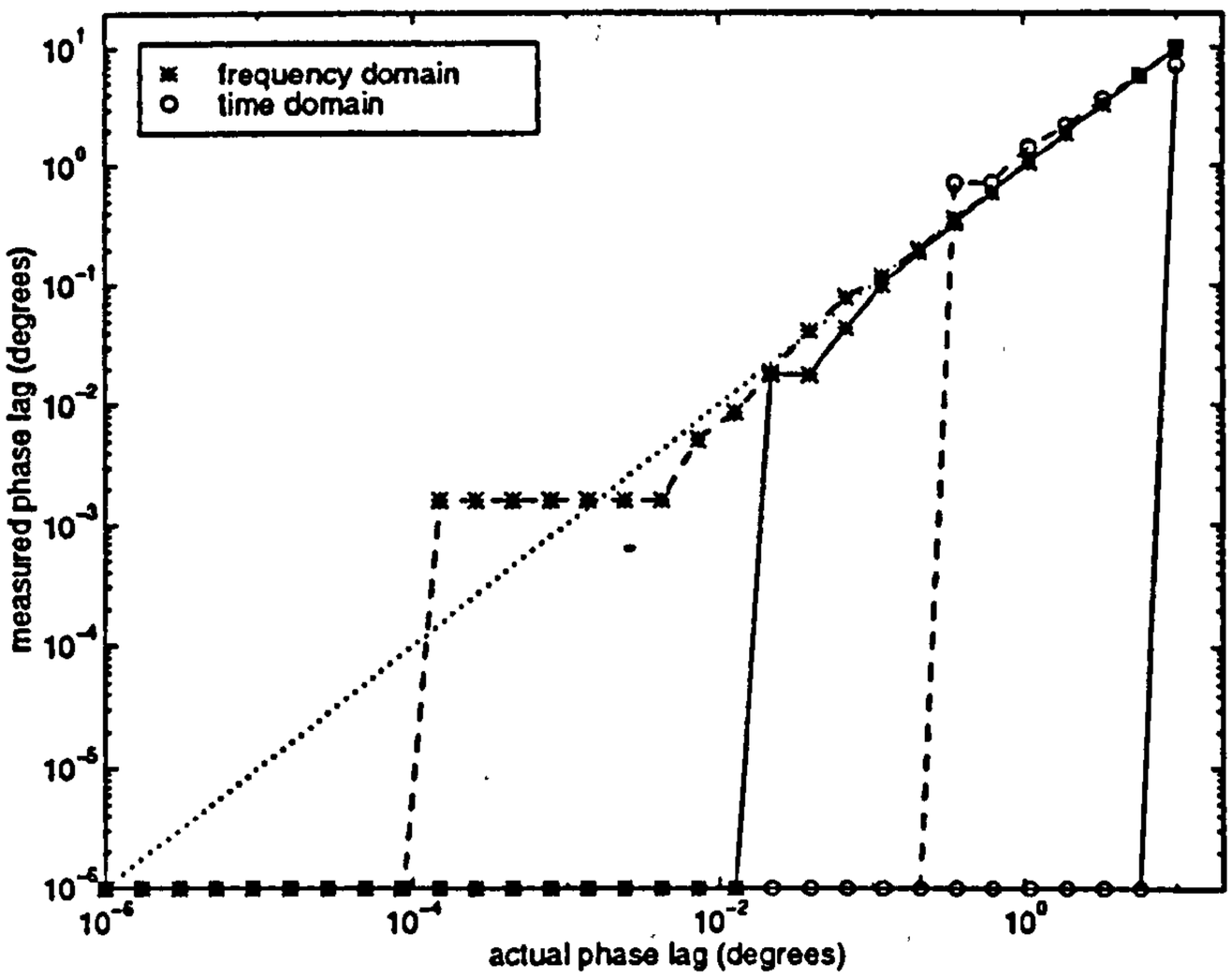

Figure G-3 *Effect of K on measured phase lag for N = 9, K = 50 (solid line) and 500 (dashed line).*

We can compare the theoretical detection limits with those observed, by converting time to phase delay. From equation (G.3):

$$\Delta\Theta_t = 360\Delta t_0 f = 360 f / f_s = 360 / K \qquad \text{(G.11)}$$

From equation (G.8), if amplitude shift is limiting:

$$\Delta\Theta_f = 360\Delta t_a f = 360 f / \pi f 2^N = 360 / \pi 2^N \qquad \text{(G.12)}$$

So the theoretical detection limits are:

$\Delta\Theta_t = 7.2$ ($K = 50$), $\Delta\Theta_t = 0.72$ ($K = 500$), $\Delta\Theta_f = 0.22°$ (independent of K).

It can be seen that:

1. The actual detection limits are all below the theoretical (guaranteed) limits, as expected.

2. Values of $\Delta\Theta_t$ are slightly below the predicted guaranteed limits, while those of $\Delta\Theta_f$ are significantly so. This may be attributed to the fact that, since the frequency domain approach uses the entire record, then it is far more likely that there will be a chance amplitude shift somewhere in the record.

3. $\Delta\Theta_f$ has a decreased detection threshold for higher values of K, whereas equation (G.12) predicts the threshold to be constant with K. This can probably be explained by the above observation: the higher value of K results in a larger number of samples, and hence an even greater likelihood of a chance amplitude shift detection.

4. While the frequency domain detection threshold is reduced significantly for increased K, the accuracy is poor until a value of $\Delta\Theta_f$ is reached which, as predicted, is independent of K.

The effect of varying N is shown in Figure G-4. It can be seen that, even for a constantly low value of $K = 50$, increasing N will lead to increasingly sensitive frequency domain measurement. The time domain measurement is virtually unaffected[1] by changes in N.

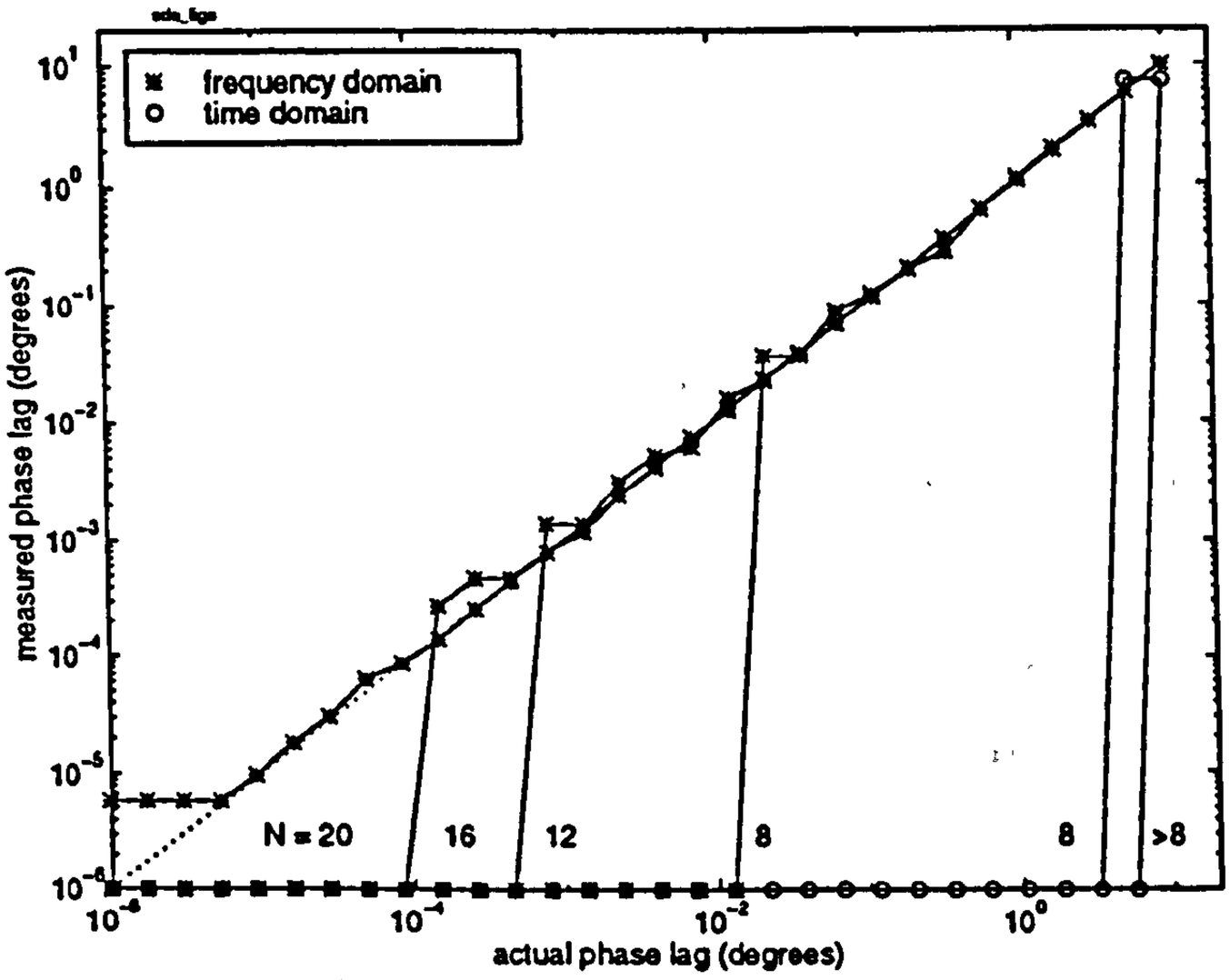

Figure G-4 *Effect of N on measured phase lag for K = 50, N = 8, 12, 16, 20.*

We can investigate whether time domain measurement is ever superior, or whether, as asserted in section 3, frequency domain measurement will always detect both phase and amplitude shifts: we set parameters such that $\Delta t_\theta << \Delta t_a$, guaranteeing that phase shift detection will always be the most sensitive. Figure G-5 illustrates the case for $K = 25 \cdot \pi 2^N$. Frequency domain sensitivity is slightly higher than time domain sensitivity, and its resolution is better, supporting the supposition.

[1] The increase in sensitivity when $N = 8$ is probably due to a lucky coincidence in the positioning of A/D voltage levels.

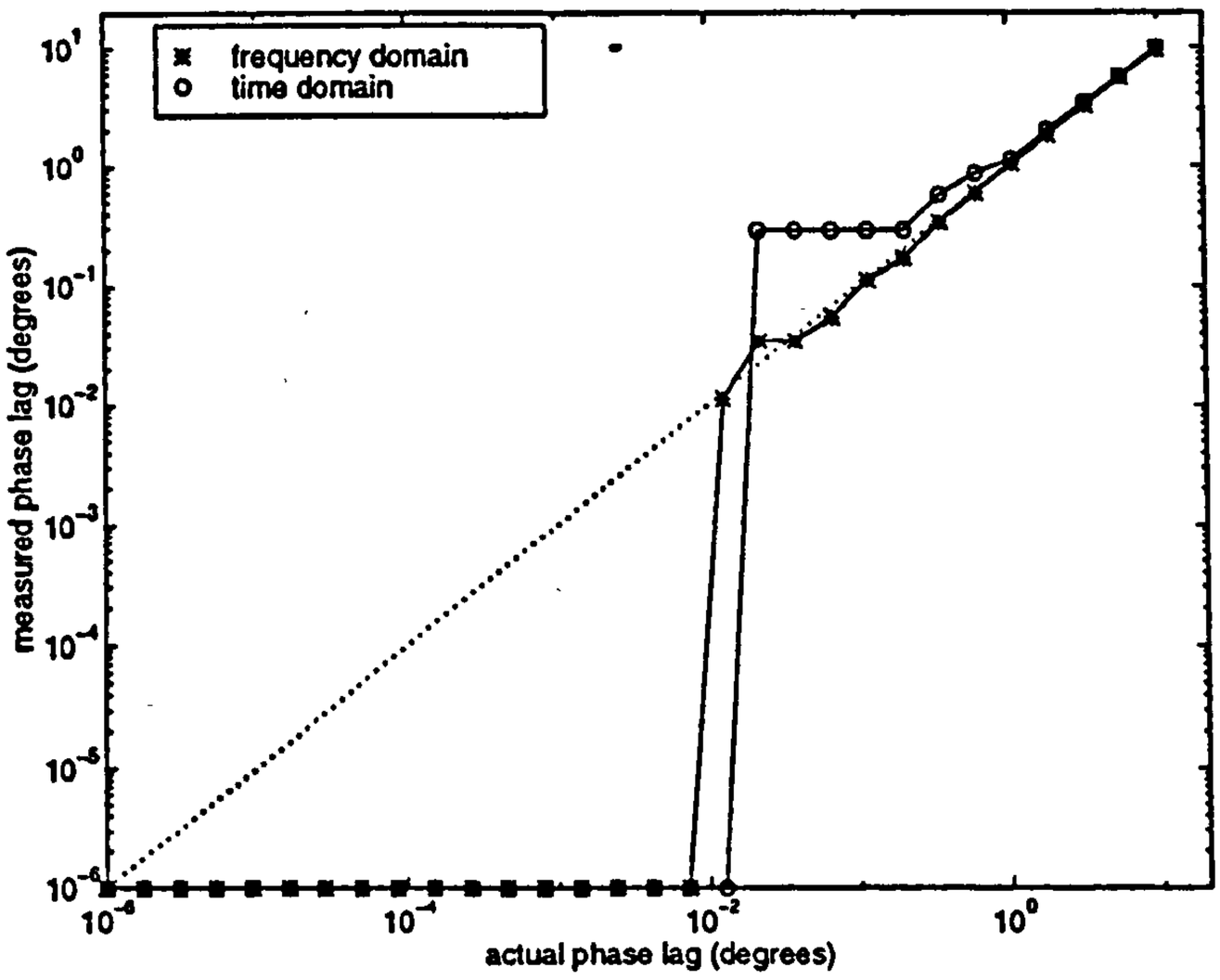

Figure G-5 *Measured phase lag for phase shift detection ($\Delta t_s = 25\ \Delta t_y$). $N = 4$, $K = 1250$.*

Finally, the effect of noise is investigated. Gaussian noise was added to the notional waveform before digitization. The measured phase accuracy was calculated in the frequency domain, and using 2 techniques in the time domain: using a "first arrival" transversal filter algorithm, as described by Jansen et al [69]; and using a simple threshold detection, with the threshold set at 1/2 signal amplitude. The actual phase lag was frozen at a large value of $\Delta\Theta = 20°$ (so that time domain techniques yield good accuracy at low noise), and the phase error[1], is plotted against the relative noise level in dB. The results are shown in Figure G-6.

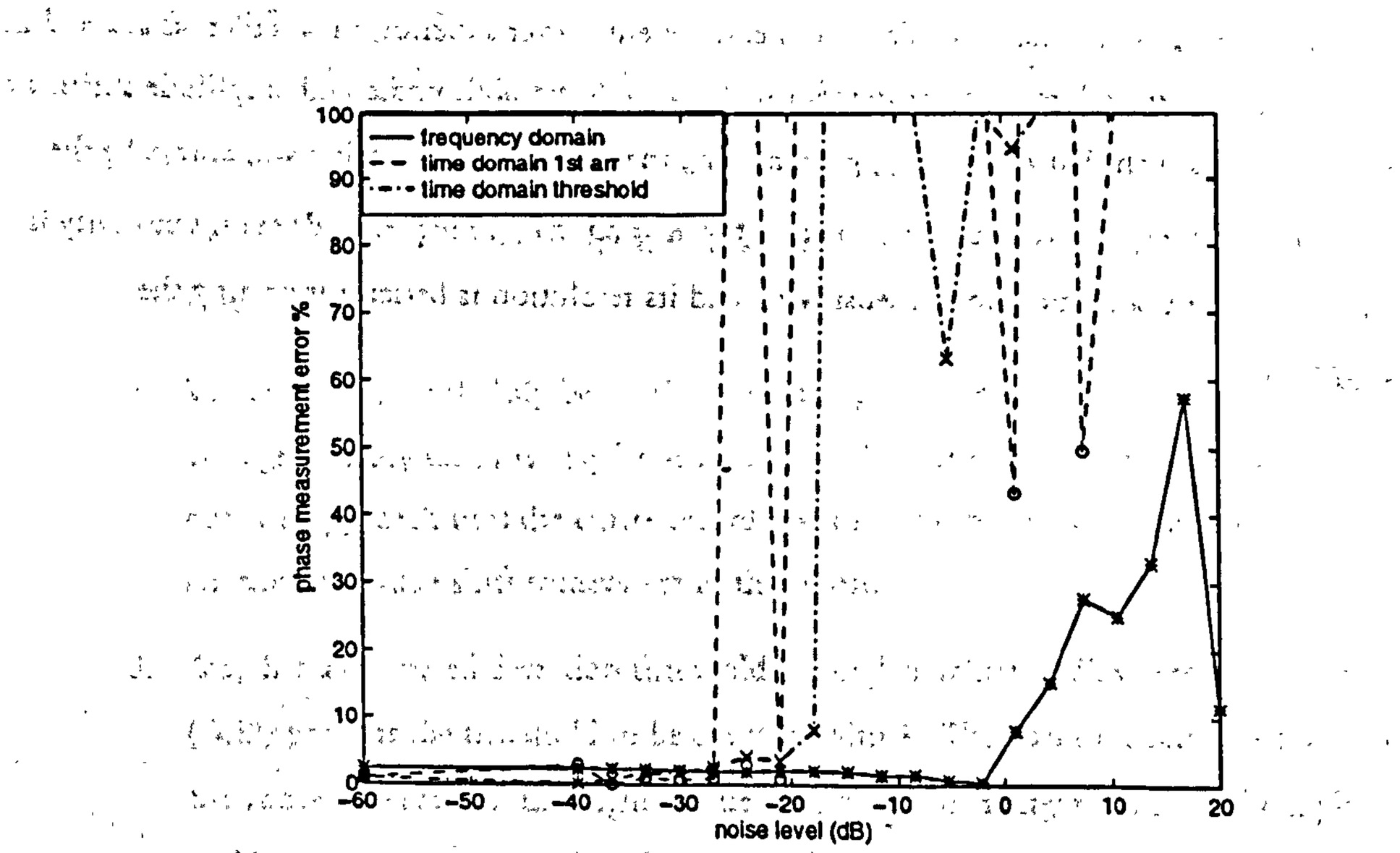

Figure G-6 *Effect of noise level on measured phase error. $K = 200$, $N = 10$, $\Delta\Theta = 20°$.*

[1] The measured phase lags were averaged 20 times to reduce the random effects of the noise.

Clearly, frequency domain measurement maintains reasonable accuracy at higher levels of noise than time domain measurement – up to 0dB instead of -20dB. In the time domain, threshold detection is slightly more resilient than "first arrival" detection, but it is only practical in cases where the signal amplitude is constant or known.

G.4 OTHER SOURCES OF PHASE ERROR

Phase jitter of the A/D converter clock may contribute significantly towards phase error: phase jitter is essentially a random time uncertainty added to each value of sampling time. Following the above analysis, it seems likely that frequency domain measurement will be more resilient to this form of error, since the record-average of the random phase errors will tend to zero.

It is unknown how much of the above analysis is relevant to measurements made using the MLSSA system, due to the extra stage of processing. It is known that additional manipulation in the digital domain leads to increasing errors due to amplitude quantisation; therefore it may be sensible to reduce the effective number of bits N by one bit, to take account of this. There are no specifications given for MLSSA's phase accuracy.

G.4.1 Analogue measurement systems

An alternative to digitizing the data, is to measure the time of flight in the analogue domain. This is the method used by Zink & Delsasso [166], and probably by Steen. There are various possible techniques:

1. Manually measuring the time shift on the display of an analogue oscilloscope [166].
2. Electronically with purpose-built threshold circuitry.
3. Using a digitizing oscilloscope with a very high digitizing rate (eg. 100Msample/s). The frequency domain would probably not have the predicted advantages in this case, because only the leading edge of the waveform could be captured (the record length is restricted). Therefore the phase information might be "mixed up" with the f = 0 Hz line, and may not be extracted.

However, any measurements would have to use "real" impulses instead of using the processed MLSSA impulse response, and so there will be added problems of signal/noise ratio and repeatability

G.5 CONCLUSIONS

This appendix has concentrated on phase measurement error in sampled data systems. For these circumstances the following conclusions are reached:

1. The detection limit for time domain measurement is dependent mainly on the oversampling ratio, and only weakly on the A/D converter resolution; the theoretical limit is close to that observed using the MATLAB model.

2. The detection limit for frequency domain measurement depends strongly on the A/D converter resolution, and weakly on the oversampling ratio. The theoretical limit is a very pessimistic worst-case prediction.

3. Frequency domain measurement will always equal or better the sensitivity and accuracy of time domain measurement.

4. Frequency domain measurement is more resilient to added noise.

5. For the above reasons, frequency domain measurement is concluded to be the better form of analysis for sampled and digitized data.

6. It is unknown how valid the above conclusions are to measurements made using MLSSA, although it is likely that they are at least qualitatively correct.

Analogue time domain measurement is a possible alternative, although this would require greater complexity of signal generation and analysis.

APPENDIX H

REVERBERANT DECAY CURVE FITTING

This Appendix describes the algorithms that were used to calculate the reverberant decay rate from the measured Schroeder decay curve. Two methods were used:

- A straight line fit to the log decay curve. This was used for measurements on quasi-static suspensions, were there tended to be a large decay range with comparitively little noise.
- A non-linear fit to the decay curve. This was used for measurements on flowing suspensions, where there was a small decay range with a high noise floor.

Both methods use iterative algorithms.

The problems addressed by the algorithms are:

- Decay records have a variety of usable decay ranges; this is due to the different energy densities in different frequency bands, and the different dust concentrations. As it is desirable to use the largest portion of the decay record as possible, without including non-exponential portions, so the fitted decay range should vary between records.
- Many decay records appear to display curved decay after an initial straight portion; the curvature always appeared to be one of time-decreasing decay rate ("concave" curvature).
- Some decay records have occasional steps or other irregularities.

The following two algorithms are designed to address these problems for the two differerent situations.

H.1 STRAIGHT-LINE FIT

This method assumes that there is little noise in the decay curve, and tries to find a straight line fit to the portion of the curve that shows linear decay (of the log curve)

The following algorithm processed each record iteratively to converge on a figure of decay rate for the straight line portion of decay:

1. Find the decay range, D, from the filtered impulse response (before reverse integration), by calculating the ratio of the rms. values of the initial and final 6% of the record. If $D < 15$ dB, the record is rejected as having an excessively small decay range.
2. Calculate the reverse-integrated decay curve, S_i , $i = 1, 2, ... N$, using Chu's method of noise subtraction (see equation 3.4).
3. Take the first sample i_{beg} to be that for which S_i first falls below -3dB (to reject the initial "early decay"). Take the final sample to be the last sample in the record, $i_{end} = N$.
4. Fit a least mean squares (LMS) straight line to the record from i_{beg} to i_{end} .
5. Find the sample i_x where the fitted line falls below $(D + 5)$ dB; if $i_x < i_{end}$ then make $i_{end} = i_x$.

Keep repeating steps 4 & 5 until the gradient of the fitted line changes by less than 1% between iterations. The process usually takes between 3 and 8 iterations; after 10 iterations the algorithm bails out and the record is rejected. If $(i_{end} - i_{beg}) < N / 100$, the record is rejected as having an excessively short straight line fit.

The 5dB which is added to D (in step 5) is a factor to speed up the convergence of the algorithm.

Figure H-1 shows two examples of the output produced by the algorithm. Note how, in the lower curve, the fitted line has converged onto the initial, straight line portion of the decay record.

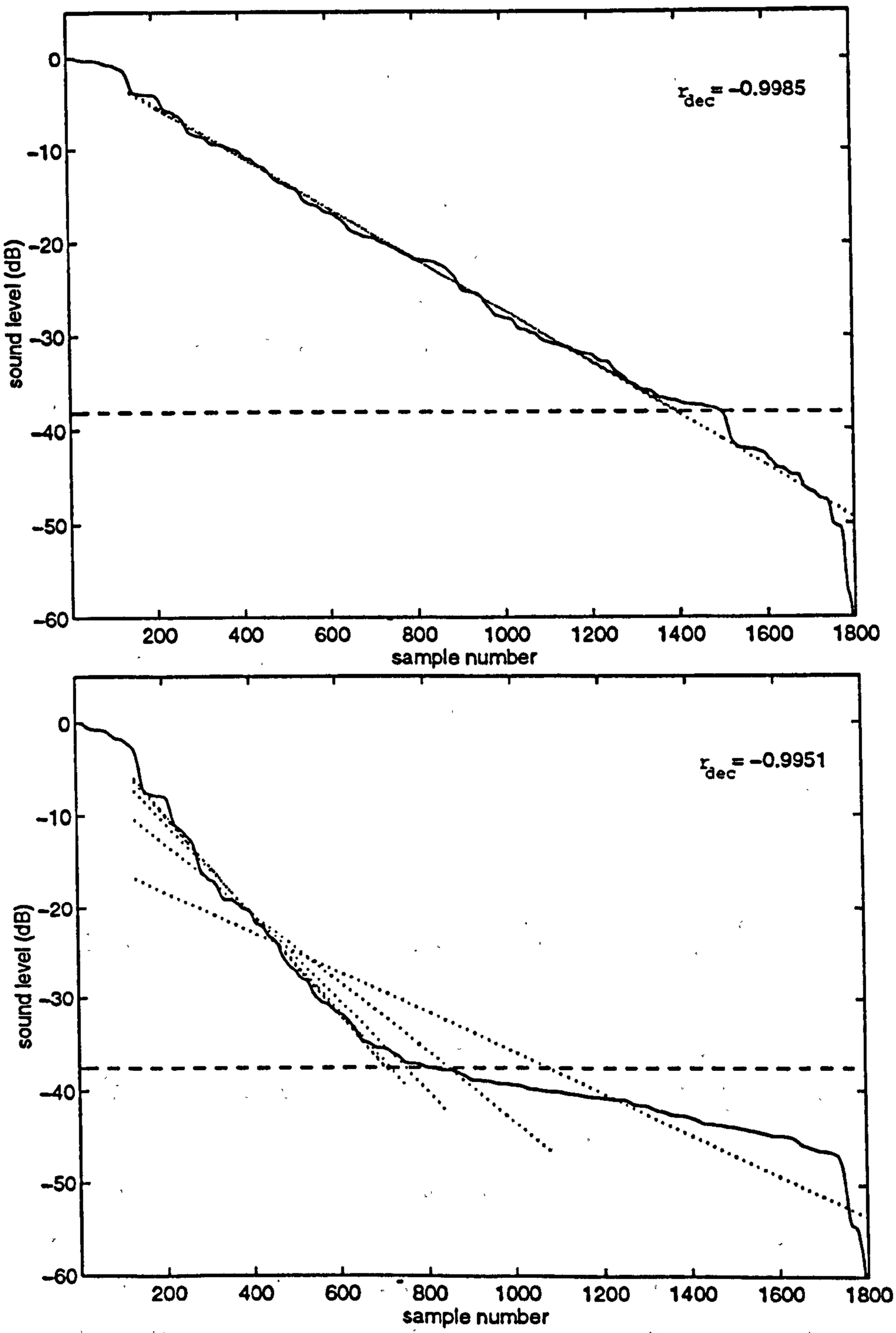

Figure H-1 *Examples of iterative decay curve fitting, for frequency band f_c = 3.9 kHz. Dotted lines are best-fit lines; dashed line is (D – 5) dB. Top: air only; bottom: dust concentration ϕ = 8.0 ppm.*

H.2 NON-LINEAR FIT

The noise subtraction technique of Chu [32] relied on subtracting the constant noise level from the IR before the reverse integration. Xiang [163],-however, approached the problem differently. He performed the reverse integration with the noise component left in, and then attempted to find a model to fit the resulting decay. Like Chu, he assumed that the noise level was constant throughout the decay, so the model consisted of an exponential term, and a linearly decreasing term that represented the reverse integration of the constant noise level. The model curve was expressed in terms of three unknowns, x_1, x_2, x_3:

$$F(\mathbf{x},t_k) = x_1 \exp(-x_2 t_k) + x_3(L - t_k) \qquad 0 \le t_k \le L$$

where L is the time duration of the record.

He showed that an optimum value of the x vector can be found to reduce the error between the model decay curve and the measured curve $d(t_k)$ by starting with an initial estimate $\mathbf{x}^0$, and iteratively applying correction values of $\Delta\mathbf{x}$ to minimise the difference between $d(t_k)$ and $F(\mathbf{x}, t_k)$.

The correction vector, $\Delta\mathbf{x}$ is found from:

$$\Delta x = A^{-1} b \tag{H.1}$$

$$\text{where } A_{ij} = \sum_{k=1}^{m} \frac{\partial F(\mathbf{x}^0,t_n)}{\partial x_i} \frac{\partial F(\mathbf{x}^0,t_n)}{\partial x_j}, \quad i, j = 1,2,3, \text{ and } m \ge 3 \tag{H.2}$$

$$b_i = \sum_{k=1}^{m} \left[d(t_k) - F(\mathbf{x}^0,t_k) \right] \frac{\partial F(\mathbf{x}^0,t_k)}{\partial x_i} \tag{H.3}$$

and where:

$$\frac{\partial F(\mathbf{x}^0,t_k)}{\partial x_1} = \exp(-x_2^0 \cdot t_k) \tag{H.4}$$

$$\frac{\partial F(\mathbf{x}^0,t_k)}{\partial x_2} = -x_1^o \cdot t_k \exp(-x_2^0 \cdot t_k) \tag{H.5}$$

$$\frac{\partial F(\mathbf{x}^0,t_k)}{\partial x_3} = L - t_k \tag{H.6}$$

The algorithm calculated the Schroeder decay curve with a proportion (40 %) of the noise subtracted using Chu's method, and then used the above equations iteratively (ignoring the early decay down to -6 dB) to calculate the best-fit values for x. The decay rate, Q, was calculated by:

$$Q = x_2 \cdot 10\log_{10} e \tag{H.7}$$

The process is illustrated for a single measurement in Figure H-2.

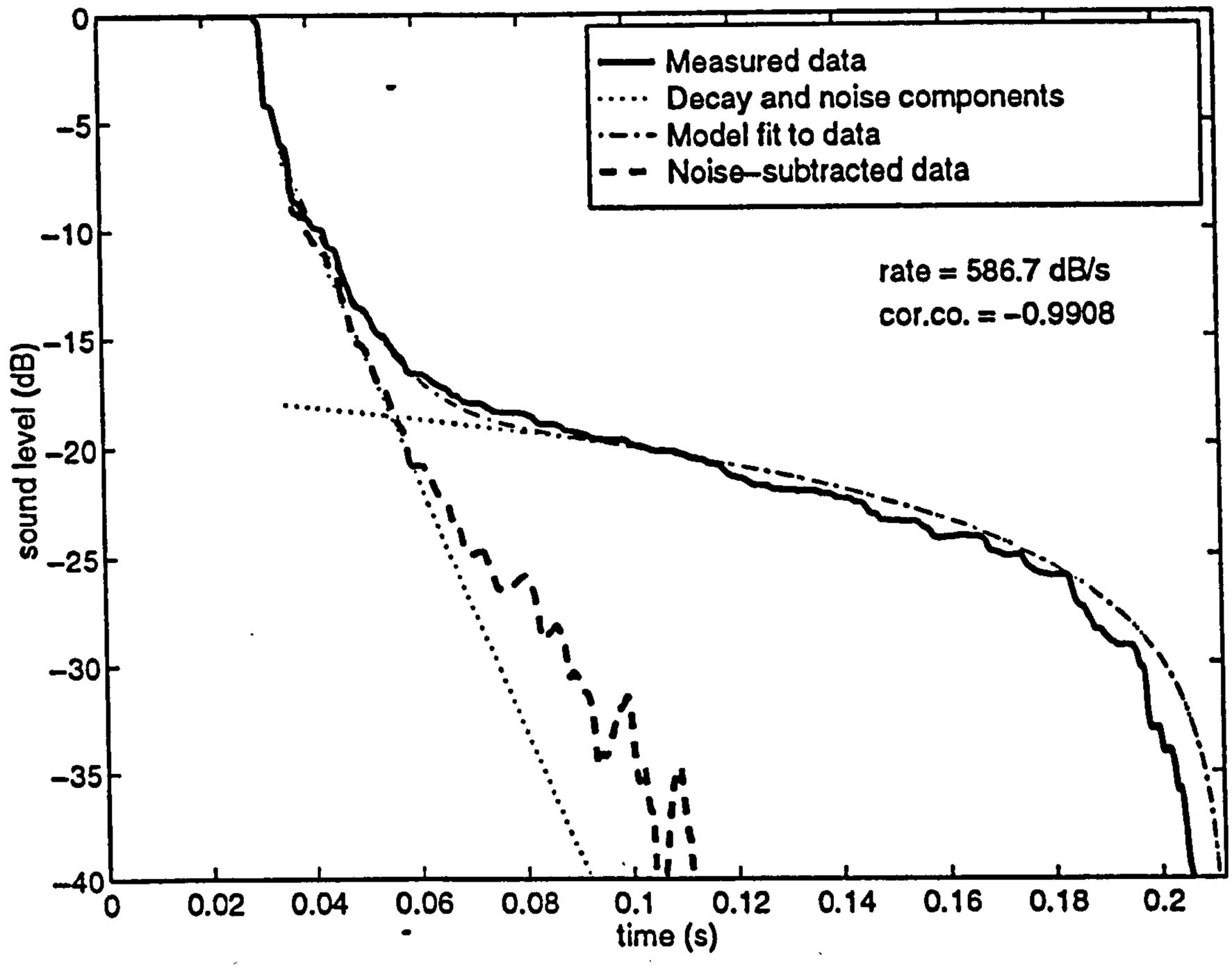

Figure H-2 Example of a fitted decay curve using Xiang's non-linear regression method. Graph shows the original measured data, the fit that the model found to the measured curve, the two components (logarithmic decay and constant noise) that were summed to produce the fitted curve, and the curve that results when the noise term is subtracted from the measured decay. Centre frequency of the modal filter is 8.45 kHz, ϕ_m = 0.035 kg/kg.

The original decay curve (solid line) shows the strong curvature caused by a high level of noise. The model fit to the curve (dot-dash line) can be seen to fit the measurement well; this curve is composed of the sum of the log decay and the constant noise components (dotted lines). When the noise component is subtracted from the measurement, the resulting curve (dashed line) is seen to be linear (with a log y-axis) over 15 dB of decay, and is well-fitted by the decay component. The final decay rate is found from this component. The correlation coefficient of the decay was calculated over the portion of the noise-corrected decay that extends from -6 dB down to the point at which the noise and decay components overlap (-18 dB in this example).